frontiers | Research Topics

Customized artificial implants: Bionic design and multiscale evaluation

Edited by
Zhenxian Chen, Yongtao Lyu, Junyan Li and Xijin Hua

Published in
Frontiers in Bioengineering and Biotechnology

ISSN 1664-8714
ISBN 978-2-8325-4945-2
DOI 10.3389/978-2-8325-4945-2

About Frontiers

Frontiers is more than just an open access publisher of scholarly articles: it is a pioneering approach to the world of academia, radically improving the way scholarly research is managed. The grand vision of Frontiers is a world where all people have an equal opportunity to seek, share and generate knowledge. Frontiers provides immediate and permanent online open access to all its publications, but this alone is not enough to realize our grand goals.

Frontiers journal series

The Frontiers journal series is a multi-tier and interdisciplinary set of open-access, online journals, promising a paradigm shift from the current review, selection and dissemination processes in academic publishing. All Frontiers journals are driven by researchers for researchers; therefore, they constitute a service to the scholarly community. At the same time, the *Frontiers journal series* operates on a revolutionary invention, the tiered publishing system, initially addressing specific communities of scholars, and gradually climbing up to broader public understanding, thus serving the interests of the lay society, too.

Dedication to quality

Each Frontiers article is a landmark of the highest quality, thanks to genuinely collaborative interactions between authors and review editors, who include some of the world's best academicians. Research must be certified by peers before entering a stream of knowledge that may eventually reach the public - and shape society; therefore, Frontiers only applies the most rigorous and unbiased reviews. Frontiers revolutionizes research publishing by freely delivering the most outstanding research, evaluated with no bias from both the academic and social point of view. By applying the most advanced information technologies, Frontiers is catapulting scholarly publishing into a new generation.

What are Frontiers Research Topics?

Frontiers Research Topics are very popular trademarks of the *Frontiers journals series*: they are collections of at least ten articles, all centered on a particular subject. With their unique mix of varied contributions from Original Research to Review Articles, Frontiers Research Topics unify the most influential researchers, the latest key findings and historical advances in a hot research area.

Find out more on how to host your own Frontiers Research Topic or contribute to one as an author by contacting the Frontiers editorial office: frontiersin.org/about/contact

Customized artificial implants: Bionic design and multiscale evaluation

Topic editors

Zhenxian Chen — Chang'an University, China
Yongtao Lyu — Dalian University of Technology, China
Junyan Li — Southwest Jiaotong University, China
Xijin Hua — University of Exeter, United Kingdom

Citation

Chen, Z., Lyu, Y., Li, J., Hua, X., eds. (2024). *Customized artificial implants: Bionic design and multiscale evaluation*. Lausanne: Frontiers Media SA.
doi: 10.3389/978-2-8325-4945-2

Table of contents

05 Editorial: Customized artificial implants: bionic design and multiscale evaluation
Zhenxian Chen, Yongtao Lyu, Junyan Li and Xijin Hua

08 Biomechanical evaluation of custom-made short implants with wing retention applied in severe atrophic maxillary posterior region restoration: A three-dimensional finite element analysis
Zhen Yang, Jingran Zhang, Zexian Xu, Xiaoqiang Liu, Jianjun Yang and Jianguo Tan

16 A single-tube-braided stent for various airway structures
Xin Tong, Yongkang Jiang, Fei Mo, Zhongqing Sun, Xiaojun Wu and Yingtian Li

27 Novel uniplanar pedicle screw systems applied to thoracolumbar fractures: a biomechanical study
Yuheng Jiang, Xiang Cui, Wei Ji, Jia Li, Yanli Shi, Jingxin Zhao, Junsong Wang, Peifu Tang and Wei Zhang

37 Biomechanical effects of screws of different materials on vertebra-pediculoplasty: a finite element study
Yan-Ni Wang, Ya-Nan Ren, Jun Han, Chao Chen, Xun Sun, Ming-Yuan Di, Yi-Ming Dou, Xin-Long Ma, Zheng Wang, Cheng-Fei Du and Qiang Yang

44 Biomechanical evaluation of a novel minimally invasive pedicle bone cement screw applied to the treatment of Kümmel's disease in porcine vertebrae
Xiang Ma, Qing Feng, Xingze Zhang, Xiaolei Sun, Longwei Lin, Lin Guo, Lijun An, Shenglin Cao and Jun Miao

55 Finite element study of sagittal fracture location on thoracolumbar fracture treatment
Xilong Cui, Junjun Zhu, Wanmei Yang, Yuxiang Sun, Xiuling Huang, Xiumei Wang, Haiyang Yu, Chengmin Liang and Zikai Hua

65 Design of a lightweight universal talus implant using topology optimization
Ahmed H. Hafez, Marwan El-Rich, Tao Liu, Nadr Jomha and Andreas Schiffer

75 Inverse design of anisotropic bone scaffold based on machine learning and regenerative genetic algorithm
Wenhang Liu, Youwei Zhang, Yongtao Lyu, Sergei Bosiakov and Yadong Liu

87 Biomechanical evaluation of a novel individualized zero-profile cage for anterior cervical discectomy and fusion: a finite element analysis
Yang Wang, Yang Liu, Aobo Zhang, Qing Han, Jianhang Jiao, Hao Chen, Xuqiang Gong, Wangwang Luo, Jing Yue, Xue Zhao, Jincheng Wang and Minfei Wu

99 Biomechanical analysis and clinical observation of 3D-printed acetabular prosthesis for the acetabular reconstruction of total hip arthroplasty in Crowe III hip dysplasia
Yuchen Liu, Fuyang Wang, Jiawei Ying, Minghao Xu, Yuan Wei, Junlei Li, Hui Xie, Dewei Zhao and Liangliang Cheng

110 Biomechanical stability of oblique lateral interbody fusion combined with four types of internal fixations: finite element analysis
Jiayu Hao, XianSheng Tang, Nizhou Jiang, Hong Wang and Jian Jiang

122 Effect of carbon-fiber-reinforced polyetheretherketone on stress distribution in a redesigned tumor-type knee prosthesis: a finite element analysis
Han Wu, Yu Guo and Wei Guo

137 3D-printed custom implant for the management of "locked" posterior dislocation of the shoulder joint with reverse Hill-Sachs lesion: a case report
Yongrong Hu, Kunhai Yang, Hao Liu, Liping Wang, Song Wang, Xiang Zhang, Bo Qu and Hongsheng Yang

144 Designing customized temporomandibular fossa prosthesis based on envelope surface of condyle movement: validation via *in silico* musculoskeletal simulation
Jun-Lin Wang, Jing Wang, Ke-Nan Chen, Jian-Qiao Guo, Xiang-Liang Xu and Chuan-Bin Guo

155 Biomechanical evaluation of a novel anterior transpedicular screw-plate system for anterior cervical corpectomy and fusion (ACCF): a finite element analysis
Shengbin Huang, Qinjie Ling, Xinxin Lin, Hao Qin, Xiang Luo and Wenhua Huang

166 Is it reasonable to shorten the length of cemented stems? A finite element analysis and biomechanical experiment
Junyan Li, Liang Xiong, Chao Lei, Xinyu Wu and Xinzhan Mao

174 Incomplete insertion of pedicle screws triggers a higher biomechanical risk of screw loosening: mechanical tests and corresponding numerical simulations
Jie-Xiang Yang, Lin Luo, Jin-Hui Liu, Nan Wang, Zhi-Peng Xi and Jing-Chi Li

frontiers | Frontiers in Bioengineering and Biotechnology

TYPE Editorial
PUBLISHED 14 May 2024
DOI 10.3389/fbioe.2024.1425080

OPEN ACCESS

EDITED AND REVIEWED BY
Markus O. Heller,
University of Southampton, United Kingdom

*CORRESPONDENCE
Yongtao Lyu,
yongtaolu@dlut.edu.cn
Junyan Li,
jyli@swjtu.edu.cn
Xijin Hua,
x.hua@exeter.ac.uk

RECEIVED 29 April 2024
ACCEPTED 03 May 2024
PUBLISHED 14 May 2024

CITATION
Chen Z, Lyu Y, Li J and Hua X (2024), Editorial: Customized artificial implants: bionic design and multiscale evaluation.
Front. Bioeng. Biotechnol. 12:1425080.
doi: 10.3389/fbioe.2024.1425080

Editorial: Customized artificial implants: bionic design and multiscale evaluation

Zhenxian Chen[1], Yongtao Lyu[2]*, Junyan Li[3]* and Xijin Hua[4]*

[1]School of Mechanical Engineering, Chang'an University, Xi'an, China, [2]School of Mechanics and Aerospace Engineering, Dalian University of Technology, Dalian, China, [3]Tribology Research Institute, Southwest Jiaotong University, Chengdu, China, [4]Department of Engineering, Faculty of Environment, Science and Economy, University of Exeter, Exeter, United Kingdom

KEYWORDS

customized artificial implants, bionic design, multiscale evaluation, biomechanics, computational simulation, experimental testing

Editorial on the Research Topic
Customized artificial implants: bionic design and multiscale evaluation

Due to individual differences, anatomical variability and complexity of working conditions, traditional "one-size-fits-all" implants cannot fulfill the clinical requirements. With the concept of precision medicine or personalized medicine being proposed and hotly discussed, more surgeons and engineers are designing, manufacturing, evaluating, and applying customized artificial implants. Meanwhile, advanced technologies such as 3D printing and multiscale computer simulations are promoting the development of customized artificial implants. Especially, customized artificial implants are booming in orthopedics and orthodontic surgeries recently. Customized orthopedic implants can offer remarkable precision and fit, improve functionality, reduce pain and inflammation, and accelerate healing. However, challenges to implement precision design and evaluation arise not only from the design need to consider bionic structures, kinematical function, mechanical performances, and biological function but also from the performance and functional evaluation involving multiscale computational simulations and comprehensive experimental testing. There is still a lack of knowledge on customized principles, design methods, evaluation systems, new material applications, and surgical plans. Advancements have been made to delve into the role of bionic design in precision treatment and long-term success, as well as the importance of multiscale evaluation to ensure the safety and efficiency of these life-changing devices.

Irregular bone defects or resection areas are common in orthopedic clinical practice, and anatomical matching design is crucial for artificial implants (Wang et al., 2022). Hu et al. designed and used a 3D-printed custom prosthesis for a patient with irregular humeral defects accompanied by shoulder joint "locking" dislocation and reverse Hill-Sachs injury. Liu et al. reported a 3D-printed integrated acetabular prosthesis and modular acetabular prosthesis for the acetabular reconstruction of total hip arthroplasty in Crowe III hip dysplasia. Wang et al. designed a novel individualized porous titanium alloy zero-profile cage for anterior cervical discectomy and fusion based on the morphological characteristics of the intervertebral space. However, in fact, customized artificial implant not only requires anatomical matching but also need to deeply focus on mechanical matching and kinematical matching. Wang et al. designed

an innovative temporomandibular joint (TMJ) fossa prosthesis based on the envelope surface of condyle movement. This customized design of fossa prosthesis not only successfully achieved a wider condylar range of motion but also reduced the muscle activation for jaw opening on the surgical side and resistance on the intact side than traditional commercial implants.

Except for customized orthopedic implants, customized breast implants, dental implants, and stents have been developed and studied. Tong et al. proposed a customized design strategy for the single-tube-braided airway stents to meet various airway structures, investigated the radial stiffness of the stents and deformation upon compression using a theoretical model, and evaluated their mechanical properties and functions using experimental testing. The proposed customized stents adapt well to different airway structures.

The customized implant is costly and time-consuming due to its customized nature (Hafez et al.). Artificial intelligence or machine learning may help to improve the drawbacks of long design cycles, such as quickly obtaining a patient's bone geometry and mechanical property (Lu et al., 2023), and creating the 3D model of artificial implants (Burge et al., 2023). Triply periodic minimal surface (TPMS) is widely used in the design of bone scaffolds for large bone detects due to its structural advantages. Liu et al. proposed a new inverse design of an anisotropic TPMS bone scaffold based on the mechanical properties of bone structures using machine learning and a regenerative genetic algorithm. Combining machine learning with the traditional optimization method achieves higher design efficiency, and the entire design process is easily controlled.

Multiscale evaluation of customized implants encompasses a range of assessments that consider the implant's performance and interaction with the body at various levels, from the macroscopic to the microscopic. Musculoskeletal (MSK) multibody dynamics (MBD) model has a remarkable advantage in simulating human macro physical activities and getting joint force and motion, ligament force, muscle force or activation. Wang et al. adopted a mandibular MSK MBD model to evaluate the jaw opening-closing motions, mandibular muscle activation, and contact forces of the customized TMJ fossa prosthesis. The finite element analysis (FEA) method can be used to quantify the stress and strain of artificial implants from a microscopic point of view. Yang et al. analyzed the position, structure, and spread area of the wing fixture of a new customized implant applied in severe atrophic maxillary posterior region restoration using FEA. Combining the advantages of MSK MBD simulation and FEA, the coupling analysis method of both (Zhang et al., 2017; Hua et al., 2022) and the FE MSK MBD model (Li et al., 2019) are the current development trend of multiscale evaluation. Meanwhile, a combination of theoretical models or computer simulation and biomechanical experiments are recommended to comprehensively evaluate the safety, efficacy stability of artificial implants (Li et al.). In addition, clinical case observation and report are equally important for systematically evaluating customized implants (Hu et al.), which should be combined with the aforementioned methods. Clinical trials and patient outcomes provide real-world data that feed back into the design process, ensuring continuous improvement and refinement. The traditional experimental methods and devices do not work on most customized artificial implants. New test standards, technologies, and equipment need to be established and developed for testing the rising customized designs.

Overall, customized artificial implants represent a significant leap forward in medical technology. This Research Topic of articles contributes to promote the development of customized artificial implants in bionic design, multiscale evaluation, and translation. New technology based on machine learning and new materials have been introduced into the precise design of customized artificial implants. Bionic design methods based on joint kinematics and the mechanical properties of bone structures are developed for customized artificial implants. The exploitation and application of novel approaches, testing techniques, and standards in evaluation are still scarce. The challenges remain in the high-efficiency, accurate, and quick design and evaluation of customized artificial implants.

Author contributions

ZC: Writing–review and editing. YL: Writing–review and editing. JL: Writing–review and editing. XH: Writing–review and editing.

Funding

The author(s) declare that financial support was received for the research, authorship, and/or publication of this article. This work was supported by Shaanxi Province Natural Science Foundation (2023-JC-YB-402).

Conflict of interest

The authors declare that the research was conducted in the absence of any commercial or financial relationships that could be construed as a potential conflict of interest.

Publisher's note

References

Burge, T. A., Jeffers, J. R. T., and Myant, C. W. (2023). Applying machine learning methods to enable automatic customisation of knee replacement implants from CT data. *Sci. Rep.* 13, 3317. doi:10.1038/s41598-023-30483-5

Hua, X., Li, J., De Pieri, E., and Ferguson, S. J. (2022). Multiscale biomechanics of the biphasic articular cartilage in the natural hip joint during routine activities. *Comput. Methods Programs Biomed.* 215, 106606. doi:10.1016/j.cmpb.2021.106606

Li, J., Lu, Y., Miller, S. C., Jin, Z., and Hua, X. (2019). Development of a finite element musculoskeletal model with the ability to predict contractions of three-dimensional muscles. *J. Biomechanics* 94, 230–234. doi:10.1016/j.jbiomech.2019.07.042

Lu, Y., Yang, Z., Zhu, H., and Wu, C. (2023). Predicting the effective compressive modulus of human cancellous bone using the convolutional neural network method. *Comput. Methods Biomech. Biomed. Engin* 26, 1150–1159. doi:10.1080/10255842.2022.2112183

Wang, L., Geng, W., He, K., and Guo, K. (2022). Convenient design method for customized implants based on bionic vein structure features. *Front. Bioeng. Biotechnol.* 10, 929133. doi:10.3389/fbioe.2022.929133

Zhang, J., Chen, Z., Wang, L., Li, D., and Jin, Z. (2017). A patient-specific wear prediction framework for an artificial knee joint with coupled musculoskeletal multibody-dynamics and finite element analysis. *Tribol. Int.* 109, 382–389. doi:10.1016/j.triboint.2016.10.050

frontiers | Frontiers in Bioengineering and Biotechnology

TYPE Original Research
PUBLISHED 09 February 2023
DOI 10.3389/fbioe.2023.1137779

OPEN ACCESS

EDITED BY
Zhenxian Chen,
Chang'an University, China

REVIEWED BY
Hai Zhang,
University of Washington, United States
Hongchang Lai,
Shanghai Jiao Tong University, China

*CORRESPONDENCE
Jianjun Yang,
yjjqd@qdu.edu.cn
Jianguo Tan,
kqtanjg@bjmu.edu.cn

†These authors have contributed equally to this work and share first authorship

SPECIALTY SECTION
This article was submitted to Biomechanics, a section of the journal Frontiers in Bioengineering and Biotechnology

RECEIVED 04 January 2023
ACCEPTED 25 January 2023
PUBLISHED 09 February 2023

CITATION
Yang Z, Zhang J, Xu Z, Liu X, Yang J and Tan J (2023), Biomechanical evaluation of custom-made short implants with wing retention applied in severe atrophic maxillary posterior region restoration: A three-dimensional finite element analysis. *Front. Bioeng. Biotechnol.* 11:1137779. doi: 10.3389/fbioe.2023.1137779

Biomechanical evaluation of custom-made short implants with wing retention applied in severe atrophic maxillary posterior region restoration: A three-dimensional finite element analysis

Zhen Yang[1,2†], Jingran Zhang[2,3†], Zexian Xu[4,5], Xiaoqiang Liu[1,2], Jianjun Yang[4,5*] and Jianguo Tan[1,2*]

[1]Department of Prosthodontics, Peking University School and Hospital of Stomatology, Beijing, China, [2]Peking University School and Hospital of Stomatology & National Center of Stomatology & National Clinical Research Center for Oral Diseases & National Engineering Laboratory for Digital and Material Technology of Stomatology & Beijing Key Laboratory of Digital Stomatology & Research Center of Engineering and Technology for Computerized Dentistry Ministry of Health & NMPA Key Laboratory for Dental Materials, Beijing, China, [3]Department of Periodontology, Peking University School and Hospital of Stomatology, Beijing, China, [4]Department of Oral and Maxillofacial Surgery, the Affiliated Hospital of Qingdao University, Qingdao, China, [5]School of Stomatology of Qingdao University, Qingdao, China

Severe bone atrophy in the maxillary posterior region poses a big challenge to implant restoration. Digitally designed and customized short implants with wing retention provide a safer and minimally invasive implant restoration scheme in such circumstances. Small titanium wings are integrated with the short implant supporting the prosthesis. Using digital designing and processing technology, the wings fixed by titanium screws can be flexibly designed, providing the main fixation. The design of the wings will influence the stress distribution and implant stability. This study analyzes the position, structure, and spread area of the wings fixture scientifically by means of three-dimensional finite element analysis. The design of the wings is set to linear, triangular, and planar styles. Under the simulated vertical and oblique occlusal forces, the implant displacement and stress between the implant and the bone surface are analyzed at different bone heights of 1 mm, 2 mm, and 3 mm. The finite element results show that the planar form can better disperse the stress. By adjusting the cusp slope to reduce the influence of lateral force, short implants with planar wing fixtures can be used safely even if the residual bone height is only 1 mm. The results of the study provide a scientific basis for the clinical application of this new customized implant.

KEYWORDS

atrophy, finite elements, stress distribution, dental implant, custom-made

1 Introduction

Alveolar bone resorption occurs due to local inflammation and a long-time lack of physiological stimulation after tooth loss. Pneumatization of the maxillary sinus is more likely to lead to a severe reduction of residual bone height (RBH), which brings a big challenge to implant restoration in the maxillary posterior region (Bitinas and Bardijevskyt, 2021). According to the 6th ITI Consensus, short implants of a diameter ≤6 mm can be chosen as

a valid treatment option in atrophic ridge cases. However, studies have revealed that they have a higher variability and lower predictability in survival rates (85%–100%) than standard ones (95%–100%) (Jung et al., 2018). Sufficient bone tissue is considered a critical condition for implant anchorage. Therefore, transalveolar sinus floor elevation (tSFE) with simultaneous implant placement is proposed in situations with RBH above 4 mm (Pjetursson and Lang, 2014; Qian et al., 2020). However, it has been found that the RBH of some patients is below 4 mm, and sometimes even only 1–2 mm. Weaker maxillary sinus floor bones increase the risk of maxillary sinus membrane perforation in tSFE treatment, so lateral sinus floor elevation with delayed implant placement is recommended. However, this technique would prolong the recovery time and cause more suffering for patients (Gonzalez et al., 2014; Testori et al., 2019). Moreover, when the RBH is below 1.5 mm, only cortical bone is left, and effective graft regeneration may not be possible (Taschieri et al., 2015).

Zygomatic implants reported by Bedrossian are developed to use when the RBH in the maxillary posterior area is extremely insufficient. This implant is about 30–52.5 mm in length and should be placed via the sinus cavities and anchored in the zygoma for stability. A few cases have shown favorable results for this technique, but further long-term clinical observation is still lacking (Varghese et al., 2021). In addition, the technique is more invasive and complex, and is often associated with serious complications such as infection, bleeding, and nerve damage. Therefore, it is not widely used in clinics. For patients with severe bone deficiency in the maxillary posterior region, especially those with RBH of less than 3 mm, there is no good clinical treatment at present. Subperiosteal implants have been re-proposed following the development of modern digital dentistry (Gellrich et al., 2017). The subperiosteal implants gain stability through the use of large-area spread titanium plate fixation. Although the plate can be individually designed to ensure fitness, poor blood flow of soft tissue still can be caused by extensive flap surgery. Nevertheless, the use of subperiosteal implants has facilitated the conception and development of innovative bone anchorage systems for oral restorations.

We have developed a new type of implant named Yang's Implant (Xu et al., 2022). This implant, as described above, is composed of a short implant and retaining wings. But unlike the subperiosteal implant, Yang's implant has an implanted part and abutment structure, and the platform switching structure is maintained to ensure soft tissue closure formation around the implant after implantation. The wing retention is fixed by titanium screws, which can be flexibly designed and provide the main fixation. In the circumstance of RBH being less than 4 mm, the stability and stress condition of Yang's implant is still unclear. However, three-dimensional finite element analysis (3D-FEA) models have been established, which are useful to guide the design and innovation of Yang's implant to better realize the clinical applications.

2 Materials and methods

2.1 Sinus geometric modeling

Initial data was obtained from patients' CBCT. The thresholding operation was performed to extract the relevant structural information of the maxilla to reconstruct the point cloud data model, then geometric modeling and a three-dimensional (3D) finite element model of the maxillary sinus were carried out with the software Mimics 24.0 (Materialises, Leuven, Belgium). After that, the local finite element model was refined with the software Hypermesh 2017 (Altair, Troy, USA) to generate an editable maxillary sinus model with RBH of less than 4 mm. The height of RBH was set up to 1 mm, 2 mm, and 3 mm, respectively.

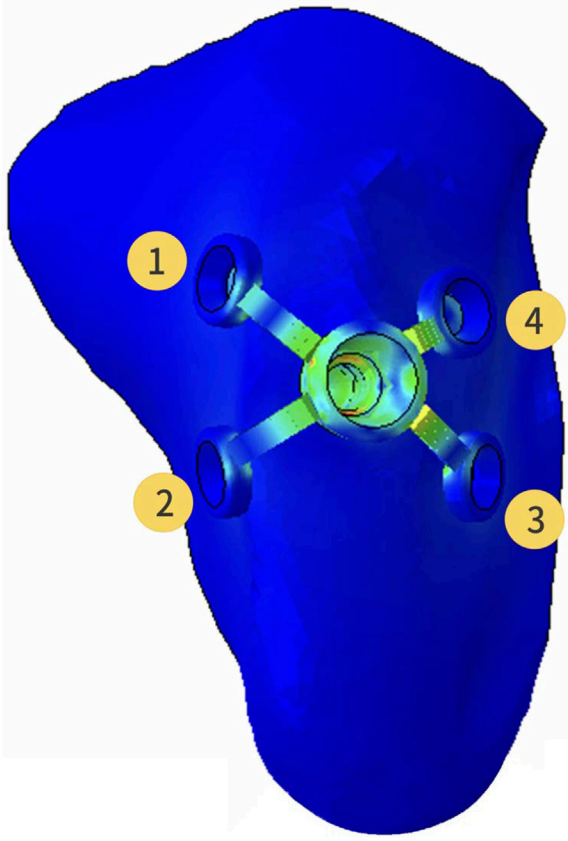

FIGURE 1
Three-dimensional finite element model of the partial maxilla and Yang's implant; Representative numbers of different direction wings.

2.2 Yang's implant geometric modeling

Registered CBCT data with model scanning data was used to obtain a virtual 3D bone reconstruction model of the patient. The position and shape of Yang's implant was designed by 3Shape dental system (3Shape, Copenhagen, Denmark) as described previously (Xu et al., 2022), and the associated file was saved in standard tessellation language (STL) format. The STL format file was imported into Hypermesh software to form the Yang's implant network model. The position of the wings responsible for retention of the implant could be moved and adjusted in this model. In this study, the implant restoration model of a left upper first molar was established. The wings were distributed in different directions on the buccal or lingual side, and they were represented with numbers, as shown in Figure 1. Named wing numbers of 13 as linear style

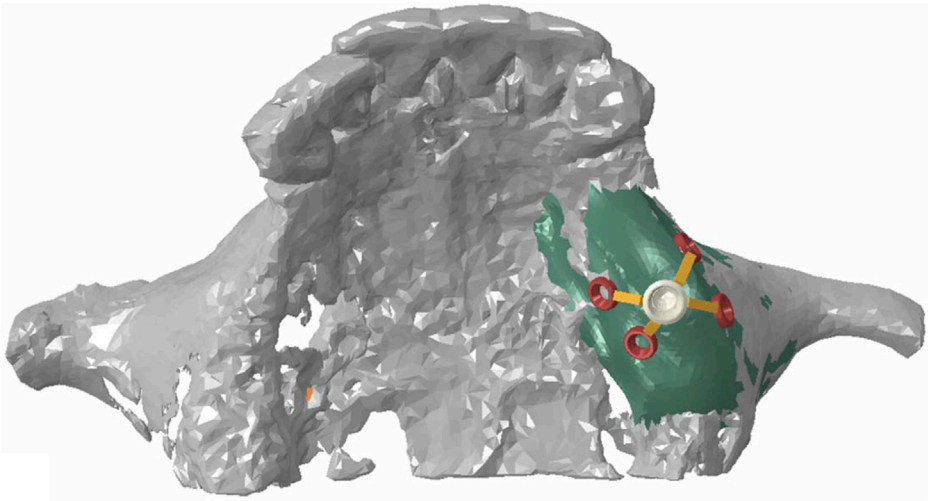

FIGURE 2
Assembly diagram of maxillary model and Yang's implant model.

TABLE 1 Material properties.

Material	Young's modulus (MPa)	Poisson's ratio
Titanium implant	103,400	0.35
Cortical bone	13,700	0.3
Cancellous bone (D3)	1370	0.3
Sinus membrane	58	0.45

(LS), 134 as triangular style (TS), and 1234 as planar style (PS), and the names were used for subsequent analysis.

2.3 Model assembly and material properties

The refined mesh model of the maxillary sinus was generated into a local geometry model, and the generated local geometry model was combined with the model of the implant through Boolean operations (Figure 2).

The material properties of different kinds of tissues and implants in the model were set to be homogeneous, isotropic, and linear elastic. The Young's modulus and Poisson's ratio of materials shown in Table 1 were taken from the previous study (Yan et al., 2015).

2.4 Interface conditions

To obtain the initial stability of Yang's implant, the interface between the implant and bone was assumed as a friction interface. It was modeled using non-linear frictional contact elements that allow for tiny displacements between the implant and the bone. The friction coefficient between the implant and bone/callus was set to 0.2. After 3 months, it was determined that osseointegration was formed. The friction coefficient was adjusted to infinity and tested the stress distribution of Yang's implants on the bone under the situation of different directions of force.

2.5 Loading and boundary conditions

Parts of the maxillary sinus model that interfered with the implant were removed. The maxillary sinus mesh in the hole-edge area was reconstructed and optimized to ensure the quality of the calculation mesh. The maxillary sinus and implant model was assigned to the unit attribute, the unit type was set to higher-order tetrahedron C3D10M.

The average occlusal force of 150 N was loaded in a vertical direction on the top of the crown (0°) and at an angle of 45° (45°) to the long axis of the crown (Figure 3). Abaqus 2018 software (Dassault Systèmes, Paris, France) was used for calculation, and the results were outputted after post-processing. Different RBH heights were set and measured the von Mises stress at the implant-bone interface of differently designed implants. To assess the distribution of stresses, von Mises stresses were visualized with stress contour plots. Biomechanical effects were also analyzed by comparing the maximum displacement of the implants.

When the RBH was only 1mm, a force of 150 N was applied at angles of 20° and 30° to the long axis of the crown, respectively. Calculations were made with the same method. The von Mises stress at the implant-bone interface in the LS, TS, and PS groups was recorded and compared with the stress at 0° and 45°.

3 Results

3.1 Implant displacement

The change of RBH, the direction of force, and the design of implant wing retention all affected the displacement of the implant. With the decrease of RBH, the displacement of the implant increased. The PS group could control the implant displacement by about 11.5 μm when the RBH remained 2 or 3 mm and the force was given perpendicularly. Under such conditions, the implant displacements of groups LS and TS were higher, at about 22.1 μm at 3 mm and 32.1 μm–40.3 μm at RBH 2 mm. In the case where the RBH was reduced to 1 mm, implant displacements of the LS and TS groups were obviously higher, exceeding 50 μm. However, the PS group would

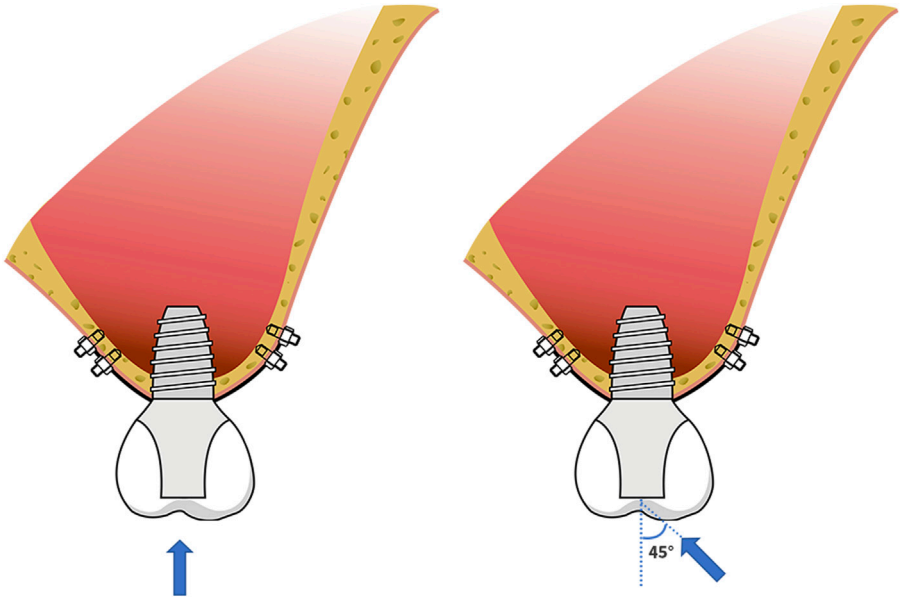

FIGURE 3
Schematic diagram of force loading; the force of 150 N loaded in a vertical direction on the top of the crown (0°) and at an angle of 45° (45°) to the long axis of the crown.

better maintain the displacement of the implant at 19.5 μm (Figure 4A). Compared to the force direction of 0°, a 45° force would shapely increase the displacement of the implant. Nevertheless, the planar retention style better maintained the implant stability compared to the other two groups. When RBH was reduced from 3 mm to 1 mm, the maximum displacement of the implant could still be controlled below 100 μm (Figure 4B).

3.2 Stress distribution at the implant-bone interface

The highest stress on the bone tended to increase as the height of the alveolar ridge decreased. Stress was gathered on the cortical bone around the neck of the implant and the retention wing. A force of 150N was applied perpendicularly to the direction of the crown. When the RBH was 3 mm, the maximum von Mises stress of the LS and TS groups was above 50 MPa, and the LS group was much higher than the TS group, at about 65.1 MPa. Compared to these two groups, the PS group was much lower, at about only 30.2 MPa. The maximum von Mises stress on crestal cortical bone slowly increased when RBH was decreased to 2 mm. The LS and TS groups could maintain the stress around 65.4–70.8 MPa, while the PS group kept the stress still below 40 MPa. However, the stress in the LS and TS groups increased significantly when the RBH reached 1 mm; compared to RBH 2 mm, the stress nearly doubled, soaring to 120.3 MPa. In these circumstances, the wing design of the planar style had outstanding advantages. The stress in this group could be controlled stably below 40 MPa (Figure 5).

When the force was applied at 45° oblique to the direction of the crown, the maximum von Mises stress on the cortical bone obviously increased. In this situation, much of the force was concentrated around the implant neck. The linear style wing design was not suitable for resisting the 45° force even when the RBH was 3 mm, and the maximum stress far exceeded 200 MPa. Compared with the LS group, group TS reduced the stress to about 116.2MPa, and the lowest stress was shown in group PS, at about 91.9 MPa. However, even using the planar design form, when RBH remained only 1 mm or 2mm, the pressure on the cortical bone would increase at a faster rate. The stress reached 158.1 MPa at RBH 2 mm and 218.5 MPa at RBH 1 mm. Additionally, maximum stress also increased in group TS and group LS when RBH was less than 3 mm, to about 225.1–355.7MPa and 434.2–482.7 MPa, respectively (Figure 6).

When RBH was only 1mm, more stress distribution showed regardless of the wings' forms. Clinically, the impact of adverse lateral force on implant restorations could be reduced by changing the cusp slope of the crown, and adjusting the direction of the force to represent the inclination adjustment of the cusp. We applied a 150N force oblique to the crown at an angle of 20° and 30°, respectively, to test the stress distribution. As the force moved, stress gathered around the implant neck gradually shifted from the center to the opposite side of the force (Figure 7A). When the force was set to 20°, the maximum stress in group LS was about 200 MPa, and the stress in group TS could be controlled at 157.1 MPa. When the force was changed to 30°, the maximum stress in the LS group increased obviously to 410.7 MPa, and also increased in the TS group, reaching 228 MPa. For the PS group, when the force was given at 45°, the maximum stress exceeded 200 MPa. When the force direction was changed to 20° or 30°, the maximum stress could be well controlled below 150 MPa (Figure 7B). In group PS, when the vertical force or 20° force was given, the maximum stress concentration was at the edge of the hole on the outside surface of the cortical bone. When 30° and 45° forces were applied, the greatest stress concentration existed at the medial cortical bone of the hole margin (Figure 7C).

4 Discussion

The concept of submucosal implants was first proposed in the 1940s. Initially, this implant was placed under the periosteum, anchored directly

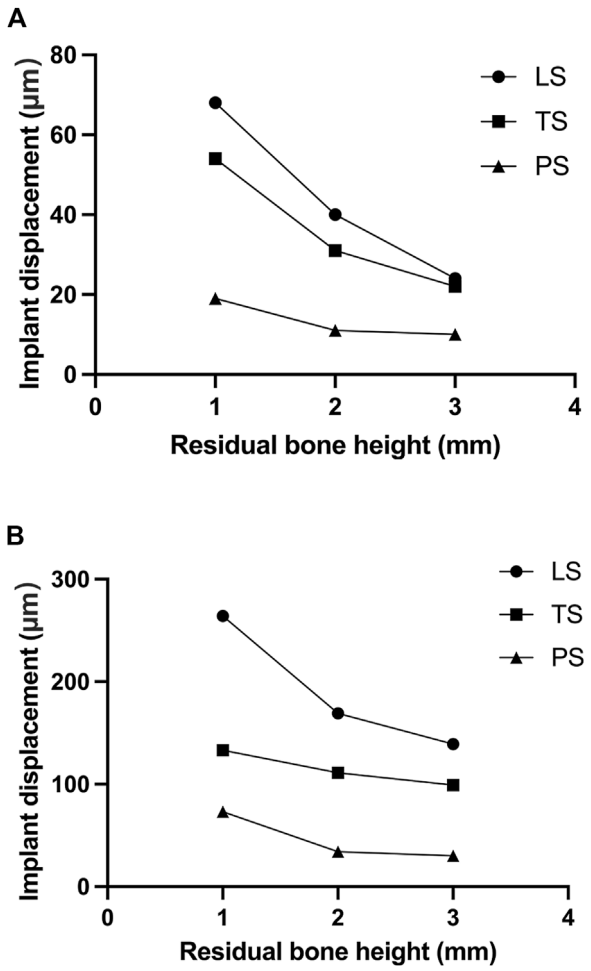

FIGURE 4
Implant displacement changes of different residual bone heights and different wing designs under forces in different directions; **(A)** 0°; **(B)** 45°.

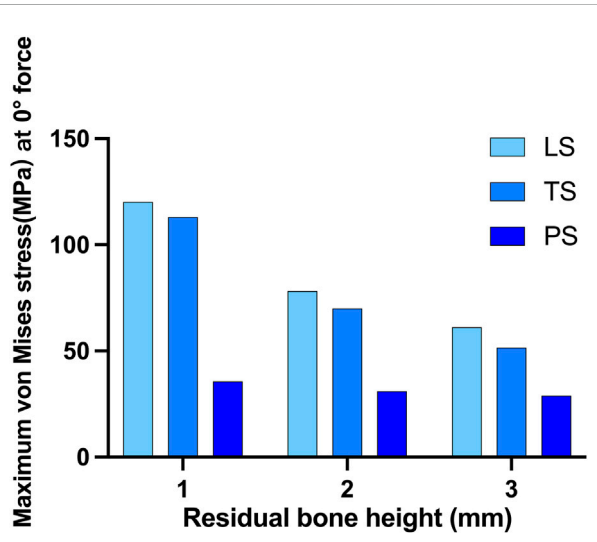

FIGURE 5
Maximum von Mises stress on crestal cortical bone of different residual bone heights and different wing designs at 0° force.

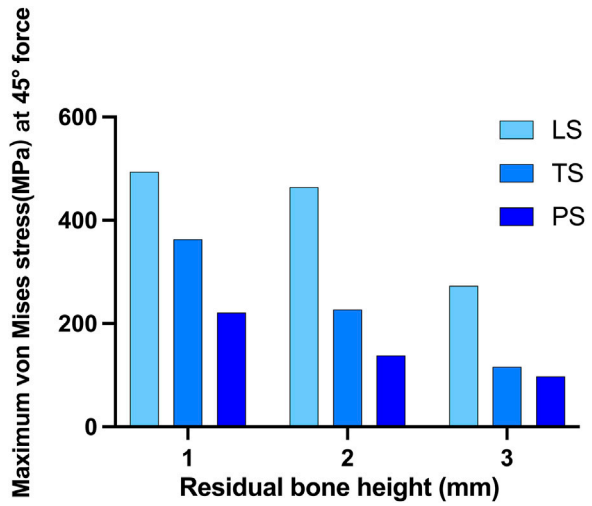

FIGURE 6
Maximum von Mises stress on crestal cortical bone of different residual bone heights and different wing designs at 45° force.

to the bone surface by means of a large-area spread plate *via* screw fixation (Silvestri and Carlotti, 1995). It solved the restoration problem of patients with severe bone atrophy to some extent. Nevertheless, the use of submucosal implants decreased in the late 1970s. One of the important reasons for the rapid decline of subperiosteal implants was that the fixed plate and post-column were integrally cast, so tiny mucosa inflammation could spread rapidly and lead to failure (Schou et al., 2000; Nemtoi et al., 2022). With the development of digital dentistry, subperiosteal implants have been re-proposed (Gellrich et al., 2017; Nemtoi et al., 2022). CAD/CAM techniques can make the retained titanium plate closely fit the bone surface in order to obtain satisfactory retention. However, the problem of one-piece manufacturing is not solved. The wing retention of the Yang's implant we developed borrows the idea of the retention plate from submucosal implants. But our implant has an implanted part, and the implant and the abutment are two sections, between which a platform switching structure is used. The platform switching connection is proven to have a better soft tissue seal around the implant, thus effectively preventing infection and marginal bone resorption. Meanwhile, Yang's implant can be customized with CAD/CAM techniques and precisely machined with a seven-axis lathe, so that the wings can fit tightly to the bone surface and form good retention.

3D-FEA has been widely used in dental research. It can be an excellent method for modeling complex structures and analyzing their mechanical properties (Trivedi, 2014). With this technique, it is possible to simulate complex structures on a microscopic scale to observe further stress distribution that is clinically impossible to observe (Turker et al., 2021). Yang's implant provides an effective method for implant restorations of patients with RBH less than 4 mm. In this circumstance, reliance on osseointegration between the implant component and the residual bone will not be sufficient for effective primary stability. The wing retained by titanium screws around the implant can provide critical retention. Larger wing spreading areas bring better support, but a larger flap elevation area is also required during the operation, which does harm to the blood supply of the soft tissue. Additionally, the direction of the wing also affects the stress distribution, thus influencing the stability of the implant. In this study, 3D-

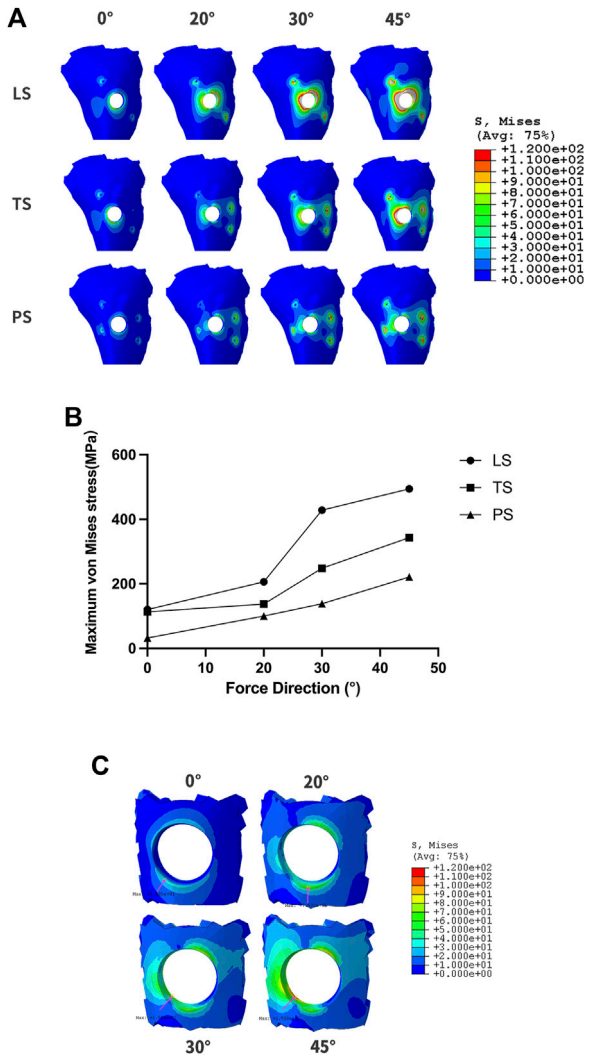

FIGURE 7
The changes of maximum von Mises stress according to different force directions and wing designs at RBH 1 mm. **(A)**. The diagram of maximum von Mises stress distribution; **(B)**. Value changes of maximum von Mises stress; **(C)**. The stress distribution at the hole-edge of the PS group.

FEA was established to analyze the stress distribution of Yang's implant with different designs and numbers of wings at different RBHs. During the process of implant surgery, the gingival flap is first performed, then the implant is placed. After the surgery, the gingiva is sutured. The most important function of the healed gingiva is to form a good soft tissue seal around the implant neck to prevent complications such as infection. It has no effect on the osseointegration stability of Yang's implant, so the gingival factor was not analyzed in the model. The result of the study is significant for further clinical design and application.

Micromotion is defined as a phenomenon that occurs at the interface of two components leading to the displacement of one component relative to the second one (Winter et al., 2013). Large micromotion at the bone-implant interface is harmful. Over 150 μm micromotion will induce the formation of fibrous connective tissue, thus interfering with implant osseointegration (Brunski, 1993; Szmukler-Moncler et al., 1998; Barnes et al., 2019). The wing retention structures of Yang's implants mainly account for the primary implant displacement. From the results of the study, a linear wing form has a poor ability to stabilize the initial displacement of the implant, especially under an oblique force. The triangular design is more conducive to the spread and dispersion of force. The planar style could distribute the occlusal force over surrounding cortical bone, effectively controlling the distribution of the implant and maintaining initial stability. When lateral force is applied, the implant displacement could still be guaranteed to be less than 100 μm even if the RBH is 1 mm. From the perspective of displacement control, the planar design form could better meet clinical application requirements.

According to Wolff's law of bone transformation, the bone's response to absorption or healing is directly related to stress in the bone (Frost, 1994). Excessive distribution of stress concentration is one of the important factors involved in time-dependent marginal bone loss, with inevitable progression compromising post-implantation stability. Marginal bone resorption usually begins in the cortical bone and progresses toward the apex (Wang et al., 2020). In addition, progressive bone loss is regarded as the first step of peri-implantitis (Galindo-Moreno et al., 2015). Maximum principal stress consists of tensile stress and compressive stress. Previous studies revealed that tensile stress promotes bone deposition while compressive stress promotes bone resorption (Zhong et al., 2013). A satisfactory design should have the ability to effectively disperse stress to avoid excessive stress concentration. Von Mises stress is commonly used in 3D-FEA studies to summarize the overall stress condition and the distribution of compressive stress and tensile stress can be analyzed by a stress distribution map. The maximum force and distribution range map must be taken into consideration to comprehensively determine the ideal design form of Yang's implant. The ideal design can effectively diminish stress concentration in supporting bone and realize stable implant restoration when the RBH is seriously insufficient. The results showed that the planar style had outstanding advantages. When vertical force was loaded, the maximum von Mises stress in this group could be controlled stably below 40MPa, even when the RBH was only 1 mm left. Oblique forces, which are quite common during normal mastication, cause more stress than axial forces (Tepper et al., 2002). Nevertheless, the PS group could still effectively control the maximum stress value when the RBH was 3 mm. From the map of stress distribution, the planar form had the advantage of dispersing the force concentrated around the hole compared to the liner and triangular groups. The maximum stress induced by the lateral force increases significantly as RBH further decreases. The 3D-FEA established in this paper simulated that the remaining bone volume was only 1 mm, which is an extreme circumstance of severe RBH deficiency in clinical practice. At this time, only the maxillary sinus floor composed of a thin layer of hard compact bone remains (Taschieri et al., 2015). The bone marrow space and blood supply are relatively poor in dense tissue. Blood vessels, capable of transporting oxygen and nutrients, are crucial for bone regeneration (Filipowska et al., 2017). So, in this case, the fresh bone powder implanted by lateral sinus floor elevation would hardly survive. We expect that Yang's implant with the planar form of wings could be applied in such extreme bone conditions. However, the maximum stress was beyond 200 MPa if a 45° force was loaded. It is a useful method to adjust the inclination of the cusps to eliminate the harmful effects of lateral stress during mastication. A previous study showed when remaining tooth tissue was weak, the stress concentration could be reduced by adjusting the inclination of the tooth cusp after post-core crown restoration, thus reducing the rate of root fracture (Liu et al., 2014). Accordingly, we

adjusted the direction of the lateral force, and the different degree of the force simulated cusp slope at different angles of the implant crown. The total stress in the PS group decreased as the force angle reduced. When the force angle was 20°, the maximum stress could be controlled below 150 MPa. Meanwhile, the compressive stress was mainly concentrated on the edge of the hole on the surface of the cortical bone opposite to the direction of the force. The maximum compressive stress shifted from the outer edge to the inner surface of the hole with the increase of the force angle (30°/45°), which could pose a potential risk of bone fracture or mucosa separation.

In summary, Yang's implant may be a good choice when a severe bone deficiency occurs in the maxillary posterior region. In clinical practice, the planar design form is suggested, which is more conducive to providing stable support in even extreme bone deficiency situations (e.g., RBH is only 1 mm). In such circumstances, it is necessary to properly adjust the cusp inclination of the implant crown to reduce the influence of harmful lateral force. The results of the 3D-FEA are the cornerstone of the large-scale clinical application of Yang's implants. In the future, the results of this study need to be compared with the accumulated clinical results.

5 Conclusion

In our finite element study, two conclusions can be drawn.

1) The customized Yang's implant can be a less traumatic and invasive method suitable for the implant restoration of patients with severe atrophic maxillary posterior regions. When the RBH in the maxillary posterior region is less than 4 mm, the stress distribution of the short implant with properly designed wings can meet the clinical requirements.
2) Compared to other styles, planar form wings can better disperse the stress and maintain the stability of the implant. By adjusting the cusp slope to reduce the influence of lateral force, the customized short implant with a planar wing fixture can be used safely even if the residual bone height is only 1 mm.

Data availability statement

The raw data supporting the conclusion of this article will be made available by the authors, without undue reservation.

Ethics statement

Written informed consent was obtained from the individual(s) for the publication of any potentially identifiable images or data included in this article.

Author contributions

ZY: experimental design, three-dimensional finite element model construction, investigation, data curation, visualization, and writing—original draft. JZ: visualization, software, and writing—original draft. ZX: methodology and resources. XL: drawing and data analysis. JY and JT: supervision, conceptualization, and funding acquisition. All authors contributed to the manuscript revision, read, and approved the submitted version.

Funding

This work was supported by the Qingdao Science and Technology Project for People (No.21-1-4-rkjk-20-nsh), the "Clinical Medicine + X" Scientific Research Project of the Medical Department of Qingdao University (No.2017M41), and the Qingdao Municipal Medical and Health Key Discipline Construction Project. This work was also supported by the Youth Foundation of Peking University School and Hospital of Stomatology (PKUSS20210114).

Acknowledgments

The authors thank Beijing Datsing Technology Company for its support in fabricating the implants. The authors thank Yujun Hou and Yong Gao senior engineers from Beijing Electro-mechanical Engineering Institute for their help in finite element modeling and analyzing.

Conflict of interest

The authors declare that the research was conducted in the absence of any commercial or financial relationships that could be construed as a potential conflict of interest.

Publisher's note

All claims expressed in this article are solely those of the authors and do not necessarily represent those of their affiliated organizations, or those of the publisher, the editors and the reviewers. Any product that may be evaluated in this article, or claim that may be made by its manufacturer, is not guaranteed or endorsed by the publisher.

Supplementary material

The Supplementary Material for this article can be found online at: https://www.frontiersin.org/articles/10.3389/fbioe.2023.1137779/full#supplementary-material

References

Barnes, S. C., Clasper, J. C., Bull, A. M. J., and Jeffers, J. R. T. (2019). Micromotion and push-out evaluation of an additive manufactured implant for above-the-knee amputees. *J. Orthop. Res.* 37 (10), 2104–2111. doi:10.1002/jor.24389

Bitinas, D., and Bardijevskyt, G. (2021). Short implants without bone augmentation vs. long implants with bone augmentation: Systematic review and meta-analysis. *Aust. Dent. J.* 66 (1), S71–S81. doi:10.1111/adj.12859

Brunski, J. B. (1993). Avoid pitfalls of overloading and micromotion of intraosseous implants. *Dent. Implantol. Update* 4 (10), 77–81.

Filipowska, J., Tomaszewski, K. A., Niedzwiedzki, L., Walocha, J. A., and Niedzwiedzki, T. (2017). The role of vasculature in bone development, regeneration and proper systemic functioning. *Angiogenesis* 20 (3), 291–302. doi:10.1007/s10456-017-9541-1

Frost, H. M. (1994). Wolff's law and bone's structural adaptations to mechanical usage: An overview for clinicians. *Angle Orthod.* 64 (3), 175–188. doi:10.1043/0003-3219(1994)064<0175:WLABSA>2.0.CO;2

Galindo-Moreno, P., Leon-Cano, A., Ortega-Oller, I., Monje, A., Valle, F O., and Catena, A. (2015). Marginal bone loss as success criterion in implant dentistry: Beyond 2 mm. *Clin. Oral Implants Res.* 26 (4), e28–e34. doi:10.1111/clr.12324

Gellrich, N. C., Rahlf, B., Zimmerer, R., Pott, P. C., and Rana, M. (2017). A new concept for implant-borne dental rehabilitation; how to overcome the biological weak-spot of conventional dental implants? *Head. Face Med.* 13 (1), 17. doi:10.1186/s13005-017-0151-3

Gonzalez, S., Tuan, M. C., Ahn, K. M., and Nowzari, H. (2014). Crestal approach for maxillary sinus augmentation in patients with ≤ 4 mm of residual alveolar bone. *Clin. Implant Dent. Relat. Res.* 16 (6), 827–835. doi:10.1111/cid.12067

Jung, R. E., Al-Nawas, B., Araujo, M., Avila-Ortiz, G., Barter, S., Brodala, N., et al. (2018). Group 1 ITI Consensus Report: The influence of implant length and design and medications on clinical and patient-reported outcomes. *Clin. Oral Implants Res.* 29 (16), 69–77. doi:10.1111/clr.13342

Liu, S., Liu, Y., Xu, J., Rong, Q., and Pan, S. (2014). Influence of occlusal contact and cusp inclination on the biomechanical character of a maxillary premolar: A finite element analysis. *J. Prosthet. Dent.* 112 (5), 1238–1245. doi:10.1016/j.prosdent.2014.04.011

Nemtoi, A., Covrig, V., Nemtoi, A., Stoica, G., Vatavu, R., Haba, D., et al. (2022). Custom-made direct metal laser sintering titanium subperiosteal implants in oral and maxillofacial surgery for severe bone-deficient patients-A pilot study. *Diagn. (Basel)* 12 (10), 2531. doi:10.3390/diagnostics12102531

Pjetursson, B. E., and Lang, N. P. (2014). Sinus floor elevation utilizing the transalveolar approach. *Periodontol. 2000* 66 (1), 59–71. doi:10.1111/prd.12043

Qian, S. J., Mo, J. J., Si, M. S., Qiao, S. C., Shi, J. Y., and Lai, H. C. (2020). Long-term outcomes of osteotome sinus floor elevation with or without bone grafting: The 10-year results of a randomized controlled trial. *J. Clin. Periodontol.* 47 (8), 1016–1025. doi:10.1111/jcpe.13260

Schou, S., Pallesen, L., Hjorting-Hansen, E., Pedersen, C. S., and Fibaek, B. (2000). A 41-year history of a mandibular subperiosteal implant. *Clin. Oral Implants Res.* 11 (2), 171–178. doi:10.1034/j.1600-0501.2000.110210.x

Silvestri, K. D., and Carlotti, A. E. (1995). Subperiosteal implant: Serving the dental profession for over 50 years. *R. I. Dent. J.* 28 (1), 11–23.

Szmukler-Moncler, S., Salama, H., Reingewirtz, Y., and Dubruille, J. H. (1998). Timing of loading and effect of micromotion on bone-dental implant interface: Review of experimental literature. *J. Biomed. Mater Res.* 43 (2), 192–203. doi:10.1002/(sici)1097-4636(199822)43:2<192::aid-jbm14>3.0.co;2-k

Taschieri, S., Testori, T., Corbella, S., Weinstein, R., Francetti, L., Di Giancamillo, A., et al. (2015). Platelet-rich plasma and deproteinized bovine bone matrix in maxillary sinus lift surgery: A split-mouth histomorphometric evaluation. *Implant Dent.* 24 (5), 592–597. doi:10.1097/ID.0000000000000293

Tepper, G., Haas, R., Zechner, W., Krach, W., and Watzek, G. (2002). Three-dimensional finite element analysis of implant stability in the atrophic posterior maxilla: A mathematical study of the sinus floor augmentation. *Clin. Oral Implants Res.* 13 (6), 657–665. doi:10.1034/j.1600-0501.2002.130613.x

Testori, T., Weinstein, T., Taschieri, S., and Wallace, S. S. (2019). Risk factors in lateral window sinus elevation surgery. *Periodontol. 2000* 81 (1), 91–123. doi:10.1111/prd.12286

Trivedi, S. (2014). Finite element analysis: A boon to dentistry. *J. Oral Biol. Craniofac Res.* 4 (3), 200–203. doi:10.1016/j.jobcr.2014.11.008

Turker, N., Alkis, H. T., Sadowsky, S. J., and Sebnem Buyukkaplan, U. (2021). Effects of occlusal scheme on all-on-four abutments, screws, and prostheses: A three-dimensional finite element study. *J. Oral Implantol.* 47 (1), 18–24. doi:10.1563/aaid-joi-D-19-00334

Varghese, K. G., Gandhi, N., Kurian, N., Daniel, A. Y., Dhawan, K., Joseph, M., et al. (2021). Rehabilitation of the severely resorbed maxilla by using quad zygomatic implant-supported prostheses: A systematic review and meta-analysis. *J. Prosthet. Dent.* doi:10.1016/j.prosdent.2021.11.007

Wang, X., Zhang, T., Yang, E., Gong, Z., Shen, H., Wu, H., et al. (2020). Biomechanical analysis of grafted and nongrafted maxillary sinus augmentation in the atrophic posterior maxilla with three-dimensional finite element method. *Scanning* 2020, 1–8. doi:10.1155/2020/8419319

Winter, W., Klein, D., and Karl, M. (2013). Effect of model parameters on finite element analysis of micromotions in implant dentistry. *J. Oral Implantol.* 39 (1), 23–29. doi:10.1563/AAID-JOI-D-11-00221

Xu, Z., Yang, Z., and Yang, J. (2022). Digital workflow for the design, manufacture, and application of custom-made short implants with wing retention device. *Front. Bioeng. Biotechnol.* 10, 885746. doi:10.3389/fbioe.2022.885746

Yan, X., Zhang, X., Gao, J., Matsushita, Y., Koyano, K., Jiang, X., et al. (2015). Maxillary sinus augmentation without grafting material with simultaneous implant installation: A three-dimensional finite element analysis. *Clin. Implant Dent. Relat. Res.* 17 (3), 515–524. doi:10.1111/cid.12254

Zhong, Z., Zeng, X. L., Ni, J. H., and Huang, X. F. (2013). Comparison of the biological response of osteoblasts after tension and compression. *Eur. J. Orthod.* 35 (1), 59–65. doi:10.1093/ejo/cjr016

frontiers | Frontiers in Bioengineering and Biotechnology

TYPE Original Research
PUBLISHED 16 March 2023
DOI 10.3389/fbioe.2023.1152412

OPEN ACCESS

EDITED BY
Yongtao Lu,
Dalian University of Technology (DUT), China

REVIEWED BY
Qiang Chen,
Southeast University, China
Lizhong MU,
Dalian University of Technology, China

*CORRESPONDENCE
Xiaojun Wu,
wuxiaojun@xauat.edu.cn
Yingtian Li,
yt.li@siat.ac.cn

†These authors contributed equally to this work and share first authorship

SPECIALTY SECTION
This article was submitted to Biomechanics, a section of the journal Frontiers in Bioengineering and Biotechnology

RECEIVED 27 January 2023
ACCEPTED 06 March 2023
PUBLISHED 16 March 2023

CITATION
Tong X, Jiang Y, Mo F, Sun Z, Wu X and Li Y (2023), A single-tube-braided stent for various airway structures.
Front. Bioeng. Biotechnol. 11:1152412.
doi: 10.3389/fbioe.2023.1152412

A single-tube-braided stent for various airway structures

Xin Tong[1,2†], Yongkang Jiang[3†], Fei Mo[1], Zhongqing Sun[1], Xiaojun Wu[2*] and Yingtian Li[1*]

[1]Shenzhen Institute of Advanced Technology, Chinese Academy of Sciences, Shenzhen, China, [2]School of Mechanical and Electrical Engineering, Xi'an University of Architecture and Technology, Xi'an, China, [3]School of Automation, Beijing University of Posts and Telecommunications, Beijing, China

Background: Airway stent has been widely used in airway procedures. However, the metallic and silicone tubular stents are not customized designed for individual patients and cannot adapt to complicated obstruction structures. Other customized stents could not adapt to complex airway structures with easy and standardized manufacturing methods.

Object: This study aimed to design a series of novel stents with different shapes which can adapt to various airway structures, such as the "Y" shape structure at the tracheal carina, and to propose a standardized fabrication method to manufacture these customized stents in the same way.

Methods: We proposed a design strategy for the stents with different shapes and introduced a braiding method to prototype six types of single-tube-braided stents. Theoretical model was established to investigate the radial stiffness of the stents and deformation upon compression. We also characterized their mechanical properties by conducting compression tests and water tank tests. Finally, a series of benchtop experiments and *ex vivo* experiments were conducted to evaluate the functions of the stents.

Results: The theoretical model predicted similar results to the experimental results, and the proposed stents could bear a compression force of 5.79N. The results of water tank tests showed the stent was still functioning even if suffering from continuous water pressure at body temperature for a period of 30 days. The phantoms and *ex-vivo* experiments demonstrated that the proposed stents adapt well to different airway structures.

Conclusion: Our study offers a new perspective on the design of customized, adaptive, and easy-to-fabricate stents for airway stents which could meet the requirements of various airway illnesses.

KEYWORDS

airway stent, photocurable stents, braiding method, stent customization, *ex vivo* experiments

1 Introduction

Airway illnesses, such as tracheobronchomalacia (TBM) and tracheobronchial stenosis (TBS), may cause the patients to cough, wheeze, apnea and sometimes lead to profound airway obstruction which will threat patients' life (Torre et al., 2012; Mitchell et al., 2014). TBM and TBS are sometimes congenital airway malformations, but more often caused by surgical trauma, tumor compression, anastomotic hyperplasia after lung transplantation, and extrinsic compression (Carden et al., 2005; Wright et al., 2019; Xiong et al., 2019). In

clinical practice, the diseases are mainly treated by tracheostomy based long-term mechanical ventilation, aortopexy, suspension, and airway stenting (Torre et al., 2012; Mitchell et al., 2014; Fraga et al., 2016; Hysinger and Panitch, 2016). Due to the advantages in non-invasive properties during surgery and rapid post-surgery recovery, airway stenting procedures have been widely adopted to keep the airway open (Ha et al., 2019; Xiong et al., 2019).

To design airway stents used for the above-mentioned clinical practices, several requirements have to be met. First, the diameter and the radial stiffness of the airway stents must be systematically optimized, to keep the airway open and reduce the risk of unnecessary complications simultaneously. Oversized stent or too large radial stiffness will cause the airway tissue injured, e.g., mucosal ischemia, while undersized stent or too weak radial stiffness will result in migration inside airways (Murgu and Laxmanan, 2016). Second, the stent must own sufficient fatigue strength to avoid fracturing when suffered from the periodical contraction during breathing and sometimes coughing (Folch and Keyes, 2018). Finally, to avoid mucus plugging, the stent should minimize its impediment on the mucociliary clearance, so that cilia-mediated mucus can flow through the stented region (Bhora et al., 2016; Murgu and Laxmanan, 2016).

Over decades, airway stents has been constantly studied (Avasarala et al., 2019; Guibert et al., 2019; Guibert et al., 2020; Mathew et al., 2020; Paunović et al., 2021; Soriano et al., 2021; Ratwani et al., 2022). The most widely used airway stents in clinical procedures are self-expandable metallic stents (SEMS). They are designed into a series of standard dimensions and fabricated by laser cutting technique. The SEMS are standard-sized stents, but the sizes and structures of different patients vary a lot. Thus, this mismatch of the standard stents and non-standard patients' airway make it difficult for patients to select proper stents during procedures. In addition, the sharp edges of SEMS will cause mucosal trauma of the airways, inducing the growth of granulation tissues which eventually requires invasive procedures to remove the stents (Dasgupta et al., 1998; Saad et al., 2003; Almadi et al., 2017; Folch and Keyes, 2018). Silicone rubber tubular stents, compared to the metallic stents, are much safer when deployed into patients' airways due to their intrinsic soft properties. However, mucus plugs or even pneumonia may occur because the silicone stents will fully cover the airways and further block the secretions cleaning (Saji et al., 2010; Sökücü et al., 2020). To create a non-standard stent, there were trials to suture several silicone rubber tubular stents together to match complicated airway structures, such as the "Y" shape structure located at the tracheal carina. But the stents are too complicated during fabrication and still difficult to match the airway sizes perfectly (Long, 1988; Majid et al., 2012).

In the previous work, an *in vivo* molded airway stent was designed. The thermoplasticity-based single helical stent would not induce the growth of the granulation tissue and avoid blocking the mucociliary clearance, and its diameter can also be adjusted during clinical procedures (Mencattelli et al., 2021). The limitation of this work is that the single helical structure cannot adapt to complicated branches. For example, when the stent is required to support airway tissues at the tracheal carina, we had to implant three single helical stents individually instead of a Y-shape stent, which brings unnecessary complexity to clinical procedures (Dutau et al., 2004; Madan et al., 2016; Sehgal et al., 2017). Besides, the single helical structure has only one contact point at each cross-sectional area, limiting the support effect in the airway in some cases.

In this paper, we proposed a novel series of stents which can be fabricated by the same braiding method using a single soft tube, and we named this type of stents as single-tube-braided stent (STB stent) (Figure 1A). The stents are photocurable, and their diameters can be customized during the clinical procedures. The STB stents are designed to exhibit different shapes in order to adapt to varied airway structures for various airway illnesses. Altogether six different shapes of the stents (Figure 1B) were demonstrated based on clinical requirements. Type I to III stents are designed for malacia located at tracheal, bronchi and/or tracheal carina. Type IV stent can be used for tracheal intubation procedures, while Type V to VI stents could provide supports to different types of TBS. In addition to design and fabrication, we also established a theoretical model to illustrate the relationship of radial stiffness and radial deformation of the stents. Experiments were conducted to verify the model and evaluate the mechanical properties of the stents, including compressive tests and water tank tests. Then, the supporting behaviors were evaluated in phantom experiments. Finally, functional demonstrations were presented by stenting the proposed stents in the *ex vivo* trachea and bronchi harvested from a swine.

2 Material and methods

2.1 Stent design

2.1.1 Design strategy

The design strategy of STB stents is described in this section. The STB stents are designed to be braided by a single tube filled with UV-curable polymer. The tube we selected is a biocompatible silicone tube, and the softness brought by the silicone material promise the stent to exhibit easy deformation and adaptation to the airway structures. To provide sufficient supporting force to the airway, the radial stiffness is the key design criteria. In this work, the UV polymer filled into the silicone tube is liquid before curing but will turn to rigid material after ultraviolet radiation. In view of the shortcoming of the *in vivo* molding stents, the STB stent is designed as multi-helix structure, to provide sufficient supporting force and contact points to the airways. From the perspective of design, five conditions must be fully met in this work.

First and foremost, the stent must be braided by one single tube, to provide customized stents for various airway illnesses, and the stent shall be composed of $2m$ helixes. Then, a left-hand helix and a right-hand helix with the same number of coils, which is symmetric about X-Y plane, are braided as a "curve group" structure defined in this work. The structures are illustrated by purple and blue curves in Supplementary Figure S1A. Third, to provide supporting forces to airways evenly, m pairs of "curve group" are designed to distribute uniformly in circumferential. Since single curve group structure cannot be evenly distributed and thus the number of m should be larger than 1. Fourth, a start point and an end point for each helix shall be defined, and the start point of later helix shall coincide with the end point of the former helix. At last, the start point of the first helix must coincide with the end point of the last helix, as shown in subfigure II of Supplementary Figure S1B. Because curve group

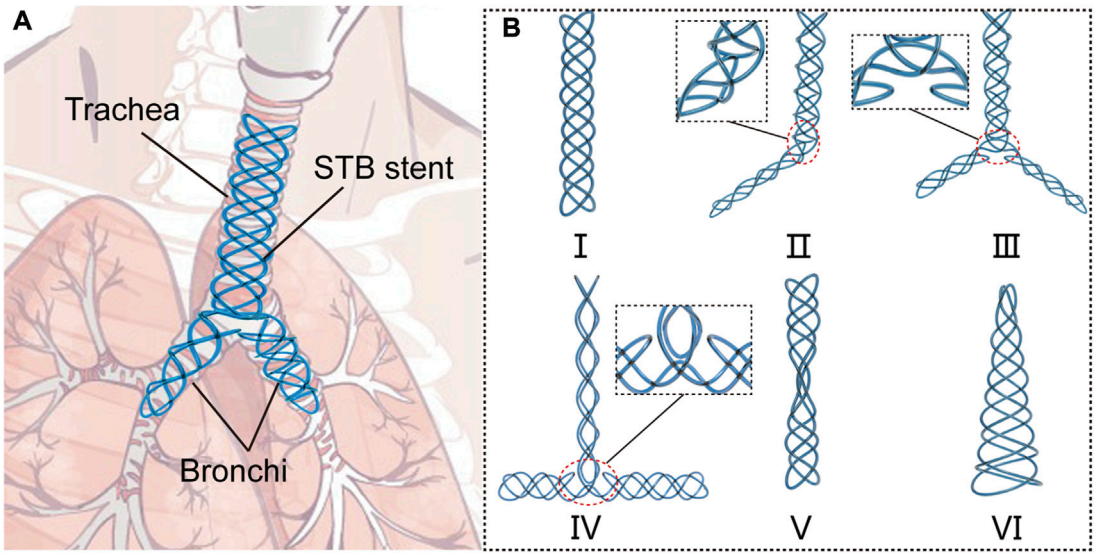

FIGURE 1
Concept of the single-tube-braided airway stent. **(A)** A schematic diagram, in which a Y-type single-tube-braided (STB) stent is implanted into the trachea and bronchi. **(B)** 6 types of STB stents for various airway structures: Type I stent, a straight stent for central airway obstruction. Type II stent, a L-shape stent to support trachea and one main bronchus. Type III stent, a Y-shape stent to support trachea and both main bronchi. Type IV stent, a T-shape stent for tracheal intubation procedures. Type V stent, an hourglass stent for tracheostenosis. Type VI stent, a conical stent for the disorder at the end of the airway.

structures have to be evenly distributed, the start point and end point of a single curve group structure have to locate at the two ends of the arc of the projected circle, whose length is $1/m + N$ or $(m-1)/m + N$ of the circumstance, where N is any natural number representing N full circles, as shown in Supplementary Figure S1C.

Although the following theory can be used to design the proposed stents with more than three pairs of curve group structures, the number of curve group structures m are selected to be 2 in this work. This is because the stents are required to avoid the impediment of mucociliary clearance, the contact area between stents and airways shall be minimized. Therefore, the stent in this work only consists of two curve group structures, indicating four helixes in total.

2.1.2 Number of coils for the stent

For a single curve group structure, the two helixes must be symmetric, so the pitch and diameter of the helix are the same and the only parameter determining the length is number of coils for each helix n. Because they are connected to each other, the turning point shall locate at the middle points of the arcs formed by the start and end points. Therefore, the number of coils for each helix n could be written as a dataset when we have decided the value of curve group is m, the dataset and each data element in the set is expressed as Eq. 1:

$$N_m = \left\{ n \middle| n = \frac{N}{2} + \frac{k}{2m} \right\} \tag{1}$$

where k equals to 1 or $m-1$.

Before deciding the actual number of coils, the relationship between the number of helical coils and the parameters of airways shall be expressed.

$$n_{theory} = \frac{l}{P} \tag{2}$$

where n_{theory} is the calculated helical coil number according to the length of diseased airway, P is the required pitch of helix after the stent is expanded in the airway, which will be discussed in Section 2.3.2, l is the length of the airway region need to be supported (Figure 2A).

However, n_{theory} is the minimum value in theory and may not equals any one data element n in the dataset N_m. Therefore, the number of coils for each helix in practice ($n_{practical}$) should be no smaller than n_{theory} to ensure a sufficient supporting, and the value should be selected from the dataset N_m. Therefore, Eq. 3 expresses the way to select $n_{practical}$.

$$n_{practical} = \min\ \left(N_m \left(find \left(N_m \geq N_{theory} \right) \right) \right) \tag{3}$$

2.1.3 Pitch and diameter of the stent

Once the number of helical coils of STB stents have been determined, the rest works to conduct is to decide the pitches and diameters of the stents. The four helixes of the stent are bonded to each other at their interaction points exhibiting numbers of rhombic structures (Figure 2A), which will keep the number of coils as a constant. The determination of the parameters starts from the molding process.

The stents will be winded onto the mold for consistency, so the diameter of the mold plus the twice the diameter of the tube shall be smaller than the diameter of human main bronchi (12 mm in general). The diameter shall be as small as possible, but not too small to unnecessarily enhance the difficulty in manufacturing.

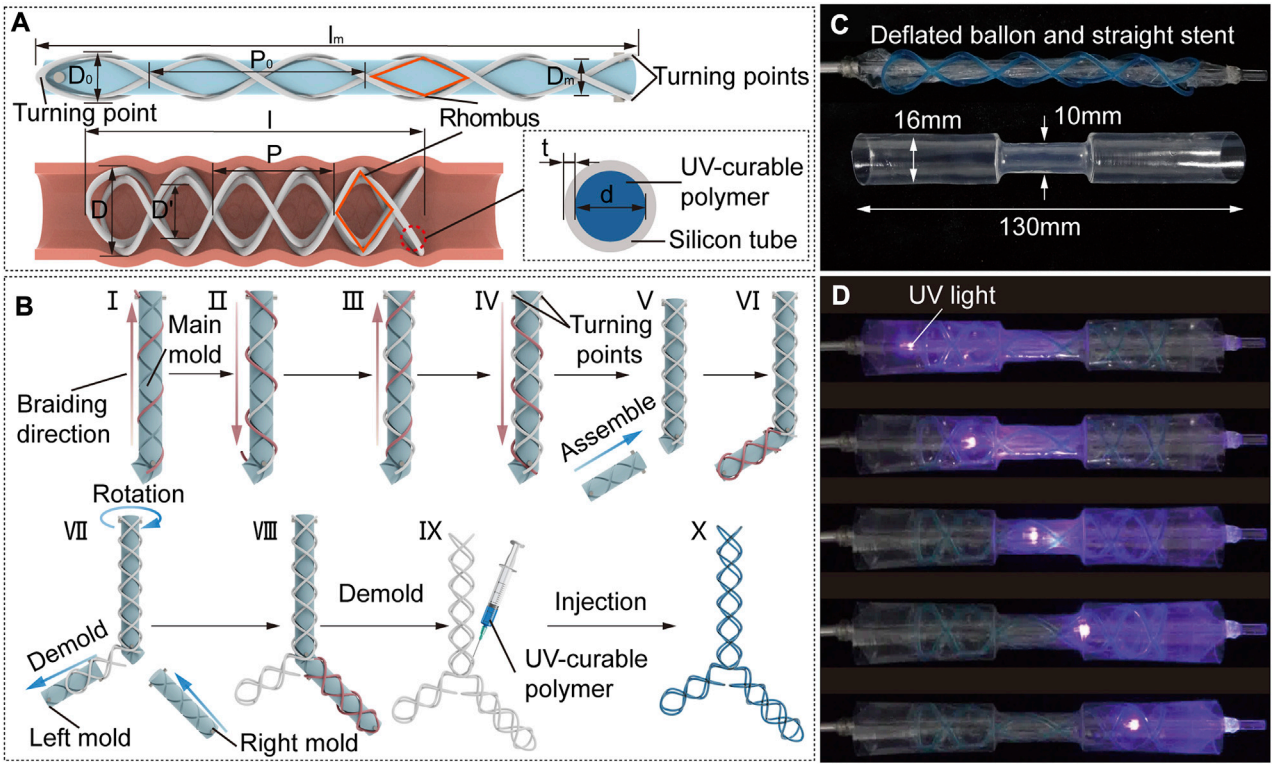

FIGURE 2
STB stent design strategy, fabrication and curing process. **(A)** Design parameters of an uncured STB stent on a mold (top), a cured STB stent in an airway (bottom left), and inner structure of the STB stent (bottom right). **(B)** Fabrication steps. A silicone rubber tube is manually winded along the grooves on the mold. Steps I to IV sequentially described the steps to wind the four helixes, and the tube highlighted in red represents the ongoing operation in these steps. Steps V to VIII separately illustrates braiding the second and the third branches of the stent. Step IX presents the injection of the UV-curable polymer. The ready-to use stent is shown in step X. **(C)** Initial straight stent on a balloon catheter, and a phantom tracheal model with a simulated stricture in the middle. **(D)** Curing process. The uncured stent is delivered into the model across the area of the stricture. Expand the stent radially by balloon dilation to conform with the model. Cure the stent with UV light provided by an optical fiber.

Since we have the diameter of mold D_m and the actual number of helical coils n_{real}, we can easily obtain the pitch of mold P_0 by Eq. 4 (detail derivate process can be found in Supplementary Material "Derivation processes of Equation 4" and Supplementary Figure S2).

$$P_0 = \sqrt[2]{\pi^2\left(D'^2 - D_m^2\right) + P^2} \tag{4}$$

where $D' = D - 4(d + 2t)$ is the inner diameter of expanded STB stent in airway, d and t are the inner diameter and thickness of the silicone tube used to fabricate the stents, and D is 3 mm larger than the trachea of human in diameter (15 mm–20 mm in general) to produce a similar preload against the trachea and prevent the stents from migration.

The length of mold l_m can be calculated by $l_m = n_{practical}P_0$, where P_0 is the pitch of the initial STB stent as shown in Figure 2B.

2.2 Stent fabrication and curing process

Here, the materials we chose, the fabrication method and curing process are described in this section. In this work, we selected a silicone tube with a thickness of 0.15 mm and the UV-curable polymer we selected with high elastic modulus (about 1,790 MPa measured with MARK-10, Mark-10 Corporation, NY, through a standard uniaxial extension test) and relatively low creep.

To braid the proposed STB stent of diverse shapes, we designed a modular molding technology (Figure 2B). The modular molds can be assembled into different configurations to fabricate different stents. The whole set of molds comprise main mold, left mold, and right mold with grooves on each of them, which is manufactured by a 3D printer (Ultimaker S3, Ultimaker B.V., MA). The grooves on the mold are braiding tracks to guide the braiding of the tube.

The braiding process is described in detail in Figure 2B. All the stents begin with winding the tube on the main mold, which are used to fabricate Type I, V and VI stents as shown in Figure 1B. The steps I to IV sequentially describe the steps to wind the four helixes, and the tube highlighted in red represents the ongoing operation in these steps. The whole braiding process is presented in Supplementary Video S1. The fabrication of other types of stents is built on the straight stent and requires the assembly of right and/or left mold onto the main mold. Step V illustrates assembling the left mold onto the main mold to form the L-shape mold, which is used to fabricate Type II stent. In step VI, the first four steps shall be repeated in sequence to braid the second branch of the stent. To fabricate the Type III and IV

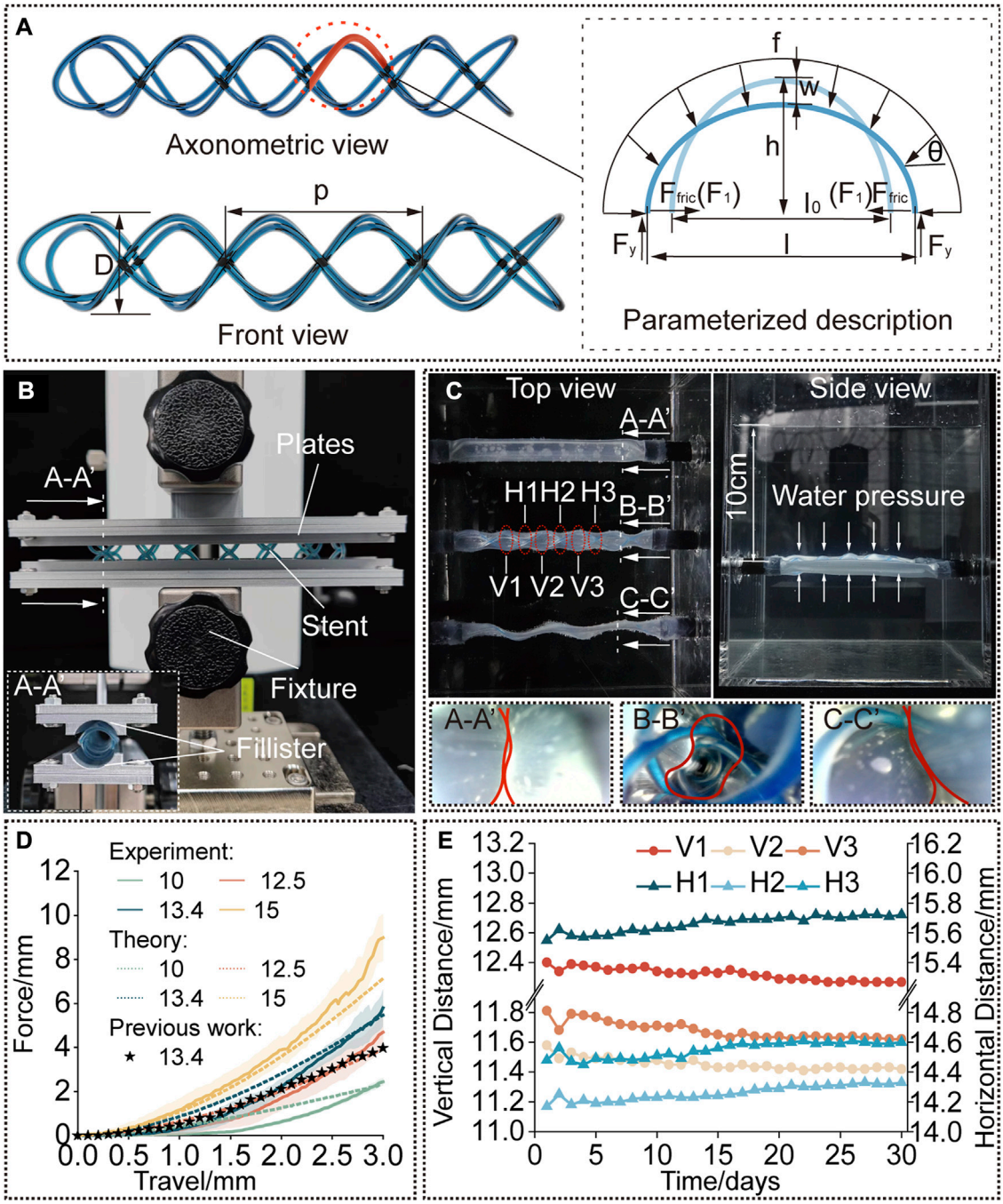

FIGURE 3
Modelling and characterization. **(A)** A rendered graph of a straight stent and a diagram of its deformation analysis. **(B)** Compression test setup. The cured stent was positioned between the two plates with fillisters and compressed by a force-measuring platform. **(C)** Water tank test setup. The stent is kept inside the phantom tracheal model at 37°C and a water pressure at a depth of 10 cm was applied. **(D)** Compression force *versus* travel distance. Experimental results compared to the predicted results to verify the model and compared to the results for the single helical stent with the same parameters. **(E)** Diameters of the stent [interpreted by the vertical and horizontal distances as shown in **(C)**] *versus* time (30 days).

stents, the left mold should be first demolded and the right mold is then assembled onto the main mold as shown in step VII;. In step VIII, the second branch of the stent is braided by the above-mentioned steps. In step IX, the stent is demolded, and the UV-curable polymer is injected into the tube. The ready-to use stent filled with polymer is shown in step X.

The curing process is described in detail. The ready-to-use stent will be placed on a balloon catheter, with which the stent will be delivered to the airways. We used an hourglass-shape transparent pipe to represent the trachea with stricture, which was designed to be consistent with the anatomical shape of an adult trachea. The balloon catheter and pipe are shown in Figure 2C. As for curing

process, the stent positioned on the uninflated balloon catheter is first delivered into the pipe. Then the balloon is inflated to expand the stent so that the stent could adapt to the varied pipe diameters. After that, we keep the inflation and insert an optical fiber connected to a UV-light source through the central lumen of the balloon catheter, to deliver UV-light to cure the polymer. The end of UV optical fiber can be positioned at different points along with the balloon to ensure fully curing of the stent. Finally, we deflate the balloon and remove the catheter, leaving the cured stent in the pipe (Supplementary Video S2).

2.3 Modelling and experimental method

In this section, we established a model to investigate the radial stiffness of the STB stents, and meanwhile we performed a series of experiments to investigate their mechanical properties. The deformation of the STB stent under uniformly distributed loading was studied in the first set of experiments, to verify the model. The second set of experiments investigated the fatigue performance of STB stents over time under radial loading (water pressure at a depth of 10 cm). The modeling and experiments are described below.

2.3.1 Model

The stents used in clinical procedures are usually oversized than the airways to prevent the stent from migration and hence suffer from compressive forces due to the elasticity of the tissue. Breathing and coughing of patients can further improve the compressive force. We established a theoretical model to establish the relationship between the compressive force and the radial deformation of the STB stent. This model shows how the parameters influence the stiffness of STB stents, such as the cross-section area of cured polymer, diameter D and helical angle of STB stent.

Based on the design configuration, we assume that the force applied on all helixes are the same. To simplify the calculation, half coil of a single helix is chosen for analysis (Figure 3A). The curve can be considered as half of an elliptical beam, which will be pressed by a uniformly distributed loading force f. Then, we can express the compressed ellipse by Eq. 5:

$$\frac{4x^2}{l^2} + \frac{y^2}{(h-w)^2} = 1 \tag{5}$$

where $h = \frac{D}{2}$ is the equation of minor axis of the compressed ellipse, w is the deflection of middle point on the beam, and the major axis of the compressed ellipse $l = \sqrt[2]{D^2 + (\frac{D}{2})^2}$.

The perimeter of the semi-ellipse is kept constant due to the inextensibility of the cured polymer, we can get the relationship of the axes before and after compression:

$$\left(\frac{l}{2}\right)^2 + (h-w)^2 = \left(\frac{l_0}{2}\right)^2 + h^2 \tag{6}$$

where, l_0 is the initial major axis of ellipse. This equation is calculated based on the approximated calculation formula of the perimeter of ellipse, which is generally written as $L = \pi\sqrt[2]{2\left((l_0/2)^2 + h^2\right)}$. In this equation, L is the perimeter of ellipse (Muir, 1902).

The horizontal and vertical component of the uniformly distributed loading force f is expressed as Eq. 7

$$f_x = f\cos\theta;\ f_y = f\sin\theta \tag{7}$$

where,

$$\begin{cases} \sin\theta = -\dfrac{(h-w)x}{\sqrt[2]{\left(\frac{l}{2}\right)^4 - x^2\left[\left(\frac{l}{2}\right)^2 - (h-w)^2\right]}} \\ \cos\theta = \dfrac{\frac{l}{2}\sqrt[2]{\left(\frac{l}{2}\right)^2 - x^2}}{\sqrt[2]{\left(\frac{l}{2}\right)^4 - x^2\left[\left(\frac{l}{2}\right)^2 - (h-w)^2\right]}} \end{cases}$$

Then, we can obtain the reaction force by Eq. 8:

$$F_y = \int_{-\frac{l}{2}}^{0} f_y dx \tag{8}$$

The friction between the beam and the internal wall of the airway was assumed as below (the detailed explanations refer to Supplementary Material "Explanation for Equation 9" and Supplementary Figure S3):

$$F_{fric} = \frac{2\mu A E w^2}{L^* l} \tag{9}$$

where μ is the friction coefficient, A is the cross-sectional area of the beam.

Then, the moment applied to point x_0, which could be at any point on the beam, can be written as:

$$M = F_y\left(x_0 + \frac{l}{2}\right) - \int_{-\frac{l}{2}}^{x_0} f_y(x_0 - x)dx - \int_{-\frac{l}{2}}^{x_0} f_x\left(y(x_0) - y(x)\right)dx - F_{fric}y(x_0) \tag{10}$$

In general, the equation of deflection w can be expressed as Eq. 11.

$$EIw'' = -M \tag{11}$$

Therefore, we can obtain the relationship between deflection w and the uniformly distributed loading f by substituting Eq. 10 into Eq. 11 and integrating the corresponding expression.

2.3.2 Experimental method

The stiffness of the airway stent shall be strong to provide sufficient radial support to keep the airway open during breathing and sometimes coughing. Therefore, we conducted a few sets of experiments. The experiment aims to prove that the stents fabricated with the selected tube own sufficient stiffness for clinical procedures.

2.4 Radial stiffness

First, the stents were designed with the diameter of 13.4 mm and pitch of 18.6 mm, to compare the radial stiffness to our previously published work (Mencattelli et al., 2021) which had already proved

its practicability in *in vivo* animal experiments. Second, the cured diameter of the stents was chosen as the variate, whose initial diameter before balloon dilation was kept the same, to investigate the influence of diameter on the radial stiffness in response to compressive loading, and the results were also compared to the results predicted by the proposed model. The parameters of the STB stent before curing were calculated according to Eq. 4. To conduct the tests, the stents were radially compressed by a displacement of 0 mm–3 mm, which is referred to the research work (Mencattelli et al., 2021). Force data was collected 20 points per second, and each trial were repeated for three times. The results are presented in Figure 3D.

The testing platform consists of a lifting platform with a force gauge (MARK-10, Mark-10 Corporation, NY) and two parallel plates with curved fillisters, between which the stents are positioned, as shown in Figure 3B. The curvature of the fillisters matched the unloaded diameters of the stents (10 mm, 12.5 mm, 13.4 mm, and 15 mm) and each plate covered a circumferential angle of 20°C on each side of the stent. We assume that the deformation of the stents in the experiment is similar to that under radial loading. To simulate the slippery in airways, the stents and fillisters were lubricated (Multi-Use Performance Lubricant with Teflon, DuPont, NY).

2.5 Fatigue property

After implanted, the stents are suffering from continuously radial loads at body temperature over a long period of time. Therefore, to evaluate the performance of stents in a simulated environment, we performed water-tank tests. The proposed stents were delivered into a phantom tracheal models, which was placed under 37°C water (Figure 3C). According to reference, the continuous positive airway pressure (CPAP) to treat airway disorders has been proven effective, and the value of the applied pressure which is sufficient to maintain respiration equals to a water pressure at a depth of 5 cm–10 cm (Pizer et al., 1986; WEIGLE, 1990; Panitch et al., 1994).

The phantom tracheal model was casted with silicone with an inner diameter of 10 mm and a thickness of 0.2 mm (The detailed material constants based on Yeoh model are: $C_1 = 1.0 \times 10^{-1}, C_2 = 1.69 \times 10^{-1}, C_3 = 2.66 \times 10^{-4}$). According to (Ha et al., 2019), the properties of the silicon had been proved with biaxial testing experiments to exhibit similar mechanical property to the actual trachea. This tracheal model was easier to collapse radially because of its soft property. This means we simulated a worse case of TBM, when the tracheal cartilages completely lose their functions and cannot provide supports to the tracheal tissue, to evaluate the performance of our stents (see Supplementary Figure S4).

As a comparison, three phantom tracheal models were side-by-side positioned in a water tank under a depth of 10 cm. The ends of the phantoms were glued and sealed to rigid tubes, which passed through the holes in the wall of the tank. To produce a similar preload against the trachea, the diameter of stents implanted in the tracheal model is 3 mm larger than the diameter of the phantom. As shown in Figure 3C, an STB stent was cured inside the middle phantom with a cured outer diameter of 13 mm, a single helical stent whose diameter and pitch are the same with the STB stent was delivered into the bottom phantom, while the phantom on the top has nothing inside. The endoscopic views at the bottom of Figure 3C show that only the phantom with the STB stent did not collapse (Supplementary Video S3, Figure S5).

3 Results

3.1 Mechanical properties

The results show the radial stiffness of the stents were presented in Figure 3D, and the stiffness was interpreted by the external compressive force. It is obvious that a cured STB stent with a larger diameter exhibits a stronger ability to resist a compressive force. If compressed no more than 1.8 mm, the resistance ability for external compressive force of the STB stent, whose pitch is 13.4 mm and silicone tube is 1 mm in diameter, is similar to that of our previous single helical stent. However, when compressed displacement exceeds 1.8 mm, the resistance ability of STB stent is larger than that of the single helical stent. This means that the proposed stent has proved its resistance ability for external compressive force is large enough to meet clinical requirements (Ha et al., 2019; Mencattelli et al., 2021).

The results predicted with the model showed similar trend to the experimental results in Figure 3D which verified the effectiveness of the above-mentioned model. In the first stage of compression, the predicted results were a little bigger than the experimental results. The differences decreased with the increase of compressive displacement. In the second stage, the experimental results increased with an even faster rate and showed larger values than the predicted ones. The reasons behind are discussed here. 1) In the model, we assumed that the elliptical beam suffered a uniformly distributed load (Supplementary Figure S6A). However, due to the fabrication error in practice, the stents cannot always match well with the fillisters of plates (Supplementary Figures S6B). The mismatch made the uniformly distributed load a concentrated force and provided less constraints to the boundary of the stents. Therefore, in the first stage, the stents were easier to deform with a smaller compressive force. 2) After the stents were compressed for a few millimeters, the compressed stents fully contacted with the fillisters. If continue the compression, in theory, the compressed stents should elongate along the axial direction of the stents (Supplementary Figures 6C, 6E). But as illustrated in Supplementary Figure S6D, the stents would deform into the gap between the plates, resulting in irregular deformation. A large portion of the compression force would be transmitted to the region to induce the irregular deformation rather than compressing the stent as a whole. This may be the reason leading to larger forces than the predicted ones in the second stage.

Figure 3E shows the radial deformation of the STB stent over a period of 30 days. In each measurement, 6 sets of data were recorded, and they are three pairs of horizontal distances (H1, H2, and H3) and three pairs of vertical distances (V1, V2, and V3). The details are explained in Figure 3C; Supplementary Figure S7. The outer diameter of the STB stent decreased from 13 mm to 11.4 mm during the 30 days. The change of diameter is 1.6 mm, which is smaller than 3 mm stated above, and the stent could still maintain the airway open. Therefore, it is safe to conclude that the STB stent would not fail for 30 days even if it is stented in a worse simulated diseased airway.

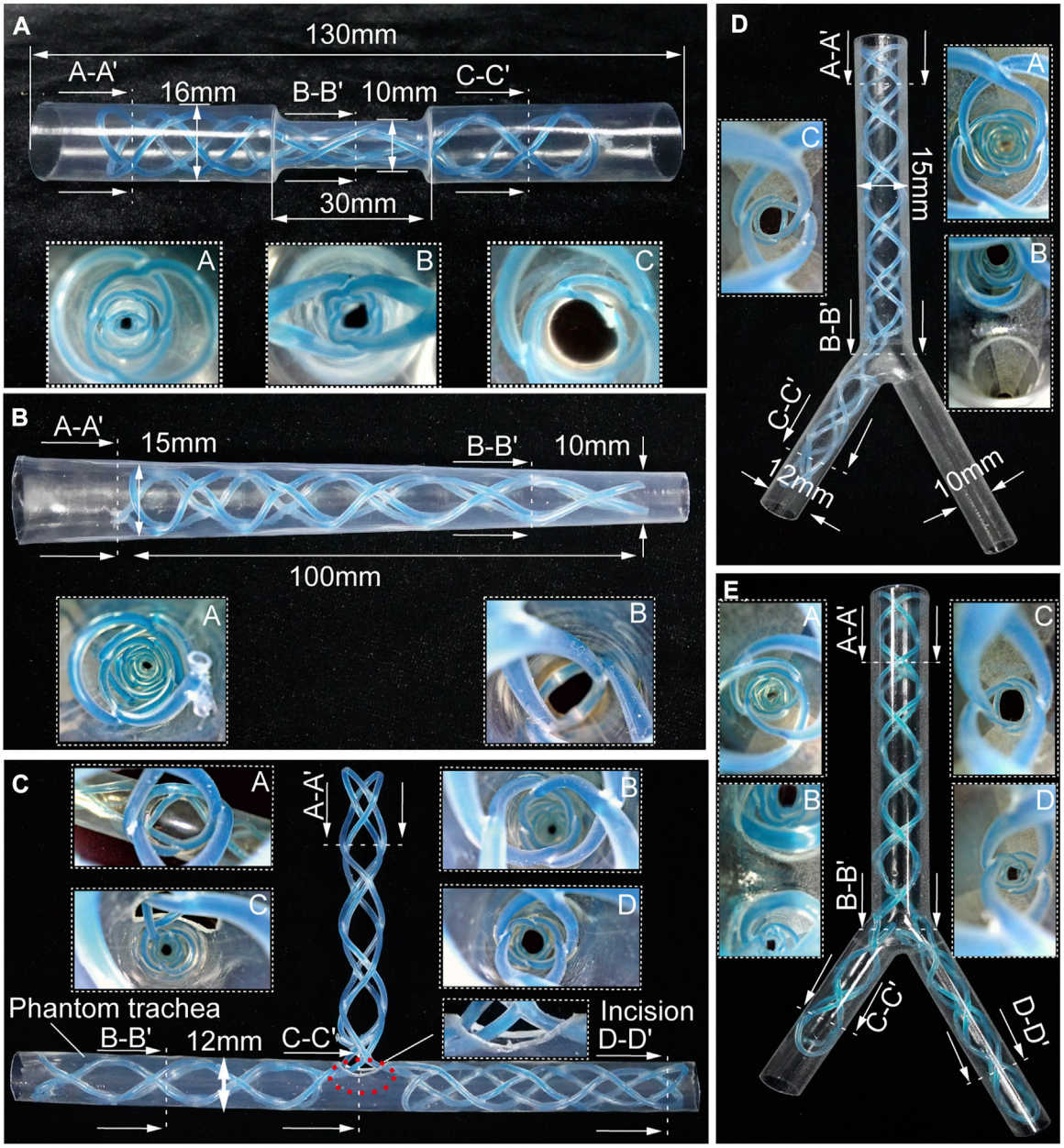

FIGURE 4
Benchtop experiments. Different shapes of the stents cured inside the corresponding phantom tracheal models with endoscopic views. **(A, B)** Molded straight stents inside tracheal phantom model with insets showing endoscopic views. **(C–E)** Molded complicated-shaped stents inside a phantom model of tracheal and bronchi with insets showing endoscopic views.

3.2 Benchtop and ex-vivo experiments

The STB stent proposed in this paper can be designed to produce different types of stents for various airway structures. To demonstrate stenting the STB stents in different airway structures, we designed, fabricated and cured the rest five types of stents, including stents in hourglass shape, conical shape, T shape, L shape, and Y shape. We also fabricated five different phantom airway models accordingly (Figure 4).

3.2.1 Benchtop experiments

Airway stenosis shows diameter decrease in airways. Stenting in such an area is the variation of airway stents in diameter. The hourglass shape stent, illustrated in Figure 4A, was obtained by curing an initial soft straight stent in a tracheal model with a narrowed region to simulate stenosis. The tracheal model, which was fabricated by a heat shrinkable tube with a wall thickness of 0.5 mm, is 130 mm in length, with a outer diameter of 16 mm, while the narrowed region is 30 mm in length and 10 mm in outer diameter. Compared the diameters at point A and point

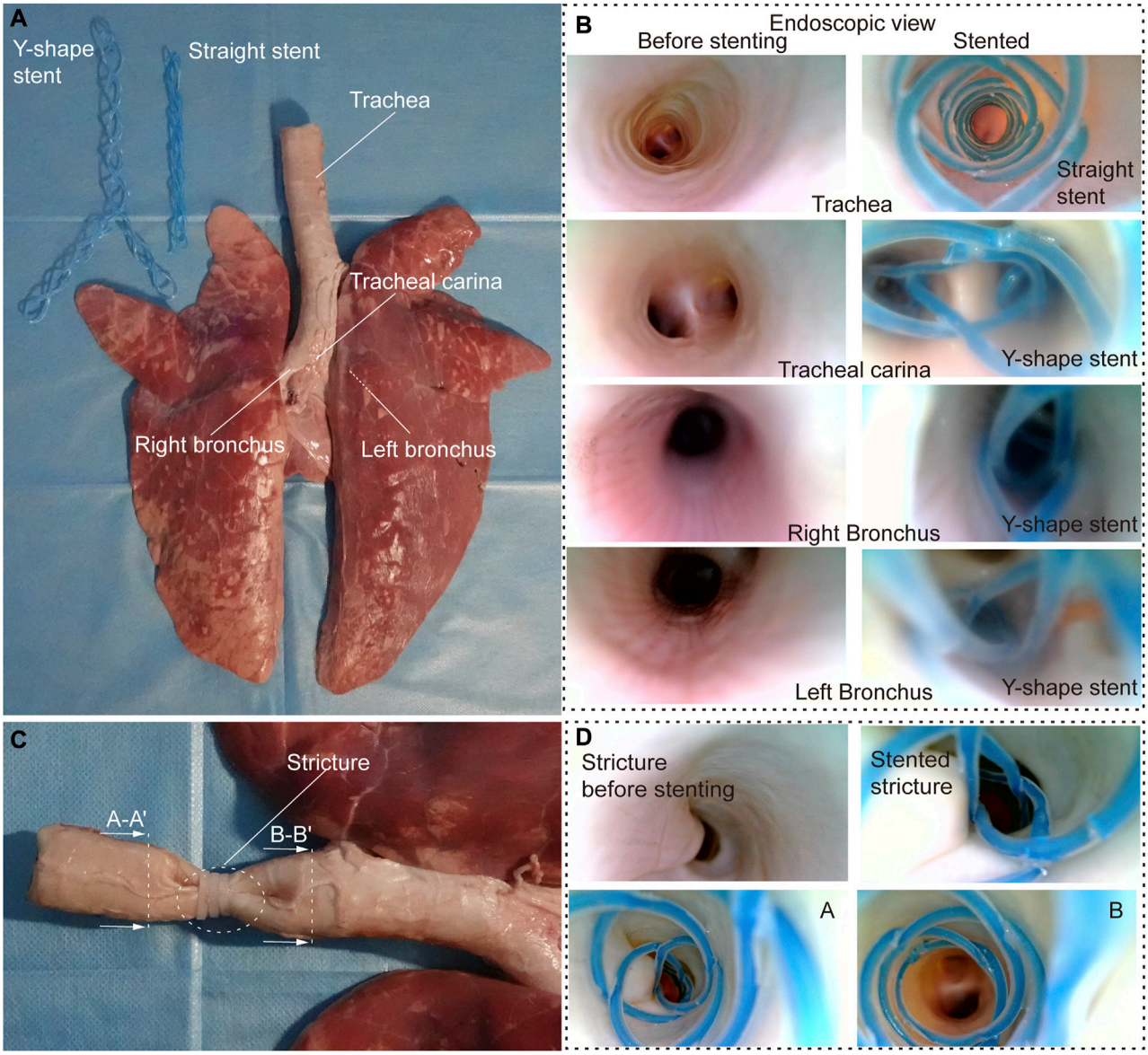

FIGURE 5
Ex vivo experiments. **(A)** *Ex vivo* swine airways and two types of stents used in the experiment. **(B)** Endoscopic view before (left) and after (right) stenting of the inner walls of the trachea, trachea carina, right and left bronchus. **(C)** Stricture created to simulate stenosis in the *ex vivo* trachea. **(D)** Endoscopic view before and after stenting in *ex vivo* trachea with stenosis.

C, the diameter at point B was much smaller, which is observed with an endoscope. This proved the stents adapted well to both the normal trachea model and the narrowed tracheal model.

Similarly, when the stenosis occurs at one end of airways, the conical stent will be a good choice. As shown in Figure 4B, a conical STB stent was cured in a conical tracheal model, and the endoscopic view clearly showed that the stent formed could match the inner wall of the phantom well. Therefore, it is safe to conclude that the straight STB stent could adapt to varied airway diameters.

The other three types of stents (T shape, L shape, and Y shape) investigated whether the proposed STB stent could provide support to different airway regions in more complicated scenarios. The T shape stent shown in Figure 4C was implanted into a tracheal model with incisions to simulate the functions of tracheostomy tubes. In Figures 4D, E, we 3D printed a transparent tracheobronchial model (transparent resin, Projet, SD system) to illustrate STB stent adapted to the trachea and bronchi at the same time. This 3D printed model with a thickness of 1 mm simulated a trachea with the outer diameter of 15 mm and the bronchi with outer diameters of 10 mm and 12 mm separately. The L shape stent and Y shape stent were delivered into and cured inside the model (Figures 4D, E). The results illustrates the proposed stents can be used for various complicated airway illness (Supplementary Video S4).

3.2.2 *Ex vivo* evaluation

To further evaluate the stenting performance of STB stents in real airways, we performed *ex vivo* experiments with trachea and

bronchi harvested from a swine (Figure 5A). The inner diameters of the trachea and bronchi are 17 mm, 13 mm, and 12 mm respectively, and endoscopic inspection were performed as shown in Figure 5B.

We tested the stents in normal airways to validate their basic functions and the delivering procedures. We cured a straight and a Y-shape STB stent separately, and endoscopic inspection were performed. It is clear that the stents adapted to the inner walls of the trachea well, and no visual mechanical injuries caused by the deployment procedure was found (Figure 5B). After that, to simulate the trachea stenosis, we manually created a 2-cm length stricture in the middle of the *ex vivo* swine trachea, by externally compressing the trachea wall with three zip ties (Figure 5C). The stricture constrained airway and left only approximately 1/5 of its original inner cross-sectional area, which simulated a severe tracheal stenosis (upper left panel in Figure 5D). To simulate the clinical procedure, we delivered a straight STB stent covered the stricture area. The stent was delivered with the above-mentioned balloon catheter, which is also used to conduct balloon dilation to open the stricture area by a little bit. The dilated stricture reopened to approximately 2/5 of its original cross-sectional area. The stent was successfully cured in the area and could support the trachea to avoid future stenosis. The endoscopic inspection is shown in (Figure 5D) and (Supplementary Video S5).

4 Discussion

This paper proposed a single-tube-braided airway stents for various airway illness. The contribution of this work is summarized here. We explained the design strategy and fabrication method for the proposed stents and six types of stents have been prototyped to demonstrate their adaptation to different airway structures. We also established a model to predict the influence of the design parameters on the radial stiffness of the stents under external compression. Then, experimentally verifications were conducted to investigate the deformation of the stents in response to external loads. It showed that the cured STB stents could bear a compression force of 5.79N, which is 145% of what could be tolerated by the previous stents, and proved the proposed stent has met the clinical requirements on stent stiffness. In addition, the fatigue property of the proposed stents was tested, and the stent could keep the phantom tracheal model open when suffered continuously loads of 10-cm water pressure at body temperature for a period of 30 days. Moreover, benchtop experiments and *ex vivo* evaluations on swine trachea and bronchi were conducted to further validate the practicability and adaptation of the proposed stents.

Our stent, compared to the commercial self-expandable metallic stents (SEMS), would not cause injuries to the tissue, and the geometrical design would not induce the growth of granulation tissues which may require invasive procedures to remove the stents out of the airway. In terms of the comparison with silicon stents in clinical trials, our stents can reduce the impediment on mucus flow and has less possibility to cause mucus plugs. In addition, the proposed stent shares the same advantage with the previous work that the stents can be easily screwed out of airways to reduce the chances to hurt the tissues, but this stent could provide more reliable and uniform supports to the trachea than the previous work. Moreover, the proposed braiding method provides possibility to manufacture all types of airways stents with the same fabrication technique.

5 Limitations of the study

Our study demonstrated the potential of STB stents, but there are still limitations which require further investigation in future works. 1) Fabrication: To fabricate a STB stent, we manually braided the tube on a 3D printed mold, which is not a standard fabrication technique. The errors in fabrication will add inaccuracy to the theoretical prediction. Thus, an automatic braiding equipment shall be built to improve the fabrication precision in the future. 2) Modeling: In this paper, to simplify the modeling process, we chose half elliptical beam as the representative for analysis. We also made a few assumptions or used approximated calculations formulas. Even though the modeling showed similar results to the experiments, the accuracy of theoretical model is limited. 3) Experiment: It is normal to find both continual and fluctuant breathes in real breathing. But in the water tank tests, the silicone tube was placed under water with the inner space connected to the atmosphere. The experiment only provided static tests but no dynamic physiological conditions were simulated. 4) Animal test: Only *ex vivo* experiment was conducted in this work. To further evaluate the practicability of STB stents in clinic procedures, we still need to conduct *in vivo* experiments to test the proposed stents in future.

Data availability statement

The raw data supporting the conclusion of this article will be made available by the authors, without undue reservation.

Ethics statement

The animal study was reviewed and approved by Shenzhen Advanced Animal Study Service Center. Written informed consent was obtained from the owner for the participation of their animal in this study.

Author contributions

XT, YJ, and YL designed the research. XT and YL conceived the original concept. XT performed the analytical and numerical work, conducted the experiments, and analyzed the data. FM and YJ assisted in the modeling. ZS and XW interpreted and discussed the experiments. XT and YJ wrote the original draft. XW advised the study and assisted in the writing of the manuscript. XT and YL revised the manuscript. YL supervised the research. All authors contributed to the preparation of the manuscript.

Funding

This work was supported by the National Natural Science Foundation of China under grant 62003334, Shenzhen Science and Technology Program under grant JCYJ20210324115609025, and National Major Scientific Instruments and Equipments Development Project of National Natural Science Foundation of China under grant 52227807.

Conflict of interest

The authors declare that the research was conducted in the absence of any commercial or financial relationships that could be construed as a potential conflict of interest.

Publisher's note

All claims expressed in this article are solely those of the authors and do not necessarily represent those of their affiliated organizations, or those of the publisher, the editors and the reviewers. Any product that may be evaluated in this article, or claim that may be made by its manufacturer, is not guaranteed or endorsed by the publisher.

Supplementary material

The Supplementary Material for this article can be found online at: https://www.frontiersin.org/articles/10.3389/fbioe.2023.1152412/full#supplementary-material

References

Almadi, M. A., Barkun, A., and Martel, M. (2017). Plastic vs. self-expandable metal stents for palliation in malignant biliary obstruction: A series of meta-analyses. *Official J. Am. Coll. Gastroenterology| ACG* 112 (2), 260–273. doi:10.1038/ajg.2016.512

Avasarala, S. K., Freitag, L., and Mehta, A. C. (2019). Metallic endobronchial stents: A contemporary resurrection. *Chest* 155 (6), 1246–1259. doi:10.1016/j.chest.2018.12.001

Bhora, F. Y., Ayub, A., Forleiter, C. M., Huang, C.-Y., Alshehri, K., Rehmani, S., et al. (2016). Treatment of benign tracheal stenosis using endoluminal spray cryotherapy. *JAMA Otolaryngology–Head Neck Surg.* 142 (11), 1082–1087. doi:10.1001/jamaoto.2016.2018

Carden, K. A., Boiselle, P. M., Waltz, D. A., and Ernst, A. (2005). Tracheomalacia and tracheobronchomalacia in children and adults: An in-depth review. *Chest* 127 (3), 984–1005. doi:10.1378/chest.127.3.984

Dasgupta, A., Dolmatch, B. L., Abi-Saleh, W. J., Mathur, P. N., and Mehta, A. C. (1998). Self-expandable metallic airway stent insertion employing flexible bronchoscopy: Preliminary results. *Chest* 114 (1), 106–109. doi:10.1378/chest.114.1.106

Dutau, H., Toutblanc, B., Lamb, C., and Seijo, L. (2004). Use of the dumon Y-stent in the management of malignant disease involving the carina: A retrospective review of 86 patients. *Chest* 126 (3), 951–958. doi:10.1378/chest.126.3.951

Folch, E., and Keyes, C. (2018). Airway stents. *Ann. Cardiothorac. Surg.* 7 (2), 273–283. doi:10.21037/acs.2018.03.08

Fraga, J. C., Jennings, R. W., and Kim, P. C. (2016). *Seminars in pediatric surgery*. Elsevier.Pediatric tracheomalacia

Guibert, N., Didier, A., Moreno, B., Lepage, B., Leyx, P., Plat, G., et al. (2019). Treatment of complex airway stenoses using patient-specific 3D-engineered stents: A proof-of-concept study. *Thorax* 74 (8), 810–813. doi:10.1136/thoraxjnl-2018-212732

Guibert, N., Saka, H., and Dutau, H. (2020). Airway stenting: Technological advancements and its role in interventional pulmonology. *Respirology* 25 (9), 953–962. doi:10.1111/resp.13801

Ha, J., Mondal, A., Zhao, Z., Kaza, A. K., and Dupont, P. E. (2019). Pediatric airway stent designed to facilitate mucus transport and atraumatic removal. *IEEE Trans. Biomed. Eng.* 67 (1), 177–184. doi:10.1109/tbme.2019.2910551

Hysinger, E. B., and Panitch, H. B. (2016). Paediatric tracheomalacia. *Paediatr. Respir. Rev.* 17, 9–15. doi:10.1016/j.prrv.2015.03.002

Long, J. A. (1988). *A method of monocanalicular silicone intubation*. NJ: SLACK Incorporated Thorofare, 204–205.

Madan, K., Dhooria, S., Sehgal, I. S., Mohan, A., Mehta, R., Pattabhiraman, V., et al. (2016). A multicenter experience with the placement of self-expanding metallic tracheobronchial Y stents. *J. Bronchology and Interventional Pulmonol.* 23 (1), 29–38. doi:10.1097/lbr.0000000000000250

Majid, A., Fernandez-Bussy, S., Kent, M., Folch, E., Fernandez, L., Cheng, G., et al. (2012). External fixation of proximal tracheal airway stents: A modified technique. *Ann. Thorac. Surg.* 93 (6), e167–e169. doi:10.1016/j.athoracsur.2012.01.094

Mathew, R., Hibare, K., Dalar, L., and Roy, W. E. (2020). Tracheobronchial stent sizing and deployment practices airway stenting practices around the world: A survey study. *J. Thorac. Dis.* 12 (10), 5495–5504. doi:10.21037/jtd-20-2080

Mencattelli, M., Mondal, A., Miale, R., Van Story, D., Peine, J., Li, Y., et al. (2021). *In vivo* molding of airway stents. *Adv. Funct. Mater.* 31 (20), 2010525. doi:10.1002/adfm.202010525

Mitchell, M. E., Rumman, N., Chun, R. H., Rao, A., Martin, T., Beste, D. J., et al. (2014). Anterior tracheal suspension for tracheobronchomalacia in infants and children. *Ann. Thorac. Surg.* 98 (4), 1246–1253. doi:10.1016/j.athoracsur.2014.05.027

Muir, T. (1902). Formula for the perimeter of an ellipse. *Nature* 66 (1703), 174–175. doi:10.1038/066174c0

Murgu, S. D., and Laxmanan, B. (2016). Biomechanical properties of airway stents: Implications for clinical practice. *J. Bronchology and Interventional Pulmonol.* 23 (2), 89–91. doi:10.1097/lbr.0000000000000267

Panitch, H. B., Allen, J. L., Alpert, B. E., and Schidlow, D. V. (1994). Effects of CPAP on lung mechanics in infants with acquired tracheobronchomalacia. *Am. J. Respir. Crit. care Med.* 150 (5), 1341–1346. doi:10.1164/ajrccm.150.5.7952562

Paunović, N., Bao, Y., Coulter, F. B., Masania, K., Geks, A. K., Klein, K., et al. (2021). Digital light 3D printing of customized bioresorbable airway stents with elastomeric properties. *Sci. Adv.* 7 (6), eabe9499. doi:10.1126/sciadv.abe9499

Pizer, B., Freeland, A., and Wilkinson, A. (1986). Prolonged positive airway pressure for severe neonatal tracheobronchomalacia. *Archives Dis. Child.* 61 (9), 908–909. doi:10.1136/adc.61.9.908

Ratwani, A. P., Davis, A., and Maldonado, F. (2022). Current practices in the management of central airway obstruction. *Curr. Opin. Pulm. Med.* 28 (1), 45–51. doi:10.1097/mcp.0000000000000838

Saad, C. P., Murthy, S., Krizmanich, G., and Mehta, A. C. (2003). Self-expandable metallic airway stents and flexible bronchoscopy: Long-term outcomes analysis. *Chest* 124 (5), 1993–1999. doi:10.1378/chest.124.5.1993

Saji, H., Furukawa, K., Tsutsui, H., Tsuboi, M., Ichinose, S., Usuda, J., et al. (2010). Outcomes of airway stenting for advanced lung cancer with central airway obstruction. *Interact. Cardiovasc. Thorac. Surg.* 11 (4), 425–428. doi:10.1510/icvts.2010.238196

Sehgal, I. S., Dhooria, S., Madan, K., Pattabhiraman, V., Mehta, R., Goyal, R., et al. (2017). Placement of tracheobronchial silicone Y-stents: Multicenter experience and systematic review of the literature. *Lung India Official Organ Indian Chest Soc.* 34 (4), 311. doi:10.4103/0970-2113.209241

Söküçü, S. N., Özdemir, C., Tural Önür, S., Dalar, L., and Altın, S. (2020). Comparison of silicon and metallic bifurcated stents in patients with malignant airway lesions. *Clin. Respir. J.* 14 (3), 198–204. doi:10.1111/crj.13114

Soriano, L., Khalid, T., Whelan, D., O'Huallachain, N., Redmond, K. C., O'Brien, F. J., et al. (2021). Development and clinical translation of tubular constructs for tracheal tissue engineering: A review. *Eur. Respir. Rev.* 30 (162), 210154. doi:10.1183/16000617.0154-2021

Torre, M., Carlucci, M., Speggiorin, S., and Elliott, M. J. (2012). Aortopexy for the treatment of tracheomalacia in children: Review of the literature. *Italian J. Pediatr.* 38 (1), 62–69. doi:10.1186/1824-7288-38-62

Weigle, C. G. (1990). Treatment of an infant with tracheobronchomalacia at home with a lightweight, high-humidity, continuous positive airway pressure system. *Crit. Care Med.* 18 (8), 892–894. doi:10.1097/00003246-199008000-00023

Wright, C. D., Li, S., Geller, A. D., Lanuti, M., Gaissert, H. A., Muniappan, A., et al. (2019). Postintubation tracheal stenosis: Management and results 1993 to 2017. *Ann. Thorac. Surg.* 108 (5), 1471–1477. doi:10.1016/j.athoracsur.2019.05.050

Xiong, X.-f., Xu, L., Fan, L.-l., Cheng, D.-y., and Zheng, B.-x. (2019). Long-term follow-up of self-expandable metallic stents in benign tracheobronchial stenosis: A retrospective study. *BMC Pulm. Med.* 19 (1), 33–10. doi:10.1186/s12890-019-0793-y

frontiers | Frontiers in Bioengineering and Biotechnology

TYPE Original Research
PUBLISHED 30 May 2023
DOI 10.3389/fbioe.2023.1172934

OPEN ACCESS

EDITED BY
Junyan Li,
Southwest Jiaotong University, China

REVIEWED BY
Yuanqiao Wu,
Boston University, United States
Jonathan Kusins,
NuVasive, United States

*CORRESPONDENCE
Junsong Wang,
waterandfood2022@163.com
Peifu Tang,
pftang301@126.com
Wei Zhang,
bszw@hotmail.com

RECEIVED 24 February 2023
ACCEPTED 25 April 2023
PUBLISHED 30 May 2023

CITATION
Jiang Y, Cui X, Ji W, Li J, Shi Y, Zhao J, Wang J, Tang P and Zhang W (2023), Novel uniplanar pedicle screw systems applied to thoracolumbar fractures: a biomechanical study.
Front. Bioeng. Biotechnol. 11:1172934.
doi: 10.3389/fbioe.2023.1172934

Novel uniplanar pedicle screw systems applied to thoracolumbar fractures: a biomechanical study

Yuheng Jiang[1,2,3], Xiang Cui[1,2], Wei Ji[1], Jia Li[1,2], Yanli Shi[4], Jingxin Zhao[1,2], Junsong Wang[1,2]*, Peifu Tang[1,2]* and Wei Zhang[1,2]*

[1]Department of Orthopedics, Chinese PLA General Hospital, Beijing, China, [2]National Clinical Research Center for Orthopaedics, Sports Medicine and Rehabilitation, Beijing, China, [3]Department of Orthopedics, General Hospital of Southern Theater Command of PLA, Guangzhou, China, [4]Anesthesia and Operation Center, The First Medical Center of Chinese PLA General Hospital, Beijing, China

Objective: In this study, the advantages of the internal fixation configuration composed of uniplanar pedicle screws in the treatment of thoracolumbar fractures were verified by biomechanical experimental methods, which provided the basis for subsequent clinical experiments and clinical applications.

Methods: A total of 24 fresh cadaveric spine specimens (T12-L2) were utilized to conduct biomechanical experiments. Two different internal fixation configurations, namely, the 6-screw configuration and the 4-screw/2-NIS (new intermediate screws) configuration, were tested using fixed-axis pedicle screws (FAPS), uniplanar pedicle screws (UPPS), and polyaxial pedicle screws (PAPS) respectively. The spine specimens were uniformly loaded with 8NM pure force couples in the directions of anteflexion, extension, left bending, right bending, left rotation, and right rotation, and the range of motion (ROM) of the T12-L1 and L1-L2 segments of the spine was measured and recorded to access biomechanical stability.

Results: No structural damage such as ligament rupture or fracture occurred during all experimental tests. In the 6-screw configuration, the ROM of the specimens in the UPPS group was significantly better than that of the PAPS group but weaker than those of the FAPS group ($p < 0.01$). In the 4-screw/2-NIS configuration, the results were identical to the biomechanical test results for the 6-screw configuration ($p < 0.01$).

Conclusion: Biomechanical test results show that the internal fixation configuration with UPPS can maintain the stability of the spine well, and the results are better than that of PAPS. UPPS has both the biomechanical advantages of FAPS and the superiority of easy operation of PAPS. We believe it is an optional internal fixation device for minimally invasive treatment of thoracolumbar fractures.

KEYWORDS

biomechanical study, uniplanar pedicle screw, intermediate screw, thoracolumbar fractures, screw tulip design

1 Introduction

Thoracolumbar fractures are a common consequence of external forces that result in continuous destruction of thoracic and lumbar vertebrae. With the increasing global aging population, the incidence of such fractures is on the rise. Pedicle screw and rod configuration is the most used surgical intervention. The surgery includes key steps such as fracture reduction and spinal stabilization. Fixed-axis pedicle screws (FAPS) have been the standard equipment for open internal fixation of the spine. However, during the operation of traditional open surgery, the soft tissue retraction may cause muscle crushing injury, destroy the muscle attachment point, *etc.*, which may cause postoperative pain and fatigue of the lower back muscles, extended recovery time, and in extreme cases, spinal function impairment.

In recent years, the use of posterior spine minimally invasive screw placement has become increasingly popular due to its effectiveness in addressing the limitations of traditional open surgery. By limiting the surgical approach's breadth, minimally invasive surgery reduces soft tissue injury and the probability of postoperative low back pain and muscle weakening. FAPS must, however, be placed in the same plane and at the same depth during operation to allow for the connecting rod's smooth insertion. The limited exposure of the minimally invasive surgical field and variations in surgeon expertise make inserting the connecting rod for FAPS challenging, resulting in increased operation time and variability in the operation's outcome.

Surgeons are continuously seeking new pedicle screw fixation systems that are more convenient for minimally invasive surgery while maintaining biomechanical advantages. Among the available solutions, the polyaxial pedicle screw (PAPS) has been commonly employed. However, its overall biomechanics are weaker than those of fixed-axis pedicle screws (FAPS), resulting in the loss of vertebral body anterior height during the healing process (Yao et al., 2021). We must therefore create new pedicle internal fixation products that are stronger biomechanically and have superior therapeutic outcomes.

To ensure the overall biomechanical advantage of internal fixation and facilitate minimally invasive surgical operations, we designed a new uniplanar pedicle screw (UPPS) (Figure 1). The screw head of UPPS has a limited range of motion within one plane while remaining fixed in other planes. Theoretically, the free movement of the screw head on the axial plane of the body does not sacrifice the stiffness of the entire internal fixation structure on the sagittal plane, and at the same time facilitates the insertion of the connecting rod. UPPS offers the advantages of both FAPS and PAPS and is ideal for minimally invasive posterior spinal surgery (Peck et al., 2021).

In addition, our previous conducted research using the finite element method and found that a four pedicle screws and two modified new intermediate screws (NIS) had similar biomechanical advantages compared to the six-pedicle screw configuration (Li et al., 2020; Guo et al., 2021). This configuration allows bilateral intermediate screws to reach the center of the injured vertebra, elevate the depressed endplate, and maintain its reduction position more efficiently than the traditional parallel configuration of pedicle screws. The new configuration can enhance internal fixation strength and enable simultaneous vertebroplasty and bone grafting

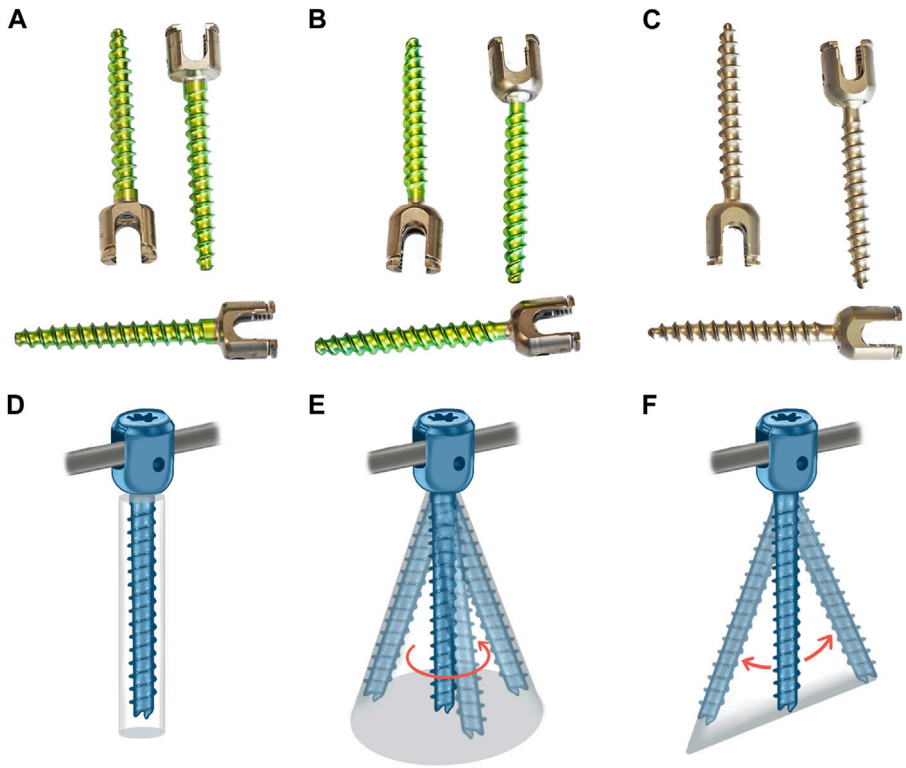

FIGURE 1
Three different pedicle screws and their schematic diagrams: **(A)** FAPS; **(B)** PAPS; **(C)** UPPS; **(D)** FAPS; **(E)** PAPS; **(F)** UPPS.

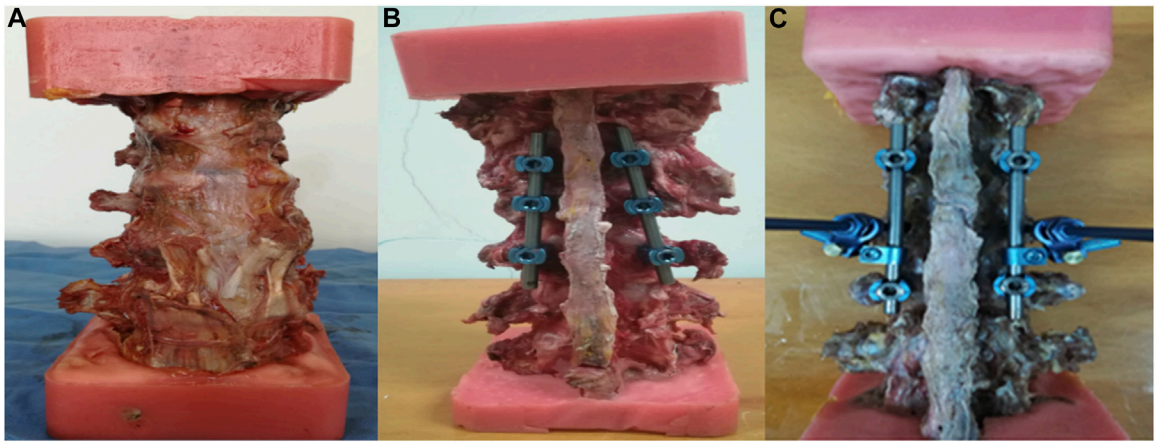

FIGURE 2
Show the spinal specimen and samples after internal fixation procedures. **(A)** Normal fresh cadaveric spine specimens; **(B)** 6-screw configuration; **(C)** 4-screw/2-NIS configuration.

procedures by surgeons. However, further research is needed to determine whether UPPS is applicable to this new configuration.

In this paper, the range of motion of the vertebral body in the T12-L1 and L1-L2 segments was measured using different internal fixation devices through biomechanical research methods. The biomechanical advantages of the UPPS internal fixation system were verified by comparing the differences in the vertebral body movements in the six spatial directions, including flexion, extension, left bending, right bending, left rotation, and right rotation. The following report presents the results of our research.

2 Materials and methods

2.1 Design and manufacture of uniplanar pedicle screws and new intermediate screws

The 3D model of UPPS was created using Solidworks software (Dassault Systèmes, Concord, MA, United States). This screw has an inner diameter of 4.1 mm and an outer diameter of 6 mm, and its hollow design enables minimally invasive insertion, with a 2 mm diameter hollow lumen. Unlike FAPS, the UPPS has a head-shank connection that allows for a ±30° range of motion on the body axis. Spot welding is used in the manufacturing process to minimize the movement of the head-shank in other directions.

The new intermediate screw was developed based on the USS® cannulated schanz screw. The NIS design features threads situated at the one-third shank, with a smooth section in the middle.

2.2 Specimen preparation

A total of 24 normal fresh cadaveric spine specimens (T12-L2) were carefully selected for this study. Each specimen was examined visually and with X-ray observation to ensure that no damage to the functional unit of the spine or abnormal bony structures were present. After removing the superficial muscle, fat and soft tissue, the inter-articular ligament and intervertebral disc structure were preserved. The specimens were then wrapped in double-layer plastic bags and stored at −20°C for later use. Prior to testing, the specimens were thawed at room temperature for 5 h. To create a model of fracture, cuneiform osteotomy was performed on the L1 vertebral body. The sample, test purpose, process, and post-test treatment process were approved by the Guangdong Provincial Medical Biomechanics Laboratory and related units, and all the procedures were carried out in accordance with the ethics guidelines established by the Chinese PLA General Hospital, Beijing, China.

2.3 Groups

The biomechanical test comprised two parts. In the first part, we aimed to investigate the biomechanical differences among UPSS, FAPS, and PAPS for the short-segment 6-screw configuration, respectively. The three groups were labeled as follows:1) 6-UPPS 2) 6-FAPS 3) 6-PAPS. The second part of the experiment was designed to compare the biomechanical differences of the three types of pedicle screws in the 4-screw configuration with two-NIS. This was labeled as follows: 1) 4-UPPS/2-NIS; 2) 4-FAPS/2-NIS; 3) 4-PAPS/2-NIS (Figure 2). To ensure proper experimental design and grouping, we equally divided the 24 specimens into 6 groups, with 4 samples in each group.

2.4 Surgical operation

In the first part of the experiment, 6 pedicle screws were inserted into each specimen, with two screws placed in each of the T12, L1, and L2 segments. The screws were all 6.0 mm in diameter and 45 mm in length and connected longitudinally by connecting rods without cross-links. A standard surgical procedure was followed by the same experienced surgeon, adhering strictly to the manufacturer's specifications for screw placement.

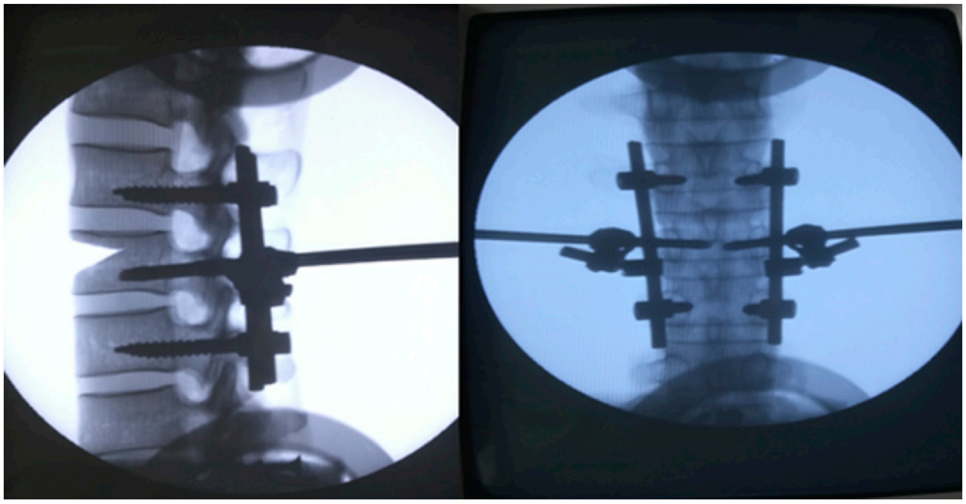

FIGURE 3
X-rays were used to confirm the success of the internal fixation insertion.

In the second part of the experiment, 4 pedicle screws were inserted into each specimen, with 2 screws placed in each of the T12 and L2 levels. The newly developed NIS screw was inserted laterally at the L1 level, which is hollow and has inner and outer diameters of 5.2 and 6 mm, respectively. The NIS screw was connected to the longitudinal rod connecting the T12 and L1 pedicle screws through a connecting device. The rest of the surgical procedure was the same as in the first part, and was performed by a deputy chief physician with extensive surgical experience.

After the placement of internal fixation for each specimen was completed, the effectiveness of the placement was confirmed by taking an X-ray (Figure 3).

2.5 Biomechanical tests

To maintain the mechanical properties of fresh specimens and ensure accurate test results, the entire test procedure for each specimen must be completed within 8 h. In the event of ligament rupture, fracture, or intervertebral disc herniation, testing of the affected specimen must be discontinued, and a replacement specimen must be used for subsequent testing.

The testing process is to place the specimen on the pure force couple loading table, fix the L2 vertebral body, and allow the T12 vertebral body to move freely. The T12 vertebral body is connected with the force couple loading link, and the 8NM pure force couple is uniformly loaded on the six degrees of freedom of flexion, extension, left bending, right bending, left rotation, and right rotation. The motion and force characteristics of the specimen are evaluated under the same loading conditions.

The motion capture system and EVaRT software (Motion Analysis Company, United States) were used to measure the absolute value of range of motion (ROM) of each segment of the specimen (Figure 4). The system employs the Edge-8 high-speed infrared capture lens, which can achieve fast (response time <0.001s) and high-precision (0.001 mm) capture of Marker point space coordinates.

2.6 Statistical analysis

Statistical analysis was performed using SPSS 19.0 software, and the results were presented in the form of mean ± standard deviation. Statistical differences between groups were compared using one-way ANOVA. Significance was defined as $p < 0.05$.

3 Results

3.1 Spinal ROM in 6-screw configuration group

During the biomechanical testing of the 6-screw configuration, no instances of ligament rupture or bony structure compromise were observed in any of the specimens.

3.1.1 ROM of T12-L1 level

At the T12-L1 level, with the 6-screw configuration composed of UPPS, the ROM of the spine in six degrees of freedom of flexion, extension, left curvature, right curvature, left rotation, and right rotation was 0.44° ± 0.04°, 0.73° ± 0.01°, 0.46° ± 0.02°, 0.63° ± 0.05°, 0.52° ± 0.01°, and 0.50° ± 0.06°, respectively. These results are significantly better than the 6-screw configuration composed of PAPS at all degrees of freedom levels ($p < 0.01$) (Figure 5). Besides, in specimens using FAPS, the ROM at the T12-L1 level was also found to be superior to those using PAPS (Supplementary Table S1).

3.1.2 ROM of L1-L2 level

At the L1-L2 level, with the 6-screw configuration composed of UPPS, the ROM of the spine under loads of flexion, extension, left

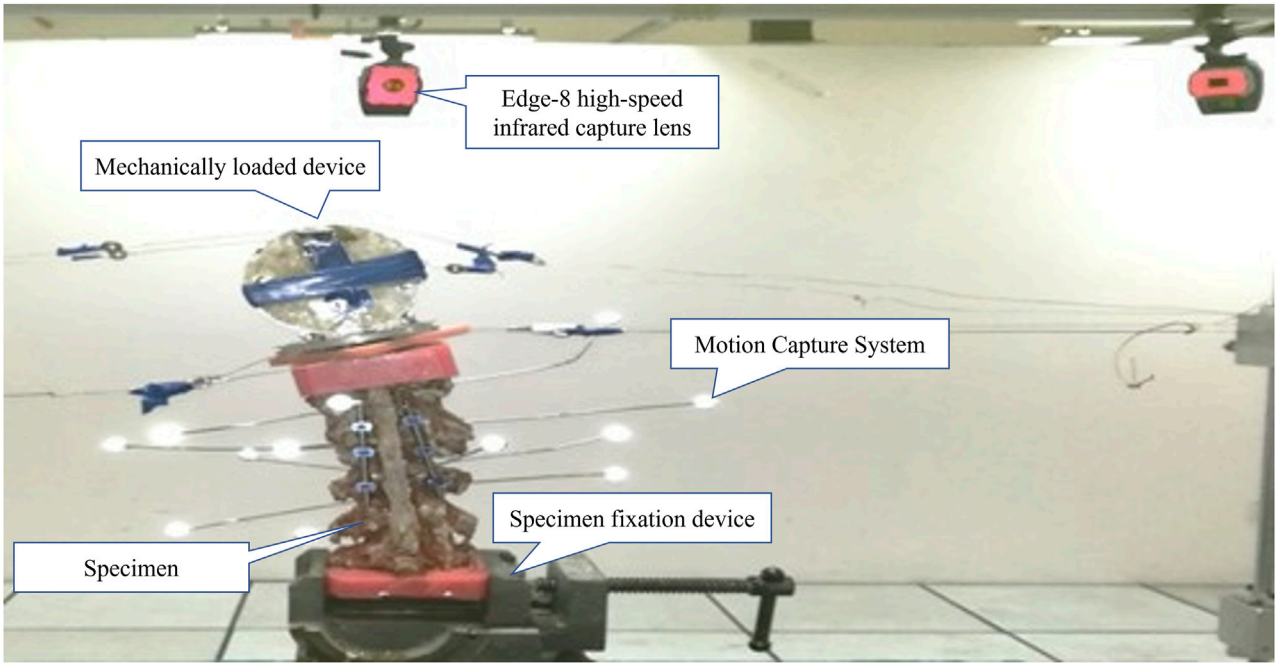

FIGURE 4
Sample in motion capture system.

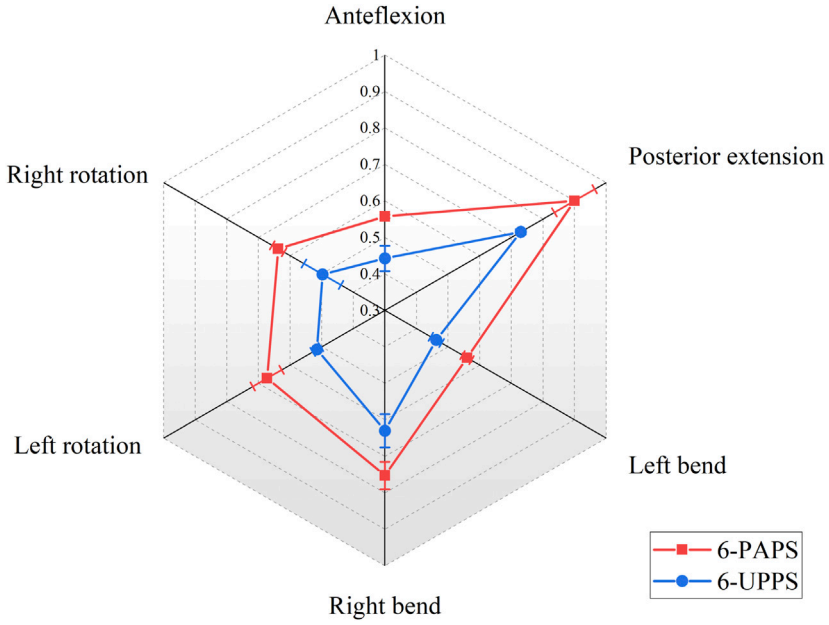

FIGURE 5
Show the ROM (°) of the T12-L1 segment in 6-screw configurations.

curve, right curve, left rotation, and right rotation were 0.63° ± 0.09°, 0.51° ± 0.05°, 0.48° ± 0.02°, 0.58° ± 0.04°, 0.54° ± 0.03°, and 0.47° ± 0.01°, respectively. Similar to the T12-L1 level, this result was also significantly better than the 6-screw configuration composed of PAPS at all degrees of freedom levels ($p < 0.01$) (Figure 6). The specimens utilizing FAPS demonstrated superior spinal range of motion at the L1-L2 level compared to those using PAPS as well (Supplementary Table S2).

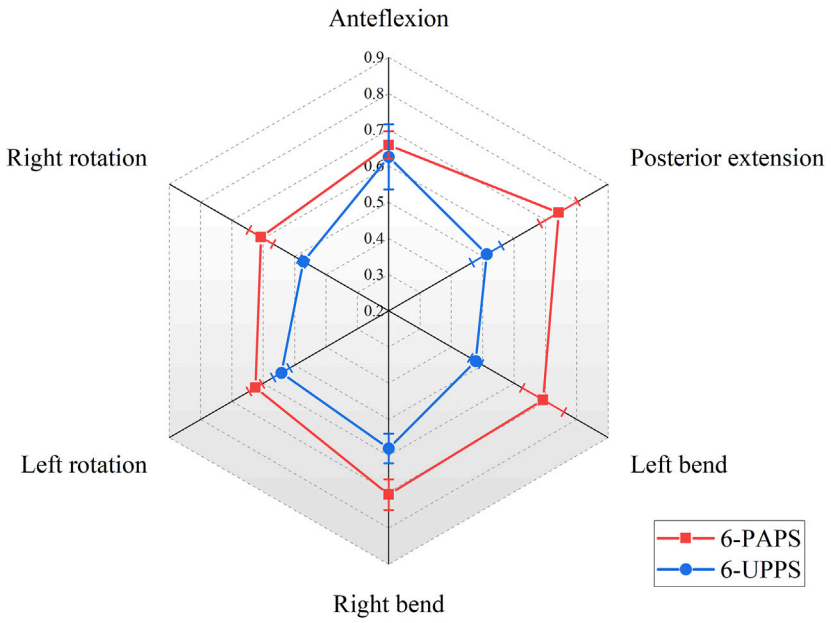

FIGURE 6
Show the ROM (°) of the L1-L2 segment in 6-screw configurations.

3.2 Spinal ROM in 4-screw/2-NIS configuration group

During the biomechanical testing of the 4-screw/2-NIS configuration, no significant damage or destruction of load-bearing structures such as ligaments or bony structures were observed.

3.2.1 ROM of T12-L1 level

The internal fixation configuration composed of 4 UPPS and 2 NIS made the ROM of the spine model at the T12-L1 level under flexion, extension, left bending, right bending, left rotation, and right rotation force couples to be 0.52° ± 0.01°, 0.71° ± 0.06°, 0.76° ± 0.03°, 0.64° ± 0.02°, 0.76° ± 0.04°, and 0.64° ± 0.02°, respectively. The results were superior to the configuration consisting of 4 PAPS/2 NIS ($p < 0.01$) (Figure 7). In addition, ROM of the spine at the T12-L1 level in specimens that utilized 4-FAPS/2-NIS was found to be superior compared to those utilizing 4-PAPS/2-NIS (Supplementary Table S3).

3.2.2 ROM of L1-L2 level

At the L1-L2 level, the 4-UPPS/2-NIS configuration also showed better spinal stability than 4-PAPS/2-NIS ($p < 0.01$) (Figure 8). The ROM under flexion, extension, left bending, right bending, left rotation and right rotation couples were 0.55° ± 0.03°, 0.68° ± 0.04°, 0.66° ± 0.01°, 0.69° ± 0.06°, 0.67° ± 0.04°, and 0.64° ± 0.04°, respectively. Additionally, according to the results of the experiment, ROM of the spine at the L1-L2 level in specimens that utilized 4-FAPS/2-NIS was also found to be superior compared to those utilizing 4-PAPS/2-NIS (Supplementary Table S4).

4 Discussion

This study provides evidence that UPPS confers unquestionable biomechanical advantages in spinal surgery. Biomechanical testing of both 6-screw and 4-screw configurations revealed no damage or destruction to load-bearing structures such as ligaments and bones. Additionally, we measured the ROM of each spine segment in six degrees of spatial freedom. ROM partially reflects the mechanical stability of the fused vertebral body in biomechanical experiments. Our findings indicate that the use of UPPS screws results in superior biomechanical stability compared to PAPS models. These results have significant implications for the treatment of spinal pathologies with minimally invasive surgery, expanding the range of available surgical options.

Minimally invasive spine surgery minimizes the incidence of postoperative low back pain and weakness in patients with open posterior spine surgery. Clinical application also verified the protection effect of the back muscles by the minimally invasive spine surgery. Kim et al. compared the trunk muscle strength of patients who underwent open posterior spinal fixation and those who underwent percutaneous internal fixation and found that the lumbar spine extension improved by more than 50% in patients who underwent percutaneous fixation, but not in patients who underwent open surgery (Kim et al., 2005). Kawaguchi et al. (1994) performed muscle biopsies on patients who underwent spinal revision surgery and observed atrophy of both type I and type II muscle fibers, extensive branching of fibrous tissue, and a "moth-eaten" appearance (Zhao et al., 2000). This behavior is caused by muscle compression, similar to the use of pneumatic tourniquets in extremity surgery. Additionally, denervation is thought to be the mechanism of muscle degeneration and atrophy after traditional

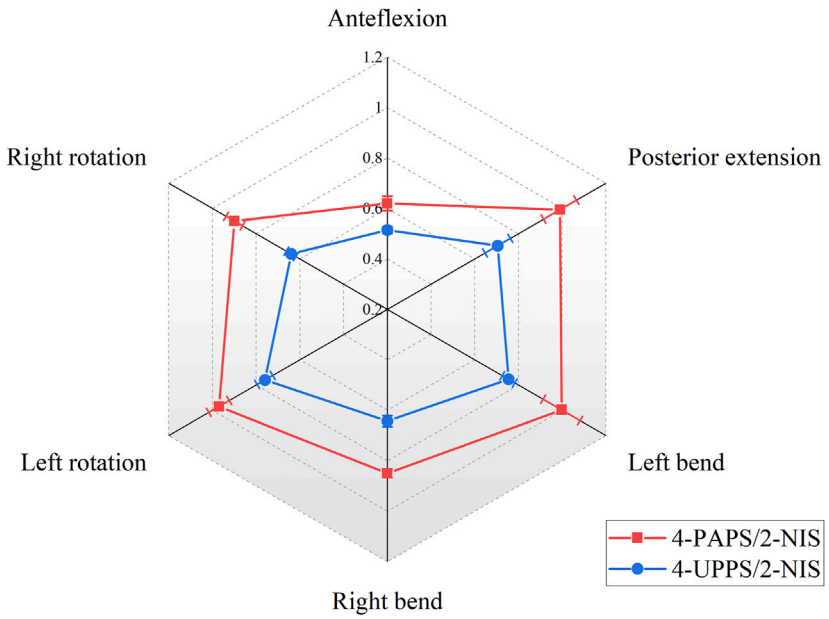

FIGURE 7
Show the ROM (°) of the T12-L1 segment in 4-screw/2-NIS configurations.

open surgery. Multifidus, a muscle with a single-segmental distribution of nerves, is particularly vulnerable to injury (Hodges et al., 2006). Prolonged stretches can cause damage at the neuromuscular junction, leading to muscle denervation and postoperative muscle degeneration and atrophy.

Given the advantages of minimally invasive surgery, a matching pedicle screw design is required. The conventional FAPS is secured between the threaded section and the head, which provides high mechanical stability after vertebral body fusion. Our research further supported this claim. At levels of T12-L1 and L1-L2, FAPS screws had the least ROM values across all setups, indicating greater biomechanical stability. However, the use of FAPS requires precise alignment of the pedicle screw caps of each spinal segment on the same horizontal line to ensure insertion of the connecting rod. Unfortunately, the limited exposure of the minimally invasive surgical field and the challenging passage of the rod make it difficult to perform this task. Moreover, the already constrained operating environment is made even more constrained by the employment of the screw sleeve throughout the surgical procedure. This leads to prolongation of operation time and poor treatment outcomes in some patients. Thus, the benefits of minimally invasive surgery may be outweighed by the challenges posed by the FAPS system.

In 2001, Foley et al. (2001) have developed the PAPS system. Using the geometric trajectory principle, the connecting rod can be inserted into the deep muscle precisely and conveniently. It has undergone revolutionary changes and is currently the most widely used pedicle fixation device for minimally invasive posterior spine surgery. However, due of the mobility between the PAPS head and threaded component, the total configuration's sagittal mechanical strength is decreased. Its surgical impact is also less than that of FAPS since it cannot be employed as a tool for fracture reduction and lacks intervertebral compression and distraction capabilities.

This study demonstrated that the ROM of the spine was the largest in the configuration composed of PAPS, indicating that the stability of the spine was worse. This is consistent with other research findings. Palmisani reported in a retrospective study that the use of polyaxial pedicle screws which are less rigid and might therefore increase the risk of loss of correction with time (Palmisani et al., 2009). A study by Shim also found that the use of PAPS is not conducive to restoring the height of the anterior column of the vertebral body and correcting kyphosis (Shim and Seo, 2022). A previous finite element study of ours also confirmed that the stabilization of the spine was worse with PAPS than with FAPS. In addition, during flexion and extension of the spine, the overall von Mises stress of the internal fixation using PAPS was higher, indicating that the biomechanical performance of the internal fixation was poor (Li et al., 2020).

UPPS was designed to address the fixation challenges encountered during minimally invasive spine surgery, particularly in situations where the use of PAPS is not desirable from a biomechanical standpoint. Our findings support the notion that UPPS offers superior biomechanical benefits compared to PAPS. Although our experimental data show that FAPS has higher biomechanical stability than UPPS, there might not be a significant difference between the two in clinical practice. Yebin confirmed that the therapeutic effects of UPPS and FAPS were comparable in the follow-up period of 12–18 months through a retrospective research of 204 patients. Patients treated with UPPS experienced less intraoperative bleeding and spent less time in the hospital. Additionally, when it comes to restoring the anterior vertebral body's height following surgery, UPPS and FAPS have comparable results (Ye et al., 2022). This demonstrates that UPPS

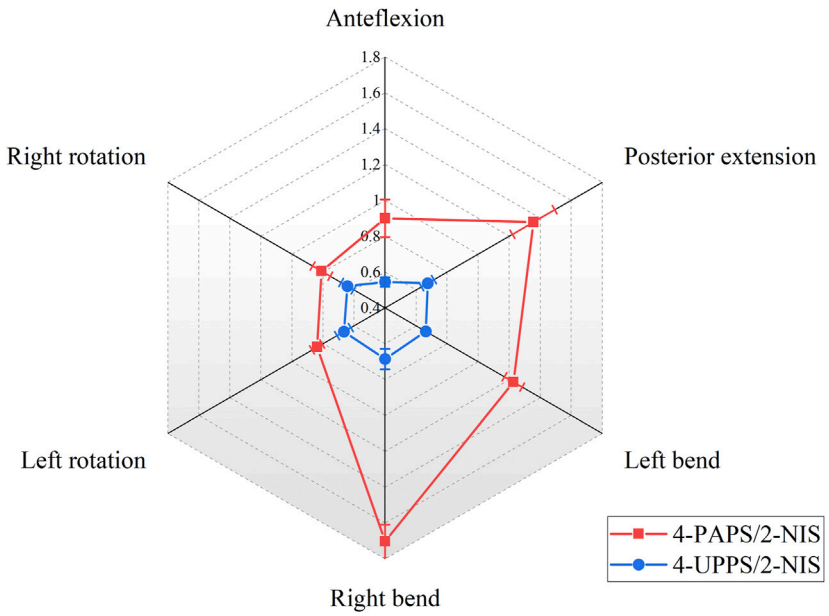

FIGURE 8
Show the ROM (°) of the L1-L2 segment in 4-screw/2-NIS configurations.

combines the advantages of FAPS and PAPS, ensuring sufficient biomechanical stability while facilitating the operation and reducing the risk of postoperative complications.

The biomechanics benefits of UPPS have also been supported by earlier investigations. Ye and Luo compared the ultimate load of FAPS, UPPS, and PAPS for internal fixation failure in static and dynamic biomechanical tests. They confirmed that UPPS has better axial mechanical stiffness than PAPS, which can reduce the risk of loss of reduction (Ye et al., 2017). The use of long segmental fixation for spinal fusion in this work, however, raises concerns about multi-segment damage and aberrant stress distribution. Liu et al. (2019) tested three types of screws and recorded two parameters that affect the retentive force including the tilt angle and the nut tightening torque. They found that the tulip-rod interface of FAPS frequently has a tilt angle, and this greatly reduces the retentive force. Therefore, Serhan et al. (2010) advocated for the use of polyaxial or uniplanar screws at the distal end of long spinal constructs since these screws increase the strength of the rod-tulip interface, and tilt angle occurs frequently at the distal end of long spinal constructs.

Intermediate screw have been developed to facilitate vertebroplasty and reduction maneuver (Baaj et al., 2011; Wang et al., 2012; Liao et al., 2017; Basaran et al., 2019). According to our prior article's finite element analysis, the configuration of employing two new intermediate screws instead of two pedicle screws in the center can give appropriate biomechanical strength for the treatment of vertebral fractures (Li et al., 2020; Guo et al., 2021). In this paper, we continued our prior study by conducting biomechanical experiments using the newly designed intermediate screw. The results demonstrated that the 4UPPS/2NIS configuration was superior to 4PAPS/2NIS, consistent with the findings of the 6-screw configuration. In addition, the new intermediate screws offer benefits for both vertebroplasty and fracture reduction simultaneously. The new intermediate screw is placed in a manner, that is, more outside-in than typical pedicle screws, which enables it to reach the center of the fractured vertebral body and elevate the compressed endplate for better maintenance of reduction. Additionally, the newly created NIS nail features a lateral window at the distal end, that is, practical for bone grafting or filling with bone cement, enabling concurrent vertebroplasty during the procedure. By contrast, the traditional use of short-segment fixation requires the middle pedicle screw to be pulled out for bone cement filling or bone grafting after fracture reduction, then reinserted after vertebroplasty, which interrupts the normal operation and prolongs the operation time (Chen et al., 2014; Li et al., 2016). Our designed NIS simplifies the surgical procedure by allowing for vertebroplasty through the lateral window after reduction and fixation.

There are several limitations to this study that need to be addressed. Firstly, the biomechanical specimens used in this study were derived from normal spines, and the biomechanical characteristics of pathological spines, such as those with osteoporosis, may differ. Secondly, this study did not test the ultimate load of internal fixation, which could provide additional information on the stability of the constructs. Additionally, there are various similar screws available in clinical practice, but this study only compared one type of FAPS and PAPS. These are issues that warrant more study.

5 Conclusion

The biomechanical test findings revealed that the configuration employing the innovative UPPS had strong biomechanical benefits

and assured spine stability. UPPS combines the biomechanical advantages of FAPS with the ease of use of PAPS. It is an optional minimally invasive internal fixation device for the treatment of thoracolumbar fractures.

Data availability statement

The original contributions presented in the study are included in the article/Supplementary Material, further inquiries can be directed to the corresponding authors.

Ethics statement

The studies involving human participants were reviewed and approved by the Chinese PLA general hospital. The patients/participants provided their written informed consent to participate in this study.

Author contributions

WZ and PT did the conception and design. YJ, YS, and WJ performed the acquisition of data. JZ and XC performed the analysis and interpretation of data. JL and WZ critically revised the article. All authors reviewed the submitted version of the manuscript. WZ, PT, and JW approved the final version of the manuscript on behalf of all authors. YJ and JL supervised the study. YJ, XC, and WJ contributed equally to this work.

Funding

This work was supported by National Key Research and Development Program of China (2022YFC2504302) and Innovation Program in Military Medicine of Chinese People's Liberation Army (16CXZ043).

Conflict of interest

The authors declare that the research was conducted in the absence of any commercial or financial relationships that could be construed as a potential conflict of interest.

Publisher's note

All claims expressed in this article are solely those of the authors and do not necessarily represent those of their affiliated organizations, or those of the publisher, the editors and the reviewers. Any product that may be evaluated in this article, or claim that may be made by its manufacturer, is not guaranteed or endorsed by the publisher.

Supplementary material

The Supplementary Material for this article can be found online at: https://www.frontiersin.org/articles/10.3389/fbioe.2023.1172934/full#supplementary-material

References

Baaj, A. A., Reyes, P. M., Yaqoobi, A. S., Uribe, J. S., Vale, F. L., Theodore, N., et al. (2011). Biomechanical advantage of the index-level pedicle screw in unstable thoracolumbar junction fractures. *J. Neurosurg. Spine* 14, 192–197. doi:10.3171/2010.10.SPINE10222

Basaran, R., Efendioglu, M., Kaksi, M., Celik, T., Mutlu, İ., and Ucar, M. (2019). Finite element analysis of short- versus long-segment posterior fixation for thoracolumbar burst fracture. *World Neurosurg.* 128, e1109–e1117. doi:10.1016/j.wneu.2019.05.077

Chen, C., Lv, G., Xu, B., Zhang, X., and Ma, X. (2014). Posterior short-segment instrumentation and limited segmental decompression supplemented with vertebroplasty with calcium sulphate and intermediate screws for thoracolumbar burst fractures. *Eur. Spine J. Off. Publ. Eur. Spine Soc. Eur. Spinal Deform. Soc. Eur. Sect. Cerv. Spine Res. Soc.* 23, 1548–1557. doi:10.1007/s00586-014-3374-z

Foley, K. T., Gupta, S. K., Justis, J. R., and Sherman, M. C. (2001). Percutaneous pedicle screw fixation of the lumbar spine. *Neurosurg. Focus* 10, 1–9. doi:10.3171/foc.2001.10.4.11

Guo, H., Li, J., Gao, Y., Nie, S., Quan, C., Li, J., et al. (2021). A finite element study on the treatment of thoracolumbar fracture with a new spinal fixation system. *Biomed. Res. Int.* 2021, 1–9. doi:10.1155/2021/8872514

Hodges, P., Holm, A. K., Hansson, T., and Holm, S. (2006). Rapid atrophy of the lumbar multifidus follows experimental disc or nerve root injury. *Spine* 31, 2926–2933. doi:10.1097/01.brs.0000248453.51165.0b

Kawaguchi, Y., Matsui, H., and Tsuji, H. (1994). Back muscle injury after posterior lumbar spine surgery: Part 2: Histologic and histochemical analyses in humans. *Spine* 19, 2598–2602. doi:10.1097/00007632-199411001-00018

Kim, D.-Y., Lee, S.-H., Chung, S. K., and Lee, H.-Y. (2005). Comparison of multifidus muscle atrophy and trunk extension muscle strength: Percutaneous: Versus: Open pedicle screw fixation. *Spine* 30, 123–129. doi:10.1097/01.brs.0000148999.21492.53

Li, J., Zhang, L.-C., Li, J., Zhang, H., Zhao, J.-X., and Zhang, W. (2020). A hybrid uniplanar pedicle screw system with a new intermediate screw for minimally invasive spinal fixation: A finite element analysis. *Biomed. Res. Int.* 2020, 1–9. doi:10.1155/2020/5497030

Li, Q., Yun, C., and Li, S. (2016). Transpedicular bone grafting and pedicle screw fixation in injured vertebrae using a paraspinal approach for thoracolumbar fractures: A retrospective study. *J. Orthop. Surg.* 11, 115. doi:10.1186/s13018-016-0452-4

Liao, J.-C., Chen, W.-P., and Wang, H. (2017). Treatment of thoracolumbar burst fractures by short-segment pedicle screw fixation using a combination of two additional pedicle screws and vertebroplasty at the level of the fracture: A finite element analysis. *BMC Musculoskelet. Disord.* 18, 262. doi:10.1186/s12891-017-1623-0

Liu, P.-Y., Lai, P.-L., and Lin, C.-L. (2019). A biomechanical investigation of the retentive force of pedicle screw structures for different screw tulip designs. *Clin. Biomech. Bristol Avon* 70, 23–30. doi:10.1016/j.clinbiomech.2019.06.003

Palmisani, M., Gasbarrini, A., Brodano, G. B., De Iure, F., Cappuccio, M., Boriani, L., et al. (2009). Minimally invasive percutaneous fixation in the treatment of thoracic and lumbar spine fractures. *Eur. Spine J. Off. Publ. Eur. Spine Soc. Eur. Spinal Deform. Soc. Eur. Sect. Cerv. Spine Res. Soc.* 18, 71–74. doi:10.1007/s00586-009-0989-6

Peck, J. H., Cadel, E., Palepu, V., Ferrell, B. M., and Warner, C. H. (2021). Mechanical performance of thoracolumbosacral pedicle screw systems: An analysis of data submitted to the Food and Drug Administration. *J. Biomech.* 125–110551. doi:10.1016/j.jbiomech.2021.110551

Serhan, H., Hammerberg, K., O'Neil, M., Sturm, P., Mardjetko, S., and Crawford, A. (2010). Intraoperative techniques to reduce the potential of set-screw loosening in long spinal constructs: A static and fatigue biomechanical investigation. *J. Spinal Disord. Tech.* 23, e31–e36. doi:10.1097/BSD.0b013e3181c982a1

Shim, J.-H., and Seo, E.-M. (2022). Efficacy and radiographic analysis of minimally invasive posterior mono-axial pedicle screw fixation in treating thoracolumbar burst fractures. *J. Clin. Med.* 11, 516. doi:10.3390/jcm11030516

Wang, H., Li, C., Liu, T., Zhao, W.-D., and Zhou, Y. (2012). Biomechanical efficacy of monoaxial or polyaxial pedicle screw and additional screw insertion at the level of fracture, in lumbar burst fracture: An experimental study. *Indian J. Orthop.* 46, 395–401. doi:10.4103/0019-5413.98827

Yao, W., Zhou, T., Huang, K., Dai, M., Mo, F., Xu, J., et al. (2021). A comparison of monoaxial pedicle screw versus polyaxial pedicle screw in short-segment posterior fixation for the treatment of thoracolumbar fractured vertebra. *Ann. Transl. Med.* 9, 669. doi:10.21037/atm-21-881

Ye, B., Yan, M., Zhu, H., Duan, W., Hu, X., Ye, Z., et al. (2017). Novel screw head design of pedicle screw for reducing the correction loss in the patients with thoracolumbar vertebral fractures: A biomechanical study. *Spine* 42, E379–E384. doi:10.1097/BRS.0000000000001808

Ye, B., Ye, Z., Yan, M., Huang, P., Tu, Z., Wang, Z., et al. (2022). Effection of monoplanar pedicle screw on facet joint degeneration in thoracolumbar vertebral fractures. *BMC Musculoskelet. Disord.* 23, 407. doi:10.1186/s12891-022-05360-3

Zhao, W.-P., Kawaguchi, Y., Matsui, H., Kanamori, M., and Kimura, T. (2000). Histochemistry and morphology of the multifidus muscle in lumbar disc herniation: Comparative study between diseased and normal sides. *Spine* 25, 2191–2199. doi:10.1097/00007632-200009010-00009

frontiers | Frontiers in Bioengineering and Biotechnology

TYPE Brief Research Report
PUBLISHED 29 June 2023
DOI 10.3389/fbioe.2023.1225925

OPEN ACCESS

EDITED BY
Xijin Hua,
University of Exeter, United Kingdom

REVIEWED BY
Xuesong Zhu,
The First Affiliated Hospital of Soochow University, China
Jun Zou,
Soochow University, China

*CORRESPONDENCE
Cheng-Fei Du,
ddccfb31@hotmail.com
Qiang Yang,
yangqiang1980@126.com

†These authors have contributed equally to this work

RECEIVED 20 May 2023
ACCEPTED 21 June 2023
PUBLISHED 29 June 2023

CITATION
Wang Y-N, Ren Y-N, Han J, Chen C, Sun X, Di M-Y, Dou Y-M, Ma X-L, Wang Z, Du C-F and Yang Q (2023), Biomechanical effects of screws of different materials on vertebra-pediculoplasty: a finite element study. *Front. Bioeng. Biotechnol.* 11:1225925. doi: 10.3389/fbioe.2023.1225925

Biomechanical effects of screws of different materials on vertebra-pediculoplasty: a finite element study

Yan-Ni Wang[1†], Ya-Nan Ren[2,3†], Jun Han[1], Chao Chen[1], Xun Sun[1], Ming-Yuan Di[1], Yi-Ming Dou[1], Xin-Long Ma[1], Zheng Wang[4], Cheng-Fei Du[2,3*] and Qiang Yang[1*]

[1]Department of Spine Surgery, Tianjin Hospital, Tianjin University, Tianjin, China, [2]Tianjin Key Laboratory for Advanced Mechatronic System Design and Intelligent Control, School of Mechanical Engineering, Tianjin University of Technology, Tianjin, China, [3]National Demonstration Center for Experimental Mechanical and Electrical Engineering Education, Tianjin University of Technology, Tianjin, China, [4]Department of Orthopaedics, Chinese People's Liberation Army General Hospital, Beijing, China

Background: The effects of cannulated screws made of polyetheretherketone (PEEK) on the biomechanical properties of the vertebral body during vertebra-pediculoplasty remain unclear. This study aimed to investigate whether PEEK screws have the potential to replace titanium alloy screws.

Methods: The surgical model of two different materials of screws was constructed using the finite element method. The biomechanical effects of the two models on the vertebral body under different working conditions were compared.

Results: ① The peak von Mises stress of PEEK screws was significantly lower than that of titanium screws, with a reduction ranging from 52% to 80%. ② The von Mises stress values for the injured T12 spine were similar for both materials. Additionally, the segmental range of motion and intervertebral disc pressure showed no significant difference between the two materials.

Conclusion: PEEK screws demonstrated advantages over titanium screws and may serve as a viable alternative for screw materials in vertebra-pediculoplasty.

KEYWORDS

screw, finite element analysis, biomechanics, PEEK, vertebra-pediculoplasty

1 Introduction

Vertebra-Pediculoplasty has emerged as a novel treatment approach for managing split and delayed osteoporotic vertebral fractures that were at risk of cement dislocation (Noritaka et al, 2021). It addressed the issue of poor clinical outcomes associated with balloon kyphoplasty for cleft osteoporotic vertebral fractures (Takahashi et al, 2019). The method involved using cannulated screws inserted into the cement block, in combination with balloon kyphoplasty, to create a "pedicle" (Noritaka et al, 2021). Traditional screws were primarily made of titanium, which offered excellent mechanical properties and good biocompatibility. However, their elastic modulus significantly differed from that of bone tissue, thereby increasing the risk of implant-related complications such as screw loosening or fracture, degeneration of adjacent segments, and long-term complications like pseudarthrosis (Zhang and Rong, 2020).

TABLE 1 Material properties of thoracolumbar spine and screws (POLIKEIT et al, 2003; Stavros et al, 2020; Tan et al, 2021).

Component	Young's modulus (MPa) Osteoporosis (normal)	Poisson's ratio Osteoporosis (normal)	Element type
Cortical	8,040 (12,000)	0.3 (0.3)	C3D8R
Cancellous	34 (100)	0.2 (0.3)	C3D4
Posterior element	2,345 (3,500)	0.25 (0.3)	C3D4
Endplate	670 (1,000)	0.4 (0.4)	C3D8R
bone cement	3,000	0.4	C3D4
Titanium screws	110,000	0.28	C3D4
PEEK screws	3,600	0.25	C3D4
Nucleus pulposus	Mooney-Rivlin, C1 = 0.18, C2 = 0.03		C3D8RH
Annulus fibers	Calibrated stress-strain curves		Spring
Facet cartilage	Neo-Hookean, C10 = 2		C3D8RH
Annulus ground	Mooney-Rivlin, C1 = 0.18, C2 = 0.045		C3D8RH
Ligament	Calibrated deflection–force curves		Spring

To overcome these limitations, this study proposed the use of polyether-ether-ketone (PEEK) material as an alternative to titanium alloy screws. PEEK has been extensively studied as an orthopedic implant material since the 1990 s (Kurtz and Devine, 2007). It has been a semi-crystalline polymer that exhibited excellent mechanical properties, favorable biocompatibility, X-ray penetrability, and other desirable physical and chemical properties, making it a promising material for orthopedic implants (Panayotov et al, 2016). Furthermore, its elastic modulus closely resembles that of normal human bone tissue, reducing stress-shielding effects (Zhao et al, 2020; Mrówka et al, 2021). Hence, this study aimed to evaluate the potential benefits of using PEEK screws in vertebra-pediculoplasty to minimize the risks associated with titanium alloys.

As vertebra-pediculoplasty was a relatively new method, the biomechanical effects in clinical practice remained unclear. Finite element (FE) analysis served as a valuable tool for assessing the biomechanical parameters of vertebral columns (Marien et al, 2017), and several studies have been conducted to evaluate the biomechanical properties of titanium and PEEK retention bars and spacers during surgery (Li et al, 2023). However, studies on titanium and PEEK screws have been limited to *in vitro* experiments (Lindtner et al, 2018; Stavros et al, 2020). Therefore, this research employed finite element analysis to compare the biomechanical effects of PEEK and titanium screws in vertebra-pediculoplasty, utilizing a finite element model of the human T11-L1 segment. The findings of this study may provide valuable theoretical guidance for the clinical application of screw materials.

2 Materials and methods

2.1 Establishment of normal thoracolumbar and osteoporotic fracture models

The CT data of a healthy 30-year-old male were imported into Mimics software (Materialise Technologies, Leuven, Belgium) to initially create a geometric model of the thoracolumbar spine (T11-L1). The thoracolumbar spine model was then imported into 3-Matic (Materialise Technologies, Leuven, Belgium) for individual processing of each vertebral body, resulting in a more accurate model structure in Geomagic software (Geomagic Inc., North Carolina, United States). The model was further processed in HyperMesh software (Altair Engineering Corp, Michigan, United States) for meshing, material property assignment, and assembly. Finally, the model was imported into Abaqus software (Dassault Systemes, PA, United States) for calculations and analysis (Tan et al, 2021). The elastic modulus of the osteoporotic vertebral structures was determined based on POLIKEIT et al (POLIKEIT et al, 2003), and specific material properties were determined according to previous studies (SHIM et al, 2008), as shown in Table 1.

2.2 Establishment of surgical model

The hollow lateral screw geometry was created in SolidWorks and imported into HyperMesh to assemble it with the vertebral body. The vertebral body-screw connection was simulated using a "binding" constraint, completing the vertebral screw fusion model. Two postoperative models of different materials (titanium and PEEK) for screw placement into the vertebral body were established based on vertebra-pediculoplasty. The cannulated screws used were 6.5 mm in diameter and 50 mm long. During the operation, bone cement was injected into the vertebral body through the hollow screw, and it diffused around the side hole of the screw, wrapping the screw evenly in a cylindrical shape (WANG et al, 2014). Each cannulated screw was injected with 2 ml of bone cement, and a cylindrical block with a radius of 8 mm and a height of 9.95 mm was created in SolidWorks to simulate the bone cement block. The screws of the two different materials had the same structure and shape. The establishment of the surgical operation model is illustrated in Figure 1.

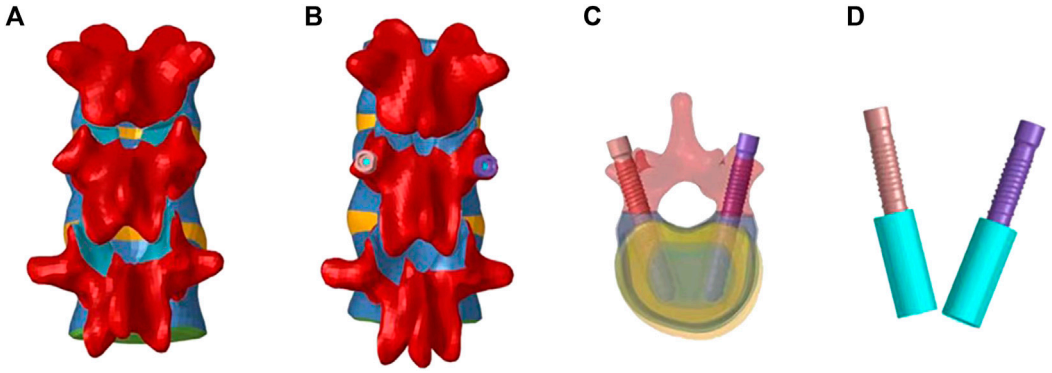

FIGURE 1
Establishment of the model after screw operation. **(A)**: Schematic diagram before T11-L1; **(B)**: Schematic diagram of T11-L1; **(C)**: Screw placement; **(D)**: Screw-cement model.

2.3 Loads and boundary conditions

A follower load of 500 N was applied to the upper surface of the T11 vertebral body to simulate physiological compressive loading. A moment load of 7.5 N m was applied to the T11 vertebral body to simulate forward flexion, back extension, lateral bending, and axial rotational motion. During loading, all degrees of freedom of the lower surface of the L1 vertebral body were constrained. (LIAO et al, 2017; DU et al, 2021).

2.4 Main outcome indicators

The maximum von Mises stresses of the screws and the injured T12 vertebral structure were compared for each model with different materials under various gestures such as flexion, extension, left bending, right bending, left rotation, and right rotation. Additionally, the segmental range of motion and intervertebral disc pressure were also evaluated.

3 Results

3.1 Verification of the normal thoracolumbar vertebrae finite element model

The range of motion (ROM) of the vertebral body was calculated under different postures. The ROMs of the T11-T12 segments were found to be 7.4°, 8.9°, and 4.6° for flexion and extension, lateral bending, and axial rotation, respectively. Similarly, the ROMs of the T12-L1 segments were 7.2°, 8.7°, and 3.8° for the corresponding postures. These results were compared with previous experimental data, and they were consistent with the findings reported in the literature (PANJABI et al, 1994; LIANG et al, 2015).

3.2 Maximum stress results of the screw

In the six models, the peak von Mises stress of the PEEK screws was 17.52 MPa, 9.125 MPa, 16.66 MPa, 8.48 MPa, 14.94 MPa, and 17.8 MPa. On the other hand, the peak stress of the titanium alloy screws was 89.03 MPa, 29.93 MPa, 69.06 MPa, 31.37 MPa, 90.88 MPa, and 37.48 MPa (e.g., Figure 2A). Upon comparison, it was observed that the maximum von Mises stress on PEEK screws was significantly lower than that on titanium screws.

3.3 Maximum Stress Analysis of Injured Vertebral T12 Structure and Analysis of Segmental Range of Motion and Intervertebral Disc Pressure

There were no significant differences in the maximum stress of the T12 cortical bone in the injured vertebra when using PEEK screws compared to titanium alloy screws under the six different states. Similarly, no noticeable differences were found in the maximum stress of the T12 cancellous bone or the analysis of the endplates (e.g. Figure 2B–D). Furthermore, the analysis of the range of motion of the vertebral body and the intervertebral disc pressure in the T11-L1 segment yielded similar results (e.g. Figure 2E, F). Upon comparing the results of the finite element analysis, it was concluded that different materials have minimal impact on the vertebral body.

4 Discussion

Due to its unique properties, PEEK has gained significant interest in bone implant research. The use of PEEK in orthopedic screws offers a promising avenue for exploration. In this study, we conducted a simulation-based analysis to assess the potential of PEEK as a substitute for the conventional titanium alloy used in screw fabrication. PEEK is a semi-crystalline polymer with excellent properties such as high modulus, melting point, processing performance, and strength (KULKARNI et al, 2007). Its elastic modulus closely resembles cortical bone, which reduces stress-shielding effects (MO et al, 2019). Additionally, PEEK is radiolucent, biocompatible, and does not cause artifacts during magnetic resonance scanning.

Recent efforts have focused on optimizing the mechanical and biological properties of PEEK through various methods such as 3D printing, coating, chemical modification, and the introduction of

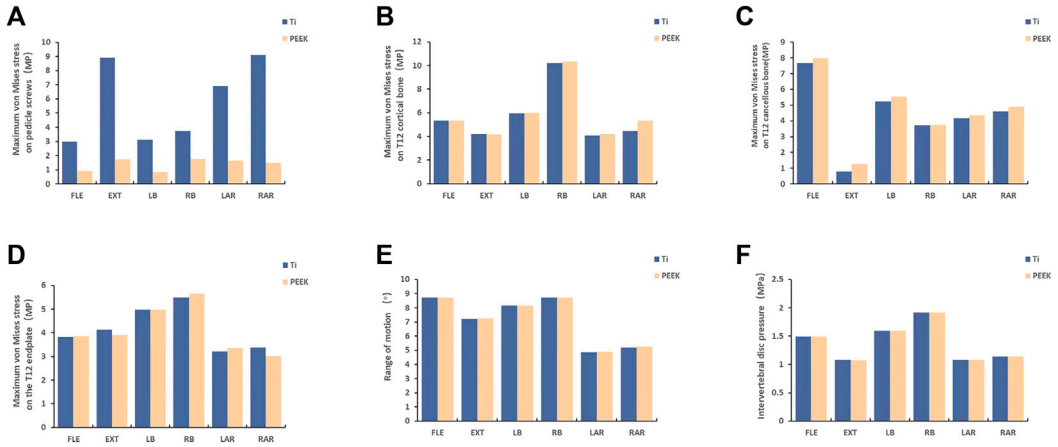

FIGURE 2
The stress results of the structure of the vertebra body [**(A)** The result of stress on pedicle screw; **(B, C, D)**: The stress results of the T12 structure of the injured vertebra; **(E, F)**: the result of the segmental range of motion and intervertebral disc pressure; FL = flexion, EX = extension, LB = left bending, RB = right bending, LAR = left axial rotation, and RAR = right axial rotation].

bioactive or antibacterial substances (Chen et al, 2022). These modifications aim to enhance the overall properties of PEEK and facilitate the treatment of bone injuries, making PEEK materials a promising option for lumbar spine repair.

In recent years, numerous studies have explored the factors that influence screw stability, including screw diameter, shape, length, thread shape, implantation method, angle, and combination (ABSHIRE et al, 2001; KINER et al, 2008; SENGUPTA and Herkowitz, 2012; Karami et al, 2015; JENDOUBI et al, 2018; NAKASHIMA et al, 2019). The current study investigates the effect of screw material in finite element analysis to provide further insights.

By comparing the von Mises stress of screws made from different materials under different vertebral body motions, our analysis reveals that PEEK screws have a significant advantage in reducing peak stress compared to titanium alloy screws. Specifically, the range of reduction observed in the von Mises stress with PEEK screws ranges between 52% and 80%. The observed reduction in peak stress indicates that the use of PEEK screws may lead to reduce the incidence of screw loosening, thereby establishing its potential as a promising alternative material. Some experiments have confirmed the idea that PEEK screws have a low risk of loosening. Richard Lintner et al (Lindtner et al, 2018) conducted cyclic loading tests on ten cadaveric lumbar vertebrae to compare the performance of carbon fiber-reinforced PEEK (CF/PEEK) and standard titanium pedicle screws in reducing screw loosening. The study found that PEEK and CF/PEEK screw/rod configurations had a significant advantage over titanium screws in reducing screw loosening. Similarly, Stavros Oikonomidis (Stavros et al, 2020) conducted cyclic loading tests on ten freshly frozen human cadaveric lumbar vertebrae to investigate the loosening rate of pedicle screws made of CFR/PEEK compared to titanium. The study concluded that the use of CFR/PEEK pedicle screws could reduce the rate of screw loosening. Further investigation is warranted to compensate for the lack of clinical studies using pedicle screws made of PEEK. One avenue for exploration is to compare relevant trials involving PEEK rods. Qian Jiaming et al (QIAN et al, 2022) and Huang Weimin et al (Huang et al, 2016) conducted follow-up studies for 6 months and 2 years, respectively, on patients who underwent posterior lumbar pedicle internal fixation and multi-level fixation using PEEK material. The results of the studies showed no instances of screw fracture or loosening during the respective follow-up periods. Although further clinical follow-up studies are required to ascertain the superiority of PEEK screws over other materials in preventing screw loosening, recent research suggests that PEEK screws may have similar benefits to PEEK rods in this regard.

When assessing the risk of screw fracture, it is important to consider the ratio of peak stress to yield stress rather than focusing solely on stress magnitude. The ratio of peak stress to yield stress for PEEK screws ranged from 8% to 17%, while for titanium screws, it fell within the range of 3%–12% (PEEK: 100 MPa, titanium: 750 MPa). The higher percentage for PEEK screws suggests a potential escalation of breakage risk (e.g., Figure 3), consistent with prior findings by FAN et al (FAN et al, 2021). However, there have been no reported cases of PEEK rod fracture, possibly due to the load experienced under physiological conditions being insufficient to cause rupture. Consequently, screw breakage is unlikely to occur.

Previous investigations have examined the load transmission properties of titanium alloy posterior screw rod systems and PEEK screws in posterolateral lumbar fixation. These studies indicated that the titanium alloy system can transmit approximately 67% of the axial compressive load, while the natural upright state can bear only about 20% of the load (CUNNINGHAM and POLLY, 2002; AHN et al, 2008). PEEK screws have favorable characteristics such as biocompatibility, radiolucency, and a lower elastic modulus compared to titanium alloy screws. These characteristics allow PEEK screws to transfer more load to the front column, improving the load distribution between the front and rear columns. A finite element study by GARNET et al (GORNET et al, 2011) supported this finding, demonstrating that a titanium rod bore at least 6% more load than a PEEK rod. This evidence suggests that the principal advantage of PEEK screws lies in mitigating stress concentration on the screw.

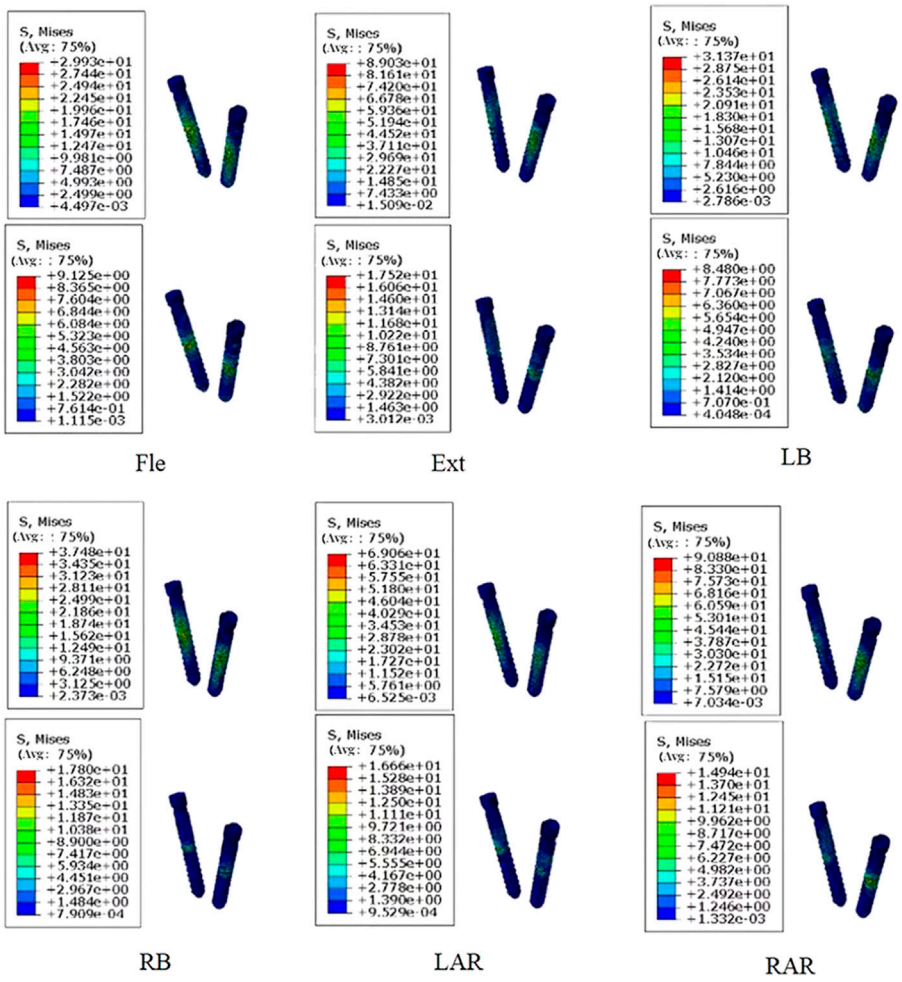

FIGURE 3
Comparison of stress distribution of screws made of two materials under different loading directions. (The figure shows titanium alloy material at the top and PEEK material at the bottom).

Next, we analyze the finite element results of the vertebral structure. The von Mises stress of the vertebral body, as well as the segmental Range of Motion and Intervertebral Disc Pressure, were obtained through finite element analysis under various conditions. The results show that the stability of the vertebral body remains largely unaffected. Similar findings have been reported in related investigations. Nomidis et al (Stavros et al, 2020) conducted biomechanical experiments using cadaveric specimens and found no macroscopic changes in the vertebral structure. Additionally, YEAGER et al (YEAGER et al, 2015) compared PEEK and titanium rods using human lumbar spine specimens and concluded that both materials offered comparable stability under different loading modes. While PEEK may not match the strength and rigidity of titanium alloys, it possesses adequate strength and rigidity to maintain spinal stability and endure physiological biomechanical demands. The elastic modulus of PEEK closely matches that of bone tissue, allowing PEEK screws to conform to micro-movements and deformations of interconnected spinal bones. This feature reduces the likelihood of stress concentration and ensures a secure connection. Moreover, PEEK demonstrates exceptional biocompatibility, minimizing the risk of inflammatory responses or tissue rejection. PEEK screws can integrate stably with the surrounding bone tissue, exhibiting biostability comparable to that of titanium screws. The adaptive nature of PEEK material to bone morphology enables it to establish minute biological interconnections with bone tissue, enhancing the stability of PEEK screw integration with the spinal bone and reducing the risk of loosening. However, the development of more ideal internal fixation materials warrants further exploration through basic scientific research and clinical trials.

Several limitations should be considered when interpreting the results of this study. Firstly, the finite element model used is based on theoretical numerical simulations and may not fully capture the complexity of the human spine system, as it does not account for factors such as cyclic loads and the influence of muscles. Secondly, the thoracic and lumbar spine models used are limited to a single subject, and the number of models is small, which may limit the generalizability of the findings. Lastly, this study represents a preliminary exploration of finite element analysis. Further research and exploration are necessary to establish a solid

foundation for the long-term development of PEEK material in lumbar spine repair.

5 Conclusion

In conclusion, PEEK screws demonstrate comparable efficacy to titanium alloy screws in providing segmental stability post-surgery. Additionally, PEEK screws facilitated the prevention of loosening, which was a great clinical advantage. Moreover, the radiolucent nature of PEEK screws facilitates postoperative imaging without interfering with radiation therapy. Thus, the PEEK or PEEK composite material may emerge as a viable alternative for screw materials in clinical practice. (Sato et al, 2018).

Data availability statement

The original contributions presented in the study are included in the article/Supplementary Material, further inquiries can be directed to the corresponding authors.

Author contributions

All authors listed have made a substantial, direct, and intellectual contribution to the work and approved it for publication.

Funding

This study was supported by the National Key R&D Program of China (2020YFC1107402), National Natural Science Foundation of China (81871782), Tianjin Science Fund for Distinguished Young Scholars (18JCJQJC47900), Medical Innovation Fund for Clinical Application of National Clinical Research Center for Orthopedics, Sports Medicine and Rehabilitation (2021-NCRC-CXJJ-ZH-22), Tianjin Key Medical Discipline (Specialty) Construction Project (TJYXZDXK-026A).

Conflict of interest

The authors declare that the research was conducted in the absence of any commercial or financial relationships that could be construed as a potential conflict of interest.

Publisher's note

All claims expressed in this article are solely those of the authors and do not necessarily represent those of their affiliated organizations, or those of the publisher, the editors and the reviewers. Any product that may be evaluated in this article, or claim that may be made by its manufacturer, is not guaranteed or endorsed by the publisher.

References

Abshire, B. B., Kambic, H. E., and Valdevit, A. (2001). Characteristics of pullout failure in conical and cylindrical pedicle screws after full insertion and back-out. *Spine J.* 1, 408–414. doi:10.1016/s1529-9430(01)00119-x

Ahn, Y. H., Chen, W. M., Lee, K. Y., Park, K. W., and Lee, S. J. (2008). Comparison of the load-sharing characteristics between pedicle-based dynamic and rigid rod devices. *Biomed. Mater.* 3 (4), 044101. doi:10.1088/1748-6041/3/4/044101

Chen, J., Cao, G., Li, L., Cai, Q., Dunne, N., and Li, X. (2022). Modification of polyether ether ketone for the repairing of bone defects. *Biomed. Mater. (Bristol, Engl.* 17 (4), 042001. doi:10.1088/1748-605x/ac65cd

Cunningham, B. W., and Polly, D. W. (2002). The use of interbody cage devices for spinal deformity: A biomechanical perspective. *Clin. Orthop. Relat. Res.* 394, 73–83. doi:10.1097/00003086-200201000-00009

Du, C. F., Cai, X. Y., Gui, W., Sun, M. S., Liu, Z. X., Liu, C. J., et al. (2021). Does oblique lumbar interbody fusion promote adjacent degeneration in degenerative disc disease:A finite element analysis. *Comput. Biol. Med.* 128, 104122. doi:10.1016/j.compbiomed.2020.104122

Fan, W., Guo, L. X., and Zhang, M. (2021). Biomechanical analysis of lumbar interbody fusion supplemented with various posterior stabilization systems. *Eur. Spine J.* 30 (8), 2342–2350. doi:10.1007/s00586-021-06856-7

Gornet, M. F., Chan, F. W., Coleman, J. C., Murrell, B., Nockels, R. P., Taylor, B. A., et al. (2011). Biomechanical assessment of a PEEK rod system for semi-rigid fixation of lumbar fusion constructs. *J. Biomech. Eng.* 133 (8), 081009. doi:10.1115/1.4004862

Huang, W., Chang, Z., Song, R., Zhou, K., and Yu, X. (2016). Non-fusion procedure using PEEK rod systems for lumbar degenerative diseases: Clinical experience with a 2-year follow-up. *BMC Musculoskelet. Disord.* 17 (1), 53–57. doi:10.1186/s12891-016-0913-2

Jendoubi, K., Bendjaballah, M., and Slimane, N. (2018). Effects of the insertion type and depth on the pedicle screw pullout strength: A finite element study. *Appl. Bionics Biomech.* 2018, 1460195. doi:10.1155/2018/1460195

Karami, K. J., Buckenmeyer, L. E., Kiapour, A. M., Kelkar, P. S., Goel, V. K., Demetropoulos, C. K., et al. (2015). Biomechanical evaluation of the pedicle screw insertion depth effect on screw stability under cyclic loading and subsequent pullout. *J. spinal Disord. Tech.* 28 (3), E133–E139. doi:10.1097/bsd.0000000000000178

Kiner, D. W., Bartol, S. W., Vaidya, R., Yeni, Y. N., and Vaidya, R. (2008). Biomechanical analysis of different techniques in revision spinal instrumentation: Larger diameter screws versus cement augmentation. *Spine* 33, 2618–2622. doi:10.1097/brs.0b013e3181882cac

Kulkarni, A. G., Hee, H. T., and Wong, H. K. (2007). Solis cage (PEEK) for anterior cervical fusion: Preliminary radiological results with emphasis on fusion and subsidence. *Spine J.* 7 (2), 205–209. doi:10.1016/j.spinee.2006.03.002

Kurtz, Steven M., and Devine, John N. (2007). PEEK biomaterials in trauma, orthopedic, and spinal implants. *Biomaterials* 28 (32), 4845–4869. ISSN 0142-9612. doi:10.1016/j.biomaterials.2007.07.013

Liao, J. C., Chen, W. P., and Wang, H. (2017). Treatment of thoracolumbar burst fractures by short-segment pedicle screw fixation using a combination of two additional pedicle screws and vertebroplasty at the level of the fracture:a finite element analysis. *BMC Musculoskelet. Disord.* 18 (1), 262. doi:10.1186/s12891-017-1623-0

Li, J., Cao, S., Guo, D., Zhang, Q. C., He, X. J., Li, H. P., et al. (2023). Finite element analysis of polyetheretherketone and titanium rods in posterior lumbar interbody fusion. *Chin. J. Tissue Eng. Res.* 27 (22), 3445–3450. doi:10.12307/2023.398

Liang, D., Ye, L. Q., Jiang, X. B., Yang, P., Zhou, G. Q., Yao, Z. S., et al. (2015). Biomechanical effects of cement distribution in the fractured area on osteoporotic vertebral compression fractures:a three-dimensional finite element analysis. *J. Surg. Res.* 195 (1), 246–256. doi:10.1016/j.jss.2014.12.053

Lindtner, R. A., Schmid, R., Nydegger, T., Konschake, M., and Schmoelz, W. (2018). Pedicle screw anchorage of carbon fiber-reinforced PEEK screws under cyclic loading. *Eur. Spine J.* 27, 1775–1784. doi:10.1007/s00586-018-5538-8

Marien, C., Arnaud, G., Saget, M., Dupré, J. C., Doumalin, P., Brémand, F., et al. (2017). Biomechanical analysis of the thoracolumbar spine under physiological loadings: Experimental motion data corridors for validation of finite element models. *Proc. Institution Mech. Eng. Part H J. Eng. Med.* 231 (10), 975–981. doi:10.1177/0954411917719740

Mo, S., Mehrjou, B., Tang, K., Wang, H., Huo, K., Qasim, A. M., et al. (2019). Dimensional-dependent antibacterial behavior on bioactive micro/nano polyetheretherketone (PEEK) arrays. *Chem. Eng. J.* 392, 123736. doi:10.1016/j.cej.2019.123736

Mrówka, M., Machoczek, T., Jureczko, P., Joszko, K., Gzik, M., Wolański, W., et al. (2021). Mechanical, chemical, and processing properties of specimens manufactured from poly-ether-ether-ketone (PEEK) using 3D printing. *Materials* 14 (11), 2717. doi:10.3390/ma14112717

Nakashima, D., Ishii, K., Nishiwaki, Y., Kawana, H., Jinzaki, M., Matsumoto, M., et al. (2019). Quantitative CT-based bone strength parameters for the prediction of novel spinal implant stability using resonance frequency analysis: A cadaveric study involving experimental micro-CT and clinical multislice CT. *Eur. Radiol. Exp.* 3 (1), 1–8. doi:10.1186/s41747-018-0080-3

Noritaka, Y., Yoshiro, Y., Nishimura, T., Yamashiro, T., Shimozaki, K., Mori, A., et al. (2021). Vertebra-pediculoplasty: A new approach to treatment of split-type and delayed-union osteoporotic vertebral fracture with a risk of cement dislodgement. *World Neurosurg.* 155, e55–e63. doi:10.1016/j.wneu.2021.07.142

Panayotov, I. V., Orti, V., Cuisinier, F., and Yachouh, J. (2016). Polyetheretherketone (PEEK) for medical applications. *J. Mater Sci. Mater Med.* 27, 118. doi:10.1007/s10856-016-5731-4

Panjabi, M. M., Oxland, T. R., Lin, R. M., and McGowen, T. W. (1994). Thoracolumbar burst fracture.A biomechanical investigation of its multidirectional flexibility. *Spine* 19 (5), 578–585. doi:10.1097/00007632-199403000-00014

Polikeit, A., Nolte, L. P., and Ferguson, S. J. (2003). The effect of cement augmentation on the load transfer in an osteoporotic functional spinal unit finite-element analysis. *Spine* 28 (10), 991–996. doi:10.1097/01.brs.0000061987.71624.17

Qian, J., Li, C. G., Yin, X. C., Chen, C., Zheng, H. Y., Zhu, Y. G., et al. (2022). Polyetheretherketone versus titanium rods used in pedicle screw fixation for lumbar degenerative diseases. *Orthop. J. China* 30 (9), 1–5. doi:10.3977/j.issn.1005-8478.2022.09.06

Sato, T., Yonezawa, I., Todo, M., Takano, H., and Kaneko, K. (2018). Biomechanical effects of implant materials on posterior lumbar interbody fusion: Comparison of polyetheretherketone and titanium spacers using finite element analysis and considering bone density. *J. Biomed. Sci. Eng.* 11 (04), 45–59. doi:10.4236/jbise.2018.114005

Sengupta, D. K., and Herkowitz, H. N. (2012). Pedicle screw-based posterior dynamic stabilization: Literature review. *Adv. Orthop.* 2012, 1–7. doi:10.1155/2012/424268

Shim, C. S., Park, S. W., Lee, S. H., Lim, T. J., Chun, K., and Kim, D. H. (2008). Biomechanical evaluation of an interspinous stabilizing device, locker. *Locker. Spine (Phila Pa 1976)* 33 (22), E820–E827. doi:10.1097/brs.0b013e3181894fb1

Stavros, O., Johannes, G., Jan, B., Madita, E., Andreas, P., Horst, F., et al. (2020). Biomechanical effects of posterior pedicle screw-based instrumentation using titanium versus carbon fiber reinforced PEEK in an osteoporotic spine human cadaver model. *Clin. Biomech.* 80, 105153. ISSN 0268-0033. doi:10.1016/j.clinbiomech.2020.105153

Takahashi, S., Hoshino, M., Yasuda, H., Hori, Y., Ohyama, S., Terai, H., et al. (2019). Characteristic radiological findings for revision surgery after balloon kyphoplasty. *Sci. Rep.* 9, 18513–18517. doi:10.1038/s41598-019-55054-5

Tan, Q., Liu, Z., Zhao, Y., Huang, X. y., Bai, H., Yang, Z., et al. (2021). Biomechanical comparison of four types of instrumentation constructs for revision surgery in lumbar adjacent segment disease: A finite element study. *Comput. Biol. Med.* 134, 104477. doi:10.1016/j.compbiomed.2021.104477

Wang, W., Baran, G. R., Garg, H., Betz, R. R., Moumene, M., and Cahill, P. J. (2014). The benefits of cement augmentation of pedicle screw fixation are increased in osteoporotic bone: AFinite element analysis. *Spine deform.* 2 (4), 248–259. doi:10.1016/j.jspd.2014.03.002

Yeager, M. S., Cook, D. J., and Cheng, B. C. (2015). *In vitro* comparison of dynesys, PEEK, and titanium constructs in the lumbar spine. *Adv. Orthop.* 2015, 895931. doi:10.1155/2015/895931

Zhang, J., and Rong, Q. (2020). Effect of new titanium alloy on biomechanical behavior of dental implant. *J. Syst. Simul.* 32 (11), 2100–2104. doi:10.16182/j.issn1004731x.joss.19-FZ0521

Zhao, G., Qin, M., and Liu, Y. (2020). Optimizing fused deposition molding process parameters for improving forming strength of polyetheretherketone. *Chin. J. Mech. Eng-En.* 56, 216–222. doi:10.3901/JME.2020.03.216

frontiers | Frontiers in Bioengineering and Biotechnology

TYPE Original Research
PUBLISHED 05 July 2023
DOI 10.3389/fbioe.2023.1218478

OPEN ACCESS

EDITED BY
Zhenxian Chen,
Chang'an University, China

REVIEWED BY
Christian Liebsch,
Ulm University Medical Center, Germany
Teng Lu,
Xi'an Jiaotong University, China

*CORRESPONDENCE
Jun Miao,
mj6688@163.com

†These authors have contributed equally to this work

RECEIVED 07 May 2023
ACCEPTED 26 June 2023
PUBLISHED 05 July 2023

CITATION
Ma X, Feng Q, Zhang X, Sun X, Lin L, Guo L, An L, Cao S and Miao J (2023), Biomechanical evaluation of a novel minimally invasive pedicle bone cement screw applied to the treatment of Kümmel's disease in porcine vertebrae. *Front. Bioeng. Biotechnol.* 11:1218478. doi: 10.3389/fbioe.2023.1218478

Biomechanical evaluation of a novel minimally invasive pedicle bone cement screw applied to the treatment of Kümmel's disease in porcine vertebrae

Xiang Ma[1,2†], Qing Feng[1†], Xingze Zhang[1,2†], Xiaolei Sun[1], Longwei Lin[1,2], Lin Guo[1], Lijun An[3], Shenglin Cao[3] and Jun Miao[1*]

[1]Tianjin Hospital, Tianjin University, Tianjin, China, [2]Tianjin Medical University, Tianjin, China, [3]Chengde Medical College, Hebei, China

Background and objective: Treatment of Kümmel's Disease (KD) with pure percutaneous kyphoplasty carries a greater likelihood of bone cement displacement due to hardened bone and defect of the peripheral cortex. In this study, we designed a novel minimally invasive pedicle bone cement screw and evaluate the effectiveness and safety of this modified surgical instruments in porcine vertebrae.

Methods: 18 mature porcine spine specimens were obtained and soaked in 10% formaldehyde solution for 24 h. 0.5000 mmol/L EDTA-Na_2 solution was used to develop *in vitro* osteoporosis models of porcine vertebrae. They were all made with the bone deficiency at the anterior edge of L1. These specimens were randomly divided into 3 groups for different ways of treatment: Group A: pure percutaneous kyphoplasty (PKP) group; Group B: unilateral novel minimally invasive pedicle bone cement screw fixation combined with PKP group; Group C: bilateral novel minimally invasive pedicle bone cement screw fixation combined with PKP group. The MTS multi-degree of freedom simulation test system was used for biomechanical tests, including axial loading of 500 N pressure, range of motion (ROM) in flexion, extension, left/right lateral bending, and left/right axial rotation at 5 Nm, and the displacement of bone cement mass at maximum angles of 5° and 10°.

Result: The three groups were well filled with bone cement, no leakage or displacement of bone cement was observed, and the height of the vertebrae was higher than pre-operation ($p < 0.05$). In the left/right axial rotation, the specimens were still significantly different ($p < 0.05$) from the intact specimens in terms of ROM after PKP. In other directions, ROM of all group had no significant difference ($p < 0.05$) and was close to the intact vertebrae. Compared with PKP group, the relative displacement of bone cement in groups B and C was smaller ($p < 0.05$).

Conclusion: In the *in vitro* animal vertebral models, the treatment of KD with the placement of novel pedicle minimally invasive bone cement screw combined with PKP can effectively restore the vertebral height, improve the stability of the affected vertebra and prevent the displacement of bone cement. Biomechanically, there is no significant difference between bilateral and unilateral fixation.

KEYWORDS
Kümmel's disease, osteoporosis, novel bone cement screw, biomechanics, porcine

1 Introduction

Kümmel's disease (KD), a rare type of osteoporotic vertebral compression fracture (OVCF), is characterized by an intravertebral vacuum cleft (IVC)in radiological imaging (Qi HR. et al., 2022; Gou et al., 2023). Patients with OVCF can experience relief of symptoms with non-surgical treatment, but about 1/3 of patients may have persistent low back pain and kyphosis, which may develop into KD (Duan et al., 2019). KD presents with back pain without obvious causes or after minor trauma based on osteoporosis, followed by a long or short asymptomatic period. Eventually, prolonged spine pain reappears in the same area and cannot be relieved, leading to the development of kyphosis (Qi J. et al., 2022; Li et al., 2023).

KD generally does not heal spontaneously, and alternative treatments such as bed rest and stent fixation have shown limited success for the treatment. They are often not sufficient to address the underlying bone deficiency and may lead to persistent symptoms and potential complications (Wang et al., 2020; Zhang et al., 2022). Moreover, patients are usually the elderly, and long-term bed rest can lead to various complications. Therefore, KD patients usually need surgical treatment such as percutaneous vertebroplasty (PVP) and percutaneous kyphoplasty (PKP) (Niu et al., 2017; Zhang et al., 2021). Internal fixation should also be considered when the patient's kyphosis is significant and compresses the spinal cord or neural structures (Gan et al., 2021; Huang et al., 2021; Han et al., 2022). Compared with common OVCF, KD tends to have a longer course of disease and have a greater likelihood of bone cement displacement after surgery due to the presence of hardened bone and defect of the peripheral cortex on either side of the IVC (Chen et al., 2015; Li et al., 2017). The hardened bone makes it difficult for bone cement to penetrate the cancellous bone and form a uniform and cohesive mass within the vertebral body (Li et al., 2017; Liu JB. et al., 2022). Displacement of bone cement can lead to nerve and spinal cord damage (Yang et al., 2008).

Currently, some studies have proposed cement augmentation combined with short segmental fixation to strengthen bone cement anchoring, but these methods are difficult to achieve minimally invasive treatment (Wang et al., 2021; Liu Y. et al., 2022; Zhang et al.,

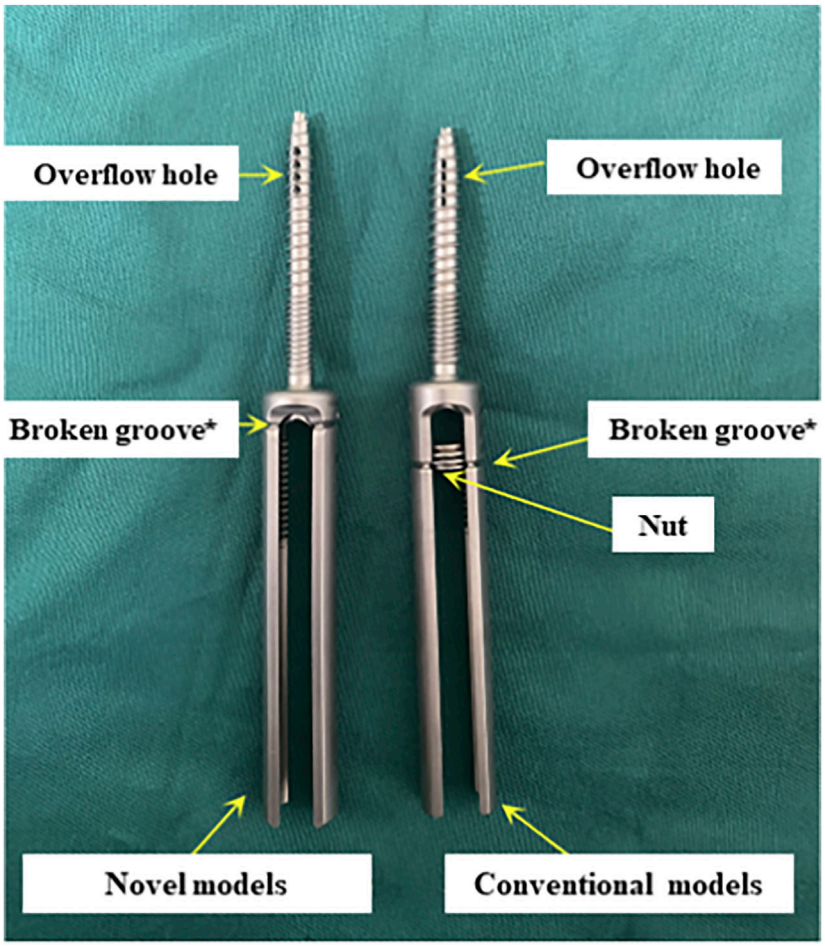

FIGURE 1
Novel and conventional cannulated pedicle screw. *, representing our improvements.

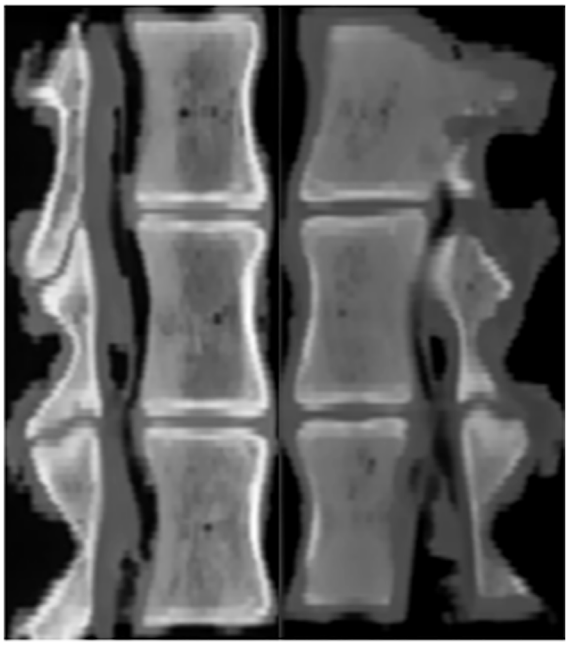

FIGURE 2
Sagittal reconstruction CT images before (left) and after (right) decalcification.

2022). The short segmental fixation could be not required for patients with KD without neurological compression symptoms. To address these clinical issues, we considered strengthening the interaction force between bone cement and bone tissue directly through pedicle screws in the treatment of KD with defect of the peripheral cortex. And the problem of wearing the muscles and other soft tissue due to the excess caudal design of the conventional pedicle bone cement screws should be further avoided (Figure 1). In this study, 18 *in vitro* specimens of KD were prepared to evaluate and analysis the effectiveness and safety of fixing bone cement mass using this modified surgical instrument.

2 Materials and methods

2.1 Material selection and preparation

This study was performed using 18 thoracolumbar vertebrae T14 (T15) -L2 harvested from mature pigs (weight 110–130 kg). The porcine thoracic vertebrae have 14–15 segments and the lumbar vertebrae have 6–7 segments. Prior to their use in the study, the pigs were healthy and not exposed to any environmental factors that could affect their bone quality. All specimens were rigorously inspected to ensure that there were no defects. CT scan in the imaging department of Tianjin Hospital confirmed that the structure of them was intact and no deficiency (Figure 2). The paravertebral muscles and other soft tissues on both sides of the specimen were removed, and the intervertebral disc, spinous process, interspinous ligament, posterior longitudinal ligament, facet joint, ligamentum flavum and transverse process were preserved. Rinse with water and soak in 10% formaldehyde solution for 24 h. The study design and subjects are presented in Figure 3.

2.2 Preparation of KD specimens

The 18 triple vertebrae specimens were completely immersed in 0.5000 mmol/L EDTA-Na_2 decalcification solution (pH 7.3 ± 0.1) (Lee et al., 2011; Hsieh et al., 2020; Liu JB. et al., 2022). Bone mineral density (BMD) of all vertebral bodies was measured weekly and the solution was changed until the percentage loss of BMD value reached 30%. After all specimens met the criteria of osteoporosis, a conical vertebral bone defect with a diameter of 16 mm and a depth of 30 mm was created in L1 of each specimen using a grinding drill. The animal model of KD was prepared by smearing the cancellous bone surface in the cone-shaped defect with bone wax to simulate the hardened bone at the defect site. L1 of each specimen was compressed to 1/2 the height of the original vertebral body by biomechanical testing machine (ElectroForce 3510, Bose) (Figure 4).

2.3 Surgical methods and experimental grouping

18 triple vertebrae specimens were randomly divided into 3 groups, which were recorded as group A, B, and C (n = 6/group). Group A underwent pure PKP; Group B underwent unilateral pedicle cement screw fixation combined with PKP; Group C underwent bilateral pedicle cement screw fixation combined with PKP.

The details of PKP surgical were performed based on standard procedure (Lei et al., 2020). The puncture position was adjusted according to the IVC to ensure that the tip cone was located in the cleft. The tip cone was withdrawn, and the guide drill was inserted in sequence to a distance of approximately 3–5 mm from the posterior edge of the vertebral body. The collapsed vertebral tissue was opened with a balloon to create a cemented cavity. Apply the PKP working sleeve to push the prepared bone cement along the vertebral arch in slow and staged injections, stopping the procedure immediately if high resistance is encountered or if the bone cement is close to the posterior wall of the vertebral body. The amount of bone cement was selected as 8 mL according to the size of the porcine vertebrae, and the distribution of the bone cement in the vertebral bone was observed. The curing time of the bone cement was 15 min. After waiting for sufficient time and confirming the curing of the bone cement, the pusher and working cannula were rotated and then withdrawn.

The following were details of the surgical procedure for novel pedicle bone cement screw fixation combined with PKP. The surface projections of the bilateral pedicle margin of the diseased vertebra were used as the pedicle screw entry point. Firstly, 1.5 mL bone cement was pushed in with the bone cement pusher, and appropriately sized pedicle bone cement screw were placed without penetration from the anterior cortical aspect. Bone cement was injected along this pedicle screw so that so that the cement flowing out of the anterior and lateral holes of the pedicle screw fused with the previously injected cement and became a single unit. After the cement had set, and the tail of the pedicle screw was broken.

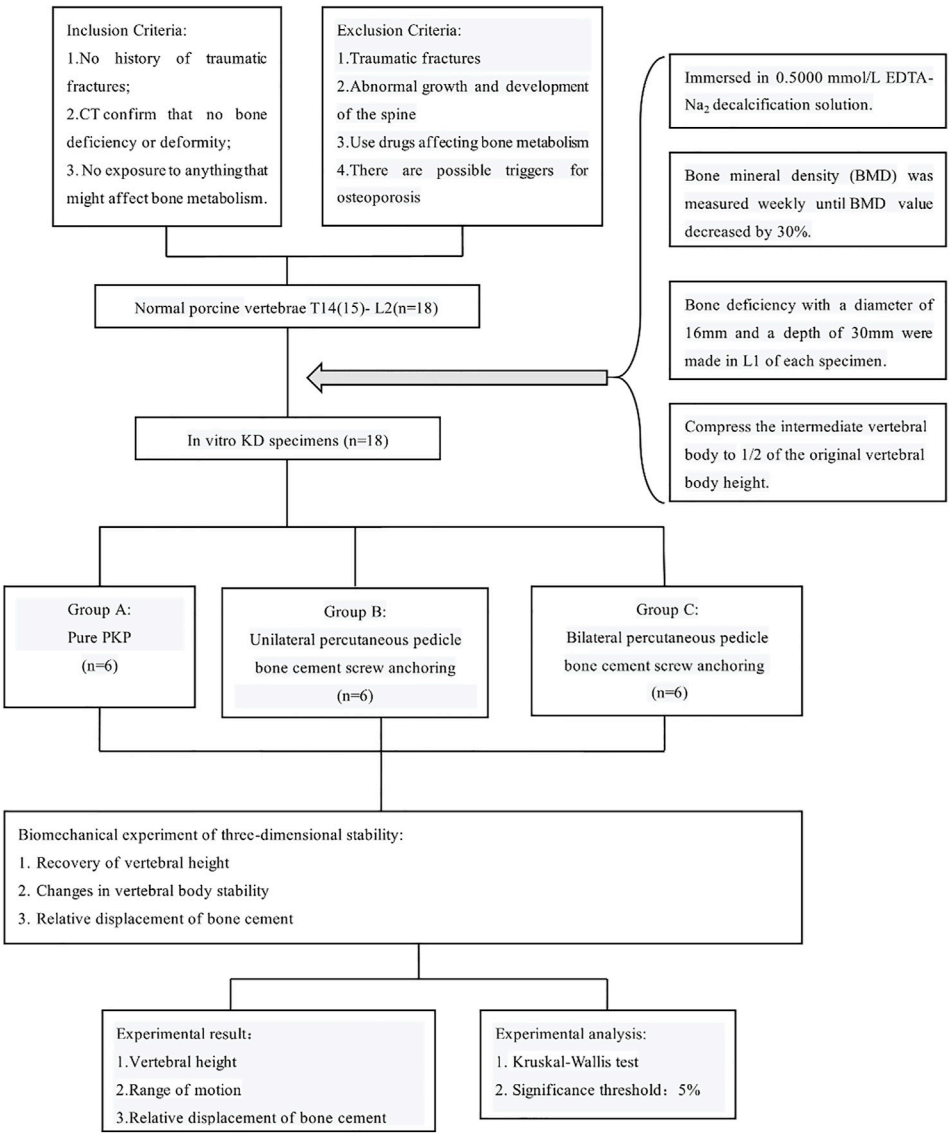

FIGURE 3
Flow chart of the study design.

CT was performed on all specimens immediately after surgery. Observation of cement filling, screw placement, vertebral body injury and spinal cord compression (Figure 5).

2.4 Three-dimensional stability biomechanical experiments

The upper and lower vertebrae of each specimen were embedded with denture base resin without crossing the intervertebral disc at depth. And in the procedure, try to make the part fixed to the MTS multi-degree of freedom simulation test system (MTS, Bionix 370.02, Figure 6) as regular in shape as possible, so that the specimens were sufficiently fixed during movement and did not become skewed. The upper and lower bases of each specimen were tightly attached to respective bases of the test machine with the T12/L1 and L1/L2 discs in a horizontal neutral position. The specimens were preloaded at a rate of 1 mm/min and stopped when the force reaches 100 N. The purpose was to eliminate creep movement and to make the vertebrae fully fixed in the mold so that they would not slip off and affect the determination of the value. The test force was set to zero after adequate fixation was completed. An axial load of 500 N was applied to simulate the mass of the upper body. The specimens were kept moist by spraying physiological saline every 5 min during the test to reduce the error caused by evaporative water loss.

2.4.1 ROM testing of vertebrae

By adjusting the tightness of the screws fixing the specimen until the constraint force in each direction was shown as 0 on the sensor. The 5 Nm force was then applied to the specimen to complete the flexion, extension, left/right lateral flexion and left/right axial rotation, and the maximum activity angle was recorded.

FIGURE 4
Compression process of specimens by biomechanical testing machine (ElectroForce 3510, Bose).

FIGURE 5
The postoperative CT scan shows satisfactory bone cement filling and accurate placement of the pedicle screws. No vertebral damage or spinal cord compression occurred during the operation. **(A)** pure PKP; **(B)** unilateral pedicle cement screw fixation combined with PKP group; **(C)** bilateral pedicle cement screw fixation combined with PKP group.

2.4.2 Bone cement relative displacement test

Each postoperative specimen underwent movements with the same force applied at maximum angles of 5° and 10° in each direction, completing each movement six times. Set the angular speed to 0.003 rad/s. The specimens were scanned by CT after movement to observe the relative displacement of the bone cement.

2.5 Statistical analysis

SPSS 26.0 software (IBM, United States) was used for statistical analysis. The means and SD ($\bar{X}$ ±s) were calculated for BMD during specimen decalcification. Medians and interquartile range [M(IQR)] were calculated for the data on the height of the vertebral body, ROM and bone cement displacement in each of these groups. The Kruskal–Wallis test was used for the comparative analysis of experimental results among different groups. The 5% significance threshold indicated a difference.

3 Results

3.1 BMD during specimen decalcification

The changes in regional bone mineral density (BMD) from normal to osteoporotic status were shown in Figure 7. The initial BMD was recorded as 1.34 ± 0.15 g/cm^2, and after being treated with EDTA for 7 weeks, the BMD decreased to 0.89 ± 0.16 g/cm^2. After

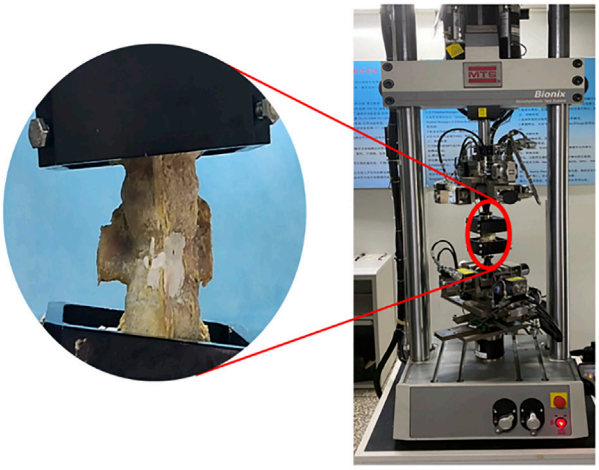

FIGURE 6
Three-dimensional stability biomechanical experiments.

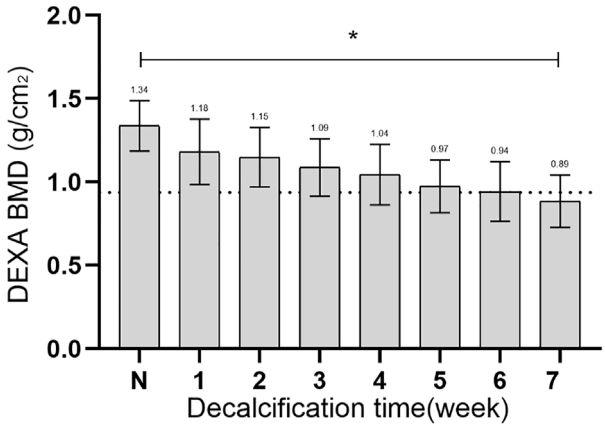

FIGURE 7
The changes in BMD from normal to osteoporotic status. N, the initial BMD; *, statistical differences.

EDTA treatment for 7 weeks, the BMD decreased to below 30% of the normal vertebral value ($p < 0.05$), indicating the onset of osteoporosis in the experiment.

3.2 The recovery status of vertebral height

The vertebral heights at 500 N of axial compression in each group were shown in Table 1. There was no statistical difference in vertebral body height before treatment ($p > 0.05$) and after treatment ($p > 0.05$). After different treatments, all three groups had higher vertebral heights than before surgery ($p < 0.05$).

3.3 Range of motion

ROM measured at 5 Nm in six directions for intact vertebral specimens (N), KD specimens (KD), postoperative group A (A), postoperative group B (B), and postoperative group C (C) were shown in Figure 8; Table 2. Statistical analysis showed that the ROM of the KD specimens was greater ($p < 0.05$) compared to the N control group, except for right lateral bending. In the left/right axial rotation, the specimens were still significantly different ($p < 0.05$) from the intact specimens in terms of ROM after pure PKP.

3.4 Relative displacement of bone cement

All specimens underwent 6 times of activity with different deflection angles in 6 directions of flexion, extension, left/right lateral bending, left/right axial rotation. After repeated movement with 5° as the maximum activity angle, no significant displacement of bone cement was seen in all vertebrae on the CT images. After repeated movement with 10° as the maximum activity angle, the relative displacement of the bone cement in each group is shown in Table 3, and the partial post-activation CT of the bone cement is shown in Figure 9. Compared with pure PKP, pedicle cement screw fixation combined with PKP can significantly reduce the relative displacement of the bone cement ($p < 0.05$).

4 Discussion

With the aging of society, osteoporosis has become the most common bone metabolic disease which is characterized by low bone density and leaving the affected bones susceptible to fracture (Song et al., 2022). KD is a complication or end-stage manifestation of vertebral compression fractures and once it occurs, it can seriously affect the patient's quality of life and survival, requiring more

TABLE 1 M(IQR) of the vertebral heights (mm) at 500 N of axial compression in each group, $n = 6$.

Group	Pre-treatment	Post-treatment	Wilcoxon signed-rank test	
			Z-value	*p*-value
A	121.02 (23.66)	131.06 (16.99)	1.782	0.075
B	109.27 (32.04)	121.84 (31.91)	2.201	0.028
C	121.85 (25.96)	137.36 (24.17)	2.201	0.028
H-value	0.881	1.205		
p-value	0.644	0.548		

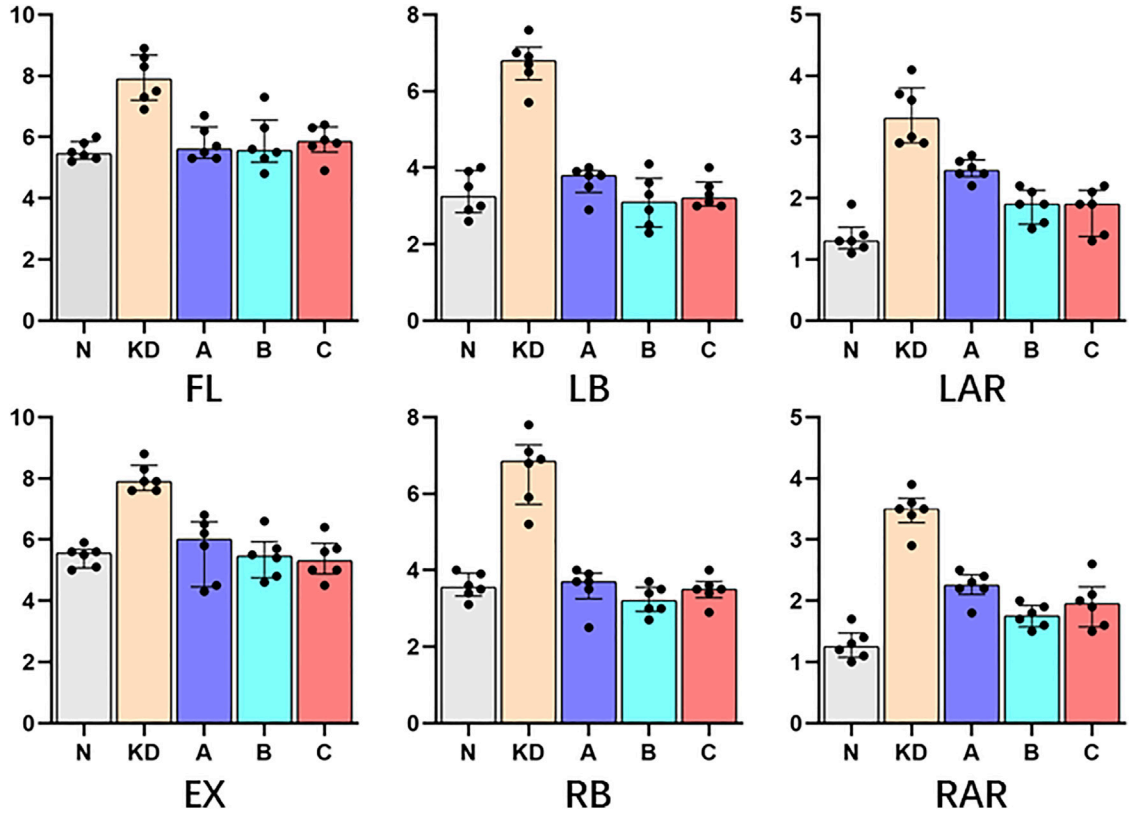

FIGURE 8
ROM (°) were indicated as the medians and interquartile range [M(IQR)].

TABLE 2 ROM (°) was shown with M (IQR); "N", intact lumbar spine; "KD", KD specimens; "A", PKP; "B", unilateral pedicle cement screw fixation combined with PKP; "C", bilateral pedicle cement screw fixation combined with PKP. FL, flexion; EX, extension; LB, left lateral bending; RB, right lateral bending; LAR, left axial rotation; RAR, right axial rotation. *, statistical difference with "N"; ▲, statistical difference with KD.

	N (n = 6)	KD (n = 6)	A (n = 6)	B (n = 6)	C (n = 6)
FL	5.45 (0.57)	7.90 (1.48)*	5.60 (1.03)▲	5.55 (1.38)▲	5.85 (0.83)
EX	5.55 (0.60)	7.90 (0.83)*	6.00 (2.13)	5.45 (1.17)▲	5.30 (1.00)▲
LB	3.25 (1.10)	6.80 (0.85)*	3.80 (0.57)	3.10 (1.27)▲	3.20 (0.63)▲
RB	3.55 (0.60)	6.85 (1.55)	3.70 (0.67)	3.20 (0.63)▲	3.50 (0.43)▲
LAR	1.30 (0.35)	3.30 (0.90)*	2.45 (0.27)*	1.90 (0.55)▲	1.90 (0.75)▲
RAR	1.25 (0.40)	3.50 (0.40)*	2.25 (0.32)*	1.75 (0.35)▲	1.95 (0.65)

TABLE 3 Relative displacement (mm) of bone cement with 10° as the maximum activity angle. "*", statistical difference ($p < 0.05$) compared to the A group.

Group	M (P_{25}, P_{75})	Kruskal–Wallis test	
		H-value	p-value
A	3.50 (1.50,6.48)	8.307	0.016
B	0.00 (0.00,0.55)*		
C	0.00 (0.00,0.43)*		

aggressive surgical treatment (Zhang et al., 2022; Gou et al., 2023). With the leap forward in minimally invasive spine technology over the last decade, the traditional open fixation-fusion surgical approach is not the best choice for patients with no nerve compression symptoms (Huang et al., 2018). PVP and PKP are more widely used in clinical practice because of its advantages in terms of economic cost, operative time, blood loss, and radiation exposure. However, they have some postoperative risks, such as loosening of the cement mass, displacement, and fracture of the cement mass, resulting in adverse consequences such as neurological impairment and re-aggravation of the posterior convexity deformity.

There is a significant technical gap in the current approach to reduce postoperative cement displacement in KD. In order to solve these clinical problems, pedicle bone cement screw can act as a "bridge" to link the bone cement with the surrounding bone tissue while being placed percutaneously and minimally invasively, reducing the incidence

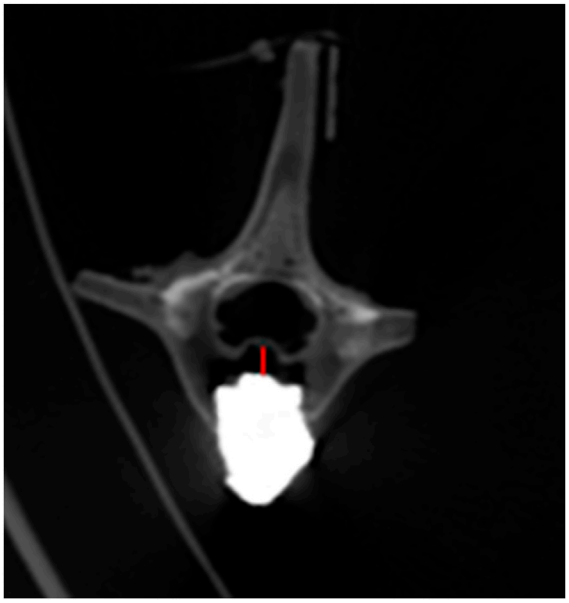

FIGURE 9
Bone cement displacement after movement. The red line represents the maximum displacement distance.

of bone cement loosening and displacement. It can be implanted into the diseased vertebra through the puncture needle used in the PKP/PVP treatment of KD, without causing additional trauma (Figure 10). The front end of the pedicle screw is equipped with multiple bone cement overflow hole, which can directly inject bone cement and fuse with the bone cement injected by PKP/PVP, ensuring a strong and anchored connection between the screw and bone cement. Meanwhile, the screw provides a fixed point of stability for the bone cement in the vertebral body. By connecting to the pedicle, the screw can anchor the bone cement in place, preventing it from loosening or displacing over time.

4.1 Preparation of KD specimens

Biomechanical testing of new spinal implants *in vitro* is essential for their safety and efficacy (Lee et al., 2011). However, the limited availability of human cadavers leads to inconsistent specimen quality, making it difficult to obtain enough specimens for controlled experiments to explore the effects of these implants (Lee et al., 2011; Hsieh et al., 2023). The vertebrae of other large mammals are morphologically and biomechanically different from the human vertebrae, and their experimental parameters are not directly transferable to the human spine. However, due to the similarity of the porcine spine to the human in terms of size, nutritional make-up, bone structure, and mineral metabolism, it has been frequently used in some studies to verify the effectiveness of spinal fusion and internal fixation, and to a certain extent to draw clinically relevant conclusions (Lee et al., 2011; Hsieh et al., 2020; Laznovsky et al., 2022).

To model osteoporosis, demineralization can be performed using reagents such as hydrochloric acid and hydrogen peroxide, but the models prepared using these methods differ from the pathological process of human osteoporosis, which is more like osteomalacia (Elfar et al., 2014; Stewart et al., 2020). EDTA is a chelating agent that binds to the metal ion Ca^{2+} and acts more slowly, preserving the natural biological structure of collagen better than the stronger and faster acting hydrochloric or nitric acids (Lee et al., 2011). After 7 weeks, the difference in BMD values of the vertebrae before and after decalcification was more than 30%. Since there is currently no investigation data on peak BMD in porcine spine, the percentage of BMD loss was measured using the human osteoporosis standard, where 25% loss is considered an indicator of osteoporosis (Lee et al., 2011; Siris et al., 2014).

In the preparation of *in vitro* osteoporotic specimens, treatment with 10% formaldehyde solution for 24 h was a common approach in previous biomechanical experimental studies because of the prolonged exposure to ambient temperature (Lee et al., 2011; Hsieh et al., 2022). This preservative measure inevitably causes

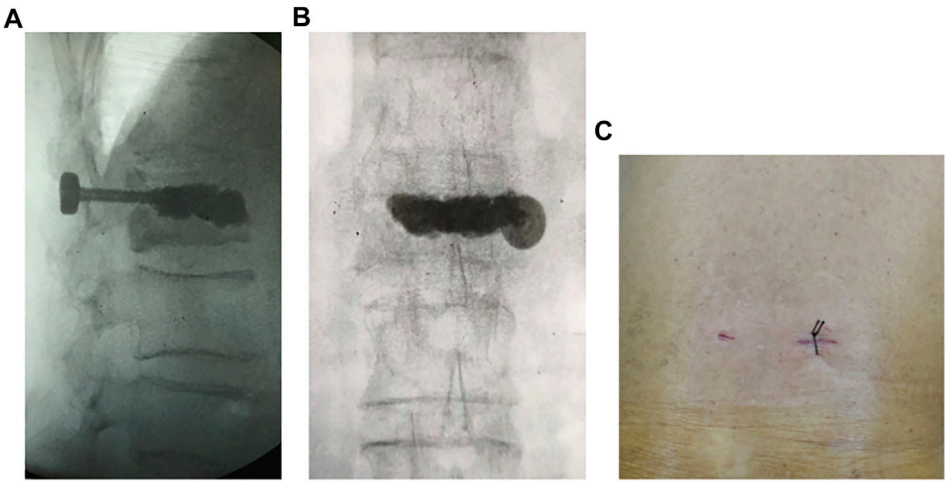

FIGURE 10
Intraoperative fluoroscopic and incisional photograph of a patient with KD treated with a novel minimally invasive pedicle bone cement screw: **(A)** lateral view **(B)** anteroposterior view **(C)** incisional view (1.5 cm).

changes in the biomechanical properties, focusing particularly on Young's modulus and impact energy in short time applications (Currey et al., 1995; Holewijn et al., 2017). This alteration makes it necessary to use smaller moments and slower angular velocities in the experiments to avoid damaging the specimens, which can also affect the experimental results to some extent.

4.2 Recovery of vertebral body height

In clinical practice, it has been found that KD occurs most commonly at the thoracolumbar junction, which is also the common location for osteoporotic vertebral fractures. From a biomechanical perspective, one important reason for the development of KD from vertebral microfractures is that the shear stress in the thoracolumbar segment changes after a large range of motion (Li et al., 2011). Following vertebral fracture, the vertebral morphology changes, mainly characterized by loss of vertebral height and spinal kyphosis (Röllinghoff et al., 2013). In this study, we found that satisfactory vertebral height was achieved regardless of the use of pedicle bone cement screw or not. This result is similar to the clinical treatment outcomes reported by Noriega et al. (2019) (Wang et al., 2021). It can be concluded that using the novel type of pedicle screw combined with PKP for the treatment of KD can achieve good effectiveness in static standing position. The restoration of vertebral height can prevent spinal center of gravity shifting, which in turn restores the internal biomechanical environment of the vertebrae and reduces the risk of nonunion (Cao et al., 2020; Najjar et al., 2023).

Both PVP and PKP are commonly used for vertebral compression fractures. Patients with severe OVCF can be treated with PVP in a prone position with the chest and hips resting on soft pillows to maintain spinal hyperextension to help restore vertebral body height (Chin et al., 2006; Shin et al., 2009; Yu et al., 2020). Since this experiment used an *in vitro* specimen, we had to use a balloon to expand the vertebral body when repairing the vertebral height.

4.3 Changes in vertebral body stability

After making the specimens into IVC-like vertebrae, ROM was significantly increased compared to intact vertebrae under 5 Nm torque. In the experiment, we observed that the increased instability mainly occurred at the site of the discontinuous cortical bone. Restoring the stability of the vertebral body is also a clear need in the treatment of KD (Yokoyama et al., 2013). The ROM of the vertebral body is an important parameter of vertebral stability. According to Denis' three-column theory, recompression of the spine may be influenced by spinal stability (Denis, 1983). Low spinal stability may lead to an increased risk of recompression. In this study, filling with bone cement reduced the maximum displacement of the KD specimens and approached the intact vertebrae, which was also demonstrated by some related studies (Dai et al., 2022). However, in the PKP group, the specimens still differed from the intact vertebrae in terms of stability during rotation. This result suggests that the stability of the vertebral body can be further increased by pedicle screw fixation, thus reducing the incidence of recompression.

4.4 Relative displacement of bone cement

An important purpose of PKP and PVP is to return the patient to normal living conditions as soon as possible, which requires that the patient be able to perform the angle required after surgery. It is also required to reduce the probability of bone cement displacement during this period (Qi HR. et al., 2022). The gold standard in biomechanical testing is to apply moments to the specimens (Wilke et al., 1998). However, due to the *in vitro* osteoporotic specimens we used, which was more flexible than undecalcified specimens, this torque may result in a significant movement of the lumbar spine that should not have been accomplished. In previous studies, maximum rotational value was similar, with a range of 4.05° to 7.10° for lying and 9° to 14° for standing (Yeager et al., 2014; Breen et al., 2019; Daniel et al., 2023). In consideration of the maximum ROM of L12-L2 and avoiding excessive damage to the experimental specimen during the experiment, 5° was used to simulate ROM for lying and 10° to simulate ROM of standing (Yeager et al., 2014; Breen et al., 2019; Daniel et al., 2023).

Previous clinical case reports have also shown displacement of bone cement, but our experimental results generally have a higher displacement rate (Korovessis et al., 2013), perhaps due to the extreme smoothness of the cortical bone defect and the complete coverage of the cancellous bone surface by bone wax in our experimental models to better control the number of variables. The KD model designed in the experiment meets the clinical and radiographic characteristics of intravertebral cleft (Formica et al., 2016; Qi J. et al., 2022). This makes it possible that the measured displacement of the bone cement in the experiment indicates the trend and magnitude of displacement. The screw can release bone cement through the lateral hole at the front end of the screw, thoroughly filling the cracks in the vertebral body, so that the bone cement and the screw are connected as a whole. At the same time, the screw connects the strongest part of the bone at the pedicle, and ultimately reinforces the interaction between the bone cement and the surrounding bone tissue as a "bridge". This achieves the function of preventing the bone cement from loosening and displacing.

4.5 Study limitations

The experiment has convincingly demonstrated that the novel bone cement screws provide excellent fixation of bone cement masses, providing them with less mobility and more stability. However, the experiment has certain limitations. First, the specimens used were porcine spines prepared by formaldehyde solution and EDTA, which inevitably led to altered the soft tissue properties and thus the overall biomechanical properties and therefore cannot be identical to human specimens. Second, the number of specimens was small, and more data are needed to support the results. Third, during the experiments, shear forces were still unavoidable, with a maximum value of 0.3 Nm. To obtain more reliable test results, these forces had to be reduced further, even to pure moments. Finally, the bone cement relative displacement

was linked to the ROM, which is not correspond to the common recommendations in previous studies.

5 Conclusion

In an *in vitro* animal vertebral body model, the application of a new minimally invasive cemented screw for Kümmel's disease meets the need for restoration of vertebral body height. It also possesses a stronger effect of fixing the vertebral body and limiting bone cement displacement compared to pure PKP. From the viewpoint of biomechanics, both unilateral and bilateral anchoring have better effects, which provides strong evidence and guidance for later clinical application.

Data availability statement

The raw data supporting the conclusion of this article will be made available by the authors, without undue reservation.

Ethics statement

The animal study was reviewed and approved by Tianjin Hospital, Tianjin University, Tianjin, China. Written informed consent was obtained from the individual(s) for the publication of any potentially identifiable images or data included in this article.

Author contributions

All authors listed have made a substantial, direct, and intellectual contribution to the work and approved it for publication.

Conflict of interest

The authors declare that the research was conducted in the absence of any commercial or financial relationships that could be construed as a potential conflict of interest.

Publisher's note

All claims expressed in this article are solely those of the authors and do not necessarily represent those of their affiliated organizations, or those of the publisher, the editors and the reviewers. Any product that may be evaluated in this article, or claim that may be made by its manufacturer, is not guaranteed or endorsed by the publisher.

References

Breen, A., Hemming, R., Mellor, F., and Breen, A. (2019). Intrasubject repeatability of *in vivo* intervertebral motion parameters using quantitative fluoroscopy. *Eur. Spine J.* 28, 450–460. doi:10.1007/s00586-018-5849-9

Cao, Z., Wang, G., Hui, W., Liu, B., Liu, Z., and Sun, J. (2020). Percutaneous kyphoplasty for osteoporotic vertebral compression fractures improves spino-pelvic alignment and global sagittal balance maximally in the thoracolumbar region. *PLoS One* 15, e0228341. doi:10.1371/journal.pone.0228341

Chen, L., Dong, R., Gu, Y., and Feng, Y. (2015). Comparison between balloon kyphoplasty and short segmental fixation combined with vertebroplasty in the treatment of kümmell's disease. *Pain Physician* 18, 373–381. doi:10.36076/ppj.2015/18/373

Chin, D. K., Kim, Y. S., Cho, Y. E., and Shin, J. J. (2006). Efficacy of postural reduction in osteoporotic vertebral compression fractures followed by percutaneous vertebroplasty. *Neurosurgery* 58, 695–700. doi:10.1227/01.neu.0000204313.36531.79

Currey, J. D., Brear, K., Zioupos, P., and Reilly, G. C. (1995). Effect of formaldehyde fixation on some mechanical properties of bovine bone. *Biomaterials* 16, 1267–1271. doi:10.1016/0142-9612(95)98135-2

Dai, H., Liu, Y., Han, Q., Zhang, A., Chen, H., Qu, Y., et al. (2022). Biomechanical comparison between unilateral and bilateral percutaneous vertebroplasty for osteoporotic vertebral compression fractures: A finite element analysis. *Front. Bioeng. Biotechnol.* 10, 978917. doi:10.3389/fbioe.2022.978917

Daniel, E. S., Lee, R. Y. W., and Williams, J. M. (2023). The reliability of video fluoroscopy, ultrasound imaging, magnetic resonance imaging and radiography for measurements of lumbar spine segmental range of motion *in-vivo*: A review. *J. Back Musculoskelet. Rehabil.* 36, 117–135. doi:10.3233/bmr-210285

Denis, F. (1983). The three column spine and its significance in the classification of acute thoracolumbar spinal injuries. *Spine (Phila Pa 1976)* 8, 817–831. doi:10.1097/00007632-198311000-00003

Duan, Z. K., Zou, J. F., He, X. L., Huang, C. D., and He, C. J. (2019). Bone-filling mesh container versus percutaneous kyphoplasty in treating Kümmell's disease. *Arch. Osteoporos.* 14, 109. doi:10.1007/s11657-019-0656-4

Elfar, J., Menorca, R. M., Reed, J. D., and Stanbury, S. (2014). Composite bone models in orthopaedic surgery research and education. *J. Am. Acad. Orthop. Surg.* 22, 111–120. doi:10.5435/00124635-201402000-00006

Formica, M., Basso, M., Cavagnaro, L., Formica, C., Zanirato, A., and Felli, L. (2016). Kümmell disease: Illustrative case for definition criteria. *Spine J.* 16, e707–e708. doi:10.1016/j.spinee.2016.03.035

Gan, D. H., Fang, M. Z., Xue, H. P., Tan, G. Q., Li, N. H., Li, Z. C., et al. (2021). Clinical observations of kummell disease treatment through percutaneous fixation combined with vertebroplasty. *Orthop. Surg.* 13, 1505–1512. doi:10.1111/os.12935

Gou, P. G., Jing, W. L., Zhou, J. M., Wang, R., Wang, Z., Chang, F., et al. (2023). Magnetic resonance imaging negative spine trauma followed by a delayed intravertebral vacuum cleft-kummell's disease: A case report and literature review. *Orthop. Surg.* 15, 366–370. doi:10.1111/os.13559

Han, X., Yang, D., Xie, X., and Chai, L. (2022). Screw cutting vertebrae after short-segment pedicle screw fixation combined with kyphoplasty in kummell disease: A case report. *Asian J. Surg.* 45, 2940–2942. doi:10.1016/j.asjsur.2022.06.113

Holewijn, R. M., Faraj, S. S. A., Kingma, I., van Royen, B. J., de Kleuver, M., and van der Veen, A. J. (2017). Spinal biomechanical properties are significantly altered with a novel embalming method. *J. Biomech.* 55, 144–146. doi:10.1016/j.jbiomech.2017.02.012

Hsieh, M. K., Lee, D. M., Li, Y. D., Peng, C. C., Tsai, T. T., Lai, P. L., et al. (2023). Biomechanical evaluation of position and bicortical fixation of anterior lateral vertebral screws in a porcine model. *Sci. Rep.* 9 (13), 454. doi:10.1038/s41598-023-27433-6

Hsieh, M. K., Li, Y. D., Li, Y. C., Liu, M. Y., Tsai, T. T., Lai, P. L., et al. (2022). Improved fixation stability for repairing pedicle screw loosening using a modified cement filling technique in porcine vertebrae. *Sci. Rep.* 17 (12), 2739. doi:10.1038/s41598-022-06724-4

Hsieh, M. K., Liu, M. Y., Chen, J. K., Tsai, T. T., Lai, P. L., Niu, C. C., et al. (2020). Use of longer sized screws is a salvage method for broken pedicles in osteoporotic vertebrae. *Sci. Rep.* 26 (10), 10441. doi:10.1038/s41598-020-67489-2

Huang, Y. S., Hao, D. J., Feng, H., Zhang, H. P., He, S. M., Ge, C. Y., et al. (2018). Comparison of percutaneous kyphoplasty and bone cement-augmented short-segment pedicle screw fixation for management of kummell disease. *Med. Sci. Monit.* 24, 1072–1079. doi:10.12659/msm.905875

Huang, Z. B., Yan, S. F., Li, S. Y., Liu, J. H., Fan, S. W., and Zhao, F. D. (2021). Short-segment pedicle screw fixation combined with vertebroplasty for the treatment of Kummell disease with kyphosis. *Zhongguo Gu Shang* 34, 694–700. doi:10.12200/j.issn.1003-0034.2021.08.002

Korovessis, P., Vardakastanis, K., Repantis, T., and Vitsas, V. (2013). Balloon kyphoplasty versus KIVA vertebral augmentation-comparison of 2 techniques for osteoporotic vertebral body fractures: A prospective randomized study. *Spine (Phila Pa 1976)* 38, 292–299. doi:10.1097/brs.0b013e31826b3aef

Laznovsky, J., Brinek, A., Zikmund, T., Boudova, M., Vojtova, L., Dorazilova, J., et al. (2022). Automatic 3D analysis of the *ex-vivo* porcine lumbar interbody fusion based on

X-ray micro computed tomography data. *Comput. Biol. Med.* 145, 105438. doi:10.1016/j.compbiomed.2022.105438

Lee, C. Y., Chan, S. H., Lai, H. Y., and Lee, S. T. (2011). A method to develop an *in vitro* osteoporosis model of porcine vertebrae: Histological and biomechanical study. *J. Neurosurg. Spine* 14, 789–798. doi:10.3171/2010.12.spine10453

Lei, F., He, W., Tian, X., Li, Z., Zheng, L., Kang, J., et al. (2020). Prophylactic percutaneous kyphoplasty treatment for nonfractured vertebral bodies in thoracolumbar for osteoporotic patients. *Biomed. Res. Int.* 2020, 1–7. doi:10.1155/2020/8593516

Li, H., Liang, C. Z., Shen, C. C., and Chen, Q. X. (2011). Decreases in fluid shear stress due to microcracks: A possible primary pathogenesis of kummell's disease. *Med. Hypotheses* 77, 897–899. doi:10.1016/j.mehy.2011.08.005

Li, H. K., Hao, D. J., Yang, J. S., Huang, D. G., Yu, C. C., Zhang, J. N., et al. (2017). Percutaneous kyphoplasty versus posterior spinal fixation with vertebroplasty for treatment of kummell disease: A case-control study with minimal 2-year follow-up. *Med. Baltim.* 96, e9287. doi:10.1097/md.0000000000009287

Li, Y. M., Qian, Y. F., Shen, G. J., Tang, C. X., Zhong, X. Q., and He, S. Q. (2023). Percutaneous mesh-container-plasty versus percutaneous kyphoplasty for the treatment of kummell's disease: A retrospective cohort study. *J. Orthop. Surg. Res.* 18, 260. doi:10.1186/s13018-023-03753-1

Liu, J. B., Zuo, R., Zheng, W. J., Li, C. Q., Zhang, C., and Zhou, Y. (2022a). The accuracy and effectiveness of automatic pedicle screw trajectory planning based on computer tomography values: An *in vitro* osteoporosis model study. *BMC Musculoskelet. Disord.* 23, 165. doi:10.1186/s12891-022-05101-6

Liu, Y., Su, Y., Xu, Y., Wang, S., Gao, L., Zheng, X., et al. (2022b). The use of three-column enhanced percutaneous vertebroplasty to treat kummell's disease. *J. Pain Res.* 15, 2919–2926. doi:10.2147/jpr.s370578

Najjar, E., Mardashti, A., Komaitis, S., Karouni, F., Vatkar, A., and Quraishi, N. A. (2023). Does kyphoplasty affect the global sagittal alignment in patients with osteoporotic vertebral fractures? A systematic review and meta-analysis. *Eur. Spine J.* 32, 38–45. doi:10.1007/s00586-022-07479-2

Niu, J., Song, D., Zhou, H., Meng, Q., Meng, B., and Yang, H. (2017). Percutaneous kyphoplasty for the treatment of osteoporotic vertebral fractures with intravertebral fluid or air: A comparative study. *Clin. Spine Surg.* 30, 367–373. doi:10.1097/bsd.0000000000000262

Noriega, D. C., Rodríguez-Monsalve, F., Ramajo, R., Sánchez-Lite, I., Toribio, B., and Ardura, F. (2019). Long-term safety and clinical performance of kyphoplasty and SpineJack® procedures in the treatment of osteoporotic vertebral compression fractures: A pilot, monocentric, investigator-initiated study. *Osteoporos. Int.* 30, 637–645. doi:10.1007/s00198-018-4773-5

Qi, H. R., Qi, J., Sun, Y., Gao, J. Y., Sun, J. M., and Wang, G. D. (2022a). Bone microarchitecture and metabolism in elderly male patients with signs of intravertebral cleft on MRI. *Eur. Radiol.* 32, 3931–3943. doi:10.1007/s00330-021-08458-9

Qi, J., Hu, Y., Yang, Z., Dong, Y., Zhang, X., Hou, G., et al. (2022b). Incidence, risk factors, and outcomes of symptomatic bone cement displacement following percutaneous kyphoplasty for osteoporotic vertebral compression fracture: A single center study. *J. Clin. Med.* 11, 7530. doi:10.3390/jcm11247530

Röllinghoff, M., Zarghooni, K., Zeh, A., Wohlrab, D., and Delank, K. S. (2013). Is there a stable vertebral height restoration with the new radiofrequency kyphoplasty? A clinical and radiological study. *Eur. J. Orthop. Surg. Traumatol.* 23, 507–513. doi:10.1007/s00590-012-1026-8

Shin, J. J., Chin, D. K., and Yoon, Y. S. (2009). Percutaneous vertebroplasty for the treatment of osteoporotic burst fractures. *Acta Neurochir. (Wien)* 151, 141–148. doi:10.1007/s00701-009-0189-5

Siris, E. S., Adler, R., Bilezikian, J., Bolognese, M., Dawson-Hughes, B., Favus, M. J., et al. (2014). The clinical diagnosis of osteoporosis: A position statement from the national bone health alliance working group. *Osteoporos. Int.* 25, 1439–1443. doi:10.1007/s00198-014-2655-z

Song, S., Guo, Y., Yang, Y., and Fu, D. (2022). Advances in pathogenesis and therapeutic strategies for osteoporosis. *Pharmacol. Ther.* 237, 108168. doi:10.1016/j.pharmthera.2022.108168

Stewart, A. J., Miles, A. W., and Fletcher, J. W. A. (2020). Influence of pilot hole diameter in cancellous screw fixation in a reduced density animal bone model. *Clin. Biomech. (Bristol, Avon)* 80, 105152. doi:10.1016/j.clinbiomech.2020.105152

Wang, B., Wang, Y., Zhang, H., Yan, L., Kong, L., He, S., et al. (2021). A novel bone cement screw system combined with vertebroplasty for the treatment of kummell disease with bone deficiency at the vertebral anterior border: A minimum 3-year follow-up study. *Clin. Neurol. Neurosurg.* 201, 106434. doi:10.1016/j.clineuro.2020.106434

Wang, W., Liu, Q., Liu, W. J., Li, Q. B., Cai, L., and Wang, Z. K. (2020). Different performance of intravertebral vacuum clefts in kummell's disease and relevant treatment strategies. *Orthop. Surg.* 12, 199–209. doi:10.1111/os.12609

Wilke, H. J., Wenger, K., and Claes, L. (1998). Testing criteria for spinal implants: Recommendations for the standardization of *in vitro* stability testing of spinal implants. *Eur. Spine J.* 7, 148–154. doi:10.1007/s005860050045

Yang, S. C., Chen, W. J., Yu, S. W., Tu, Y. K., Kao, Y. H., and Chung, K. C. (2008). Revision strategies for complications and failure of vertebroplasties. *Eur. Spine J.* 17, 982–988. doi:10.1007/s00586-008-0680-3

Yeager, M. S., Cook, D. J., and Cheng, B. C. (2014). Reliability of computer-assisted lumbar intervertebral measurements using a novel vertebral motion analysis system. *Spine J.* 1 (14), 274–281. doi:10.1016/j.spinee.2013.10.048

Yokoyama, K., Kawanishi, M., Yamada, M., Tanaka, H., Ito, Y., Hirano, M., et al. (2013). In not only vertebroplasty but also kyphoplasty, the resolution of vertebral deformities depends on vertebral mobility. *AJNR Am. J. Neuroradiol.* 34, 1474–1478. doi:10.3174/ajnr.a3424

Yu, H., Li, Y., Yao, X., Lin, J., Pan, Y., Zhuang, H., et al. (2020). Application of percutaneous vertebroplasty and percutaneous kyphoplasty in treating Kummell's patients with different stages and postural correction status. *Expert Rev. Med. Devices* 17, 357–364. doi:10.1080/17434440.2020.1736039

Zhang, C., Wen, T., Li, C., Ruan, D., and He, Q. (2021). Cluster phenomenon of vertebral refractures after posterior pedicle screw fixation in a patient with glucocorticosteroid-induced kummell's disease: A treatment dilemma. *Arch. Osteoporos.* 16, 93. doi:10.1007/s11657-021-00941-6

Zhang, L., Wang, J. C., Wang, Y. X., and Feng, X. M. (2022). Comparison of high- and low-viscosity cement percutaneous vertebroplasty with manipulative reduction for the treatment of kummell's disease: A retrospective cohort study. *J. Back Musculoskelet.* 35, 301–307. doi:10.3233/bmr-191778

frontiers | Frontiers in Bioengineering and Biotechnology

TYPE Original Research
PUBLISHED 07 August 2023
DOI 10.3389/fbioe.2023.1229218

OPEN ACCESS

EDITED BY
Junyan Li,
Southwest Jiaotong University, China

REVIEWED BY
Christian Liebsch,
Ulm University Medical Center, Germany
Mehran Moazen,
University College London,
United Kingdom

*CORRESPONDENCE
Zikai Hua,
eddie_hua@shu.edu.cn
Chengmin Liang,
liangchm@163.com

RECEIVED 26 May 2023
ACCEPTED 26 July 2023
PUBLISHED 07 August 2023

CITATION
Cui X, Zhu J, Yang W, Sun Y, Huang X, Wang X, Yu H, Liang C and Hua Z (2023), Finite element study of sagittal fracture location on thoracolumbar fracture treatment.
Front. Bioeng. Biotechnol. 11:1229218.
doi: 10.3389/fbioe.2023.1229218

Finite element study of sagittal fracture location on thoracolumbar fracture treatment

Xilong Cui[1,2,3], Junjun Zhu[1], Wanmei Yang[2,3], Yuxiang Sun[1], Xiuling Huang[1], Xiumei Wang[1], Haiyang Yu[2,3], Chengmin Liang[2,3]* and Zikai Hua[1,3]*

[1]School of Mechatronics Engineering and Automation, Shanghai University, Shanghai, China, [2]Department of Orthopedics, Fuyang People's Hospital, Fuyang, Anhui, China, [3]Spinal Deformity Clinical and Research Center of Anhui Province, Fuyang, Anhui, China

Background: Posterior internal fixation is the main method used for the treatment of thoracolumbar fractures. Fractures often occur in the upper 1/3 of the vertebral body. However, they can also occur in the middle or lower 1/3 of the vertebral body. At present, there is no report discussing the potential effects of sagittal location on instrument biomechanics or surgical strategy. The object of this study was to investigate the effect of the sagittal location of the fracture region of the vertebral body on the biomechanics of the internal fixation system and surgical strategy.

Methods: A finite element model of the T11-L3 thoracolumbar segment was established based on a healthy person's CT scan. Different sagittal fracture location finite element models were created by resection of the upper 1/3, middle 1/3, and lower 1/3 of the L1 vertebral body. Three surgical strategies were utilized in this study, namely, proximal 1 level and distal 1 level (P1-D1), proximal 2 level and distal 1 level (P2-D1), and proximal 1 level and distal 2 levels (P1-D2). Nine fixation finite element models were created by combining fracture location and fixation strategies. Range of motion, von Mises stress, and stress distribution were analyzed to evaluate the effects on the instrument biomechanics and the selection of surgical strategy.

Results: In all three different fixation strategies, the maximum von Mises stress location on the screw did not change with the sagittal location of the fracture site; nevertheless, the maximum von Mises stress differed. The maximum rod stress was located at the fracture site, with its value and location changed slightly. In the same fixation strategy, a limited effect of sagittal location on the range of motion was observed. P2D1 resulted in a shorter range of motion and lower screw stress for all sagittal locations of the fracture compared with the other strategies; however, rod stress was similar between strategies.

Conclusion: The sagittal location of a fracture may affect the intensity and distribution of stress on the fixation system but does not influence the selection of surgical strategy.

KEYWORDS

thoracolumbar fracture, sagittal location, instrument, biomechanics, surgical strategy

Introduction

According to an epidemiological study, the incidence of spinal fractures is approximately 32.8/100 000 (Liu et al., 2018). Most fractures occurs in the thoracic spine, followed by the lumbar- and cervical spine, accounting for 41.6%, 33.7%, and 24.6% respectively (den Ouden et al., 2019). More than 14.3% of cases are burst fractures (Denis, 1983). The thoracolumbar spine is the transition region from the fixed thoracic spine to the flexible lumbar. Therefore, the thoracolumbar segment is the region where fractures occur most frequently (Holmes et al., 2001). Fracture fragments can migrate the spinal canal and potentially cause spinal cord injury. The main focus in the treatment of thoracolumbar fractures is to restore spinal stability. Burst fractures involve the anterior and middle columns, which are considered unstable (Petersilge and Emery, 1996). Internal fixation is the most important surgical option for the treatment of unstable thoracolumbar fractures. Internal fixation could be divided into anterior, posterior, and combined anterior and posterior operations. Posterior transpedicular internal fixation is the most commonly used method. Short-segment, limited long-segment, and long-segment fixation has been previously reported in the literature (El et al., 2020; Girardo et al., 2021; Liang et al., 2020). These techniques have resulted in good clinical outcomes; however, instrument loosening and breakage can occur (Mu et al., 2022).

Finite element (FE) analysis offers the advantages of good repeatability and cost-effectiveness. Thus, it has been widely used to understand and optimise the different fracture fixations, mechanical testing, and spine fracture biomechanical research (Naoum et al., 2021; Guo et al., 2021; Wong et al., 2021). Numerous studies have compared the maximum stress and distribution of different fixation methods. However, not all internal instruments have the same fracture location as predicted in clinical practice.

Studies revealed that the location and size of upper endplate injury in the coronal plane affect internal fixation and vertebral body stress. Wang and Hu found that in cases with 4/5 endplate fractures, internal fixation should not be removed after surgery (Wang and Hu., 2020). In patients with spinal tumors, the location and size could also affect spinal biomechanics (Galbusera et al., 2018). However, whether the sagittal distribution of the fractures affects the stress of internal fixation or surgical strategy has not been reported in the literature. Clinically, some researches have observed this sagittal distribution. According to the AO classification, type A3.2 is divided into upper burst fractures, lower burst fractures, and lateral burst fractures (Rosenthal et al., 2018). In the Denis classification, compression fractures are divided into Types A, B, C, and D. The fractured region of Type B, C, and D primarily located in the upper, middle, and lower regions, accounting for 62.4%, 6.09%, and 15.2%, respectively. In burst fractures, upper fractures account for 49.2%, while lower fractures account for 6.8%. Some researchers have also classified the mechanical mechanisms behind these distribution patterns. (Guo and Li., 2019).Therefore, we hypothesized that the sagittal distribution of fractures may affect the level and position of maximum mechanical stress on the internal fixation suggesting that the fracture level must be taken into account when developing a treatment algorithm.

In this study, we resected the upper 1/3, middle 1/3, and lower 1/3 of the vertebral body to simulate the sagittal distribution of different sagittal fractures, A3 burst fractures according to Vaccaro et al. (2013) Three internal fixation strategies were used, namely, one proximal and distal segment (P1D1), two proximal and one distal segment (P2D1), and one proximal and two distal segments (P1D2). The objectives of this study were to 1) investigate the effects of fracture sagittal distribution on internal fixation biomechanics, and 2) determine its potential influence on the selection of internal fixation strategy.

Materials and methods

The volunteer selection criteria: 18–30 years old, no history of spinal tumors, lower back pain, or spinal surgery, BMI 18.5–23.9 kg/m^2. A 25-year-old male with a BMI of 20.2 kg/m^2 was involved in the study with written informed consent. The study was approved by the Ethics Committee of Fu Yang Hospital (No, 2020-11, Anhui, China).

Computed tomography images of T10-L4 were obtained using a Brilliance 256 CT scanner (Philips Brilliance iCT256, Eindhoven, Netherlands). The slice thickness was 0.5 mm and the in-plane resolution was 512 × 512. A three-dimensional model of T11-L3 was established with Mimics 21.0 (Materialise, Leuven, Belgium). The cortical bone and cancellous bone were based on geometry using the "Threshold" and "Regional Growth" tools. The mesh structure was prepared using the preprocessing software Geomagic Studio 12.0 (Geomagic, Cary, NC, United States). Notably, the thickness of the cortical bone and endplate was 1 mm and 0.5 mm, respectively (Wong et al., 2003).

UGNX12.0 (Dassault Systèmes, S.A, Paris, France) was used to construct the intervertebral disc. The nucleus pulposus and annular fibers were constructed separately. Additionally, the volume ratio of the annulus fibrosus to the nucleus pulposus was set to 6:4 (Wang et al., 2013).

A baseline three-dimensional FE model of a healthy T11-L3 was created first. The following three interfaces were modelled as bonded: the vertebral body-endplate, endplate-nucleus pulposus, and nucleus pulposu-annulus fibrosus. Moreover, frictionless contact was used to simulate the sliding contact between articular cartilages. The model was assumed to be homogeneous, isotropic, and linearly elastic. The material properties used are presented in Table 1 (Park et al., 2013; Wang et al., 2018). The ligaments (i.e., the

TABLE 1 Material properties assumed for different components of the finite element (FE) model.

Spinal site	Young's modulus (MPa)	Poisson's ratio
Vertebra		
Cortical	12,000	0.3
Cancellous bone	100	0.2
Endplate	23.8	0.4
Cartilage	11	0.4
Intervertebral disc		
Nucleus pulposus	1	0.49
Annulus fibrosis	4.2	0.4
Pedicle screws and rods	110,000	0.3

TABLE 2 Material properties assumed for different components of ligaments.

Ligament	Rigidity	Strain ε (%)	Rigidity	Strain ε (%)	Rigidity	Strain ε (%)
Anterior	347	0–12.2	787	12.2–20.3	1,864	20.3
Posterior	29.5	0–11.1	61.7	11.1–23	236	23
Capsular	36	0–25	159	25–30	384	30
Intertransverse	0.3	0–18.2	1.8	18.2–23.3	10.7	23.3
Flavum	7.7	0–5.9	9.6	5.9–4.9	58.2	49
Supraspinal	2.5	0–20	5.3	20–25	34	25
Interspinal	1.4	0–13.9	1.5	13.9–20	14.7	20

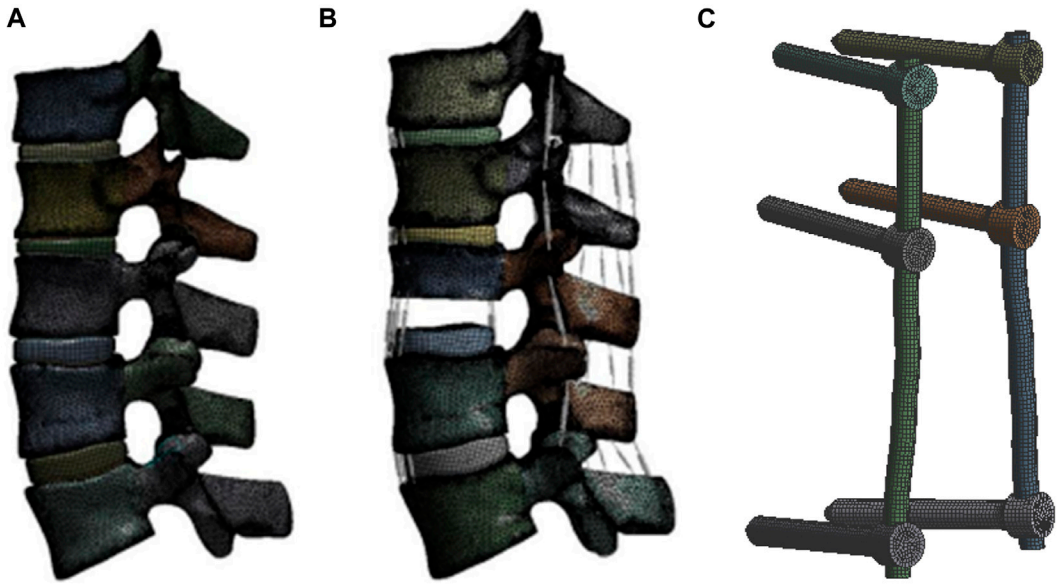

FIGURE 1
Finite element models with L3 fixed in all degree of freedom **(A)**, **(B)** 7.5 N*M moment in extension, flexion and lateral bending, **(C)** 5.5 N*M moment in axial rotation was assumed with 400 N compressive load: intact model; lower 1/3 L1 fracture model; and fixation instrument model.

anterior longitudinal ligament, posterior longitudinal ligament, ligamentum flavum, capsular ligament, and interspinous ligament) were constructed as nonlinear spring elements in ANSYS Workbench (Ansys, Pittsburgh, PA, United States), and the material properties are shown in Table 2(Rohlmann et al., 2009). After mesh convergence analysis, a total of 68,619 elements and 1,240,899 nodes were included.

Model creation for different sagittal fracture distribution

The fractured vertebra model was created using SolidWorks (Simulia, United States). The upper, middle, and lower 1/3 of L1 were resected, and the posterior structure was maintained to establish an unstable type A3.2 thoracolumbar fracture, according to the AO spinal fracture classification (Vaccaro et al., 2013) (Figure 1).

Creation of the pedicle and screw and rod models

Titanium alloy pedicle screws (6 mm × 50 mm for lumbar; 5.5 mm × 45 mm for thoracic vertebra) and rods (5.5 mm) were modeled using SolidWorks. The screws were inserted into the vertebra and connected with rods (Figure 1). Bonded contact was used between the screw and the vertebra, as well as between the screw and the rod. The mesh size was set to 1 mm for each screw and rod, and the unit included a total of 42,923 elements and 152,473 nodes.

Models of different surgical strategies

The models included upper 1/3 fracture, (U-P1D1, U-P2D1, U-P1D2), middle 1/3 fracture, (M-P1D1, M-P2D1, M-P1D2), and

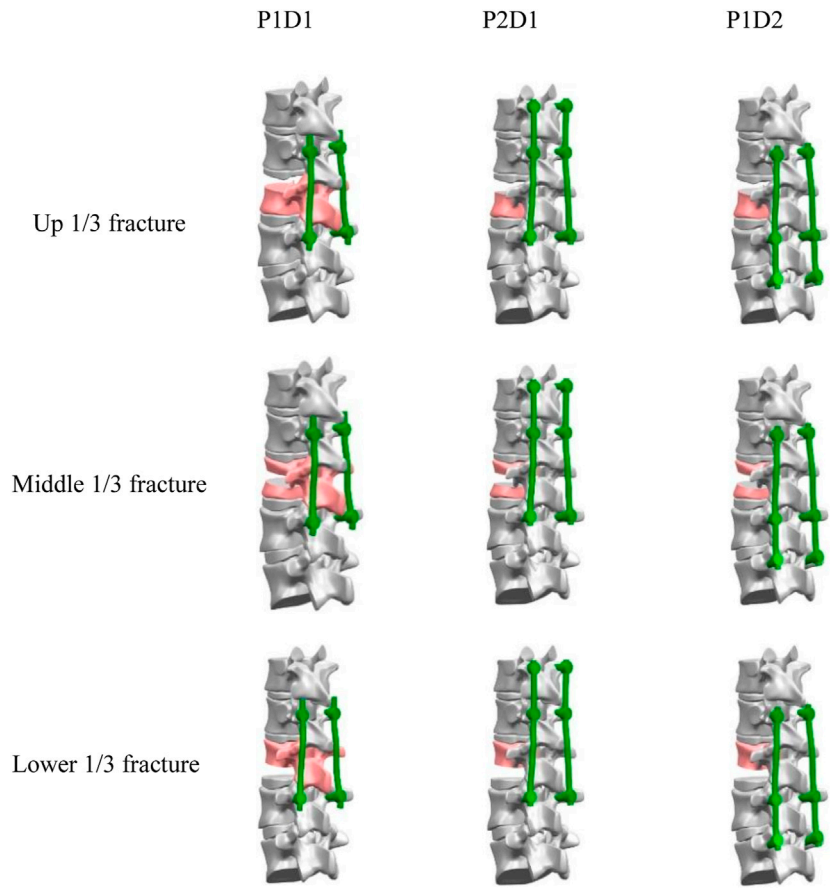

FIGURE 2
Models of different surgical strategies.

lower 1/3 fracture (L-P1D1, L-P2D1, L-P1D2) (Figure 2). Nine models were created in total.

Load and boundary

The load and boundary conditions were based on research published by Basaran et al. (2019). The L3 vertebra body was fixed in all degree of freedom. A compressive load of 400 N was applied to the top surface of T11 was applied to all the models as follower loading. Movement in coronal, sagittal, and transverse planes were evaluated, including extension, lateral bending, and rotation motions. The extension, flexion and lateral flexion moments were assumed to be 7.5 N*M, while the axial rotation moment was assumed to be 5.5 N*M.

Measurements and assessment indices

The range of motion (ROM) of T12-L2 was assessed in the nine FE models under six loading conditions. Data for the maximum von Mises stress and location were also collected and analyzed.

Results

Validation

Following the creation of the normal T12-L2 FE model, data on movement induced by 7.5 N*M in flexion, lateral bending and rotation were collected. The ROM values of the T12-L2 segment were as follows: flexion 6.36°; extension 8.12°; left bending 9.9°; right bending 7.85°; left rotation 4.61°; and right rotation 3.78°. The ROM results were comparable with those reported by (Alizadeh et al., 2013; Disch et al., 2007; Schmoelz et al., 2010) (Figure 3). To further verify the intact modle, we extracted the ROM of T11-L3 at 5.5N*M and compared it with the titro experiment. The ROM results were comparable with those reported by Couvertier et al., 2017 (Figure 3).

ROM of the T12-L2 in nine FE models

The ROM values, including flexion, extension, left and right lateral bending, and left and right axial rotation, for the three internal fixation models in the upper, middle, and lower 1/3 of L1 fractures under different motion states were presented in

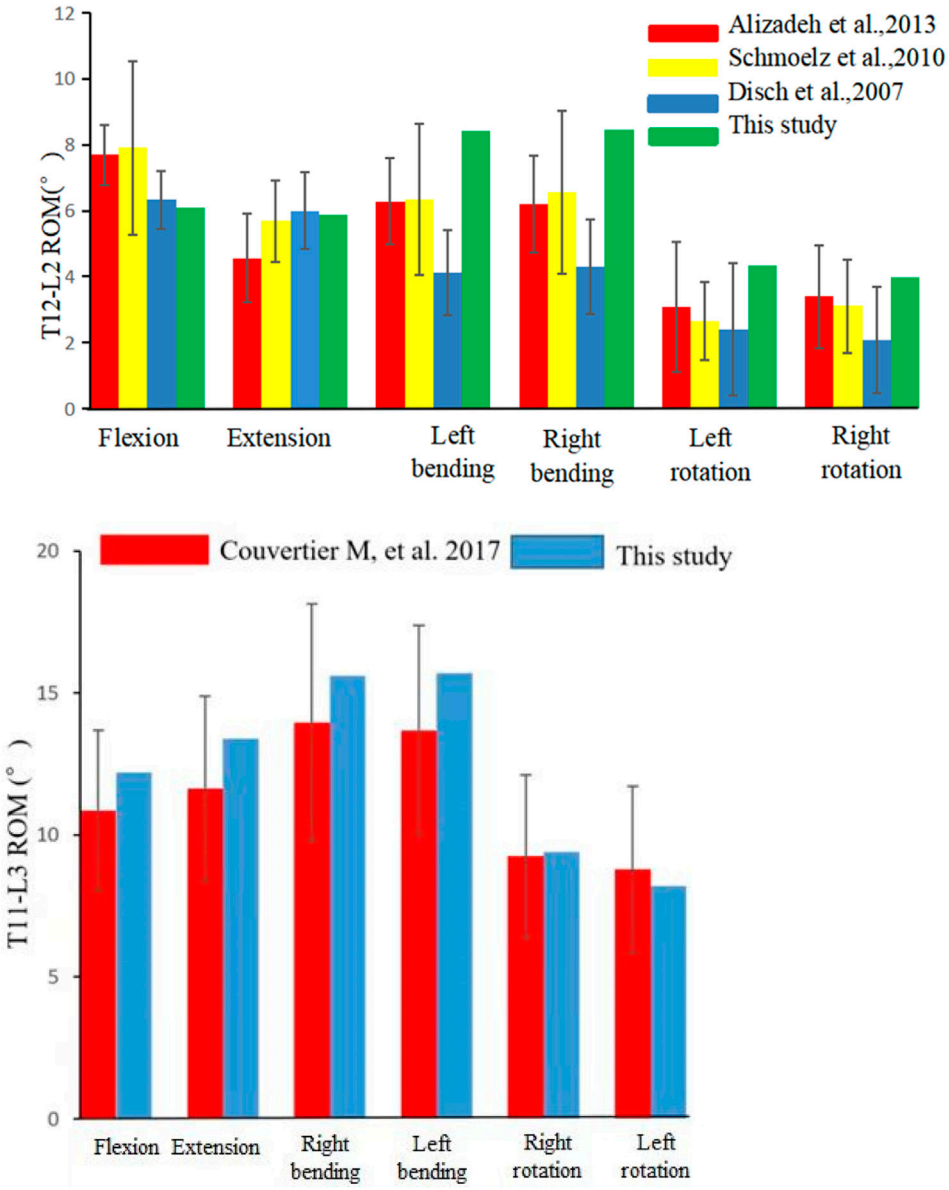

FIGURE 3
Comparison of the range of motion (ROM) of T12/L2 and T11-L3 in this study with those recorded in other studies.

Table 3. It was found that the P1-D1 fixation model showed maximum ROM in all six motion states, while the P2-D1 and P1-D2 fixation models showed no obvious difference in ROM values. It was also evident that the effect of the same fixation technique on ROM varied with different fracture locations. Across all models, flexion motion resulted in the highest ROM values with the maximum values of 11.63°, 12.85°, and 12.85° in the upper, middle, and lower 1/3 fractures, respectively, followed by extension, axial rotation, and the lowest ROM in left and right lateral bending. For the flexion motion, the P1D1, P2D1, and P1D2 fixation models could not provide sufficient stability for the fixed segments, resulting in significantly higher ROM values for all models compared to other physiological motion states.

Maximum von mises stress on the screws and rods

In all fixation models and states of motion, the maximum von Mises stress for both pedicle screws and rods was observed during flexion, while the lowest was during extension (as shown in Figures 4, 5). For upper and lower 1/3 fractures, the maximum von Mises stresses of pedicle screws in all three models were ranked in descending order as P1-D1, P1-D2 and P2-D1 models under all six physiological motion states, the maximum von Mises stresses in rods among the three models did not show significant differences. For middle 1/3 fractures, the maximum von Mises stresses in flexion and extension were identified in descending order as P1-D1, P1-D2 and P2-D1 models, however, the maximum von Mises stress values for

TABLE 3 Range of motion (ROM) of the finite element models of different fixation strategies (°).

Fracture location	Upper 1/3 fracture			Middle 1/3 fracture			Lower 1/3 fracture		
Model/Motion	P1D1	P2D1	P1D2	P1D1	P2D1	P1D2	P1D1	P2D1	P1D2
Flexion	11.63	9.93	10.07	12.85	9.17	9.59	12.85	10.83	11.00
Extension	4.77	4.60	4.26	4.75	4.57	4.40	4.75	4.57	4.40
Left bending	1.35	0.74	0.63	0.82	0.70	0.65	1.72	0.70	0.63
Right bending	1.32	0.53	0.62	1.87	0.70	0.64	1.00	0.68	0.64
Left rotation	2.20	1.70	1.85	1.90	1.80	1.90	2.17	1.79	1.92
Right rotation	2.20	1.86	1.80	1.79	1.80	1.91	2.19	1.79	1.93

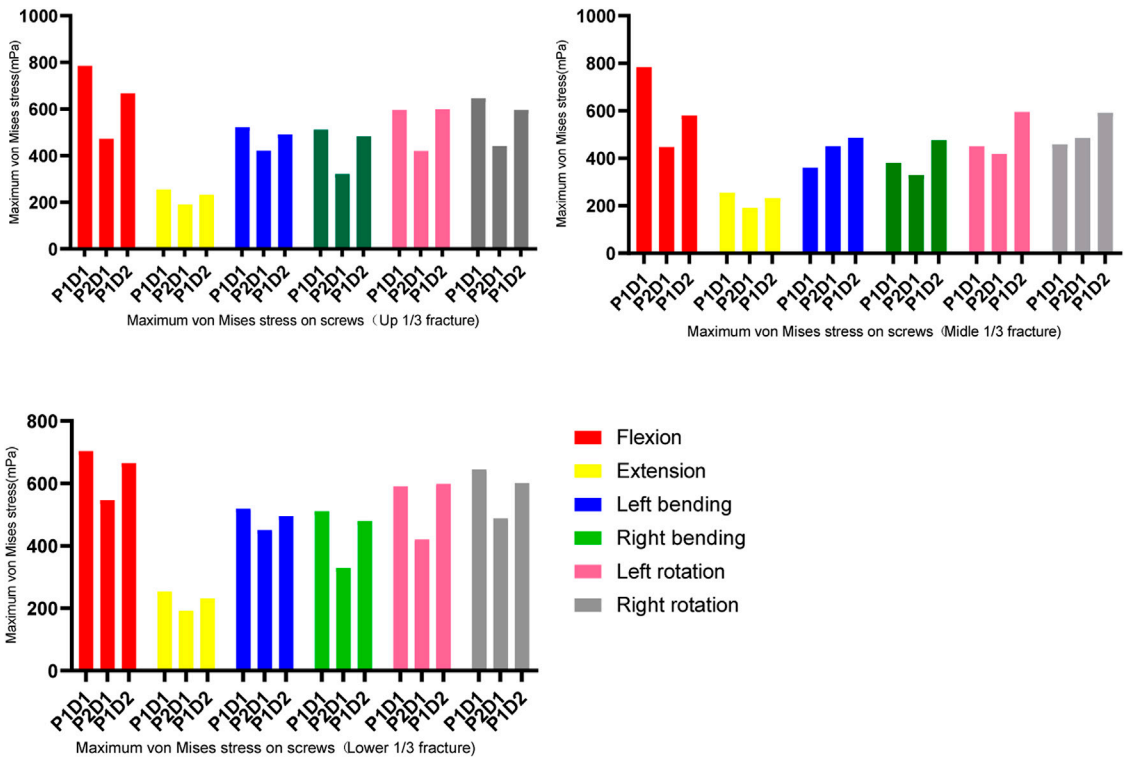

FIGURE 4
Maximum von Mises stress on the screws.

pedicle screws were observed in the P1-D2 model, with slight differences between the P1-D1 and P2-D1 models, in lateral bending and axial rotation. Similarly, in flexion and extension, the maximum von Mises stress values for rods, were observed in the P1-D1 model, while in lateral bending and axial rotation, the von Mises stress value of the rod in the P1-D1 model was the smallest, and the maximum von Mises stress values of the rod in the P1-D2 and P2-D1 models did not show significant differences.

The results shown in Figure 6, indicate that the maximum von Mises stresses for pedicle screws of all three models were majorly concentrated around the screw roots, and the maximum stresses on the rods were located in the L1 cone region, i.e., at the fracture location.

Discussion

To investigate the influence of sagittal location of vertebral body fracture on internal fixation system stress and the selection of surgical internal fixation strategy, 9 finite element models with three types of sagittal and three surgical strategies were developed in this study. The results showed in all the three sagittal models, P2D1 has a smaller ROM and less internal fixation stress. Therefore, the findings indicated that the sagittal location of the fracture does not affect the choice of surgical strategy, but can affect the level of mechanical stress on the internal fixation and their potential risk of failure.

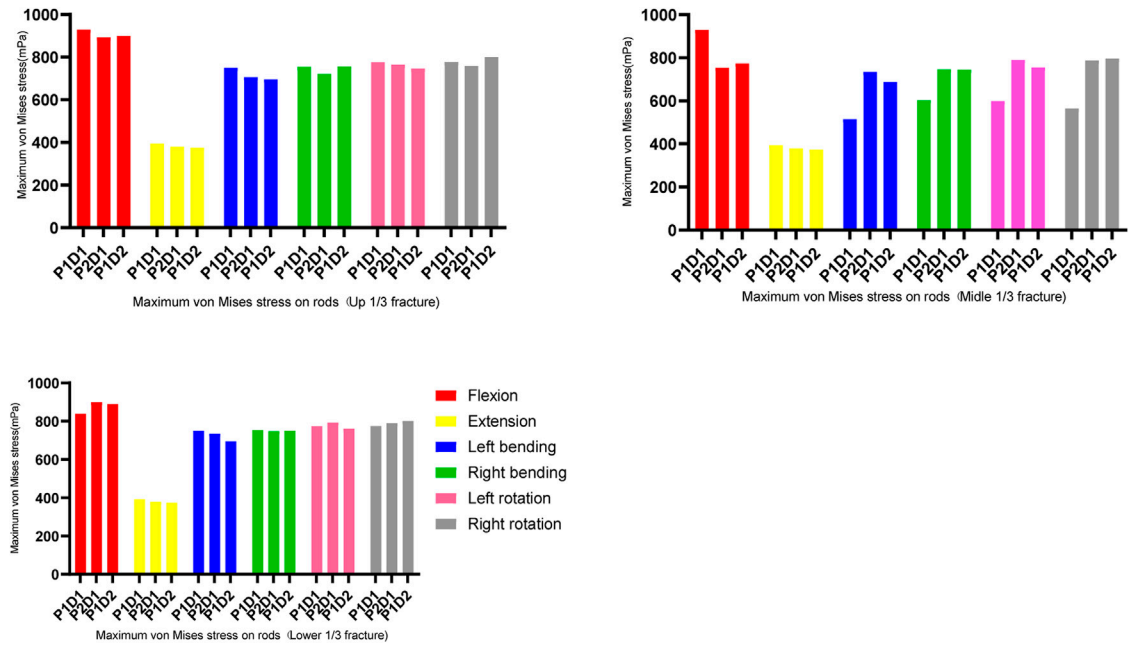

FIGURE 5
Maximum von Mises stress on the rods.

Spinal fractures often occur in the thoracolumbar segment, and L1 is the most frequently involved site, taking up 16.2%–34.4% of all spinal fractures (Holmes et al., 2001; Katsuura et al., 2016; Leucht et al., 2009). Thus, we selected L1 to establish the FE model. There are various surgical strategies available, in addition to the P1D1, P2D1, and P1D2 methods mentioned in the article. Other options include the P2D2 and the combination of P1D1 with vertebral pedicle screw fixation, etc. However, if the pedicle of the injured vertebra is fractured, the screw could not be placed. Furthermore, it is difficult to establish the FE model because the screws are exposed in upper 1/3 fractures. It is thought that P2D2 does not significantly reduce stress on screws compared with P2D1 and P1D2. P2D1 involves the fixation of more segments, thereby resulting in loss of movement. P2D2 is not recommended as the first choice for the treatment of thoracolumbar fractures (Basaran et al., 2019; Wong et al., 2021). Therefore, in this study, we selected the P1D1, P2D1, and P1D2 fixation techniques.

Multiple posterior internal fixation surgical techniques have been widely used in clinical practice, with significant effects in the treatment of thoracolumbar fractures. However, controversy remains regarding the selection of surgical strategies (Cahueque et al., 2016). In recent years, studies have analyzed the biomechanical stability of fracture regions using different internal fixation models. The majority of these studies modeled the lower 1/3 of the vertebral body resection. Nevertheless, fractures can occur in the upper, middle, and lower regions (Denis, 1983; Rosenthal et al., 2018). Additionally, L1 is the most common site of thoracolumbar fractures. Therefore, T11-L3 was chosen to establish a fracture model of upper, middle, and lower 1/3 fractures of L1. Our results show that the sagittal distribution of fractures influences the ROM.

In all models, the largest ROM was obtained at the flexion motion. This finding is consistent with those noted in previous studies (Basaran et al., 2019). Under the flexion motion, fractures in the middle and upper 1/3 are associated with the shortest and longest ROM, respectively. For example, in the P1D1 fixation model, the ROM values for the upper, middle, and lower 1/3 were 11.63°, 9.93°, and 10.07°, respectively. The probable cause is that fractures located in the middle 1/3 have more uniform internal fixation stress is more uniform and greater stability. The pedicle plays an important role in the stability of the spine. When the fracture is located in the upper 1/3, the pedicle is involved, thereby increasing the ROM.

The biomechanical stability of fixation models is related to the extent and location of fixation (Wang et al., 2018). This study showed no significant difference in the ROM of extension, lateral bending, and axial rotation between the P2D1 and P1D2 models at the three fracture levels. The ROM values for both models were lower than those recorded for the P1D1 model at all six states of motion. This implies that six-screw fixation in the fracture area could provide more spinal stability than short-segment fixation. Theoretically, the addition of the fixation segment provides additional fixation points for fracture reduction and kyphosis correction. This is consistent with the conclusions of previous studies (Jindal et al., 2020; Xu et al., 2019).

In all models, the maximum screw stress was obtained under flexion motion. The distance between the fracture position and the screw affects the instrument stress (Zhang et al., 2021). Our findings showed that, under the same type of internal fixation, the fracture location altered (reduced or increased) the stress on the screw but did not affect the maximum stress location (Figures 4, 6).

It has been documented that stress concentration occurs in adjacent segments under short-segment fixation. This may cause looseness and breakage due to fatigue by increased bearing stress of

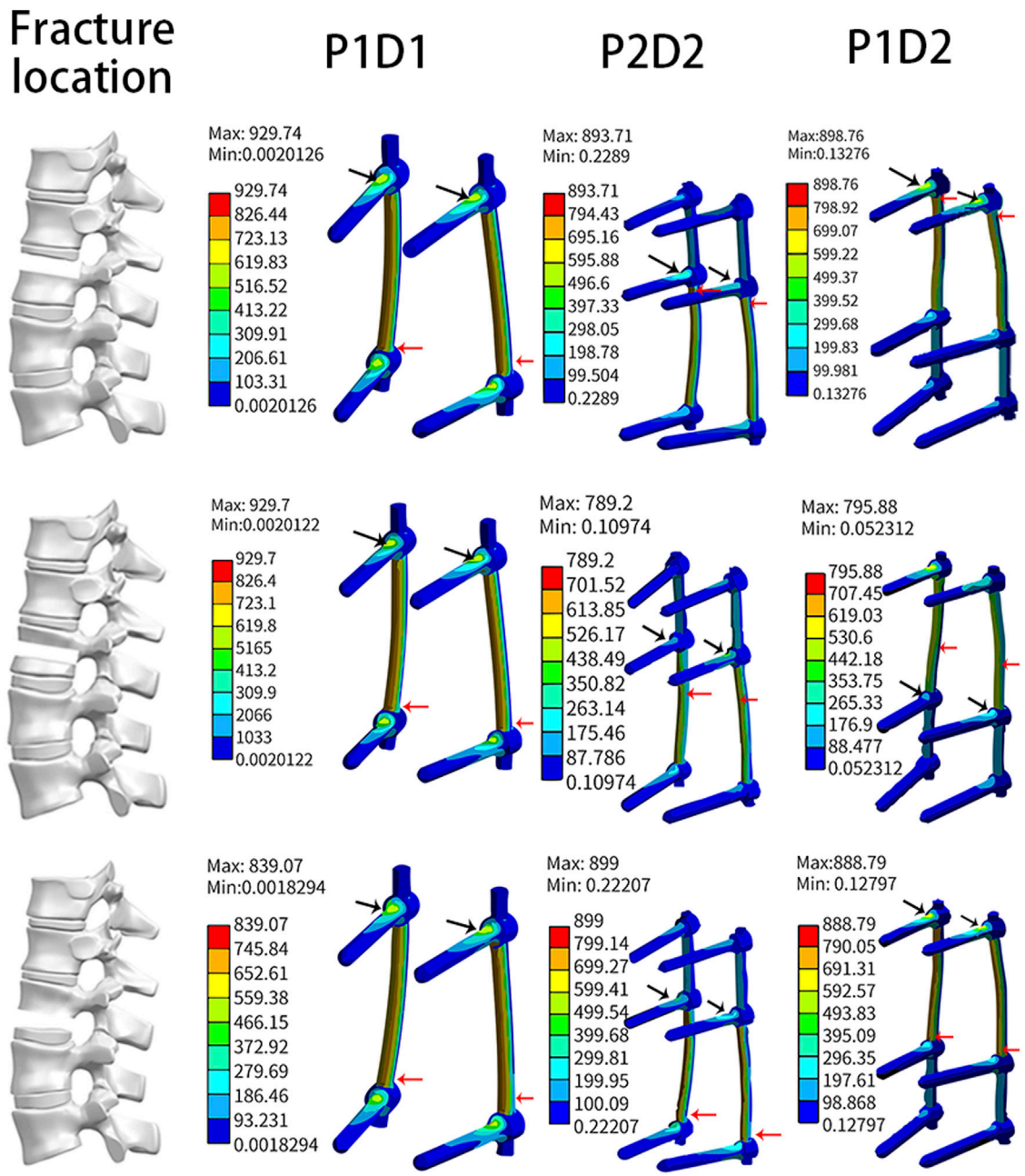

FIGURE 6
Maximum stress location on the screw and rod.

the internal fixation (Jindal et al., 2020). The results of this study further indicated that an increase in the number of screws can reduce the average stress, thus reducing the risk of screw breakage (Xu et al., 2019). In the three fracture distributions analyzed in this study, the maximum stress of P1D2 and P2D1 was significantly lower than that of P1D1. This result was comparable with those reported in previous studies (Wu et al., 2019). Our results showed that P2D1 was considered more appropriate in this setting than P1D2, comparable with previous studies (C. E. Wong et al., 2021). Clinically, this method has proven to be an effective alternative for fixation (Modi et al., 2009). However, they did not consider the sagittal location variation of the fractures.

The fracture site was the most unstable region of the constructs. Hence the maximum stress on the rods occurred across the fractures site that was in line with previous studies (Wong et al., 2021). In the present study, the site of maximum stress on the rod shifted downward in parallel with the location of the fracture, and the stress value changed accordingly. For the three fixation strategies, the maximum stress on the instrument in the upper and lower 1/3 fracture models was similar. In the middle 1/3 fracture model, P2D1 and P1D1 were associated with similar stress. The stress noted for these techniques was higher than that recorded for P1D1. These findings could guide physicians regarding the clinical management of type A3 fractures.

This study had several limitations. Although finite element analysis is a valid method in biomechanical studies, it still does not fully simulate the comparison of human treatments. Experimental results of finite element analysis represent a new clinical trend rather than definitive conclusions (Lewis et al., 2021). Under 7.5 N*M moments, the fracture models may seriously deform. We did not validate the fracture models. In this study pertaining to the somewhat simplified and idealized material properties used in the simulation, such as the nonlinear behavior of spinal ligaments, the viscoelasticity of intervertebral discs, and the varying degrees of degeneration - all of which differ from cadaveric specimens. And what's more, pure structural resection does not reflect the complexity of fracture morphology. Only the A3 fracture models were established in this study and the boundary conditions in terms of the complex segmental motion of the human spine in the thoracolumbar segment were simplified Thus, models with actual ROM and with other fracture subtypes should be warranted in the future. The screw thread size should be considered for more realistic screw stress analyses in future studies. In addition, using a nonlinear material constitutive model is necessary to study the localized failure of internal fixation systems. However, the stress trends for the different procedures observed in this study are comparable to previous studies. Finally, although there are numerous posterior internal fixation methods used to treat fractures, only three techniques were modeled in this study. Further investigations should be performed to evaluate more biomechanical properties of other models concerning other posterior internal fixation methods.

Conclusion

The sagittal location of fractures did not affect the choice of surgical strategies; however, it affected the magnitude of stress and distribution of the internal fixation system.

Data availability statement

The raw data supporting the conclusion of this article will be made available by the authors, without undue reservation.

Ethics statement

The studies involving human participants were reviewed and approved by ethics committee of Fuyang people's hospital. The patients/participants provided their written informed consent to participate in this study.

Author contributions

Conceptualization, XC, CL and ZH; methodology, JZ, XH, HY and XW; investigation, WY, YS and XC; data analysis, XW, WY and YS; writing—original draft preparation, XC, WY and YS; Writing—review and editing, XC, JZ and YS; funding acquisition, XC and CL; resources, HY and CL; supervision, XH and ZH. All authors contributed to the article and approved the submitted version.

Funding

This study was supported by the Key Project of Natural Science of Bengbu Medical College (grant numbers: BYKY2019226ZD and BYKY2019227ZD).

Conflict of interest

The authors declare that the research was conducted in the absence of any commercial or financial relationships that could be construed as a potential conflict of interest.

Publisher's note

All claims expressed in this article are solely those of the authors and do not necessarily represent those of their affiliated organizations, or those of the publisher, the editors and the reviewers. Any product that may be evaluated in this article, or claim that may be made by its manufacturer, is not guaranteed or endorsed by the publisher.

References

Alizadeh, M., Kadir, M. R. A., Fadhli, M. M., Fallahiarezoodar, A., Azmi, B., Murali, M. R., et al. (2013). The use of X-shaped cross-link in posterior spinal constructs improves stability in thoracolumbar burst fracture: A finite element analysis. *J. Orthop. Res.* 31 (9), 1447–1454. doi:10.1002/jor.22376

Basaran, R., Efendioglu, M., Kaksi, M., Celik, T., Mutlu, I., and Ucar, M. (2019). Finite element analysis of short-versus Long-Segment posterior fixation for thoracolumbar burst fracture. *World Neurosurg.* 128, e1109–e1117. doi:10.1016/j.wneu.2019.05.077

Cahueque, M., Cobar, A., Zuniga, C., and Caldera, G. (2016). Management of burst fractures in the thoracolumbar spine. *J. Orthop.* 13 (4), 278–281. doi:10.1016/j.jor.2016.06.007

Couvertier, M., Germaneau, A., Saget, M., Dupré, J., Doumalin, P., Brémand, F., et al. (2017). Biomechanical analysis of the thoracolumbar spine under physiological loadings: Experimental motion data corridors for validation of finite element models. *Proc. Institution Mech. Eng. Part H J. Eng. Med.* 231 (10), 975–981. doi:10.1177/0954411917719740

den Ouden, L. P., Smits, A. J., Stadhouder, A., Feller, R., Deunk, J., and Bloemers, F. W. (2019). Epidemiology of spinal fractures in a level one trauma center in The Netherlands. *Spine* 44 (10), 732–739. doi:10.1097/BRS.0000000000002923

Denis, F. (1983). The three column spine and its significance in the classification of acute thoracolumbar spinal injuries. *Spine (Phila Pa 1976)* 8 (8), 817–831. doi:10.1097/00007632-198311000-00003

Disch, A. C., Luzzati, A., Melcher, I., Schaser, K. D., Feraboli, F., and Schmoelz, W. (2007). Three-dimensional stiffness in a thoracolumbar en-bloc spondylectomy model: A biomechanical *in vitro* study. *Clin. Biomech.* 22 (9), 957–964. doi:10.1016/j.clinbiomech.2007.07.010

El, B. H., Saleh, A. K., Elsherief, F., Abuomira, I., and Elkawary, A. I. (2020). Short-Segment fixation of thoracolumbar fractures with incorporated screws at the level of fracture. *Orthop. Surg.* 12 (1), 170–176. doi:10.1111/os.12590

Galbusera, F., Qian, Z., Casaroli, G., Bassani, T., Costa, F., Schlager, B., et al. (2018). The role of the size and location of the tumors and of the vertebral anatomy in determining the structural stability of the metastatically involved spine: A finite element study. *Transl. Oncol.* 11 (3), 639–646. doi:10.1016/j.tranon.2018.03.002

Girardo, M., Masse, A., Risitano, S., and Fusini, F. (2021). Long versus short segment instrumentation in osteoporotic thoracolumbar vertebral fracture. *Asian Spine J.* 15 (4), 424–430. doi:10.31616/asj.2020.0033

Guo, H., Li, J., Gao, Y., Nie, S., Quan, C., Li, J., et al. (2021). A finite element study on the treatment of thoracolumbar fracture with a new spinal fixation system. *Biomed. Res. Int.* 2021, 1–9. doi:10.1155/2021/8872514

Guo, L. X., and Li, W. J. (2019). A biomechanical investigation of thoracolumbar burst fracture under vertical impact loads using finite element method. *Clin. Biomech. (Bristol, Avon)* 68, 29–36. doi:10.1016/j.clinbiomech.2019.05.018

Holmes, J. F., Miller, P. Q., Panacek, E. A., Lin, S., Horne, N. S., and Mower, W. R. (2001). Epidemiology of thoracolumbar spine injury in blunt trauma. *Acad. Emerg. Med.* 8 (9), 866–872. doi:10.1111/j.1553-2712.2001.tb01146.x

Jindal, R., Jasani, V., Sandal, D., and Garg, S. K. (2020). Current status of short segment fixation in thoracolumbar spine injuries. *J. Clin. Orthop. Trauma* 11 (5), 770–777. doi:10.1016/j.jcot.2020.06.008

Katsuura, Y., Osborn, J. M., and Cason, G. W. (2016). The epidemiology of thoracolumbar trauma: A meta-analysis. *J. Orthop.* 13 (4), 383–388. doi:10.1016/j.jor.2016.06.019

Leucht, P., Fischer, K., Muhr, G., and Mueller, E. J. (2009). Epidemiology of traumatic spine fractures. *Injury* 40 (2), 166–172. doi:10.1016/j.injury.2008.06.040

Lewis, G. S., Mischler, D., Wee, H., Reid, J. S., and Varga, P. (2021). Finite element analysis of fracture fixation. *Curr. Osteoporos. Rep.* 19, 403–416. doi:10.1007/s11914-021-00690-y

Liang, C., Liu, B., Zhang, W., Yu, H., Cao, J., and Yin, W. (2020). Clinical effects of posterior limited Long-Segment pedicle instrumentation for the treatment of thoracolumbar fractures. *J. Invest. Surg.* 33 (1), 25–30. doi:10.1080/08941939.2018.1474301

Liu, B., Zhu, Y., Liu, S., Chen, W., Zhang, F., and Zhang, Y. (2018). National incidence of traumatic spinal fractures in China. *Medicine* 97 (35), e12190. doi:10.1097/MD.0000000000012190

Modi, H. N., Chung, K. J., Seo, I. W., Yoon, H. S., Hwang, J. H., Kim, H. K., et al. (2009). Two levels above and one level below pedicle screw fixation for the treatment of unstable thoracolumbar fracture with partial or intact neurology. *J. Orthop. Surg. Res.* 4, 28. doi:10.1186/1749-799X-4-28

Mu, S., Wang, J., and Gong, S. (2022). Mechanical analysis of posterior pedicle screw system placement and internal fixation in the treatment of lumbar fractures. *Comput. Math. Methods Med.* 2022, 1–10. doi:10.1155/2022/6497754

Naoum, S., Vasiliadis, A. V., Koutserimpas, C., Mylonakis, N., Kotsapas, M., and Katakalos, K. (2021). Finite element method for the evaluation of the human spine: A literature overview. *J. Funct. Biomater.* 12, 43. doi:10.3390/jfb12030043

Park, W. M., Kim, K., and Kim, Y. H. (2013). Effects of degenerated intervertebral discs on intersegmental rotations, intradiscal pressures, and facet joint forces of the whole lumbar spine. *Comput. Biol. Med.* 43 (9), 1234–1240. doi:10.1016/j.compbiomed.2013.06.011

Petersilge, C. A., and Emery, S. E. (1996). Thoracolumbar burst fracture: Evaluating stability. *Semin. Ultrasound CT MR* 17 (2), 105–113. doi:10.1016/s0887-2171(96)90010-4

Rohlmann, A., Zander, T., Rao, M., and Bergmann, G. (2009). Realistic loading conditions for upper body bending. *J. Biomech.* 42 (7), 884–890. doi:10.1016/j.jbiomech.2009.01.017

Rosenthal, B. D., Boody, B. S., Jenkins, T. J., Hsu, W. K., Patel, A. A., and Savage, J. W. (2018). Thoracolumbar burst fractures. *Clin. Spine Surg.* 31 (4), 143–151. doi:10.1097/BSD.0000000000000634

Schmoelz, W., Schaser, K. D., Knop, C., Blauth, M., and Disch, A. C. (2010). Extent of corpectomy determines primary stability following isolated anterior reconstruction in a thoracolumbar fracture model. *Clin. Biomech.* 25 (1), 16–20. doi:10.1016/j.clinbiomech.2009.09.010

Vaccaro, A. R., Oner, C., Kepler, C. K., Dvorak, M., Schnake, K., Bellabarba, C., et al. (2013). AOSpine thoracolumbar spine injury classification system: Fracture description, neurological status, and key modifiers. *Spine (Phila Pa 1976)* 38 (23), 2028–2037. doi:10.1097/BRS.0b013e3182a8a381

Wang, H., Mo, Z., Han, J., Liu, J., Li, C., Zhou, Y., et al. (2018). Extent and location of fixation affects the biomechanical stability of short- or long-segment pedicle screw technique with screwing of fractured vertebra for the treatment of thoracolumbar burst fractures: An observational study using finite element analysis. *Med. Baltim.* 97 (26), e11244. doi:10.1097/MD.0000000000011244

Wang, P., and Hu, X. (2020). Biomechanical finite element analysis of superior endplate collapse after thoracolumbar fracture surgery. *Ann. Transl. Med.* 8 (12), 753. doi:10.21037/atm-20-4091

Wang, S., Park, W. M., Gadikota, H. R., Miao, J., Kim, Y. H., Wood, K. B., et al. (2013). A combined numerical and experimental technique for estimation of the forces and moments in the lumbar intervertebral disc. *Comput. Method. Biomec.* 16 (12), 1278–1286. doi:10.1080/10255842.2012.668537

Wong, C. E., Hu, H. T., Tsai, C. H., Li, J. L., Hsieh, C. C., and Huang, K. Y. (2021). Comparison of posterior fixation strategies for thoracolumbar burst fracture: A finite element study. *J. Biomech. Eng.* 143 (7), 071007. doi:10.1115/1.4050537

Wong, C., Gehrchen, P. M., Darvann, T., and Kiaer, T. (2003). Nonlinear finite-element analysis and biomechanical evaluation of the lumbar spine. *IEEE Trans. Med. Imaging* 22 (6), 742–746. doi:10.1109/TMI.2003.814783

Wu, Y., Chen, C. H., Tsuang, F. Y., Lin, Y. C., Chiang, C. J., and Kuo, Y. J. (2019). The stability of long-segment and short-segment fixation for treating severe burst fractures at the thoracolumbar junction in osteoporotic bone: A finite element analysis. *PLoS One* 14 (2), e0211676. doi:10.1371/journal.pone.0211676

Xu, M., Yang, J., Lieberman, I., and Haddas, R. (2019). Stress distribution in vertebral bone and pedicle screw and screw-bone load transfers among various fixation methods for lumbar spine surgical alignment: A finite element study. *Med. Eng. Phys.* 63, 26–32. doi:10.1016/j.medengphy.2018.10.003

Zhang, T., Wang, Y., Zhang, P., Xue, F., Zhang, D., and Jiang, B. (2021). Different fixation pattern for thoracolumbar fracture of ankylosing spondylitis: A finite element analysis. *PLoS One* 16 (4), e0250009. doi:10.1371/journal.pone.0250009

frontiers | Frontiers in Bioengineering and Biotechnology

TYPE Original Research
PUBLISHED 24 August 2023
DOI 10.3389/fbioe.2023.1228809

OPEN ACCESS

EDITED BY
Junyan Li,
Southwest Jiaotong University, China

REVIEWED BY
Xing Peng,
Southwest Jiaotong University, China
Francesca Berti,
Polytechnic University of Milan, Italy

*CORRESPONDENCE
Andreas Schiffer,
andreas.schiffer@ku.ac.ae
Marwan El-Rich,
marwan.elrich@ku.ac.ae

RECEIVED 25 May 2023
ACCEPTED 07 August 2023
PUBLISHED 24 August 2023

CITATION
Hafez AH, El-Rich M, Liu T, Jomha N and Schiffer A (2023), Design of a lightweight universal talus implant using topology optimization.
Front. Bioeng. Biotechnol. 11:1228809.
doi: 10.3389/fbioe.2023.1228809

Design of a lightweight universal talus implant using topology optimization

Ahmed H. Hafez[1], Marwan El-Rich[1,2]*, Tao Liu[3], Nadr Jomha[4] and Andreas Schiffer[1]*

[1]Department of Mechanical Engineering, Khalifa University, Abu Dhabi, United Arab Emirates, [2]Healthcare Engineering Innovation Center (HEIC), Khalifa University of Science and Technology, Abu Dhabi, United Arab Emirates, [3]Human Performance Lab, Faculty of Kinesiology, University of Calgary, Calgary, AB, Canada, [4]Faculty of Medicine and Dentistry, University of Alberta, Edmonton, AB, Canada

Total talus replacement is a promising alternative treatment for talus fractures complicated by avascular necrosis and collapse. This surgical option replaces the human talus bone with a customized talus implant and can maintain ankle joint functionality compared to traditional treatment (e.g., ankle fusion). However, the customized implant is costly and time-consuming due to its customized nature. To circumvent these drawbacks, universal talus implants were proposed. While they showed clinically satisfactory results, existing talus implants are heavier than biological talus bones as they are solid inside. This can lead to unequal weight between the implant and biological talus bone, and therefore leading to other complications. The reduction of the implants' weight without compromising its performance and congruency with surrounding bones is a potential solution. Therefore, this study aims to design a lightweight universal talus implant using topology optimization. This is done through establishing the loading and boundary conditions for three common foot postures: neutral, dorsi- and plantar-flexion. The optimized implant performance in terms of mass, contact characteristics with surrounding joint cartilage and stress distributions is studied using a 3D Finite Element (FE) model of the ankle joint. The mass of the optimized implant is reduced by approximately 66.6% and its maximum stresses do not exceed 70 MPa, resulting in a safety factor of 15.7. Moreover, the optimized and solid implants show similar contact characteristics. Both implants produced peak contact pressures that were approximately 19.0%–196% higher than those produced by the biological talus. While further mechanical testing under *in-vivo* loading conditions is required to determine clinical feasibility, preliminarily, the use of a lightweight universal implant is expected to provide the patient with a more natural feel, and a reduced waiting period until surgery.

KEYWORDS

talus implant design, bioinspired design, total talus replacement, finite element analysis, topology optimization, contact pressure, cartilage

1 Introduction

The talus bone, with its unique geometry and large articular surface, plays a significant role in load transmission and foot movement as it serves as the connection point between the leg and the foot (Liu et al., 2020). Given its poor blood supply and large cartilage-covered surface area, coupled with the non-existence of muscular or tendinous attachments, the talus is more susceptible to

avascular necrosis (AVN). AVN is the death of bone tissue due to restricted blood supply (Tonogai et al., 2017), and may be a result of fractures (Trovato et al., 2018), high-energy injuries (Katsui et al., 2019), trauma, steroid use, metabolic or idiopathic causes (Bowes et al., 2019), and osteosarcoma (bone cancer) (Huang et al., 2021). Ultimately, talar collapse manifests in the form of ankle joint incongruity leading to pain, stiffness and restricted movement (Bowes et al., 2019).

A common surgical treatment is ankle arthrodesis (fusion) where the talus is fixated to the tibia or to both the tibia and calcaneus. While this procedure provides acceptable pain relief, it results in the loss of hindfoot and ankle movement as well as increased stresses on the surrounding joints (Bowes et al., 2019). A more favorable alternative is total talus replacement (TTR) surgery, which results in a higher rate of pain relief (Tonogai et al., 2017), preserved range of motion and joint function as well relatively easier surgeries and reduced recovery periods (Hussain, 2020). Since TTRs are typically patient-specific, the custom-made implant's design process can be time-consuming and costly, resulting in increased periods between surgical decision and implantation (Liu et al., 2020). To solve the drawbacks, universal talar prostheses have been previously developed and were proved to be feasible (Trovato et al., 2018; Bowes et al., 2019; Trovato, 2016; Trovato et al., 2017; Liu et al., 2022a). Due to the universal nature, these types of implants can be mass produced. Both the waiting time between diagnosis and surgery as well as the associated design and production costs can be reduced (Trovato et al., 2017). However, when comparing the weight of the talus implant to the biological talus bone, existing universal talus implants are generally up to several times heavier, given the use of ceramics and metals as implant materials (West and Rush, 2021). This can lead to unequal weight of the left and right foot and potential complications.

In order to enhance implant structures, topology optimization (TO) is typically used. TO is a procedure that optimizes material distribution in a defined design space in order to achieve higher performance structures, typically ones with lighter weight while maintaining mechanical properties (Kladovasilakis et al., 2020). For TTRs, a single study is known to have employed TO in their design process. In that study, a comparison was made between a topologically optimized scaffold and a rational scaffold of the inner structure of a talus replacement in three postures corresponding to peak gait cycle loads. The implant used was a recreation of a cadaveric talus, and the simulation excluded the fibula as well as the adjacent bones' cartilages (Kang et al., 2022). This exclusion likely decreases the accuracy of the resulting stress distributions, thereby affecting the optimized implant geometry and expected performance under more anatomically-accurate conditions.

This study focused on the design of a universal talus implant, under three loading scenarios, using topology optimization to obtain an enhanced structure that benefits from the advantages of a universal implant as well as addresses some limitations of the aforementioned study by including the fibula and the bones' cartilages in the model. The optimized implant's performance (mass, stresses and contact pressures) is then assessed, in comparison with the non-optimized solid implant and biological talus, using finite element analysis (FEA).

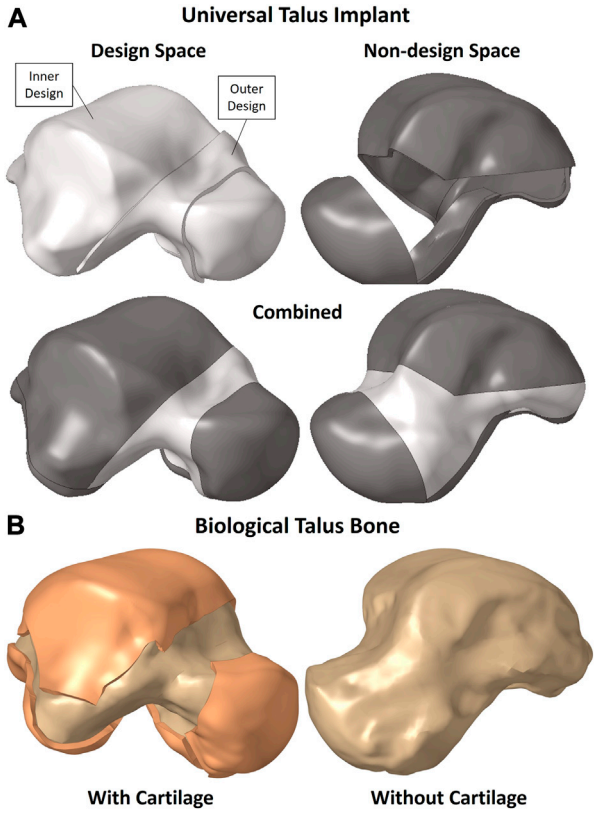

FIGURE 1
(A) Universal talus implant and **(B)** biological talus bone setup.

2 Materials and methods

2.1 Geometry acquisition

The universal talus implant's geometry was obtained from an earlier study (Trovato et al., 2017) where a talus (among 91 tali) with the least total deviation from the rest of the tali was selected, and was uniformly further scaled up by 0.5 mm to compensate for the cartilage existing on a biological talus bone.

The ankle joint geometry, including the biological talus bone, was obtained from an earlier study (Trovato et al., 2018) where a dissected cadaveric foot (right side) was CT scanned under three postures: +20° dorsiflexion (DF, foot pointed upwards), 0° neutral standing (NS, standing position), and −20° plantarflexion (PF, foot pointed downwards). The angles were selected to represent a wide range of flexion angles of the foot where the postures are typically experienced when ascending/descending stairs, for example, (Brockett and Chapman, 2016). The obtained images were then imported into MIMICS (Materialize, NV, Belgium, Version 20.0) where the bones were created, and then cleaned using Geomagic (3D Systems®, Morrisville, USA, Version 2014) to ultimately obtain the 3D geometry. The cartilage, presented in

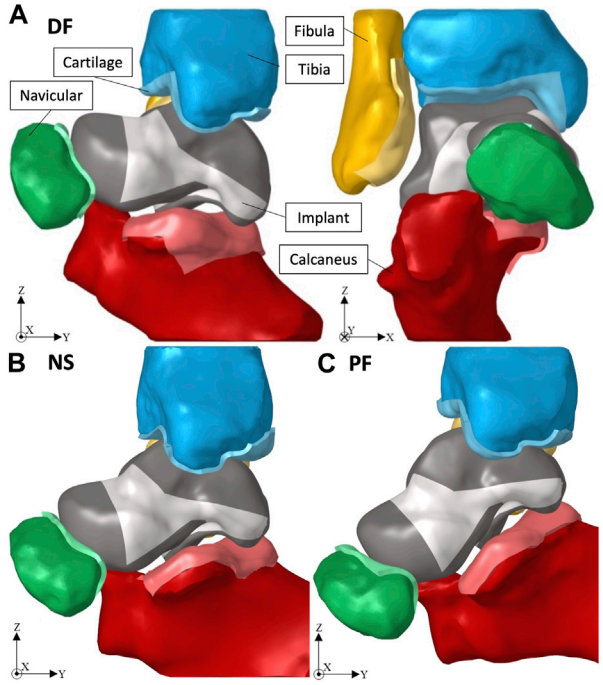

FIGURE 2
Ankle joint in **(A)** +20° DF, **(B)** 0° NS, and **(C)** −20° PF.

greater detail in Section 2.3, was created using Hypermesh (Altair®, Troy, United States, Version 2021), by extruding the shell elements on the articular surfaces of the adjacent bones, as well as the biological talus, by 1.5 mm (Liu et al., 2022a). Throughout the study, the term 'ankle joint' is used to represent all the five bones (including the navicular and calcaneus), not strictly the anatomical ankle joint composed of the talus, tibia, and fibula. Additionally, the term 'adjacent bones' refers to the aforementioned ankle joint without the talus. Finally, unless stated otherwise, the terms 'implant' and 'universal implant' are used interchangeably.

2.2 Biological talus bone and universal implant setup

The solid implant geometry, shown in Figure 1A, was partitioned to easily allow its modification for different FEA setups as well as the optimization while preserving the mesh for consistency. It was divided into the design space (in white) and non-design space (in grey). The outer sections, namely, the outer design space and entire non-design space, are 1 mm-thick solids. The biological talus bone, presented in greater detail in Section 2.3, is shown in Figure 1B with and without its cartilage. For the purposes of this study, the biological talus was used strictly for comparison, not optimization.

The partitions were not randomly created; rather they were defined to maintain the implant's function in terms of contact between the non-design space partitions with their respective adjacent bones' cartilages while accounting for additive manufacturing (AM) constraints. The main consideration was to allow the metal powders used in powder-based AM to be removed, hence the availability of an outer design space as well instead of only having an enclosed inner design space where the powders would remain trapped.

2.3 Finite element model

The following section describes the setup for both implants, namely, the optimized and solid implants, in addition to the biological talus.

2.3.1 Solid implant and ankle joint FE setup

Given that the obtained ankle joint's 3D geometry was of the biological bones, the solid implant was 'best-fit' aligned with the biological talus using Geomagic, and then the adjacent bones were translated away from the implant to avoid interference when creating their cartilage layers. Figure 2 shows the ankle joint FE setup, with the solid implant, in dorsiflexion (DF, +20°), neutral standing (NS, 0°), and plantarflexion (PF, −20°) respectively.

The simulation of each posture, using Optistruct solver (Altair®, Troy, United States, Version 2021), includes three consecutive, large-displacement, non-linear static load steps: 1) the adjacent bones are returned to their respective CT scan position to establish contact with the implant which is fixed in place; 2) the implant freely adjusts itself with the adjacent bones which remain fixed in their positions at the end of load step 1; 3) a compressive force of 2000 N is applied to the tibia in the direction of gravity (negative *Z*-axis). Note that the magnitude of the compressive force (2000 N) equates to approximately three to four times a person's weight and was chosen in accordance with a previous study (Liu et al., 2022a). More complex or extreme loading conditions were not considered in this work. Both the tibia and fibula are equation-constrained to move together in the *Z*-axis to mimic their realistic combined motion (Liu et al., 2022a).

All the defined loads, displacements and equation constraints are applied to reference points representing rigid body motion of a set of elements on the adjacent bones. The only exception is the implant whose defined displacements are applied to the nodes on the outer surface of its outer design space.

To reduce computational difficulties, the non-articular surfaces of the adjacent bones were meshed using three-node triangular shell elements while the articular surfaces were meshed using four-node quad elements. All the shell elements were assigned a thickness of 1 mm. For the cartilage, the articular surface's four-node elements were extruded 1.5 mm, distributed over four equal layers, to create solid eight-node hexahedral elements.

Since the implant is an artificial replacement for the biological talus, no cartilage was created on its surface, rather its volume was uniformly scaled up by 0.5 mm to account for the natural cartilage thickness. For the non-design sections, their outer surfaces were first shell-meshed using four-node quad elements (for the main areas that will be in contact with the adjacent bones' cartilages) while surrounded by three-node triangular elements. The shell mesh of the five aforementioned sections was then mapped across each respective solid section, from its outer to its inner surface, creating eight-node hexahedral and six-node pentahedral solid elements. For the outer-design section, since it does not establish any contact, its outer surface was meshed with quad-

TABLE 1 Model material properties.

Component	Material Behavior	Mechanical Properties	
Bones (cortical bone)	Linear elastic	E = 19 GPa, ν = 0.3	Liu et al. (2022a)
Cartilage	Hyperelastic (Ogden)	μ_1 = 2.43 MPa, α_1 = 12.45, D_1 = 0.176 $\frac{1}{MPa}$	Liu et al. (2022a)
Implant (Ti-6Al-4V)	Linear elastic	E = 107 GPa, ν = 0.323, ρ = 4,405 $\frac{kg}{m^3}$	Ansys Workbench (2020)

dominated mixed shell elements. Finally, the inner-design section was meshed using four-node tetrahedral solid elements.

Herein, the implant, cartilages, and bones were assumed to be homogeneous isotropic solids, and their assigned material models and properties are summarized in Table 1. Additionally, surface-to-surface contacts were defined between the cartilages of the adjacent bones and their related contact areas on the outer surfaces of the respective non-design space of the implants. A static friction coefficient, μ_s = 0.01 (frictionless contact), was defined between the contact pairs, and separation was allowed after contact (Liu et al., 2022a).

2.3.2 Biological talus FE setup

As for the ankle joint FE setup involving the biological talus, a visual demonstration is shown in an earlier study (Liu et al., 2022a). A setup similar, in terms of loading and material properties, to that in Section 2.3.1 was utilized where the biological talus was in place of the solid implant. The selected rigid body set of elements were on the non-contact shell elements. The talus and its cartilage were meshed identically to the aforementioned adjacent bones (see Section 2.3.1). In this particular case, the surface contacts were defined between the adjacent bone cartilages and their related contact areas on the talus' cartilage surface.

2.3.3 Optimized implant FE setup

The optimized universal implant, presented further in Section 3.1, is visualized in isolation from the ankle joint in this study, as shown in Figure 5B. After TO (defined in Section 2.5), the updated finite element (FE) model of the ankle joint with the optimized implant, a setup identical to that of the solid implant in Section 2.3.1, was used for all three postures. The non-optimized (solid) implant was substituted with the optimized one in order to evaluate the performance of the latter. The only difference is the optimized implant's mesh, which due to its complex geometry, was fully meshed using four-node tetrahedral solid elements.

2.4 Mesh sensitivity analysis

To verify that the simulation results are independent of the solid implant's mesh, a sensitivity analysis was conducted. The ankle joint, in NS only, was simulated by varying the total number of elements of the implant while maintaining the mesh setup described in Section 2.3.1.

Based on the results, beyond 376,156 elements (100,083 nodes) the stress values varied minimally, where for at least a 4.2% increase in the total number of elements leads to an increase of at most 1.7% in either von Mises or contact stress, the solid implant was deemed to be mesh insensitive. Therefore, the model selected for further FE simulations and optimizations was the one with 414,111 elements (118,218 nodes). It possesses a sufficiently high number of elements, which will be required for a more detailed representation of the optimized topology; while it simultaneously has less elements, for computational efficiency, than the model with the finest mesh.

2.5 Topology optimization setup

The mesh and the material properties used for the implant are as described in Section 2.3.1. To further expand on Section 2.2, in the context of TO, the definitions of the design and non-design spaces, shown in Figure 1A, are important. The non-design space is the section that remains unchanged and is not optimized while the design space is the section that changes and is optimized, hence the partitions created in the implant.

For the loading conditions of the implant, the output nodal contact forces on the non-design sections from the FEA of the implant (resulting from the analysis in Section 2.3.1), in all three postures, were directly applied as loads on the same nodes of the implant (since the same mesh was used). All nodal contact forces belonging to each posture were placed in a load step of their own for a total of three linear static load steps. For example, Figure 3 shows the DF load step, where the size of each arrow is proportional to the magnitude of each nodal contact force.

The inertia relief 'INREL' parameter was activated which allows the software to run the static analysis without constraints, and instead, the applied loads are balanced out by nodal accelerations (automatically determined by Optistruct).

For the TO setup, the objective was to minimize the total volume $V(\boldsymbol{\rho})$ of the design space, which is the combination of both the 'Inner Design' and 'Outer Design' sections, as shown in Figure 1A. A von Mises (VM) static stress constraint was applied to the entire implant where the maximum VM stress of element e, $\sigma_{vm,e}$, may not exceed 75 MPa. The TO problem can be formulated as follows:

$$minimize\, V(\boldsymbol{\rho}) = \sum_{e=1}^{N} \rho_e \; w.r.t.\; \rho_e \tag{1}$$

$$subject\, to\, \sigma_{vm,e} \leq 75\,\text{MPa} \tag{2}$$

where

$$0.01 \leq \rho_e \leq 1, where\, e = 1, \ldots, N \tag{3}$$

The design variable is the relative density ρ of each element in the design space, where the relative density is the ratio of the optimized element's volume to the same element's non-optimized volume (which is a solid). Each element e, ranging from 1 to N number of finite elements, is assigned the design variable ρ_e.

The 75 MPa limit was selected to maintain a sufficiently high safety factor (SF, where SF is the ratio of the material's yield strength, 1,100 MPa for Ti-6Al-4V (Ansys Workbench, 2020), to the

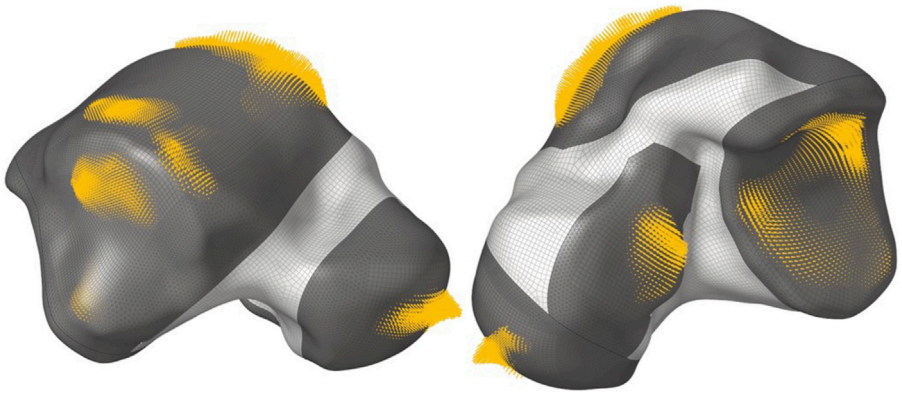

FIGURE 3
Nodal contact forces in dorsiflexion.

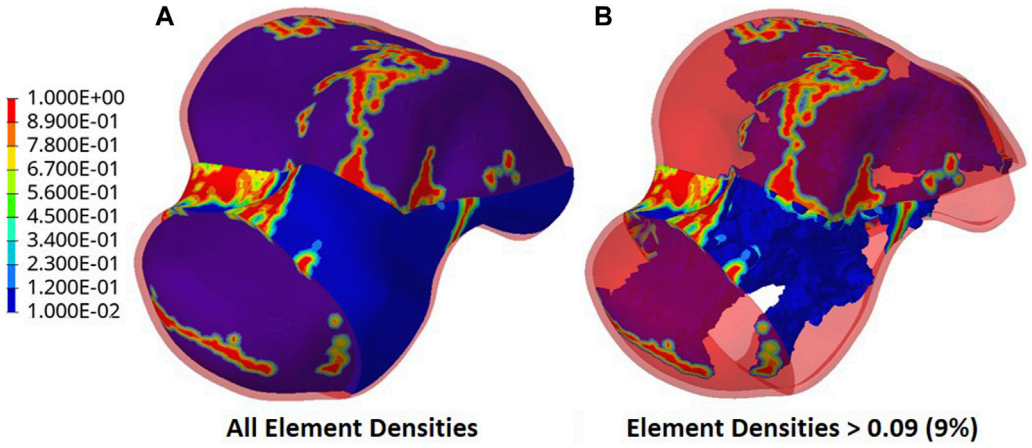

FIGURE 4
Optimized implant element density contours for **(A)** all densities and **(B)** densities >0.09.

maximum VM stress in the model) against yielding while still obtaining a relatively lightweight structure.

3 Results

3.1 Optimized geometry

The output of the optimization is the element density contour plot where the element densities (relative densities) of each element are shown. The relative density is the ratio of the optimized element's volume to the volume of the same non-optimized element. The values range from 0.01 (1%) to 1 (100%), where a (near) zero value represents a void (no material) and a value of one represents a solid (material). The element density contour plot of the optimized implant is shown for all densities in Figure 4A, and densities >0.09 in Figure 4B. Since the non-design space is not optimized, it is made transparent in Figure 4 for better visualization.

To extract the surface of the optimized geometry, the Hypermesh post-processing tool 'OSSmooth' was used and an iso-density boundary surface was extracted with a selected threshold density of 9%. The selected threshold density was based on requiring the removal of low-density solid elements while maintaining connections in some areas between the design and non-design space. The resulting optimized geometry's non-design and optimized design spaces are shown in Figure 5A while the solidified geometry, used for further analysis as defined in Section 2.3.3, is shown in Figure 5B. The masses of the design and non-design spaces, as well as the total masses of both the optimized and solid (non-optimized) implants are plotted in Figure 6A for a material density of 4,405 $\frac{kg}{m^3}$, corresponding to Ti-6Al-4V (Ansys Workbench, 2020).

3.2 Stress comparisons

To ensure the safety of the optimized implant, in addition to verifying that the optimization stress constraints were satisfied, a VM stress evaluation was conducted. For comparison of the optimized and solid implants as well as the biological talus, the

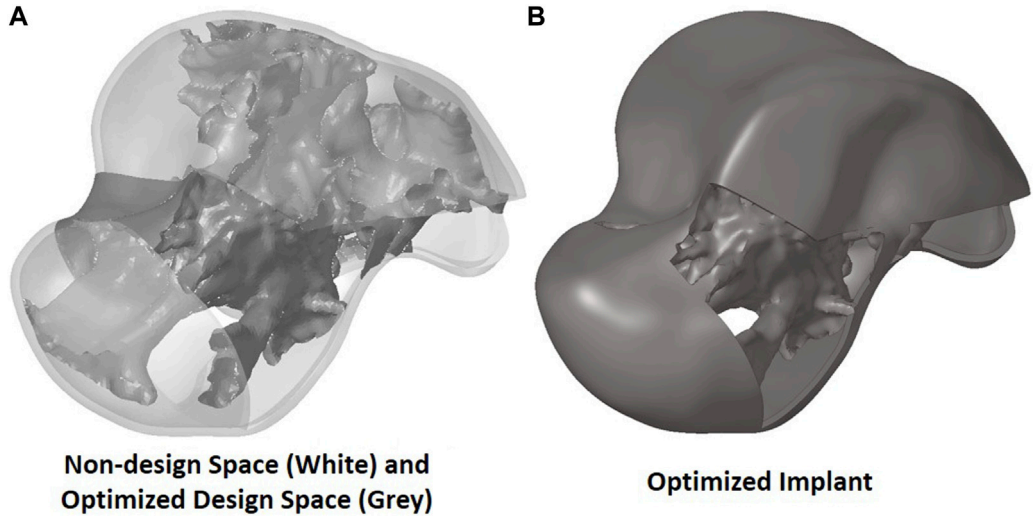

FIGURE 5
Optimized implant geometry **(A)** with non-design and optimized design spaces and **(B)** overall.

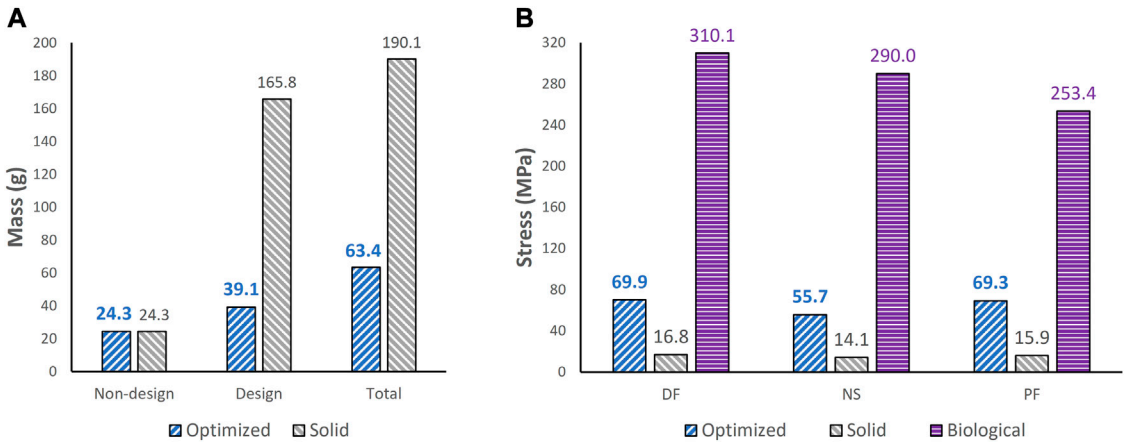

FIGURE 6
Comparisons of **(A)** mass between optimized and non-optimized (solid) implants and **(B)** maximum von Mises stress between optimized and solid implants, and biological talus.

maximum VM stresses are plotted in Figure 6B and the stress contours are shown in Figure 7 for all three postures. Note that the cartilage of the biological talus is hidden in Figure 7 for visualization and ease of comparison, and the grey sections were defined as rigid body sets, hence the nonexistence of stress contours.

3.3 Contact pressure comparisons

The effect of the optimized implant on the adjacent cartilages' contact characteristics was considered. Since a higher pressure, beyond a certain limit, could lead to bone fracture (Liu et al., 2022a), any talus implant should ideally have contact pressures and areas similar to those of the biological bone. For comparison of the optimized and solid implants as well as the biological talus, the maximum contact pressures are plotted in Figure 8. For the optimized implant and biological talus, the contact pressure contours of the adjacent cartilages in DF, NS, and PF are shown in Figure 9. As for the solid implant, the equivalent contours are not shown since the contact pressure patterns were identical to those produced by the optimized implant, and exhibit negligible maximum pressure differences, as seen in Figure 8.

4 Discussion

4.1 Results discussion

Based on Figures 4, 5, the material appears to be distributed in a way that is mostly governed by the load transfer paths, and is removed in the

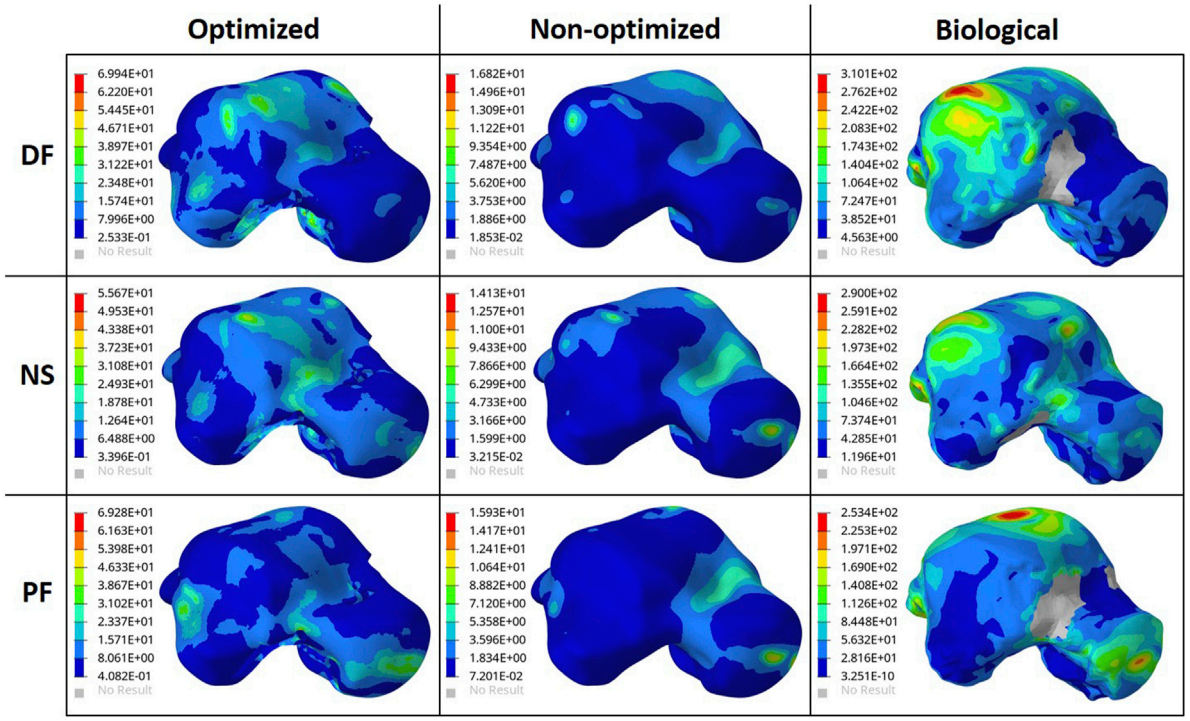

FIGURE 7
Von Mises Stress (MPa) contours for the optimized and non-optimized (solid) implants, and biological talus.

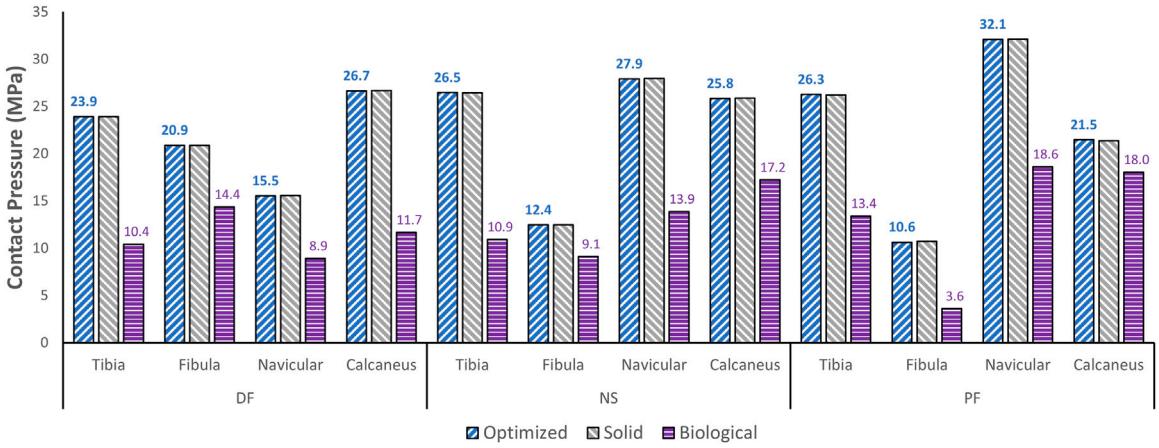

FIGURE 8
Maximum contact pressure comparisons between the optimized and solid implants, and biological talus.

sections that are less stressed. This leads to an optimal material distribution that reduces the implant's mass while rendering it safe for implantation by reinforcing the sections that transfer the load. For the summarized masses in Figure 6A, it is evident that the optimized implant weighs considerably less than the solid, non-optimized one. This lightweight implant design is expected to provide the patient with a more natural feel similar to that offered by the biological bone.

As for the stresses in all three postures in the optimized implant, based on Figure 6B; Figure 7, they are lower than the defined 75 MPa stress constraint. Additionally, the overall SF (lowest of the three postures, in DF) under static loading conditions is approximately 15.7. Accordingly, the optimized implant is deemed to be safe given its high SF. Additionally, as expected, it has higher stresses than the solid implant due to the availability of less material. For the biological talus, given its low elastic modulus, it experienced the highest stress across all three postures.

Finally, based on Figures 8, 9, the optimized and solid implants' contact pressures on the adjacent cartilages are identical in all three

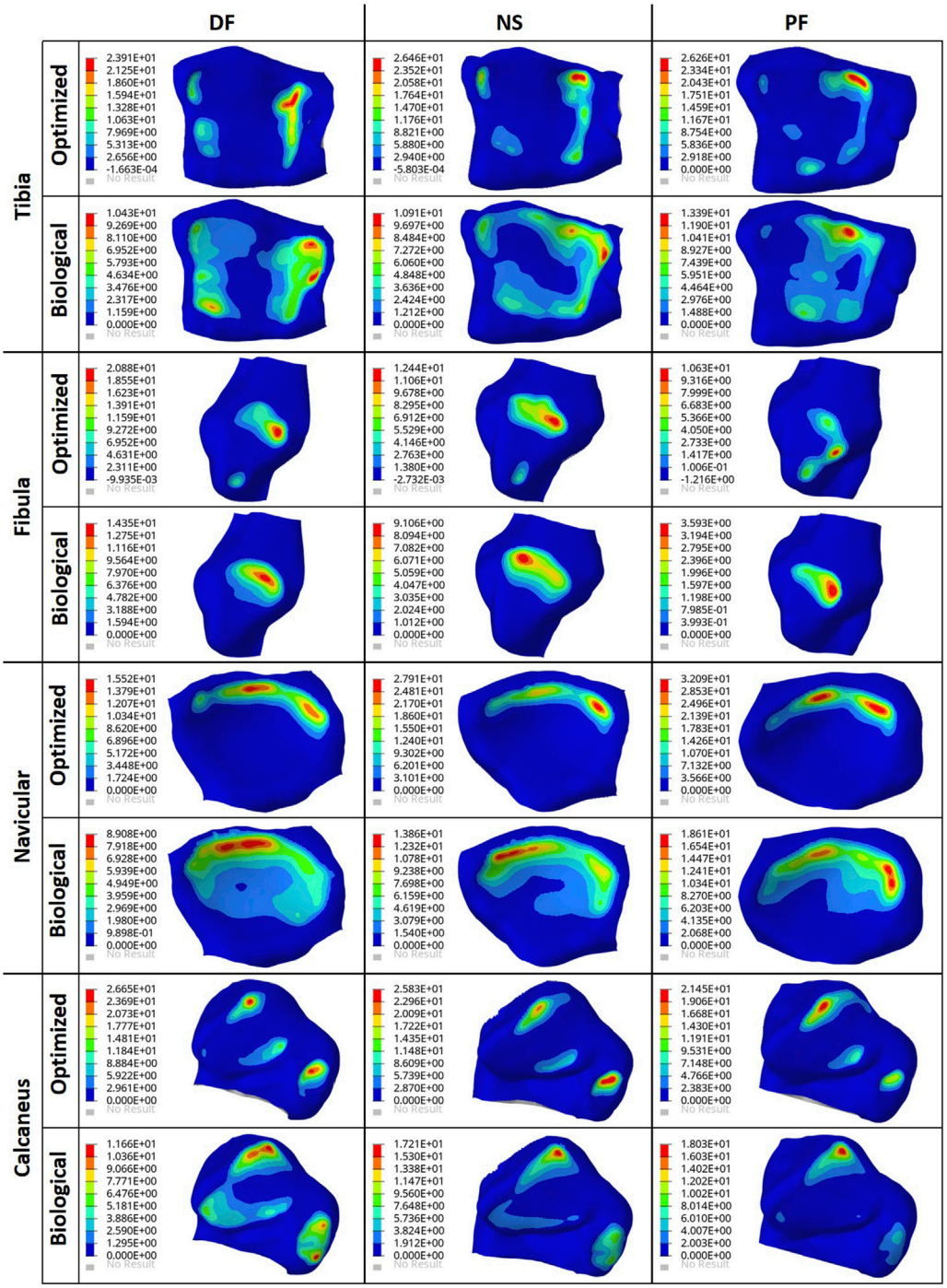

FIGURE 9
Contact pressure (MPa) contours for the optimized implant and biological talus.

postures. While this could partially be attributed to the nature of the material used for the implant which is considerably stiffer than cortical bone (Liu et al., 2022a), it is more likely that this is due to the unchanged articular surfaces (since they are a part of the non-design space). The biological bone has the lowest contact pressures with a significant peak pressure difference, relative to the implants. It produced peak pressures approximately 15.9%–66.2% lower than those produced by both implants. Additionally, on average, the contact areas appear to be higher for the biological talus in comparison to the implants. This could be attributed to the less stiff nature of cortical bone, but more significantly, this is likely due to the cartilage layer on the biological talus. Hence, adding an artificial cartilage layer on the implant surface could help in alleviating contact pressure peaks and guard against bone fractures near the bone/implant interfaces. Increased contact areas and reduced contact pressures due to the addition of a

compliant layer on top of the metal-based implant were also found in a recent study (Liu et al., 2022b).

The results of this study deem the usage of optimized universal implants a feasible alternative to traditional custom-made ones. The patient is expected to benefit from a more natural feel as a result of the optimized implant's lightweight nature as well as reduced times until surgical implantation given the universal nature. More generally, this study can help define a framework on how to approach the optimization of talus implants to obtain higher-performance and more economical total talus replacements.

4.2 Limitations and future work

Future work on the topic should focus on addressing the limitations of the present study. The optimization should be conducted for different types of loading such as dynamic (based on the human gait cycle), fatigue, and impact loading, that is not only limited to a single plane (sagittal in this research), but also to coupled out of plane loading and motion such as in the frontal plane. For the adjacent bones, more subjects could be used for optimization based on a variety of higher-quality bone geometries, rather than a single geometry. Moreover, more anatomically accurate ankle joint setups can be used in which both cortical and cancellous bone properties are considered, alongside the use of ligaments and muscles. Ligaments were not included in this comparative study given that the same postures and boundary conditions were used for all three tali and static loading was assumed. While the ligaments can play a significant role under dynamic loading, ligament usage is expected to have a minimal impact on the results when loads are applied statically (Liu et al., 2022a). To possibly reduce contact pressures, the usage of other materials (or a combination) could be explored. Additionally, to reduce the potential of stress concentrations without significantly increasing the implant's weight, the use of a porous structure within the design space can be explored. This would likely offer enhanced energy absorption and buffering effects, which are beneficial for the long-term performance of the implant (Peng et al., 2022).

Finally, it is worth noting that, while a constant elastic modulus was assumed throughout the implant, in practice, the mechanical behavior of the component may vary spatially. In particular, lower thickness sections realized through AM have been shown to possess a lower elastic modulus as compared to their bulk equivalent (Danielli et al., 2023). Hence, the computed geometry may not exhibit the intended optimality and safety criteria in the additively manufactured part. Consequently, the fabricated implants would need to be mechanically tested to validate the study's results and ensure safety.

5 Conclusion

This study focused on optimizing a universal talus implant, for total talus replacement, using topology optimization. For three postures, an FE model was developed for the biological talus, the solid implant, and similarly for the optimized implant post-optimization.

The major findings pertaining to the optimized universal implant are as follows. Its mass is significantly reduced (by approximately 66.6%). Based on maximum von Mises stresses in all three postures, it evidently satisfies the stress constraints (≤75 MPa) set in the optimization. Additionally, it is deemed to be safe in that it withstands 2000 N of static loading in all three postures with a safety factor of 15.7. This is based on the worst-case posture, dorsiflexion, with the highest maximum stress among all three. As for its effect on the surrounding cartilage, its maximum contact pressures were identical to those of the solid implant, therefore that aspect remained unaffected by the optimization.

Data availability statement

The raw data supporting the conclusion of this article will be made available by the authors, without undue reservation.

Author contributions

AH: Investigation, Validation, Data curation, Visualization, Writing—Original draft. ME-R: Conceptualization, Methodology, Supervision, Writing—Review and Editing. TL: Investigation, Data curation. NJ: Conceptualization, Manuscript review. AS: Conceptualization, Methodology, Supervision, Writing—Review and Editing, Funding acquisition. All authors contributed to the article and approved the submitted version.

Funding

This study was funded by Khalifa University through the Competitive Internal Research Award (CIRA) 2018 [grant number CIRA-2018-128].

Conflict of interest

The authors declare that the research was conducted in the absence of any commercial or financial relationships that could be construed as a potential conflict of interest. A patent application has been submitted for design characteristics of a universal talus prosthesis but has not been commercialized.

Publisher's note

References

Ansys Workbench (2020). *Static structural, engineering data, engineering data sources, additive manufacturing materials*. Canonsburg, Pennsylvania: ANSYS, Inc.

Bowes, J., Adeeb, S., Grosvenor, A., Beaupre, L., and Jomha, N. (2019). Development and implantation of a universal talar prosthesis. *Front. Surg.* 6, 63. doi:10.3389/fsurg.2019.00063

Brockett, C. L., and Chapman, G. J. (2016). Biomechanics of the ankle. *Orthop. Trauma* 30 (3), 232–238. doi:10.1016/j.mporth.2016.04.015

Danielli, F., Berti, F., Nespoli, A., Colombo, M., Villa, T., La Barbera, L., et al. (2023). Towards the development of a custom talus prosthesis produced by SLM: design Rules and Verification. *J. Mech. Sci. Technol.* 37 (3), 1125–1130. doi:10.1007/s12206-022-2109-z

Huang, J., Xie, F., Tan, X., Xing, W., Zheng, Y., and Zeng, C. (2021). Treatment of osteosarcoma of the talus with a 3D-printed talar prosthesis. *J. Foot Ankle Surg.* 60 (1), 194–198. doi:10.1053/j.jfas.2020.01.012

Hussain, R. (2020). Metallic 3D printed total talus replacement: a case study. *J. Foot Ankle Surg.* 60, 634–641. doi:10.1053/j.jfas.2020.10.005

Kang, Y., Kim, S., Kim, J., Lee, J., and Park, J. (2022). Evaluating the validity of lightweight talar replacement designs: rational models and topologically optimized models. *Biomaterials Res.* 26 (1), 10. doi:10.1186/s40824-022-00256-8

Katsui, R., Takakura, Y., Taniguchi, A., and Tanaka, Y. (2019). Ceramic artificial talus as the initial treatment for comminuted talar fractures. *Foot Ankle Int.* 41 (1), 79–83. doi:10.1177/1071100719875723

Kladovasilakis, N., Tsongas, K., and Tzetzis, D. (2020). Finite element analysis of orthopedic hip implant with functionally graded bioinspired lattice structures. *Biomimetics* 5 (3), 44. doi:10.3390/biomimetics5030044

Liu, T., Ead, M., Cruz, S. D., Jomha, N., Adeeb, S., El-Rich, M., et al. (2022b). Polycarbonate-urethane coating can significantly improve talus implant contact characteristics. *J. Mech. Behav. Biomed. Mater.* 125, 104936. doi:10.1016/j.jmbbm.2021.104936

Liu, T., Jomha, N., Adeeb, S., El-Rich, M., and Westover, L. (2020). Investigation of the average shape and principal variations of the human talus bone using statistic shape model. *Front. Bioeng. Biotechnol.* 8, 656. doi:10.3389/fbioe.2020.00656

Liu, T., Jomha, N., Adeeb, S., El-Rich, M., and Westover, L. (2022a). The evaluation of artificial talus implant on ankle joint contact characteristics: a finite element study based on four subjects. *Med. Biol. Eng. Comput.* 60 (4), 1139–1158. doi:10.1007/s11517-022-02527-x

Peng, X., Huang, Q., Zhang, G., Li, J., Zhang, X., Lu, Y., et al. (2022). Compensating the anisotropic mechanical properties of electron beam melting-based gyroid scaffolds using structural design. *Int. J. Mech. Sci.* 226, 107442. doi:10.1016/j.ijmecsci.2022.107442

Tonogai, I., Hamada, D., Yamasaki, Y., Wada, K., Takasago, T., Tsutsui, T., et al. (2017). Custom-made alumina ceramic total talar prosthesis for idiopathic aseptic necrosis of the talus: report of two cases. *Case Rep. Orthop.* 2017, 1–7. doi:10.1155/2017/8290804

Trovato, A., Bornes, T., El-Rich, M., Dhillon, S., Adeeb, S., and Jomha, N. (2018). Analysis of a generic talar prosthetic with a biological talus: a cadaver study. *J. Orthop.* 15 (1), 230–235. doi:10.1016/j.jor.2018.01.015

Trovato, A., El-Rich, M., Adeeb, S., Dhillon, S., and Jomha, N. (2017). Geometric analysis of the talus and development of a generic talar prosthetic. *Foot Ankle Surg.* 23 (2), 89–94. doi:10.1016/j.fas.2016.12.002

Trovato, A. (2016). *The development and analysis of a generic talus bone prosthetic*. Edmonton: Ph. D, University of Alberta.

West, T., and Rush, S. (2021). Total talus replacement: case series and literature review. *J. Foot Ankle Surg.* 60 (1), 187–193. doi:10.1053/j.jfas.2020.08.018

frontiers | Frontiers in Bioengineering and Biotechnology

TYPE Original Research
PUBLISHED 07 September 2023
DOI 10.3389/fbioe.2023.1241151

OPEN ACCESS

EDITED BY
Andrew T. M. Phillips,
Imperial College London,
United Kingdom

REVIEWED BY
Qiang Chen,
Southeast University, China
Linjie Wang,
Imperial College London,
United Kingdom

*CORRESPONDENCE
Yadong Liu,
doctoryadong@163.com

RECEIVED 16 June 2023
ACCEPTED 25 August 2023
PUBLISHED 07 September 2023

CITATION
Liu W, Zhang Y, Lyu Y, Bosiakov S and Liu Y (2023), Inverse design of anisotropic bone scaffold based on machine learning and regenerative genetic algorithm. *Front. Bioeng. Biotechnol.* 11:1241151. doi: 10.3389/fbioe.2023.1241151

Inverse design of anisotropic bone scaffold based on machine learning and regenerative genetic algorithm

Wenhang Liu[1], Youwei Zhang[1], Yongtao Lyu[1,2], Sergei Bosiakov[3] and Yadong Liu[4]*

[1]Department of Engineering Mechanics, Dalian University of Technology, Dalian, China, [2]DUT-BSU Joint Institute, Dalian University of Technology, Dalian, China, [3]Faculty of Mechanics and Mathematics, Belarusian State University, Minsk, Belarus, [4]Department of Orthopedics, Dalian Municipal Central Hospital Affiliated of Dalian University of Technology, Dalian, China

Introduction: Triply periodic minimal surface (TPMS) is widely used in the design of bone scaffolds due to its structural advantages. However, the current approach to designing bone scaffolds using TPMS structures is limited to a forward process from microstructure to mechanical properties. Developing an inverse bone scaffold design method based on the mechanical properties of bone structures is crucial.

Methods: Using the machine learning and genetic algorithm, a new inverse design model was proposed in this research. The anisotropy of bone was matched by changing the number of cells in different directions. The finite element (FE) method was used to calculate the TPMS configuration and generate a back propagation neural network (BPNN) data set. Neural networks were used to establish the relationship between microstructural parameters and the elastic matrix of bone. This relationship was then used with regenerative genetic algorithm (RGA) in inverse design.

Results: The accuracy of the BPNN-RGA model was confirmed by comparing the elasticity matrix of the inverse-designed structure with that of the actual bone. The results indicated that the average error was below 3.00% for three mechanical performance parameters as design targets, and approximately 5.00% for six design targets.

Discussion: The present study demonstrated the potential of combining machine learning with traditional optimization method to inversely design anisotropic TPMS bone scaffolds with target mechanical properties. The BPNN-RGA model achieves higher design efficiency, compared to traditional optimization methods. The entire design process is easily controlled.

KEYWORDS

machine learning, genetic algorithm, triply periodic minimal surfaces, inverse design, arrangement anisotropy

1 Introduction

Bone is a crucial part of the human body, serving various functions such as body support, protection of internal organs, and mineral storage. With the increasing aging population, the number of people suffering from joint diseases is also rising, leading to a greater demand for external repair techniques for bone defects (Gruskin et al., 2012; Li et al., 2015; Lin et al., 2020). Currently, the most important treatment method for repairing bone defects is bone tissue

engineering scaffolds that can guide bone tissue regeneration (Henkel et al., 2013; Tang et al., 2016; Zhu et al., 2021). The triply periodic minimal surface (TPMS) is an ideal model for designing scaffolds in bone tissue engineering due to its zero mean curvature and high specific surface area, which is similar to natural bone (Yan et al., 2015; Bobbert et al., 2017). However, it should be noted that different parts of bone tissue have varying mechanical properties, and the mechanical properties of the same bone tissue may differ in different directions. Therefore, it is crucial to develop an inverse design method for bone scaffolds based on the mechanical properties of bone structures.

The current research on TPMS bone scaffold mainly focuses on optimizing its structure to achieve the target performance. For example, (Yánez et al., 2018), systematically investigated stress conditions under compression and torsion of different types of Gyroid porous structures with varying porosity models (Rajagopalan and Robb, 2006). Proposed two bracket models, the P-type bracket and the regular voxel bracket in the TPMS unit. They found that the stress distribution of the P-unit bracket was better than that of other units with smaller strains (Wieding et al., 2014). Optimized the configuration parameters of titanium alloy scaffolds with opening characteristics, making the scaffolds have similarly elastic to human bone and satisfactory pore size. Overall, the research on TPMS bone scaffolds still needs to be improved, focusing on optimizing their structures to improve their performance. Unlike the previous uniform arrangement, the anisotropic TPMS structure is introduced in this article. This structure is more in line with the real structure of bone, which is also anisotropic.

To realize the inverse design, the machine learning (ML) based method is resorted due to its low computational cost, high adaptability to various physical problems, and good independence from physical models. ML-based method is a data-driven method, and its effectiveness depends on the amount of prepared data and the algorithm employed (Wang et al., 2021). Besides, the use of ML for inverse design has matured in metamaterials. For example, the artificial neural network (ANN) was employed by (Peurifoy et al., 2018) to approximate the inverse design of photonic crystals. The deep-learning-based model comprising two bidirectional ANN was established to design and optimize the chiroptical metamaterials at specific wavelengths (Ma et al., 2018). Recently, the Gauss-Bayesian model involving Bayesian optimization using Gaussian kernel was proposed to realize the inverse design of various acoustic metamaterials for predesignated functionality (Zheng et al., 2020). While ML methods have been effectively utilized in the inverse design of metamaterials, their application in bone implants is still limited and requires further investigation.

The present study aimed to inversely design complex bone scaffolds using anisotropic TPMS structures. The target for inverse design was the partial elasticity matrix of bone. A mapping relationship between structural parameters and mechanical properties using the back propagation neural network (BPNN) neural network was established in our design method. Then, a regenerative genetic algorithm (RGA) was embedded in machine learning for inverse search to obtain the desired structure (Figure 1). Finally, several sets of design targets and high-precision finite element (FE) simulations were used to demonstrate the validity and generalizability of the BPNN-RGA model.

2 Materials and methods

2.1 Anisotropic TPMS structures

Arrangement anisotropy refers to the fact that the number of TPMS unit cells arranged in each direction is different while the length of the structure in each direction remains constant. The whole structure had different mechanical properties, such as Young's modulus, in different directions. As shown in Figure 2A, the unit cell structure, normal arrangement structure, and anisotropic arrangement structure of four types of TPMS required for inverse design are displayed. As shown in Figure 2B, the change in compressive modulus in different directions of the structure varies with the number of units in the y-direction of the given coordinate system in Figure 2A. It should be noted that when only the modulus in the y-direction is changed, the moduli in the x-direction and z-direction were the same (the number in x and z directions is kept "2"). A more complicated structural design can be made if the numbers in the three directions are different.

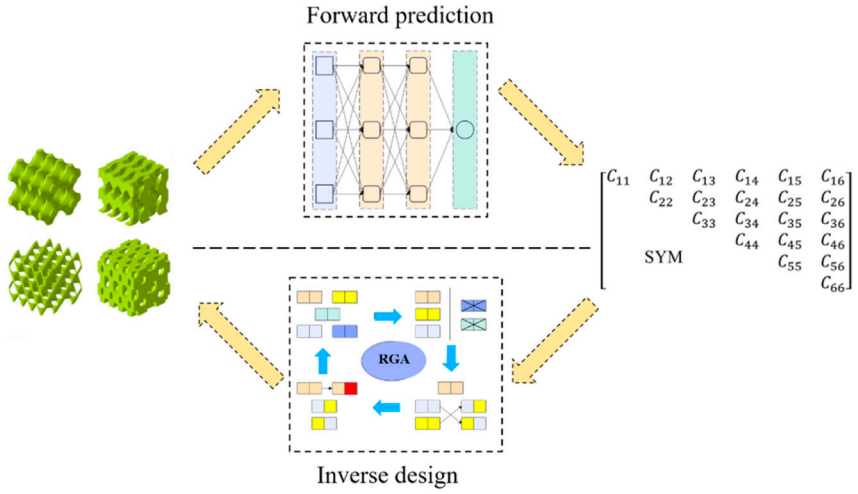

FIGURE 1
Flow chart of forward prediction and inverse design.

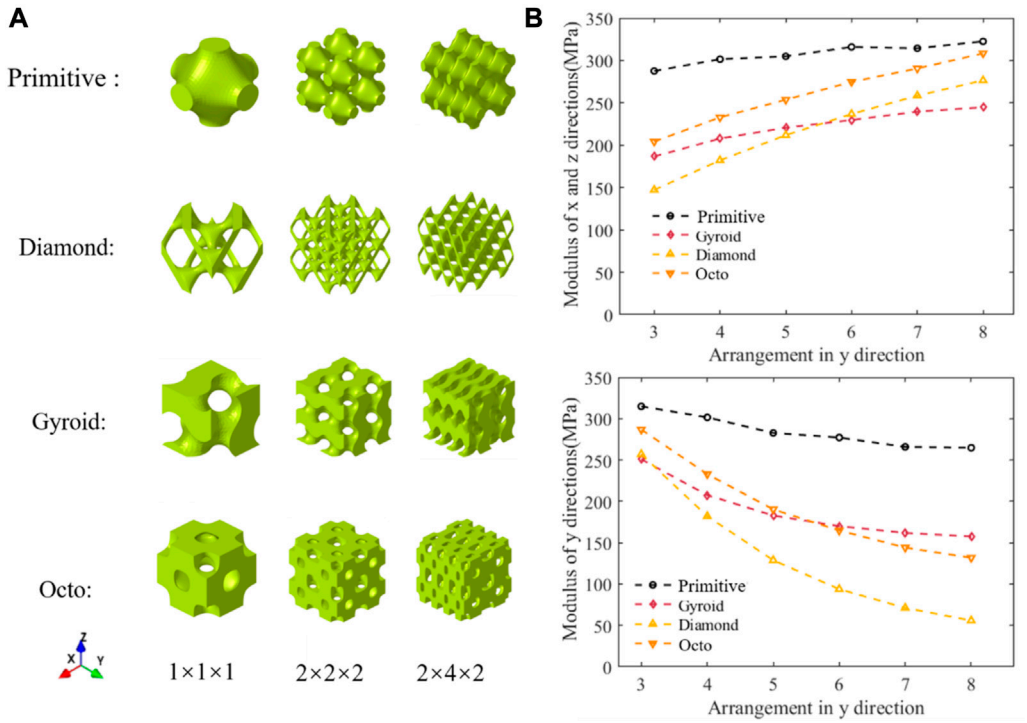

FIGURE 2
Schematic diagram of structure and their performance. **(A)** Structures of various arrangements **(B)** Variation of compression modulus with the number of arrangements.

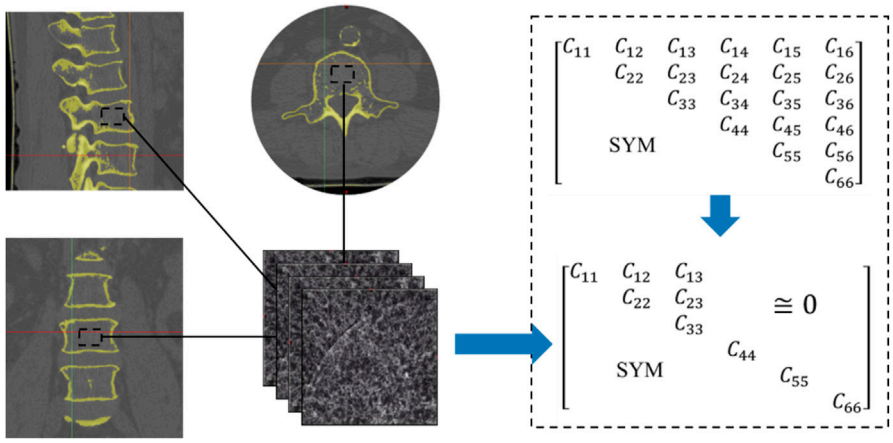

FIGURE 3
CT images of bone structure and its stiffness matrix.

Anisotropic TPMS structures can be generated by controlling the parameters of the surface equations. The anisotropic Primitive scaffold was characterized using the following equation:

$$U_S = \cos\left(\frac{2\pi m}{L}x\right) + \cos\left(\frac{2\pi n}{L}y\right) + \cos\left(\frac{2\pi l}{L}z\right) - t$$

where m, n, and l are the arrangement numbers of the anisotropic Primitive unit cell in the x, y, and z directions, respectively; t is the surface control coefficient, which is related to porosity φ; L is the dimension of the design structure in the x, y, and z directions.

The FE method was used to calculate the equivalent stiffness matrix of the human bone from computed tomography (CT) images (Figure 3). The 2D image is re-established as a 3D model by superposition, and then the finite element method is utilized to solve the C_{ij}, with 1,2,3 in the parameters corresponding to the x, y, and z directions, respectively, as detailed in the literature

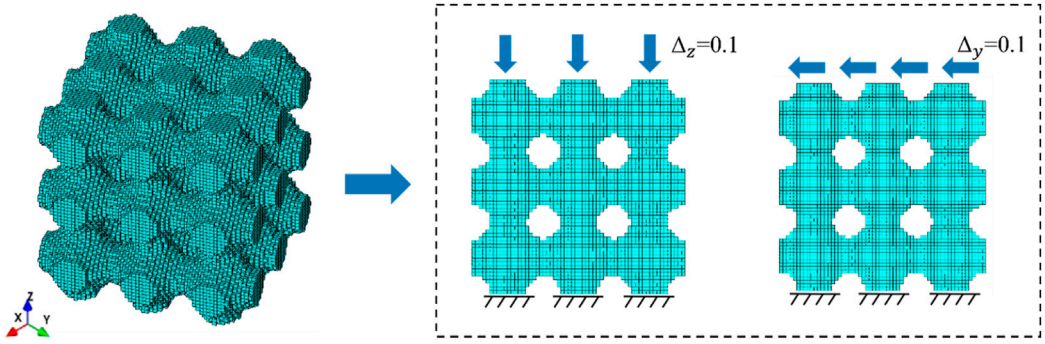

FIGURE 4
Two loading conditions of the TPMS structure.

(Xiao et al., 2021; Lu et al., 2022). The stiffness matrix was then compared with those in the existing literature to verify its rationality (Kalouche et al., 2010; Wang et al., 2016). The analysis of the equivalent elastic matrix data shows that it is difficult to achieve inverse design of the elastic matrix if the TPMS was uniformly arranged in space. A previous study has shown that, in a specific direction, the mechanical properties of TPMS scaffolds can be significantly improved by adjusting structural anisotropy (Peng et al., 2022). This feature was used to create structures with various mechanical properties in all directions.

2.2 Establishment of machine learning database

The ML method is largely database dependent, so enough data are required to perform the inverse design. To generate the data set for ML to predict the equivalent stiffness matrix of TPMS, we obtained the 3D scatter plot from the TPMS surface equation and used the scatter plot to generate the unit node information. The range of variation of the number of structural arrangements is set to 3–8. The range of variation of porosity is set to 50%–75%. The element node information was imported into ANSYS (v.18.0, Ansys Inc., Canonsburg, PA, United States) to generate the FE model. Moreover, FE calculations were performed according to different boundary conditions. TPMS surface parameters and the results of FE calculation were used as the training set of neural networks.

As shown in the Figure 4, the compression and shear terms in the stiffness matrix were solved using the unidirectional compression and pure shear conditions. The lower surface of the TPMS structure was completely fixed and a displacement load of 0.1 was applied to the upper edge face. The length L was 10.00 mm, and the elements were first-order hexahedral solid elements (Solid185). The Young's modulus for the component material was 10.00 GPa, and the Poisson ratio was 0.30 (Hak et al., 2014; Wu et al., 2018). It should be noted that Young's modulus of the designed configuration was changed to 100 GPa for the low porosity bone due to the significant difference between the two bone moduli (Collins et al., 2021).

2.3 Forward prediction using BPNN

ML can be used to quickly predict problems that are previously difficult to solve (Yan et al., 2018; Chen et al., 2019). The BPNN is a representative ML algorithm inspired by the biological neural network of the human brain (Lu et al., 2019). BPNN could be regarded as a non-linear operator, which takes an input vector X and returns the hypothesis value of the output vector y, as given in equation:

$$y = \mathrm{BPNN}(\boldsymbol{X}) = \mathrm{BPNN}(c, \varphi, t, m, n, l)$$

where c is a label used to distinguish different TPMS structures, and c is an integer, the value of which is between 1 and 4 (Figure 5).

A typical BPNN is shown in Figure 6. The first layer of the BPNN was the input layer, the last layer was the output layer, and two hidden layers were introduced between them. When the input information $\boldsymbol{X}$ was transferred into a neuron node in the hidden layer, as shown in Figure 6, the neuron node would give an approximation adjusted by a nonlinear activation function. The nonlinear relationship between the input variables and the medium approximation h_j was captured in hidden layer 1.

$$h_j = f\left[\left(\sum_{i=1}^{6} w_{ij}^{(1)} x_i\right) + b_j^{(1)}\right], j = 1 \to m$$

where $w_{ij}^{(1)}$ is the weight connecting the input variable i and the neuron node j , $b_j^{(1)}$ is the related bias, and f is the nonlinear activation function which is continuous and differentiable.

Through two hidden layers, this approximation is mapped into the output variable $\tilde{y}_j$ corresponding to the neuron node j by a linear transfer function ϕ.

$$\tilde{y} = \sum_{j=1}^{6} \tilde{y}_j = \sum_{j=1}^{6} \phi\left(w_j^{(3)} h_j + b^{(3)}\right)$$

where $w_j^{(3)}$ is the weight connecting the neuron j and the output variable $b^{(3)}$ is the related bias. If the actual output $\tilde{y}$ is different to the target output y, a back propagation of error based on gradient error theory is required to iteratively adjust the weight coefficients in the network to minimize the difference through the mean square error (MSE) function.

Two neural networks, BPNN1 and BPNN2, were trained after determining the optimal structure of the neural network. The

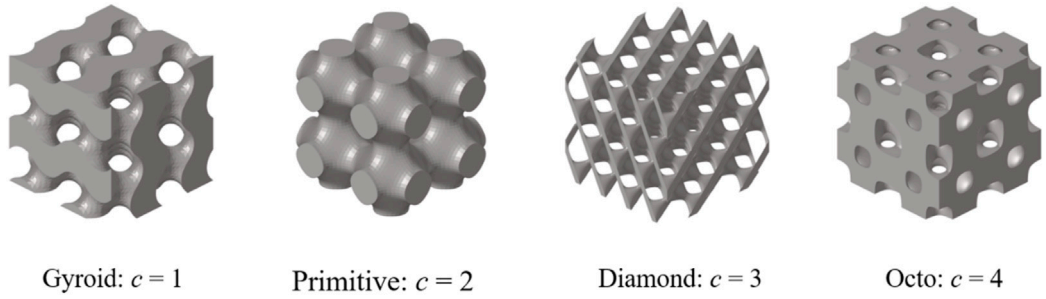

FIGURE 5
Machine learning label of TPMS structures.

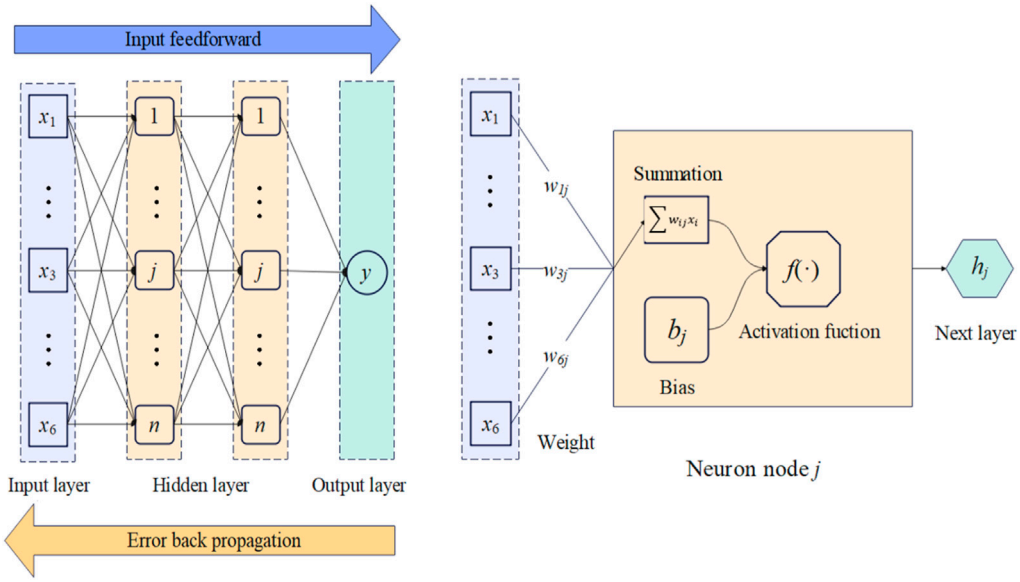

FIGURE 6
The structure of the BPNN neural network.

BPNN1 was used to train the mapping relationship between the structure and the compressive modulus, and BPNN2 was used to train the mapping relationship between the structure and the shear modulus.

2.4 Inverse design using BPNN-RGA

The RGA was employed to search for the TPMS configuration, of which the equivalent stiffness matrix was closest to the objective one, as illustrated in Figure 7. The individuals of the RGA were TPMS configurations, and chromosomes were surface equation parameters. A ML model was used to map the relationship between the surface parameters and the equivalent stiffness. The model's fitness was determined by comparing the absolute value of the difference between the fitting stiffness and the target stiffness. The smaller the absolute value, the better the fitness. A single output was used to ensure the neural network's accuracy. Moreover, a regeneration step based on the traditional genetic algorithm was incorporated in this article. Regenerating two structures with the same design parameters but different x, y, and z arrangements was involved in this step. This step aimed to change the direction of load application and obtain the compression or shear properties of the same structure in different directions. Without adding new neural networks, the accuracy of multi-output neural networks was improved in this approach.

TPMS structures with different porosities, arrangement numbers, and cell types were generated as the initial population. The first step in the genetic algorithm was to evaluate the fitness of the individuals in the population. Individuals with lower fitness scores were more likely to undergo cross-mutation, while those with higher fitness scores may also undergo cross-mutation but with a lower probability. After completing the mutations and crossovers, the parents and children were sorted together. The top

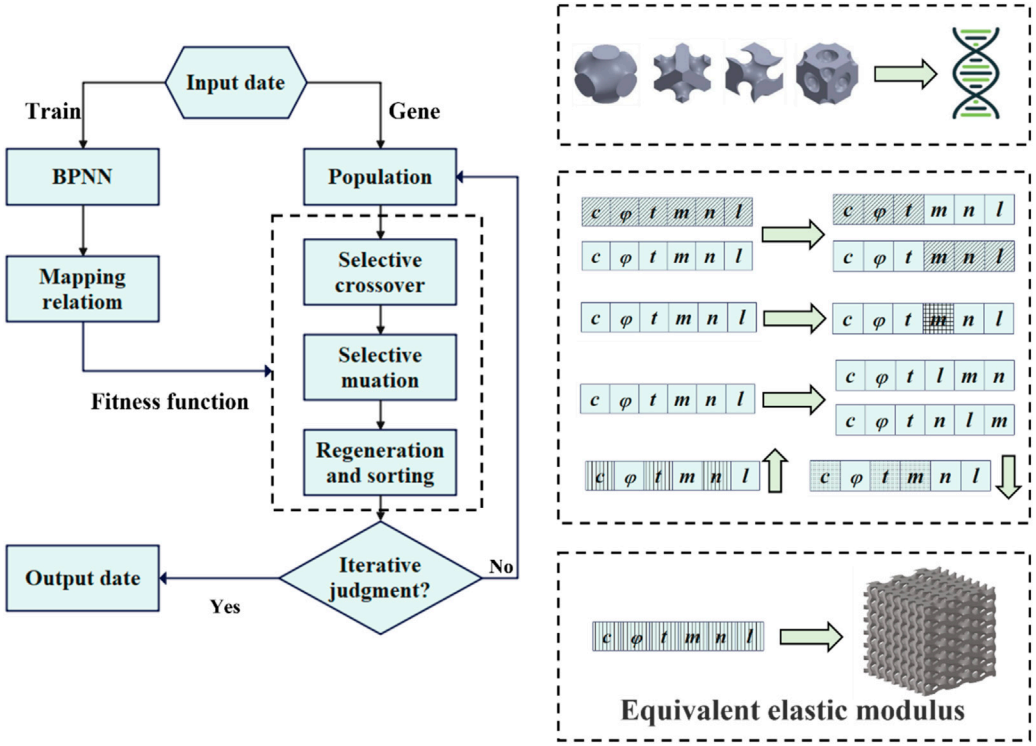

FIGURE 7
Flow chart of the inverse search using genetic algorithm.

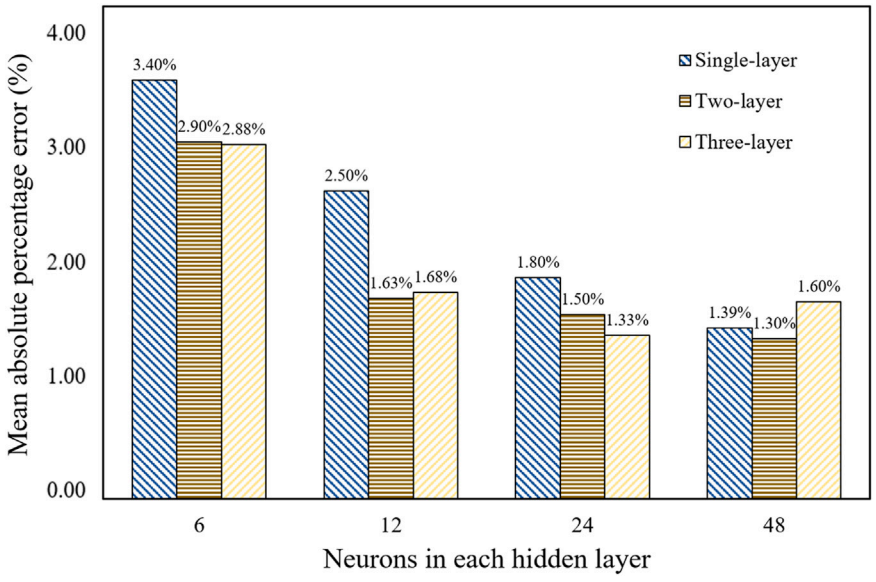

FIGURE 8
Comparison of the neural network errors with different structures.

2,000 individuals with the highest fitness were selected as the new population, and the next round of mutation and crossover sorting was carried out. The best-adapted individual was recorded each time, and if the error did not decrease after 20 consecutive iterations, it was considered that the best individual had been found. At this point, the outputs were the structural design parameters.

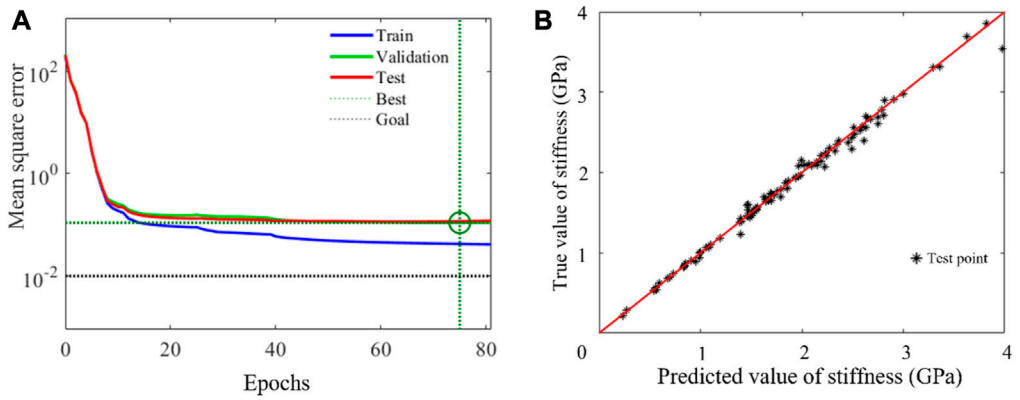

FIGURE 9
Error analysis of neural network model. **(A)** The mean square error **(B)** The test results of the BPNN network.

TABLE 1 Data sensitivity analysis.

Number of data	Data calculation time (h)	Network training time (s)	Percentage relative error (%)
400	0.36	3	3.5
1,200	1.1	8	2.4
2,000	1.8	8	1.8
4,000	3.6	26	1.4
8,000	7.2	34	1.2

3 Result

3.1 Optimization of the neural network model

We generated 8,000 TPMS configurations and computed their equivalent stiffness matrixes using the FE method, among which 7,000 configurations were used in the training set and 1,000 configurations in the test set. Once the database was established, it was crucial to determine the optimal BPNN structure, including the number of hidden layers and neurons in each layer. The quality of the neural network structure was evaluated based on the mean absolute percentage error (MAPE). The MAPE for the stiffness of each architecture is shown in Figure 8. It can be seen that the BPNN architecture with two hidden layers and 48 neurons in each hidden layer has the minimal error. Therefore, the neural network structure was used to predict the modulus.

The convergent behavior of the selected BPNN architecture is shown in Figure 9A. It was also indicated that there was no overfitting phenomenon because the established BPNN model performed well with training and test datasets. In order to verify the reliability of the neural network, the trained network was loaded, the newly generated input data was given, and the comparison between the fitted output data and that of the FE calculation was made. The result is shown in Figure 9B. It can be seen that the BPNN has a high predictive accuracy even when it is used to predict untrained data. A sensitivity analysis of the number of trainings was also conducted and the results are shown in Table 1. The time consumed to compute the samples was also labeled.

3.2 Inverse design based on the porous bone

The stiffness matrix of porous bone was calculated from CT images. However, due to the anisotropy of porous bone, there were still nine different design goals, even after omitting items close to zero. The inverse design of the spine bone focused on the structure's performance in compression rather than shear. Therefore, the compressive moduli in three directions (C_{11}, C_{22}, C_{33}) were considered as the primary design target, while the shear moduli related to (C_{44}, C_{55}, C_{66}) were the secondary design target. The other non-diagonal items related to compression (C_{12}, C_{13}, C_{23}) were used as the verification items, and their errors should not be too large. Using the regenerative genetic algorithm in inverse design, the two neural networks BPNN1 and BPNN2, combined with the function of the regenerative genetic algorithm, we can obtain the structural design parameters that meet the six design objectives:

$$\boldsymbol{X}_{best} = (c, \varphi, t, m, n, l) = (1, 67\%, 0.52, 7, 8, 3)$$

The corresponding TPMS structure was Gyroid, the structural porosity was 67%, and the numbers in the x, y, and z directions were 7, 8, and 3, respectively. The stress distribution under compression is shown in Figure 10. The proposed supporting reaction force can be

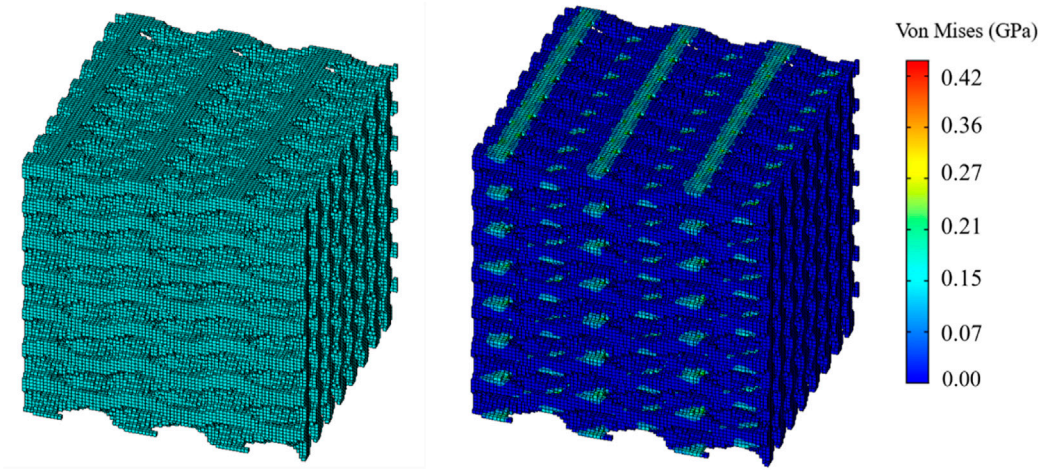

FIGURE 10
Verification of the design structure using the FE simulation.

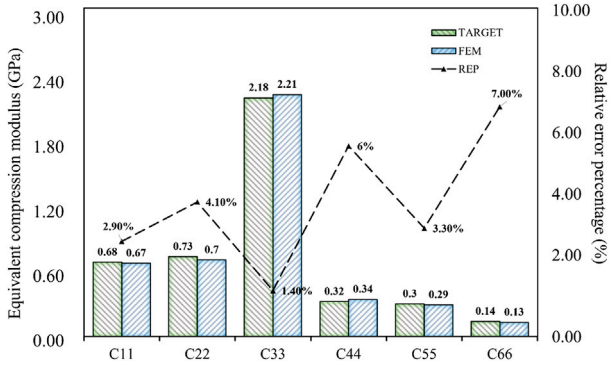

FIGURE 11
Error analysis of six design objectives of porous bone.

obtained through formula calculation (Feng et al., 2021; Lu et al., 2022), and the partial stiffness matrix of the structure was compared with the target value. The comparison between the results and the target value is as shown in Figure 11. Error analysis in terms of both numerical magnitude and relative error percentage (REP).

The results of the simulation demonstrated that the BPNN-RGA method could achieve the inverse design with a maximum absolute error of 0.03 GPa and a maximum relative error percentage of 7.00%, when the design targets were the compression and the shear modulus in three directions. The secondary design target had the most significant error percentage due to its small magnitude.

When the design targets were reduced to three, such as the compressive modulus in three directions, the relative error percentage became almost negligible (Figure 12). Therefore, achieving indiscriminate prediction of three or fewer design objectives within the current inverse design domain was possible. When the design target was only the three-dimensional compressive modulus, the maximum absolute error was limited to 0.04 GPa, and the maximum relative error percentage was limited to 2.00%. It can be concluded that the BPNN-RGA method has the higher design accuracy for the fewer design targets, as demonstrated by the decrease in relative error percentage.

3.3 Inverse design based on other porous bones

The data presented in this article was obtained through the analysis of porous bone CT images. While its validity had been confirmed (Kalouche et al., 2010; Wang et al., 2016), it should be noted that it was served as an illustrative example. Due to the irregular arrangement of trabecular bone in porous bone, the modulus of different positions can vary greatly, and the ratio of modulus in each direction may be inconsistent. The three-dimensional compressive modulus from existing literature (Wu et al., 2018) was used as the design target to demonstrate the universality of the inverse design domain of the BPNN-RGA model (Figure 13).

As shown in Figure 13, the BPNN-RGA model still has good solutions for different compressive moduli and proportions. The corresponding TPMS structure was Primitive, the structural porosity was 52%, and the numbers in the *x*, *y*, and *z* directions were 3, 6, and 6, respectively. The maximum error of the structure is less than 3.00%. In addition to the inverse design of porous bone with a small modulus, low porosity bone with a relatively large modulus was also inverse designed. Design goals for low porosity bone from existing literature (Wang et al., 2016).

As shown in Figure 14, the design error of BPNN-RGA for low porosity bone is still controlled within 3.00%. The corresponding TPMS structure was Octo, the structural porosity was 58%, and the numbers in the x, y, and z directions were 4, 5, and 5, respectively. In addition, the analysis of the historical output data of the RGA showed that when the control error was around 5.00%, several unit cell structures can satisfy the design requirements (Figure 15). These unit cells had different arrangement numbers in three directions and different porosity levels, providing more options for selecting the most appropriate porosity and structures for machining based on machining constraints.

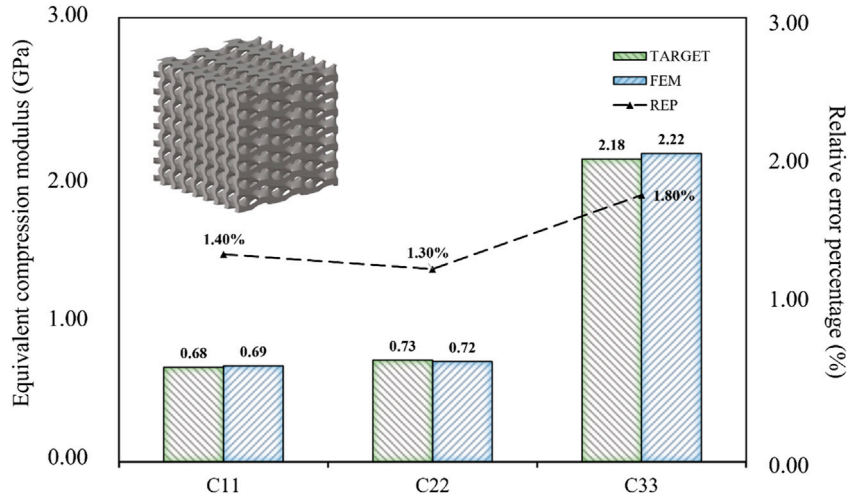

FIGURE 12
Error analysis of three design objectives of porous bone.

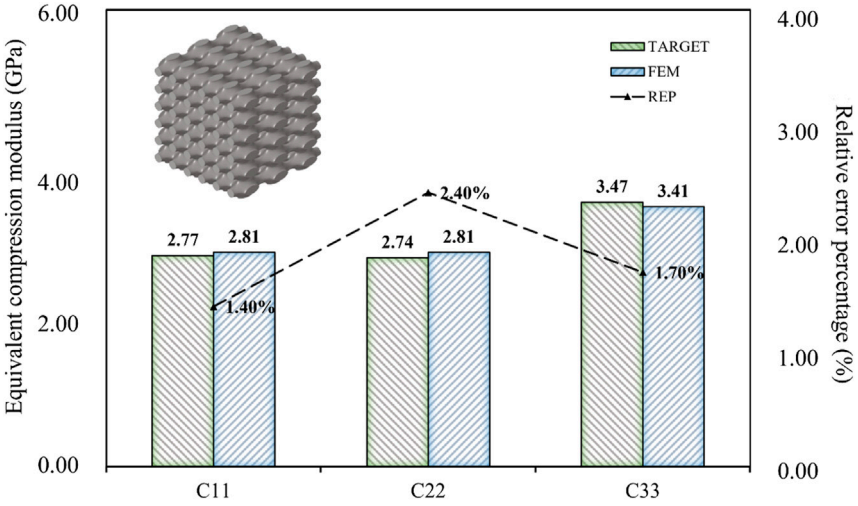

FIGURE 13
Error analysis of high porous bone based on existing literature.

4 Discussion

In the present study, a BPNN-RGA model was developed to design complex bone scaffolds, and a simulation error analysis was performed to verify the accuracy of the model. The present study indicates that complex bone scaffolds can be designed efficiently and accurately using the BPNN-RGA model.

In some ways, the design method based on neural networks was more efficient than other optimization methods. A comparative discussion with other bone scaffold design methods is given below: The randomization method based on computer aided design has been proven effective in simulating real bone through the randomization process (Mullen et al., 2010). However, this method requires many trials to achieve the expected performance. The design of unknown design targets could not be efficient. Although the BPNN-RGA model depends on data, when the data is accumulated enough, the neural network can find the internal relationship between the data to predict the unknown data accurately, which cannot be achieved by traditional randomization methods.

Except randomization, comparison with topology optimization methods is also a focus (Guest and Prevost, 2007). Utilized solid isotropic material with penalization based structural optimization to develop a topology optimization technique for finding a scaffold with pores in the shape of a Schwartz primitive structure. The topology optimization method was also used to match the stiffness matrix of the scaffold material to the stiffness matrix of anisotropic natural bone. Although topology optimization can realize the design

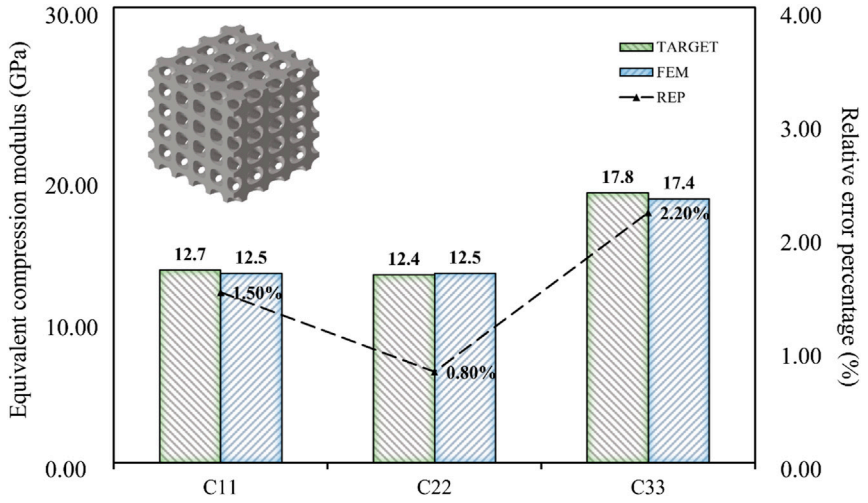

FIGURE 14
Error analysis of low porosity bone based on existing literature.

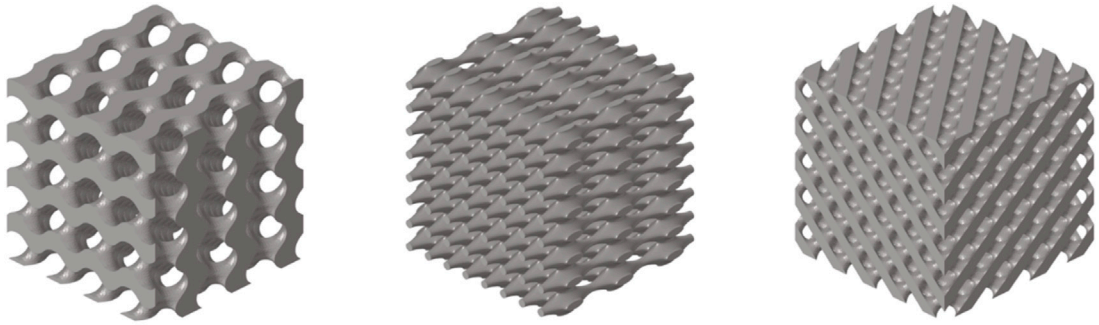

FIGURE 15
Several other structural diagrams that meet the design error.

of complex bones the designed structure may have gray units that affect the printing of the structure. It should be noted that although additive manufacturing (AM) can produce structures in any shape, the quality of the structures may vary greatly depending on the design and fabrication parameters (Wang et al., 2013). As the BPNN-RGA method is designed based on the TPMS structure, which has been widely used in bone scaffolds, there is no need to worry about manufacturing. The dimension of the design target is reduced using the parameters of the surface equation instead of the three-dimensional structures, which improves the design efficiency.

In addition, the selectivity of the design results are also the highlights of the BPNN-RGA model. When the design error was set to approximately 5.00%, we found various unit cells suitable for inverse design with the same design goals, which provided us with more options to select. The difference between the different types of TPMS structures, if they all met the design objectives, was the porosity. A successful implant must meet mechanical requirements that match the surrounding tissue to reduce stress shielding and prevent mechanical failure. However, except these considerations, it is also important to consider cell attachment and growth, as well as the transportation of nutrients and metabolic wastes for optimal biocompatibility (Langer and Vacanti, 1999; Hollister, 2009). Bone regeneration in porous implants *in vivo* involves the recruitment and penetration of cells from the surrounding bone tissue and vascularization (Karageorgiou and Kaplan, 2005). The porosity of a structure is linked to nutrient exchange and the size of its specific surface area. Therefore, when designing structures that meet specific requirements, we can make a decision based on the porosity of the structure (Story et al., 1998; Lewandrowski et al., 2000).

The limitation of the BPNN-RGA model is that the design field is limited to four TPMS structures. When there are more than six targets in the inverse design, some inaccuracies may occur due to the design field. To address this issue, one of the methods is to increase the variety of TPMS structures, and the

other method is to increase the number of single-cell arrays. Furthermore, the efficiency of the BPNN-RGA model is reflected in its repeated use. The time cost of building the model may be higher if it is used only once. This is also a common feature of all machine learning models.

5 Conclusion

In this paper, a new inverse design method BPNN-RGA was proposed to inversely design anisotropic bone scaffolds. In this method, anisotropy was introduced into the arrangement of bone scaffolds based on traditional TPMS structures, and the bone stiffness matrix calculated from CT images was used as the inverse design target. The results of the FE calculation were used in neural network training to find the mapping relationship between the structural parameters and the elastic modulus. RGA was used in inverse design to find the structure meeting the target modulus. Multiple bone data were used to verify the universality and accuracy of the BPNN-RGA method. The results showed that the average error was less than 3.00%, when the design targets was three mechanical performance parameters and about 5.00% when the design targets was six. Compared with the traditional optimization method, the proposed BPNN-RGA model achieves high design efficiency. Moreover, the results of the design have the characteristics of stability and selectivity.

Data availability statement

Original research data in the study are included in the article, further inquiries can be directed to the corresponding author.

Author contributions

WL, YZ, YoL, SB, and YaL: conceptualization, methodology, formal analysis, simulation, writing-original draft. WL, YoL, and SB: conceptualization, analysis, writing-review and editing. YZ and YoL: resources, writing-review and editing, supervision. All authors contributed to the article and approved the submitted version.

Funding

This study was supported by the National Natural Science Foundation of China (12072066), the Liaoning Provincial Natural Science Foundation of China (2022-YGJC-21), the Natural Science Foundation of Dalian (21Z11019, 2021RQ025), the Dalian Science and Technology Innovation Fund (2022JJ13SN077) and the DUT-BSU joint research grant (ICR2303), Dalian University of Technology.

Conflict of interest

The authors declare that the research was conducted in the absence of any commercial or financial relationships that could be construed as a potential conflict of interest.

Publisher's note

All claims expressed in this article are solely those of the authors and do not necessarily represent those of their affiliated organizations, or those of the publisher, the editors and the reviewers. Any product that may be evaluated in this article, or claim that may be made by its manufacturer, is not guaranteed or endorsed by the publisher.

References

Bobbert, F. S. L., Lietaert, K., Eftekhari, A. A., Pouran, B., Ahmadi, S. M., Weinans, H., et al. (2017). Additively manufactured metallic porous biomaterials based on minimal surfaces: A unique combination of topological, mechanical, and mass transport properties. *Acta Biomater.* 53, 572–584. doi:10.1016/j.actbio.2017.02.024

Chen, G., Li, T., Chen, Q., Ren, S., Wang, C., and Li, S. (2019). Application of deep learning neural network to identify collision load conditions based on permanent plastic deformation of shell structures. *Comput. Mech.* 64 (2), 435–449. doi:10.1007/s00466-019-01706-2

Collins, M. N., Ren, G., Young, K., Pina, S., Reis, R. L., and Oliveira, J. M. (2021). Scaffold fabrication technologies and structure/function properties in bone tissue engineering. *Adv. Funct. Mater.* 31 (21), 2010609. doi:10.1002/adfm.202010609

Feng, J. W., Liu, B., Lin, Z. W., and Fu, J. Z. (2021). Isotropic porous structure design methods based on triply periodic minimal surfaces. *Mater. Des.* 210, 110050. doi:10.1016/j.matdes.2021.110050

Gruskin, E., Doll, B. A., Futrell, F. W., Schmitz, J. P., and Hollinger, J. O. (2012). Demineralized bone matrix in bone repair: history and use. *Adv. Drug Deliv. Rev.* 64 (12), 1063–1077. doi:10.1016/j.addr.2012.06.008

Guest, J. K., and Prevost, J. H. (2007). Design of maximum permeability material structures. *Comput. Methods Appl. Mech. Eng.* 196 (4-6), 1006–1017. doi:10.1016/j.cma.2006.08.006

Hak, D. J., Lindeque, B. G. P., Mauffrey, C., Seligson, D., and Lindeque, B. (2014). Use of carbon-fiber-reinforced composite implants in orthopedic surgery. *Orthopedics* 37 (12), 825–830. doi:10.3928/01477447-20141124-05

Henkel, J., Woodruff, M. A., Epari, D. R., Steck, R., Glatt, V., Dickinson, I. C., et al. (2013). Bone regeneration based on tissue engineering conceptions - a 21st century perspective. *Bone Res.* 1, 216–248. doi:10.4248/br201303002

Hollister, S. J. (2009). Scaffold design and manufacturing: from concept to clinic. *Adv. Mater.* 21 (32-33), 3330–3342. doi:10.1002/adma.200802977

Kalouche, I., Crepin, J., Abdelmoumen, S., Mitton, D., Guillot, G., and Gagey, O. (2010). Mechanical properties of glenoid cancellous bone. *Clin. Biomech. (Bristol, Avon)* 25 (4), 292–298. doi:10.1016/j.clinbiomech.2009.12.009

Karageorgiou, V., and Kaplan, D. (2005). Porosity of 3D biomaterial scaffolds and osteogenesis. *Biomaterials* 26 (27), 5474–5491. doi:10.1016/j.biomaterials.2005.02.002

Langer, R. S., and Vacanti, J. P. (1999). Tissue engineering: the challenges ahead. *Sci. Am.* 280 (4), 86–89. doi:10.1038/scientificamerican0499-86

Lewandrowski, K. U., Gresser, J. D., Bondre, S. P., Silva, A. E., Wise, D. L., and Trantolo, D. J. (2000). Developing porosity of poly(propylene glycol-co-fumaric acid) bone graft substitutes and the effect on osteointegration: A preliminary histology study in rats. *J. Biomaterials Science-Polymer Ed.* 11 (8), 879–889. doi:10.1163/156856200744075

Li, Y., Chen, S. K., Li, L., Qin, L., Wang, X. L., and Lai, Y. X. (2015). Bone defect animal models for testing efficacy of bone substitute biomaterials. *J. Orthop. Transl.* 3 (3), 95–104. doi:10.1016/j.jot.2015.05.002

Lin, X., Patil, S., Gao, Y. G., and Qian, A. R. (2020). The bone extracellular matrix in bone formation and regeneration. *Front. Pharmacol.* 11, 757. doi:10.3389/fphar.2020.00757

Lu, X., Giovanis, D. G., Yvonnet, J., Papadopoulos, V., Detrez, F., and Bai, J. (2019). A data-driven computational homogenization method based on neural networks for the nonlinear anisotropic electrical response of graphene/polymer nanocomposites. *Comput. Mech.* 64 (2), 307–321. doi:10.1007/s00466-018-1643-0

Lu, Y., Huo, Y., Zou, J., Li, Y., Yang, Z., Zhu, H., et al. (2022). Comparison of the design maps of TPMS based bone scaffolds using a computational modeling framework simultaneously considering various conditions. *Proc. Inst. Mech. Eng. H.* 236 (8), 1157–1168. doi:10.1177/09544119221102704

Ma, W., Cheng, F., and Liu, Y. (2018). Deep-learning-enabled on-demand design of chiral metamaterials. *ACS Nano* 12 (6), 6326–6334. doi:10.1021/acsnano.8b03569

Mullen, L., Stamp, R. C., Fox, P., Jones, E., Ngo, C., and Sutcliffe, C. J. (2010). Selective laser melting: A unit cell approach for the manufacture of porous, titanium, bone in-growth constructs, suitable for orthopedic applications. II. Randomized structures. *J. Biomed. Mater. Res. Part B Appl. Biomaterials* 92B (1), 178–188. doi:10.1002/jbm.b.31504

Peng, X., Huang, Q., Zhang, G., Li, J., Zhang, X., Lu, Y., et al. (2022). Compensating the anisotropic mechanical properties of electron beam melting-based Gyroid scaffolds using structural design. *Int. J. Mech. Sci.* 226, 107442. doi:10.1016/j.ijmecsci.2022.107442

Peurifoy, J., Shen, Y., Jing, L., Yang, Y., Cano-Renteria, F., DeLacy, B. G., et al. (2018). Nanophotonic particle simulation and inverse design using artificial neural networks. *Sci. Adv.* 4(6), eaar4206. doi:10.1126/sciadv.aar4206

Rajagopalan, S., and Robb, R. A. (2006). Schwarz meets schwann: design and fabrication of biomorphic and durataxic tissue engineering scaffolds. *Med. Image Anal.* 10 (5), 693–712. doi:10.1016/j.media.2006.06.001

Story, B. J., Wagner, W. R., Gaisser, D. M., Cook, S. D., and Rust-Dawicki, A. M. (1998). *In vivo* performance of a modified CSTi dental implant coating. *Int. J. Oral Maxillofac. Implants* 13 (6), 749–757.

Tang, D., Tare, R. S., Yang, L. Y., Williams, D. F., Ou, K. L., and Oreffo, R. O. C. (2016). Biofabrication of bone tissue: approaches, challenges and translation for bone regeneration. *Biomaterials* 83, 363–382. doi:10.1016/j.biomaterials.2016.01.024

Wang, D., Yang, Y. Q., Liu, R. C., Xiao, D. M., and Sun, J. F. (2013). Study on the designing rules and processability of porous structure based on selective laser melting (SLM). *J. Mater. Process. Technol.* 213 (10), 1734–1742. doi:10.1016/j.jmatprotec.2013.05.001

Wang, X., Xu, S., Zhou, S., Xu, W., Leary, M., Choong, P., et al. (2016). Topological design and additive manufacturing of porous metals for bone scaffolds and orthopaedic implants: A review. *Biomaterials* 83, 127–141. doi:10.1016/j.biomaterials.2016.01.012

Wang, H., Xiao, S.-H., and Zhang, C. (2021). Novel planar auxetic metamaterial perforated with orthogonally aligned oval-shaped holes and machine learning solutions. *Adv. Eng. Mater.* 23 (7), 2100102. doi:10.1002/adem.202100102

Wieding, J., Wolf, A., and Bader, R. (2014). Numerical optimization of open-porous bone scaffold structures to match the elastic properties of human cortical bone. *J. Mech. Behav. Biomed. Mater* 37, 56–68. doi:10.1016/j.jmbbm.2014.05.002

Wu, D., Isaksson, P., Ferguson, S. J., and Persson, C. (2018). Young's modulus of trabecular bone at the tissue level: A review. *Acta Biomater.* 78, 1–12. doi:10.1016/j.actbio.2018.08.001

Xiao, P., Haque, E., Zhang, T., Dong, X. N., Huang, Y., and Wang, X. (2021). Can DXA image-based deep learning model predict the anisotropic elastic behavior of trabecular bone? *J. Mech. Behav. Biomed. Mater* 124, 104834. doi:10.1016/j.jmbbm.2021.104834

Yan, C. Z., Hao, L., Hussein, A., and Young, P. (2015). Ti-6Al-4V triply periodic minimal surface structures for bone implants fabricated via selective laser melting. *J. Mech. Behav. Biomed. Mater.* 51, 61–73. doi:10.1016/j.jmbbm.2015.06.024

Yan, W. T., Lin, S., Kafka, O. L., Lian, Y. P., Yu, C., Liu, Z. L., et al. (2018). Data-driven multi-scale multi-physics models to derive process-structure-property relationships for additive manufacturing. *Comput. Mech.* 61 (5), 521–541. doi:10.1007/s00466-018-1539-z

Yánez, A., Cuadrado, A., Martel, O., Afonso, H., and Monopoli, D. (2018). Gyroid porous titanium structures: A versatile solution to be used as scaffolds in bone defect reconstruction. *Mater. Des.* 140, 21–29. doi:10.1016/j.matdes.2017.11.050

Zheng, B., Yang, J., Liang, B., and Cheng, J.-c. (2020). Inverse design of acoustic metamaterials based on machine learning using a Gauss–Bayesian model. *J. Appl. Phys.* 128 (13). doi:10.1063/5.0012392

Zhu, G. Y., Zhang, T. X., Chen, M., Yao, K., Huang, X. Q., Zhang, B., et al. (2021). Bone physiological microenvironment and healing mechanism: basis for future bone-tissue engineering scaffolds. *Bioact. Mater.* 6 (11), 4110–4140. doi:10.1016/j.bioactmat.2021.03.043

frontiers | Frontiers in Bioengineering and Biotechnology

TYPE Original Research
PUBLISHED 07 September 2023
DOI 10.3389/fbioe.2023.1229210

OPEN ACCESS

EDITED BY
Junyan Li,
Southwest Jiaotong University, China

REVIEWED BY
Zikai Hua,
Orthotek Laboratory, China
Diane Gregory,
Wilfrid Laurier University, Canada

*CORRESPONDENCE
Jincheng Wang,
jinchengwangjlu@163.com
Minfei Wu,
wumf@jlu.edu.cn

RECEIVED 26 May 2023
ACCEPTED 14 August 2023
PUBLISHED 07 September 2023

CITATION
Wang Y, Liu Y, Zhang A, Han Q, Jiao J, Chen H, Gong X, Luo W, Yue J, Zhao X, Wang J and Wu M (2023), Biomechanical evaluation of a novel individualized zero-profile cage for anterior cervical discectomy and fusion: a finite element analysis.
Front. Bioeng. Biotechnol. 11:1229210.
doi: 10.3389/fbioe.2023.1229210

Biomechanical evaluation of a novel individualized zero-profile cage for anterior cervical discectomy and fusion: a finite element analysis

Yang Wang[1], Yang Liu[1], Aobo Zhang[1], Qing Han[1], Jianhang Jiao[1], Hao Chen[1], Xuqiang Gong[1], Wangwang Luo[1], Jing Yue[2], Xue Zhao[3], Jincheng Wang[1]* and Minfei Wu[1]*

[1]Department of Orthopedics, The Second Hospital of Jilin University, Changchun, China, [2]Department of Anesthesiology, The Second Hospital of Jilin University, Changchun, China, [3]Department of Endocrinology and Metabolism, First Hospital of Jilin University, Changchun, China

Introduction: Anterior cervical discectomy and fusion (ACDF) is a standard procedure for treating symptomatic cervical degenerative disease. The cage and plate constructs (CPCs) are widely employed in ACDF to maintain spinal stability and to provide immediate support. However, several instrument-related complications such as dysphagia, cage subsidence, and adjacent segment degeneration have been reported in the previous literature. This study aimed to design a novel individualized zero-profile (NIZP) cage and evaluate its potential to enhance the biomechanical performance between the instrument and the cervical spine.

Methods: The intact finite element models of C3-C7 were constructed and validated. A NIZP cage was designed based on the anatomical parameters of the subject's C5/6. The ACDF procedure was simulated and the CPCs and NIZP cage were implanted separately. The range of motion (ROM), intradiscal pressure (IDP), and peak von Mises stresses of annulus fibrosus were compared between the two surgical models after ACDF under four motion conditions. Additionally, the biomechanical performance of the CPCs and NIZP cage were evaluated.

Results: Compared with the intact model, the ROM of the surgical segment was significantly decreased for both surgical models under four motion conditions. Additionally, there was an increase in IDP and peak von Mises stress of annulus fibrosus in the adjacent segment. The NIZP cage had a more subtle impact on postoperative IDP and peak von Mises stress of annulus fibrosus in adjacent segments compared to CPCs. Meanwhile, the peak von Mises stresses of the NIZP cage were reduced by 90.0–120.0 MPa, and the average von Mises stresses were reduced by 12.61–17.56 MPa under different motion conditions. Regarding the fixation screws, the peak von Mises stresses in the screws of the NIZP cage increased by 10.0–40.0 MPa and the average von Mises stresses increased by 2.37–10.10 MPa.

Conclusion: The NIZP cage could effectively reconstruct spinal stability in ACDF procedure by finite element study. Compared with the CPCs, the NIZP cage had better biomechanical performance, with a lower stress distribution on the cage and a more moderate effect on the adjacent segmental discs. Therefore, the NIZP

cage could prevent postoperative dysphagia as well as decrease the risk of subsidence and adjacent disc degeneration following ACDF. In addition, this study could serve as a valuable reference for the development of personalized instruments.

KEYWORDS

cervical spine, finite element analysis, anterior cervical discectomy and fusion, Cage, biomechanics

Introduction

Cervical degenerative disease is a chronic, structural deterioration of the cervical spine associated with aging and physiological deterioration (Teraguchi et al., 2014; Theodore, 2020; Lee et al., 2021). MRI screenings have shown that between 47.4% and 86.3% of individuals over the age of 50 have cervical disc degeneration, with the C5/6 segment being the most commonly affected (Teraguchi et al., 2014). The symptoms of cervical degenerative disease typically involve cervical axial pain, numbness and weakness in the limbs, and even neurological deficits, resulting in a significantly decreased quality of life (Theodore, 2020). Conservative treatments are generally effective for patients with mild symptoms or a short duration of the disease; However, surgical intervention is a preferable alternative for patients with cervical degenerative disease suffering from severe neurological symptoms and ineffective conservative management (Scholz et al., 2020; Heijdra Suasnabar et al., 2023).

Anterior cervical discectomy and fusion (ACDF) has been a standard procedure for the treatment of symptomatic cervical degenerative disease (Fraser and Hartl, 2007; Zou et al., 2017; Sun et al., 2018). Cage was first proposed by Bagby et al. and was made of stainless steel with a hollow structure (Bagby, 1988). Since then, the cage has been optimized in terms of materials and processes, which has gradually become the preferred internal fixation device for spinal fusion surgery (Zdeblick and Phillips, 2003; Shen et al., 2022). At present, the most frequently performed internal fixation devices in clinical practice are cage and plate constructs (CPCs). The devices have the capability to directly decompress the nerves, restore the height of intervertebral space, and maintain the mechanical stability of the cervical spine. Nevertheless, previous literature has reported several instrument-related complications, such as dysphagia, cage subsidence, and adjacent segment degeneration (Fountas et al., 2007; Moussa et al., 2018). For conventional CPCs, the contact area between the cage and endplates is limited due to the irregular surface of the upper and lower endplates. This limited contact area, prone to relative stress concentration and uneven distribution, potentially resulting in cage subsidence and instrument fracture (Zhang et al., 2022; Sun et al., 2023).

In recent years, with the refinement of individualized medical models, there has been an increase in the design of individualized spinal instruments (Spetzger et al., 2016). Zhang et al. (2022) constructed a novel individualized titanium mesh that improved the compatibility of the implant with the cervical spine as well as decreased implant-related complications. It has been reported that the titanium plates are an important factor contributing to postoperative dysphagia and heterotopic ossification (Sun et al., 2018; Scholz et al., 2020; Guo et al., 2021). To address this, zero-profile cage has been introduced to replace titanium plate fixation with screw-only fixation, which could prevent complications associated with titanium plates (Sun et al., 2018). However, previous reports have demonstrated a higher risk of subsidence for implantation of zero-profile cage compared to conventional CPCs (Lee et al., 2015; Chen et al., 2016). Therefore, it was necessary to design a novel individualized zero-profile (NIZP) cage to prevent instrument-related complications for ACDF.

Finite element (FE) analysis is a crucial *in vitro* experiment that allows for realistic simulation of spinal surgery and evaluation of the biomechanical performance of the spine. Several studies have investigated the biomechanical effects of internal fixation devices on ACDF using FE analysis (Moussa et al., 2018; Hua et al., 2020; Zhou et al., 2021). Consequently, this study aimed to design a NIZP cage for ACDF and evaluate the biomechanical differences between CPCs and NIZP cage. Additionally, it could provide biomechanical evidence for further optimization of cervical cage.

Materials and methods

Finite element model of the cervical spine

A three-dimensional FE model of C3-C7 was first reconstructed based on computed tomography scans with 0.8 mm intervals (Dual Source CT; Siemens, Munich, Germany) of a 32-year-old healthy male volunteer (height: 175 cm; weight: 63 kg). This study was performed in strict accordance with the Declaration of Helsinki (2003) and approved by the Ethics Committee of the Second Hospital of Jilin University (Ethical batch number: SB2020189). All details of the experiment were explained to the volunteer and his informed consent was obtained. The computed tomography data were imported into Mimics software v21.0 (Materialise, Inc., Leuven, Belgium) in DICOM format to reconstruct the geometry of the cervical spine model. The initial C3-C7 model was then smoothed and polished using Magics software v21.0 (Materialise, Inc., Leuven, Belgium). Then, solid models of intervertebral discs, facet joints, and endplates were constructed in 3-Matic software v13.0 (Materialise, Inc., Leuven, Belgium). Afterwards, these components of FE model were meshed in Hypermesh v16.0 (Altair Engineering, Troy, Michigan, United States). The vertebral body, intervertebral disc, facet joints, and endplates were constructed using 3D

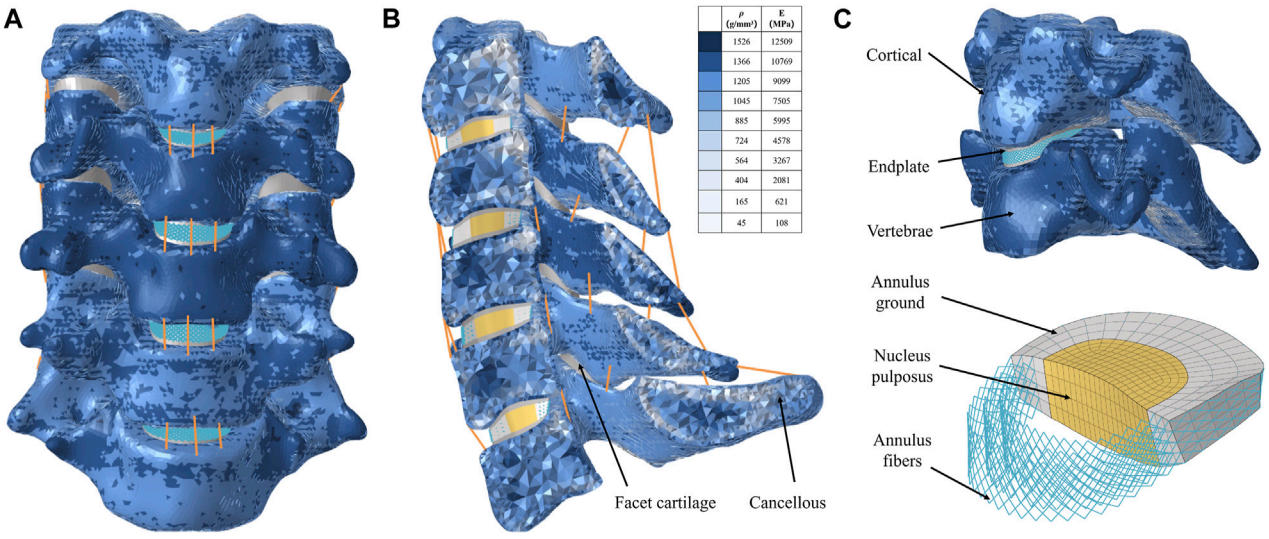

FIGURE 1
Finite element model for intact C3-7 cervical spine. **(A)** Intact model, **(B)** Left-view section of the finite element model, **(C)** Cortical bone, endplate, annulus ground, nucleus pulposus, and annulus fiber.

TABLE 1 Material properties of the finite element model.

Component	Element type	Young modulus (MPa)	Poisson's ratio	Crosssection (mm^2)	References
Vertebrae	C3D4	$\rho = 47 + 1.112*HU$	0.3	-	Rho et al., 1995; Sun et al., 2023; Wo et al., 2021
		$E = 0.63\rho^{1.35}$			
Intervertebral disc					Zhang et al., 2022; Shen et al., 2022
Nucleus pulposus	C3D8	1.0	0.49	-	
Annulus fibers	T3D2	110.0	0.3	-	
Annulus fibrosus substance	C3D8	4.2	0.49	-	
Endplate	C3D8	500.0	0.4	-	Wo et al. (2021)
Facet joint cartilage	C3D8	10.4	0.4	-	Wo et al. (2021)
Ligament					Shen et al., 2022; Zhang et al., 2022
Anterior longitudinal ligament	T3D2	10.0	0.3	6.0	
Posterior longitudinal ligament	T3D2	10.0	0.3	5.0	
Interspinous ligament	T3D2	1.5	0.3	10.0	
Supraspinous ligament	T3D2	1.5	0.3	5.0	
Capsular ligament	T3D2	10.0	0.3	46.0	
ligamentum flavum	T3D2	1.5	0.3	5.0	
Implants (Ti6Al4V)	-				Zhang et al. (2022)
NIZP cage, screws	C3D4	110, 000	0.3	-	
CPCs	C3D4	110, 000	0.3	-	

NIZP cage, a novel individualized zero-profile (NIZP) cage; CPCs, cage and plate constructs.

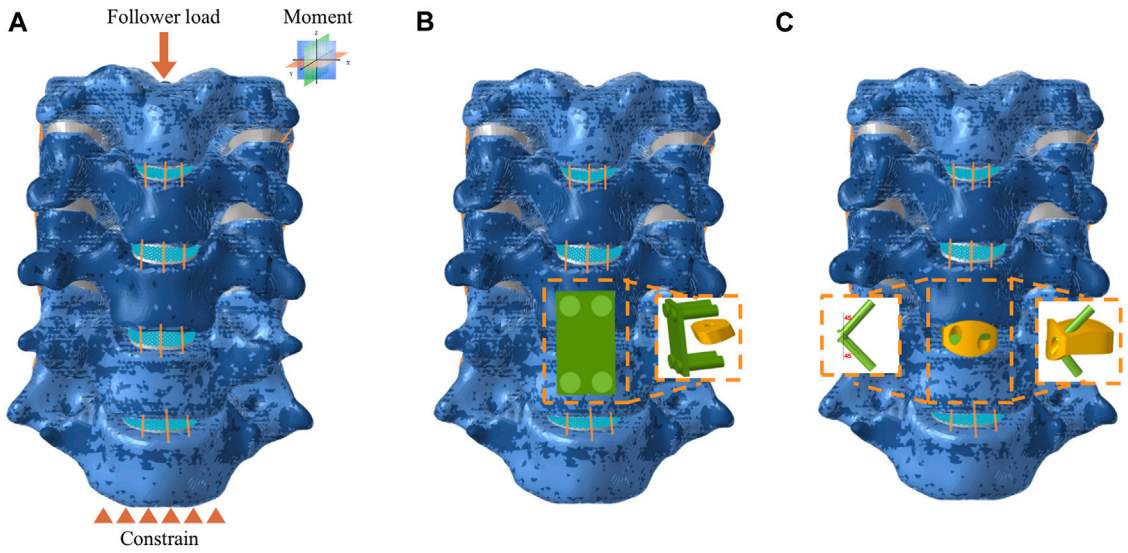

FIGURE 2
Finite element model for anterior cervical discectomy and fusion. **(A)** Intact model subject to force and constrain, **(B)** CPCs model, **(C)** NIZP cage model.

TABLE 2 Mesh convergence test of the mesh density of the FE model.

Case	Element size (mm)	Number of elements	Percentage change in peak von mises stress
Reference case	0.5	211,030	-
Case A	0.8	100,044	<5%
Case B	1.2	50,600	>5%
Case C	1.5	34,754	>5%

solid elements with isotropic properties (Hua et al., 2020; Shen et al., 2022; Zhang et al., 2022).

The element type of the vertebral body was divided into a four-node tetrahedral mesh (C3D4), and the intervertebral disc, facet joints, and endplates were divided into an eight-node hexahedral mesh (C3D8) (Wo et al., 2021). According to the empirical formulation of Rho et al., the material properties of the vertebrae were attached to the FE model based on computed tomography gray values in Mimics software v21.0 (Rho et al., 1995; Sun et al., 2023). The intervertebral disc was further divided into two parts with a volume ratio of 7:3: nucleus pulposus and annulus fibrosus (Zhang et al., 2022). The nucleus pulposus was modeled as having isotropic, incompressible, fluid-like properties (Kallemeyn et al., 2010). The annulus fibrosus was simulated by annulus fibers wrapped around an annulus fibrosus substance. And the annulus fiber was a mesh structure composed of truss elements that experienced tension only, with an inclination angle between 15° and 45° to the transverse plane (Mo et al., 2017; Zhang et al., 2022). The cervical ligaments, including anterior longitudinal ligament, posterior longitudinal ligament, interspinous ligament, supraspinous ligament, capsular ligament, and ligamentum flavum, were modeled using tension-only truss elements and connected to the adjacent vertebrae (Figure 1) (Shen et al., 2022; Zhang et al., 2022). All components were imported into Abaqus software v6.14 (SIMULIA Inc.) in inp format. The facet joints covered by articular cartilage layer with surface-to-surface contact and a frictional coefficient set at 0.1, and other contact surfaces were defined as Tie contact (Wo et al., 2021; Shen et al., 2022). All material properties and element types of the components of cervical spine were shown in Table 1 (Rho et al., 1995; Wo et al., 2021; Shen et al., 2022; Zhang et al., 2022; Sun et al., 2023).

Design of a novel individualized porous titanium alloy zero-profile cage

The NIZP cage for ACDF was designed in Magics software v21.0 (Materialise, Inc., Leuven, Belgium). Initially, the morphology of the intervertebral space was depicted by extracting the lower surface of the C5 vertebra and the upper surface of the C6 vertebra. Subsequently, a novel cage was designed based on the morphological characteristics of the intervertebral space, aiming to increase the contact area between the implant and the cervical spine. To prevent the cage from entering the spinal canal during fixation screw insertion, an arc-shaped restrictor plate was constructed in front of the cage. The height of the restrictor plate was determined by measuring the intervertebral space height of C5 and C6. Finally, in order to maximize the length of the screw track within the vertebral body and enhance spinal stability, two screws were implanted in the C5 and C6 vertebrae at a 45° angle in the sagittal plane, respectively. The fixation screws had a diameter of 4 mm and a length of

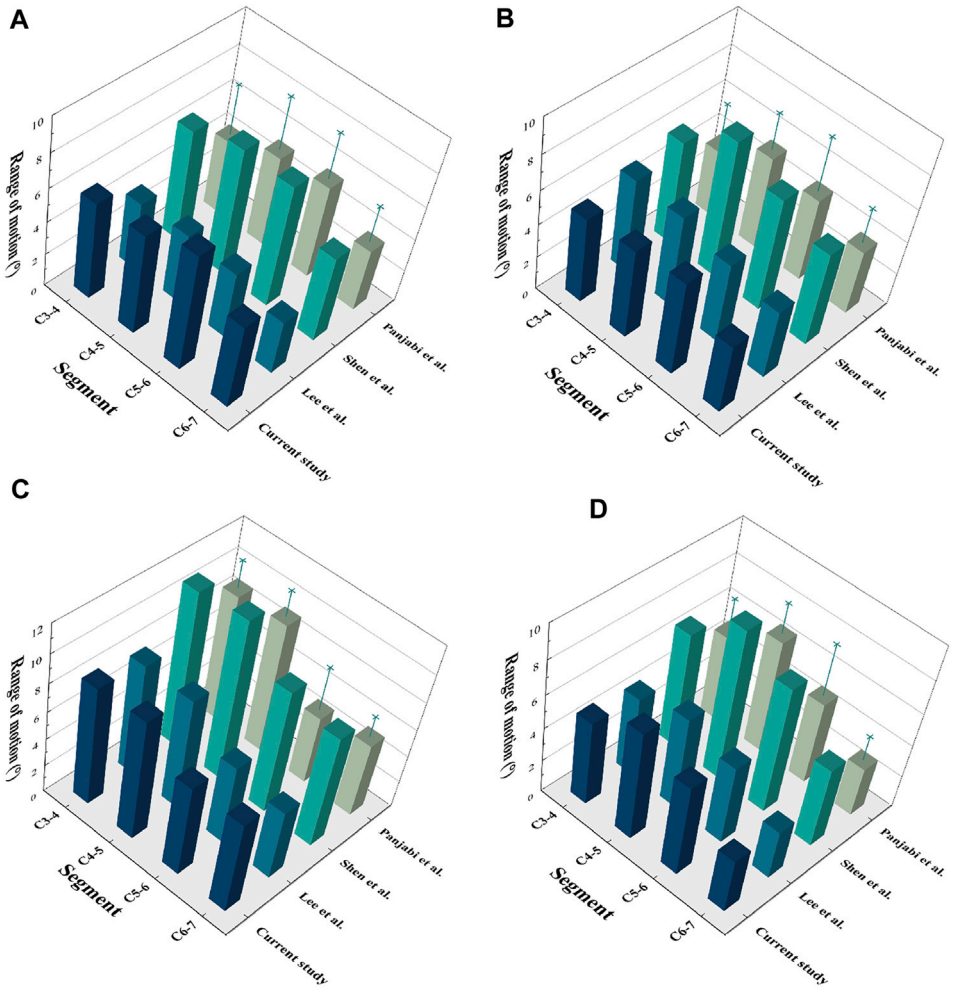

FIGURE 3
Validation of the C3-7 intact model. **(A)** Flexion, **(B)** Extension, **(C)** Lateral bending, **(D)** Axial rotation.

16 mm. Furthermore, the NIZP cage was manufactured from titanium alloy (Ti6Al4V) to enhance the osseointegration performance of the implant (Epasto et al., 2019).

FE model of ACDF procedure

The ACDF procedure was performed on the C5-C6 segment in the research. At this segment, the anterior longitudinal ligament and intervertebral disc were completely resected. Then two surgical implants, including CPCs and NIZP cage, were simulated and implanted in the C5-C6 intervertebral spaces, respectively (Figures 2B,C). The CPCs are composed of a conventional cage, a titanium plate, and four screws. The titanium plate was fixed anteriorly to the intervertebral space by four screws. As for the NIZP cage, it consists of only a individualized cage and two screws. The cage was implanted into the intervertebral space and secured by two screws. For all surgical models, the contact surfaces between the cage, screws, and the vertebra were defined as Tie contact to simulate complete bony fusion (Zhang et al., 2022). The material properties of these implants are listed in Table 1 (Zhang et al., 2022).

Mesh convergence

In this research, a mesh convergence test was conducted to validate the influence of mesh refinement on the predictions of the FE model (Shen et al., 2022). The element size of the C3-C7 was set at four different sizes for comparative analysis (Table 2). The element size of the FE model was set at 0.5, 0.8, 1.2, and 1.5 mm in the four cases, respectively. By comparing the peak von Mises stress values predicted by the reference case, the corresponding values of cases A, B, and C were considered accurate within 5% of the reference case. Notably, Case A demonstrated a higher accurate compared to the other cases, maintaining a prediction accuracy of 98% over the reference case model in less computation time.

Boundary and loading conditions

As shown in Figure 2A, the intact C3-C7 segment was modeled in the FE analysis. The lower surface of the C7 vertebrae was constrained in all directions, while a follower load of 73.6 N was applied to the upper surface of the C3 vertebra to simulate the weight

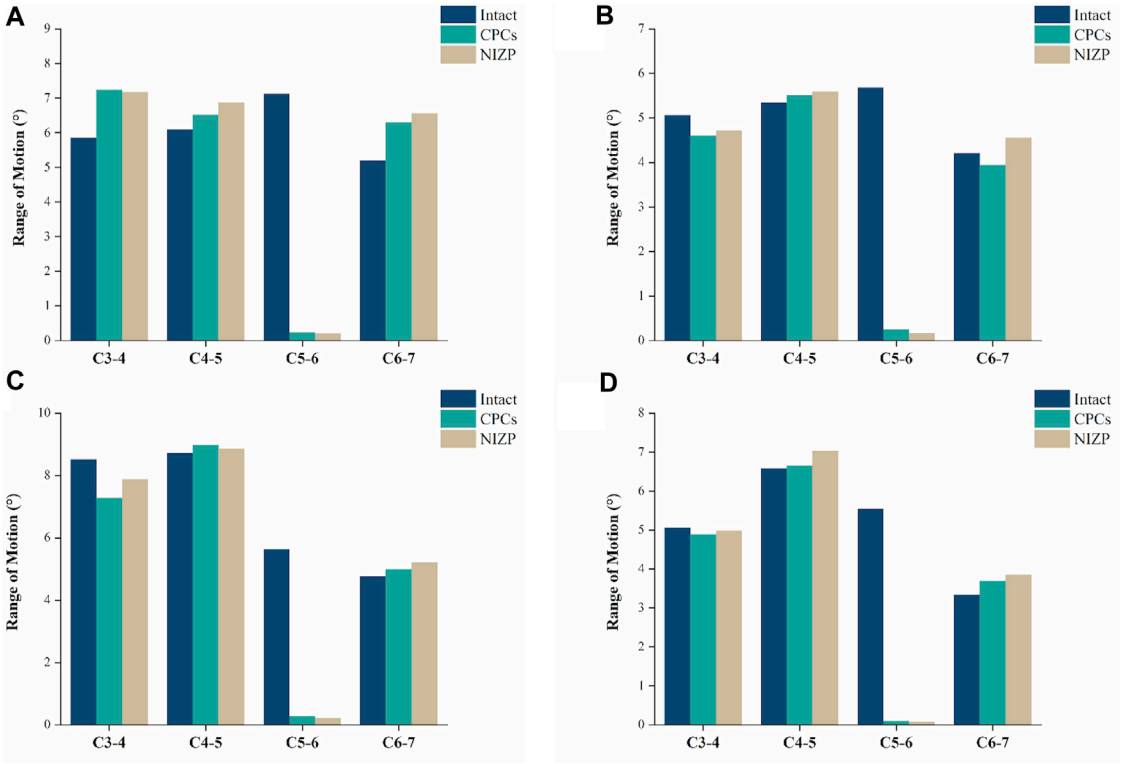

FIGURE 4
Comparison of the range of motion for the three models under four motion conditions. **(A)** Flexion, **(B)** Extension, **(C)** Lateral bending, **(D)** Axial rotation.

of the head and muscle force. Moreover, a 1.0 N m moment was performed on the upper surface of the C3 vertebra to simulate flexion, extension, axial rotation, or lateral bending (Sun et al., 2023). The range of motion (ROM) for each segment was calculated based on the relative motions of each vertebra in each motion condition (Panjabi et al., 2001). The ROM of each segment in the intact FE model was compared to previously published data to validate the model's effectiveness. The differences in biomechanical characteristics of the two surgical implants were compared in each motion condition. Furthermore, the ROM of each segment, intradiscal pressure (IDP) in adjacent segments and peak von Mises stress of the annulus fibrosus in adjacent segments were tested under all motion conditions.

Results

Validation of the cervical FE model

To validate the cervical FE model, a follower load of 73.6 N and a moment of 1.0 N-m were applied to the upper surface of the C3 vertebrae, while a constraint was applied to the lower surface of C7. The intervertebral ROMs were compared with the results of published *in vitro* experiments as well as FE experiments (Panjabi et al., 2001; Lee et al., 2016; Shen et al., 2022) (Figure 3). The ROMs of the intact model at C3/4, C4/5, C5/6, and C6/7 were 5.85°, 6.09°, 7.12°, and 5.20°, respectively, in flexion; 5.06°, 5.35°, 5.68°, and 4.21°, respectively, in extension; 8.52°, 8.72°, 5.62°, and 4.76°, respectively, in lateral bending; and 5.06°, 6.58°, 5.54°, and 3.34°, respectively, in axial rotation. The prediction results of the cervical FE model were consistent with the results reported in the previous literature.

ROMs after surgery

As shown in Figure 4, the ROMs at C5/6 for the intact, CPCs and NIZP cage models were 7.12°, 0.24°, and 0.20° in flexion; 5.68°, 0.25°, and 0.16° in extension; 5.62°, 0.28°, and 0.22° in lateral bending; and 5.54°, 0.10°, and 0.08° in axial rotation, respectively. Compared to the intact model, the ROMs of the two surgical models were significantly decreased under four motion conditions. In addition, postoperative ROMs in adjacent segments increased in both the CPCs and NIZP groups, especially in flexion.

Intradiscal pressure in adjacent segments

IDP at C4/5 and C6/7 are presented in Figures 5A,B. At C4/5, the IDP of the intact, CPCs and NIZP cage models were 0.28 MPa, 0.31 MPa, and 0.29 MPa in flexion; 0.15 MPa, 0.16 MPa, and 0.16 MPa in extension; 0.19 MPa, 0.21 MPa, and 0.20 MPa in lateral bending; and 0.14 MPa, 0.15 MPa, and 0.14 MPa in axial rotation, respectively. As for C6/7, the IDP of three models were

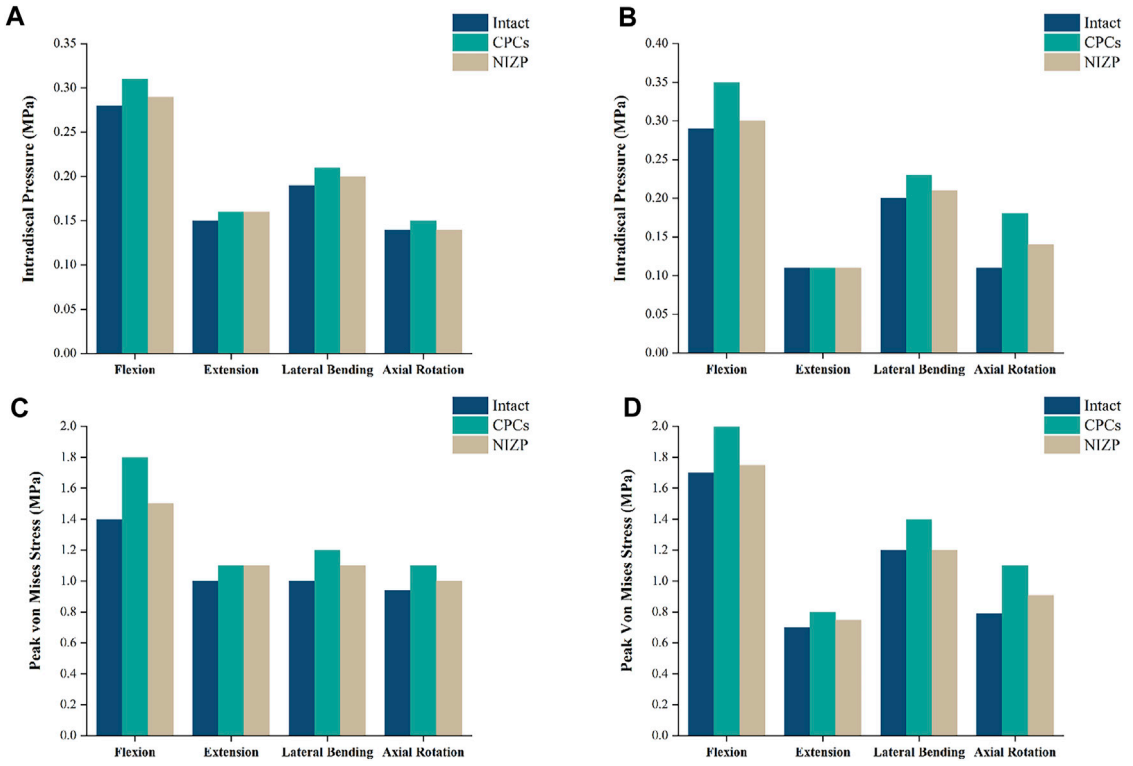

FIGURE 5
Comparison of intradiscal pressure and peak von Mises stresses in adjacent segments for the three models under four motion conditions. **(A)** IDP in C4/5, **(B)** IDP in C6/7, **(C)** Peak von Mises stresses in C4/5, **(D)** Peak von Mises stresses in C6/7.

0.29 MPa, 0.35 MPa, and 0.30 MPa in flexion; 0.11 MPa, 0.11 MPa, and 0.11 MPa in extension; 0.20 MPa, 0.23 MPa, and 0.21 MPa in lateral bending; and 0.11 MPa, 0.18 MPa, and 0.14 MPa in axial rotation, respectively. Compared with the intact model, the IDP in adjacent segments increased in both surgical models under four motion conditions, with a more pronounced variation in the CPCs mode (Figure 6).

Peak von mises stress of annulus fibrosus in adjacent segments

Peak von Mises stress on the annulus fibrosus at C4/5 and C6/7 are presented in Figures 5C,D. For C4/5, the peak von Mises stresses of annulus fibrosus of the intact, CPCs and NIZP models were 1.40 MPa, 1.80 MPa, and 1.50 MPa in flexion; 1.00 MPa, 1.10 MPa, and 1.10 MPa in extension; 1.00 MPa, 1.20 MPa, and 1.10 MPa in lateral bending; and 0.94 MPa, 1.10 MPa, and 1.05 MPa in axial rotation, respectively. At C6/7, the peak stresses of annulus fibrosus of three models were 1.70 MPa, 2.00 MPa, and 1.75 MPa in flexion; 0.70 MPa, 0.80 MPa, and 0.75 MPa in extension; 1.20 MPa, 1.40 MPa, and 1.20 MPa in lateral bending; and 0.79 MPa, 1.10 MPa, and 0.91 MPa in axial rotation, respectively. Peak von Mises stresses on the annulus fibrosus of adjacent segments were increased owing to internal fixation devices, especially the CPCs. The stress cloud maps of the annulus fibrosus are shown in Figure 7.

Von mises stress of internal fixation systems

As shown in Figure 8, the peak and average von Mises stresses of two internal fixation systems - CPCs and NIZP - are compared under different motion conditions. Among them, the peak von Mises stresses in the cage for the CPCs and NIZP models were 540.0 MPa and 440.0 MPa, 430.0 MPa and 310.0 MPa, 450.0 MPa and 330.0 MPa, and 410.0 MPa and 320.0 MPa in flexion, and extension, lateral bending, and axial rotation, respectively. In addition, the average von Mises stresses in the cage for two surgical models were 33.17 MPa and 19.61 MPa, 35.10 MPa and 22.49 MPa, 34.19 MPa and 16.63 MPa, and 28.15 MPa and 15.48 MPa under four motion conditions, respectively. As for plate or screw, the peak von Mises stresses for two surgical models were 140.0 and 180.0 MPa, 200.0 and 220.0 MPa, 150.0 and 160.0 MPa, and 120.0 and 150.0 MPa under four motion conditions, respectively. And the average von Mises stresses in cage for two surgical models were 17.46 MPa and 24.24 MPa, 21.20 MPa and 23.57 MPa, 16.28 MPa and 26.38 MPa, and 14.07 MPa and 22.97 MPa under four motion conditions, respectively. The stress distributions of the internal fixation systems are shown in Figure 9.

Discussion

Anterior cervical discectomy and fusion (ACDF) is widely acknowledged as the most common and effective treatment for cervical degenerative diseases (Zou et al., 2017; Sun et al., 2018).

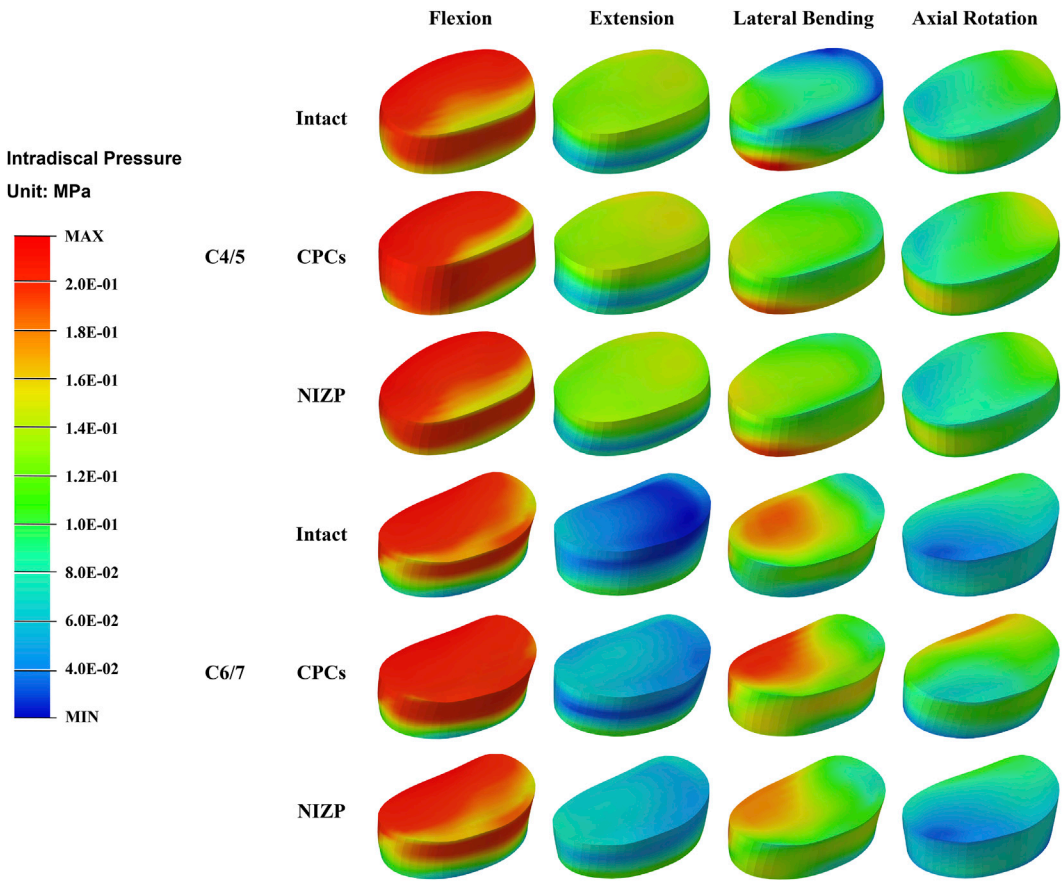

FIGURE 6
The stress distribution of disc in adjacent segments for the three models under four motion conditions.

CPCs plays an important role in ACDF. Previous studies have demonstrated that the implantation of titanium plates in the anterior approach stabilizes spinal structures and promotes fusion (Zou et al., 2017; Guo et al., 2021). However, this approach may irritate the esophagus and increase the risk of postoperative dysphagia (Xiao et al., 2017; Liu et al., 2020). To address these concerns, the NIZP cage was designed to decrease implant-related complications. In this study, a finite element model of C3-C7 segment was constructed to evaluate the biomechanical performance of the NIZP cage. In ACDF procedure, surgeons only need to expose the prevertebral soft tissue of diseased segment to implant the NIZP cage, thereby reducing excessive irritation of the esophagus and minimizing postoperative dysphagia. ROM was evaluated in this study to determine the efficacy of implants in maintaining structural stability of the cervical spine. The results revealed that both the implants effectively reduced the ROM at the surgical segment under four motion conditions, compare to the intact model. Moreover, the ROMs of the NIZP cage was slightly lower than that of the CPCs. It was relevant to a better fit with the upper and lower cervical endplates. However, there was no statistically significant difference between the two models. Zhang et al. (2016) conducted FE analysis and cadaveric studies to demonstrate that a cage that closely matched the cervical spine provided better stability during flexion and extension motion compared to the conventional cage. It is worth mentioning that the ROMs at the C4/5 and C6/7 were increased in both surgical models, especially in flexion and extension motion. To compensate for the lost ROM in the surgical segment, the cervical spine increased the ROM in the adjacent segment to maintain postoperative ROM. Previous *in vitro* mechanical experiments (Eck et al., 2002) and FE analysis (Zhou et al., 2021) similarly concluded that there was a corresponding increase in the mobility of the upper and lower segments after ACDF. In general, the stability of spinal structure was well reconstructed by both CPCs and NIZP cage after ACDF.

Stress distribution is frequently utilized in FE studies to evaluate the risk of subsidence and fixation failure, with von Mises stress serving as a crucial indicator (Wo et al., 2021). Following ACDF, cage subsidence is a prevalent complication, with reported subsidence rates ranging from 8% to 34%. This subsidence could contribute to kyphotic deformity, nerve impairment, *etc.* (Zhang et al., 2016; Sun et al., 2018; Jin et al., 2021; Zhang et al., 2022). Inadequate compatibility between the cage and the spine endplate leads to uneven stress distribution and stress concentration, ultimately posing a potential risk of cage subsidence (Shen et al., 2022; Zhang et al., 2022). A NIZP cage was constructed in this study based on the anatomical characteristics of the cervical spine, in order to enhance the compatibility between the cage and the endplate. Comparing the stress distributions of the two implants, it revealed that the NIZP cage had a reduction in peak von Mises stresses by 90.0–120.0 MPa and average von Mises stresses by 12.61–17.56 MPa

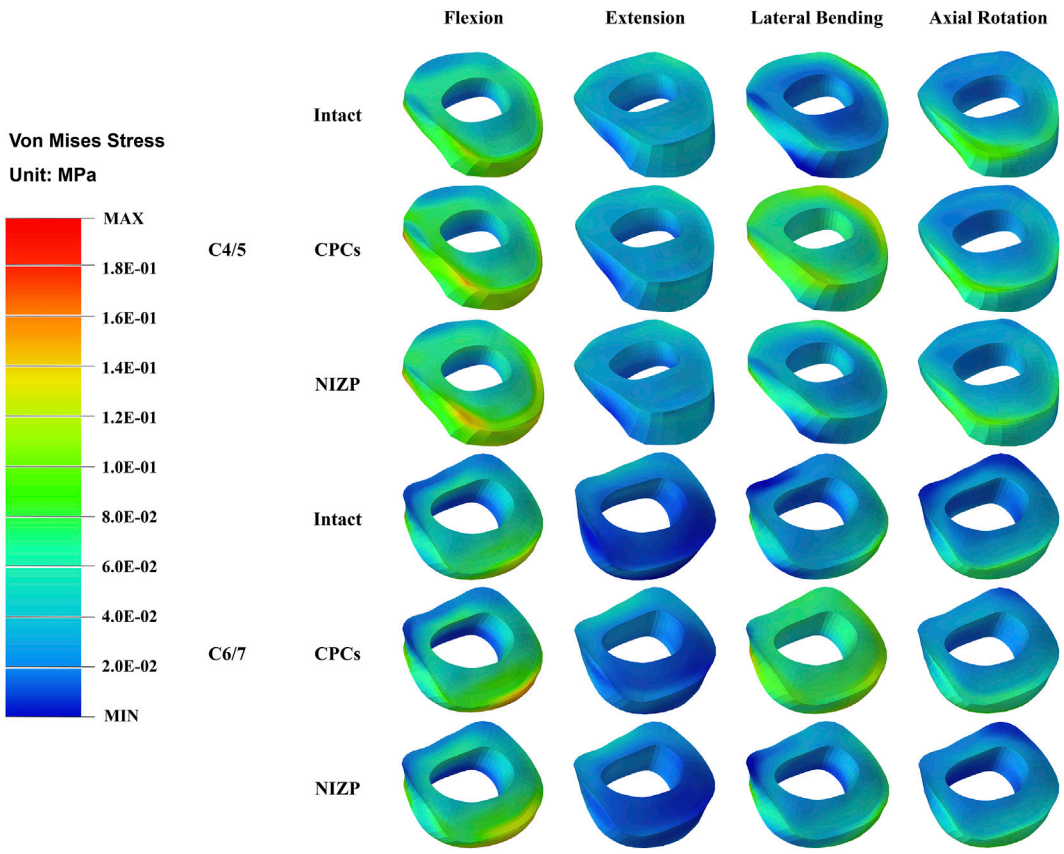

FIGURE 7
The stress distribution of annulus fibrosus in adjacent segments for the three models under four motion conditions.

compared to CPCs under the four motion conditions. As shown in the stress cloud maps, the stresses in CPCs were mainly concentrated in the edge areas, particularly in the front area of the cage. In contrast, the stresses in the NIZP cage were more evenly distributed in the inner areas and the anterior restrictor plate. This indicated that a well-matched implant could decrease the peak stress and improve stress distribution, thereby reducing the risk of cage subsidence. Several studies also support this perspective (Zhang et al., 2022; Sun et al., 2023), stating that increasing the contact area through improved conformity of the implant to the endplate can prevent excessive stress concentration and reduce the risk of implant subsidence.

Disc degeneration in adjacent segments represents an important complication after spinal surgery (Fountas et al., 2007). To assess the risk of adjacent segment degeneration, the IDP and the peak von Mises stresses of annulus fibrosus in the adjacent segments were measured respectively in this study. For both surgical groups, the postoperative IDPs of C4/5 and C6/7 were higher than those of the intact model. And the IDP of the CPCs group were slightly higher than those of the NIZP group under most motion conditions. Specifically, under flexion and axial rotation conditions, the IDP in the CPCs group increased by 7.14% in C4/5 segment, and by 17.24% and 36.36% in C6/7 segment, respectively, compared to the NIZP group. It is well known that the motion unit of the cervical spine consists of the upper and lower vertebrae and an intervertebral disc (Theodore, 2020). After ACDF, an intervertebral disc structure was sacrificed and replaced by a titanium alloy. The loss of a motion unit led to a corresponding increase in ROMs of adjacent segments, which resulted in an increase in IDP and annulus fibrosus stresses (Eck et al., 2002). Similarly, Zhang et al. (2022) concluded that the increase in ROM of the adjacent segments after surgery contributed to further disc compression or stretching, resulting in increased stresses. Overall, the NIZP cage facilitates the decrease of the risk of disc degeneration in the adjacent segment after ACDF compared to CPCs.

In addition, fixation screws are an important component of the two implants. Compared to the screw-plate device of CPCs, the NIZP cage exhibited an increase in peak von Mises stresses in the screws within a range of 10.0–40.0 MPa, and an increase in average von Mises stresses within a range of 2.37–10.10 MPa under various motion conditions. As shown in the stress cloud map, the stresses of the screw-plate device were primarily concentrated in the contact area between the screws and the titanium plate under different motion conditions. However, in the contact area between the screws and the vertebral body, the stresses were distributed more uniformly. On the contrary, the stresses in the screws of the NIZP cage were primarily concentrated in the contact area between the screws and the vertebral body, especially in the upper screws. Since the fixation pattern of NIZP cage relied on only two screws, it was inevitable that the stress increased and the stress concentrated in the screws. It is worth mentioning that the peak von Mises stress in the screw

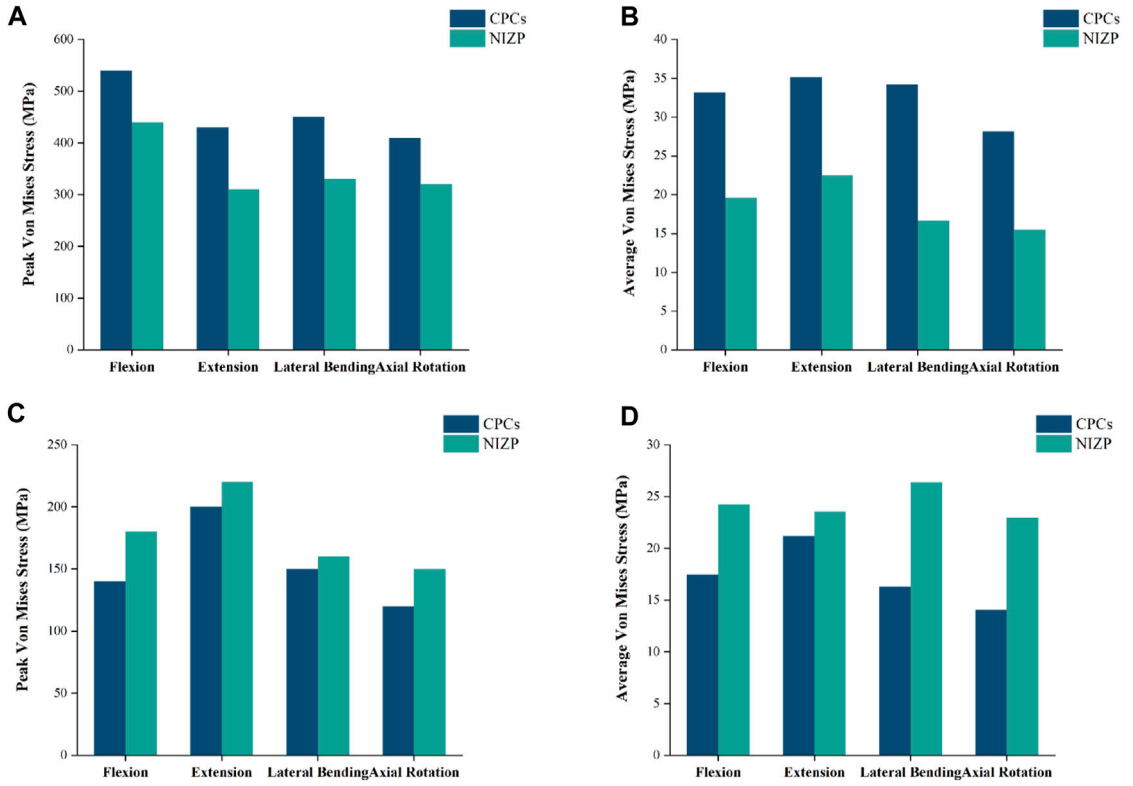

FIGURE 8
Comparison of peak or average von Mises stresses for the CPCs and NIZP cage under four motion conditions. **(A)** Peak von Mises stresses for cage of the two instrument, **(B)** Average von Mises stresses for cage of the two instrument, **(C)** Peak von Mises stresses for fixation screws of the two instrument, **(D)** Average von Mises stresses for fixation screws of the two instrument.

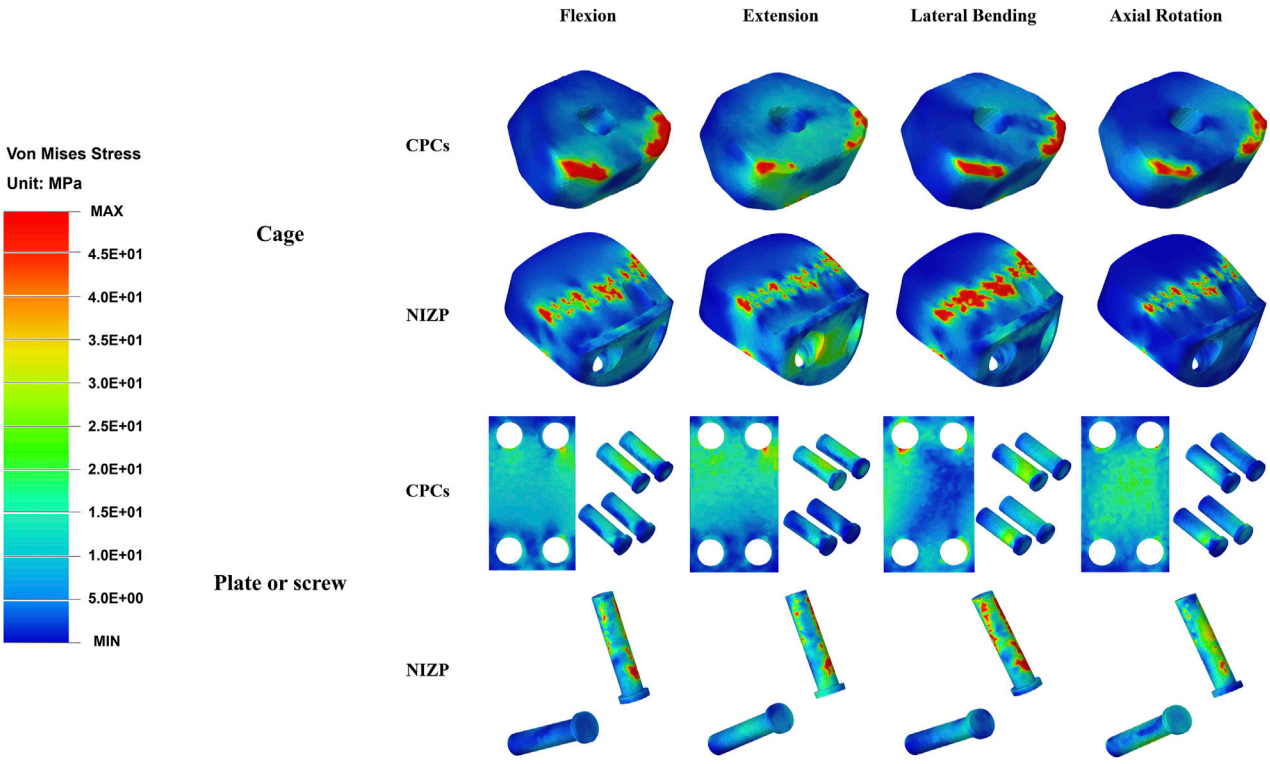

FIGURE 9
The stress distribution of the CPCs and NIZP cage under four motion conditions.

is far less than the yield strength of the titanium alloy, which is not sufficient to cause screw fracture or failure (Zhang et al., 2018).

The study has several limitations that should be acknowledged. Firstly, only FE analysis was performed to test the biomechanical performance of the NIZP cage. However, further validation is needed through animal and clinical experiments. Secondly, the finite element model was simplified within an acceptable range, including material properties, boundary conditions, and contact relations. The influence of the cervical muscles on the biomechanics was not considered, which means that the study cannot completely simulate the actual situation after ACDF. Thirdly, although the cages used in the study have porous structures, solid structures were employed for all the analyses to ensure better convergence of the calculations. And the fourth, the finite element analysis was based on data from only one patient. Additionally, *in vitro* biomechanical experiments and clinical studies will be conducted in the future to evaluate the findings of this study.

Conclusion

The NIZP cage could effectively reconstruct spinal stability after ACDF by FE analysis. The NIZP cage demonstrated superior biomechanical performance compared to CPCs, resulting in a lower stress distribution on the cage and a more moderate effect on the adjacent segmental discs. Therefore, the NIZP cage could prevent postoperative dysphagia as well as decrease the risk of subsidence and adjacent disc degeneration after ACDF. In addition, this study could serve as a valuable reference for the development of personalized instruments.

Data availability statement

The original contributions presented in the study are included in the article/Supplementary Material, further inquiries can be directed to the corresponding authors.

Ethics statement

The studies involving humans were approved by the Ethics Committee of the Second Hospital of Jilin University. The studies were conducted in accordance with the local legislation and institutional requirements. Written informed consent for participation was not required from the participants or the participants and legal guardians/next of kin in accordance with the national legislation and institutional requirements. Written informed consent was obtained from the individual(s) for the publication of any potentially identifiable images or data included in this article.

Author contributions

MW and JW conceived and designed the study. YW, YL, and AZ collected the required images and established the finite element models. YW, QH, XG, and HC performed the literature search and data collection. YW and YL performed the first analysis of the results and drafted the article. YW, AZ, JJ, and WL revised the manuscript. MW, JJ, QH, JY, XZ, and JW provided the financial support. All authors contributed to the article and approved the submitted version.

Funding

This work was supported by the National Natural Science Foundation of China (Grant Numbers: 82072456 and 82272504); the National Key R&D Program of China (Grant Number: 2018YFB1105100); the Department of Science and Technology of Jilin Province, P.R.C (Grant Numbers: 20200404202YY, 20210204104YY, YDZJ202201ZYTS135, YDZJ202201ZYTS290, 20200403086SF, 20210101321JC, 20220204119YY, YDZJ202201ZYTS131, YDZJ202201ZYTS129, 20220401084YY, 202201ZYTS505, YDZJ202301ZYTS076, 20210101439JC, and 20200201453JC); Department of Finance of Jilin Province (Grant Numbers: 2020SCZT037); Jilin Province Development and Reform Commission, P.R.C (Grant Number: 2018C010 and 2022C043-5); Interdisciplinary Integration and Cultivation Project of Jilin University (Grant number: JLUXKJC2020307); and Research Fund of the First Hospital of Jilin University (2021-zl-01).

Conflict of interest

The authors declare that the research was conducted in the absence of any commercial or financial relationships that could be construed as a potential conflict of interest.

Publisher's note

References

Bagby, G. W. (1988). Arthrodesis by the distraction-compression method using a stainless steel implant. *Orthopedics* 11 (6), 931–934. doi:10.3928/0147-7447-19880601-13

Chen, Y., Lu, G., Wang, B., Li, L., and Kuang, L. (2016). A comparison of anterior cervical discectomy and fusion (ACDF) using self-locking stand-alone polyetheretherketone (PEEK) cage with ACDF using cage and plate in the treatment of three-level cervical degenerative spondylopathy: A retrospective study with 2-year follow-up. *Eur. Spine J.* 25 (7), 2255–2262. doi:10.1007/s00586-016-4391-x

Eck, J. C., Humphreys, S. C., Lim, T. H., Jeong, S. T., Kim, J. G., Hodges, S. D., et al. (2002). Biomechanical study on the effect of cervical spine fusion on adjacent-level

intradiscal pressure and segmental motion. *Spine (Phila Pa* 27(22), 2431–2434. doi:10.1097/00007632-200211150-00003

Epasto, G., Distefano, F., Mineo, R., and Guglielmino, E. (2019). Subject-specific finite element analysis of a lumbar cage produced by electron beam melting. *Med. Biol. Eng. Comput.* 57 (12), 2771–2781. doi:10.1007/s11517-019-02078-8

Fountas, K. N., Kapsalaki, E. Z., Nikolakakos, L. G., Smisson, H. F., Johnston, K. W., Grigorian, A. A., et al. (2007). Anterior cervical discectomy and fusion associated complications. *Spine (Phila Pa* 32(21), 2310–2317. doi:10.1097/BRS.0b013e318154c57e

Fraser, J. F., and Hartl, R. (2007). Anterior approaches to fusion of the cervical spine: A meta analysis of fusion rates. *J. Neurosurg. Spine* 6 (4), 298–303. doi:10.3171/spi.2007.6.4.2

Guo, X., Zhou, J., Tian, Y., Kang, L., and Xue, Y. (2021). Biomechanical effect of different plate-to-disc distance on surgical and adjacent segment in anterior cervical discectomy and fusion - a finite element analysis. *BMC Musculoskelet. Disord.* 22 (1), 340. doi:10.1186/s12891-021-04218-4

Heijdra Suasnabar, J. M., Vleggeert-Lankamp, C. L. A., Goedmakers, C. M. W., de Vries, F., Arts, M. P., and van den Akker-van Marle, M. E. (2023). Cost effectiveness of implanting a prosthesis after anterior cervical discectomy for radiculopathy: results of the NECK randomized controlled trial. *Spine J.* 23 (6), 851–858. doi:10.1016/j.spinee.2023.02.003

Hua, W., Zhi, J., Ke, W., Wang, B., Yang, S., Li, L., et al. (2020). Adjacent segment biomechanical changes after one- or two-level anterior cervical discectomy and fusion using either a zero-profile device or cage plus plate: A finite element analysis. *Comput. Biol. Med.* 120, 103760. doi:10.1016/j.compbiomed.2020.103760

Jin, Z. Y., Teng, Y., Wang, H. Z., Yang, H. L., Lu, Y. J., and Gan, M. F. (2021). Comparative analysis of cage subsidence in anterior cervical decompression and fusion: zero profile anchored spacer (ROI-C) vs. Conventional cage and plate construct. *Front. Surg.* 8, 736680. doi:10.3389/fsurg.2021.736680

Kallemeyn, N., Gandhi, A., Kode, S., Shivanna, K., Smucker, J., and Grosland, N. (2010). Validation of a C2-C7 cervical spine finite element model using specimen-specific flexibility data. *Med. Eng. Phys.* 32 (5), 482–489. doi:10.1016/j.medengphy.2010.03.001

Lee, J. B., Park, J. H., Lee, J. J., Lee, H. J., Kim, I. S., Hur, J. W., et al. (2021). Influence of dynamic neck motion on the clinical usefulness of multi-positional MRI in cervical degenerative spondylosis. *Eur. Spine J.* 30 (6), 1542–1550. doi:10.1007/s00586-021-06760-0

Lee, J. H., Park, W. M., Kim, Y. H., and Jahng, T. A. (2016). A biomechanical analysis of an artificial disc with a shock-absorbing core property by using whole-cervical spine finite element analysis. *Spine (Phila Pa 1976)* 41 (15), E893–E901. doi:10.1097/BRS.0000000000001468

Lee, Y. S., Kim, Y. B., and Park, S. W. (2015). Does a zero-profile anchored cage offer additional stabilization as anterior cervical plate? *Spine (Phila Pa 1976)* 40 (10), E563–E570. doi:10.1097/BRS.0000000000000864

Liu, J., Wang, R., Wang, H., Wang, Y., Lv, D., Diao, P., et al. (2020). Biomechanical comparison of a new memory compression alloy plate versus traditional titanium plate for anterior cervical discectomy and fusion: A finite element analysis. *Biomed. Res. Int.* 2020, 1–10. doi:10.1155/2020/5769293

Mo, Z., Li, Q., Jia, Z., Yang, J., Wong, D. W., and Fan, Y. (2017). Erratum to: biomechanical consideration of prosthesis selection in hybrid surgery for bi-level cervical disc degenerative diseases. *Eur. Spine J.* 26 (1), 298. doi:10.1007/s00586-016-4799-3

Moussa, A., Tanzer, M., and Pasini, D. (2018). Cervical fusion cage computationally optimized with porous architected Titanium for minimized subsidence. *J. Mech. Behav. Biomed. Mater* 85, 134–151. doi:10.1016/j.jmbbm.2018.05.040

Panjabi, M. M., Crisco, J. J., Vasavada, A., Oda, T., Cholewicki, J., Nibu, K., et al. (2001). Mechanical properties of the human cervical spine as shown by three-dimensional load-displacement curves. *Spine (Phila Pa 1976)* 26 (24), 2692–2700. doi:10.1097/00007632-200112150-00012

Rho, J. Y., Hobatho, M. C., and Ashman, R. B. (1995). Relations of mechanical properties to density and CT numbers in human bone. *Med. Eng. Phys.* 17 (5), 347–355. doi:10.1016/1350-4533(95)97314-f

Scholz, M., Onal, B., Schleicher, P., Pingel, A., Hoffmann, C., and Kandziora, F. (2020). Two-level ACDF with a zero-profile stand-alone spacer compared to conventional plating: A prospective randomized single-center study. *Eur. Spine J.* 29 (11), 2814–2822. doi:10.1007/s00586-020-06454-z

Shen, Y. W., Yang, Y., Liu, H., Qiu, Y., Li, M., Ma, L. T., et al. (2022). Biomechanical evaluation of intervertebral fusion process after anterior cervical discectomy and fusion: A finite element study. *Front. Bioeng. Biotechnol.* 10, 842382. doi:10.3389/fbioe.2022.842382

Spetzger, U., Frasca, M., and Konig, S. A. (2016). Surgical planning, manufacturing and implantation of an individualized cervical fusion titanium cage using patient-specific data. *Eur. Spine J.* 25 (7), 2239–2246. doi:10.1007/s00586-016-4473-9

Sun, B., Han, Q., Sui, F., Zhang, A., Liu, Y., Xia, P., et al. (2023). Biomechanical analysis of customized cage conforming to the endplate morphology in anterior cervical discectomy fusion: A finite element analysis. *Heliyon* 9 (1), e12923. doi:10.1016/j.heliyon.2023.e12923

Sun, Z., Liu, Z., Hu, W., Yang, Y., Xiao, X., and Wang, X. (2018). Zero-profile versus cage and plate in anterior cervical discectomy and fusion with a minimum 2 Years of follow-up: A meta-analysis. *World Neurosurg.* 120, e551–e561. doi:10.1016/j.wneu.2018.08.128

Teraguchi, M., Yoshimura, N., Hashizume, H., Muraki, S., Yamada, H., Minamide, A., et al. (2014). Prevalence and distribution of intervertebral disc degeneration over the entire spine in a population-based cohort: the wakayama spine study. *Osteoarthr. Cartil.* 22 (1), 104–110. doi:10.1016/j.joca.2013.10.019

Theodore, N. (2020). Degenerative cervical spondylosis. *N. Engl. J. Med.* 383 (2), 159–168. doi:10.1056/NEJMra2003558

Wo, J., Lv, Z., Wang, J., Shen, K., Zhu, H., Liu, Y., et al. (2021). Biomechanical analysis of cervical artificial disc replacement using cervical subtotal discectomy prosthesis. *Front. Bioeng. Biotechnol.* 9, 680769. doi:10.3389/fbioe.2021.680769

Xiao, S., Liang, Z., Wei, W., and Ning, J. (2017). Zero-profile anchored cage reduces risk of postoperative dysphagia compared with cage with plate fixation after anterior cervical discectomy and fusion. *Eur. Spine J.* 26 (4), 975–984. doi:10.1007/s00586-016-4914-5

Zdeblick, T. A., and Phillips, F. M. (2003). Interbody cage devices. *Spine (Phila Pa 1976)* 28 (15 Suppl. l), S2–S7. doi:10.1097/01.BRS.0000076841.93570.78

Zhang, C., Lu, B., Wang, H., Guo, Z., Paley, V., and Volinsky, A. A. (2018). Vacuum pressureless sintering of Ti-6Al-4V alloy with full densification and forged-like mechanical properties. *J. Mater. Eng. Perform.* 27 (1), 282–292. doi:10.1007/s11665-017-3019-6

Zhang, F., Xu, H. C., Yin, B., Xia, X. L., Ma, X. S., Wang, H. L., et al. (2016). Can an endplate-conformed cervical cage provide a better biomechanical environment than a typical non-conformed cage? A finite element model and cadaver study. *Orthop. Surg.* 8 (3), 367–376. doi:10.1111/os.12261

Zhang, K. R., Yang, Y., Ma, L. T., Qiu, Y., Wang, B. Y., Ding, C., et al. (2022). Biomechanical effects of a novel anatomic titanium mesh cage for single-level anterior cervical corpectomy and fusion: A finite element analysis. *Front. Bioeng. Biotechnol.* 10, 881979. doi:10.3389/fbioe.2022.881979

Zhou, J. M., Guo, X., Kang, L., Zhao, R., Yang, X. T., Fu, Y. B., et al. (2021). Biomechanical effect of C(5)/C(6) intervertebral reconstructive height on adjacent segments in anterior cervical discectomy and fusion - a finite element analysis. *Orthop. Surg.* 13 (4), 1408–1416. doi:10.1111/os.13010

Zou, S., Gao, J., Xu, B., Lu, X., Han, Y., and Meng, H. (2017). Anterior cervical discectomy and fusion (ACDF) versus cervical disc arthroplasty (CDA) for two contiguous levels cervical disc degenerative disease: A meta-analysis of randomized controlled trials. *Eur. Spine J.* 26 (4), 985–997. doi:10.1007/s00586-016-4655-5

frontiers | Frontiers in Bioengineering and Biotechnology

TYPE Original Research
PUBLISHED 15 September 2023
DOI 10.3389/fbioe.2023.1219745

OPEN ACCESS

EDITED BY
Zhenxian Chen,
Chang'an University, China

REVIEWED BY
Jincheng Wang,
Second Affiliated Hospital of Jilin University, China
Xianjiu Lu,
Qingdao University, China

*CORRESPONDENCE
Dewei Zhao,
zhaodewei2016@163.com
Liangliang Cheng,
liangliang30766@163.com

†These authors share first authorship

RECEIVED 09 May 2023
ACCEPTED 04 September 2023
PUBLISHED 15 September 2023

CITATION
Liu Y, Wang F, Ying J, Xu M, Wei Y, Li J, Xie H, Zhao D and Cheng L (2023), Biomechanical analysis and clinical observation of 3D-printed acetabular prosthesis for the acetabular reconstruction of total hip arthroplasty in Crowe III hip dysplasia.
Front. Bioeng. Biotechnol. 11:1219745.
doi: 10.3389/fbioe.2023.1219745

Biomechanical analysis and clinical observation of 3D-printed acetabular prosthesis for the acetabular reconstruction of total hip arthroplasty in Crowe III hip dysplasia

Yuchen Liu[1†], Fuyang Wang[1†], Jiawei Ying[1], Minghao Xu[1], Yuan Wei[2], Junlei Li[1], Hui Xie[1], Dewei Zhao[1*] and Liangliang Cheng[1*]

[1]Department of Orthopedics, Affiliated Zhongshan Hospital of Dalian University, Dalian, China, [2]Affiliated Zhongshan Hospital of Dalian University, Dalian, China

Objective: This study aimed to evaluate the biomechanical effectiveness of 3D-printed integrated acetabular prosthesis (IAP) and modular acetabular prosthesis (MAP) in reconstructing the acetabulum for patients with Crowe III developmental dysplasia of the hip (DDH). The results of this study can provide a theoretical foundation for the treatment of Crowe III DDH in total hip arthroplasty (THA).

Methods: Finite element (FE) analysis models were created to reconstruct Crowe III DDH acetabular defects using IAP and MAP. The contact stress and relative micromotion between the acetabular prosthesis and the host bone were analyzed by gradually loading in three increments (210 N, 2100 N, and 4200 N). In addition, five patients with Crowe III DDH who underwent IAP acetabular reconstruction were observed.

Results: At the same load, the peak values of IAP contact stress and relative micromotion were lower than those of MAP acetabular reconstruction. Under jogging load, the MAP metal augment's peak stress exceeded porous tantalum yield strength, and the risk of prosthesis fracture was higher. The peak stress in the bone interface in contact with the MAP during walking and jogging was higher than that in the cancellous bone, while that of IAP was higher than that of the cancellous bone only under jogging load, so the risk of MAP cancellous bone failure was greater. Under jogging load, the relative micromotion of the MAP reconstruction acetabular implant was 45.2 μm, which was not conducive to bone growth, while under three different loads, the relative micromotion of the IAP acetabular implant was 1.5–11.2 μm, all <40 μm, which was beneficial to bone growth. Five patients with IAP acetabular reconstruction were followed up for 11.8 ± 3.4 months, and the Harris score of the last follow-up was 85.4 ± 5.5. The imaging results showed good stability of all prostheses with no adverse conditions observed.

Conclusion: Compared with acetabular reconstruction with MAP, IAP has a lower risk of loosening and fracture, as well as a better long-term stability. The application of IAP is an ideal acetabular reconstruction method for Crowe III DDH.

KEYWORDS

developmental dysplasia of the hip, acetabular reconstruction, 3D printing, integral acetabular prosthesis, modular acetabular prosthesis, finite element analysis

1 Introduction

Development dysplasia of the hip (DDH) is characterized by abnormalities in the anatomy of the acetabulum and femur. This anatomical abnormality increases the contact stress of the hip joint, resulting in hip instability, impingement, and pathological state of the labrum, and finally develops into osteoarthritis (Gala et al., 2016). Osteoarthritis, secondary to hip dysplasia, includes thinning of articular cartilage, narrowing of joint space, subchondral cystic lesions, and even hip joint deformation. The clinical manifestations are hip joint pain and limited activity, which seriously affect the quality of daily life (Garcia et al., 2022). Although there are several alternatives to hip preservation, many adult patients with DDH eventually require hip replacement (Schmitz et al., 2020).

Total hip arthroplasty (THA) can relieve hip pain symptoms and improve hip function in patients with DDH and is the main surgical procedure for adult DDH (Zhang et al., 2022). Based on the subluxation height relative to the inter-teardrop line, DDH was divided into four types according to Crowe's classification. The acetabular morphological deformity in Crowe III is more obvious than those in Crowe types I, II, and IV, resulting in more incredible difficulty of acetabular reconstruction and the installation of the acetabular prosthesis in THA, especially for the restoration of the hip rotational center and the reconstruction of bone defect (Wen et al., 2021). The traditional methods mainly include bone grafting, high hip center, and medial protrusio technique (Mou et al., 2020). However, the structural bone graft has problems, such as bone resorption and collapse (Goto et al., 2021). The internal or upward movement of the rotation center has the disadvantages of offset reduction and leg length discrepancy (Kleemann et al., 2003; Liu et al., 2018; Mou et al., 2020). For Crowe III DDH, choosing a more appropriate acetabular reconstruction method is an urgent issue for clinicians.

In recent years, with the development of the 3D printing technology, personalized orthopedic implant devices have provided solutions to many problems (Mirkhalaf et al., 2023). The 3D printing technology originated in the 1980s can provide preoperative visual and tactile evaluation and prepare individualized prostheses for different degrees and parts of orthopedic injuries, thus achieving improved surgical outcomes and reduced postoperative complications (Lee et al., 2020; Pu et al., 2021). Meanwhile, the 3D printing technology provides a new idea for acetabular reconstruction in patients with Crowe III DDH, which can personalize the design of metal augments and acetabular cups according to the acetabular bone defects in Crowe III DDH patients. We use screws to fix the metal augment on the bone defect and place the acetabular cup, which not only ensures the complete coverage of the acetabular cup but also restores the hip center of rotation and achieves the biomechanical stability of the acetabular cup (Zhang et al., 2020). However, the modular acetabular prosthesis (MAP) with multiple components (acetabular cup + metal augment + metal screw) poses a risk of inter-component failure (Strahl et al., 2023). To reduce the complex intra-operative manipulation and the potential of prosthetic loosening for the MAP, the integrated acetabular prosthesis (IAP) designed by the 3D printing technology may achieve better initial and long-term stability. This could effectively reduce the incidence of adverse events after acetabular reconstruction in patients with Crowe III DDH.

Additionally, selecting the appropriate acetabular prosthesis material is a key factor to the success of the surgery. Porous tantalum is currently the ideal orthopedic implant material for prosthesis repair. Its low modulus of elasticity prevents stress-shielding; a high coefficient of friction enhances the initial stability of the prosthesis; and the design of a bone trabecular structure promotes the ingrowth of new bone tissue (Junlei Li et al., 2020). Therefore, porous tantalum, which has more stable physicochemical properties, superior biomechanical performance, and better osseointegration ability, was chosen as the material for the acetabular prosthesis in this study.

Furthermore, the differences between the two acetabular prostheses regarding adaptability and biomechanical properties will be verified. In this study, a model of the acetabular bone defect of Crowe III DDH was established to simulate THA, and the initial stability of IAP and MAP acetabular reconstruction under different loads was compared and analyzed, which provides a reference for clinical selection of appropriate acetabular reconstruction from a biomechanical perspective.

2 Materials and methods

2.1 Establishment of the acetabular bone defect model of Crowe III DDH

The subject, a 60-year-old man (175 cm; 70 kg) with Crowe III DDH, agreed and signed the informed consent form. A Siemens 64-row spiral CT scanner was used to scan the hip with a thickness of 0.5 mm. The CT image was stored in the standard Digital Imaging and Communications in Medicine (DICOM) format in Mimics 21 (The Materialise Group, Leuven, Belgium), a medical 3D reconstruction software. Appropriate gray values were selected to distinguish bone and tissue, and the three-dimensional model of the original hip was established (Wang et al., 2021) (Figure 1A). Then, the reconstructed model was imported into 3-Matic (The Materialise Group, Leuven, Belgium) software for surface optimization processing, such as model surface defect repair, smoothing, and accurate surface function.

2.2 Establishment and assembly of the acetabular prosthesis model

According to the size of the acetabulum of the subject, the acetabular cup component of the MAP was constructed in CAD

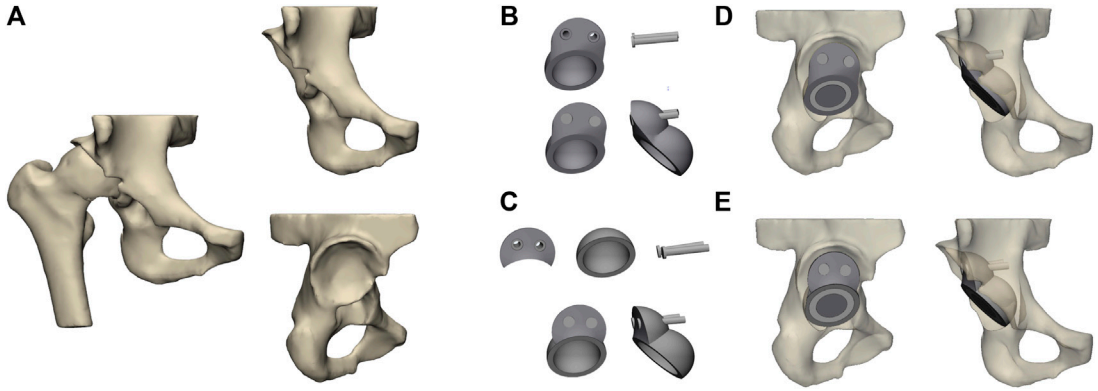

FIGURE 1
Establishment and assembly of models. **(A)** Geometrical model of the hip joint of the Crowe III developmental dysplasia of the hip (DDH); **(B)** integrated acetabular prosthesis (IAP) components; **(C)** modular acetabular prosthesis (MAP) components; **(D)** assembly of IAP acetabular reconstruction; **(E)** assembly of MAP acetabular reconstruction.

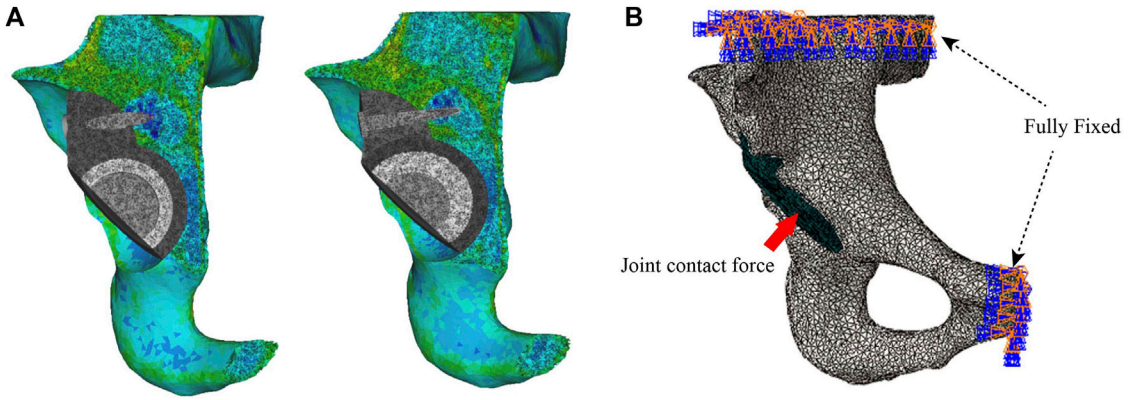

FIGURE 2
Setting of material properties, boundary conditions, and loads. **(A)** Setting the material properties of the iliac and acetabular prostheses and **(B)** loading and boundary conditions of FE modeling.

(SolidWorks 2016; SolidWorks Corp, United States), and the diameter of the acetabular cup designed in this study was 50 mm. The anteversion angle of the acetabular cup was adjusted to 15° and the abduction angle was 45° (Pour et al., 2023). In CAD software, the IAP and metal augment were designed according to the acetabular bone defect's size after the acetabular cup's placement. Two screws (length: 35 mm and diameter: 6.0 mm) were used to fix the IAP and metal augment (Figures 1B, C). The parameters of the femoral head prosthesis were designed according to the diameter of the femoral head, and the 32-mm femoral ceramic head and corresponding polyethylene liner were implanted. Since the femoral part was not involved in this study, to save the calculation time of the Finite element (FE) model, the construction of the femoral and femoral stem prosthesis was omitted in this paper. In addition, to facilitate the application of the load, the femoral head of the prosthesis was simplified to a hemisphere in FE analysis (Wang et al., 2022). Finally, the aforementioned model was non-fluid-assembled in 3-Matic (Figures 1D, E).

2.3 Establishment of the FE model

FE model was meshed with tetrahedral 4-node elements (C3D4). To obtain the actual structure and calculation proportion of the model, the mesh size was set to 1 mm, which has been validated by Dutt (2015). All models being analyzed were assumed to be continuous, isotropic, and with homogeneous linear elastic materials. The model was re-imported into Mimics 21, and material assignments were assigned according to the corresponding areas of the cortical and cancellous bone obtained by CT scanning (Guo et al., 2022) (Figure 2A). Table 1 lists the parameters of various materials (Fu et al., 2018).

2.4 Setting of the model parameters

The previously assembled models were imported into Abaqus 2021 (Simulia Corp, Providence, RI, United States). Based on the previous studies setting frictional contact interactions, the

TABLE 1 Material properties defined in the finite element (FE) models.

Components	Materials	Elastic Modulus (MPa)	Poisson's ratio (*v*)
Cortical bone	Cortical bone	17,300	0.265
Cancellous bone	Cancellous bone	400	0.2
Screws	Titanium alloy	110,600	0.326
Acetabular cup	Tantalum	8,963	0.31
Metal augment			
Integrated cup			
Ceramic femoral head	Ceramics	350,000	0.22
Liner	Polyethylene	800	0.45

friction coefficient between the bone–metal augment interface and the bone–acetabular cup interface was set to 0.8, the interface between the acetabular cup and the metal augment was established to a non-frictional connection, and the rest of the interfaces were tied connection (Du et al., 2020). In addition, fixed constraint boundary conditions were set on the pubis and the superior part of the ilium to prevent the model from moving during the analysis (Akrami et al., 2018) (Figure 2B). Based on the results of peak stresses in the unilateral hip joint reported in most of the literature, the hip contact force is 30% BW for double-legged standing (Xiong et al., 2022), 300% BW for walking, and 600% BW for jogging (Bergmann et al., 2001; Kitamura et al., 2022). The body weight of the volunteers was 70 kg. Therefore, in this study, we applied loads of 210 N, 2100 N, and 4200 N of hip contact forces to the rotation center of the femoral head (Soloviev et al., 2023).

2.5 Clinical application of the IAP in the acetabular reconstruction of Crowe III DDH

General data of patients: After obtaining the approval of the institutional ethics committee of the Affiliated Zhongshan Hospital of Dalian University, we performed a retrospective study that enrolled five patients with Crowe III DDH treated with 3D-printed porous tantalum IAP for THA in our hip joint department from January 2021 to January 2022. There were one male and four female patients with an average age of 65.2 ± 8.5 years.

Inclusion criteria: 1) Diagnosis of Crowe III DDH complicated with hip osteoarthritis and 2) patients agreed to hip replacement and signed the informed consent form.

Exclusion criteria: 1) The ages of the patients were below 30 years or above 80 years and 2) the primary diseases of the hip joint were other autoimmune diseases, infectious arthritis, or neoplastic conditions.

Preoperative design and preparation of the prosthesis: The CT data of the patient's hip joint were reconstructed on a computer, and the position of the acetabular cup was simulated in the true acetabulum position. The superolateral bone defect of the acetabular cup was filled with a sphere, forming an interconnected double spherical structure matched with the true and false acetabulum. A smooth curved transition between the edge of the acetabular prosthesis and the outer plate of the iliac crest should be carried out to avoid excessive protrusion of the outside of the augmentation device and preserve the nail hole position. The screw diameter, length, and fixation direction were designed according to the simulation design, defect location, and amount of residual bone. To avoid stress-shielding, the final structure of the IAP model was made porous by Magics (Materialise, Belgium). Finally, we imported the porous IAP model data into the 3D printer and used the laser powder bed fusion technology to prepare the prosthesis using tantalum powder (Figures 3A–E).

Surgical procedure: After the patient was anesthetized, the operation was performed via the posterolateral approach with the patient in the lateral decubitus position. The exposure and preparation of the acetabulum were the same as that for the posterolateral THA. The fibrotic scar tissue, thickened joint capsule, and surrounding hyperplastic osteophyte were removed intraoperatively. The acetabular reamer file was used to grind it to the preoperative planned size in the true and false acetabulum position. The 3D printing IAP was implanted and fixed with metal screws, finally installing the inner lining and femoral head prosthesis. The range of motion was checked adequately after hip reduction and before closing the incision (Figure 3F).

Postoperative management: The antero-posterior projection X-ray of the hip after the operation showed that the acetabular prosthesis was well-positioned with appropriate abduction and anteversion angle. Antibiotics were dripped for infection prophylaxis within 24 h. After resuscitation from anesthesia, patients should have ankle flexion and extension activities and quadriceps isometric muscle strength training under guidance. Partial weight-bearing exercise was allowed 24–48 h after the surgery, and the full weight-bearing exercise was permitted 2 weeks post-surgery.

2.6 Evaluation criteria

First, the stability of two acetabular prostheses in the Crowe III DDH acetabular reconstruction was evaluated by the contact stress and relative micromotion between the acetabular prosthesis and the host bone. Second, for the selected cases of the acetabular IAP

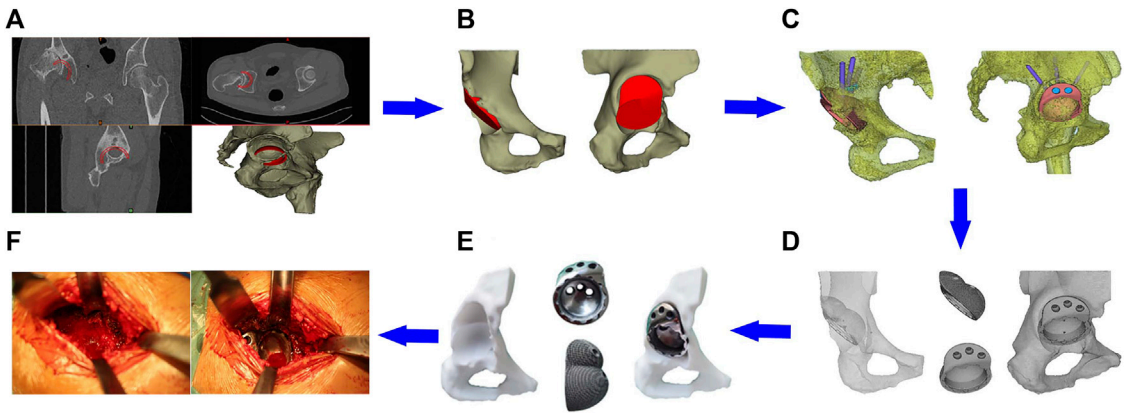

FIGURE 3
Clinical application of the IAP. **(A)** Acetabular cup placement in true acetabular position; **(B)** establishment of the integrated acetabular cup model; **(C)** design of the nail hole and screw direction; **(D)** porous treatment of IAP model; **(E)** preoperative model adaptation analysis; **(F)** surgical procedure.

reconstruction for Crowe III DDH in this article, we used the Harris hip score to evaluate hip joint function and used imaging examination to assess whether there were transparent line, displacement, aseptic loosening, osteolysis, and bone growth between the prosthesis and the bone surface.

3 Results

3.1 Validation of the developed FE model

The FE model used in this study for MAP acetabular reconstruction under walking and jogging loads had been validated through comparison with previous biomechanical models. The results of implant peak stress from Fu et al. (2018) (50.25 MPa for walking and 75.86 MPa for jogging) and relative micromotion under walking load (12.61 μm) from Wang et al. (2022) were compared with those of our study: implant peak stress of 52.3 MPa (walking) and 83.1 MPa (jogging), along with a relative micromotion of 13.7 μm under walking load. The results are similar, verifying that our FE model is suitable for further analysis.

3.2 Comparison of stress distribution in contact between the IAP and MAP

The bone interface in contact with the acetabular prosthesis is divided into the cortical bone and cancellous bone. The peak stress of the cortical bone interface was located at the edge of the cortical bone in contact with the acetabular prosthesis, and the peak stress of the cancellous bone interface was situated at the junction of the cancellous bone and the end edge of the metal screw. The peak stress at the cortical bone interface in contact with the IAP was 5.5 Mpa (210 N), 10.7 Mpa (2100 N), and 22.4 Mpa (4200 N), and the peak stress at the cancellous bone interface was 1.6 Mpa (210 N), 2.7 Mpa (2100 N), and 5.6 Mpa (4200 N) (Figures 4A, C, E). The peak stress at the cortical bone interface in contact with the MAP was 5.7 Mpa (210 N), 12.6 Mpa (2100 N), and 25.8 Mpa (4200 N), and the peak stress in the cancellous bone interface was 2.2 Mpa (210 N), 3.5 Mpa (2100 N), and 6.8 Mpa (4200 N) (Figures 4B, D, F).

3.3 Comparison of stress distribution between IAP and MAP implants

The peak stress of the IAP implant was located in the part of contact with the acetabular cortical bone, which was 12.7 Mpa (210 N), 16.2 Mpa (2100 N), and 25.8 Mpa (4200 N) (Figures 5A, C, E). The peak stress of the MAP implant was located at the lower one-third portion of the screw of the fixed metal augment, which was 17.6 Mpa (210 N), 52.3 Mpa (2100 N), and 83.1 Mpa (4200 N). The peak stress of the MAP metal augment was located at the nail hole, which was 12.2 Mpa (210 N), 20.6 Mpa (2100 N), and 54.2 Mpa (4200 N) (Figures 5 B, D, F).

3.4 Comparison of the relative micromotion of the IAP and MAP concerning the host bone

The peak micromotion of the IAP relative to the host bone was 1.5 μm (210 N), 8.9 μm (2100 N), and 11.2 μm (4200 N) (Figures 6A, C, E). The peak micromotion of the MAP relative to the host bone was 9.7 μm (200 N), 13.7 μm (2100 N), and 45.2 μm (4200 N) (Figures 6B, D, F).

3.5 Clinical follow-up results of patients

The follow-up time for patients was 11.8 ± 3.4 months. The preoperative Harris hip score was 46.5 ± 4.8, increasing to 80.1 ± 6.6 at 3 months postoperative and 85.4 ± 5.5 at the final follow-up. No surgical site swelling, infection, or postoperative complications were observed during the last follow-up. In addition, all patients' anteroposterior projection X-ray of the hip showed no adverse conditions such as radiolucent lines, loosening, and osteolysis around the 3D-printed IAP and bone surface (Figures 7A–C).

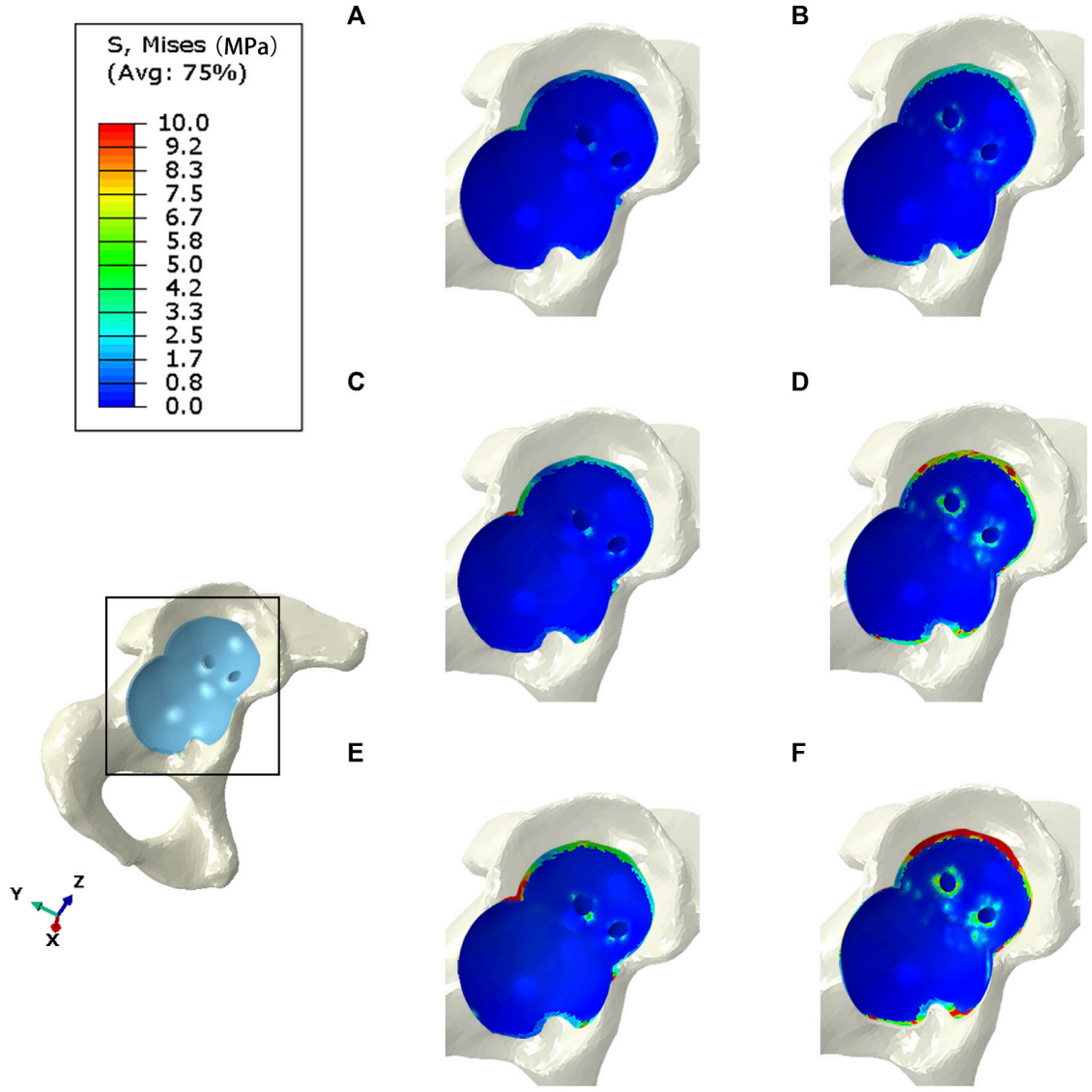

FIGURE 4
Stress distribution of bones contacted by IAP and MAP. **(A,B)** 210 N; **(C,D)** 2100 N; **(E,F)** 4200 N.

4 Discussion

The lack of adequate acetabular bone coverage on the superolateral part of the acetabular cup during the THA of Crowe III DDH will affect the initial stability of the acetabular cup (Crowe et al., 1979). The selection of an appropriate acetabular reconstruction method is the key to ensuring the biomechanical stability of the acetabular cup. The 3D printing technology provides a new choice for acetabular reconstruction in Crowe III DDH patients (Zhang et al., 2020). The IAP and MAP designed by the 3D printing technology can not only restore the rotation center of the hip joint, leg length discrepancy, and the muscle tension around the hip joint but also provide a stable and practical support for the acetabular cup to keep it in an ideal position. However, there is a lack of biomechanical research comparing the stability of the interface between the IAP and MAP acetabular components and the host bone.

To help clinicians better understand hip biomechanics and prevent complications, the FE analysis has been widely used in orthopedic implant design and preoperative planning. Compared to other experiments, it can not only simulate the biomechanical performance of implants as prostheses with good fidelity but also demonstrate higher efficiency and conserve resources (Fallahnezhad et al., 2023). This study used the FE analysis to evaluate the biomechanical advantages and disadvantages of the IAP and MAP by assessing the contact stress and relative micromotion between the acetabular prosthesis and the host bone under different loads.

The acetabular cup and metal augment used in the present study were porous tantalum materials. The yield strength of porous tantalum has been reported to be 35–51 Mpa (Wang et al., 2023). Under the maximum load, the peak stresses of the IAP and MAP as porous tantalum implants were 25.8 Mpa (contacting the edge of the cortical bone) and 54.2 MPa (at the nail hole of the

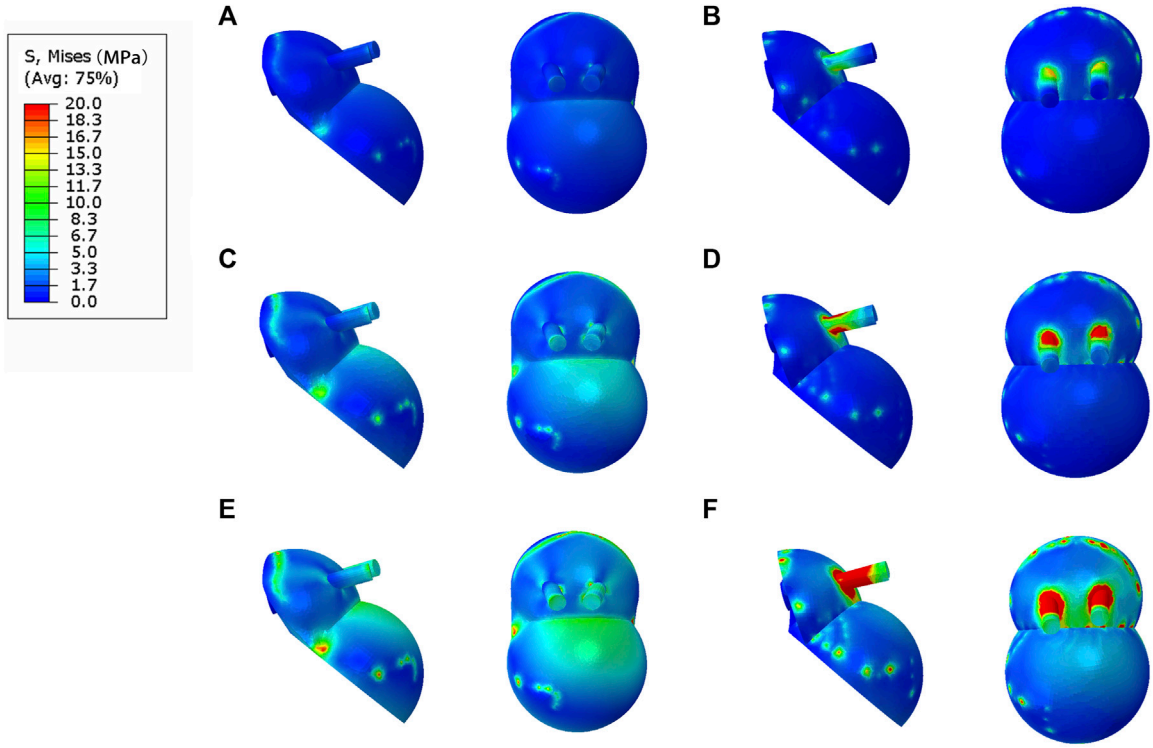

FIGURE 5
Stress distribution of IAP and MAP implants. **(A,B)** 210 N; **(C,D)** 2100 N; **(E,F)** 4200 N.

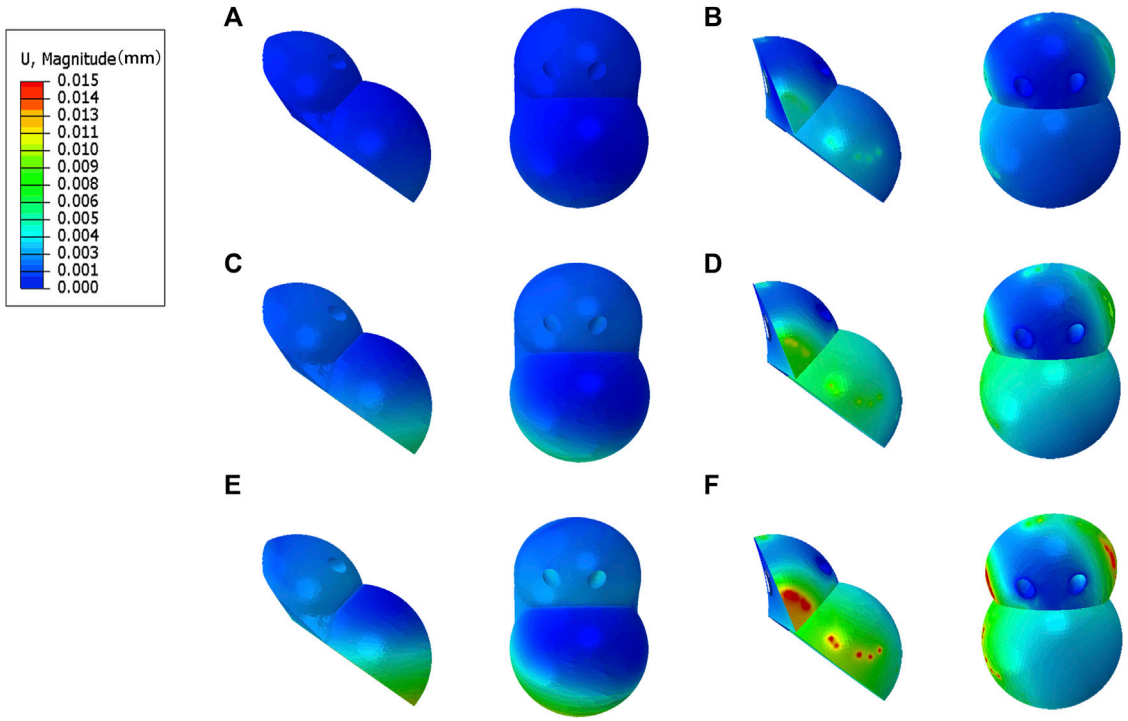

FIGURE 6
Relative micromotion distribution of the IAP and MAP relative to the host bone. **(A,B)** 210 N; **(C,D)** 2100 N; **(E,F)** 4200 N.

FIGURE 7
A 65-year-old male patient with Crowe III DDH who underwent 3D-printed IAP acetabular reconstruction. **(A)** Preoperative X-ray image; **(B)** immediate postoperative X-ray image; **(C)** postoperative last follow-up X-ray image.

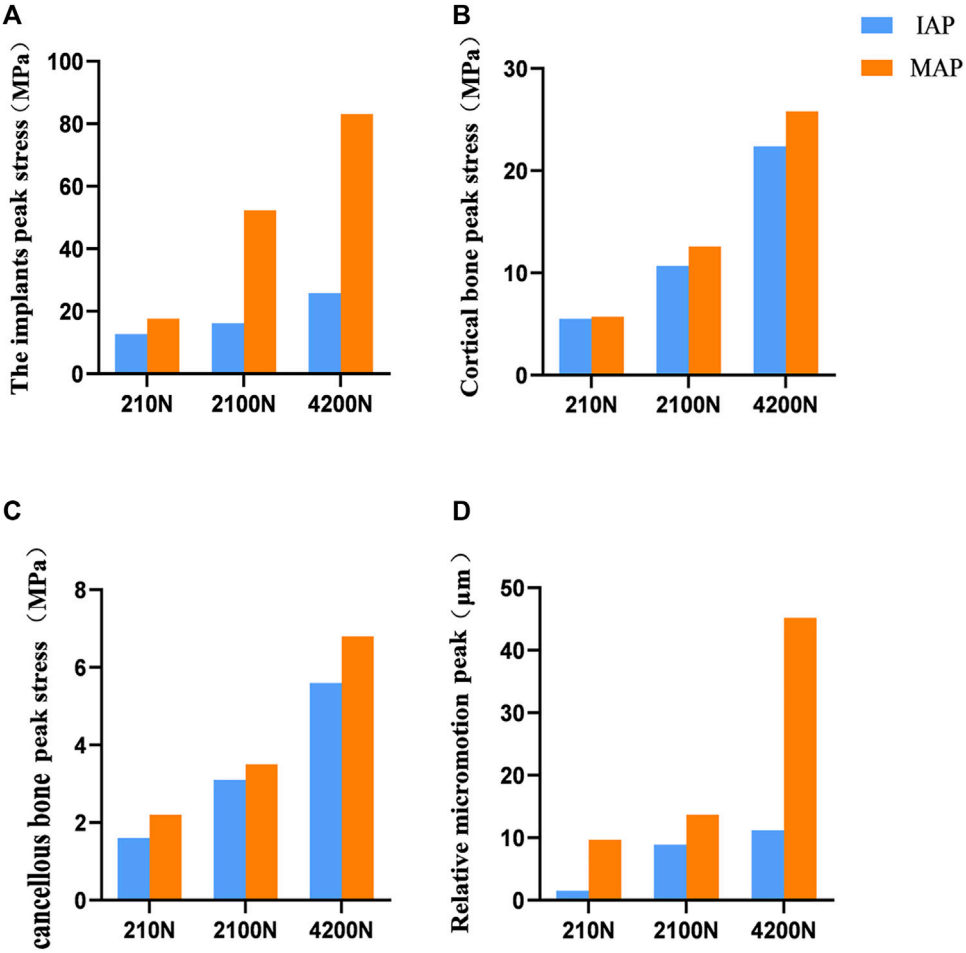

FIGURE 8
Comparison of contact stress and relative micromotion between the IAP and MAP. **(A)** Peak stress of the implant. **(B)** Peak stress of the cortical bone. **(C)** Peak stress of the cancellous bone. **(D)** Peak micromotion of the acetabular prosthesis relative to the host bone.

metal augment), and the peak stress of the MAP was more significant than the yield strength of porous tantalum. Therefore, the MAP is prone to failure and fracture when it reaches the exercise load immediately after operation. At the same time, under the same load, compared with MAP acetabular reconstruction, IAP, as an implant, had more uniform force and lower peak stress, which reduced the risk of prosthesis fracture (Figure 8A).

The mean yield strengths of cancellous and cortical bones near the acetabulum was 3.3 and 93.4 Mpa, respectively (Fu et al., 2018). Under a double-legged standing load, the peak interface stress between the cortical bone and the MAP was 5.7 MPa, and for the cancellous bone, it was 2.2 MPa. Similarly, the interface peak stress between the cortical bone and the IAP was 5.5 MPa, and for the cancellous bone, it was 1.6 MPa.

Notably, the peak stresses at the interface of cortical and cancellous bones in contact with both the MAP and IAP were found to be below their respective yield strengths. According to the aforementioned data, the bone strength around the acetabulum is strong enough to support the patient to stand after acetabular reconstruction. Furthermore, the research has shown that a relative micromotion of less than 40 μm between the acetabular prosthesis and the host bone promotes bone ingrowth, which is beneficial for the long-term stability of the acetabular prosthesis (Kaku et al., 2015). Under a double-legged standing load, the relative micromotion of the MAP and IAP was 9.7 and 1.5 μm, respectively, which facilitated bone ingrowth, indicating that the two acetabular prostheses were stable under the standing load.

Under the exercise load, the peak interface stress of the MAP in walking and jogging contact with the cancellous bone was 3.5 and 6.8 Mpa, respectively, which were higher than the yield strength of the cancellous bone. However, the peak stress (5.6 Mpa) of the IAP exposed to the cancellous bone only exceeded the yield strength of the cancellous bone under the jogging load (Figures 8B, C). Therefore, compared with IAP acetabular reconstruction, the MAP cancellous bone has a higher risk of failure, and prosthesis fixation is unreliable and prone to loosening. Under jogging load, the micromotion of the MAP relative to the host bone was more than 40 μm, which was not conducive to bone growth and affected the long-term stability of the acetabular prosthesis. In contrast, the relative micromotion of the IAP to the host bone under three different loads was much smaller than the critical condition of bone growth, and the condition of bone growth was better, which was beneficial to the long-term stability of the acetabular prosthesis (Figure 8D). Therefore, according to the results of FE analysis, the IAP is safer than the MAP in acetabular reconstruction.

In summary, during the early postoperative exercise, with the high stress in MAP nail holes and MAP metal screws, the prosthesis has a higher risk of fracture and loosening. In contrast, the IAP not only effectively disperses the stress on the screws, reducing high-stress areas between the prosthesis and the host bone, thus lowering the risk of prosthesis fracture and loosening, but also provides more favorable conditions for bone ingrowth, promoting the long-term stability of the prosthesis. Regarding the reasons behind such biomechanical differences, we believe that in Crowe III DDH acetabular reconstructions, the integrated design of the IAP can effectively achieve uniform stress transfer in the acetabular prosthesis. Additionally, the fixation of multiple metal screws also provides enhanced stability for the IAP. On the contrary, the multi-component design of the MAP makes the acetabular prosthesis stress distribution uneven, and the contact between the components will cause the prosthesis to loosen due to the change in biomechanical load. Therefore, from the biomechanical perspective, the IAP reconstruction of the acetabulum can provide more excellent biomechanical properties while maintaining reliable structural strength.

In clinical applications, a high loosening and fracture rate of the acetabular prosthesis after follow-up for acetabular defect reconstruction using the MAP was also reported in the literature Borland et al. (2012); Cassar-Gheiti et al. (2021). In this study, five Crowe III DDH patients undergoing IAP acetabular reconstruction were clinically followed up. The hip function of all patients was significantly improved, and the quality of life of patients was greatly improved. The imaging results showed that the acetabular prosthesis is firmly fixed with no signs of loosening or fracture observed, indicating the satisfactory stability of the prosthesis. This clinical result has further confirmed the validity of the biomechanical results of this study.

The limitations of this study are as follows: 1) The influence of muscles and soft tissues around the hip joint was not considered in this study: only hip contact forces were used for testing, which might not accurately reflect hip joint motion under physiological loading patterns. 2) The results of this study were generated based on computer simulations and were not validated using cadaveric bone for biomechanical studies. 3) No clinical case comparison was performed primarily because the FE analysis results of the MAP model indicated higher clinical application risks. Therefore, clinical validation was carried out exclusively on IAP cases. 4) This study merely referenced prior research for mesh configuration and did not perform mesh sensitivity analysis. Despite these limitations, our findings may help orthopedic surgeons to select a more appropriate acetabular reconstruction method in clinical practice.

5 Conclusion

In this study, the biomechanics of the IAP- and MAP-reconstructed Crowe III DDH acetabulum designed by 3D printing technology were evaluated by the FE analysis. The results show that the risk of loosening and fracture of the prosthesis is lower and the long-term stability is better with the IAP than with the MAP reconstructed acetabulum, suggesting that the IAP may have more excellent biomechanical properties than the MAP in Crowe III DDH acetabular reconstruction. Clinical follow-up of five patients with Crowe III DDH acetabular reconstruction by IAP showed good clinical efficacy, which has further verified the effectiveness of the IAP reconstruction of the acetabulum. These results can provide a biomechanical reference for the selection of clinical treatment.

Data availability statement

The original contributions presented in the study are included in the article/Supplementary Material. Further inquiries can be directed to the corresponding authors.

Ethics statement

The studies involving human participants were reviewed and approved by the institutional ethics committee of the Affiliated Zhongshan Hospital of Dalian University. The patients/participants provided their written informed consent to participate in this study. Written informed consent was obtained from the individual(s) for the publication of any potentially identifiable images or data included in this article.

Author contributions

YL conducted experiments and edited the entire manuscript. FW and JY wrote the first draft and finalized the manuscript. MX and YW were involved in establishing and analyzing the finite element models. JL and HX were involved in polishing and revising the manuscript language. DZ and LC were involved in the supervision and resources. All authors contributed to the article and approved the submitted version.

Funding

This research was funded by the Dalian Key Medical Specialty Construction Fund Project "Peak Plan-2021-243."

Conflict of interest

The authors declare that the research was conducted in the absence of any commercial or financial relationships that could be construed as a potential conflict of interest.

Publisher's note

References

Akrami, M., Craig, K., Dibaj, M., Javadi, A. A., and Benattayallah, A. (2018). A three-dimensional finite element analysis of the human hip. *J. Med. Eng. Technol.* 42 (7), 546–552. doi:10.1080/03091902.2019.1576795

Bergmann, G., Deuretzbacher, G., Heller, M., Graichen, F., Rohlmann, A., Strauss, J., et al. (2001). Hip contact forces and gait patterns from routine activities. *J. Biomech.* 34 (7), 859–871. doi:10.1016/s0021-9290(01)00040-9

Borland, W. S., Bhattacharya, R., Holland, J. P., and Brewster, N. T. (2012). Use of porous trabecular metal augments with impaction bone grafting in management of acetabular bone loss. *Acta Orthop.* 83 (4), 347–352. doi:10.3109/17453674.2012.718518

Cassar-Gheiti, A. J., Mei, X. Y., Afenu, E. A., Safir, O. A., Gross, A. E., and Kuzyk, P. R. T. (2021). Midterm outcomes after reconstruction of superolateral acetabular defects using flying buttress porous tantalum augments during revision total hip arthroplasty. *J. Arthroplasty* 36 (8), 2936–2941. doi:10.1016/j.arth.2021.03.040

Crowe, J. F., Mani, V. J., and Ranawat, C. S. (1979). Total hip replacement in congenital dislocation and dysplasia of the hip. *J. Bone Jt. Surg. Am.* 61 (1), 15–23. doi:10.2106/00004623-197961010-00004

Du, Y., Fu, J., Sun, J., Zhang, G., Chen, J., Ni, M., et al. (2020). Acetabular bone defect in total hip arthroplasty for crowe II or III developmental dysplasia of the hip: A finite element study. *Biomed. Res. Int.* 2020, 1–12. doi:10.1155/2020/4809013

Dutt, A. (2015). Effect of mesh size on finite element analysis of beam. *SSRG -IJME* 2, 8–10. doi:10.14445/23488360/IJME-V2I12P102

Fallahnezhad, K., O'Rourke, D., Bahl, J. S., Thewlis, D., and Taylor, M. (2023). The role of muscle forces and gait cycle discretization when assessing acetabular cup primary stability: A finite element study. *Comput. Methods Programs Biomed.* 230, 107351. doi:10.1016/j.cmpb.2023.107351

Fu, J., Ni, M., Chen, J., Li, X., Chai, W., Hao, L., et al. (2018). Reconstruction of severe acetabular bone defect with 3D printed Ti6Al4V augment: A finite element study. *Biomed. Res. Int.* 2018, 1–8. doi:10.1155/2018/6367203

Gala, L., Clohisy, J. C., and Beaulé, P. E. (2016). Hip dysplasia in the young adult. *J. Bone Jt. Surg. Am.* 98 (1), 63–73. doi:10.2106/jbjs.O.00109

Garcia, S., Demetri, L., Starcevich, A., Gatto, A., and Swarup, I. (2022). Developmental dysplasia of the hip: controversies in management. *Curr. Rev. Musculoskelet. Med.* 15 (4), 272–282. doi:10.1007/s12178-022-09761-8

Goto, E., Umeda, H., Otsubo, M., and Teranishi, T. (2021). Cemented acetabular component with femoral neck autograft for acetabular reconstruction in Crowe type III dislocated hips. *Bone Jt. J.* 103-b (2), 299–304. doi:10.1302/0301-620x.103b2.Bjj-2020-1214.R1

Guo, Z., Peng, Y., Shen, Q., Li, J., He, P., Yuan, P., et al. (2022). Reconstruction with 3D-printed prostheses after type I + II + III internal hemipelvectomy: finite element analysis and preliminary outcomes. *Front. Bioeng. Biotechnol.* 10, 1036882. doi:10.3389/fbioe.2022.1036882

Junlei Li, L. Q., Yang, K., Ma, Z., Wang, Y., Cheng, L., Zhao, D., et al. (2020). Materials evolution of bone plates for internal fixation of bone fractures: A review. *J. Mater. Sci. Technol.* 36 (0), 190–208. doi:10.1016/j.jmst.2019.07.024

Kaku, N., Tabata, T., and Tsumura, H. (2015). Influence of cup-center-edge angle on micro-motion at the interface between the cup and host bone in cementless total hip arthroplasty: three-dimensional finite element analysis. *Eur. J. Orthop. Surg. Traumatol.* 25 (8), 1271–1277. doi:10.1007/s00590-015-1697-z

Kitamura, K., Fujii, M., Iwamoto, M., Ikemura, S., Hamai, S., Motomura, G., et al. (2022). Effect of coronal plane acetabular correction on joint contact pressure in periacetabular osteotomy: A finite-element analysis. *BMC Musculoskelet. Disord.* 23 (1), 48. doi:10.1186/s12891-022-05005-5

Kleemann, R. U., Heller, M. O., Stoeckle, U., Taylor, W. R., and Duda, G. N. (2003). THA loading arising from increased femoral anteversion and offset may lead to critical cement stresses. *J. Orthop. Res.* 21 (5), 767–774. doi:10.1016/s0736-0266(03)00040-8

Lee, U. L., Lim, J. Y., Park, S. N., Choi, B. H., Kang, H., and Choi, W. C. (2020). A clinical trial to evaluate the efficacy and safety of 3D printed bioceramic implants for the reconstruction of zygomatic bone defects. *Mater. (Basel)* 13 (20), 4515. doi:10.3390/ma13204515

Liu, B., Gao, Y. H., Ding, L., Li, S. Q., Liu, J. G., and Qi, X. (2018). Computed tomographic evaluation of bone stock in patients with crowe type III developmental dysplasia of the hip: implications for guiding acetabular component placement using the high hip center technique. *J. Arthroplasty* 33 (3), 915–918. doi:10.1016/j.arth.2017.10.021

Mirkhalaf, M., Men, Y., Wang, R., No, Y., and Zreiqat, H. (2023). Personalized 3D printed bone scaffolds: A review. *Acta Biomater.* 156, 110–124. doi:10.1016/j.actbio.2022.04.014

Mou, P., Liao, K., Chen, H. L., and Yang, J. (2020). Controlled fracture of the medial wall versus structural autograft with bulk femoral head to increase cup coverage by host bone for total hip arthroplasty in osteoarthritis secondary to developmental dysplasia of the hip: A retrospective cohort study. *J. Orthop. Surg. Res.* 15 (1), 561. doi:10.1186/s13018-020-02088-5

Pour, A. E., Tung, W. S., Donnelley, C. A., Tommasini, S. M., and Wiznia, D. H. (2023). Hip abduction can Be considered the sole posterior precaution strategy to lower the rate of impingement after posterior approach total hip arthroplasty with large femoral head: A computer simulation study. *J. Arthroplasty* 38, 1385–1391. doi:10.1016/j.arth.2023.01.027

Pu, F., Liu, J., Shi, D., Huang, X., Zhang, J., Wang, B., et al. (2021). Reconstruction with 3D-printed prostheses after sacroiliac joint tumor resection: A retrospective case-control study. *Front. Oncol.* 11, 764938. doi:10.3389/fonc.2021.764938

Schmitz, M. R., Murtha, A. S., and Clohisy, J. C. (2020). Developmental dysplasia of the hip in adolescents and young adults. *J. Am. Acad. Orthop. Surg.* 28 (3), 91–101. doi:10.5435/jaaos-d-18-00533

Soloviev, D., Maslov, L., and Zhmaylo, M. (2023). Acetabular implant finite element simulation with customised estimate of bone properties. *Mater. (Basel)* 16 (1), 398. doi:10.3390/ma16010398

Strahl, A., Boese, C. K., Ries, C., Hubert, J., Beil, F. T., and Rolvien, T. (2023). Outcome of different reconstruction options using allografts in revision total hip arthroplasty for severe acetabular bone loss: A systematic review and meta-analysis. *Arch. Orthop. Trauma Surg.* doi:10.1007/s00402-023-04843-9

Wang, X., Zhou, K. J. H., Li, Y., Xie, H., and Wang, B.-J. (2023). Preparation, modification, and clinical application of porous tantalum scaffolds. *Front. Bioeng. Biotechnol.* 11, 1127939. doi:10.3389/fbioe.2023.1127939

Wang, Y., Wang, M., Li, C., Nakamura, Y., Deng, L., Yamako, G., et al. (2022). Biomechanical effect of metal augment and bone graft on cup stability for acetabular reconstruction of total hip arthroplasty in hip dysplasia: A finite element analysis. *BMC Musculoskelet. Disord.* 23 (1), 277. doi:10.1186/s12891-022-05168-1

Wang, Y., Yamako, G., Okada, T., Arakawa, H., Nakamura, Y., and Chosa, E. (2021). Biomechanical effect of intertrochanteric curved varus osteotomy on stress reduction in femoral head osteonecrosis: A finite element analysis. *J. Orthop. Surg. Res.* 16 (1), 465. doi:10.1186/s13018-021-02614-z

Wen, X., Zuo, J., Liu, T., Gao, Z., and Xiao, J. (2021). Bone defect map of the true acetabulum in hip dysplasia (Crowe type II and III) based on three-dimensional image reconstruction analysis. *Sci. Rep.* 11 (1), 22955. doi:10.1038/s41598-021-02448-z

Xiong, B., Yang, P., Lin, T., Xu, J., Xie, Y., Guo, Y., et al. (2022). Changes in hip joint contact stress during a gait cycle based on the individualized modeling method of "gait-musculoskeletal system-finite element. *J. Orthop. Surg. Res.* 17 (1), 267. doi:10.1186/s13018-022-03094-5

Zhang, H., Guan, J. Z., Zhang, Z., Chen, X. T., Ma, X. D., Zhao, J. N., et al. (2022). Restoring rotation center in total hip arthroplasty for developmental dysplasia of the hip with the assistance of three dimensional printing technology: A pilot study. *Orthop. Surg.* 14 (1), 119–128. doi:10.1111/os.13183

Zhang, H., Liu, Y., Dong, Q., Guan, J., and Zhou, J. (2020). Novel 3D printed integral customized acetabular prosthesis for anatomical rotation center restoration in hip arthroplasty for developmental dysplasia of the hip crowe type III: A case report. *Med. Baltim.* 99 (40), e22578. doi:10.1097/md.0000000000022578

frontiers | Frontiers in Bioengineering and Biotechnology

TYPE Original Research
PUBLISHED 25 September 2023
DOI 10.3389/fbioe.2023.1260693

OPEN ACCESS

EDITED BY
Zhenxian Chen,
Chang'an University, China

REVIEWED BY
Hanxing Zhu,
Cardiff University, United Kingdom
Chi-Tay Tsai,
Florida Atlantic University, United States

*CORRESPONDENCE
Hong Wang,
whwl@dlut.edu.cn
Jian Jiang,
rejustin@sina.com

†These authors have contributed equally to this work and share first authorship

RECEIVED 18 July 2023
ACCEPTED 04 September 2023
PUBLISHED 25 September 2023

CITATION
Hao J, Tang X, Jiang N, Wang H and Jiang J (2023), Biomechanical stability of oblique lateral interbody fusion combined with four types of internal fixations: finite element analysis. *Front. Bioeng. Biotechnol.* 11:1260693. doi: 10.3389/fbioe.2023.1260693

Biomechanical stability of oblique lateral interbody fusion combined with four types of internal fixations: finite element analysis

Jiayu Hao[1†], XianSheng Tang[2†], Nizhou Jiang[1], Hong Wang[1*] and Jian Jiang[1*]

[1]Department of Spine Surgery, Dalian Municipal Central Hospital, Dalian University of Technology, Dalian, China, [2]Department of Engineering Mechanics, Dalian University of Technology, Dalian, China

Objective: Using finite element analysis to identify the optimal internal fixation method for oblique lateral lumbar interbody fusion (OLIF), providing guidance for clinical practice.

Methods: A finite element model of the L4 – L5 segment was created. Five types of internal fixations were simulated in the generated L4-L5 finite element (FE) model. Then, six loading scenarios, i.e., flexion, extension, left-leaning, right-leaning, rotate left, and rotate right, were simulated in the FE models with different types of fixations. The biomechanical stability of the spinal segment after different fixations was investigated.

Results: Regarding the range of motion (ROM) of the fused segment, OLIF + Bilateral Pedicle Screws (BPS) has a maximum ROM of 1.82° during backward bending and the smallest ROM in all directions of motion compared with other models. In terms of the von Mises stress distribution on the cage, the average stress on every motion direction of OLIF + BPS is about 17.08MPa, and of OLIF + Unilateral Vertebral Screw - Pedicle Screw (UVS-PS) is about 19.29 MPa. As for the von Mises stress distribution on the internal fixation, OLIF + BPS has the maximum internal fixator stress in left rotation (31.85 MPa) and OLIF + Unilateral Pedicle Screw (UPS) has the maximum internal fixator stress in posterior extension (76.59 MPa). The data of these two models were smaller than those of other models.

Conclusion: OLIF + BPS provides the greatest biomechanical stability, OLIF + UPS has adequate biomechanical stability, OLIF + UVS-PS is inferior to OLIF + UPS synthetically, and OLIF + Double row vertical screw (DRVS) and Individual OLIF (IO) do not present significant obvious advantages.

KEYWORDS

finite element analysis, OLIF, internal fixation, biosolid mechanics, CAGE

Introduction

Currently, lumbar fusion surgery (LIF), including posterior lumbar fusion (PLIF) or transforaminal lumbar fusion (TLIF), is widely used in clinical practice (Huang et al., 2022). However, insertion of the fusion through a posterior approach requires the removal of the posterior structures of the vertebral body, which can affect vertebral stability. Additionally,

repeated traction on the dural sac and nerve roots during the procedure may lead to nerve injury. Multiple surgical approaches have been attempted to minimize complications.

Oblique lateral lumbar interbody fusion (OLIF) is considered one of the best options for lumbar fusion (Aleinik et al., 2021). In 1997, Mayer (Mayer, 1997) described a minimally invasive anterior approach to the lumbar spine through a retroperitoneal approach at the L2-L5 level and a transabdominal approach at the L5-S1 level, which first proposed OLIF. In OLIF, the cage enters the disc from the oblique lateral side, preserving the small posterior joints, muscles, and other tissues. In 2012, Silvestre et al. (Silvestre et al., 2012) improved Mayer's approach to the procedure, resulting in the OLIF that is currently used. OLIF is a discectomy implant fusion performed through the anatomical gap between the retroperitoneal lumbar major muscle anteriorly and the aorta. The mechanisms of OLIF include restoring disc height, increasing posterior longitudinal ligament tension, and improving the sagittal sequence of the spine. (Alimi et al., 2014; Liu et al., 2019).

Compared to other lumbar fusion methods, OLIF has the following advantages (Huang et al., 2022; Liu et al., 2022; Zhang et al., 2022). First, OLIF allows the cage to enter the lumbar spine anteriorly without opening the spinal canal or damaging the posterior muscles, ligaments, and bony structures. This preserves more bone, which is particularly important for patients with disc degeneration combined with osteoporosis. Second, by removing sufficient disc tissue and providing a large contact area with the endplate, the fusion device significantly enhances the supporting strength of the fusion. Third, OLIF reduces the possibility of damaging the lumbar muscles and lumbosacral nerves. Fourth, the interbody fusion used in OLIF is much larger compared to conventional posterior fusions, and it is placed across the endplate, which significantly enhances its biomechanical stability. In addition, OLIF has the advantages of a low complication rate, less surgical blood loss, shorter operative time, and shorter patient hospital stay (Mobbs et al., 2015; Lu and Lu, 2019; Aleinik et al., 2021). Joseph et al. (2015) reported a complication rate of 20.2% (380/1885) after TLIF, whereas Abe et al. (2017) reported a complication rate of 1.2% (2/155) after OLIF, indicating a significant reduction in innerve injury with OLIF. Moreover, the OLIF procedure preserves more of the anatomy, theoretically providing more resistance during motion (Kim et al., 2005).

It has also been suggested that OLIF leads to lumbar instability and increases the risk of fusion subsidence and fracture (Abe et al., 2017; Quillo-Olvera et al., 2018; Bereczki et al., 2021). After OLIF, especially in osteoporotic patients, surgical injury can lead to instability of the corresponding lumbar segment, subsidence, and displacement of the fusion cage, which can ultimately result in surgical failure (Malham et al., 2015). Therefore, in most cases, OLIF requires reinforcement with internal fixation devices to enhance the stability of the fusion (Cappuccino et al., 2010; Shasti et al., 2019). The internal fixation system must maintain good function until firm bony fusion is achieved. For lumbar fusion, the stiffness of the internal fixation system at the operative segment and its ability to share the load of the fusion apparatus is fundamental to bone healing or fusion. The combination of fusion inserted through OLIF with posterior internal fixation instrumentation results in a stronger and more stable structure (Kim et al., 2005; Niemeyer et al., 2006; Kornblum et al., 2013). Different types of internal fixation devices play important roles in maintaining the stability of the operated segment and reducing fusion device complications (Pham et al., 2016; Xu et al., 2018). Fusion device complications are related to bone density, fusion level, disc position, disc height, and pedicle screw internal fixation (Kim et al., 2013; Oh et al., 2017). Fusion settling is a major factor in revision surgery after OLIF (Alimi et al., 2014; Tempel et al., 2018). Local healing is better facilitated if the load transmitted through the fusion device can be increased without fusion settling.

There is limited research on the biomechanical stability of OLIF combined with internal fixation. This study aims to identify an OLIF supplementary internal fixation method that can provide the best spinal stability. We established a normal vertebral body model and five surgical models and compared their biomechanical stability using finite element (FE) analysis. In these 5 models, although the Individual OLIF (IO) model did not have any additional internal fixation, we still established its model as a reference.

Methods

Three-dimensional FE model of the lumbar spine

A female volunteer (age: 39 years old, height: 169.0 cm, weight: 60.0 kg) with lumbar degenerative disease was recruited. The entire lumbar spine was scanned using a NEUVIZ 64-row spiral CT scanner with a slice thickness of 0.1 mm. Appropriate gray values were selected to distinguish bone and tissues. The images of the L4-L5 segment were selected from the complete lumbar spine image, as this is the most commonly used in OLIF surgery. The computed tomography images were stored in the format of Digital Imaging and Communications in Medicine (DICOM). The DICOM data were imported into Mimics Research 20.0 (Materialise, Belgium) for the three-dimensional (3D) reconstruction of Lumbar 4-5 segments. Then the reconstructed model was imported into Geomagic Wrap 2021 (Reverse Engineering Software, United States) for surface optimization, eliminating defects in the initial model. After the smoothing process was completed, the vertebral body of the spine model was offset inward by 0.5 mm. The hollow part between the original model and the offset model was added to the anterior vertebral body as cortical bone and the inner body was used as cancellous bone. The cortical bone on the upper and lower surfaces of the vertebral body is set as an endplate with a thickness of 0.5 mm. The cartilage part was first created by creating an appropriately sized cylinder in SolidWorks 2019 (CAD software, Dassault Systems, United States), and then performing Boolean operations on the L4 and L5 endplates that fit with the cylinder to generate the cartilage. The fusion device and bone screw were established in Solidworks 2019 with corresponding dimensions. Finally, all the models were imported into 3-material (Metric, Belgium) to adjust the screw positions, perform Boolean operations, generate four screw layout schemes, and import the inp file into Abaqus 6.14 after generating the mesh. The ligaments were established in Abaqus 6.14 with seven major ligaments created at appropriate locations: Anterior

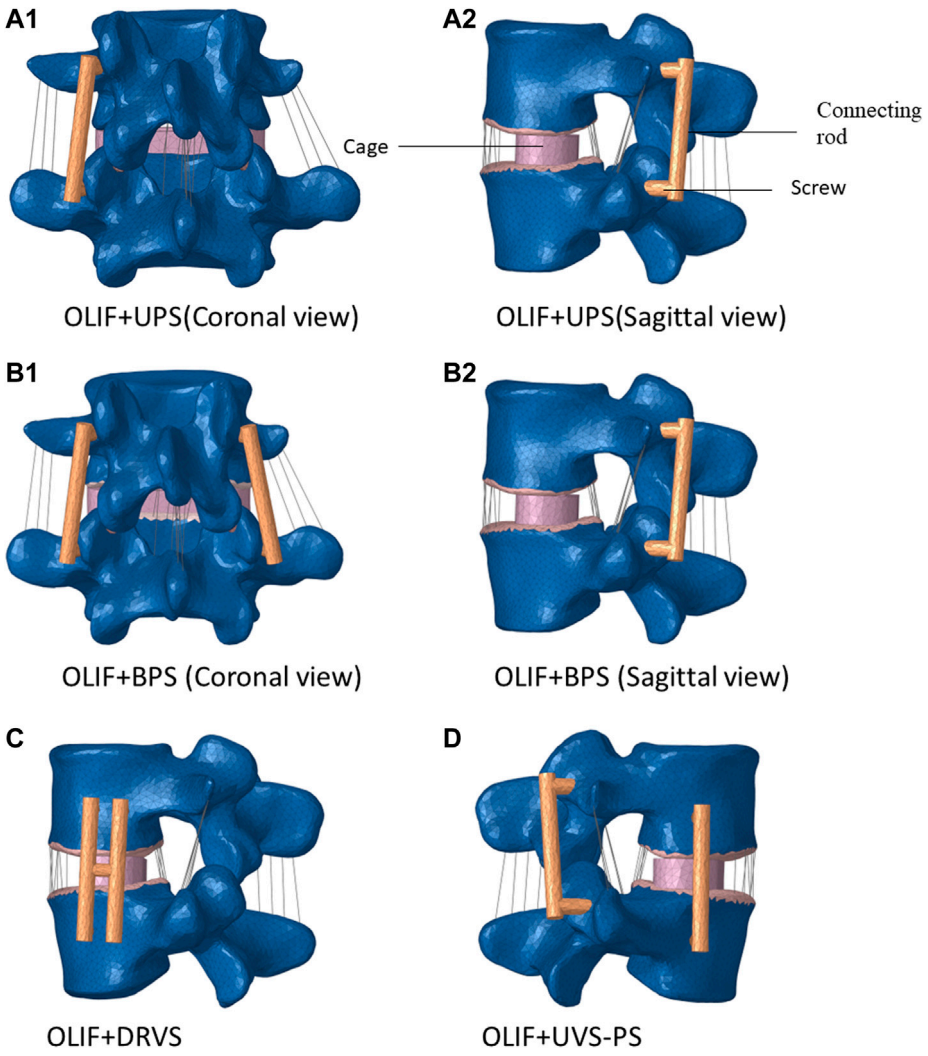

FIGURE 1
Four types of internal fixation models. (OLIF: Oblique lateral lumbar interbody fusion, UPS: Unilateral Pedicle Screw, BPS: Bilateral Pedicle Screws, DRVS: Double row vertical screw, UVS-PS: Unilateral Vertebral Screw-Pedicle Screw).

Longitudinal Ligament (ALL), Posterior Longitudinal Ligament (PLL), Ligamentum Flavum (LF), Intertransverse Ligament (ITL), Supraspinous Ligament (SL), and Interspinous Ligament (ISL).

In the interaction setting, the bonding surface of cortical bone and cancellous bone were bound, the fusion device was bound to the lower surface of the L4 segment and the upper surface of the L5 segment, the ligament was bound to the outer surface of cortical bone, the bone screw was bound to the surface of the hole after Boolean operation of the spine. The friction contact coefficient between the cartilage and the surface of the upper and lower articular processes was set to 0.1 (Cai et al., 2022). The bone parts in the complete FE model of the L4-L5 segments include cortical bone, cancellous bone, and cartilage parts. The cortical bone thickness was set to 0.5 mm based on CT image estimation and another research (Cai et al., 2022). The element type for cortical bone, cancellous bone, fusion cage, and bone screw was C3D4, the element type of ligament was T3D2, and the element type of cartilage was C3D4. The developed L4-L5 spinal segment model was meshed using C3D4 elements after a mesh convergence study.

FE models of the internal fixation and cage

In the present study, the Individual OLIF (IO) model and OLIF combined with four internal fixation models were established (Figure 1). The cage measures 45.0 mm in length, 17.0 mm in width, and 14.0 mm in height. The length of the screw is 45.0 mm and the diameter is 6.5 mm. The connecting rod has a length of 50.0 mm and a diameter of 5.5 mm. The fusion device and internal fixation were established by corresponding dimensions in Solidworks 2019. During the FE simulation, the entire nucleus pulposus and fibrous ring were removed. In the Individual OLIF (IO) model, fusion cages were implanted in the intervertebral space, and no internal fixation

TABLE 1 Material properties, element type, and number for the component in the FE model of the spinal segment.

Component	E [MPa]	ν	Element type	References
Bony Structures				
Cortical bone	12,000	0.3	C3D4	Burstein et al. (1976)
Cancellous bone	1,500	0.3	C3D4	Lindahl (1976)
Posterior bone	3,500	0.3	C3D4	Shirazi-Adl et al. (1986)
End plate	12,000	0.3	C3D4	Grant et al. (2001)
Facet cartilage	20	0.3	C3D4	
Intervertebral disc				
Annulus fibrosus	Calibrated stress-strain curves			
Nucleus pulposus	Mooney–Rivlin, C1 = 0.12, C2 = 0.03			
Implants				
Cage	22,000	0.3	C3D4	
Internal fixation	110,000	0.3	C3D4	

(*E represents Young's modulus and ν represents the Poisson's ratio).

TABLE 2 Material properties, element type, number, and cross-sectional area of the ligaments in the FE model.

Ligament	E1*[Mpa]	E2* [Mpa]	ε12**	Element type (number)	Area [mm^2]	Reference
Anterior Longitudinal Ligament	7.8	20.0	0.12	T3D2 (7)	32.4	Moramarco et al. (2010)
Posterior Longitudinal Ligament	1.0	2.0	0.11	T3D2 (6)	5.2	
Ligamentum Flavum	1.5	1.5	0.06	T3D2 (3)	84.2	
Intertransverse Ligament	10.0	59.0	0.18	T3D2 (3)	1.8	Chazal et al. (1985)
Supraspinous Ligament	3.0	5.0	0.2	T3D2 (4)	25.2	
Interspinous Ligament	13.2	42.6	0.15	T3D2 (4)	35.1	
Ligament	E [Mpa]	ν	Element type (number)		Area [mm2]	Reference
Capsular Ligament	24.4	0.3	T3D2 (6)		23.8	Tyndyka et al. (2007)

(*E1 denotes the Young's modulus of the first phase and E2 denotes the Young's modulus of the second phase; ε12** denotes the strain transition between two bilinear moduli E_1 and E_2.).

was implanted. In the OLIF + Unilateral Pedicle Screw (OLIF + UPS) model, while implanting a fusion cage in the intervertebral space, screws were implanted in one side of the pedicle, and the upper and lower screws were connected by connecting rods. In the OLIF + Double row vertical screw (OLIF + DRVS) model, while implanting a fusion cage in the intervertebral space, double row screws were implanted in the lateral vertebral body, which was connected by connecting rods. At the same time, a transverse connection was added at the level of the intervertebral disc to connect the bilateral connecting rods. In the OLIF + Unilateral Vertebral Screw - Pedicle Screw (OLIF + UVS-PS) model, a fusion cage was implanted in the intervertebral space, screws were implanted in one side of the pedicle, and screws were implanted in the same side of the vertebral body. The pedicle screws and vertebral screws were connected by connecting rods, respectively. In the OLIF + Bilateral Pedicle Screws (OLIF + BPS) model, a fusion cage was implanted in the intervertebral space, screws were implanted in both pedicle screws, and the upper and lower screws were connected by connecting rods.

Definition of the properties of the materials

Linear elastic material models were used for the bony tissues. Facet cartilage and intervertebral discs were modeled using Neo-Hookean and Mooney-Rivlin hyperelastic materials (Du et al., 2014; Cai et al., 2020; Cai et al., 2022; Liu et al., 2022). The nucleus pulposus constituted 50% of the disc and the cortical bone thickness was 0.5 mm (Cai et al., 2022; Zhang et al., 2022). The material parameters of the tissue model are shown in Table 1. The material used in the cage is Poly ether ether ketone (PEEK), and the material used for internal fixation is titanium alloy. Linear elastic material models were used for the spinal cage

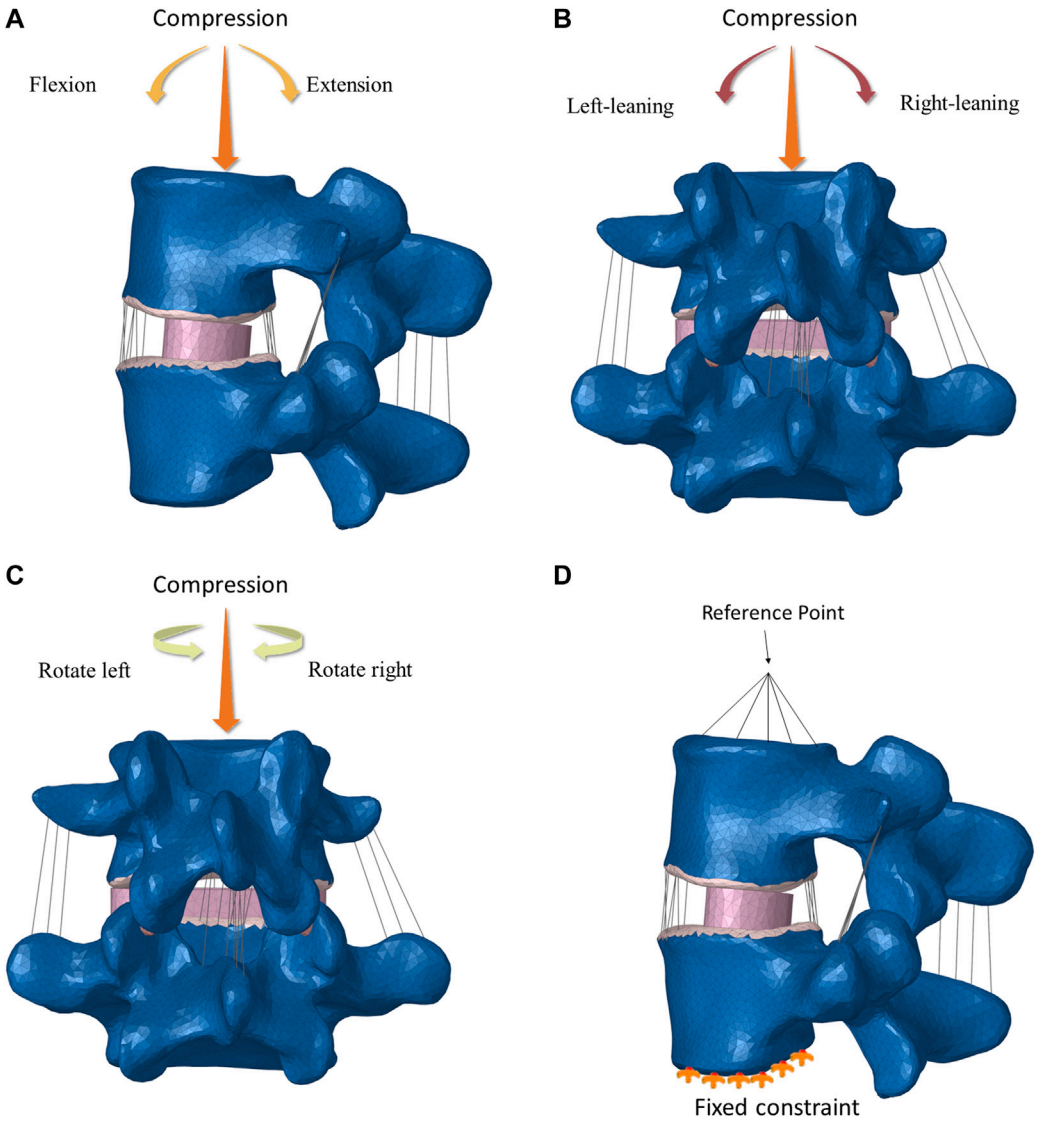

FIGURE 2
Six activity directions and boundary conditions.

and internal fixation components. Therefore, an elastic modulus of 22000 MPa and Poisson's ratio of 0.3 were defined for the cage, and an elastic modulus of 110000 MPa and Poisson's ratio of 0.3 were defined for internal fixation. All ligaments were meshed using tension truss elements (T3D2). Based on literature data, the bilinear elastic material model described the mechanical behavior of ALL, PLL, LF, ITL, SSL, and ISL, while the linear elastic material model described the mechanical behavior of CL. (Table 2).

The setting of the loading and boundary conditions

In the FE L4-L5 spinal fixation models, the spinal cage was fully constrained to its adjacent bony parts. The screws were fully constrained to their surrounding bone tissues, and the connecting bars and screws were also fully constrained to each other. Six loading scenarios (flexion and extension, leaning-left and leaning-right, rotate right and rotate left) were simulated in the FE L4-L5 spinal fixation models to mimic the daily activities (Figure 2). In all the loading scenarios, a vertically downward load of 200.0 N was applied in the model to simulate the body weight. Boundary conditions were established to fix the lower surface of L5, a reference point was established at the center of the upper surface of L4, the reference point was coupled with the upper surface, a torque of 5 N m and a concentrated force perpendicular to the upper surface of the vertebral body of 200 N were applied to the reference point, and the forces on the spine were jointly simulated. After the settings were applied, the results were calculated.

IO model has 232,411 nodes and 1424600 elements. OLIF + UPS model has 228,770 nodes and 1393400 elements. OLIF + DRVS

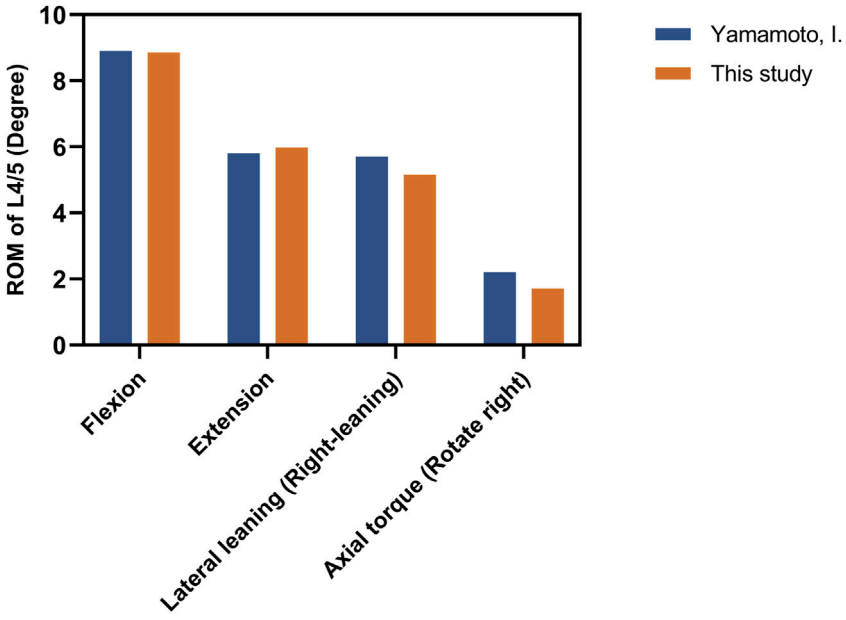

FIGURE 3
The comparision of ROM between the intact model and the previous *in vitro* experimental study. (Unit:degree).

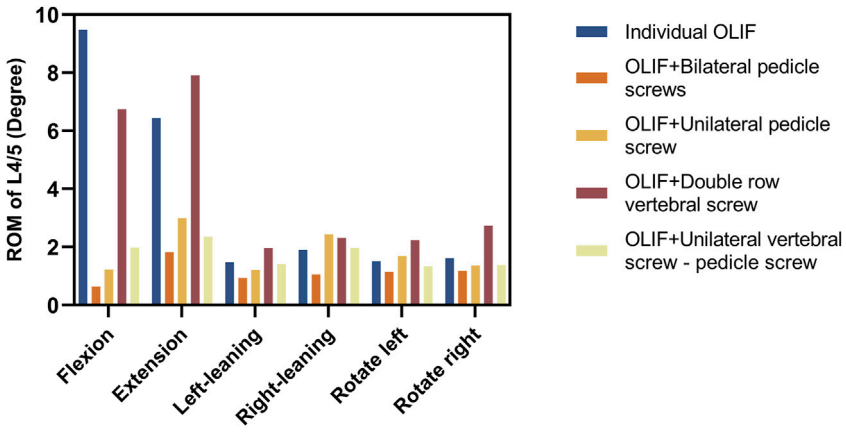

FIGURE 4
The ranges of motion (ROM) of fusion segments (Unit:degree).

model has 232,840 nodes and 1415121 elements. OLIF + UVS-PS model has 229,094 nodes and 1390833 elements. OLIF + BPS model has 242,659 nodes and 1808364 elements. The mesh size of bones ranges from 0.5 to 2.5. The mesh size of the cage ranges from 1.2 to 4.5. The mesh size of the screw ranges from 0.5 to 2.5.

Results

Validation of the FE spinal model

Apply 10 N m to our model and compare the ROM of fused segments with cadaver studies (Yamamoto et al., 1989). Our results fall within the range of variation, demonstrating our model's reliability (Figure 3).

Ranges of motion (ROM) of the fused spinal segment

The ultimate goal of OLIF surgery is to make the fusion segment as a whole part, and thus the angle of vertebral body movement can directly reflect the effectiveness of the surgery. The ROM of the fused segment is expressed as an angle, which directly reflects the stability of the fused segment. The less ROM, the more stable of fusion segment and the less risk of complication (Cai et al., 2022). The

TABLE 3 The ROM of fusion segments (Unit: degree).

Name	Flexion	Extension	Left-leaning	Right-leaning	Rotate left	Rotate right
Individual OLIF	9.48	6.44	1.47	1.90	1.51	1.61
OLIF + Bilateral pedicle screws	0.64	1.82	0.93	1.05	1.14	1.18
OLIF + Unilateral pedicle screw	1.22	2.99	1.20	2.44	1.69	1.36
OLIF + Double row vertebral screw	6.74	7.91	1.96	2.31	2.24	2.73
OLIF + Unilateral vertebral screw - pedicle screw	1.98	2.35	1.40	1.97	1.33	1.38

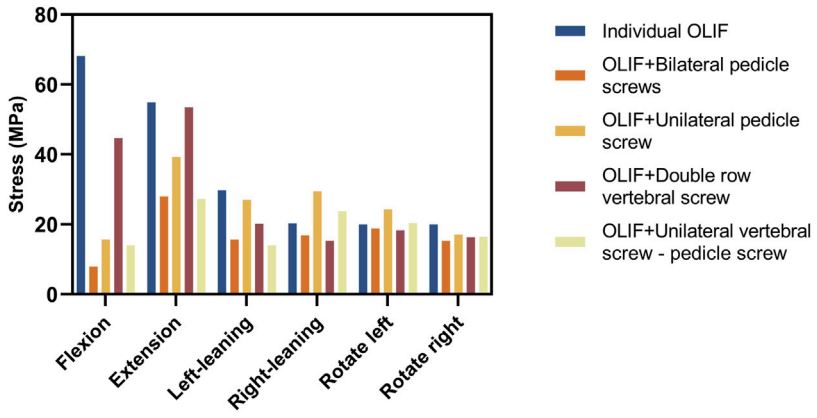

FIGURE 5
Maximum von Mises stresses distributed on the cage (Unit: MPa).

ROM of the surgical model under a combined load of 200 N and 5 N m is shown in Figure 4 and Table 3. In the flexion group, the ROM of IO was 9.48°, and the ROM of OLIF + DRVS was 6.74°. In the backward bending group, the ROM of IO was 6.44°, and the ROM of OLIF + DRVS was 7.91°. These four data are significantly greater than the data of other models in various motion directions. OLIF + BPS has a maximum ROM of 1.82° during backward bending and has the smallest ROM in all directions of motion. OLIF + UPS is similar to OLIF + UVS-PS, and both models are slightly inferior to OLIF + BPS overall, but the difference is not very significant.

Distribution of the von mises stress in the cage and internal fixations

The greater the stress distributed on the fusion cage and internal fixation, the higher the likelihood of complications is to occur, such as cage settlement, endplate collapse, fractures, and screw loosening and fracture (Villa et al., 2014; Singhatanadgige et al., 2021; Qin et al., 2022). The distribution of the von Mises stress on the Cage is shown in Figures 5, 6; Table 4. In the flexion group, the von Mises stress of IO was 68.15 MPa, and of OLIF + DRVS was 44.64 MPa. In the backward bending group, the von Mises stress of IO was 54.07 MPa, and of OLIF + DRVS was 53.42 MPa. These four data are significantly greater than the data of other models in various motion directions. The data of OLIF + BPS and OLIF + UVS-PS are similar and are less than others. The average stress on every motion direction of OLIF + BPS is about 17.08 MPa and of OLIF + UVS-PS is about 19.29 MPa.

The distribution of the von Mises stress on the internal fixation is shown in Figures 7, 8; Table 5. In flexion and posterior extension, the maximum internal fixation stresses on OLIF + DRVS and OLIF + UVS-PS were significantly greater than those in the other models. OLIF + DRVS had the maximum internal fixator stress in forward bending (155.9 MPa), and OLIF + UVS-PS had the maximum internal fixator stress in posterior backward bending (105.8 MPa). OLIF + BPS had the maximum internal fixator stress in left rotation (31.85 MPa), and OLIF + UPS had the maximum internal fixator stress in posterior extension (76.59 MPa). The data of these two models were smaller than in the other models.

Discussion

This study aims to identify an OLIF supplementary internal fixation method that can provide the best spinal stability. In the present study, the biomechanical stability of the L4-L5 spinal segment using different fixations was investigated using FE analysis. Five different models, e.g., OLIF + DRVS, OLIF + UPS, IO, OLIF + BPS, OLIF + UVS-PS, were simulated and the ROM of the fused spinal segment and stress distribution in the cage and internal fixations were investigated (Cai et al., 2022). All intervertebral discs in the figures have been replaced by fusion cages.

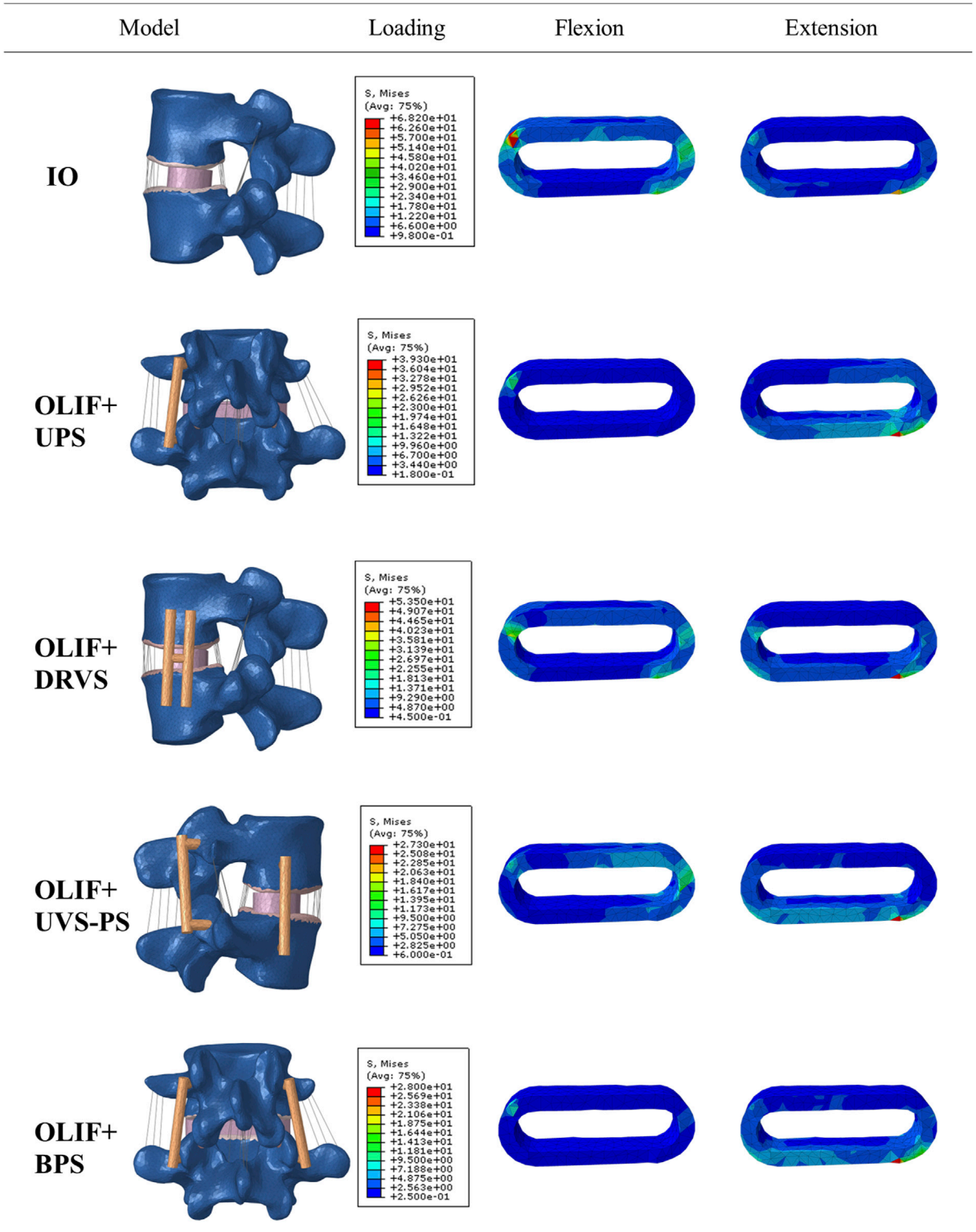

FIGURE 6
Cloud map of stress distribution in the fusion device during flexion and extension.

By comparing the ROM of different models, we found that OLIF + BPS has the least ROM in each motion mode. On the one hand, this indicates that OLIF + BPS provides a more stable load-sharing on the fusion, facilitates bone healing or fusion, and has the most stable fusion-vertebral body interface, reducing the likelihood of complications such as fusion loosening. On the other hand, the IO and OLIF + DRVS had the greatest ROM in flexion and extension motion compared to all surgical models. This implies that postoperative patients who accept one

10.3389/fbioe.2023.1260693

TABLE 4 The maximum stress of the cage (Unit: MPa).

Name	Flexion	Extension	Left-leaning	Right-leaning	Rotate left	Rotate right
Individual OLIF	68.15	54.87	29.72	20.29	19.98	19.99
OLIF + Bilateral pedicle screws	7.919	27.98	15.65	16.85	18.82	15.29
OLIF + Unilateral pedicle screw	15.63	39.23	26.96	29.42	24.24	17.11
OLIF + Double row vertebral screw	44.64	53.42	20.16	15.33	18.27	16.31
OLIF + Unilateral vertebral screw - pedicle screw	13.99	27.22	13.96	23.7	20.37	16.52

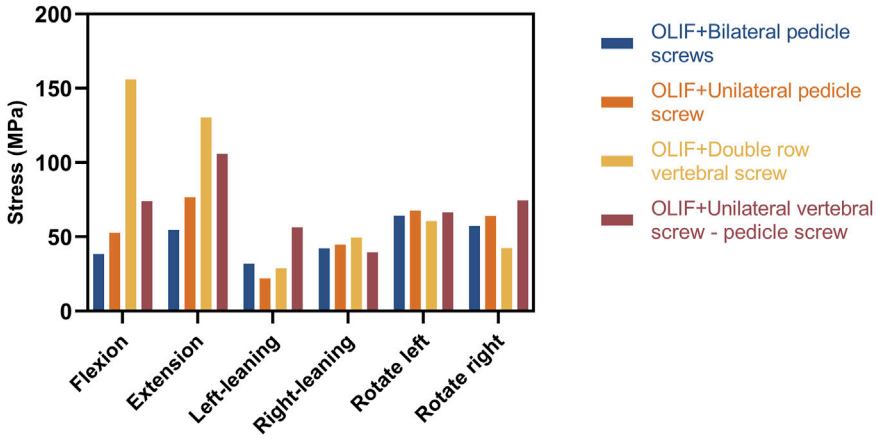

FIGURE 7
Maximum von Mises stresses distributed on the internal fixation sytem (Unit: MPa).

of these two operations are more likely to experience pain due to lumbar instability. The excessive motion indicates a weaker fusion-vertebral body interface, increasing the risk of cage loosening, displacement, or even prolapse.

The maximum stress on the IO and OLIF + DRVS fusion cages during flexion and extension is significantly greater than that on OLIF + BPS and OLIF + UVS-PS. This indicates that IO and OLIF + DRVS are more prone to fusion cage settlement compared to OLIF + BPS and OLIF + UVS-PS. This result is consistent with the study by Guofang Fang et al. They found that OLIF + BPS can reduce the maximum stress on the endplate, thereby reducing the incidence of cage settlement. Compared to OLIF + BPS, the IO method of OLIF surgery generates more pressure, especially in terms of extension and flexion, which may be a potential risk factor for cage settlement (Fang et al., 2020). In addition, in our study, the maximum stress on the fusion cage during forward flexion and backward extension is significantly greater than in other directions, mostly occurring in the upper front or lower back. This indicates that the fusion cage is more likely to enter the vertebral body in an inclined posture (Figure 6). This is consistent with the research results of Fang, G. et al. (Fang et al., 2020). The maximum cage stress in the OLIF + UPS was less than that in the IO and OLIF + DRVS, but greater than that in OLIF + BPS and OLIF + UVS-PS. Under different motion loads, the cage was less stressed in the OLIF + BPS and OLIF + UVS-PS. Only in flexion and rotating right, the maximum cage stress was greater in OLIF + UVS-PS than in OLIF + BPS. In the rest of the motion loads, the maximum cage stress was similar in both internal fixation methods, indicating a lower likelihood of cage subsidence in both models.

The maximum internal fixation stresses for OLIF + UVS-PS were significantly greater in flexion, extension, and rotating left compared to the other models, except for OLIF + DRVS. These results indicate that the components of OLIF + DRVS and OLIF + UVS-PS are more likely to fracture. The maximum internal fixation stresses for OLIF + UPS and OLIF + BPS were smaller and similar in all motion directions. The maximum internal fixator stress of OLIF + BPS was greater than that of OLIF + UPS only in left rotating. Therefore, OLIF + BPS is the least likely to experience a component fracture due to metal fatigue, followed by OLIF + UPS. These findings are consistent with the study by Cai, X. Y. et al., where the maximum stress of OLIF + DRVS was significantly greater than that of OLIF + UPS and OLIF + BPS (Cai et al., 2022).

The performance of the ROM and maximum stresses of OLIF + BPS were better than the other models under the same loading conditions. This indicates that OLIF + BPS can limit the movement of the surgical segment, share the stress of the fusion and endplate, maintain the effect of indirect decompression after OLIF, and further improve its stability with significant biomechanical advantages. However, OLIF + BPS cannot be performed in a single position and requires intraoperative changes in the patient's position. OLIF + UPS were slightly less effective than OLIF + BPS in terms of internal fixation, but still provided good biomechanical stability in all directions of motion and did not require intraoperative changes in the patient's position. OLIF + UVS-PS is inferior to OLIF +

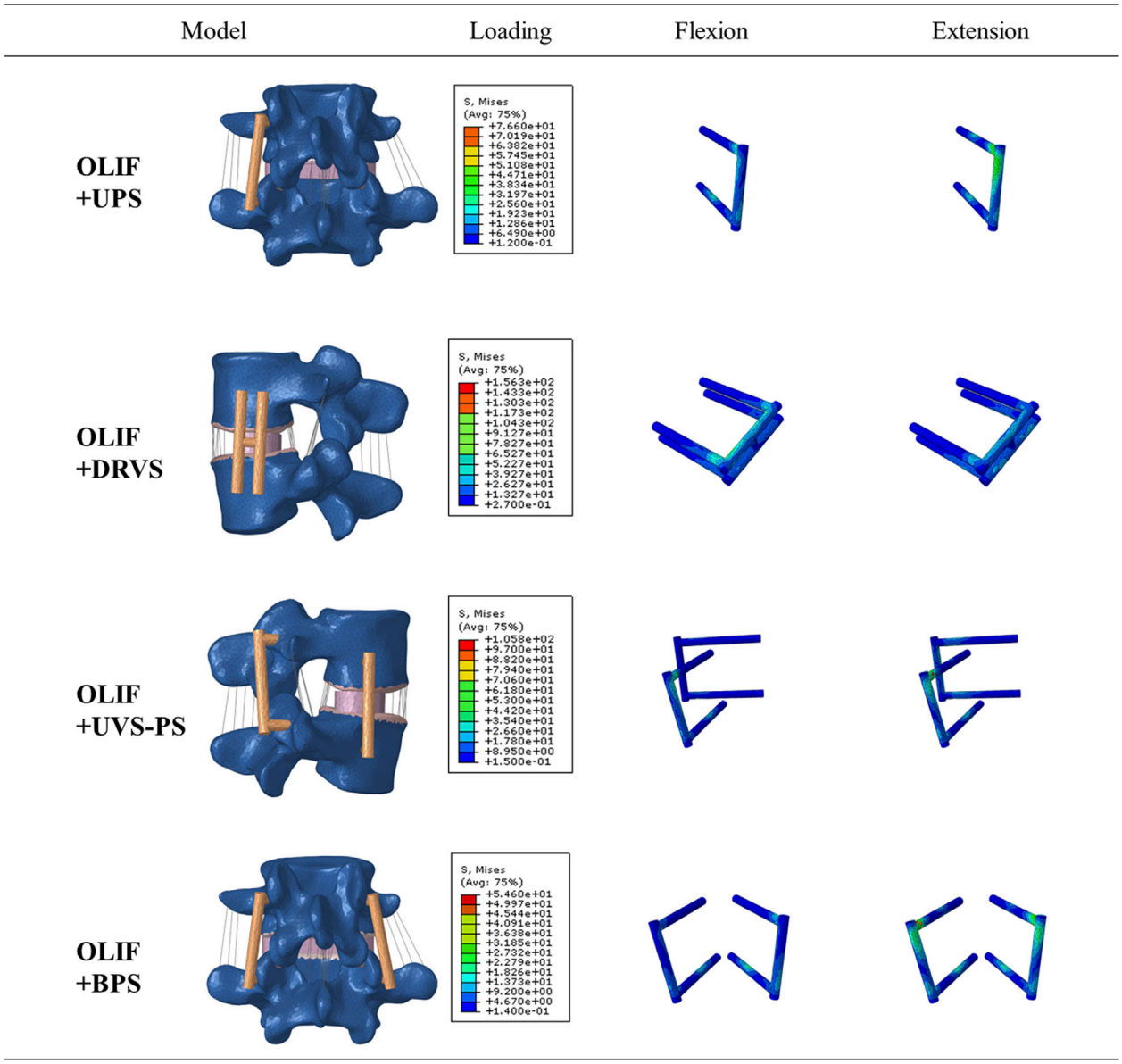

FIGURE 8
Internal fixation strss distribution cloud map during flexion and extension.

TABLE 5 Maximum stress on the internal fixation system (Unit: MPa).

Name	Flexion	Extension	Left-leaning	Right-leaning	Rotate left	Rotate right
OLIF + Bilateral pedicle screws	38.49	54.56	31.85	42.24	64.2	57.26
OLIF + Unilateral pedicle screw	52.82	76.59	21.98	44.78	67.52	64.13
OLIF + Double row vertebral screw	155.9	130.2	28.82	49.74	60.66	42.49
OLIF + Unilateral vertebral screw - pedicle screw	73.88	105.8	56.38	39.61	66.37	74.58

UPS in terms of internal fixation stress, patient economic burden, and surgical procedure. Moreover, the vertebral screws of OLIF + UVS-PS were only subjected to a small amount of stress, which indicates that vertebral screws may not be necessary (Figure 8). The ROM and maximum fusion stresses of IO and OLIF + DRVS are inferior to those of the other models, which indicates that the incidence of fusion subsidence and vertebral instability may be higher in these two models than in the other models. Only one of the two vertebral screws in OLIF + DRVS was significantly stressed, and the crossbeam was almost unstressed, which indicates that it may not be necessary to add two

vertebral screws to the vertebral body and connect them through the crossbeam (Figure 8).

Although the present study comprehensively investigated different implantation methods, some limitations should be acknowledged. First, only the FE analysis is performed in the present study and no cadaver study was performed, which may result in conclusions deviating from the actual situation. Second, this study did not simulate soft tissues except for the ligaments and intervertebral discs such as muscles, fascia, and fat. These soft tissues provide slight traction due to their elasticity. However, currently, there is no evidence to prove that this traction force affects the biomechanical stability after lumbar surgery. What's more, it is conventionally believed that early postoperative lumbar spine surgery often requires limiting lumbar muscle activity. Therefore, even without simulating soft tissues like muscles, the results will not be affected (Williamson et al., 2007). Third, simplified FE models of the cage and screw are used in the present study. However, the texture on the surface of the fusion device and the thread of the screw do not affect the overall mechanical performance, so removing the texture on their surface will not affect the results of this study. In summary, further experimental research on cadaveric biomechanics is still necessary for future investigations. Despite these limitations, our research findings can still assist spinal surgeons in selecting the most suitable fixation strategy in clinical practice.

Conclusion

It is concluded from the present study that OLIF + BPS has the best biomechanical stability, but it requires changing the patient's position during the surgery, which reduces the simplicity of the surgery. OLIF + UPS provides adequate biomechanical stability. OLIF + UVS-PS is inferior to OLIF + UPS in terms of internal fixation stress, patient economic burden, and surgical procedure. IO and OLIF + DRVS do not have significant advantages in biomechanical stability, and may only be of value in exceptional circumstances. Based on the biomechanical analysis, OLIF + BPS is recommended for OLIF surgery. OLIF + UPS can be used as an alternative.

Data availability statement

The original contributions presented in the study are included in the article/Supplementary material, further inquiries can be directed to the corresponding author.

Ethics statement

The studies involving humans were approved by the Ethics Committee of Dalian Central Hospital. The studies were conducted in accordance with the local legislation and institutional requirements. The participants provided their written informed consent to participate in this study. Written informed consent was obtained from the individual(s) for the publication of any potentially identifiable images or data included in this article.

Author contributions

JH: Writing–original draft. XT: Writing–original draft. NJ: Writing–review and editing. HW: Writing–review and editing. JJ: Writing–review and editing.

Funding

The authors declare financial support was received for the research, authorship, and/or publication of this article. This research was funded by the Guangdong Medical Science and Technology Research Fund Project, grant number A2020417; Guangzhou Science and Technology Plan Project, grant number 202102020033; Natural Science Foundation of Liaoning Province, 2022-MS-443.

Conflict of interest

The authors declare that the research was conducted in the absence of any commercial or financial relationships that could be construed as a potential conflict of interest.

Publisher's note

All claims expressed in this article are solely those of the authors and do not necessarily represent those of their affiliated organizations, or those of the publisher, the editors and the reviewers. Any product that may be evaluated in this article, or claim that may be made by its manufacturer, is not guaranteed or endorsed by the publisher.

References

Abe, K., Orita, S., Mannoji, C., Motegi, H., Aramomi, M., Ishikawa, T., et al. (2017). Perioperative complications in 155 patients who underwent oblique lateral interbody fusion surgery: perspectives and indications from a retrospective, multicenter survey. *Spine (Phila Pa 1976)* 42 (1), 55–62. doi:10.1097/brs.0000000000001650

Aleinik, A. Y., Mlyavykh, S. G., and Qureshi, S. (2021). Lumbar spinal fusion using lateral oblique (Pre-psoas) approach (review). *Sovrem. Tekhnologii Med.* 13 (5), 70–81. doi:10.17691/stm2021.13.5.09

Alimi, M., Hofstetter, C. P., Cong, G. T., Tsiouris, A. J., James, A. R., Paulo, D., et al. (2014). Radiological and clinical outcomes following extreme lateral interbody fusion. *J. Neurosurg. Spine* 20 (6), 623–635. doi:10.3171/2014.1.spine13569

Bereczki, F., Turbucz, M., Kiss, R., Eltes, P. E., and Lazary, A. (2021). Stability evaluation of different oblique lumbar interbody fusion constructs in normal and osteoporotic condition - a finite element based study. *Front. Bioeng. Biotechnol.* 9, 749914. doi:10.3389/fbioe.2021.749914

Burstein, A. H., Reilly, D. T., and Martens, M. (1976). Aging of bone tissue: mechanical properties. *J. Bone Joint Surg. Am.* 58 (1), 82–86.

Cai, X. Y., Bian, H. M., Chen, C., Ma, X. L., and Yang, Q. (2022). Biomechanical study of oblique lumbar interbody fusion (OLIF) augmented with different types of instrumentation: a finite element analysis. *J. Orthop. Surg. Res.* 17 (1), 269. doi:10.1186/s13018-022-03143-z

Cai, X. Y., Sun, M., Huang, Y., Liu, Z., Liu, C., Du, C., et al. (2020). Biomechanical effect of L ₄ –L ₅ intervertebral disc degeneration on the lower lumbar spine: A finite element study. *Orthop. Surg.* 12 (3), 917–930. doi:10.1111/os.12703

Cappuccino, A., Cornwall, G. B., Turner, A. W. L., Fogel, G. R., Duong, H. T., Kim, K. D., et al. (2010). Biomechanical analysis and review of lateral lumbar fusion constructs. *Spine (Phila Pa 1976)* 35 (26), S361–S367. doi:10.1097/brs.0b013e318202308b

Chazal, J., Tanguy, A., Bourges, M., Gaurel, G., Escande, G., Guillot, M., et al. (1985). Biomechanical properties of spinal ligaments and a histological study of the supraspinal ligament in traction. *J. Biomechanics* 18 (3), 167–176. doi:10.1016/0021-9290(85)90202-7

Du, C., Mo, Z., Tian, S., Wang, L., Fan, J., Liu, S., et al. (2014). Biomechanical investigation of thoracolumbar spine in different postures during ejection using a combined finite element and multi-body approach. *Int. J. Numer. Method Biomed. Eng.* 30 (11), 1121–1131. doi:10.1002/cnm.2647

Fang, G., Lin, Y., Wu, J., Cui, W., Zhang, S., Guo, L., et al. (2020). Biomechanical comparison of stand-alone and bilateral pedicle screw fixation for oblique lumbar interbody fusion surgery-A finite element analysis. *World Neurosurg.* 141, e204–e212. doi:10.1016/j.wneu.2020.05.245

Grant, J. P., Oxland, T. R., and Dvorak, M. F. (2001). Mapping the structural properties of the lumbosacral vertebral endplates. *Spine (Phila Pa 1976)* 26 (8), 889–896. doi:10.1097/00007632-200104150-00012

Huang, S., Min, S., Wang, S., and Jin, A. (2022). Biomechanical effects of an oblique lumbar interbody fusion combined with posterior augmentation: a finite element analysis. *BMC Musculoskelet. Disord.* 23 (1), 611. doi:10.1186/s12891-022-05553-w

Joseph, J. R., Smith, B. W., La Marca, F., and Park, P. (2015). Comparison of complication rates of minimally invasive transforaminal lumbar interbody fusion and lateral lumbar interbody fusion: a systematic review of the literature. *Neurosurg. Focus* 39 (4), E4. doi:10.3171/2015.7.focus15278

Kim, M. C., Chung, H. T., Cho, J. L., Kim, D. J., and Chung, N. S. (2013). Subsidence of polyetheretherketone cage after minimally invasive transforaminal lumbar interbody fusion. *J. Spinal Disord. Tech.* 26 (2), 87–92. doi:10.1097/bsd.0b013e318237b9b1

Kim, S. M., Lim, T. J., Paterno, J., Park, J., and Kim, D. H. (2005). Biomechanical comparison: stability of lateral-approach anterior lumbar interbody fusion and lateral fixation compared with anterior-approach anterior lumbar interbody fusion and posterior fixation in the lower lumbar spine. *J. Neurosurg. Spine* 2 (1), 62–68. doi:10.3171/spi.2005.2.1.0062

Kornblum, M. B., Turner, A. W., Cornwall, G. B., Zatushevsky, M. A., and Phillips, F. M. (2013). Biomechanical evaluation of stand-alone lumbar polyether-ether-ketone interbody cage with integrated screws. *Spine J.* 13 (1), 77–84. doi:10.1016/j.spinee.2012.11.013

Lindahl, O. (1976). Mechanical properties of dried defatted spongy bone. *Acta Orthop. Scand.* 47 (1), 11–19. doi:10.3109/17453677608998966

Liu, C., Wang, J., and Zhou, Y. (2019). Perioperative complications associated with minimally invasive surgery of oblique lumbar interbody fusions for degenerative lumbar diseases in 113 patients. *Clin. Neurol. Neurosurg.* 184, 105381. doi:10.1016/j.clineuro.2019.105381

Liu, Z. X., Gao, Z. W., Chen, C., Cai, X. Y., and Ren, Y. N. (2022). Effects of osteoporosis on the biomechanics of various supplemental fixations co-applied with oblique lumbar interbody fusion (OLIF): a finite element analysis. *BMC Musculoskelet. Disord.* 23 (1), 794. doi:10.1186/s12891-022-05645-7

Lu, T., and Lu, Y. (2019). Comparison of biomechanical performance among posterolateral fusion and transforaminal, extreme, and oblique lumbar interbody fusion: A finite element analysis. *World Neurosurg.* 129, e890–e899. doi:10.1016/j.wneu.2019.06.074

Malham, G. M., Parker, R. M., Blecher, C. M., and Seex, K. A. (2015). Assessment and classification of subsidence after lateral interbody fusion using serial computed tomography. *J. Neurosurg. Spine* 23 (5), 589–597. doi:10.3171/2015.1.spine14566

Mayer, H. M. (1997). A new microsurgical technique for minimally invasive anterior lumbar interbody fusion. *Spine (Phila Pa 1976)* 22 (6), 691–699. doi:10.1097/00007632-199703150-00023

Mobbs, R. J., Phan, K., Malham, G., Seex, K., and Rao, P. J. (2015). Lumbar interbody fusion: techniques, indications and comparison of interbody fusion options including PLIF, TLIF, MI-TLIF, OLIF/ATP, LLIF and ALIF. *J. Spine Surg.* 1 (1), 2–18. doi:10.3978/j.issn.2414-469X.2015.10.05

Moramarco, V., Pérez del Palomar, A., Pappalettere, C., and Doblaré, M. (2010). An accurate validation of a computational model of a human lumbosacral segment. *J. Biomech.* 43 (2), 334–342. doi:10.1016/j.jbiomech.2009.07.042

Niemeyer, T. K., Koriller, M., Claes, L., Kettler, A., Werner, K., and Wilke, H. J. (2006). *In vitro* study of biomechanical behavior of anterior and transforaminal lumbar interbody instrumentation techniques. *Neurosurgery* 59 (6), 1271–1277. doi:10.1227/01.neu.0000245609.01732.e4

Oh, K. W., Lee, J. H., Lee, J. H., Lee, D. Y., and Shim, H. J. (2017). The correlation between cage subsidence, bone mineral density, and clinical results in posterior lumbar interbody fusion. *Clin. Spine Surg.* 30 (6), E683–e689. doi:10.1097/bsd.0000000000000315

Pham, M. H., Jakoi, A. M., and Hsieh, P. C. (2016). Minimally invasive L5-S1 oblique lumbar interbody fusion with anterior plate. *Neurosurg. Focus* 41, 1. doi:10.3171/2016.2.focusvid.1692

Qin, Y., Zhao, B., Yuan, J., Xu, C., Su, J., Hao, J., et al. (2022). Does cage position affect the risk of cage subsidence after oblique lumbar interbody fusion in the osteoporotic lumbar spine: A finite element analysis. *World Neurosurg.* 161, e220–e228. doi:10.1016/j.wneu.2022.01.107

Quillo-Olvera, J., Lin, G. X., Jo, H. J., and Kim, J. S. (2018). Complications on minimally invasive oblique lumbar interbody fusion at L2-L5 levels: a review of the literature and surgical strategies. *Ann. Transl. Med.* 6 (6), 101. doi:10.21037/atm.2018.01.22

Shasti, M., Koenig, S. J., Nash, A. B., Bahrami, S., Jauregui, J. J., O'Hara, N. N., et al. (2019). Biomechanical evaluation of lumbar lateral interbody fusion for the treatment of adjacent segment disease. *Spine J.* 19 (3), 545–551. doi:10.1016/j.spinee.2018.09.002

Shirazi-Adl, A., Ahmed, A. M., and Shrivastava, S. C. (1986). Mechanical response of a lumbar motion segment in axial torque alone and combined with compression. *Spine (Phila Pa 1976)* 11 (9), 914–927. doi:10.1097/00007632-198611000-00012

Silvestre, C., Mac-Thiong, J. M., Hilmi, R., and Roussouly, P. (2012). Complications and morbidities of mini-open anterior retroperitoneal lumbar interbody fusion: oblique lumbar interbody fusion in 179 patients. *Asian Spine J.* 6 (2), 89–97. doi:10.4184/asj.2012.6.2.89

Singhatanadgige, W., Sukthuayat, A., Tanaviriyachai, T., Kongtharvonskul, J., Tanasansomboon, T., Kerr, S. J., et al. (2021). Risk factors for polyetheretherketone cage subsidence following minimally invasive transforaminal lumbar interbody fusion. *Acta Neurochir. (Wien)* 163 (9), 2557–2565. doi:10.1007/s00701-021-04923-y

Tempel, Z. J., McDowell, M. M., Panczykowski, D. M., Gandhoke, G. S., Hamilton, D. K., Okonkwo, D. O., et al. (2018). Graft subsidence as a predictor of revision surgery following stand-alone lateral lumbar interbody fusion. *J. Neurosurg. Spine* 28 (1), 50–56. doi:10.3171/2017.5.spine16427

Tyndyka, M. A., Barron, V., McHugh, P. E., and O'Mahoney, D. (2007). Generation of a finite element model of the thoracolumbar spine. *Acta Bioeng. Biomech.* 9 (1), 35–46.

Villa, T., La Barbera, L., and Galbusera, F. (2014). Comparative analysis of international standards for the fatigue testing of posterior spinal fixation systems. *Spine J.* 14 (4), 695–704. doi:10.1016/j.spinee.2013.08.032

Williamson, E., White, L., and Rushton, A. (2007). A survey of post-operative management for patients following first time lumbar discectomy. *Eur. Spine J.* 16 (6), 795–802. doi:10.1007/s00586-006-0207-8

Xu, D. S., Walker, C. T., Godzik, J., Turner, J. D., Smith, W., and Uribe, J. S. (2018). Minimally invasive anterior, lateral, and oblique lumbar interbody fusion: a literature review. *Ann. Transl. Med.* 6 (6), 104. doi:10.21037/atm.2018.03.24

Yamamoto, I., Panjabi, M. M., Crisco, T., and Oxland, T. (1989). Three-dimensional movements of the whole lumbar spine and lumbosacral joint. *Spine (Phila Pa 1976)* 14 (11), 1256–1260. doi:10.1097/00007632-198911000-00020

Zhang, S., Liu, Z., Lu, C., Zhao, L., Feng, C., Wang, Y., et al. (2022). Oblique lateral interbody fusion combined with different internal fixations for the treatment of degenerative lumbar spine disease: a finite element analysis. *BMC Musculoskelet. Disord.* 23 (1), 206. doi:10.1186/s12891-022-05150-x

frontiers | Frontiers in Bioengineering and Biotechnology

TYPE Original Research
PUBLISHED 26 September 2023
DOI 10.3389/fbioe.2023.1243936

OPEN ACCESS

EDITED BY
Zhenxian Chen,
Chang'an University, China

REVIEWED BY
Zikai Hua,
Orthotic Laboratory, China
Jingyu Zhang,
Tianjin Hospital, China

*CORRESPONDENCE
Wei Guo,
bonetumor@163.com
Yu Guo,
tezuka1989@126.com

RECEIVED 21 June 2023
ACCEPTED 11 September 2023
PUBLISHED 26 September 2023

CITATION
Wu H, Guo Y and Guo W (2023), Effect of carbon-fiber-reinforced polyetheretherketone on stress distribution in a redesigned tumor-type knee prosthesis: a finite element analysis. *Front. Bioeng. Biotechnol.* 11:1243936. doi: 10.3389/fbioe.2023.1243936

Effect of carbon-fiber-reinforced polyetheretherketone on stress distribution in a redesigned tumor-type knee prosthesis: a finite element analysis

Han Wu[1,2], Yu Guo[1,2]* and Wei Guo[1,2]*

[1]Department of Musculoskeletal Tumor, People's Hospital, Peking University, Beijing, China, [2]Beijing Key Laboratory of Musculoskeletal Tumor, Beijing, China

Background: Surgery for bone tumors around the knee often involves extensive resection, making the subsequent prosthetic reconstruction challenging. While carbon fiber-reinforced polyetheretherketone (CF-PEEK) has been widely used in orthopedic implants, its application in tumor-type prosthesis is limited. This study aims to evaluate the feasibility of using 30wt% and 60wt% carbon fiber-reinforced polyetheretherketone (CF30-PEEK and CF60-PEEK) as materials for a redesigned tumor-type knee prosthesis through numerical analysis.

Methods: A knee joint model based on CT data was created, and the resection and prosthetic reconstruction were simulated. Three finite element models of the prostheses, representing the initial and updated designs with CoCrMo and CFR-PEEK components, were constructed. Loading conditions during standing and squatting were simulated with forces of 700 N and 2800 N, respectively. Finite element analysis was used to analyze the von Mises stress and stability of all components for each prosthesis type.

Results: After improvements in both material and design, the new Type 3 prosthesis showed significantly lower overall stress with stress being evenly distributed. Compared with the initial design, the maximum von Mises stress in Type 3 was reduced by 53.9% during standing and 74.2% during squatting. In the standing position, the maximum stress in the CF30-PEEK femoral component decreased by 57.3% compared with the initial design which was composed of CoCrMo, while the stress in the CF60-PEEK cardan shaft remained consistent. In the squatting position, the maximum stress in the femoral component decreased by 81.9%, and the stress in the cardan shaft decreased by 46.5%.

Conclusion: The incorporation of CF30-PEEK effectively transmits forces and reduces stress concentration on the femoral component, while CF60-PEEK in the redesigned cardan shaft significantly reduces stress while maintaining stiffness. The redesigned prosthesis effectively conducts loading force and demonstrates favorable biomechanical characteristics, indicating the promising potential of utilizing CF30-PEEK and CF60-PEEK materials for tumor-type knee prostheses. The findings of this study could provide novel insights for the design and development of tumor-type knee prostheses.

KEYWORDS

tumor-type prosthesis, prosthetic reconstruction, carbon-fiber-reinforced polyetheretherketone, finite element analysis, stress distribution

1 Introduction

Aggressive bone and soft tissue tumors around the knee often require extensive surgical resection, and functional reconstruction with tumor-type knee prosthesis. The limitations of widely used metallic materials in orthopedic prostheses, such as titanium alloys and CoCrMo, have been highlighted in numerous studies. The most common drawbacks are the heavy weight due to high density, and the significant difference in elastic modulus between the metal implants (ranging from 100 to 200 GPa) and human bones (3–20 GPa). The modulus mismatch, also known as the stress shielding effect, can lead to small fractures, aseptic loosening, and ultimately implant failure (Sumner, 2015). Additionally, certain metal ions released by wear particles are toxic to bone and tissue cells, causing inflammation in adjacent tissues (Okazaki and Gotoh, 2005; Scharf et al., 2014; Armstead et al., 2017). Therefore, updating the materials used for prosthetic fabrication is crucial.

Implants that offer suitable mechanical properties, excellent wear resistance, and low cytotoxicity form the basis for successful osteointegration. Carbon/polymer composites have gained significant interest due to their exceptional mechanical properties. Among these composites, carbon-fiber-reinforced polyetheretherketone (CF-PEEK) has been extensively studied in orthopedics over the past few decades, following the successful utilization of pure polyetheretherketone (PEEK) (Theivendran et al., 2021). CF-PEEK provides translucency under X-ray imaging, eliminating scattering effects and enabling the evaluation of early tumor recurrence and precise radiotherapy while minimizing the impact on surrounding soft tissues (Zimel et al., 2015; Nevelsky et al., 2017). CF-PEEK filled with 30wt% short carbon fiber (CF30-PEEK) demonstrates excellent mechanical properties, with a tensile strength (175–209 MPa) and elastic modulus (16–24 GPa) (Bonnheim et al., 2019; Avanzini et al., 2022) significantly lower than those of metals, closely resembling the properties of bone (50–100 MPa and 7–30 GPa) (Morgan et al., 2018). This resemblance effectively avoids stress shielding and subsequent implant loosening or failure (Sha et al., 2009). Additionally, CF-PEEK exhibits favorable wear resistance when articulating against ceramic and metallic materials (Scholes and Unsworth, 2007; Brockett et al., 2016), and its wear particles do not demonstrate significant cytotoxicity (Utzschneider et al., 2010), thereby extending the prosthesis lifespan. To date, CF-PEEK has been investigated in various applications, including spinal cages (Schwendner et al., 2023), fixation systems (Boriani et al., 2018; Cofano et al., 2020), knee joint prostheses (Koh et al., 2019), and intramedullary nails (Vles et al., 2019; Ziran et al., 2020).

The length, arrangement, and weight percentage of carbon fibers filled in CF-PEEK can impact its mechanical properties, providing the opportunity to manipulate them (Liao et al., 2020). While CF-PEEK with 30wt% carbon fiber is reinforced by short carbon fibers, CF-PEEK with 60wt% (CF60-PEEK) contains relatively longer or continuous carbon fibers. CF60-PEEK shares many similarities with CF30-PEEK but exhibits higher stiffness due to the utilization of long carbon fibers (Zhao et al., 2021). The elastic modulus of CF60-PEEK can range from 50 GPa to 150 GPa, depending on the orientation and volume fraction of carbon fibers (Bonnheim et al., 2019). Therefore, CF60-PEEK, possessing light weight and high stiffness, is suitable for fabricating torsion-resistant and load-bearing implants.

Due to the large bone defect, tumor-type knee prostheses are typically heavier than most knee joint implants. Therefore, replacing metallic biomaterials with CF-PEEK holds technological importance for tumor-type prostheses. With a lower density than CoCrMo alloy (7.9–8.5 g/cm^3) and Ti6Al4V alloy (4.51 g/cm^3), CF30-PEEK (1.35–1.4 g/cm^3) can reduce the weight of the prosthesis and alleviate the burden on surrounding tissues, resulting in a considerable improvement in comfort. Despite the increasing use of CF-PEEK in orthopedic trauma and spinal instrumentation, there is limited published research on tumor-type knee prostheses composed of CF-PEEK. Finite Element Analysis is an essential method for simulating stress distribution and exploring mechanical properties when designing a prosthesis (Yao et al., 2021; Zhu et al., 2021). In our previous study, we introduced an originally designed micro-motion tumor-type knee prosthesis and conducted Finite Element Analysis. However, the initial prosthesis yielded unsatisfactory results during subsequent tests. In this study, we have renewed the design and provided a numerical study of a novel tumor-type prosthesis composed of CF-PEEK. This study aims to explore the feasibility of using CF30-PEEK and CF60-PEEK as replacements for CoCrMo in tumor-type knee prostheses, and three different Finite Element models were established to analyze the von Mises stress of each component. The results of this study are expected to provide insights into the development of tumor-type knee prostheses.

2 Materials and methods

2.1 Updates in prosthesis design

Three tumor-type knee prostheses, referred to as Type 1, Type 2, and Type 3, were evaluated in this study. Type 1 represents the initial design, consisting of intramedullary stems for the femur and tibia medullary cavity, an extension rod, a distal femoral component, two flexion shafts with two shaft bushings, a cardan shaft with a cardan gasket, a tibial insert, and a proximal tibial component (Figure 1A). The cardan shaft not only links the femur and tibia but also enables controlled micro-motions within the knee joint. This design preserves knee joint flexibility for multidirectional movement while maintaining necessary constraint. However, subsequent test results of Type 1 indicated a possibility of dislocation and the need for further adjustments, leading to the development of Type 2 and Type 3 prostheses.

To reduce the risk of dislocation, the diameter of the distal end of the cardan shaft was enlarged in Type 2 and Type 3, making it wider than the gap of the tibial insert. As a result, the cardan gasket was removed to fit into the groove of the tibial component. Additionally, the neck of the cardan shaft was lengthened, and the PE tibial insert was slightly thickened accordingly. A bushing ring inside the cardan shaft was also removed. The Type 2 and Type 3 has the same geometric design, and the details of all types are shown in Supplementary Figure S1.

However, both the cardan shaft and tibial component were made of CoCrMo. Although our previous study showed that the flexion shafts and cardan shaft are not the main bearing components (Guo and Guo, 2022), it is doubtful whether retaining a metal-on-metal interface after removing the PE gasket is safe and appropriate. This

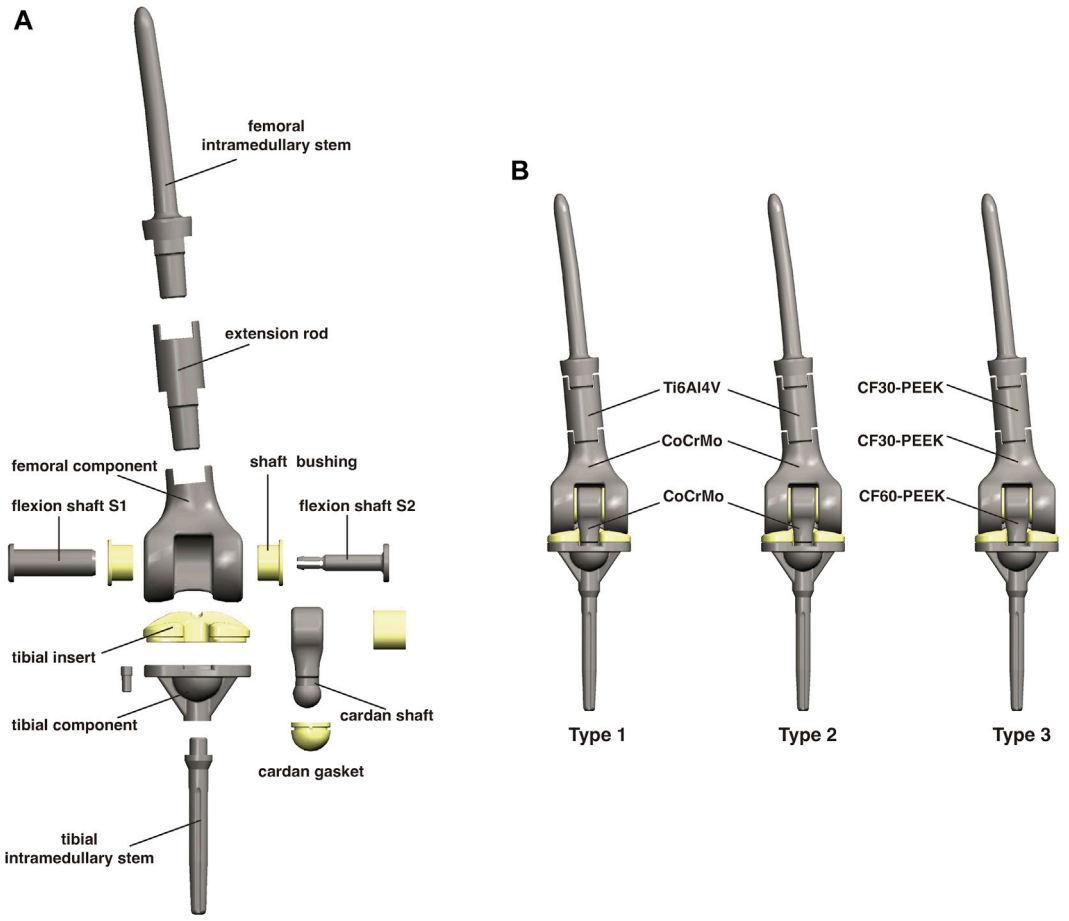

FIGURE 1
(A) A schematic diagram of the components of this micro-motion tumor-type knee prosthesis. **(B)** Differences in the materials among the three types of prostheses.

interface may not withstand repeated motion and may increase the risk of wear, especially considering the cytotoxicity of CoCrMo wear debris.

CF60-PEEK reinforced by continuous carbon fiber has shown a comparable elastic modulus (150 GPa) to CoCrMo (218 GPa), with reduced wear rates and cytotoxicity of wear debris. Therefore, to reduce the potential for wear while maintaining high stiffness, CoCrMo was replaced by CF60-PEEK for the cardan shaft, while the tibial component remained made of CoCrMo. Consequently, Type 2 (which contains a CoCrMo cardan shaft) served only as a control group in this study. Apart from the structural issues, the weight of the CoCrMo components also drew our attention. The advantages of using CF30-PEEK in tumor-type prostheses were confirmed in our previous study (Guo and Guo, 2022), and we retained the design of CF30-PEEK femoral component and extension rod in Type 3 (Figure 1B).

2.2 Finite element model construction

The CT data was derived from the same patient as our previous study (Guo and Guo, 2022), with a height of 168 cm and a weight of 70 kg. The total femur and total tibia measured 430 mm and 330 mm in length, respectively. Next, the medical modeling software Mimics 20.0 (Materialise Inc., Belgium) was used to construct the original knee joint model. The osteotomy length for the resection of the distal femur tumor was set at 128 mm, and for the proximal tibia it was set at 10.5 mm. Both osteotomy directions were perpendicular to the axis of the medullary cavity.

Subsequently, the simulated osteotomy was performed, and a custom prosthesis model was designed using engineering design software CREO 7.0 (PTC, United States). To analyze the stress distribution of three different implants in two static postures (knee joint at 0° for standing and at 90° for squatting), a finite element (FE) environment was created. The Altair Inspire software (Altair Engineering Inc., United States) was used for the pre-processing of this environment. Static structural analysis was performed using the OptiStruct 2019 solver (Altair Engineering Inc., United States). All materials were simplified to be linear elastic and isotropic, and the properties of different materials are shown in Table 1.

2.3 Loading and boundary conditions

In the loading condition, a downward load of 700 N was applied vertically to the femoral head to simulate the body's

TABLE 1 The characteristics of different materials.

Materials	Young's modulus (MPa)	Poisson's ratio	Tensile strength (MPa)	Compressive strength (MPa)
Cortical bone Rezwan et al. (2006), Guo and Guo (2022)	14,000	0.30	50–151	130–220
CoCrMo Sevimay et al. (2005), Herranz et al. (2020)	218,000	0.33	409–431	632–682
Ti6Al4V Arrazola et al. (2009), Kaleli et al. (2018), Ishfaq et al. (2021)	110,000	0.35	960–1,100	870–1,010
UHMWPE Manoj Kumar et al. (2015), Malito et al. (2018)	1,016	0.30	10.2–26.3	9.8–15.7
CF30-PEEK Sarot et al. (2010), Schwitalla and Müller (2013)	18,000	0.39	175–214	239–246
CF60-PEEK Schwitalla et al. (2015), Liao et al. (2020)	150,000	0.35	2000	800

gravity in one-legged standing. A load of 2,800 N was applied to simulate the highest loaded condition during one-legged squatting (Smith et al., 2008; Kutzner et al., 2010; Bergmann et al., 2014). In both postures, the distal end of tibia was fully constrained in all directions (Supplementary Figures S2A, B).

As shown in Supplementary Figures S2C, D, the contact conditions were varied among standard, boned and no contact. Briefly, the interfaces between the intramedullary stems and bones were bonded due to the bone cement design (indicated in blue). The interfaces between the femoral intramedullary stem, extension rod and the femoral component were also bonded because of the taper connection. For the remaining interfaces, standard contact conditions were applied (indicated in green). Additionally, some seemingly narrow gaps did not actually result in contact based on the geometric design (indicated in gray).

2.4 Model verification and data processing

Initially, the 10 Nodes tetrahedral (TET10) elements were utilized for calculations. However, during the gradual mesh refinement, increasing errors emerged and prevented the completion of the calculations. This issue could be attributed to the complexity of the model, which includes multiple components with intricate structures. Additionally, the software may automatically adjust meshes to accommodate small curvature corners, potentially distorting the meshes, which could significantly impact the stress levels and yield unreliable results (Saadlaoui et al., 2017).

For computational efficiency, the 4 Nodes tetrahedral (TET4) elements was subsequently employed for the calculation. In this study, the von Mises stress was selected as the primary parameter for evaluating biomechanical performance of the prosthesis. A convergence test was conducted on both Type 1 and Type 3 models by increasing the mesh densities (Supplementary Figures S3A, B). It was observed that convergence curve was not smooth. This could be attributed to the fact that many parameters of the model could affect mesh convergence behavior, and convergence tests may not always yield satisfactory solutions (Schmidt et al., 2009).

TABLE 2 The number of nodes and elements for each model.

	Model	Nodes	Elements
Standing	Type-1	83,163	341,411
	Type-2	80,812	333,723
	Type-3	80,812	333,723
Squatting	Type-1	83,180	339,746
	Type-2	81,739	337,572
	Type-3	81,739	337,572

Another reason for the lack of smoothness in the convergence curve may be that the models retained substantial details, resulting in different convergence rates at different locations (Schmidt et al., 2009). For instance, considering the femoral component, which is of particular interest in this study, as the mesh density increased, the smooth surfaces of the medial and lateral condyles converged at much lower mesh densities. In contrast, the intercondylar fossa with curvature features exhibited slower convergence rates (Supplementary Figures S3C, D). Theoretically, the best way to determine whether smaller element sizes would result in smooth curves without abrupt changes would be to continuously increase the mesh densities, although this approach is impractical (Bright and Rayfield, 2011).

The different rate was calculated as the percentage difference in the maximum von Mises stress between the current mesh density and the previous density (Supplementary Tables S1, S2). Regarding the different rate, there appears to be no consensus in the literature, with values of <10% or <5% both being quoted (Schmidt et al., 2009; Bright and Rayfield, 2011; Lai et al., 2015; Tseng et al., 2015). In this study, the convergence was considered to have started at where a <10% different rate was observed between successive meshes. Consequently, for most locations, the Type 1 model can be deemed to have converged at 341,411 elements and the Type 3 model at 333,723 elements, with an average mesh size of 2.0 mm (Table 2).

All the statistical analyses in this study were performed with the SPSS 22.0 software. For comparison of three groups, one-way ANOVA was performed. The differences were considered significant at $p < 0.05$.

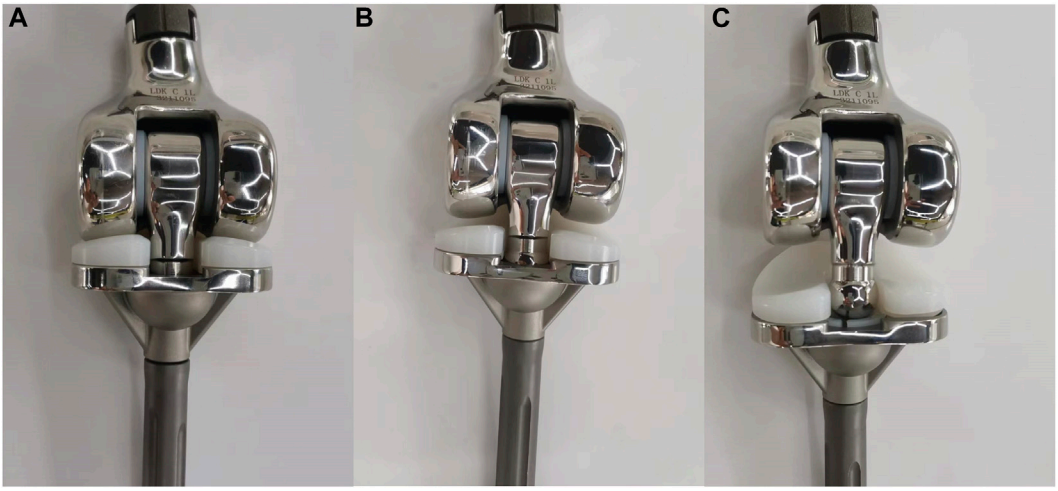

FIGURE 2
Illustration of **(A)** a normal Type 1 prosthesis, **(B)** the cardan shaft being pulled out from the cardan gasket, and **(C)** the cardan shaft fully dislocated and stuck into the tibial insert.

3 Results

3.1 Development of micro-motion tumor prosthesis

The initial design (referred to as Type 1) was first demonstrated in our previous study (Guo and Guo, 2022). For individuals in Asia and the Middle East, certain daily activities such as toileting, kneeling, and cross-legged sitting often require full flexion squatting (Hemmerich et al., 2006). However, during the subsequent static loading test of Type 1, which simulated this specific movement, unsatisfactory results were observed. It was discovered that there was a potential issue where the cardan shaft could be pulled out from the cardan gasket, leading to subluxation, or even getting stuck in the gap of the tibial insert, resulting in complete dislocation (Figure 2). This occurred when the prosthesis underwent prolonged bending at a high flexion angle with load-bearing. If this situation were to occur in a clinical utilization, it would require a revision surgery to restore the functionality of the knee joint. To address this issue, the cardan shaft was redesigned as described in the Methods section. Subsequently, the stress distribution of all three prostheses was analyzed.

3.2 Overall stress distribution and displacement of three models

The von Mises stress distribution of three models, including the proximal femur and tibia, was analyzed in this study. Figure 3A illustrates the overall stress distribution of the entire model in the standing posture. The maximum stress value was observed in Type 2 (93.63 MPa), which was higher than Type 1 (82.95 MPa) and Type 3 (38.25 MPa). As shown in Figure 3B, when squatting, Type 2 showed the highest stress value (5,662 MPa), significantly exceeding that of Type 1 (4,694 MPa) and Type 3 (1,213 MPa). For a more detailed examination, three random points around the maximum stress point were collected for statistical analysis. As shown in Figures 3C, D, the maximum stress observed in the Type 3 model was the lowest in both standing and squatting position. Compared with Type 1, Type 3 showed a distinct reduction of 53.9% in maximum von Mises stress during standing and 74.2% reduction during squatting. The maximum displacement of the entire model was shown in Figure 4. The maximum displacement was observed in the proximal femur in both positions. When standing, the maximum displacement in Type 3 (18.02 mm) was slightly higher than that of Type 1 (17.48 mm) and Type 2 (17.53 mm). In the squatting position, the maximum displacement remained highest in Type 3 (173.6 mm), significantly surpassing that of Type 1 (115.5 mm) and Type 2 (114.8 mm).

3.3 Mechanical analysis of extension rod, femoral component and tibial insert

The extension rod and femoral component of three prostheses were made of materials with different mechanical properties, which could potentially affect the stress distribution. However, as shown in Figure 5, in the standing condition, the maximum stress values observed on the extension rod were nearly identical for Type 1 (22.15 MPa), Type 2 (26.83 MPa), and Type 3 (25.48 MPa). This trend remained similar in the squatting position, with values of 1,308, 1,283, and 1,213 MPa, respectively.

There were significant differences in the stress distribution on the femoral component. In the standing condition (Figure 5A), the maximum stress on the CF30-PEEK femoral component in Type 3 (35.45 MPa) was significantly lower than that of the CoCrMo component in Type 1 (82.95 MPa) and Type 2 (93.63 MPa). Moreover, in all three types, the highest stress on the femoral

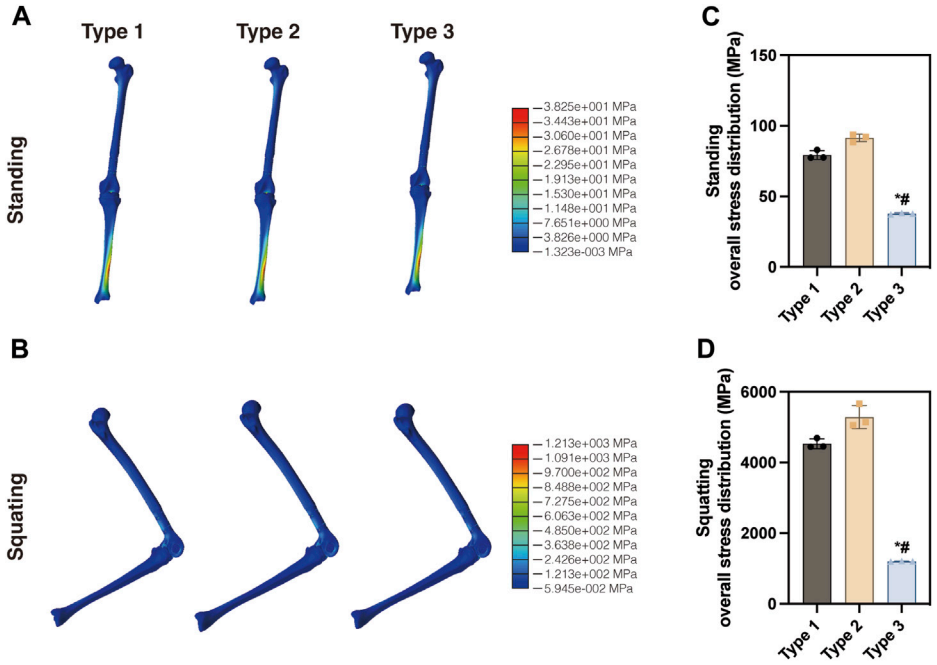

FIGURE 3
Distribution of the von Mises stress in the three entire models in the **(A)** standing position and **(B)** squatting position. Statistical analysis of the maximum von Mises stress in the **(C)** standing and **(D)** squatting position (*$p < 0.05$ compared with Type 1, #$p < 0.05$ compared with Type 2, same in the following figures).

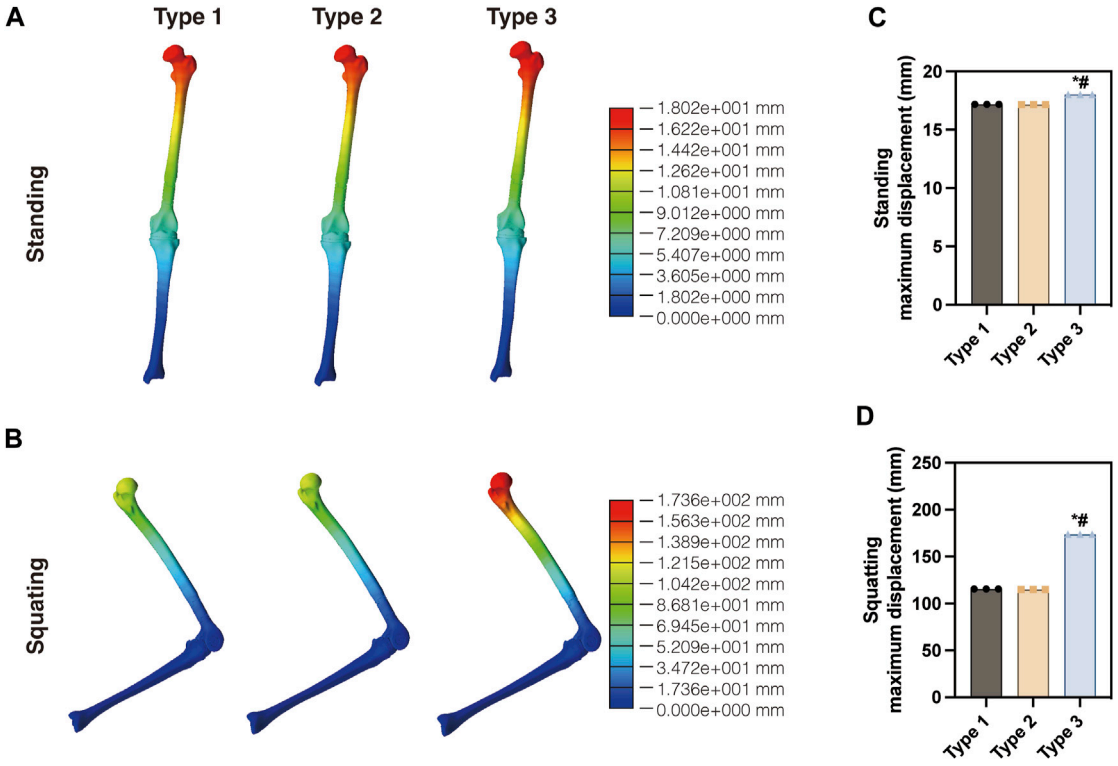

FIGURE 4
Displacement of the three models in the **(A)** standing and **(B)** squatting position. Statistical analysis of the maximum displacement in the **(C)** standing and **(D)** squatting position.

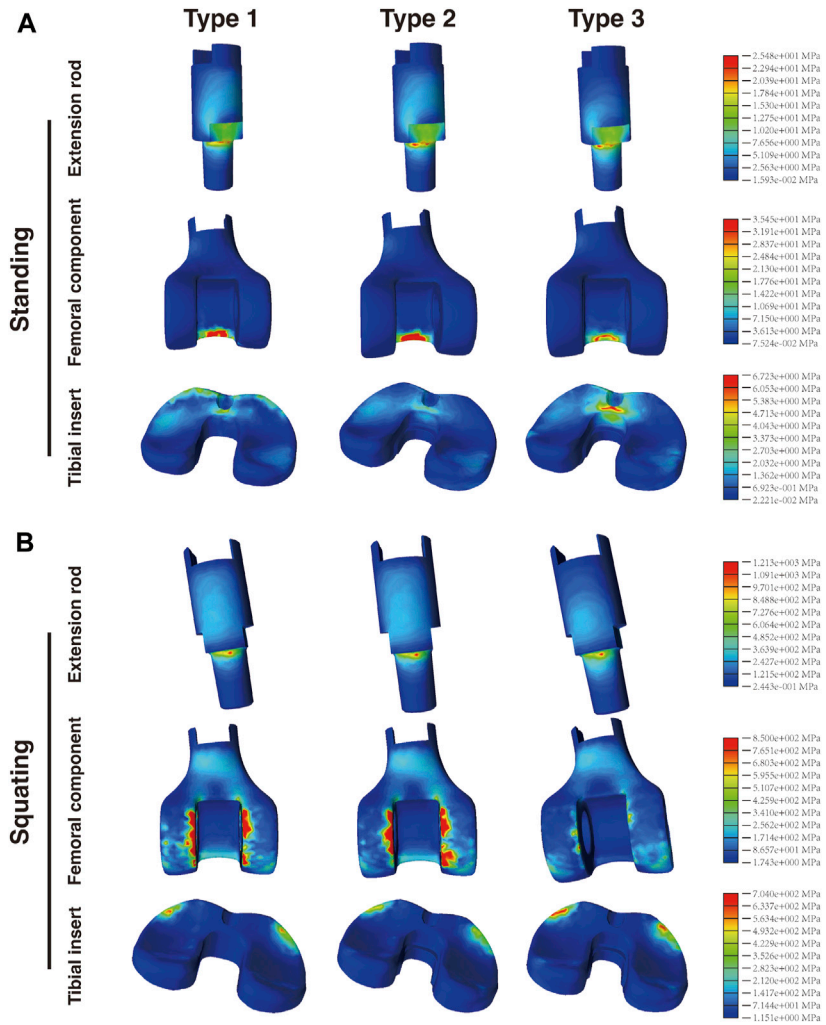

FIGURE 5
Distribution of the von Mises stress in the extension rod, femoral component and tibial insert in the **(A)** standing and **(B)** squatting position.

component appeared at the contact area with the cardan shaft, located within the region corresponding to intercondylar fossa. In the squatting condition, the maximum stress on the femoral component of Type 3 (850 MPa) was substantially lower than that of Type 1 (4,694 MPa) and Type 2 (5,662 MPa). It is noteworthy that the maximum stress in all three types of prostheses was observed at the interface between the femoral component and tibial insert (Figure 5B). Compared with Type 1, the maximum stress on the femoral component of Type 3 decreased by 57.3% and 81.9% under the standing and squatting conditions, respectively.

Regarding the tibial insert, stress concentration was observed on the anterior regions of the insert in all three types. The maximum stress observed in Type 3 (6.723 and 704 MPa) was higher than that of Type 1 (4.095 and 625.1 MPa) and Type 2 (3.853 and 519.3 MPa) in both postures (Figures 5A, B). Further analysis of the medial and lateral sides of the insert (corresponding to the medial and lateral menisci) revealed that the maximum von Mises stress on both sides of the tibial insert in Type 3 was also higher than those in the other two types (Supplementary Figure S4).

3.4 Stress analysis of connecting components

The connecting components consist of the flexion shaft S1 and flexion shaft S2 (Figure 1). S2 is inserted into S1, with two shaft bushings positioned between S1 and the femoral component. Together, these connecting components articulate the cardan shaft with the femoral component. When standing, the maximum stress on both the flexion shaft S1 (6.383 MPa) and S2 (3.137 MPa) of Type 3 was slightly higher than that of Type 1 (2.158 and 1.148 MPa, respectively) and Type 2 (5.842 and 2.545 MPa, respectively) (Figure 6A). Similarly, when squatting, Type 3 exhibited the highest stress on S1 (295.8 MPa) and S2 (71.23 MPa) among the three types, as compared with Type 1 (105.7 and 36.51 MPa, respectively) and Type 2 (169.8 and 54.06 MPa, respectively) (Figure 6B). In the standing condition, most stress located on the central area of shaft S1 and S2 in all the three types. However, when squatting, most stress was concentrated on the central area of S2 but a greater amount was found on the edge of S1. The maximum stress on all shaft bushings showed no

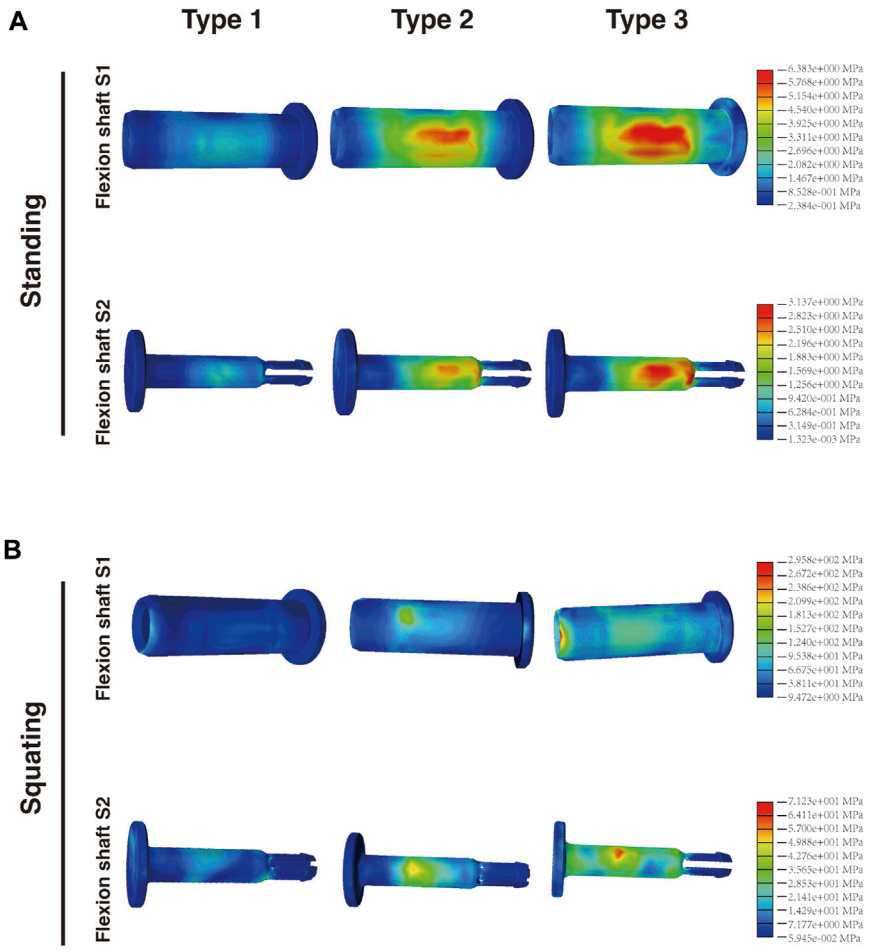

FIGURE 6
Distribution of the von Mises stress on flexion shaft S1 and S2 in the **(A)** standing and **(B)** squatting position.

significant differences among them, although Type 3 presented slightly higher stress values regardless of position (Figure 7).

3.5 Stress analysis of micro-motion components

The cardan shaft is a key distinguishing feature that sets this prosthesis apart from other distal femoral tumor-type prostheses. It serves the dual purpose of connecting the femoral and tibial components and enabling micro-motions in multiple directions, thus preserving the flexibility of the knee joint.

Figure 8 demonstrates that in Type 2 and Type 3, the cardan gasket was removed due to the enlarged distal end of the cardan shaft. Following design and material adjustments, it was observed that when standing, the maximum stress in the cardan shaft of Type 3 (26.69 MPa) was slightly higher than that of Type 1 (22.29 MPa) but lower than Type 2 (37.34 MPa). In Type 1, the majority of the stress was located at the contact area with femoral component, whereas in Type 2 and Type 3, more stress appeared on the neck of the cardan shaft. In the squatting position, the stress distribution differed from the standing posture. The maximum stress in Type 3 (996.3 MPa) was significantly lower than that in Type 1 (1862 MPa) but similar to Type 2 (970.3 MPa). The majority of high-stress was located at the flange region of upper cardan shaft, in contact with the shaft bushings, with no significant stress concentration in the neck or bottom areas. Compared with Type 1, the maximum stress on the cardan shaft of Type 3 increased by 19.7% when standing, but decreased by 46.5% when squatting.

Regarding the cardan gasket in Type 1, most of the maximum stress was observed on the edges below the top of the gasket. When squatting, stress concentration appeared at the central bottom of the gasket, which was not obvious when standing. Furthermore, in Type 1, the gasket top was in contact with the tibial insert, presenting an interface stress of approximately 0.16–0.53 MPa in the standing position and 2.06–8.52 MPa in the squatting position. It is worth noting that in Type 2 and Type 3, the upper surface of the hemisphere structure was not in contact with the bottom of the tibial insert (Supplementary Figure S1), thus showing a normal stress gradient.

Analysis of the tibial component revealed that when standing, the maximum stress in Type 3 (11.16 MPa) was lower than that of Type 1 (20.62 MPa) and Type 2 (15.78 MPa). When squatting, Type 1 showed the highest stress value of 937.8 MPa, followed by Type 3

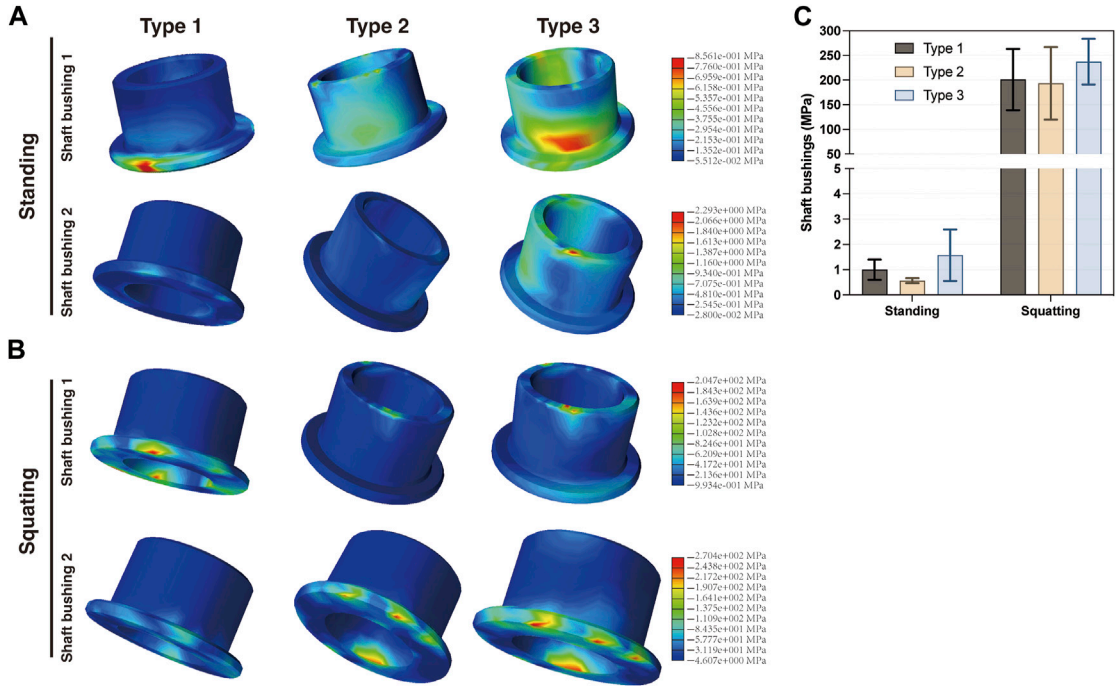

FIGURE 7
Distribution of the von Mises stress on shaft bushings in the **(A)** standing and **(B)** squatting position, and **(C)** statistical analysis of the maximum stress in three types.

(612.4 MPa) and Type 2 (532.1 MPa). The distribution of von Mises stress on the tibial component was similar among the three types in the standing or squatting position, respectively.

3.6 Stress analysis of femur, tibia, and intramedullary stems

Figure 9 demonstrates that in the standing condition, the maximum stress on the proximal femur was nearly identical between Type 1 (8.262 MPa) and Type 2 and Type 3 (both 8.222 MPa). Additionally, the maximum stress observed on the tibia was similar among Type 1 (33.61 MPa) and the other two types (both 34.02 MPa). Furthermore, there were only minor differences in the stress distribution among the femoral or tibial intramedullary stems, respectively. A similar trend was observed in the squatting condition. These findings suggest that the adjustments in design and material had minimal impact on the stress distribution of the femur, tibia, and their intramedullary stems. Figure 10 presents the maximum stress values of each component in all three types.

4 Discussion

The wide resection of bone tumors around the knee requires reconstruction with appropriate tumor-type prostheses. In our previous study (Guo and Guo, 2022), we proposed the initial design of a micro-motion tumor-type knee prosthesis. This prosthesis incorporates a crucial cardan shaft connection, which enables micro-motion between the femur and tibia, preserving the flexibility of the knee joint after implant surgery. However, during subsequent tests simulating prolonged squatting with weight-bearing, the prosthesis exhibited a potential for dislocation, leading to malfunctions of the prosthesis. Consequently, a redesign of the prosthesis became necessary. The primary cause of dislocation was the cardan shaft being pulled out from the shaft gasket and the tibial component. Therefore, the redesign primarily focused on addressing this issue through modifications to the cardan shaft, as described above.

CFR-PEEK has been successfully used in many orthopedic reconstructions. Although CF30-PEEK has not been extensively used for femoral components or load-bearing parts of joint prostheses (Koh et al., 2019; Vertesich et al., 2022), it has demonstrated good load-bearing capacity in other clinical applications and has shown stable long-term performance (Nakahara et al., 2013; Rotini et al., 2015; Schliemann et al., 2015; Boriani et al., 2018; Laux et al., 2018; Ziegler et al., 2019). Additionally, our previous study found favorable stress distribution in the femoral component made of CF30-PEEK (Guo and Guo, 2022). These findings suggest that CF30-PEEK can potentially replace CoCrMo for the femoral component, reducing the weight of the tumor-type prosthesis without compromising its strength. Therefore, in this study, we chose to retain CF30-PEEK as the material for the femoral component in Type 3.

By adjusting the arrangement and weight fraction of carbon fibers embedded in CFR-PEEK composites, CF60-PEEK exhibits an elastic modulus ranging from 50 to 150 GPa (Schwitalla et al., 2015; Xu et al., 2019; Liao et al., 2020; Souza et al., 2021). This allows for achieving higher rigidity and torsion resistance similar to metals,

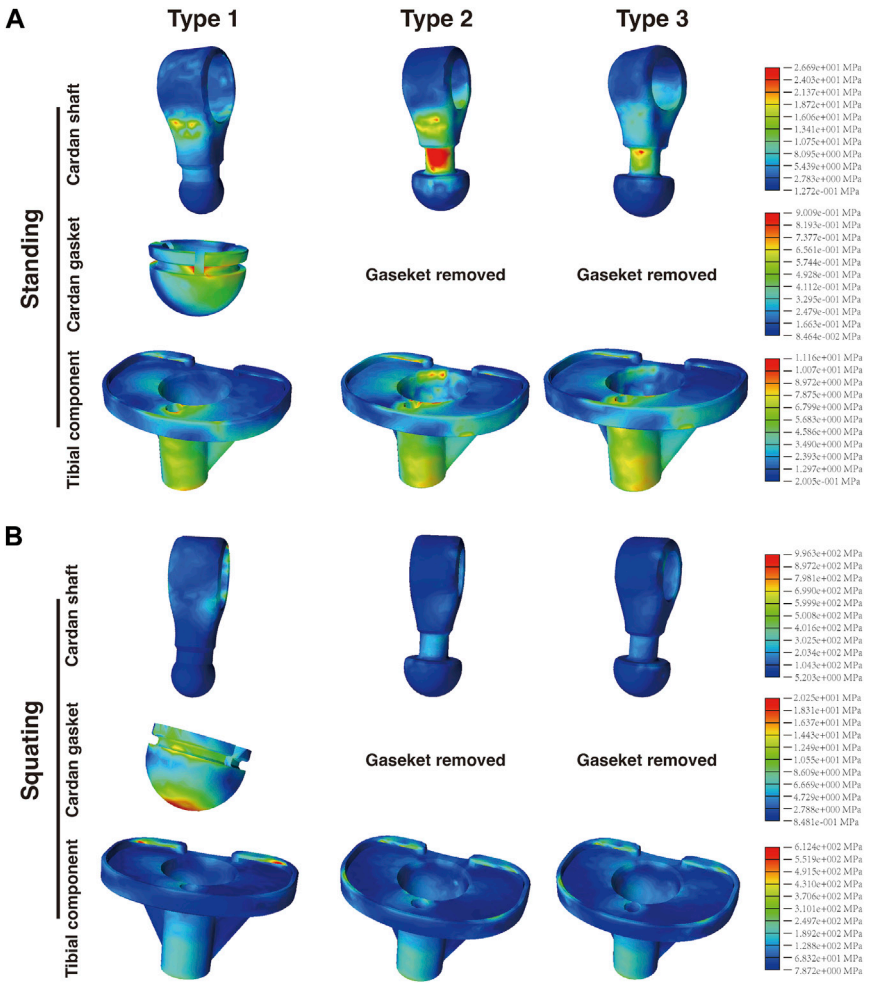

FIGURE 8
Distribution of the von Mises stress on the cardan shaft, cardan gasket, and tibial component in the **(A)** standing and **(B)** squatting position.

while maintaining a lighter weight (Verma et al., 2021). Clinical use of long carbon fiber-reinforced PEEK composites, such as the Carbofix Piccolo system, have demonstrated good load-bearing capabilities and bending resistance (Hak et al., 2014). Tests conducted by Steinberg et al. showed that tibial nails and plates made of 60wt% CFR-PEEK exhibit similar mechanical characteristics to commercially available metal implants, with lower wear performance (Steinberg et al., 2013). CF60-PEEK also demonstrates excellent wear resistance (Koh et al., 2019). The wear rate of CFR-PEEK is lower than that of metal-on-UHMWPE and metal-on-metal systems (Howling et al., 2003; Scholes and Unsworth, 2009a; Scholes and Unsworth, 2009b). Considering these characteristics, CF60-PEEK was selected as the material for the cardan shaft in this study to ensure component rigidity, stability, and high wear resistance. Its impact on stress distribution was subsequently analyzed.

Finite element analysis (FEA) is a highly effective and powerful tool for evaluating multiple variables in orthopedic implants, aiding in design optimization and predicting stress distribution (Pfeiffer, 2016). In this study, three different finite element models were developed, incorporating Young's modulus and Poisson's ratio to complete the models. To independently assess the effect of material variations on stress distribution, the Type 2 group, which had the same geometric structure as Type 3 but retained the CoCrMo composition as Type 1, served as control group as well. However, there is currently a lack of consensus on the loading or contact stress on the knee joint during movement, particularly after reconstruction with a tumor-type knee prosthesis. Research on the knee joint suggests that the peak axial force during level walking can range from 2.2 to 2.5 times body weight (BW) (Bergmann et al., 2014). In fast walking, the medial knee contact force can increase by 30%–70% compared to the standing position, and the loading is greatly influenced by muscle force (Ogaya et al., 2015; Trepczynski et al., 2018). Stair descent can generate forces up to 346% BW, while stair ascent can result in forces up to 316% BW (Kutzner et al., 2010). These values vary widely among individuals, and the estimation of contact force may have an error of 10% BW (Jung et al., 2017).

Furthermore, the load on the knee joint becomes more complex in the deep squat position (beyond 90 degrees of flexion). On one hand, the actual tibiofemoral contact forces depend on the net moments of the hamstrings or the quadriceps force in the sagittal plane (Smith et al., 2008; Kutzner et al., 2010; Bergmann et al., 2014).

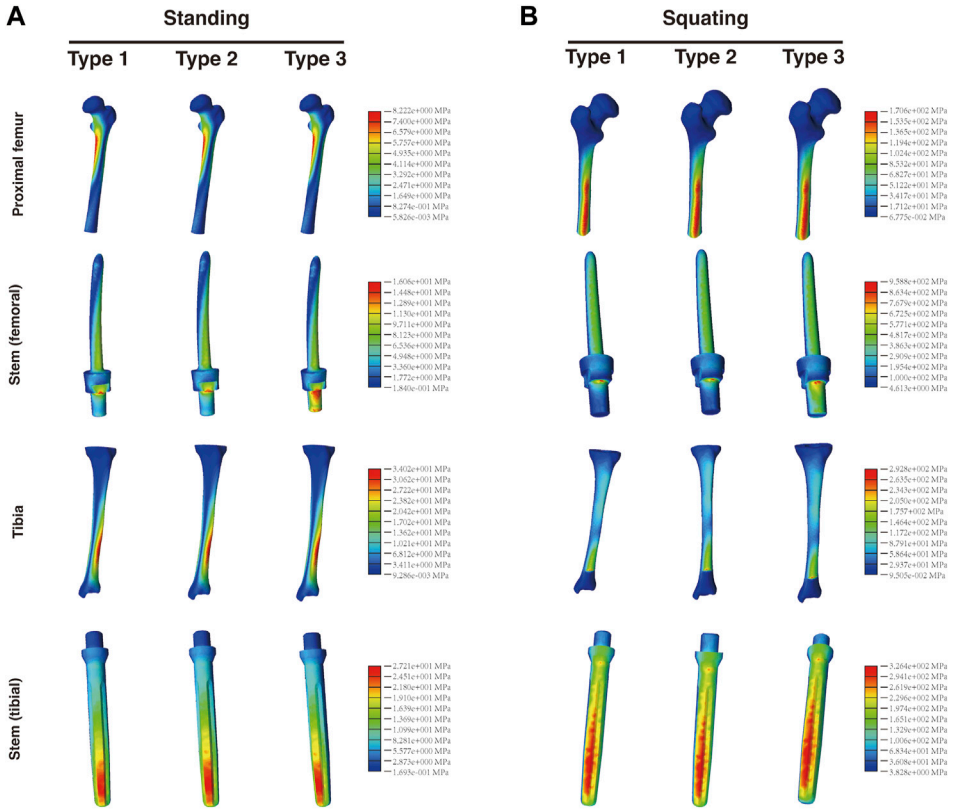

FIGURE 9
Distribution of the von Mises stress on the proximal femur, tibia, and respective intramedullary stems in the **(A)** standing and **(B)** squatting position.

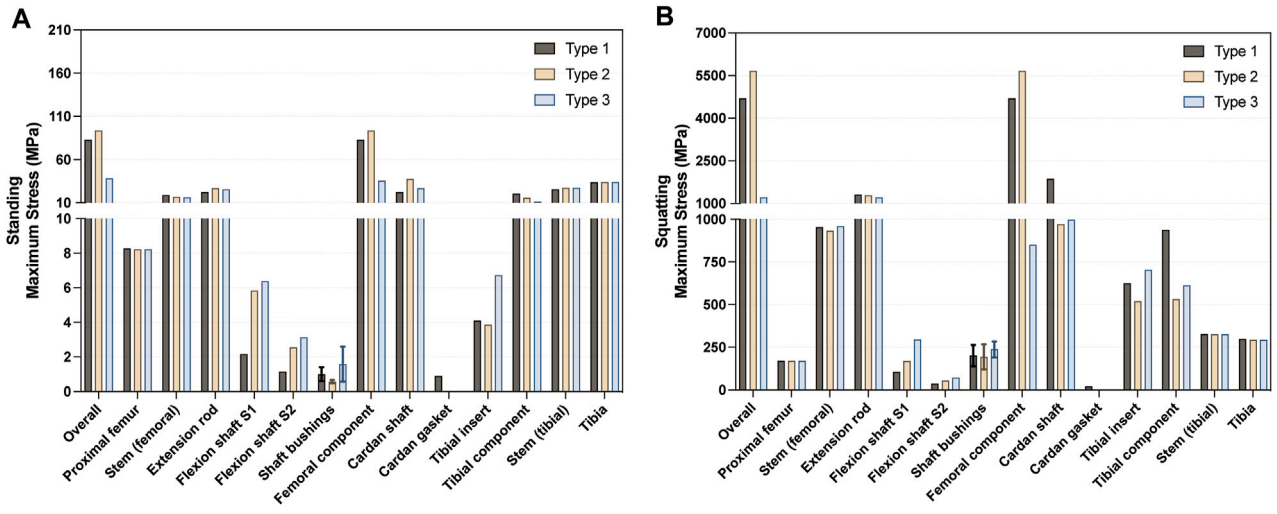

FIGURE 10
Summary of the maximum von Mises stress in each component in the **(A)** standing and **(B)** squatting position.

On the other hand, even at the same knee flexion angle, loading conditions on the knee joint can vary during activities such as stair ascent, rising from a chair, and deep squatting. For example, during one-legged flexion in stair ascending, the knee joint experiences forces equivalent to 316% BW, while during two-legged bending in deep squatting, the forces range from 240% to 253% BW (Taylor et al., 1998; Smith et al., 2008; Kutzner et al., 2010; Bergmann et al., 2014). Moreover, due to the various combinations of anatomical

structures and complex movements, determining the normal loading conditions within the knee joint is challenging (Taylor et al., 2004).

Therefore, for computational efficiency, in our study, we applied a load of 700 N to simulate the load during standing, and 2800 N to simulate the extreme load during knee bending in the gait cycle. These loads are slightly higher than those used in previous finite element studies, but align more closely with the peak loading during one-legged postures (Bergmann et al., 2014), as we aimed to encompass a wider range of the complexity and variability of knee joint loading. However, considering that patients may use assistive devices such as braces or crutches during postoperative recovery, the load settings in this study may be higher than the actual tibiofemoral contact stress under most circumstances.

Research has shown that for primary distal femoral endoprostheses, decreased survivorship is primarily attributed to soft tissue failure, aseptic loosening, and structural complications (Pala et al., 2013; Bus et al., 2017; Haijie et al., 2018; Ogura et al., 2021). In the case of revision prostheses, periprosthetic fracture and aseptic loosening are the primary causes of implant failure (Pala et al., 2013; Geiger et al., 2023). In this study, the overall von Mises stress of the newly designed prosthesis was significantly lower than that of the other two groups in both the standing and squatting position. Stress analysis of the entire model showed that, after updating the design and material, the overall stress on the Type 3 prosthesis remained consistent and evenly distributed. Additionally, there was no significant difference in the stress distribution observed at the bone-prosthesis interface between Type 3 and Type 1 in both standing and squatting positions. The von Mises stress between the bones and intramedullary stems was similar, indicating no significant stress shielding effects. This suggests that the stress in the Type 3 model is effectively transmitted from the prosthesis to the cortical bone, preventing instability between the prosthesis and bone and avoiding subsequent complications.

The displacement analysis of the entire model revealed that in the standing position, Type 3 showed similar results to the other two groups. However, during the higher load-bearing squatting position, the displacement in Type 3 significantly increased. This can be attributed to the notable difference in stiffness between the CF30-PEEK components and the CoCrMo components. The extension rod and femoral component that made of CF30-PEEK exhibit lower stiffness but higher elastic deformability, which aligns with the findings of our previous study (Guo and Guo, 2022).

Upon further analysis of the load distribution on the components, it was observed that after the design modifications, there were no significant differences in the stress distribution of the intramedullary stems of the femur and tibia, extension rod, and bushings for flexion shafts. However, notable changes were observed in the stress distribution of the components that had been replaced with new materials and the components in contact with them. When comparing the stress distribution of the femoral components, it was found that in the standing position, the region in contact with the cardan shaft (referred to as the intercondylar fossa) showed the highest stress. In the squatting position, the maximum stress shifted to the region in contact with the tibial insert. The femoral component made of CF30-PEEK exhibited significantly lower maximum stress in both standing and squatting positions, compared with the CoCrMo groups. A long-term follow-up research showed that after tumor resection and reconstruction in the knee joint, the prosthesis failure was primarily caused by mechanical facts (Henderson et al., 2011). These failures are likely linked to the weight of the prosthesis. The findings in this study highlight the positive impact of using CF30-PEEK in the femoral component, as it not only effectively reduces the weight burden but also mitigates the risks of fatigue due to stress concentration.

Analysis of the tibial insert revealed complex results. The Type 3 group showed higher maximum stress on the UHMWPE insert compared to the other two groups, in both standing and squatting postures. Further analysis revealed that both the medial and lateral regions of the tibial insert experienced elevated stress in the Type 3 group. In this study, the elastic modulus of CF30-PEEK was set at 18 GPa, significantly lower than that of CoCrMo but closer to UHMWPE. This relative modulus compatibility helps with load transfer and promotes even stress distribution (Heary et al., 2016). It was further confirmed in this study, where the von Mises stress on the CF30-PEEK femoral component was closer to that of the UHMWPE insert, compared with the CoCrMo-UHMWPE pairs. These findings suggest that the load force could be effectively transmitted from the femoral component to the tibial insert. However, it is important to note that all three groups exhibited some stress concentration at the ridge of the tibial insert. Further research is necessary to assess the potential risks of wear and fatigue associated with tibial inserts.

The flexion shaft S1 and S2 play a crucial role in articulating the femoral components and the cardan shaft. The stress concentration regions on the flexion shaft may be influenced by the transmission of axial forces from the femoral component. Regarding the cardan shaft, when comparing Type 3 with Type 2 and Type 1, the utilization of CF60-PEEK as the material along with the design updates, resulted in a similar stress distribution when standing, but a substantial reduction in stress when squatting. This reduction could hold significant importance for tumor-type prostheses, as many of tumor-type prostheses still carry a risk of breakage (Yoshida et al., 2012). Studies have reported that approximately 2%–6% of tumor patients reconstructed with rotating hinge prostheses experienced fractures at the tibial yoke, where the rotating component was inserted into the tibial tray (Myers et al., 2007). In contrast to rotating hinge implants, in this prosthesis, the bottom of the cardan shaft remains unfixed, and stress is transmitted through the femoral component to the tibial insert and tibial component. We speculate that the substantial reduction in stress on the cardan shaft could help mitigate the risk of fractures resulting from increased activity and repetitive torsion.

As for the tibial component, Type 3 exhibited slightly higher stress, although the stress difference among the three groups was minimal. The region in contact with the tibial insert experienced the highest stress, and no stress concentration was observed at the contact surface between the cardan shaft and the groove of the tibial component. The low contact pressure contributes to reducing the risk of wear at the interface between the cardan shaft and the tibial component (Grupp et al., 2010; Koh et al., 2019).

In the squatting position, certain components showed stress levels that exceeded their theoretical yield strength. However, this does not necessarily indicate component failure. The results are

influenced by various parameters such as mesh density and loading conditions. Utilizing loading conditions that are closer to physiological conditions could likely yield a more realistic stress distribution. We also acknowledge the following limitations in this study. Firstly, for computational efficiency, only Poisson's ratio and elastic modulus were considered as parameters. Incorporating additional parameters for model construction (Viceconti et al., 2005) and using viscoelastic models for specific components may offer more comprehensive insights into stress distribution (Alotta et al., 2018). Secondly, this study exclusively assessed the von Mises stress on bones and the prosthesis under two static conditions. Future research should account for the gradual changes in a post-surgery patient's gait. Incorporating dynamic motion models and analyzing the complete gait cycle would facilitate a more specific evaluation of stress distribution across a wider range of knee flexion degrees. Furthermore, a comprehensive biomechanical analysis should consider the influence of soft tissues and muscles, as they significantly impact joint loading. Additionally, combining the findings with *ex vivo* validations such as pressure-sensitive film tests would provide a more accurate assessment of the contact forces and stress distribution within the prosthesis (Khosravipour et al., 2018).

5 Conclusion

In conclusion, our study provides a novel investigation into a tumor-type prosthesis composed of CFR-PEEK, with a focus on assessing the von Mises stress distribution across its components. The results indicate that CF30-PEEK effectively transmits forces, leading to reduced stress concentration on the femoral component, while reduced weight and improved functionality. The incorporation of CF60-PEEK in the redesigned cardan shaft significantly reduces the von Mises stress while maintaining comparable stiffness. These advancements in force transmission and stress reduction are expected to enhance the stability and durability of the new tumor-type knee prosthesis. However, before introducing the prosthesis into routine clinical practice, further objective investigations on deformation and wear performance are necessary.

Data availability statement

The original contributions presented in the study are included in the article/Supplementary Material, further inquiries can be directed to the corresponding author.

Ethics statement

The studies involving human participant were reviewed and approved by the Ethics Committee of Peking University People's Hospital. The patients/participants provided their written informed consent to participate in this study.

Author contributions

Conceptualization: WG; validation, methodology, resources: HW, YG, WG; formal analysis, data collection, writing–original draft: HW; writing–review and editing: HW, YG, WG. All authors contributed to the article and approved the submitted version.

Funding

This study was supported by the Beijing Science and Technology Planning Project (grant number Z201100005520054) and the Capital Health Development Scientific Research Special Project (grant number 2020-2Z-4089).

Conflict of interest

The authors declare that the research was conducted in the absence of any commercial or financial relationships that could be construed as a potential conflict of interest.

Publisher's note

Supplementary material

The Supplementary Material for this article can be found online at: https://www.frontiersin.org/articles/10.3389/fbioe.2023.1243936/full#supplementary-material

References

Alotta, G., Barrera, O., and Pegg, E. C. (2018). Viscoelastic material models for more accurate polyethylene wear estimation. *J. Strain Analysis Eng. Des.* 53, 302–312. doi:10.1177/0309324718765512

Armstead, A. L., Simoes, T. A., Wang, X., Brydson, R., Brown, A., Jiang, B.-H., et al. (2017). Toxicity and oxidative stress responses induced by nano- and micro-CoCrMo particles. *J. Mater. Chem. B* 5, 5648–5657. doi:10.1039/C7TB01372H

Arrazola, P.-J., Garay, A., Iriarte, L.-M., Armendia, M., Marya, S., and Le Maître, F. (2009). Machinability of titanium alloys Ti6Al4V and Ti555.3. *J. Mater. Process. Technol.* 209, 2223–2230. doi:10.1016/j.jmatprotec.2008.06.020

Avanzini, A., Battini, D., Petrogalli, C., Pandini, S., and Donzella, G. (2022). Anisotropic behaviour of extruded short carbon fibre reinforced PEEK under static and fatigue loading. *Appl. Compos Mater* 29, 1041–1060. doi:10.1007/s10443-021-10004-1

Bergmann, G., Bender, A., Graichen, F., Dymke, J., Rohlmann, A., Trepczynski, A., et al. (2014). Standardized loads acting in knee implants. *PLOS ONE* 9, e86035. doi:10.1371/journal.pone.0086035

Bonnheim, N., Ansari, F., Regis, M., Bracco, P., and Pruitt, L. (2019). Effect of carbon fiber type on monotonic and fatigue properties of orthopedic grade PEEK. *J. Mech. Behav. Biomed. Mater.* 90, 484–492. doi:10.1016/j.jmbbm.2018.10.033

Boriani, S., Tedesco, G., Ming, L., Ghermandi, R., Amichetti, M., Fossati, P., et al. (2018). Carbon-fiber-reinforced PEEK fixation system in the treatment of spine tumors: A preliminary report. *Eur. Spine J.* 27, 874–881. doi:10.1007/s00586-017-5258-5

Bright, J. A., and Rayfield, E. J. (2011). The response of cranial biomechanical finite element models to variations in mesh density. *Anatomical Rec.* 294, 610–620. doi:10.1002/ar.21358

Brockett, C. L., Carbone, S., Abdelgaied, A., Fisher, J., and Jennings, L. M. (2016). Influence of contact pressure, cross-shear and counterface material on the wear of PEEK and CFR-PEEK for orthopaedic applications. *J. Mech. Behav. Biomed. Mater.* 63, 10–16. doi:10.1016/j.jmbbm.2016.06.005

Bus, M. P. A., van de Sande, M. A. J., Fiocco, M., Schaap, G. R., Bramer, J. A. M., and Dijkstra, P. D. S. (2017). What are the long-term results of MUTARS® modular endoprostheses for reconstruction of tumor resection of the distal femur and proximal tibia? *Clin. Orthop. Relat. Res.* 475, 708–718. doi:10.1007/s11999-015-4644-8

Cofano, F., Di Perna, G., Monticelli, M., Marengo, N., Ajello, M., Mammi, M., et al. (2020). Carbon fiber reinforced vs titanium implants for fixation in spinal metastases: A comparative clinical study about safety and effectiveness of the new carbon-strategy. *J. Clin. Neurosci.* 75, 106–111. doi:10.1016/j.jocn.2020.03.013

Geiger, E. J., Arnold, M. T., Hart, C. M., Greig, D., Trikha, R., Sekimura, T., et al. (2023). What is the long-term survivorship of primary and revision cemented distal femoral replacements for limb salvage of patients with sarcoma? *Clin. Orthop. Relat. Research®* 481, 460–471. doi:10.1097/CORR.0000000000002333

Grupp, T. M., Utzschneider, S., Schröder, C., Schwiesau, J., Fritz, B., Maas, A., et al. (2010). Biotribology of alternative bearing materials for unicompartmental knee arthroplasty. *Acta Biomater.* 6, 3601–3610. doi:10.1016/j.actbio.2010.04.003

Guo, Y., and Guo, W. (2022). Study and numerical analysis of von Mises stress of a new tumor-type distal femoral prosthesis comprising a peek composite reinforced with carbon fibers: finite element analysis. *Comput. Methods Biomechanics Biomed. Eng.* 25 (15), 1663–1677. doi:10.1080/10255842.2022.2032681

Haijie, L., Dasen, L., Tao, J., Yi, Y., Xiaodong, T., and Wei, G. (2018). Implant survival and complication profiles of endoprostheses for treating tumor around the knee in adults: A systematic review of the literature over the past 30 years. *J. Arthroplasty* 33, 1275–1287.e3. doi:10.1016/j.arth.2017.10.051

Hak, D. J., Mauffrey, C., Seligson, D., and Lindeque, B. (2014). Use of carbon-fiber-reinforced composite implants in orthopedic surgery. *Orthopedics* 37, 825–830. doi:10.3928/01477447-20141124-05

Heary, R. F., Parvathreddy, N. K., Qayumi, Z. S., Ali, N. S., and Agarwal, N. (2016). Suitability of carbon fiber–reinforced polyetheretherketone cages for use as anterior struts following corpectomy. *J. Neurosurg. Spine* 25, 248–255. doi:10.3171/2016.1.SPINE14291

Hemmerich, A., Brown, H., Smith, S., Marthandam, S. s. k., and Wyss, U. p. (2006). Hip, knee, and ankle kinematics of high range of motion activities of daily living. *J. Orthop. Res.* 24, 770–781. doi:10.1002/jor.20114

Henderson, E. R., Groundland, J. S., Pala, E., Dennis, J. A., Wooten, R., Cheong, D., et al. (2011). Failure mode classification for tumor endoprostheses: retrospective review of five institutions and a literature review. *JBJS* 93, 418–429. doi:10.2106/JBJS.J.00834

Herranz, G., Berges, C., Naranjo, J. A., García, C., and Garrido, I. (2020). Mechanical performance, corrosion and tribological evaluation of a Co–Cr–Mo alloy processed by MIM for biomedical applications. *J. Mech. Behav. Biomed. Mater.* 105, 103706. doi:10.1016/j.jmbbm.2020.103706

Howling, G. I., Sakoda, H., Antonarulrajah, A., Marrs, H., Stewart, T. D., Appleyard, S., et al. (2003). Biological response to wear debris generated in carbon based composites as potential bearing surfaces for artificial hip joints. *J. Biomed. Mater. Res. Part B Appl. Biomaterials* 67B, 758–764. doi:10.1002/jbm.b.10068

Ishfaq, K., Abdullah, M., and Mahmood, M. A. (2021). A state-of-the-art direct metal laser sintering of Ti6Al4V and AlSi10Mg alloys: surface roughness, tensile strength, fatigue strength and microstructure. *Opt. Laser Technol.* 143, 107366. doi:10.1016/j.optlastec.2021.107366

Jung, Y., Koo, Y., and Koo, S. (2017). Simultaneous estimation of ground reaction force and knee contact force during walking and squatting. *Int. J. Precis. Eng. Manuf.* 18, 1263–1268. doi:10.1007/s12541-017-0148-7

Kaleli, N., Sarac, D., Külünk, S., and Öztürk, Ö. (2018). Effect of different restorative crown and customized abutment materials on stress distribution in single implants and peripheral bone: A three-dimensional finite element analysis study. *J. Prosthet. Dent.* 119, 437–445. doi:10.1016/j.prosdent.2017.03.008

Khosravipour, I., Pejhan, S., Luo, Y., and Wyss, U. P. (2018). Customized surface-guided knee implant: contact analysis and experimental test. *Proc. Inst. Mech. Eng. H.* 232, 90–100. doi:10.1177/0954411917744586

Koh, Y.-G., Park, K.-M., Lee, J.-A., Nam, J.-H., Lee, H.-Y., and Kang, K.-T. (2019). Total knee arthroplasty application of polyetheretherketone and carbon-fiber-reinforced polyetheretherketone: A review. *Mater. Sci. Eng. C-MATERIALS Biol. Appl.* 100, 70–81. doi:10.1016/j.msec.2019.02.082

Kutzner, I., Heinlein, B., Graichen, F., Bender, A., Rohlmann, A., Halder, A., et al. (2010). Loading of the knee joint during activities of daily living measured *in vivo* in five subjects. *J. Biomechanics* 43, 2164–2173. doi:10.1016/j.jbiomech.2010.03.046

Lai, Y. -S., Chen, W. -C., Huang, C. -H., Cheng, C. -K, Chan, K. -K., and Chang, T. -K. (2015). The effect of graft strength on knee laxity and graft in-situ forces after posterior cruciate ligament reconstruction. *PLoS One* 10, e0127293. doi:10.1371/journal.pone.0127293

Laux, C. J., Hodel, S. M., Farshad, M., and Müller, D. A. (2018). Carbon fibre/polyether ether ketone (CF/PEEK) implants in orthopaedic oncology. *World J. Surg. Oncol.* 16, 241. doi:10.1186/s12957-018-1545-9

Liao, C., Li, Y., and Tjong, S. C. (2020). Polyetheretherketone and its composites for bone replacement and regeneration. *POLYMERS* 12, 2858. doi:10.3390/polym12122858

Malito, L. G., Arevalo, S., Kozak, A., Spiegelberg, S., Bellare, A., and Pruitt, L. (2018). Material properties of ultra-high molecular weight polyethylene: comparison of tension, compression, nanomechanics and microstructure across clinical formulations. *J. Mech. Behav. Biomed. Mater.* 83, 9–19. doi:10.1016/j.jmbbm.2018.03.029

Manoj Kumar, R., Sharma, S. K., Manoj Kumar, B. V., and Lahiri, D. (2015). Effects of carbon nanotube aspect ratio on strengthening and tribological behavior of ultra high molecular weight polyethylene composite. *Compos. Part A Appl. Sci. Manuf.* 76, 62–72. doi:10.1016/j.compositesa.2015.05.007

Morgan, E. F., Unnikrisnan, G. U., and Hussein, A. I. (2018). Bone mechanical properties in healthy and diseased states. *Annu. Rev. Biomed. Eng.* 20, 119–143. doi:10.1146/annurev-bioeng-062117-121139

Myers, G. J. C., Abudu, A. T., Carter, S. R., Tillman, R. M., and Grimer, R. J. (2007). Endoprosthetic replacement of the distal femur for bone tumours: LONG-TERM results. *J. Bone and Jt. Surg. Br.* 89, 521–526. doi:10.1302/0301-620X.89B4.18631

Nakahara, I., Takao, M., Bandoh, S., Bertollo, N., Walsh, W. R., and Sugano, N. (2013). *In vivo* implant fixation of carbon fiber-reinforced PEEK hip prostheses in an ovine model. *J. Orthop. Res.* 31, 485–492. doi:10.1002/jor.22251

Nevelsky, A., Borzov, E., Daniel, S., and Bar-Deroma, R. (2017). Perturbation effects of the carbon fiber-PEEK screws on radiotherapy dose distribution. *J. Appl. Clin. Med. Phys.* 18, 62–68. doi:10.1002/acm2.12046

Ogaya, S., Naito, H., Okita, Y., Iwata, A., Higuchi, Y., Fuchioka, S., et al. (2015). Contribution of muscle tension force to medial knee contact force at fast walking speed. *J. Mech. Med. Biol.* 15, 1550002. doi:10.1142/S0219519415500025

Ogura, K., Fujiwara, T., Morris, C. D., Boland, P. J., and Healey, J. H. (2021). Long-term competing risks for overall and cause-specific failure of rotating-hinge distal femoral arthroplasty for tumour reconstruction. *Bone and Jt. J.* 103-B, 1405–1413. doi:10.1302/0301-620X.103B8.BJJ-2020-2323.R1

Okazaki, Y., and Gotoh, E. (2005). Comparison of metal release from various metallic biomaterials *in vitro*. *Biomaterials* 26, 11–21. doi:10.1016/j.biomaterials.2004.02.005

Pala, E., Henderson, E. r., Calabrò, T., Angelini, A., Abati, C. n., Trovarelli, G., et al. (2013). Survival of current production tumor endoprostheses: complications, functional results, and a comparative statistical analysis. *J. Surg. Oncol.* 108, 403–408. doi:10.1002/jso.23414

Pfeiffer, F. M. (2016). The use of finite element analysis to enhance research and clinical practice in orthopedics. *J. Knee Surg.* 29, 149–158. doi:10.1055/s-0035-1570114

Rezwan, K., Chen, Q. Z., Blaker, J. J., and Boccaccini, A. R. (2006). Biodegradable and bioactive porous polymer/inorganic composite scaffolds for bone tissue engineering. *Biomaterials* 27, 3413–3431. doi:10.1016/j.biomaterials.2006.01.039

Rotini, R., Cavaciocchi, M., Fabbri, D., Bettelli, G., Catani, F., Campochiaro, G., et al. (2015). Proximal humeral fracture fixation: multicenter study with carbon fiber peek plate. *Musculoskelet. Surg.* 99, 1–8. doi:10.1007/s12306-015-0371-2

Saadlaoui, Y., Milan, J.-L., Rossi, J.-M., and Chabrand, P. (2017). Topology optimization and additive manufacturing: comparison of conception methods using industrial codes. *J. Manuf. Syst.* 43, 178–186. doi:10.1016/j.jmsy.2017.03.006

Sarot, J. R., Contar, C. M. M., Cruz, A. C. C. d., and de Souza Magini, R. (2010). Evaluation of the stress distribution in CFR-PEEK dental implants by the three-dimensional finite element method. *J. Mater Sci. Mater Med.* 21, 2079–2085. doi:10.1007/s10856-010-4084-7

Scharf, B., Clement, C. C., Zolla, V., Perino, G., Yan, B., Elci, S. G., et al. (2014). Molecular analysis of chromium and cobalt-related toxicity. *Sci. Rep.* 4, 5729. doi:10.1038/srep05729

Schliemann, B., Hartensuer, R., Koch, T., Theisen, C., Raschke, M. J., Kösters, C., et al. (2015). Treatment of proximal humerus fractures with a CFR-PEEK plate: 2-year results of a prospective study and comparison to fixation with a conventional locking plate. *J. Shoulder Elb. Surg.* 24, 1282–1288. doi:10.1016/j.jse.2014.12.028

Schmidt, H., Alber, T., Wehner, T., Blakytny, R., and Wilke, H.-J. (2009). Discretization error when using finite element models: analysis and evaluation of an underestimated problem. *J. Biomech.* 42, 1926–1934. doi:10.1016/j.jbiomech.2009.05.005

Scholes, S. C., and Unsworth, A. (2009a). Pitch-based carbon-fibre-reinforced poly (ether—Ether—Ketone) OPTIMA® assessed as a bearing material in a mobile bearing unicondylar knee joint. *Proc. Inst. Mech. Eng. H.* 223, 13–25. doi:10.1243/09544119JEIM471

Scholes, S. C., and Unsworth, A. (2007). The wear properties of CFR-PEEK-OPTIMA articulating against ceramic assessed on a multidirectional pin-on-plate machine. *Proc. Inst. Mech. Eng. H.* 221, 281–289. doi:10.1243/09544119JEIM224

Scholes, S. C., and Unsworth, A. (2009b). Wear studies on the likely performance of CFR-PEEK/CoCrMo for use as artificial joint bearing materials. *J. Mater. Science-Materials Med.* 20, 163–170. doi:10.1007/s10856-008-3558-3

Schwendner, M., Ille, S., Kirschke, J. S., Bernhardt, D., Combs, S. E., Meyer, B., et al. (2023). Clinical evaluation of vertebral body replacement of carbon fiber–reinforced polyetheretherketone in patients with tumor manifestation of the thoracic and lumbar spine. *Acta Neurochir.* 165, 897–904. doi:10.1007/s00701-023-05502-z

Schwitalla, A. D., Abou-Emara, M., Spintig, T., Lackmann, J., and Müller, W. D. (2015). Finite element analysis of the biomechanical effects of PEEK dental implants on the peri-implant bone. *J. Biomechanics* 48, 1–7. doi:10.1016/j.jbiomech.2014.11.017

Schwitalla, A., and Müller, W.-D. (2013). PEEK dental implants: A review of the literature. *J. Oral Implant.* 39, 743–749. doi:10.1563/AAID-JOI-D-11-00002

Sevimay, M., Turhan, F., Kiliçarslan, M. A., and Eskitascioglu, G. (2005). Three-dimensional finite element analysis of the effect of different bone quality on stress distribution in an implant-supported crown. *J. Prosthet. Dent.* 93, 227–234. doi:10.1016/j.prosdent.2004.12.019

Sha, M., Guo, Z., Fu, J., Li, J., Fan Yuan, C., Shi, L., et al. (2009). The effects of nail rigidity on fracture healing in rats with osteoporosis. *Acta Orthop.* 80, 135–138. doi:10.1080/17453670902807490

Smith, S. M., Cockburn, R. A., Hemmerich, A., Li, R. M., and Wyss, U. P. (2008). Tibiofemoral joint contact forces and knee kinematics during squatting. *Gait Posture* 27, 376–386. doi:10.1016/j.gaitpost.2007.05.004

Souza, J. C. M., Pinho, S. S., Braz, M. P., Silva, F. S., and Henriques, B. (2021). Carbon fiber-reinforced PEEK in implant dentistry: A scoping review on the finite element method. *Comput. METHODS BIOMECHANICS Biomed. Eng.* 24, 1355–1367. doi:10.1080/10255842.2021.1888939

Steinberg, E. L., Rath, E., Shlaifer, A., Chechik, O., Maman, E., and Salai, M. (2013). Carbon fiber reinforced PEEK optima—a composite material biomechanical properties and wear/debris characteristics of CF-PEEK composites for orthopedic trauma implants. *J. Mech. Behav. Biomed. Mater.* 17, 221–228. doi:10.1016/j.jmbbm.2012.09.013

Sumner, D. R. (2015). Long-term implant fixation and stress-shielding in total hip replacement. *J. Biomechanics* 48, 797–800. doi:10.1016/j.jbiomech.2014.12.021

Taylor, S. J. G., Walker, P. S., Perry, J. S., Cannon, S. R., and Woledge, R. (1998). The forces in the distal femur and the knee during walking and other activities measured by telemetry. *J. Arthroplasty* 13, 428–437. doi:10.1016/S0883-5403(98)90009-2

Taylor, W. R., Heller, M. O., Bergmann, G., and Duda, G. N. (2004). Tibio-femoral loading during human gait and stair climbing. *J. Orthop. Res.* 22, 625–632. doi:10.1016/j.orthres.2003.09.003

Theivendran, K., Arshad, F., Hanif, U.-K., Reito, A., Griffin, X., and Foote, C. J. (2021). Carbon fibre reinforced PEEK versus traditional metallic implants for orthopaedic trauma surgery: A systematic review. *J. Clin. Orthop. trauma* 23, 101674. doi:10.1016/j.jcot.2021.101674

Trepczynski, A., Kutzner, I., Schwachmeyer, V., Heller, M. O., Pfitzner, T., and Duda, G. N. (2018). Impact of antagonistic muscle co-contraction on *in vivo* knee contact forces. *J. NeuroEngineering Rehabilitation* 15, 101. doi:10.1186/s12984-018-0434-3

Tseng, Z. J, and Flynn, J. J. (2015). Convergence analysis of a finite element skull model of Herpestes javanicus (Carnivora, Mammalia): Implications for robust comparative inferences of biomechanical function. *Journal of Theoretical Biology* 365, 112–148. doi:10.1016/j.jtbi.2014.10.002

Utzschneider, S., Becker, F., Grupp, T. M., Sievers, B., Paulus, A., Gottschalk, O., et al. (2010). Inflammatory response against different carbon fiber-reinforced PEEK wear particles compared with UHMWPE *in vivo*. *Acta Biomater.* 6, 4296–4304. doi:10.1016/j.actbio.2010.06.002

Verma, S., Sharma, N., Kango, S., and Sharma, S. (2021). Developments of PEEK (polyetheretherketone) as a biomedical material: A focused review. *Eur. Polym. J.* 147, 110295. doi:10.1016/j.eurpolymj.2021.110295

Vertesich, K., Staats, K., Böhler, C., Koza, R., Lass, R., and Giurea, A. (2022). Long term results of a rotating hinge total knee prosthesis with carbon-fiber reinforced poly-ether-ether-ketone (CFR-PEEK) as bearing material. *Front. Bioeng. Biotechnol.* 10, 845859. Available at: https://www.frontiersin.org/articles/10.3389/fbioe.2022.845859 [Accessed June 10, 2023]. doi:10.3389/fbioe.2022.845859

Viceconti, M., Olsen, S., Nolte, L.-P., and Burton, K. (2005). Extracting clinically relevant data from finite element simulations. *Clin. Biomech. (Bristol, Avon)* 20, 451–454. doi:10.1016/j.clinbiomech.2005.01.010

Vles, G. F., Brodermann, M. H., Roussot, M. A., and Youngman, J. (2019). Carbon-fiber-reinforced PEEK intramedullary nails defining the niche. *Case Rep. Orthop.* 2019, 1–6. doi:10.1155/2019/1538158

Xu, Z., Zhang, M., Gao, S., Wang, G., Zhang, S., and Luan, J. (2019). Study on mechanical properties of unidirectional continuous carbon fiber-reinforced PEEK composites fabricated by the wrapped yarn method. *Polym. Compos.* 40, 56–69. doi:10.1002/pc.24600

Yao, Y., Mo, Z., Wu, G., Guo, J., Li, J., Wang, L., et al. (2021). A personalized 3D-printed plate for tibiotalocalcaneal arthrodesis: design, fabrication, biomechanical evaluation and postoperative assessment. *Comput. Biol. Med.* 133, 104368. doi:10.1016/j.compbiomed.2021.104368

Yoshida, Y., Osaka, S., Kojima, T., Taniguchi, M., Osaka, E., and Tokuhashi, Y. (2012). Revision of tumor prosthesis of the knee joint. *Eur. J. Orthop. Surg. Traumatol.* 22, 387–394. doi:10.1007/s00590-011-0848-0

Zhao, W., Yu, R., Dong, W., Luan, J., Wang, G., Zhang, H., et al. (2021). The influence of long carbon fiber and its orientation on the properties of three-dimensional needle-punched CF/PEEK composites. *Compos. Sci. Technol.* 203, 108565. doi:10.1016/j.compscitech.2020.108565

Zhu, D., Fu, J., Wang, L., Guo, Z., Wang, Z., and Fan, H. (2021). Reconstruction with customized, 3D-printed prosthesis after resection of periacetabular Ewing's sarcoma in children using "triradiate cartilage-based" surgical strategy:a technical note. *J. Orthop. Transl.* 28, 108–117. doi:10.1016/j.jot.2020.12.006

Ziegler, P., Maier, S., Stöckle, U., Gühring, M., and Stuby, F. M. (2019). The treatment of proximal humerus fracture using internal fixation with fixed-angle plates. *Dtsch. Ärzteblatt Int.* 116 (45), 757–763. doi:10.3238/arztebl.2019.0757

Zimel, M. N., Hwang, S., Riedel, E. R., and Healey, J. H. (2015). Carbon fiber intramedullary nails reduce artifact in postoperative advanced imaging. *Skelet. Radiol.* 44, 1317–1325. doi:10.1007/s00256-015-2158-9

Ziran, B. H., O'Pry, E. K., and Harris, R. M. (2020). Carbon fiber–reinforced PEEK versus titanium tibial intramedullary nailing: A preliminary analysis and results. *J. Orthop. Trauma* 34, 429–433. doi:10.1097/BOT.0000000000001756

frontiers | Frontiers in Bioengineering and Biotechnology

TYPE Case Report
PUBLISHED 09 October 2023
DOI 10.3389/fbioe.2023.1259255

OPEN ACCESS

EDITED BY
Junyan Li,
Southwest Jiaotong University, China

REVIEWED BY
Roland Manfred Klar,
University of Missouri–Kansas City, United States
Yuanqiao Wu,
Boston University, United States

*CORRESPONDENCE
Bo Qu,
50828536@qq.com
Hongsheng Yang,
hongsheng228@163.com

†These authors share first authorship

RECEIVED 17 July 2023
ACCEPTED 19 September 2023
PUBLISHED 09 October 2023

CITATION
Hu Y, Yang K, Liu H, Wang L, Wang S, Zhang X, Qu B and Yang H (2023), 3D-printed custom implant for the management of "locked" posterior dislocation of the shoulder joint with reverse Hill-Sachs lesion: a case report. *Front. Bioeng. Biotechnol.* 11:1259255. doi: 10.3389/fbioe.2023.1259255

3D-printed custom implant for the management of "locked" posterior dislocation of the shoulder joint with reverse Hill-Sachs lesion: a case report

Yongrong Hu†, Kunhai Yang†, Hao Liu, Liping Wang, Song Wang, Xiang Zhang, Bo Qu* and Hongsheng Yang*

Department of Orthopedics, Clinical Medical College and The First Affiliated Hospital of Chengdu Medical College, Chengdu, Sichuan Province, China

Introduction: Irregular bone defects of the humerus are common in clinical practice, but there are fewer reported cases of irregular humeral defects accompanied by shoulder joint "locking" dislocation and reverse Hill-Sachs injury caused by an electric shock. The choice of treatment for such cases is closely related to the extent of shoulder joint function recovery. This is a case report of a 60-year-old male patient who suffered from a shoulder joint "locking" dislocation with accompanying reverse Hill-Sachs injury due to muscle contraction after being electrically shocked at work. The patient was treated with a 3D-printed custom humeral head prosthesis for the treatment of the shoulder joint "locking" dislocation and reverse Hill-Sachs injury.

Case presentation: A 60-year-old male patient, working as a construction worker, presented to our emergency department with right shoulder pain and restricted movement for more than 30 min after an electric shock. Right humeral CT revealed a comminuted fracture of the right humeral head. D-dimer levels were significantly elevated at 3239.00 ng/mL, and oxygen partial pressure was slightly decreased at 68 mmHg. Treatment included emergency wound debridement and dressing for the electrical injury, cardioprotective measures, anticoagulation, and symptomatic management. After stabilizing the patient's condition, the patient underwent 3D-printed custom prosthesis-assisted partial replacement of the right humeral head and rotator cuff repair in the orthopedic department. Postoperatively, the patient's right shoulder joint wound healed well, and mobility was restored.

Conclusion: This case report demonstrates that the use of a 3D-printed custom prosthesis for the treatment of irregular humeral bone defects caused by specific injury mechanisms, especially cases involving shoulder joint "locking" dislocation and reverse Hill-Sachs injury, can achieve precise bone defect repair, minimize surgical trauma, and provide superior outcomes in terms of postoperative functional rehabilitation.

KEYWORDS

reverse Hill-Sachs lesion, posterior dislocation, electric shock injuries, 3D printing, shoulder joint

Introduction

Electrical injuries pose significant risks to the human body and can result in multisystem damage, including injuries to the musculoskeletal, respiratory, cardiovascular, and central nervous systems (Zhang et al., 2017). The injuries caused by electric shocks are primarily characterized by burns but can also lead to secondary damage such as fractures and dislocations. These secondary injuries often occur due to loss of consciousness and subsequent falls or as a result of involuntary muscle contractions (Kokkalis et al., 2017).

The shoulder joint, being the most mobile and unstable joint in the human body, is particularly susceptible to injuries following an electric shock. The surrounding muscles of the shoulder joint forcefully contract, pulling on the bones and causing posterior dislocation of the shoulder joint along with an anterior fracture of the humeral head. This condition, known as "locking" dislocation of the shoulder joint with associated reverse Hill-Sachs injury, presents challenges in terms of diagnosis and treatment, with literature reporting a misdiagnosis and missed diagnosis rate of up to 60% (Stone et al., 2014). This injury has been labeled a "treatment trap" due to its complex nature.

Irregular large bone defects of the humeral head present a significant challenge for orthopedic surgeons. Traditional methods of fracture fixation and shoulder joint replacement have shown limitations in long-term outcomes for irregular large bone defects accompanied by "locking" dislocation of the shoulder joint and reverse Hill-Sachs injury. However, with the rapid development of digital technology, 3D printing technology, also known as additive manufacturing, has emerged as a promising approach for surgical planning and preoperative simulations in cases of humeral head injuries.

In this case report, we present the case of a 60-year-old male patient admitted to our hospital following an electrical injury. The patient underwent treatment for a fractured right humeral head using a 3D-printed custom prosthesis. Given the unique mechanism of injury and the complexity of the case, this report aims to emphasize the necessity and importance of utilizing 3D-printed custom prostheses in the treatment of "locking" dislocation of the shoulder joint with associated reverse Hill-Sachs injury and irregular large bone defects of the humeral head. The report provides a detailed description of the patient's diagnostic and treatment process.

Case presentation

A 60-year-old middle-aged laborer had been engaged in construction activities at the worksite, required to use iron tools to mix concrete within a cement-filled barrel. Unfortunately, the construction site's electrical wires accidentally came into contact

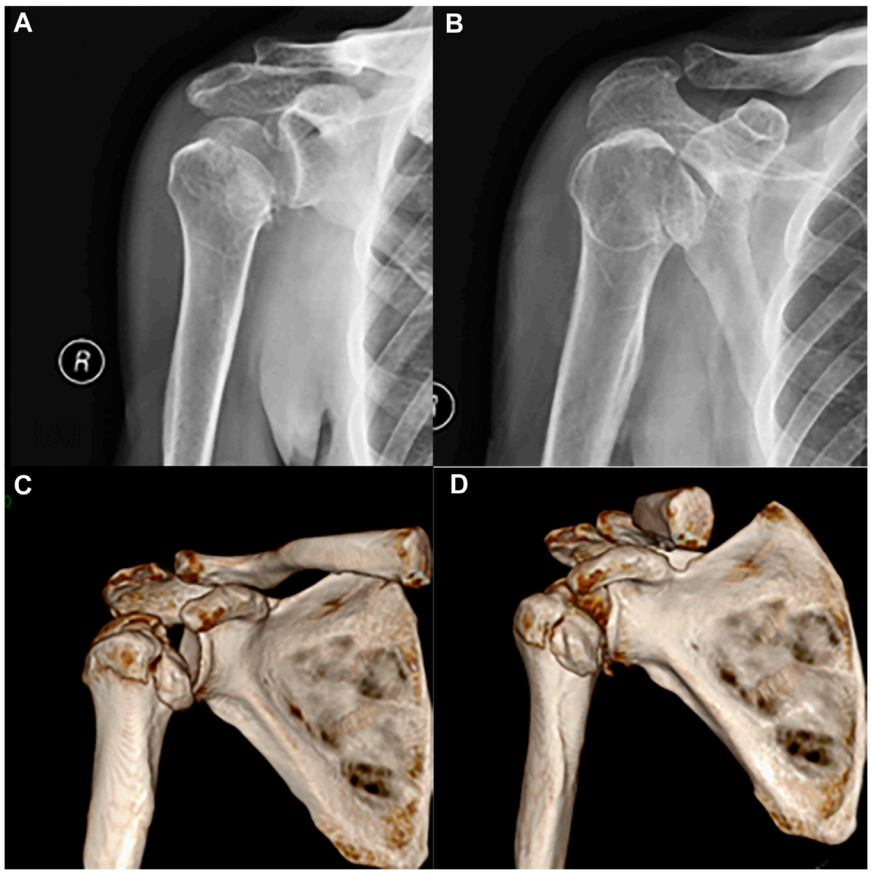

FIGURE 1
(A, B) Preoperative X-ray and **(C, D)** CT bone three-dimensional reconstruction.

TABLE 1 General information and indicators of abnormal laboratory tests upon admission.

Category	Result	Reference value	Counting unit
Gender	Male	—	—
Age	60	—	—
Past Medical History	none	—	—
Family History	none	—	—
Personal History	none	—	—
Blood Routine			
WBC	14.26	4–10	10^9/L
NE%	80.2	45–77	%
LY%	10.1	20–40	%
MO%	9.3	3–8	%
NE#	11.43	2–7.7	10^9/L
MO#	1.33	0.12–0.8	10^9/L
Liver Function, Renal Function and Cardiac Enzymes			
TP	55.6	65–85	g/L
ALB	35.2	40–55	g/L
CK	392	<200	U/L
Urine Analysis			
PRO	+-	-	—
PH	8.0	5.0–7.5	—
BLD	3+	-	—

with the cement-filled iron barrel. The electrical current from the wires was conducted through the iron barrel into his body, resulting in his electrocution (approximately 380V) and subsequent collapse. He immediately experienced chest tightness, blurred vision, and excruciating pain that immobilized his right shoulder. Promptly, his colleagues dialed emergency services (120) and swiftly transported him to the Emergency Department of the First Affiliated Hospital of Chengdu Medical College. Upon arrival, a burn care physician conducted a physical examination, noting significant tenderness and limited mobility in the right shoulder joint. However, the Dugas sign yielded a negative result (–). Furthermore, the patient had multiple electrical burn wounds on his hands and feet, characterized by volcano-shaped lesions with dry, black charred tissue inside. After confirming the patient's stable vital signs, the wounds underwent debridement and dressing. The patient received treatment at the Burn Unit. Following treatment there, the patient was further transferred to the Orthopedics Department for further evaluation.

Radiographic and three-dimensional CT scans were performed to assess the condition of the patient's right shoulder joint (Figure 1). The imaging revealed a comminuted fracture of the right humeral head with fragmented, collapsed fragments and surrounding soft tissue swelling, along with a minor amount of air. Preoperative examination demonstrated significant impairment in the patient's range of motion in the right shoulder joint. General information and indicators of abnormal laboratory tests upon admission see in Table 1.

Based on the patient's medical history and auxiliary examinations, the orthopedic physician established the following diagnoses: 1) Comminuted fracture with a substantial bone defect in the right humeral head, 2) "Locking" dislocation of the right shoulder joint accompanied by a reverse Hill-Sachs injury, 3) Proximal fracture of the right humerus, and 4) Electrical injury with necrotic electrical burns on both hands and feet. After careful deliberation, the medical team decided to proceed with a 3D-printed custom prosthesis-assisted surgery, which involved partial replacement of the right humeral head and exploration and repair of the rotator cuff, once the patient's condition stabilized. A 3D-printed model was used to simulate the surgical procedure, enabling the formulation of an effective plan that would address the remaining fracture fragments specific to the patient's case. During the design phase of the 3D-printed prosthesis, various factors were taken into account, including prosthesis compatibility, the arrangement of rotator cuff suture holes, and the integration of the prosthesis and bone contact surface to promote bone integration.

The 3D-printed prosthetic limb was fabricated using Ti-6Al-4V material, renowned for its outstanding biocompatibility and bone integration properties (Li et al., 2020). The prosthetic limb was designed utilizing Mimics software (version 20.0; Materialise, Belgium) and manufactured through 3D printing technology by Chunli Limited Company (Beijing, People's Republic of China). Before proceeding with final production, the prosthetic limb model underwent printing and testing procedures to validate our design. The entire process, commencing from the collection of patient data to the production of the prosthetic limb, typically spanned approximately 3 weeks.

The surgical procedure (Figure 2) was carried out as follows: The surgical site was accessed through the deltopectoral groove of the pectoralis major muscle. During the surgery, the greater and lesser tuberosities of the right humerus were exposed, revealing a severe fracture with small and fragmented bone pieces that could not be adequately stabilized using screws. The right humeral head was dislocated and trapped, necessitating the use of a bone lever for reduction and the installation of a resection guide. The fracture ends were trimmed with a saw, and the surrounding fragmented fragments were removed. A marrow expansion was performed at the proximal end, followed by the placement of the 3D-printed humeral head prosthesis based on the nailing plate guide. Direct visualization confirmed a good match between the 3D-printed prosthesis and the remaining right humeral head. The rotator cuff was sutured onto the 3D-printed prosthesis, and the repair and fixation of the infraspinatus muscle insertion were conducted. Fluoroscopy was utilized throughout the surgery to ensure proper positioning of the prosthesis. Postoperatively, the patient's condition was favorable, allowing for weight-bearing activities to commence on the second day. The shoulder joint exhibited limited anterior and posterior swinging movements. The surgical incision healed without complications or infection. Once the incision had fully healed, the patient was discharged for home treatment and provided with guidance for rehabilitation training. In the initial phase (0–6 weeks) after surgery, the patient was advised to use a suspension sling (with the option of an abduction pillow) for

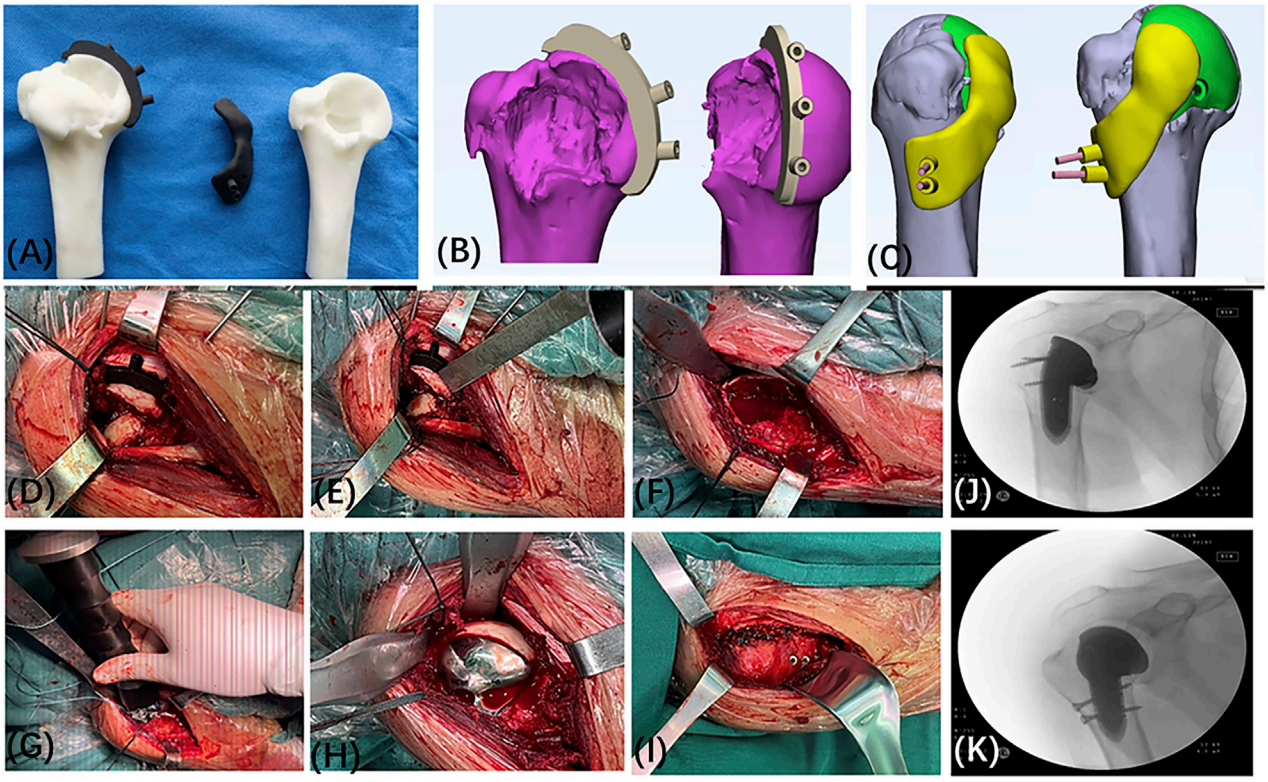

FIGURE 2
Custom 3D Printed Prosthesis Design and Surgical Procedure. **(A–C)** Preoperative Simulated Guide Plate Osteotomy and Fixation. **(D–F)** During the surgery, a significant bone defect was observed in the right humeral head. **(G–I)** Intraoperatively, the site of the humeral head injury and the position of the 3D-printed implant were confirmed. Repairs were performed on the rotator cuff and the insertion point of the infraspinatus muscle on the scapula. **(J, K)** Intraoperatively, fluoroscopy shows that the implant is well-placed.

immobilization. Passive elevation up to 120° was permitted, and pendulum exercises involving forward and backward as well as side-to-side swinging of the affected arm in a bent-over position were recommended. In the subsequent phase (7–12 weeks after surgery), the support device was removed, and resistance training, including external rotation exercises, was gradually introduced. In the third phase (after 12 weeks), comprehensive shoulder joint training was conducted to optimize the patient's shoulder joint function (Yu et al., 2020).

Postoperative follow-up was conducted to evaluate the patient's recovery. Over a 2-month period at our postoperative follow-up, notable improvements in functional and pain scores were observed between preoperative, 1-week postoperative, and 2-month postoperative assessments. The Visual Analog Scale (VAS) pain score decreased from approximately 5 points 1 week after surgery to approximately 2 points 2 months after surgery. At the 2-month mark, the patient achieved 150° of forward flexion, 90° of abduction, and 40° of extension in the shoulder joint, demonstrating significant improvement compared to preoperative and 1-week postoperative measurements (Figure 3).

Postoperative X-rays revealed no evidence of prosthesis loosening (Figures 4A, B). According to the concept of osseointegration proposed by Professor Branemark in the 1960s (Branemark et al., 2001), a permanent bone-to-bone interface, devoid of fibrous tissue intervention, was established when an implant came into contact with actively functioning bone tissue. The occurrence of osseointegration on the prosthesis surface was observed on the 2-month follow-up CT scan (Figures 4C, D).

Discussion

This case report strictly adheres to The CARE guidelines checklist 2013 edition (Gagnier et al., 2013) and provides a detailed description of a rare case involving an irregular defect of the right humerus caused by an electrical injury, accompanied by posterior dislocation of the right shoulder joint and a reverse Hill-Sachs lesion. In clinical practice, such a condition is relatively uncommon, thus further exploration is warranted regarding its complex etiology and treatment methods for irregular bone defects. In our literature search, we did not find any case reports specifically related to electrical injuries and the use of 3D printing technology for repair and treatment. Therefore, this report represents the first of its kind. However, for the repair of large irregular bone defects, previous studies have demonstrated the potential application of customized repairs using 3D printing technology. However, for the repair of irregular large segmental bone defects, existing research has demonstrated the potential application of customized repair using 3D printing technology. For example, Fiz et al. have suggested that in femoral

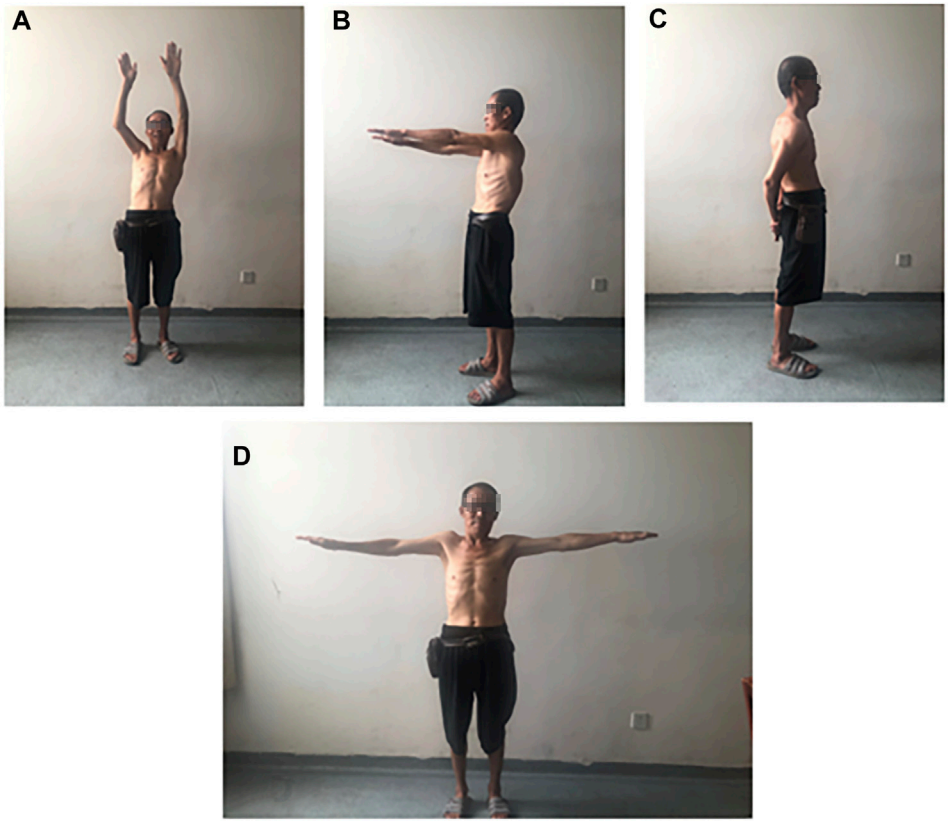

FIGURE 3
Patient's range of motion at 1 month postoperatively: **(A, B)** Forward flexion: 90°–150°, **(C)** Extension: 40°, **(D)** Abduction: 90°.

derotational osteotomy, 3D printing technology is considered a rapid and cost-effective tool for improving surgical outcomes (Fiz et al., 2017).

In this case, the patient suffered multiple electrical wounds on both hands and feet following an electrical shock. The patient also presented with a "locked" posterior dislocation of the right shoulder joint, a reverse Hill-Sachs lesion, as well as a comminuted fracture and a substantial defect of the right humeral head. We believe these injuries were a result of the burns and intense contraction of the muscles around the right shoulder joint. For such conditions, early surgical intervention is crucial to restore the morphological integrity of the humeral head and stabilize the shoulder joint. Studies have shown that conservative treatment can be considered for fresh dislocations with humeral head defects less than 25%. Manual reduction under nerve block anesthesia and the use of external fixation can achieve satisfactory stability of the shoulder joint. However, for patients with humeral head defects greater than 25%, conservative treatment is prone to result in shoulder joint deformity and loss of function, severely impacting the quality of life. Therefore, active surgical intervention should be chosen (Cirino et al., 2022).

Traditional surgical methods for this condition include McLaughlin surgery, modified McLaughlin surgery, shoulder joint replacement, and arthroscopic surgery. Although these methods can effectively restore shoulder joint stability, McLaughlin surgery and modified McLaughlin surgery are only suitable for patients with humeral head defects less than 50% (Yu et al., 2020). They have disadvantages such as long operation time, significant bleeding, extensive trauma, slow recovery, and difficulty in reconstructing bone fragments that fit the defect site. Long-term complications may include bone resorption, traumatic arthritis, and pain. While shoulder joint replacement can address joint mobility issues in the short term, this method may disrupt normal tissue structures and has drawbacks such as long operation time, significant bleeding, and substantial trauma. Additionally, prosthetic implants have a limited lifespan and may require subsequent or multiple shoulder joint replacement surgeries. Arthroscopic repair of soft tissue injuries and restoration of soft tissue balance is suitable for patients with humeral head defects less than 25%, particularly those with defects less than 20% (Martetschlager et al., 2013). This may be due to the fact that in cases with smaller humeral head defects, shoulder joint instability is primarily caused by damage to the joint capsule, labrum, and rotator cuff (Yu et al., 2020). Arthroscopic modified McLaughlin surgery also has some limitations, such as a longer learning curve, uncertain long-term outcomes, and difficulties in reducing locked posterior dislocations under arthroscopy (Du et al., 2023). Therefore, we did not choose these methods.

In this case, the extent of humeral head injury was 40%, with important structures such as the rotator cuff attached to it. The humeral head has a smooth, spherical structure that is difficult to match in shape. Therefore, we chose to use 3D printing technology to design precise implants for the surgery. Unlike traditional internal fixation devices such as plates and screws, 3D-printed implants can

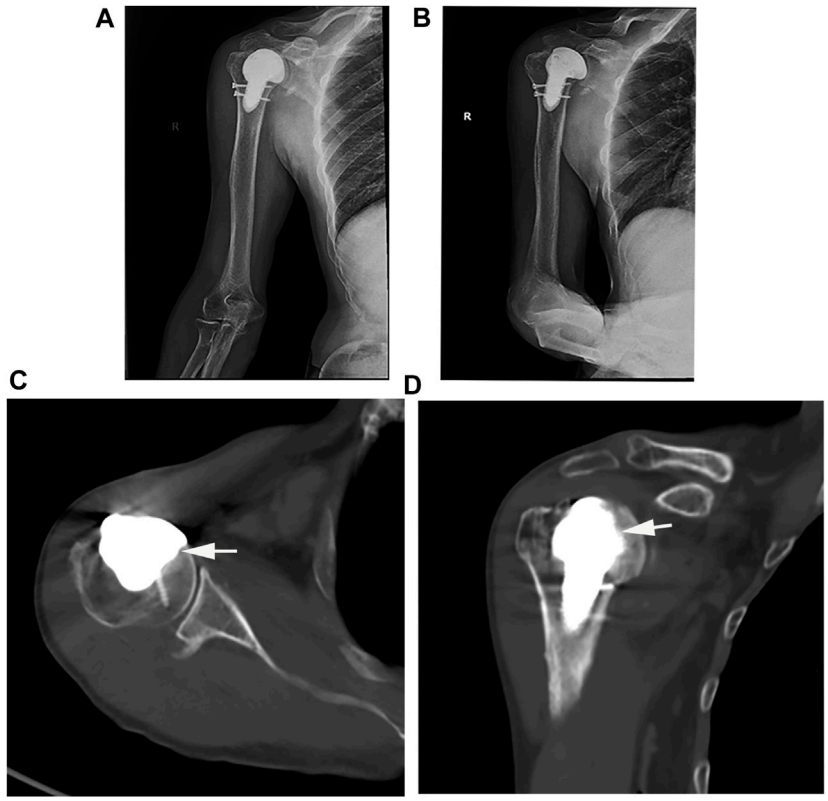

FIGURE 4
(A, B) Postoperative X-ray and **(C, D)** CT examination (White arrow: successful osseointegration).

seamlessly connect with the remaining portion of the patient's humeral head, achieving a perfect fit. This not only maximizes the preservation of normal tissue structures, reduces operation time, bleeding, and trauma, but also enables the reconstruction of the proximal anatomy of the humeral bone to facilitate the attachment and repair of a portion of the rotator cuff, thereby improving shoulder joint stability and function. We observed a secure fixation of the implant. Two months post-surgery, we noted the formation of a bony callus at the interface between the implant and the bone, indicating the feasibility of achieving osseointegration with the 3D-printed porous implant. Additionally, 3D-printed porous metal structures can provide excellent bone integration and protection of the subchondral bone and joint surfaces, facilitating bone ingrowth and shaping (Abar et al., 2022).

Regarding the limitation of a 2-month follow-up period, we acknowledge that the follow-up duration was relatively short. However, within the short span of 2 months, the patient's pain, as measured by the Visual Analog Scale (VAS) score, and shoulder joint range of motion had already shown such significant recovery, further supporting the effectiveness of this technique. Nonetheless, we plan to conduct further follow-up to gain a more comprehensive understanding of the patient's recovery. Considering the limitations of implants, the presence of implants in the body can endure for several centuries; therefore, the question of whether they will degrade inside the body should not be entertained. However, the surface roughness, morphology, and morphological characteristics of implants can significantly influence cellular behavior, encompassing aspects such as cell adhesion, proliferation, differentiation, and the corrosion behavior of implants. Consequently, most additive manufacturing technologies require post-processing to enhance their surface properties, thereby promoting osseointegration. In addition, challenges such as adhesive removal, sacrificing residual materials, microbial infections, uneven shrinkage, and resolution issues may pose limitations in the manufacturing of these implants (Alipour et al., 2022). As a result, recent research has proposed improved additive manufacturing methods to address these challenges and continues to delve into further studies to better serve patients.

Based on this case, it can be concluded that 3D printing technology offers the following advantages in treating large irregular bone defects of a special nature: 1. Customized individualized implants tailored to the specific factors causing the irregular lesion, enabling personalized and precise treatment to achieve satisfactory expected outcomes; 2. The implant surface possesses a porous and rough trabecular bone structure that better mimics the microstructure of human bones, promoting bone and soft tissue ingrowth; 3. Additive manufacturing techniques allow for customized production of implants that closely match the patient's needs. Therefore, this technology addresses the shortcomings of traditional shoulder joint surgeries for the treatment of large segmental bone defects and brings benefits to challenging cases.

Conclusion

The utilization of 3D-printed custom implants for the treatment of irregular humeral head bone defects caused by specific injury mechanisms, particularly in cases of shoulder joint "locked" posterior dislocation and reverse Hill-Sachs injury, represents a promising and advantageous option.

Data availability statement

The original contributions presented in the study are included in the article/Supplementary material, further inquiries can be directed to the corresponding authors.

Ethics statement

The studies involving humans were approved by the Ethics Committee Office of the First Affiliated Hospital of Chengdu Medical College. The studies were conducted in accordance with the local legislation and institutional requirements. The participants provided their written informed consent to participate in this study. Written informed consent was obtained from the individuals for the publication of any potentially identifiable images or data included in this article.

Author contributions

YH: Funding acquisition, Investigation, Methodology, Writing–original draft, Writing–review and editing. KY: Writing–review and editing. HL: Writing–review and editing. LW: Data collection. SW: Writing–review and editing. XZ: Methodology, Writing–review and editing. BQ: Funding acquisition, Methodology, Supervision, Writing–review and editing. HY: Funding acquisition, Methodology, Supervision, Writing–review and editing.

Funding

The authors declare financial support was received for the research, authorship, and/or publication of this article. This work was supported by Project of Sichuan Provincial Department of Science and Technology (NO: 2021YFG0324); Foundation project of Chengdu Medical College (CYZ18-32).

Conflict of interest

The authors declare that the research was conducted in the absence of any commercial or financial relationships that could be construed as a potential conflict of interest.

Publisher's note

All claims expressed in this article are solely those of the authors and do not necessarily represent those of their affiliated organizations, or those of the publisher, the editors and the reviewers. Any product that may be evaluated in this article, or claim that may be made by its manufacturer, is not guaranteed or endorsed by the publisher.

References

Abar, B., Kwon, N., Allen, N. B., Lau, T., Johnson, L. G., Gall, K., et al. (2022). Outcomes of surgical reconstruction using custom 3D-printed porous titanium implants for critical-sized bone defects of the foot and ankle. *Foot Ankle Int.* 43 (6), 750–761. doi:10.1177/10711007221077113

Alipour, S., Nour, S., Attari, S. M., Mohajeri, M., Kianersi, S., Taromian, F., et al. (2022). A review on *in vitro*/*in vivo* response of additively manufactured Ti-6Al-4V alloy. *J. Mater Chem. B* 10 (46), 9479–9534. doi:10.1039/d2tb01616h

Branemark, R., Branemark, P., Rydevik, B., and Myers, R. R. (2001). Osseointegration in skeletal reconstruction and rehabilitation: A review. *J. Rehabilitation Res. Dev.* 38 (2), 175–181.

Cirino, C. M., Kantrowitz, D. E., Cautela, F. S., Gao, M., Cagle, P. J., and Parsons, B. O. (2022). Incidence and risk factors for pseudosubluxation of the humeral head following proximal humerus fracture. *JSES Int.* 6 (3), 338–342. doi:10.1016/j.jseint.2022.01.013

Du, G., Hu, X., Wen, Y., Tan, L., Lu, M., Zhang, Y., et al. (2023). Finite element analysis of using 3D-printed porous metal support prosthesis for the treatment of giant cell tumor of the distal femur with bone defects. *J. Clin. Res. Orthop.* 8 (02), 99–109. doi:10.19548/j.2096-269x.2023.02.006

Fiz, N., Delgado, D., Sánchez, X., Sánchez, P., Bilbao, A. M., Oraa, J., et al. (2017). Application of 3D technology and printing for femoral derotation osteotomy: case and technical report. *Ann. Transl. Med.* 5 (20), 400. doi:10.21037/atm.2017.07.03

Gagnier, Joel J., Kienle, G., Altman, D. G., Moher, D., Sox, H., and Riley, D. (2013). The CARE guidelines: consensus-based clinical case reporting guideline development. *Glob. Adv. health Med.* 2 (5), 38–43. doi:10.7453/gahmj.2013.008

Kokkalis, Z. T., Iliopoulos, I. D., Antoniou, G., Antoniadou, T., Mavrogenis, A. F., and Panagiotopoulos, E. (2017). Posterior shoulder fracture-dislocation: an update with treatment algorithm. *Eur. J. Orthop. Surg. Traumatol.* 27 (3), 285–294. doi:10.1007/s00590-016-1840-5

Li, Q., Li, X., Chen, Z., Sun, H. F., Wang, H. B., Liu, H., et al. (2020). MR imaging as a precise technique to evaluate skull-base tumor volume: comparison of CT, MR imaging and FDG PET from murine and clinical data. *Chin. Orthop. J. Clin. Basic Res.* 2 (02), 105–110. doi:10.1016/j.jcms.2019.12.007

Martetschlager, F., Padalecki, J. R., and Millett, P. J. (2013). Modified arthroscopic McLaughlin procedure for treatment of posterior instability of the shoulder with an associated reverse Hill-Sachs lesion. *Knee Surg. Sports Traumatol. Arthrosc.* 21 (7), 1642–1646. doi:10.1007/s00167-012-2237-6

Stone, N., Karamitopoulos, M., Edelstein, D., Hashem, J., and Tucci, J. (2014). Bilateral distal radius fractures in a 12-year-old boy after household electrical shock: case report and literature summary. *Case Rep. Med.* 2014, 1–5. doi:10.1155/2014/235756

Yu, M., Wan, Y., Ren, B., Wang, H., Zhang, X., Qiu, C., et al. (2020). 3D printed Ti-6Al-4V implant with a micro/nanostructured surface and its cellular responses. *ACS Omega* 5 (49), 31738–31743. doi:10.1021/acsomega.0c04373

Zhang, Y., Zhou, Z., Zhang, Z., and Wu, S. (2017). A facile green synthesis of silver nanoparticles based on poly-L-lysine. *Orthop. J. China* 25 (17), 1534–1537. doi:10.1166/jnn.2017.13003

frontiers | Frontiers in Bioengineering and Biotechnology

TYPE Original Research
PUBLISHED 31 October 2023
DOI 10.3389/fbioe.2023.1273263

OPEN ACCESS

EDITED BY
Zhenxian Chen,
Chang'an University, China

REVIEWED BY
Giovanni Badiali,
University of Bologna, Italy
Kaushik Mukherjee,
Indian Institute of Technology Delhi, India

*CORRESPONDENCE
Jian-Qiao Guo,
guojianqiao@bit.edu.cn
Xiang-Liang Xu,
kqxxl@126.com

†These authors have contributed equally to this work

RECEIVED 05 August 2023
ACCEPTED 16 October 2023
PUBLISHED 31 October 2023

CITATION
Wang J-L, Wang J, Chen K-N, Guo J-Q, Xu X-L and Guo C-B (2023), Designing customized temporomandibular fossa prosthesis based on envelope surface of condyle movement: validation via *in silico* musculoskeletal simulation.
Front. Bioeng. Biotechnol. 11:1273263.
doi: 10.3389/fbioe.2023.1273263

Designing customized temporomandibular fossa prosthesis based on envelope surface of condyle movement: validation via *in silico* musculoskeletal simulation

Jun-Lin Wang[1†], Jing Wang[1†], Ke-Nan Chen[1], Jian-Qiao Guo[2*], Xiang-Liang Xu[1*] and Chuan-Bin Guo[1]

[1]Department of Oral and Maxillofacial Surgery, Peking University School and Hospital of Stomatology, National Center of Stomatology, National Clinical Research Center for Oral Diseases, National Engineering Research Center of Oral Biomaterials and Digital Medical Devices, Beijing Key Laboratory of Digital Stomatology, Research Center of Engineering and Technology for Computerized Dentistry, Ministry of Health, NMPA Key Laboratory for Dental Materials, Beijing, China, [2]MOE Key Laboratory of Dynamics and Control of Flight Vehicle, School of Aerospace Engineering, Beijing Institute of Technology, Beijing, China

Objective: This study presents an innovative articular fossa prosthesis generated by the envelope surface of condyle movement, and compares its mandible movements, muscle activities, and joint reaction forces with two temporomandibular joint (TMJ) prostheses using multibody musculoskeletal simulation.

Methods: A healthy 23-year-old female was recruited for this study. Cone-beam computed tomographic (CBCT) was performed to reconstruct the mandibular bone geometry. A customized TMJ fossa prosthesis was designed based on the subject-specific envelope surface of condyle movement (ESCM). Mandibular kinematics and jaw-closing muscle electromyography (EMG) were simultaneously recorded during maximum jaw opening-closing movements. To validate our prosthesis design, a mandibular musculoskeletal model was established using flexible multibody dynamics and the obtained kinematics and EMG data. The Biomet fossa prosthesis and the ellipsoidal fossa prosthesis designed by imitating the lower limb prostheses were used for comparison. Simulations were performed to analyze the effects of different fossa prostheses on jaw opening-closing motions, mandibular muscle activation, and contact forces.

Results: The maximum opening displacement for the envelope-based fossa prosthesis was greater than those for Biomet and ellipsoidal prostheses (36 mm, 35 mm, and 33 mm, respectively). The mandibular musculoskeletal model with ellipsoidal prosthesis led to dislocation near maximal jaw opening. Compared to Biomet, the envelope-based fossa reduced the digastric and lateral pterygoid activation at maximal jaw opening. It also reduced the maximal resistance to condylar sliding on the intact side by 63.2 N.

Conclusion: A customized TMJ fossa prosthesis was successfully developed using the ESCM concept. Our study of musculoskeletal multibody modeling has

highlighted its advantages and potential. The artificial fossa design successfully achieved a wider condylar range of motion. It also reduced the activation of jaw opening muscles on the affected side and resistance on the intact side. This study showed that an ESCM-based approach may be useful for optimizing TMJ fossa prostheses design.

KEYWORDS

articular fossa prosthesis, envelope surface, musculoskeletal simulation, flexible multibody dynamics, temporomandibular joint, mandibular movement

1 Introduction

The temporomandibular joint (TMJ) is the only movable joint of the human oral and maxillofacial region, and is actively involved in several daily activities (Zheng et al., 2019). TMJ disorders, such as tumors and ankylosis, can affect its integrity and cause joint dysfunction (Mercuri, 2000). Total joint replacement is an effective method for TMJ reconstruction and functional restoration (Sidebottom, 2008).

Currently, there are two commercially-available TMJ replacement systems approved by the Food and Drug Administration, Biomet Microfixation (Jacksonville, FL, USA) (Imola and Liddell, 2016) and TMJ Concepts (Ventura, CA, USA) (Wolford et al., 1994). Both these systems consist of condylar and fossa components (Kiehn et al., 1974). The TMJ Concepts prostheses are constructed using patient-specific cone-beam computed tomography (CBCT) data (Wolford et al., 2003). Meanwhile, Biomet has three stock components with different lengths and styles (Imola and Liddell, 2016). The Biomet artificial fossa is a flat and ellipsoidal surface, and the TMJ fossa and mandibular ramus may need to be trimmed in order to fit with it.

Existing TMJ prostheses were designed solely based on medical imaging, and cannot completely restore the physiological condylar kinematics (Zou et al., 2020). The natural condyle has sliding and rotational movements (van Loon et al., 1999). Although TMJ replacement significantly improves mandibular movement, the condylar kinematics for the prosthesis are different compared to the natural TMJ (Westermark, 2010; Gruber et al., 2015; Gonzalez-Perez et al., 2016). In particular, condylar sliding may be completely lost after TMJ replacement (Sonnenburg and Sonnenburg, 1985; Merlini and Palla, 1988; Mercuri et al., 1995). This may be because the geometry of the TMJ prosthesis restricts the condylar range of motion (ROM) (van Loon et al., 1999). *In vitro* experiments performed by Celebi et al.(2011) demonstrated that the artificial condyle is more deeply enclosed within the articular fossa compared to the natural condyle. This makes achieving the normal condylar ROM nearly impossible.

A function-based prosthesis may be designed by imitating the artificial joints of the lower limb. For example, the instantaneous center of rotation of the knee joint was considered when designing artificial knee implants (Walker, 2001). It has been observed that the physiological knee kinematics cannot be achieved by restoring its anatomical morphology alone (Wang et al., 2021). Similarly, TMJ fossa prostheses may also be custom-made based on the three-dimensional (3D) condylar movement. According to the finite element analysis using a canine model, this may result in a reasonable strain distribution (Xu et al., 2017). Reconstruction of the functional condylar surface, i.e., the envelope surface of condylar movement (ESCM), in normal adults was proposed by Huang et al. (2021). The use of the ESCM concept for designing TMJ fossa prostheses can allow physiologically accurate kinematics (Chen et al., 2022a; Chen et al., 2022b).

The ESCM surface concept has not yet been applied for the real-world design of human TMJ fossa prostheses. An important reason is the lack of systematic comparison of the effect of different TMJ prostheses on mandibular biomechanics. Radiographic, ultrasonic, magnetic, and optoelectronic tracking methods have previously been used for *in vivo* quantification of the mandibular kinematics (Woodford et al., 2020). Based on these measured kinematics data, multibody dynamics modeling provided an *in silico* method to investigate the hidden biomechanics of the mandibular musculoskeletal system. This has proven to be effective and reliable in quantifying the functional outcomes after mandibular surgery and reconstruction (Hannam et al., 2010; Hannam, 2011). Previous studies have also validated the feasibility of simulating maximal jaw opening-closing movements based on flexible multibody dynamics (Broser et al., 2021; Guo et al., 2022).

This study is the first to propose a TMJ fossa prosthesis design based on the ESCM concept. Functional outcomes of this fossa design, including mandibular movements, muscle activity, and joint reaction forces, were predicted based on musculoskeletal multibody simulations, and compared with those of the Biomet and ellipsoidal fossa prostheses. We hypothesized that the customized envelope-based fossa prosthesis would improve the functional outcomes, including condylar ROM and jaw opening muscle activations.

2 Materials and methods

2.1 Subject

This study was approved by the Institutional Review Board of Peking University School and Hospital of Stomatology, Beijing, China (Pkussirb-201947091). A 23-year-old female volunteer with no symptoms and signs of TMJ disorder or a history of TMJ disorder or orthodontic treatment was selected. Written informed consent to publish the findings was obtained.

2.2 CBCT

Skull base and mandibular CBCT scans (NewTom VG, NewTom, Imola, Italy; Voxel size: 0.3 mm, Field of view: 16 cm × 16 cm) were performed in the intercuspal position. The segmentation and 3D reconstructions were performed in stereolithographic format using CBCT data in the Proplan CMF software (version 3.0, Materialise, Leuven, Belgium).

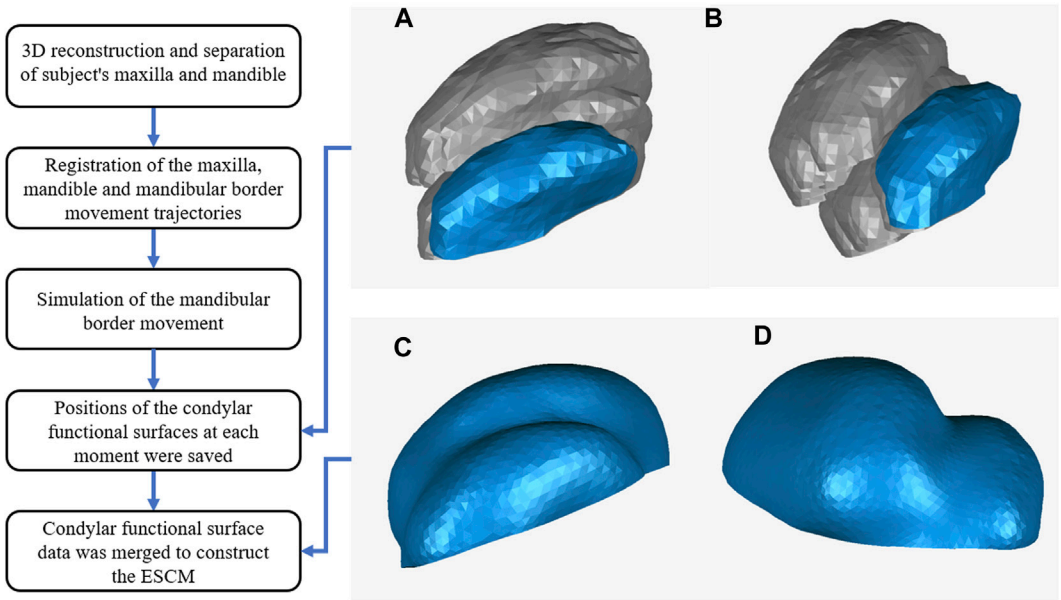

FIGURE 1
Procedure of obtaining the ESCM. The coronal section **(A)** and sagittal section **(B)** of positions of the condylar functional surfaces at each moment. The coronal section **(C)** and sagittal section **(D)** of ESCM generated by merging the condylar functional surface data.

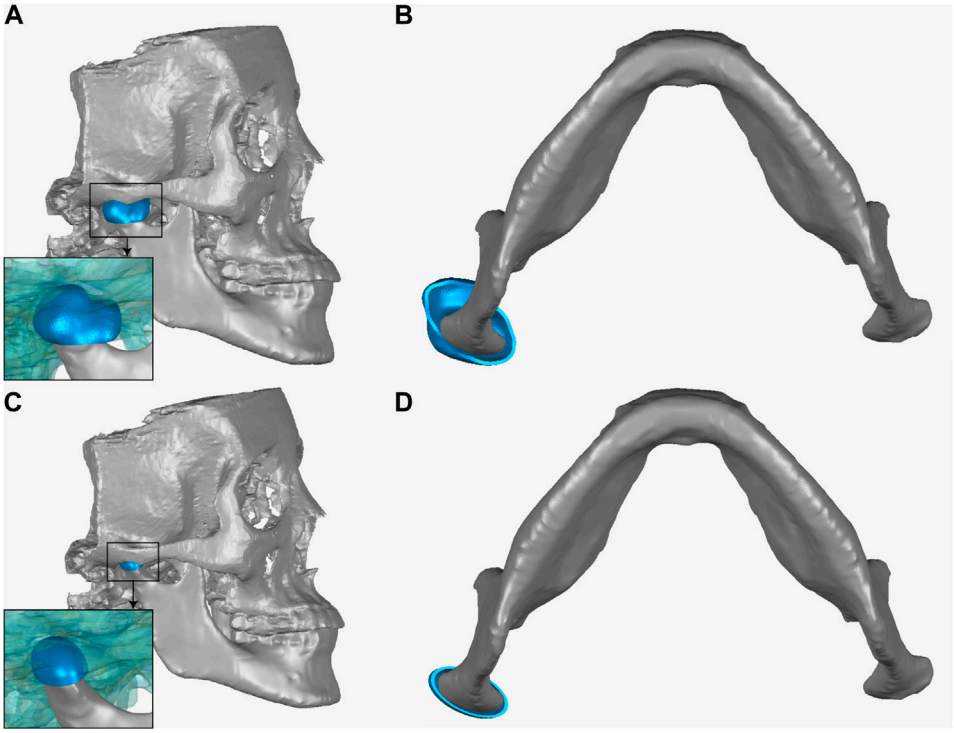

FIGURE 2
The sagittal section **(A)** and cross section **(B)** of envelope-based fossa prosthesis. The sagittal section **(C)** and cross section **(D)** of the ellipsoidal fossa prosthesis.

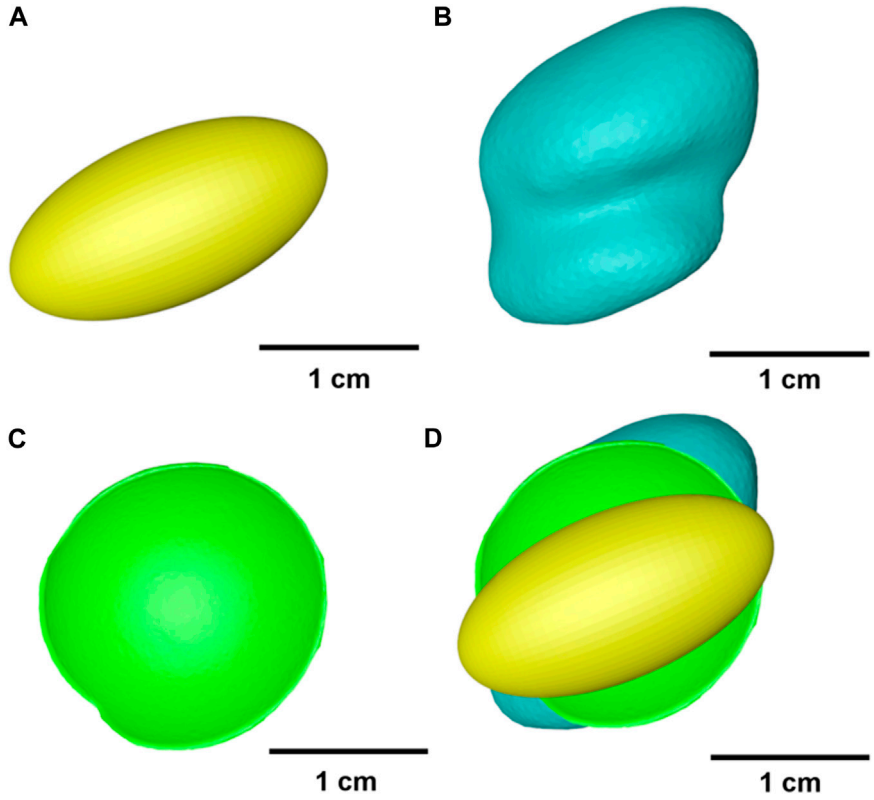

FIGURE 3
Geometry of different fossa prostheses. **(A)** Ellipsoidal fossa prosthesis. **(B)** Envelope-based fossa prothesis. **(C)** Biomet fossa prosthesis. **(D)** Comparison of the range of condylar motion.

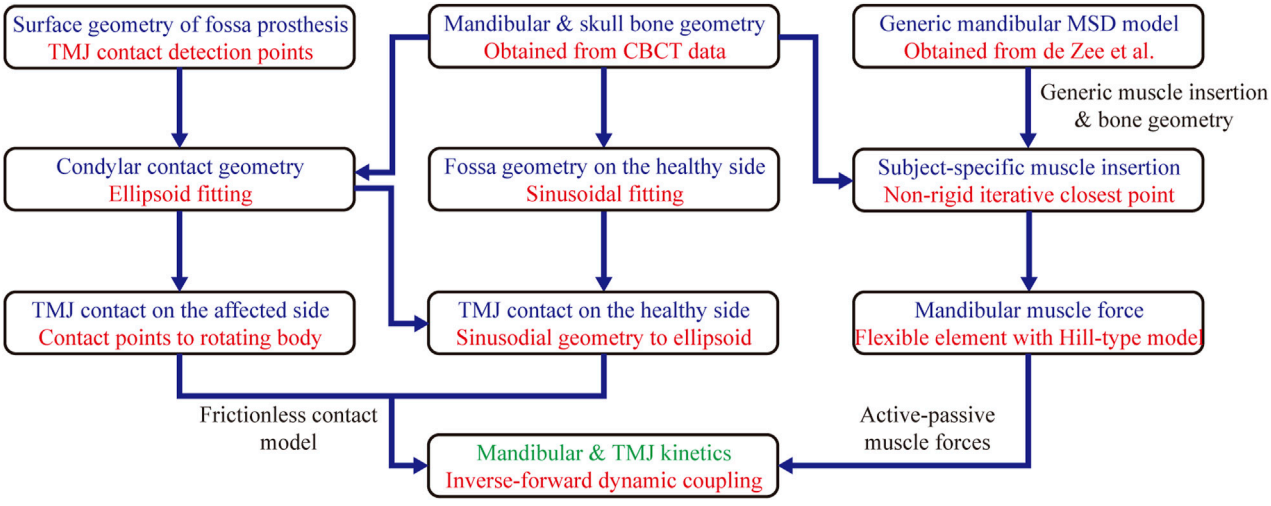

FIGURE 4
The schematic overview of establishing the subject-specific mandible musculoskeletal model. MSD, Multibody System Dynamics.

2.3 Mandibular movements and electromyography (EMG)

The subject was instructed to perform two warm-up cycles and one test cycle of maximal opening-closing movements, beginning and ending in the maximum intercuspal position (Baqaien et al., 2007; Koeppel et al., 2015). The WINJAW ultrasound system (Zebris Medical GmbH, Isny, Germany) was used to record the mandibular motion. Mandibular position relative to the upper dentition was recorded using the Trios intraoral scanner (3Shape, Copenhagen, Denmark).

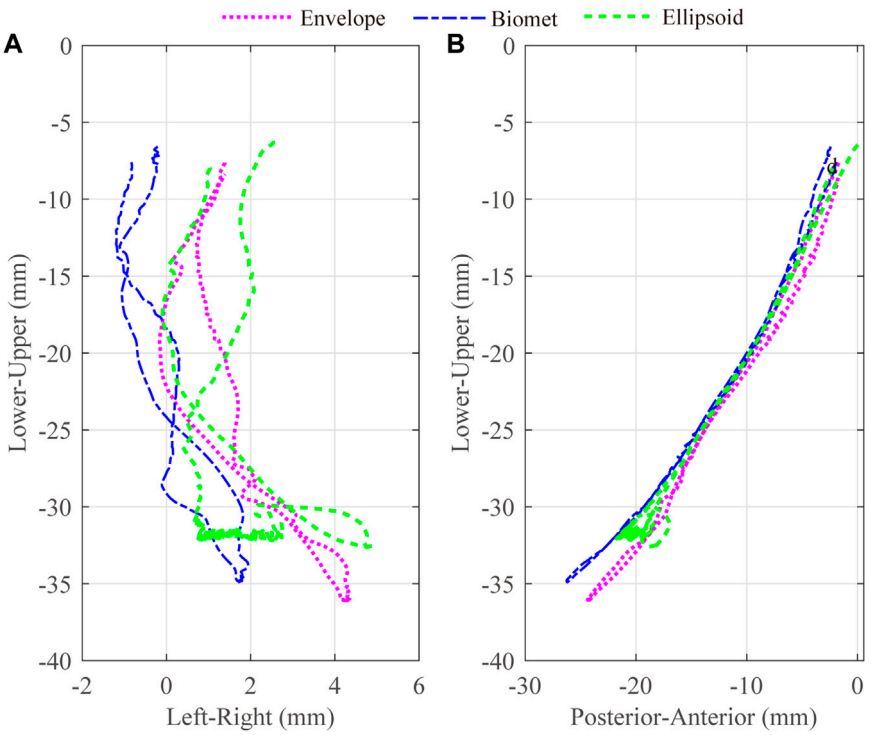

FIGURE 5
3D trajectories for the lower incisors with different artificial fossae. The axes were separated as two different panes, Left-Right **(A)** and Posterior-Anterior **(B)**.

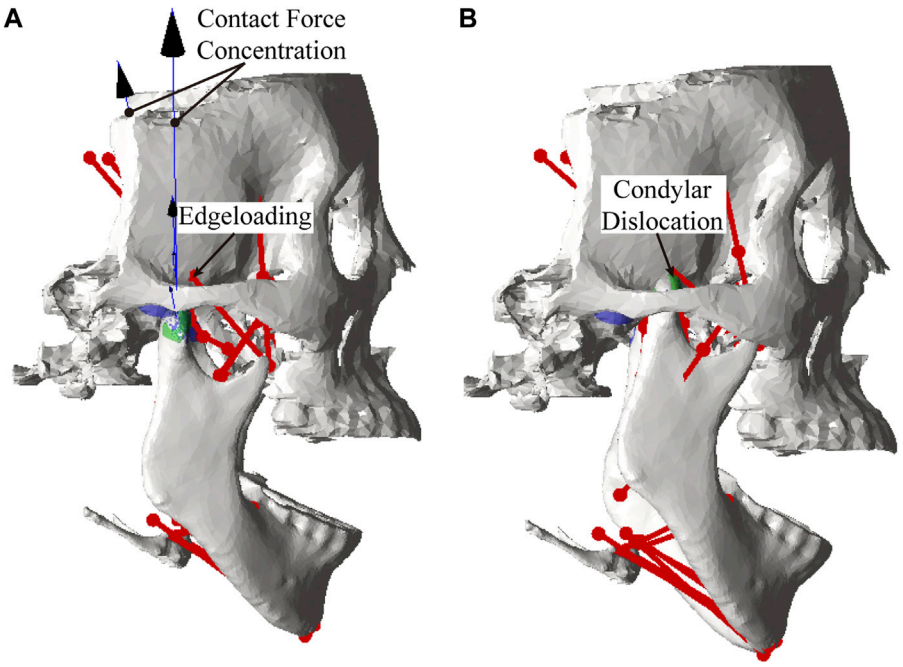

FIGURE 6
Edgeloading **(A)** and condylar dislocation **(B)** near maximal jaw opening.

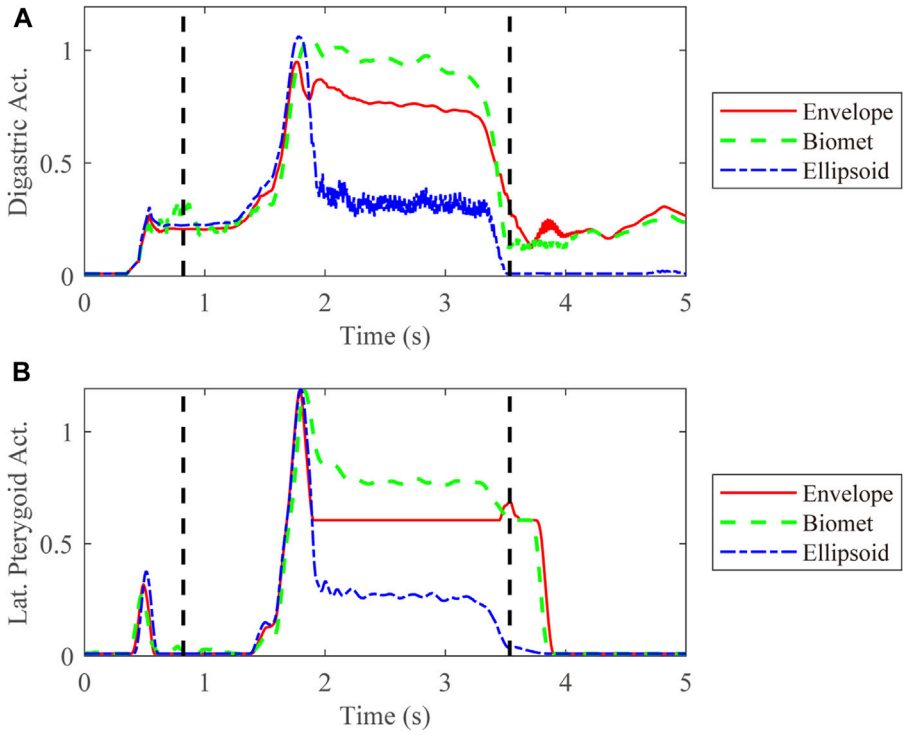

FIGURE 7
Activation of the digastric **(A)** and lateral pterygoid **(B)** muscles on the affected side. The vertical dotted line demonstrates the time range for jaw opening-closing movements. Act. = Activation. Lat. = lateral.

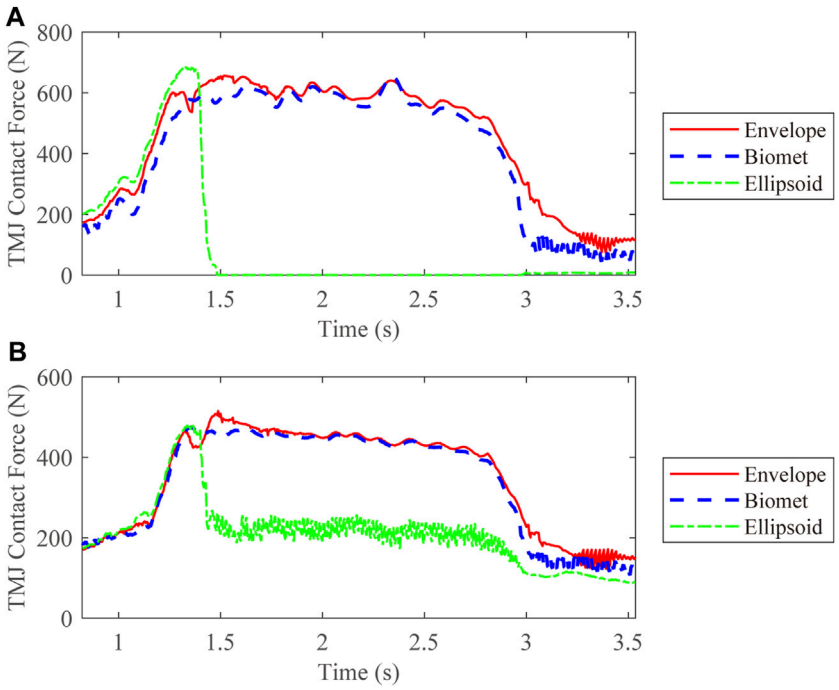

FIGURE 8
TMJ contact forces for different types of articular fossa types. **(A)** Intact side; **(B)** Affected side.

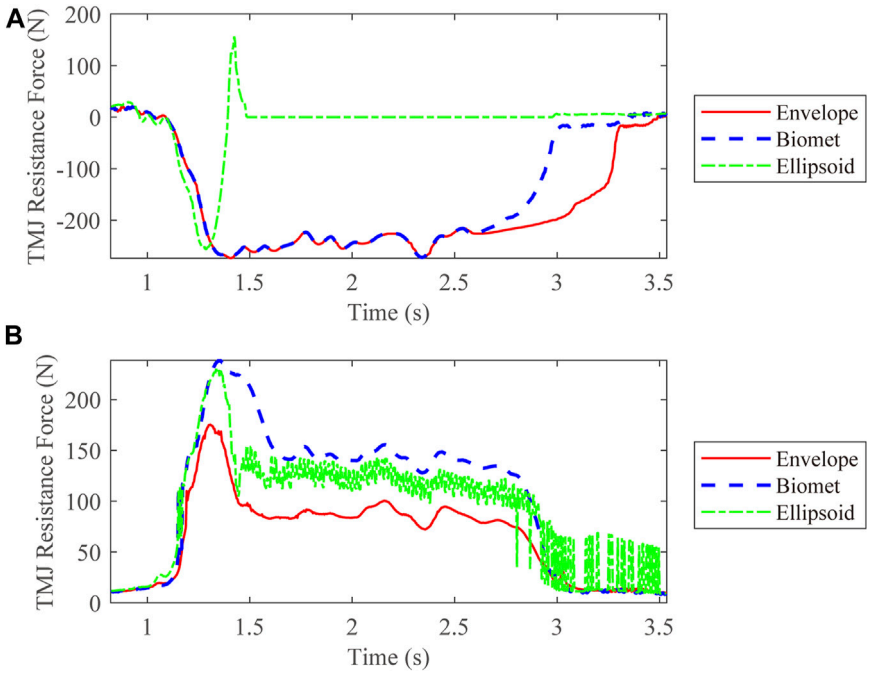

FIGURE 9
Resistance to forward condylar translation on the intact **(A)** and affected **(B)** sides.

The WINJAW EMG device (Zebris Medical GmbH, Isny, Germany) was used to simultaneously record bilateral stomatognathic muscle activities during each cycle of mandibular movements. The electrodes were positioned on the anterior temporalis and masseter muscle bellies bilaterally. The subject was instructed to perform maximum voluntary contractions (MVCs) thrice to obtain the maximal muscle force-generating capacity for each muscle (Ferrario et al., 2004; Owashi et al., 2017). Raw EMG signals were rectified and low-pass filtered (Lloyd and Besier, 2003; Guo et al., 2020), and the data were normalized using the MVC values (Quental et al., 2012). The obtained dimensionless signal was used as input to analyze muscular activation based on the first-order activation dynamics equation (Thelen, 2003; Guo et al., 2022).

2.4 TMJ fossa protheses and ellipsoidal condyle design

The TMJ fossa prothesis, based on the ESCM concept, was designed as follows. The maxilla, mandible and mandibular border movement trajectories were registered. Then according to the trajectories, the mandibular border movement was simulated, and the positions of the functional surfaces of the condyle at each moment were saved in the same 3D coordinated system. The condylar functional surface was defined as the coverage of the transverse ridge 6 mm forward. Condylar functional surface data was merged to construct the ESCM, as reported previously (Huang et al., 2021). The procedure used to obtain the ESCM is shown in Figure 1. Subsequently, the geometry of envelope surface was smoothened and refined using the Geomagic Studio software (version 2012, 3D Systems, Rock Hill, SC, USA). The envelope surface was uniformly thickened by 1 mm, and the customized fossa prosthesis was obtained (Figures 2A, B).

The Biomet fossa used in this study was obtained by increasing the overall size of the stock fossa prosthesis by 25% to fit the shape of the subject's natural fossa. An ellipsoidal fossa prosthesis was obtained by setting a hemi-ellipsoid to fit the subject's natural condyle (Figures 2C, D). The ellipsoidal fossa prosthesis was designed by imitating the lower limb joint implants and ignoring the condylar translation. The ellipsoidal fossa prosthesis was used to demonstrate the importance of condylar movements in TMJ prosthesis designing. Previous studies (Oberg et al., 1971; Zhao et al., 2019) have reported that the mandibular condyles of most adults are nearly ellipsoidal. The major (mediolateral) axis of the condyle is twice as long as the minor (anteroposterior) axis. Similarly, the mediolateral to anteroposterior diameter ratio of the ellipsoidal fossa prosthesis was 2:1.

The condylar ROMs for different fossa prostheses are shown in Figure 3. A least-squares fit of the subject-specific CBCT was used to determine the condylar radius, assuming the condylar surface to be frictionless (Yao et al., 2011; Modenese and Kohout, 2020; Guo et al., 2022). The condyle on the intact side was kept in the natural shape.

2.5 Mandibular multibody musculoskeletal model

Mandibular subject-specific musculoskeletal modeling and simulation were based on a study by Guo et al. (2022). The subject-

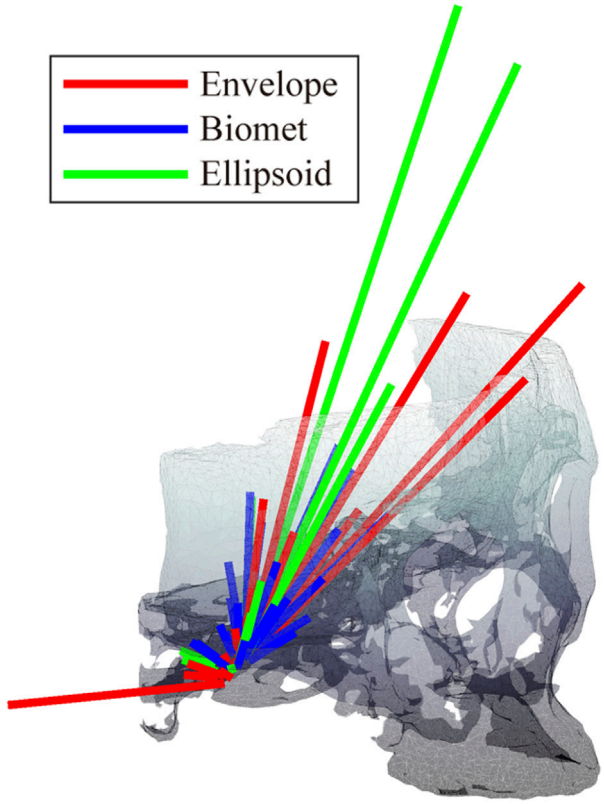

FIGURE 10
Distribution of TMJ contact forces with the condyles moving to edges of different fossa prostheses.

specific mandibular and skull geometry was obtained from the reconstructed CBCT data (Koolstra and van Eijden, 2005). The mandibular model was driven by 24 muscle bundles (de Zee et al., 2007), which were discretized by a flexible muscle element with a typical Hill-type model. Muscle insertion contours within the generic model were mapped onto the subject-specific bone morphology using the non-rigid iterative closest point algorithm.

The surface geometry of each fossa prosthesis type was extracted, and their vertices were set as contact detection points. Condylar contact geometry on the affected side was simplified as an ellipsoid, and the TMJ contact was modeled as a group of contact points to the rotating body. The normal contact force for the TMJ was calculated using a frictionless contact force model for soft materials (Flores and Ambrósio, 2010), with a friction coefficient of 0.001 (Xu et al., 2017).

Numerical simulations were performed using the inverse-forward dynamic coupling approach (Guo et al., 2022). The 3D mandibular movements were selected as the kinematic inputs to constrain the mandibular bone kinematics. Hyoid location in the intercuspal and maximal opening positions were measured using CBCT, and its movement trajectories were simplified through linear interpolation (Silva and Ambrósio, 2003; Guo et al., 2022). The musculotendon length for each muscle was calculated using the inverse dynamics approach. Motion constraints were removed during forward dynamics estimations. Mandibular muscle forces were estimated via feedback control using their lengths as the target value. A proportional derivative controller was used to calculate the activations for each muscle bundle. The schematic overview of establishing the subject-specific mandible musculoskeletal model is shown in Figure 4.

3 Results

Lower incisor movements for different artificial fossa types are shown in Figure 5. The maximum jaw opening magnitudes for the envelope-based, Biomet, and ellipsoidal fossae were 36 mm, 35 mm, and 33 mm, respectively. With an ellipsoidal fossa prosthesis implanted, the condyle of the affected side performed joint dislocation (Figure 6). Condylar ROMs on the affected side were nearly identical for the envelope-based and Biomet prostheses.

We also compared the kinetic data during jaw-opening motions. The activation of the digastric and lateral pterygoid muscles during maximal jaw opening was reduced with envelope-based fossa prosthesis compared to Biomet (Figure 7). Bilateral contact forces for the envelope-based and Biomet fossae were similar during and at maximal jaw opening. However, the TMJ with the envelope-based fossa allowed greater normal contact forces than Biomet (Figure 8). When the condyle traveled through the apex, the resistance for forward condylar translation with the envelope-based fossa decreased by 62.4 N (Figure 9). Moreover, the condylar contact force was unevenly distributed for different prostheses, and the maximal contact force for the envelope-based fossa at maximal jaw opening was greater than that for Biomet (Figure 10).

4 Discussion

Total joint replacement is commonly used to treat severe degenerative conditions of the TMJ, particularly when conservative treatment has been ineffective. A major goal of TMJ reconstruction is the restoration of normal function. However, current TMJ prostheses that conform to the anatomical shape of TMJ cannot completely restore the physiological condylar kinematics; the geometry of the prostheses reduces the condylar ROM (van Loon et al., 1999; Zheng et al., 2019; Zou et al., 2019). The present study combined the TMJ fossa prosthesis with a functional condylar surface, which was different from the commercially-available TMJ prostheses, allowing physiologically accurate kinematics (Chen et al., 2022b).

The present study was the first to apply the ESCM concept to TMJ fossa prostheses, and a subject-specific mandibular musculoskeletal model was used to simulate mandibular movements, muscle activation, and resistance forces with different prostheses. As a subject-specific model for the human mandibular musculoskeletal system, it had been validated for predicting mandibular trajectories during jaw opening-closing movements in two previous studies, one with seven healthy subjects (Guo et al., 2022), and the other with the patients suffering from oral and maxillofacial tumors (Guo et al., 2023). Calculation precision of the musculoskeletal model would be verified in the further study with patients of TMJ replacement

surgery. The kinematic results were compared among the envelope-based, stock Biomet, and ellipsoidal fossa prostheses. The maximum jaw opening magnitude for the stock Biomet fossa prosthesis was 35 mm, which was similar to the long-term outcomes for Biomet following TMJ replacement reported in previous studies (Gonzalez-Perez et al., 2016; Kanatsios et al., 2018). Compared to the Biomet, the envelope-based artificial fossa reduced jaw-opening muscle activation on the affected side and resistance on the intact side. It also increased the maximum jaw opening magnitude while maintaining the condylar ROM and bilateral contact forces. These results suggested that in terms of restoring the natural ROM of TMJ, the ESCM-based TMJ fossa prosthesis did show advantages and potential.

We developed the ellipsoidal fossa prosthesis based on the lower limb joint implants, such as the artificial hip joint (Hernigou et al., 2017). For the ellipsoidal fossa prosthesis design, we only considered condylar rotation and ignored its forward translation. We found that the ellipsoidal fossa limited the postoperative ROM of the TMJ. This indicates the importance of considering all condylar movements while designing prostheses, and reflects the rationale for envelope-based fossa prosthesis.

As showed in the results, there were advantages of the ESCM-based fossa prosthesis. It could not only improve the maximal jaw opening magnitude and condylar ROM, but also increased the efficiency of the jaw-opening process, as shown by the significant decrease in lateral pterygoid activation at maximum jaw opening. These indicated that the ESCM-based artificial fossa successfully replicated the functional anatomy of the mandibular musculoskeletal system. The physiological movement of TMJ could be affected by many factors, such as the posterior slope of articular eminence, the shape and deformation of articular disc, and traction of muscles (Mack, 1989). The articular eminence could provide a stable fulcrum for anterior condyle rotation (Van Eijden et al., 1997), while significant volume of the articular fossa and eminence bone has to be sacrificed for commercial condylar prostheses (Bai et al., 2015). In a study of 165 TMJs reconstructed using the Biomet stock prosthesis, Zhao et al. (2018) found that some patients required significant bone trimming or grafting to adjust the condyle-ramus angle and fossa for stable prosthesis implantation. As a result, the complete structure of articular eminence was damaged. On the other hand, the ESCM-based fossa prosthesis generated by the condylar functional surface data would provide physiological support and guidance for the condylar movement (Chen et al., 2022b; Chen et al., 2023). It may play a combined role of articular eminence, articular disc, capsule, ligament and so on, which could also provide the stable fulcrum for anterior condyle rotation as same as articular eminence. That increased the moment arms of the jaw-opening muscles (Spencer, 1998) and so could explain the significant decrease in digastric activation at the maximal jaw opening. Moreover, the guidance of ESCM-based fossa prosthesis for the condyle to slide forward could explain the significant decrease in lateral pterygoid activation at maximum jaw opening.

This study also had some limitations. First, the data used were obtained from a single subject. Studies with larger sample sizes will be required in the future. In addition, the subject of this study had no history of TMJ diseases, while total TMJ replacement is a biomechanical treatment option for patients with end-stage TMJ diseases (Sidebottom, 2008). For the patients whose articular fossa is damaged by the tumor and the condyle is intact and the condylar movement is normal, their envelope surfaces of condylar movement can still be obtained by the method used in this study. Moreover, in the case where the unilateral condyle is damaged but the patient could still perform normal mandibular movements, the mirroring of the intact side could be applied using the same method. This method could not be applied to those patients who were unable to perform normal mandibular movements, such as, patients with TMJ ankylosis. A method for predicting the shape of ESCM based on the facial morphology had been proposed in the previous study (Chen et al., 2023). Although further research was needed, it may be helpful in future ESCM data collection of patients with TMJ diseases whose normal mandibular movements could not be performed. Second, the complex TMJ morphology and loading patterns were simplified for our musculoskeletal models. TMJ cartilage and articular disk of the intact side were not modelled, which may have influenced the contact mechanics of the intact side. Besides, given that the mandibular kinematics would change for different other positions, more mastication loading conditions other than the maximum intercuspal position should be considered in the further study. Third, the condylar geometry on the affected side was simplified as an ellipsoid. An articular fossa prosthesis should be matched with a suitable condylar prosthesis based on the patient-specific functional anatomy. ESCM-based fossa prostheses still require some improvements. For example, the peak contact force for the envelop-based fossa was greater than that for Biomet at maximum jaw opening. This may have been because of the uneven distribution of contact forces, resulting from the bistable shape of the envelope-based fossa prosthesis, which could be influenced by the articular eminence morphology (Huang et al., 2021; Chen et al., 2022b). Compared with the envelope-based artificial fossa, the surface geometry of the Biomet fossa was flatter, making the contact force distribution more even. The uneven geometry of the envelope-based fossa prosthesis reduced the contact area with the condyle, resulting in an increased contact force. This would increase the potential for component wear, material failure, and TMJ dislocation (Kent et al., 1986; Giannakopoulos et al., 2012). Moreover, an anterior stop of the ESCM-based fossa prosthesis may be needed to avoid TMJ luxation, which will be considered in the further study. Despite these limitations, the study offers a novel perspective for TMJ fossa prostheses design. The customized envelope-based fossa prosthesis described in this study may allow the optimization of TMJ fossa prosthesis design.

5 Conclusion

A customized TMJ fossa prosthesis was successfully developed using the ESCM concept. Our study of musculoskeletal multibody modeling has highlighted its advantages and potential. The artificial fossa design successfully achieved a wider condylar ROM. It also reduced the activation of jaw opening muscles on the affected side and resistance on the intact side. This study showed that an ESCM-based approach may be useful for optimizing TMJ fossa prostheses design.

Data availability statement

The raw data supporting the conclusion of this article will be made available by the authors, without undue reservation.

Ethics statement

The studies involving humans were approved by the Institutional Review Board of Peking University School and Hospital of Stomatology, Beijing, China (Pkussirb-201947091). The studies were conducted in accordance with the local legislation and institutional requirements. The participants provided their written informed consent to participate in this study. Written informed consent was obtained from the individual(s) for the publication of any potentially identifiable images or data included in this article.

Author contributions

J-LW: Conceptualization, Data curation, Investigation, Methodology, Validation, Writing–original draft. JW: Conceptualization, Data curation, Investigation, Methodology, Validation, Writing–original draft. K-NC: Data curation, Visualization, Writing–original draft. J-QG: Funding acquisition, Resources, Software, Supervision, Writing–review and editing. X-LX: Funding acquisition, Resources, Software, Supervision, Writing–review and editing. C-BG: Conceptualization, Writing–review and editing.

Funding

The author(s) declare financial support was received for the research, authorship, and/or publication of this article. This work was supported by grants from the National Natural Science Foundations of China (grant number 12102035, 12132009), Beijing Municipal Science and Technology Commission (grant number Z201100005520055), Clinical Research Foundation of Peking University School and Hospital of Stomatology (grant number PKUSS-2023CRF205); and the Peking University Medicine Fund for World's Leading Discipline or Discipline Cluster Development (grant number BMU2022XKQ003).

Conflict of interest

The authors declare that the research was conducted in the absence of any commercial or financial relationships that could be construed as a potential conflict of interest.

Publisher's note

References

Bai, G., Yang, C., He, D., Zhang, X., and Abdelrehem, A. (2015). Application of fossa bone graft to stabilize stock total joint prosthesis in temporomandibular joint surgery. *J. Craniomaxillofac. Surg.* 43, 1392–1397. doi:10.1016/j.jcms.2015.06.048

Baqaien, M. A., Al-Salti, F. M., and Muessig, D. (2007). Changes in condylar path inclination during maximum protrusion between the ages of 6 and 12 years. *J. Oral Rehabil.* 34, 27–33. doi:10.1111/j.1365-2842.2006.01690.x

Broser, P. J., Marquetand, J., Middelmann, T., Sometti, D., and Braun, C. (2021). Investigation of the temporal and spatial dynamics of muscular action potentials through optically pumped magnetometers. *J. Electromyogr. Kinesiol.* 59, 102571. doi:10.1016/j.jelekin.2021.102571

Celebi, N., Rohner, E. C., Gateno, J., Noble, P. C., Ismaily, S. K., Teichgraeber, J. F., et al. (2011). Development of a mandibular motion simulator for total joint replacement. *J. Oral Maxillofac. Surg.* 69, 66–79. doi:10.1016/j.joms.2010.05.085

Chen, K. N., Jiang, J. Q., Wang, J. L., Sun, Y. C., Guo, C. B., and Xu, X. L. (2022a). Preliminary measurement and analysis of the condylar movement envelope surface parameters in healthy adults. *Chin. J. Stomatol.* 57, 1015–1021. doi:10.3760/cma.j.cn112144-20220630-00355

Chen, K. N., Wang, J., Chen, J. P., Wang, J. L., Sun, Y. C., Xu, X. L., et al. (2022b). Comparative study of temporomandibular articular fossa bone surface and the envelope surface of the condyle movement. *Chin. J. Dent. Res.* 25, 179–187. doi:10.3290/j.cjdr.b3317993

Chen, K., Zhang, Z., Jiang, J., Wang, J., Wang, J., Sun, Y., et al. (2023). Prediction of condylar movement envelope surface based on facial morphology. *Heliyon* 9, e17769. doi:10.1016/j.heliyon.2023.e17769

De Zee, M., Dalstra, M., Cattaneo, P. M., Rasmussen, J., Svensson, P., and Melsen, B. (2007). Validation of a musculo-skeletal model of the mandible and its application to mandibular distraction osteogenesis. *J. Biomech.* 40, 1192–1201. doi:10.1016/j.jbiomech.2006.06.024

Ferrario, V. F., Sforza, C., Zanotti, G., and Tartaglia, G. M. (2004). Maximal bite forces in healthy young adults as predicted by surface electromyography. *J. Dent.* 32, 451–457. doi:10.1016/j.jdent.2004.02.009

Flores, P., and Ambrósio, J. (2010). On the contact detection for contact-impact analysis in multibody systems. *Multibody Syst. Dyn.* 24, 103–122. doi:10.1007/s11044-010-9209-8

Giannakopoulos, H. E., Sinn, D. P., and Quinn, P. D. (2012). Biomet microfixation temporomandibular joint replacement system: a 3-year follow-up study of patients treated during 1995 to 2005. *J. Oral Maxillofac. Surg.* 70, 787–794. doi:10.1016/j.joms.2011.09.031

Gonzalez-Perez, L. M., Gonzalez-Perez-Somarriba, B., Centeno, G., Vallellano, C., and Montes-Carmona, J. F. (2016). Evaluation of total alloplastic temporo-mandibular joint replacement with two different types of prostheses: a three-year prospective study. *Med. Oral Patol. Oral Cir. Bucal.* 21, e766–e775. doi:10.4317/medoral.21189

Gruber, E. A., Mccullough, J., and Sidebottom, A. J. (2015). Medium-term outcomes and complications after total replacement of the temporomandibular joint. Prospective outcome analysis after 3 and 5 years. *Br. J. Oral Maxillofac. Surg.* 53, 412–415. doi:10.1016/j.bjoms.2014.12.010

Guo, J., Chen, J., Wang, J., Ren, G., Tian, Q., and Guo, C. (2022). EMG-assisted forward dynamics simulation of subject-specific mandible musculoskeletal system. *J. Biomech.* 139, 111143. doi:10.1016/j.jbiomech.2022.111143

Guo, J., Huang, H., Yu, Y., Liang, Z., Ambrósio, J., Zhao, Z., et al. (2020). Modeling muscle wrapping and mass flow using a mass-variable multibody formulation. *Multibody Syst. Dyn.* 49, 315–336. doi:10.1007/s11044-020-09733-1

Guo, J., Wang, J., Chen, J., Ren, G., Tian, Q., and Guo, C. (2023). Multibody dynamics modeling of human mandibular musculoskeletal system and its applications in surgical planning. *Multibody Syst. Dyn.* 57, 299–325. doi:10.1007/s11044-023-09876-x

Hannam, A. G. (2011). Current computational modelling trends in craniomandibular biomechanics and their clinical implications. *J. Oral Rehabil.* 38, 217–234. doi:10.1111/j.1365-2842.2010.02149.x

Hannam, A. G., Stavness, I. K., Lloyd, J. E., Fels, S. S., Miller, A. J., and Curtis, D. A. (2010). A comparison of simulated jaw dynamics in models of segmental mandibular resection versus resection with alloplastic reconstruction. *J. Prosthet. Dent.* 104, 191–198. doi:10.1016/S0022-3913(10)60120-5

Hernigou, P., Dubory, A., Potage, D., Roubineau, F., and Flouzat, L. C. H. (2017). Dual-mobility arthroplasty failure: a rationale review of causes and technical considerations for revision. *Int. Orthop.* 41, 481–490. doi:10.1007/s00264-016-3328-7

Huang, C., Xu, X., Li, L., Sun, Y., and Guo, C. (2021). Study on the reconstruction of a four-dimensional movement model and the envelope surface of the condyle in normal adults. *Br. J. Oral Maxillofac. Surg.* 60, 884–889. doi:10.1016/j.bjoms.2021.08.006

Imola, M. J., and Liddell, A. (2016). Temporomandibular joint reconstruction. *Curr. Opin. Otolaryngol. Head. Neck Surg.* 24, 336–342. doi:10.1097/MOO.0000000000000282

Kanatsios, S., Breik, O., and Dimitroulis, G. (2018). Biomet stock temporomandibular joint prosthesis: long-term outcomes of the use of titanium condyles secured with four or five condylar fixation screws. *J. Craniomaxillofac. Surg.* 46, 1697–1702. doi:10.1016/j.jcms.2018.07.002

Kent, J. N., Block, M. S., Homsy, C. A., Prewitt, J. M. R., and Reid, R. (1986). Experience with a polymer glenoid fossa prosthesis for partial or total temporomandibular joint reconstruction. *J. Oral Maxillofac. Surg.* 44, 520–533. doi:10.1016/s0278-2391(86)80092-1

Kiehn, C. L., Desprez, J. D., and Converse, C. F. (1974). A new procedure for total temporomandibular joint replacement. *Plast. Reconstr. Surg.* 53, 221–226. doi:10.1097/00006534-197402000-00022

Koeppel, T., Sapin-De, B. E., and Bonnet, A. S. (2015). Three dimensional functional analysis of the human mandibular movements. *Comput. Methods Biomech. Biomed. Engin.* 18, 1964–1965. doi:10.1080/10255842.2015.1069569

Koolstra, J. H., and Van Eijden, T. M. (2005). Combined finite-element and rigid-body analysis of human jaw joint dynamics. *J. Biomech.* 38, 2431–2439. doi:10.1016/j.jbiomech.2004.10.014

Lloyd, D. G., and Besier, T. F. (2003). An EMG-driven musculoskeletal model to estimate muscle forces and knee joint moments *in vivo*. *J. Biomech.* 36, 765–776. doi:10.1016/s0021-9290(03)00010-1

Mack, P. J. (1989). A computer analysis of condylar movement as determined by cuspal guidances. *J. Prosthet. Dent.* 61, 628–633. doi:10.1016/0022-3913(89)90290-4

Mercuri, L. G. (2000). The use of alloplastic prostheses for temporomandibular joint reconstruction. *J. Oral Maxillofac. Surg.* 58, 70–75. doi:10.1016/s0278-2391(00)80020-8

Mercuri, L. G., Wolford, L. M., Sanders, B., White, R. D., Hurder, A., and Henderson, W. (1995). Custom CAD/CAM total temporomandibular joint reconstruction system: preliminary multicenter report. *J. Oral Maxillofac. Surg.* 53, 106–115. doi:10.1016/0278-2391(95)90381-x

Merlini, L., and Palla, S. (1988). The relationship between condylar rotation and anterior translation in healthy and clicking temporomandibular joints. *Schweiz. monatsschr. Zahnmed.* 98, 1191–1199.

Modenese, L., and Kohout, J. (2020). Automated generation of three-dimensional complex muscle geometries for use in personalised musculoskeletal models. *Ann. Biomed. Eng.* 48, 1793–1804. doi:10.1007/s10439-020-02490-4

Oberg, T., Carlsson, G. E., and Fajers, C. M. (1971). The temporomandibular joint. A morphologic study on a human autopsy material. *Acta Odontol. Scand.* 29, 349–384. doi:10.3109/00016357109026526

Owashi, V. K. P., Sapin-De, B. E., and Bonnet, A. S. (2017). Electromyography of the masticatory muscles during biting. *Comput. Methods Biomech. Biomed. Engin.* 20, 155–156. doi:10.1080/10255842.2017.1382908

Quental, C., Folgado, J., Ambrósio, J., and Monteiro, J. (2012). A multibody biomechanical model of the upper limb including the shoulder girdle. *Multibody Syst. Dyn.* 28, 83–108. doi:10.1007/s11044-011-9297-0

Sidebottom, A. J. (2008). Guidelines for the replacement of temporomandibular joints in the United Kingdom. *Br. J. Oral Maxillofac. Surg.* 46, 146–147. doi:10.1016/j.bjoms.2006.12.001

Silva, M. T. D., and Ambrósio, J. (2003). Solution of redundant muscle forces in human locomotion with multibody dynamics and optimization tools. *Mech. Based Des. Struct. Mach.* 31, 381–411. doi:10.1081/SME-120022856

Sonnenburg, I., and Sonnenburg, M. (1985). Total condylar prosthesis for alloplastic jaw articulation replacement. *J. Maxillofac. Surg.* 13, 131–135. doi:10.1016/s0301-0503(85)80033-3

Spencer, M. A. (1998). Force production in the primate masticatory system: electromyographic tests of biomechanical hypotheses. *J. Hum. Evol.* 34, 25–54. doi:10.1006/jhev.1997.0180

Thelen, D. G. (2003). Adjustment of muscle mechanics model parameters to simulate dynamic contractions in older adults. *J. Biomech. Eng.* 125, 70–77. doi:10.1115/1.1531112

Van Eijden, T. M., Korfage, J. A., and Brugman, P. (1997). Architecture of the human jaw-closing and jaw-opening muscles. *Anat. Rec.* 248, 464–474. doi:10.1002/(sici)1097-0185(199707)248:3<464::aid-ar20>3.0.co;2-m

Van Loon, J. P., Falkenström, C. H., De Bont, L. G., Verkerke, G. J., and Stegenga, B. (1999). The theoretical optimal center of rotation for a temporomandibular joint prosthesis: a three-dimensional kinematic study. *J. Dent. Res.* 78, 43–48. doi:10.1177/00220345990780010501

Walker, P. S. (2001). A new concept in guided motion total knee arthroplasty. *J. Arthroplasty.* 16, 157–163. doi:10.1054/arth.2001.28723

Wang, Z. W., Wen, L., Luan, Y. C., Ma, D. S., Dong, X., Cheng, C. K., et al. (2021). Restoration of joint inclination in total knee arthroplasty offers little improvement in joint kinematics in neutrally aligned extremities. *Front. Bioeng. Biotechnol.* 9, 673275. doi:10.3389/fbioe.2021.673275

Westermark, A. (2010). Total reconstruction of the temporomandibular joint. Up to 8 years of follow-up of patients treated with Biomet(®) total joint prostheses. *Int. J. Oral Maxillofac. Surg.* 39, 951–955. doi:10.1016/j.ijom.2010.05.010

Wolford, L. M., Cottrell, D. A., and Henry, C. H. (1994). Temporomandibular joint reconstruction of the complex patient with the Techmedica custom-made total joint prosthesis. *J. Oral Maxillofac. Surg.* 52, 2–10. doi:10.1016/0278-2391(94)90003-5

Wolford, L. M., Pitta, M. C., Reiche-Fischel, O., and Franco, P. F. (2003). TMJ Concepts/Techmedica custom-made TMJ total joint prosthesis: 5-year follow-up study. *Int. J. Oral Maxillofac. Surg.* 32, 268–274. doi:10.1054/ijom.2002.0350

Woodford, S. C., Robinson, D. L., Mehl, A., Lee, P. V. S., and Ackland, D. C. (2020). Measurement of normal and pathological mandibular and temporomandibular joint kinematics: a systematic review. *J. Biomech.* 111, 109994. doi:10.1016/j.jbiomech.2020.109994

Xu, X., Luo, D., Guo, C., and Rong, Q. (2017). A custom-made temporomandibular joint prosthesis for fabrication by selective laser melting: finite element analysis. *Med. Eng. Phys.* 46, 1–11. doi:10.1016/j.medengphy.2017.04.012

Yao, X., Fan, S., An, G., and Wang, Z. (2011). The measurements and analysis of temporomandibular joint bony structures. *J. Pract. Stomatol.* 06, 801–804. doi:10.3969/j.issn.1001-3733.2011.06.016

Zhao, J., Zou, L., He, D., and Ellis, E. R. (2018). Comparison of bone adaptation after modification in biomet standard alloplastic temporomandibular joint prostheses. *J. Craniomaxillofac. Surg.* 46, 1707–1711. doi:10.1016/j.jcms.2018.07.024

Zhao, Q., Sun, N., Zhang, F., Song, D., Lu, Z., Sun, N., et al. (2019). Measurement of temporomandibular joint and surrounding accessory structures. *J. Shandong Univ. Health Sci.* 01, 87–91. doi:10.6040/j.issn.1671-7554.0.2018.766

Zheng, J., Chen, X., Jiang, W., Zhang, S., Chen, M., and Yang, C. (2019). An innovative total temporomandibular joint prosthesis with customized design and 3D printing additive fabrication: a prospective clinical study. *J. Transl. Med.* 17, 4. doi:10.1186/s12967-018-1759-1

Zou, L., Zhao, J., and He, D. (2019). Preliminary clinical study of Chinese standard alloplastic temporomandibular joint prosthesis. *J. Craniomaxillofac. Surg.* 47, 602–606. doi:10.1016/j.jcms.2019.01.045

Zou, L., Zhong, Y., Xiong, Y., He, D., Li, X., Lu, C., et al. (2020). A novel design of temporomandibular joint prosthesis for lateral pterygoid muscle attachment: a preliminary study. *Front. Bioeng. Biotechnol.* 8, 630983. doi:10.3389/fbioe.2020.630983

frontiers | Frontiers in Bioengineering and Biotechnology

TYPE Original Research
PUBLISHED 09 November 2023
DOI 10.3389/fbioe.2023.1260204

OPEN ACCESS

EDITED BY
Junyan Li,
Southwest Jiaotong University, China

REVIEWED BY
Xiaojun Chen,
Shanghai Jiao Tong University, China
Yuanqiao Wu,
Boston University, United States

*CORRESPONDENCE
Wenhua Huang,
huangwenhua2009@139.com
Xiang Luo,
dr-luo@163.com

†These authors have contributed equally to this work

RECEIVED 17 July 2023
ACCEPTED 30 October 2023
PUBLISHED 09 November 2023

CITATION
Huang S, Ling Q, Lin X, Qin H, Luo X and Huang W (2023), Biomechanical evaluation of a novel anterior transpedicular screw-plate system for anterior cervical corpectomy and fusion (ACCF): a finite element analysis. *Front. Bioeng. Biotechnol.* 11:1260204. doi: 10.3389/fbioe.2023.1260204

Biomechanical evaluation of a novel anterior transpedicular screw-plate system for anterior cervical corpectomy and fusion (ACCF): a finite element analysis

Shengbin Huang[1,2†], Qinjie Ling[3†], Xinxin Lin[2], Hao Qin[2], Xiang Luo[2*] and Wenhua Huang[1,4*]

[1]Department of Human Anatomy, School of Basic Medical Sciences, Guangxi Medical University, Nanning, Guangxi, China, [2]Department of Orthopedics, The Eighth Affiliated Hospital of Guangxi Medical University, Guigang, Guangxi, China, [3]Department of Spinal Surgery, The First Affiliated Hospital of Guangzhou Medical University, Guangzhou, Guangdong, China, [4]National Key Discipline of Human Anatomy, Guangdong Provincial Key Laboratory of Medical Biomechanics, Guangdong Engineering Research Center for Translation of Medical 3D Printing Application, School of Basic Medical Sciences, Southern Medical University, Guangzhou, Guangdong, China

Background and objective: Cervical fusion with vertebral body screw (VBS)-plate systems frequently results in limited biomechanical stability. To address this issue, anterior transpedicular screw (ATPS) fixation has been developed and applied preliminarily to multilevel spinal fusion, osteoporosis, and three-column injury of the cervical spine. This study aimed to compare the biomechanical differences between unilateral ATPS (UATPS), bilateral ATPS (BATPS), and VBS fixation using finite element analysis.

Materials and methods: A C6 corpectomy model was performed and a titanium mesh cage (TMC) and bone were implanted, followed by implantation of a novel ATPS-plate system into C5 and C7 to simulate internal fixation with UATPS, BATPS, and VBS. Internal fixation with UATPS comprises ipsilateral transpedicular screw-contralateral vertebral body screw (ITPS-CVBS) and cross transpedicular screw-vertebral body screw (CTPS-VBS) fixations. Mobility, the maximal von Mises stress on TMC, the stress distribution and maximal von Mises stress on the screws, and the maximum displacement of the screw were compared between the four groups.

Results: Compared with the original model, each group had a reduced range of motion (ROM) under six loads. After ACCF, the stress was predominantly concentrated at two-thirds of the length from the tail of the screw, and it was higher on ATPS than on VBS. The stress of the ATPS from the cranial part was higher than that of the caudal part. The similar effect happened on VBS. The screw stress cloud maps did not show any red areas reflective of a concentration of the stress on VBS. Compared with VBS, ATPS can bear a greater stress from cervical spine movements, thus reducing the stress on TMC. The maximal von Mises stress was the lowest with bilateral transpedicular TMC and increased with cross ATPS and with ipsilateral ATPS. ITPS-CVBS, CTPS-VBS, and BATPS exhibited a reduction of 2.3%–22.1%, 11.9%–2.7%, and 37.9%–64.1% in the maximum displacement of screws, respectively, compared with that of VBS.

Conclusion: In FEA, the comprehensive stability ranked highest for BATPS, followed by CTPS-VBS and ITPS-CVBS, with VBS demonstrating the lowest stability. Notably, utilizing ATPS for fixation has the potential to reduce the occurrence of internal fixation device loosening after ACCF when compared to VBS.

KEYWORDS

cervical spine, anterior pedicle screw, anterior surgery, corpectomy, reconstruction, biomechanics, finite element analysis

1 Introduction

Degeneration, trauma, and infection of the lower cervical spine frequently occur in the anterior column, and conventional anterior fixation with plates and screws is usually used in most cases undergoing diskectomies or corpectomis. In patients with osteoporosis or those requiring multilevel decompression and reconstruction, fixation with vertebral body screw (VBS)-plate systems frequently results in limited biomechanical stability and loosening of internal fixation devices (Singh et al., 2004). Koller et al. (2007) reviewed the literature and found the non-fusion rate of multilevel anterior cervical discectomy and fusion (ACDF) to be 20%–50% and the failure rate of anterior cervical corpectomy and fusion (ACCF) to be 30%–100%. Bayerl et al. (2019) retrospectively analyzed 21 patients who underwent two-level cervical corpectomy, and long-term postoperative follow-ups revealed that the instability rate was up to 33% after fixation only with the anterior VBS system. Hence, they recommended additional posterior spinal fusion after two-level cervical corpectomy to increase the stability of anterior fixation and reduce the failure rate and complications of surgery. However, additional posterior surgery not only increases the economic burden, but also increases surgical complications (Okawa et al., 2011; Mushkin et al., 2019).

Pedicle screw fixation can offer adequate stability of the cervical spine (Henriques et al., 2015). Biomechanical research show that ATPS performs significantly better than VBS (Koller et al., 2008a; Wu et al., 2015). Koller et al. (2008b) demonstrated that the ATPS technique for the cervical spine takes advantage of both anterior and posterior approaches and can prevent loosening of internal fixation devices. In addition, this technique can overcome the inadequacy of fixation strength of VBS in patients with osteoporosis and, thus, results in enhanced biomechanical stability. In clinical practice, the ATPS-plate system is rarely available and it is difficult to insert bilateral ATPS (BATPS) into the lower cervical spine because of the hindrance of the trachea and esophagus and the lack of other factors such as the computer navigation systems. Consequently, there are few reports of the clinical application of the ATPS fixation technique for the cervical spine. There have been many reports of unilateral transpedicular screw fixation (Aramomi et al., 2008; Yukawa et al., 2009; Ikenaga et al., 2012) or fixation with unilateral ATPS (UATPS) plus VBS (Zhang et al., 2016). However, there is paucity of literature on the differences in the stability of UATPS and BATPS for the cervical spine, and on comparative biomechanical advantages of different orientations of unilateral screws.

The action forces among the vertebral bodies of the cervical spine and their surrounding muscles and ligaments are complicated, and both animal and cadaver models have drawbacks. Hence, biomechanical finite element analysis (FEA) of the cervical spine, as a supplement to animal and cadaver studies, has been widely used. It is a tool for predicting and preparing for clinical trials. After the finite element test predictions are reasonable, *in vitro* experiments need to be conducted for analysis and verification before clinical trials.

TABLE 1 Parameters of the various tissues of the cervical spine (Polikeit et al., 2003).

Structure	Young's modulus (MPa)	Modulus (MPa) Poisson's ratio	Area (mm^2)	Element type
Cortical bone	12,000	0.3		solid186
Cancellous bone	100	0.2		solid186
Endplate	1,000	0.4		solid186
Posterior elements	3,500	0.25		solid186
Nucleus pulposus	0.2	0.4999		solid186
Annulus fibrosus	4.2	0.45		solid186
Anterior longitudinal ligament	20	0.3	38	link180
Posterior longitudinal ligament	70	0.3	20	link180
Ligamentum flavum	50	0.3	60	link180
Interspinal ligament	28	0.3	35.5	link180
Supraspinous ligament	28	0.3	35.5	link180
Capsular ligament	20	0.3	40	link180
Titanium prosthesis	116,000	0.3		solid186

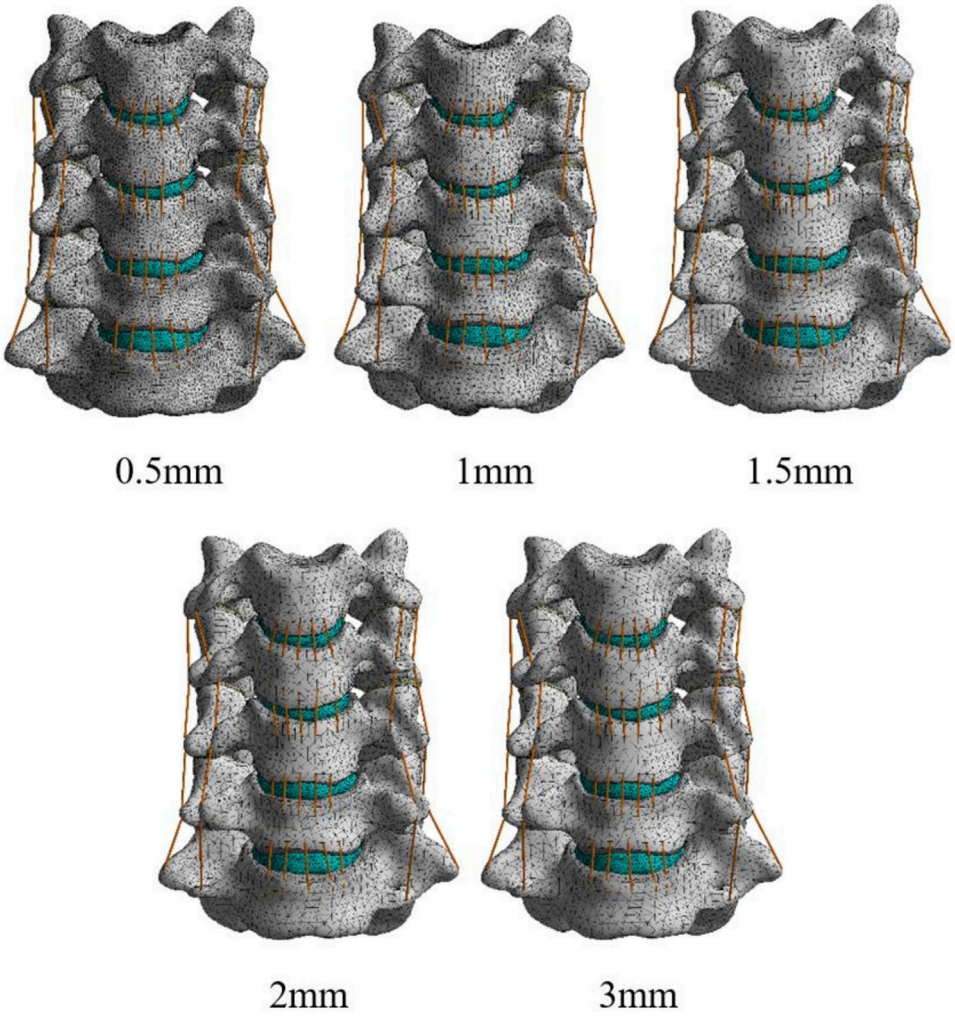

FIGURE 1
The mesh FE model.

The finite element method allows for the establishment of three-dimensional (3D) finite element models for specific scenarios and facilitates analysis of the efficacy of various therapeutic regimens (Biswas et al., 2018; Dai et al., 2022). Finite element models can also determine the engineering basis for device design and provide technical recommendations (Ling et al., 2019). This study aimed to explore the biomechanical differences between UATPS (two screw orientations), BATPS, and VBS by testing a novel ATPS-plate system for the cervical spine through finite element analysis, so as to provide a theoretical basis for the clinical use of ATPS for the cervical spine.

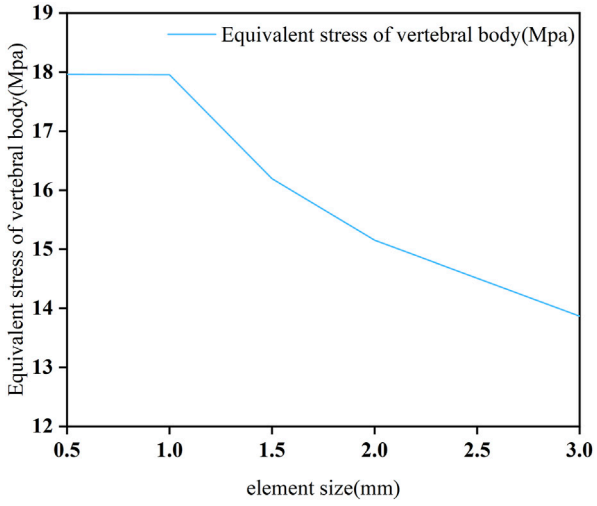

FIGURE 2
Mesh convergence analysis.

2 Materials and methods

2.1 Construction of C3–C7 finite element models

The study subject was a 32-year-old healthy male volunteer. This study was approved by the Ethics Committee of Guangxi Medical University, and informed consent was obtained from the volunteer.

TABLE 2 Mesh convergence test results.

Mesh size (mm)	Nodes	Units	Change rate of the maximal von Mises stress (%)
0.5	865,134	574,841	-
1	235,972	374,193	<5
1.5	214,571	156,216	>5
2	177,387	125,396	>5
3	143,318	110,125	>5

A 3D finite element model of C3–C7 was reconstructed with computed tomography (CT) data using Mimics 20.0 (Materialise, Leuven, Belgium). Next, the 3D model was smoothed and polished using Geomagic 12.0 (Geomagic, United States). In the model, the cortical and cancellous bone, endplate, annulus fibrosus, nucleus pulposus, posterior elements, anterior longitudinal ligament, posterior longitudinal ligament, capsular ligament, transverse ligament, ligamentum flavum, interspinous ligament, supraspinous ligament and capsular ligament were reconstructed. Table 1 lists all the material properties and element types of these tissues according to Polikeit et al. (2003).

To obtain accurate data, the mesh of the model was validated. The mesh convergence test was performed with the 3D finite element model of C3–C7, and the mesh was divided by five sizes (0.5, 1, 1.5, 2, and 3 mm) (Figure 1). The five mesh models were subjected to testing, with the maximal von Mises stress on the vertebral body being the parameter of interest. Figure 2 shows the relationship between the stress and the mesh size. Based on the calculation time and results, the requirement of a change rate of <5% for the maximal von Mises stress was met (Dai et al., 2022). Hence, the unit size of 1 mm was used as the final mesh size for this study (Table 2).

2.2 Boundary and loading conditions of FE models

Setup of the C3–C7 model (Figure 3): All facet joints were set as contact, with a friction co-efficient of 0.1 (Liu et al., 2011). All degrees of freedom of the endplate beneath C7 were restricted, and a pre-load of 50 N was applied to the endplate above C3 to simulate the weight of the head, and the additional bending moment of motion was 1 Nm (Lee et al., 2011). To validate the C3–C7 finite element model, a bending moment of 1.5 Nm was applied to the C3 plane, and the model was loaded in flexion, extension, lateral bending, and axial rotation (Lee et al., 2011), followed by calculation, data extraction, and determination of the range of motion (ROM).

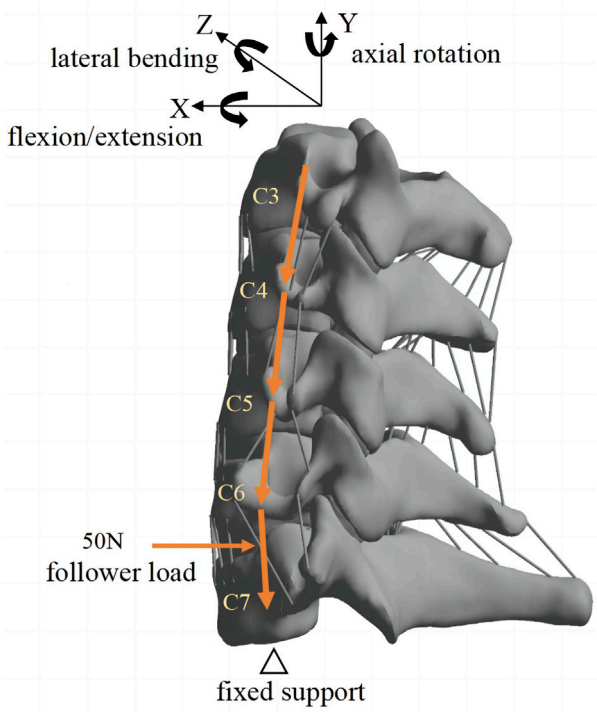

FIGURE 3
Loading and boundary conditions of the C3–C7 cervical model.

2.3 Construction of ACCF finite element model by four types of fixation

3D physical modeling was performed for a novel ATPS-plate system of the cervical spine (Patent No: ZL 2018 2 0814089.9) (Figure 4) and for a titanium mesh cage (TMC) by using Solidworks 2015 (Dassault Systemes, France). C6 corpectomy and C5/6 and C6/7 discectomy were simulated, and a TMC packed with cancellous bone was implanted into the decompression groove. The components of the screw-plate system were then assembled. For contact setup: the intervertebral disc, nucleus pulposus, and endplate were bound to each other; the screws and vertebrae contacted inseparably, the screws and plate and the plate and vertebrae contacted in a face-to-face manner. There was separable rough contact between the TMC and endplate, which did not allow for sliding. The finite element model of four types of internal fixation in ACCF following reconstruction for single-level corpectomy and decompression was simulated (Figure 5): UATPS, including ipsilateral transpedicular screw-contralateral vertebral body screw (ITPS-CVBS) and cross transpedicular screw-vertebral body screw (CTPS-VBS); BATPS; and VBS.

The 4-type finite element model was imported into Ansys Workbench 18.0 (ANSYS, United States), and working conditions were established and calculated with reference to the original model of the full set. Subsequently, the ROM, the maximal von Mises stress on TMC, the stress distribution and maximal von

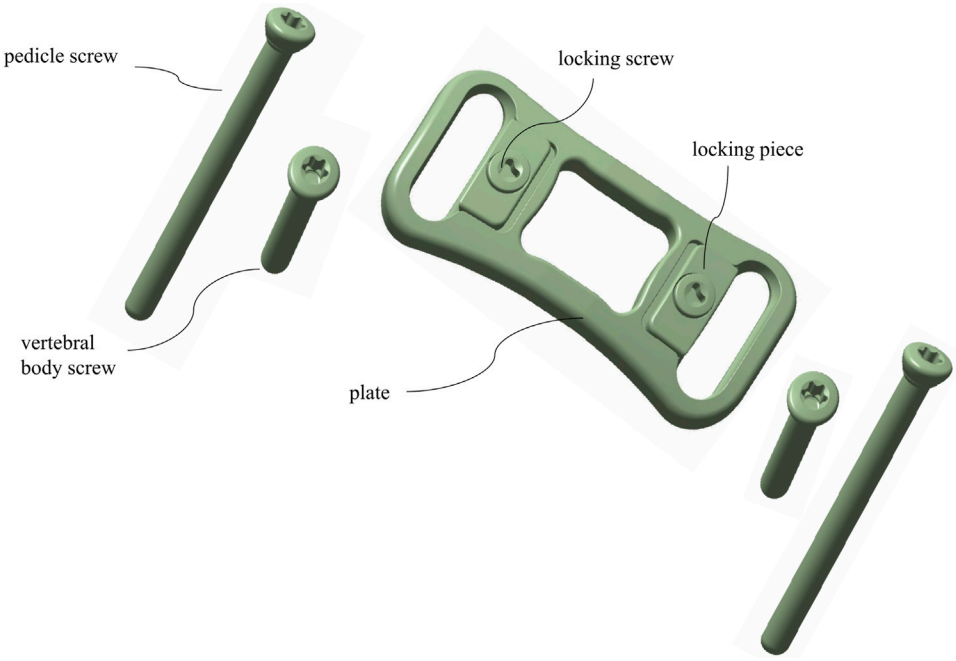

FIGURE 4
The novel anterior transpedicular screw plate systems.

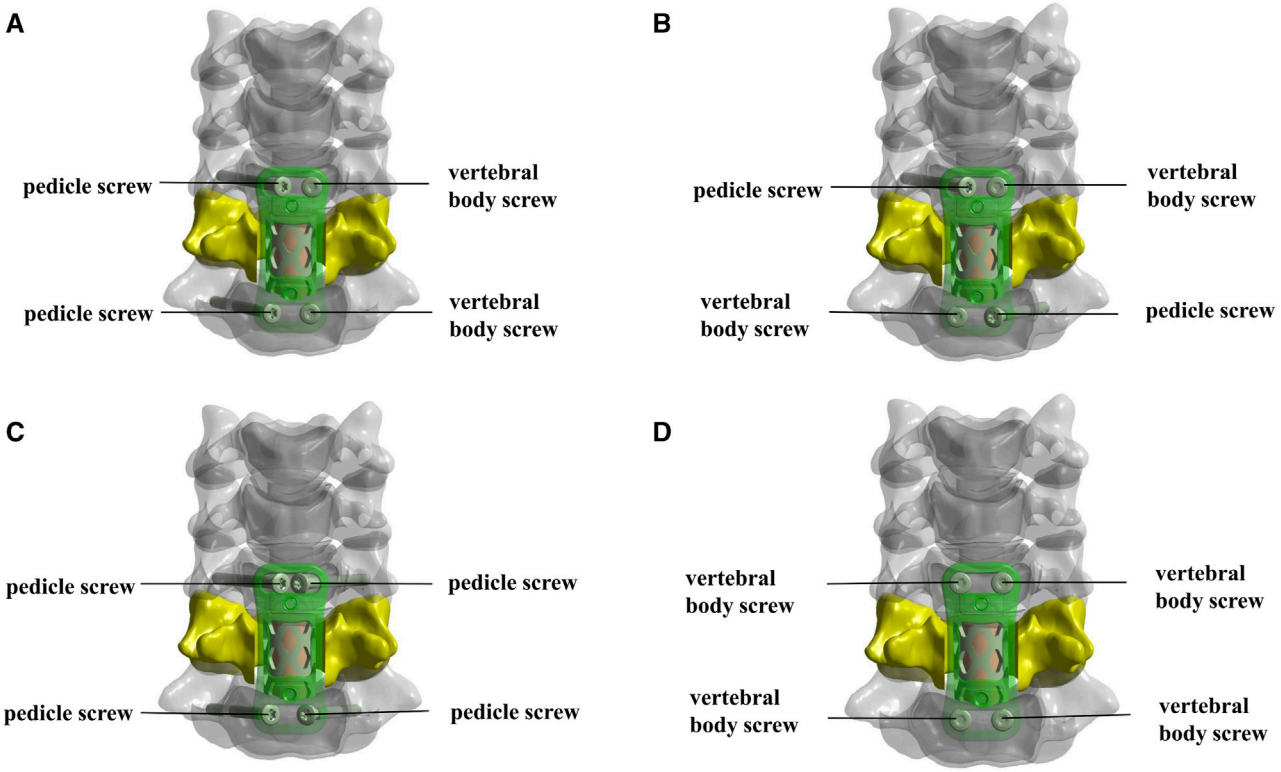

FIGURE 5
The models of four types of screw instrumentation. **(A,B)** Unilateral ATPS (UATPS): ipsilateral transpedicular screw-contralateral vertebral body screw (ITPS-CVBS, **(A)** and cross transpedicular screw-vertebral body screw (CTPS-VBS, **(B)**; **(C)** bilateral ATPS (BATPS); **(D)** vertebral body screw (VBS).

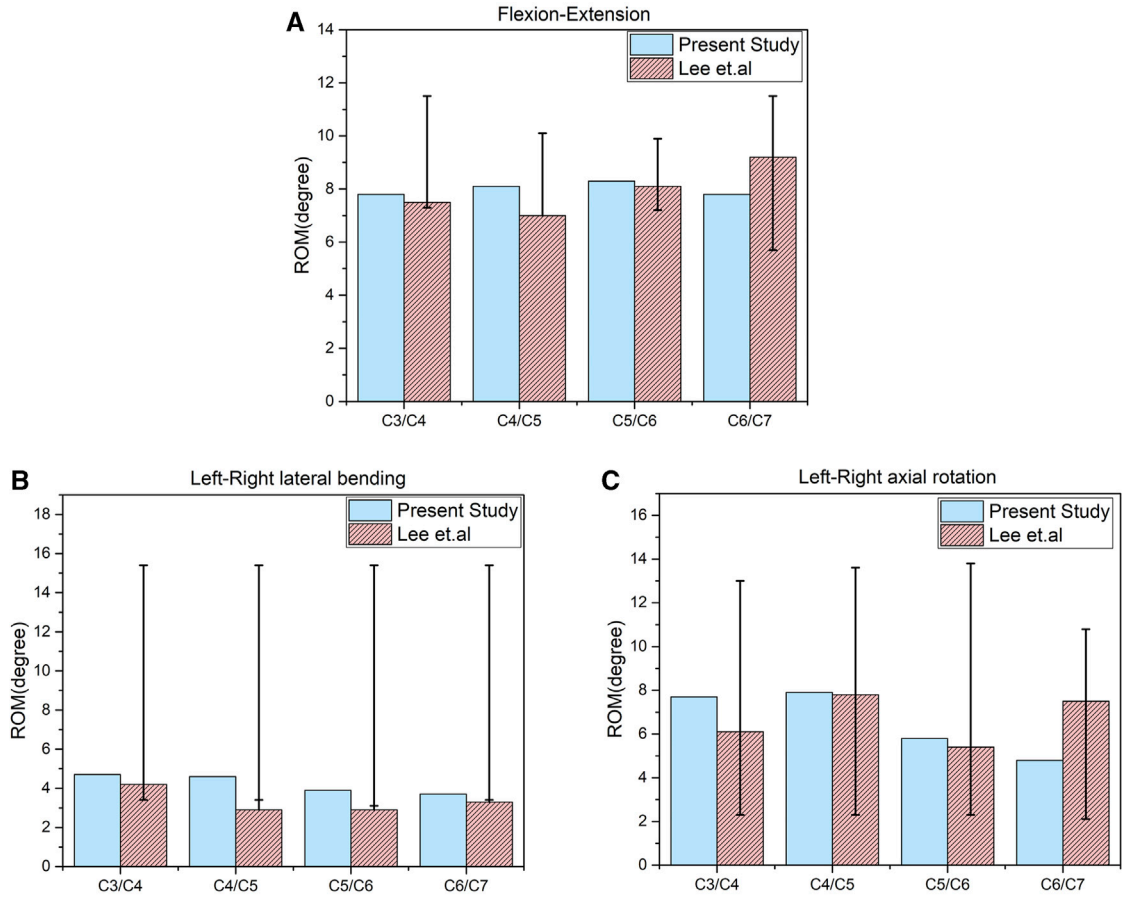

FIGURE 6
Comparison of the range of motion (ROM) of the original finite element models of C3–C7 with the previous biomechanical study. **(A)** ROM in flexion-extension. **(B)** ROM in lateral bending. **(C)** ROM in axial rotation.

Mises stress on screws, and the maximum sliding displacement of screws were analyzed for the four models.

3 Results

3.1 Validation of C3–C7 vertebral model

Under pure moments and motion loads, the predicted results of ROM were compared with the results of the validated model to assess the validity of the new model. The results were congruent with the literature (Lee et al., 2011), thus, the model was validated (Figure 6).

3.2 Range of motion (ROM)

Compared with the original model, all the internal fixation models exhibited reduced ROM in the six orientations, namely, reduction of ROM by 42.1%–48.1% in flexion, by 44.3%–47.5% in extension, by 20.2%–33.5% in left lateral bending, by 15.7%–22.1% in right lateral bending, by 20.7%–24.6% in left rotation, and by 20.0%–22.2% in right rotation. The ROM differed insignificantly between the four models and was in the ascending order: BATPS<CTPS-VBS<ITPS-CVBS<VBS (Figure 7).

3.3 Maximal von Mises stress on TMC

Under the loading conditions in flexion, extension, lateral bending, and lateral axial rotation, the maximal von Mises stress on TMC was lowest in the BATPS group (12.18, 43.58, 29.58, 30.05, 51.59, and 40.28 MPa, respectively) and highest in the VBS group (14.92, 51.10, 24.93, 36.92, 47.36, and 49.17 MPa, respectively), while that in the UATPS group was between the BATPS group and the VBS group (CTPS-VBS: 14.20, 48.41, 31.72, 33.00, 41.99, and 41.48 MPa, respectively; ITPS-CVBS: 14.64, 50.26, 32.41, 33.11, 42.03, and 42.09 MPa, respectively) (Figure 8). The stress on BATPS in flexion, extension, and lateral bending was significantly lower than that on UATPS, but the differences were insignificant in rotation. However, regardless of bilateral or unilateral ATPS, the stress on TMC was lower compared with that on VBS.

3.4 Maximal von Mises stress and stress cloud map of screws

Comparison of UATPS (ITPS-CVBS vs. CTPS-VBS) showed that the stress reduced by 37.4% on ITPS-CVBS when compared to CTPS-VBS in left bending, but the group differences were insignificant in flexion, extension, right lateral bending, and lateral rotation (Figure 9).

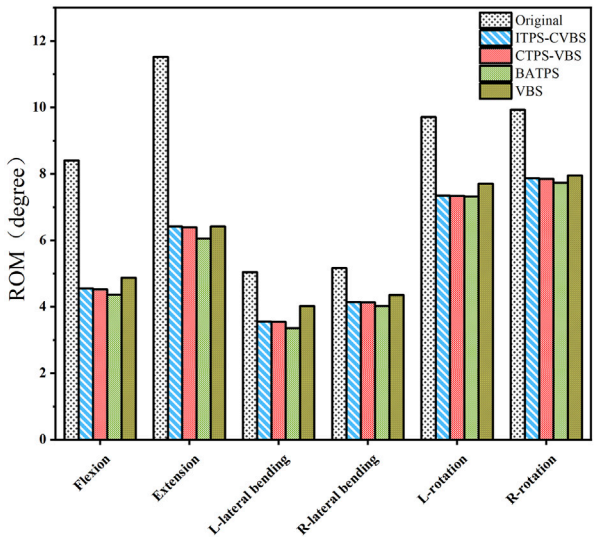

FIGURE 7
ROM of the different models of fixation.

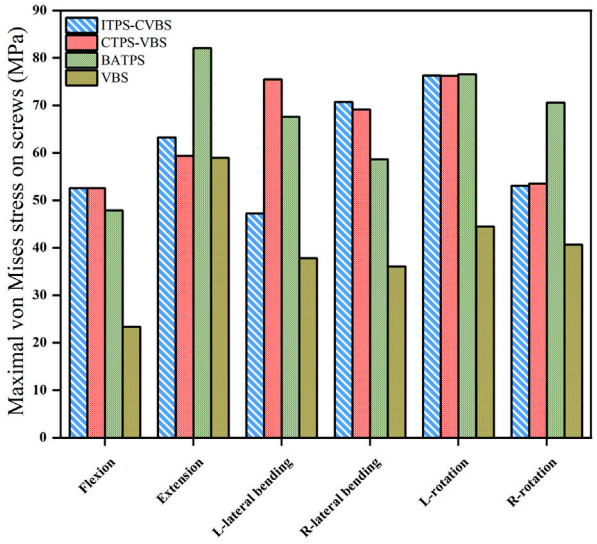

FIGURE 9
Maximal von Mises stress on screws between different groups.

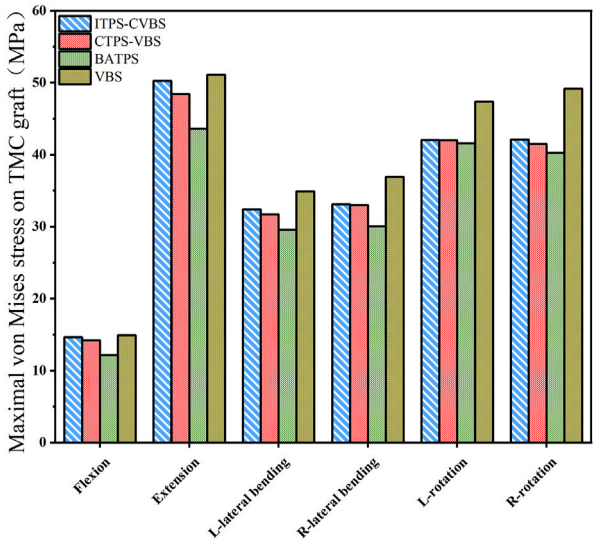

FIGURE 8
Maximal von Mises stress on TMC graft in the different groups.

BATPS endured the maximum stress of 82.07 MPa in extension. VBS endured stress of 23.38, 58.92, 78.80, 36.09, 44.56, and 40.66 MPa, respectively, under the six loads, which were significantly lower than those on transpedicular screws (ITPS-CVBS, CTPS-VBS, and BATPS) (Figure 9). Figure 10 shows the stress distribution on the screws under the six loads in each model group.

3.5 Maximum displacement of screws

The maximum displacement of screws was largest in the VBS group under loads in flexion, extension, left and right lateral bending, and left and right lateral axial rotation (Figure 10). When compared with VBS, the maximum displacement of screws reduced by 8.1%, 2.3%, 4.1%, 7.7%, 22.1%, and 6.4%, respectively, with ITPS-CVBS; by 29.4%, 11.9%, 32.7%, 16.6%, 22.1%, and 6.6%, respectively, with CTPS-VBS; and by 39.6%, 37.9%, 64.1%, 64.6%, 53.1%, and 50.7%, respectively, with BATPS (Figure 11).

4 Discussion

Following anterior cervical corpectomy, VBS or ATPS can be used for internal fixation. ATPS can anchor the three columns of the vertebra, leading to a higher stability compared with VBS. ATPS technique is insertion pedicle screw from the anterior cervical vertebra, cross-sectional insertion of ATPS into the cervical spine is key to the technique. Koller et al. (2008b) proposed that the ideal cross-sectional entry point for screws is contralateral to the pedicles for C3–C5, but is ipsilateral to the pedicles for C6–T1. Zhao et al. (2018) drew similar conclusions as Koller et al. However, in modeling, we found that the screw into the C5 vertebral body can rotate around the center of the pedicle; thus, the entry point of ATPS was ipsilateral to the pedicles, and the cortical bone of the pedicle was not penetrated (Figure 5C). Therefore, we choose the anterior pedicle screw fixation method should based on the upper and lower cervical corpectomy segment. If the upper vertebral body of the corpectomy segment is C3 or C4, we can only choose one vertebral body screw and one pedicle screw (Figures 5A, B). For C5, one vertebral body screw and one pedicle screw or two pedicle screws can be used. The lower vertebral body of the corpectomy segment is C6 or C7, and two pedicle screws can be inserted (Figure 5C). Hence, we performed C6 corpectomy with screw fixation of C5 and C7, which can meet the requirement of inserting unilateral or bilateral ATPS and VBS and allows for the following biomechanical comparisons.

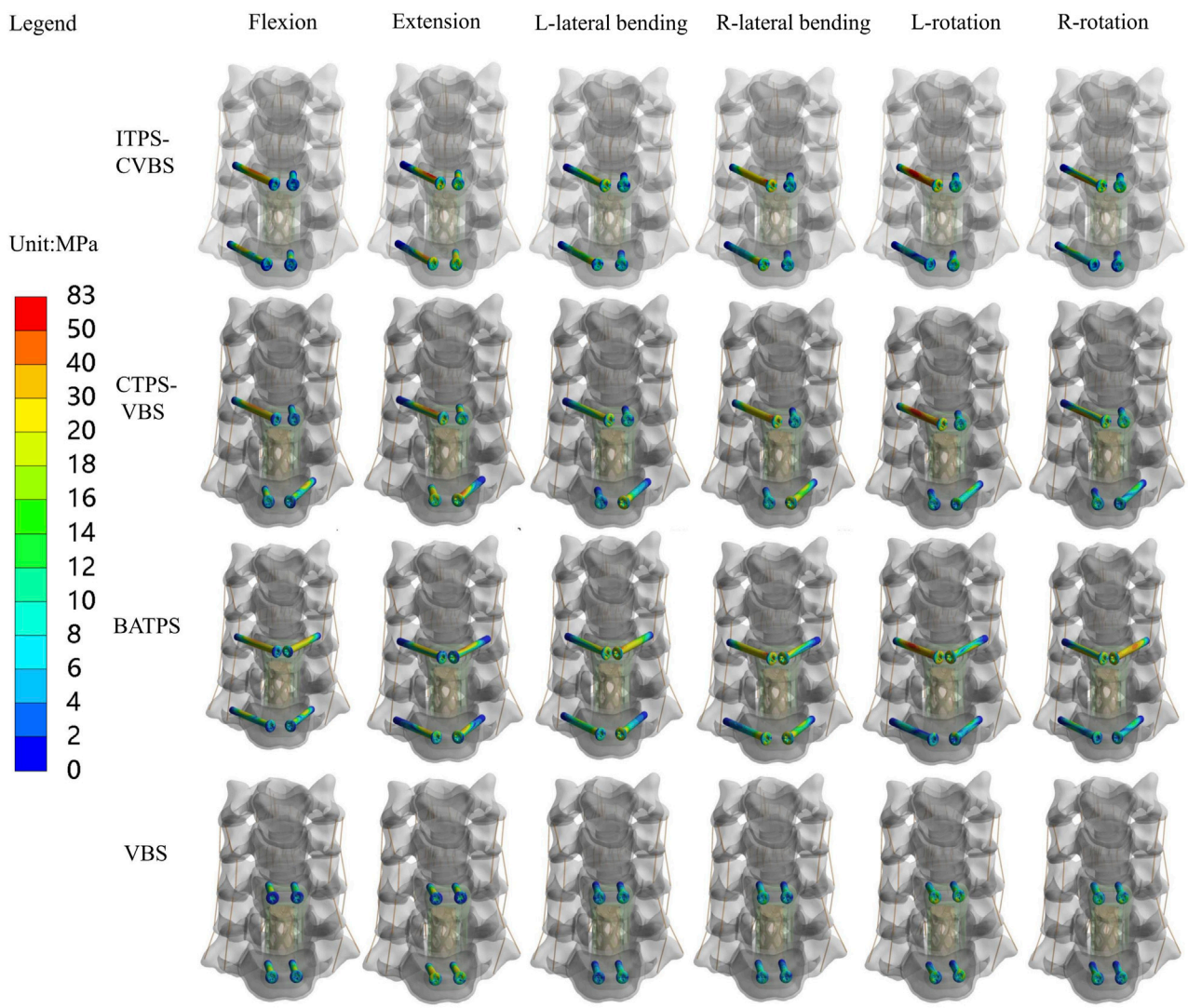

FIGURE 10
Distribution of the von Mises stress on screws between different groups.

4.1 ROM

Following cervical spinal fusion, a smaller ROM is associated with higher stability and reduced likelihood of loosening of internal fixation devices. Wu et al. (2018) simulated ATPS and VBS internal fixation with six cervical spine specimens and found that ATPS had a smaller ROM than VBS, and that ATPS internal fixation can offer adequate stability for three-column injury to the lower cervical spine. Our results demonstrated that compared with the original model, the four screw insertion methods, namely, BATPS, ITPS-CVBS, CTPS-VBS, and VBS, exhibited significantly reduced overall ROM of the cervical spine under all six loads, with the ROM in the ascending order of ATPS<ITPS-CVBS<CTPS-VBS<VBS (Figure 7). When compared with VBS, ATPS can reduce the ROM of the cervical spine, which is consistent with the findings of Wu et al. (2018). It can be inferred that the use of ATPS can reduce the ROM of the cervical spine and thus increase the stability of the cervical spine, and that such advantages may be more pronounced in the internal fixation for multilevel cervical corpectomy and spinal fusion. Notably, the number of screws used and the method of screw insertion influence the ROM of the cervical spine differently. An increased number of ATPS used is associated with a decreased ROM; given a same number of ATPS or VBS used, cross insertion of ATPS resulted in a smaller ROM and a better overall stability compared with ipsilateral insertion.

4.2 Maximal von Mises stress on TMC

Implant displacement and settlement is associated with the stress on the implant-endplate interface. An excess load of the endplate may lead to implant displacement and endplate damage, ultimately resulting in failure of the internal fixation. In this study, the maximal von Mises stress on TMC was lowest in flexion and highest in extension in each group, possibly because the screws and plate in front of the cervical spine can offset some stress in flexion. However, the magnitude of the stress varied among the different

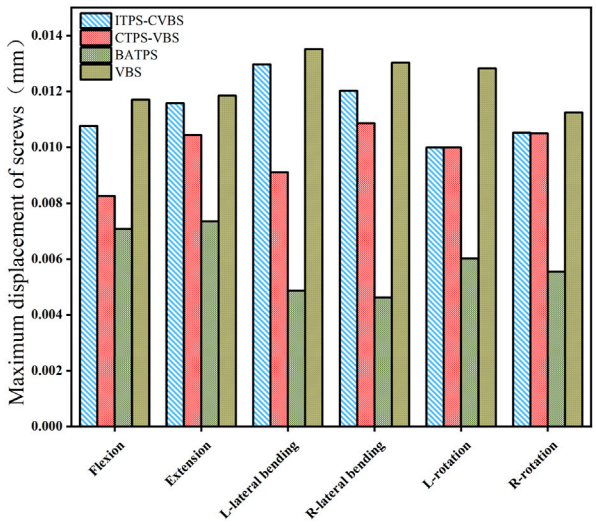

FIGURE 11
Maximum displacement of screws between different groups.

methods of fixation. Under various working conditions in motion, the maximal von Mises stress on TMC was lowest with BATPS, was lower with CTPS-VBS than with ITPS-CVBS, and was highest with VBS. Hence, internal fixation with VBS yields greater stress on TMC and is likely to cause damage to the endplate bone.

4.3 Maximal von Mises stress and stress cloud map of screws

Owing to bending, deformation, and loosening, the anchoring components and rods between the screw and bone are liable to displacement (Oda et al., 2022). Fogel et al. (2003) also reported that fracture is likely to occur in the presence of failure between the screwhead and screw. In the clinical setting, the screw is usually fractured at the junction of the nut and the plate, and the stress on this junction is key to facture of the screw. In this study, the stress cloud map showed that the stress was predominantly concentrated at a point two-thirds of the length from the tail of the screw after ACCF, the stress of the ATPS from the cranial part was higher than that of the caudal part. The maximal von Mises stress was greater on unilateral or bilateral ATPS compared with that on VBS. VBS inserted into the anterior and middle columns of the vertebral body and into the cancellous bone of the vertebral body can bear a small stress during movements of the cervical spine. In contrast, ATPS penetrates the anterior, middle, and posterior columns of the vertebral body; hence, it bears a great stress during movements of the cervical spine, thereby avoiding loosening. The screw stress cloud maps did not show any red areas reflective of a concentration of the stress on VBS in the six orientations of movement, possibly because of transfer of the stress onto the TMC. Hence, the likelihood of TMC displacement is high with VBS. With respect to UATPS fixation, the stress was reduced by 37.4% with ITPS-CVBS when compared with CTPS-VBS in left bending, possibly because no ATPS shared the stress in ITPS-CVBS at the left side of the cervical spine. Hence, in light of the maximal von Mises stress on screws and the stress cloud map, ATPS can tolerate greater stress than VBS during cervical spine movements. BATPS can balance the stress during cervical spine movements better than UATPS. In terms of UATPS, CTPS-VBS can tolerate lateral bending better than ITPS-CVBS.

4.4 Maximum displacement of screws

The maximum displacement of the screw is proposed as a stability parameter (Li et al., 2013), which can reflect the overall stability of the screw-plate system better than the ROM of the cervical spine and the stress on internal fixation devices. Screw loosening results from insufficient stress on the screw-bone interface, and the bone density of the vertebral body, the length of screw, the thread type, the screw diameter, and single or double cortical fixation all influence screw stability (Zhang et al., 2006; Matsukawa et al., 2016). Pedicle is the most abundant area of cortical bone in the cervical spine. Koller et al. (2008a) demonstrated that the fixation strength of ATPS was 2.5 times that of conventional anterior VBS. In this study, under loads in flexion, extension, lateral bending, and lateral axial rotation, the maximum displacement was largest with VBS, smallest with BATPS, and was moderate with ITPS-CVBS and CTPS-VBS. UATPS showed even smaller displacement than VBS under the six loads, suggesting a good stability, which is consistent with the literature (Koller et al., 2010; Zhao et al., 2018). With respect to UATPS, CTPS-VBS exhibited smaller screw displacement and better stability compared with ITPS-CVBS in flexion, extension, and lateral bending, but not in rotation. Hence, in terms of the ATPS technique, stability is highest with BATPS, followed by CTPS-VBS, and is lowest with ITPS-CVBS.

Taken together, based on the ROM, the maximal von Mises stress on TMC, the stress distribution and maximal von Mises stress on screws, and the maximum sliding displacement of screws, we compared different methods of anterior screw insertion into the cervical spine in ACCF and demonstrated that the stability was highest with BATPS, followed by CTPS-VBS, ITPS-CVBS, and then VBS. Hence, the ATPS technique can reduce the incidence of screw loosening and TMC displacement.

4.5 Limitations of the study

This study does have some limitations. The study investigated the initial stability of different screw fixations following single-level ACCF, and further studies need to be conducted on the ultimate mechanical properties and fatigue resistance of these screw fixations. In addition, no finite element model involves muscles, and the data may change with the addition of muscles. Furthermore, the model in this study did not simulate multilevel ACCF or osteoporosis-related working conditions. Our data are expected to change in multilevel spinal fusions and osteoporosis, but the overall trend of stability may not change. In addition, *in vitro* biomechanical testing and clinical studies need to be performed to appraise the results of this study.

4.6 Conclusion

The stability of various methods of anterior screw insertion in the cervical spine for ACCF differs. The findings of this study hold the potential to aid in the development of an optimal fixation

method for lower cervical spinal fusions, with the goal of reducing internal fixation failures following anterior cervical spinal fusions. In the context of finite element analysis (FEA), BATPS is recommended whenever feasible, and in cases where only UATPS insertion is possible, CTPS-VBS is recommended. Prior to conducting clinical trials, it remains essential to perform *in vitro* experiments to further analyze and validate the results.

Data availability statement

The original contributions presented in the study are included in the article/Supplementary Material, further inquiries can be directed to the corresponding authors.

Ethics statement

The studies involving humans were approved by the Ethics Committee of the Guangxi Medical University. The studies were conducted in accordance with the local legislation and institutional requirements. The participants provided their written informed consent to participate in this study. Written informed consent was obtained from the individual(s) for the publication of any potentially identifiable images or data included in this article.

Author contributions

SH: Writing–original draft, Writing–review and editing. QL: Writing–review and editing, Writing–original draft. XLi: Writing–original draft. HQ: Writing–original draft. XLu: Writing–review and editing. WH: Writing–review and editing.

Funding

The author(s) declare financial support was received for the research, authorship, and/or publication of this article. This work was supported by: 1) Guigang Science and Technology Project (GKZ 1834002 and 2008010); 2) Guangxi Science and Technology Project (AD17129017 and AD17195042); 3) Guangdong Postgraduate Education Innovation Project (2022JGXM029); 4) National Key and Program of China (2022YFB4600600); 5) National Natural Science Foundation of China (32271181).

Conflict of interest

The authors declare that the research was conducted in the absence of any commercial or financial relationships that could be construed as a potential conflict of interest.

Publisher's note

References

Aramomi, M., Masaki, Y., Koshizuka, S., Kadota, R., Okawa, A., Koda, M., et al. (2008). Anterior pedicle screw fixation for multilevel cervical corpectomy and spinal fusion. *Acta Neurochir. (Wien)* 150, 575–582. discussion 582. doi:10.1007/s00701-008-1574-1

Bayerl, S. H., Pohlmann, F., Finger, T., Prinz, V., and Vajkoczy, P. (2019). Two-level cervical corpectomy-long-term follow-up reveals the high rate of material failure in patients, who received an anterior approach only. *Neurosurg. Rev.* 42, 511–518. doi:10.1007/s10143-018-0993-6

Biswas, J. K., Rana, M., Majumder, S., Karmakar, S. K., and Roychowdhury, A. (2018). Effect of two-level pedicle-screw fixation with different rod materials on lumbar spine: a finite element study. *J. Orthop. Sci.* 23, 258–265. doi:10.1016/j.jos.2017.10.009

Dai, H., Liu, Y., Han, Q., Zhang, A., Chen, H., Qu, Y., et al. (2022). Biomechanical comparison between unilateral and bilateral percutaneous vertebroplasty for osteoporotic vertebral compression fractures: a finite element analysis. *Front. Bioeng. Biotechnol.* 10, 978917. doi:10.3389/fbioe.2022.978917

Fogel, G. R., Reitman, C. A., Liu, W., and Esses, S. I. (2003). Physical characteristics of polyaxial-headed pedicle screws and biomechanical comparison of load with their failure. *Spine (Phila Pa 1976)* 28, 470–473. doi:10.1097/01.BRS.0000048652.45964.2E

Henriques, T., Cunningham, B. W., Mcafee, P. C., and Olerud, C. (2015). *In vitro* biomechanical evaluation of four fixation techniques for distractive-flexion injury stage 3 of the cervical spine. *Ups. J. Med. Sci.* 120, 198–206. doi:10.3109/03009734.2015.1019684

Ikenaga, M., Mukaida, M., Nagahara, R., Yasunaga, T., Ueda, Y., and Sohma, Y. (2012). Anterior cervical reconstruction with pedicle screws after a 4-level corpectomy. *Spine (Phila Pa 1976)* 37, E927–E930. doi:10.1097/BRS.0b013e31824ff7b2

Koller, H., Acosta, F., Tauber, M., Fox, M., Martin, H., Forstner, R., et al. (2008a). Cervical anterior transpedicular screw fixation (ATPS)-Part II. Accuracy of manual insertion and pull-out strength of ATPS. *Eur. Spine J.* 17, 539–555. doi:10.1007/s00586-007-0573-x

Koller, H., Hempfing, A., Acosta, F., Fox, M., Scheiter, A., Tauber, M., et al. (2008b). Cervical anterior transpedicular screw fixation. Part I: study on morphological feasibility, indications, and technical prerequisites. *Eur. Spine J.* 17, 523–538. doi:10.1007/s00586-007-0572-y

Koller, H., Hempfing, A., Ferraris, L., Maier, O., Hitzl, W., and Metz-Stavenhagen, P. (2007). 4- and 5-level anterior fusions of the cervical spine: review of literature and clinical results. *Eur. Spine J.* 16, 2055–2071. doi:10.1007/s00586-007-0398-7

Koller, H., Schmidt, R., Mayer, M., Hitzl, W., Zenner, J., Midderhoff, S., et al. (2010). The stabilizing potential of anterior, posterior and combined techniques for the reconstruction of a 2-level cervical corpectomy model: biomechanical study and first results of ATPS prototyping. *Eur. Spine J.* 19, 2137–2148. doi:10.1007/s00586-010-1503-x

Lee, S. H., Im, Y. J., Kim, K. T., Kim, Y. H., Park, W. M., and Kim, K. (2011). Comparison of cervical spine biomechanics after fixed- and mobile-core artificial disc replacement: a finite element analysis. *Spine (Phila Pa 1976)* 36, 700–708. doi:10.1097/BRS.0b013e3181f5cb87

Li, Q. L., Li, X. Z., Liu, Y., Zhang, H. S., Shang, P., Chu, Z. M., et al. (2013). Treatment of thoracolumbar fracture with pedicle screws at injury level: a biomechanical study based on three-dimensional finite element analysis. *Eur. J. Orthop. Surg. Traumatol.* 23, 775–780. doi:10.1007/s00590-012-1076-y

Ling, Q., He, E., Zhang, H., Lin, H., and Huang, W. (2019). A novel narrow surface cage for full endoscopic oblique lateral lumbar interbody fusion: a finite element study. *J. Orthop. Sci.* 24, 991–998. doi:10.1016/j.jos.2019.08.013

Liu, C. L., Zhong, Z. C., Hsu, H. W., Shih, S. L., Wang, S. T., Hung, C., et al. (2011). Effect of the cord pretension of the Dynesys dynamic stabilisation system on the biomechanics of the lumbar spine: a finite element analysis. *Eur. Spine J.* 20, 1850–1858. doi:10.1007/s00586-011-1817-3

Matsukawa, K., Yato, Y., Imabayashi, H., Hosogane, N., Abe, Y., Asazuma, T., et al. (2016). Biomechanical evaluation of fixation strength among different sizes of pedicle screws using the cortical bone trajectory: what is the ideal screw size for optimal fixation? *Acta Neurochir. (Wien)* 158, 465–471. doi:10.1007/s00701-016-2705-8

Mushkin, A. Y., Naumov, D. G., and Evseev, V. A. (2019). Multilevel spinal reconstruction in pediatric patients under 4 years old with non-congenital pathology (10-year single-center cohort study). *Eur. Spine J.* 28, 1035–1043. doi:10.1007/s00586-018-5756-0

Oda, Y., Takigawa, T., Ito, Y., Misawa, H., Tetsunaga, T., Uotani, K., et al. (2022). Mechanical study of various pedicle screw systems including percutaneous pedicle screw in trauma treatment. *Med. Kaunas.* 58, 565. doi:10.3390/medicina58050565

Okawa, A., Sakai, K., Hirai, T., Kato, T., Tomizawa, S., Enomoto, M., et al. (2011). Risk factors for early reconstruction failure of multilevel cervical corpectomy with dynamic plate fixation. *Spine (Phila Pa 1976)* 36, E582–E587. doi:10.1097/BRS.0b013e3181e0f06a

Polikeit, A., Nolte, L. P., and Ferguson, S. J. (2003). The effect of cement augmentation on the load transfer in an osteoporotic functional spinal unit: finite-element analysis. *Spine (Phila Pa 1976)* 28, 991–996. doi:10.1097/01.BRS.0000061987.71624.17

Singh, K., Vaccaro, A. R., Kim, J., Lorenz, E. P., Lim, T. H., and An, H. S. (2004). Enhancement of stability following anterior cervical corpectomy: a biomechanical study. *Spine (Phila Pa 1976)* 29, 845–849. doi:10.1097/00007632-200404150-00005

Wu, H. H., Tang, T., Yu, X., and Pang, Q. J. (2018). Stability of two anterior fixations for three-column injury in the lower cervical spine: biomechanical evaluation of anterior pedicle screw-plate fixation. *J. Int. Med. Res.* 46, 1455–1460. doi:10.1177/0300060517734687

Wu, C., Chen, C., Wu, W., Zhao, W., Sun, P., Fan, J., et al. (2015). Biomechanical analysis of differential pull-out strengths of bone screws using cervical anterior transpedicular technique in normal and osteoporotic cervical cadaveric spines. *Spine (Phila Pa 1976)* 40, E1–E8. doi:10.1097/BRS.0000000000000644

Yukawa, Y., Kato, F., Ito, K., Nakashima, H., and Machino, M. (2009). Anterior cervical pedicle screw and plate fixation using fluoroscope-assisted pedicle axis view imaging: a preliminary report of a new cervical reconstruction technique. *Eur. Spine J.* 18, 911–916. doi:10.1007/s00586-009-0949-1

Zhang, Q. H., Tan, S. H., and Chou, S. M. (2006). Effects of bone materials on the screw pull-out strength in human spine. *Med. Eng. Phys.* 28, 795–801. doi:10.1016/j.medengphy.2005.11.009

Zhang, Z., Mu, Z., and Zheng, W. (2016). Anterior pedicle screw and plate fixation for cervical facet dislocation: case series and technical note. *Spine J.* 16, 123–129. doi:10.1016/j.spinee.2015.09.040

Zhao, L., Chen, J., Liu, J., Elsamaloty, L., Liu, X., Li, J., et al. (2018). Biomechanical analysis on of anterior transpedicular screw-fixation after two-level cervical corpectomy using finite element method. *Clin. Biomech. (Bristol, Avon)* 60, 76–82. doi:10.1016/j.clinbiomech.2018.09.008

frontiers | Frontiers in Bioengineering and Biotechnology

TYPE Original Research
PUBLISHED 17 November 2023
DOI 10.3389/fbioe.2023.1289985

OPEN ACCESS

EDITED BY
Xijin Hua,
University of Exeter, United Kingdom

REVIEWED BY
Zikai Hua,
Orthotek Laboratory, China
Alessandro Ruggiero,
University of Salerno, Italy

*CORRESPONDENCE
Xinzhan Mao,
xinzhan.mao@csu.edu.cn

RECEIVED 06 September 2023
ACCEPTED 08 November 2023
PUBLISHED 17 November 2023

CITATION
Li J, Xiong L, Lei C, Wu X and Mao X (2023), Is it reasonable to shorten the length of cemented stems? A finite element analysis and biomechanical experiment.
Front. Bioeng. Biotechnol. 11:1289985.
doi: 10.3389/fbioe.2023.1289985

Is it reasonable to shorten the length of cemented stems? A finite element analysis and biomechanical experiment

Junyan Li, Liang Xiong, Chao Lei, Xinyu Wu and Xinzhan Mao*

Department of Orthopedics, The Second Xiangya Hospital, Central South University, Changsha, Hunan, China

Background: Uncemented short stems have been shown to optimize load distribution on the proximal femur, reducing stress shielding and preserving bone mass. However, they may adversely affect the initial stability of the stems. To date, most research conducted on short stems has predominantly centered on uncemented stems, leaving a notable dearth of investigations encompassing cemented stems. Therefore, this study aimed to investigate the length of cemented stems on the transmission of femoral load patterns and assess the initial stability of cemented short stems.

Method: A series of finite element models were created by gradient truncation on identical cemented stem. The impact of varying lengths of the cemented stem on both the peak stress of the femur and the stress distribution in the proximal femur (specifically Gruen zones 1 and 7) were assessed. In addition, an experimental biomechanical model for cemented short stem was established, and the initial stability was measured by evaluating the axial irreversible displacement of the stem relative to the cement.

Result: The maximum von-Mises stress of the femur was 58.170 MPa. Spearman correlation analysis on the shortened length and von-Mises stress of all nodes in each region showed that the *p*-values for all regions were less than 0.0001, and the correlation coefficients (r) for each region were 0.092 (Gruen Zone 1) and 0.366 (Gruen Zone 7). The result of the biomechanical experiment showed that the irreversible axial displacement of the stem relative to cement was −870 μm (SD 430 μm).

Conclusion: Reducing the length of a cemented stem can effectively enhance the proximal load of the femur without posing additional fracture risk. Moreover, the biomechanical experiment demonstrated favorable initial stabilities of cemented short stems.

KEYWORDS

hip, joint arthroplasty, cemented stem, stem length, finite element analysis, biomechanics

1 Introduction

Total Hip Arthroplasty (THA), as one of the most successful surgical techniques of the 20th century, is the most effective treatment for various end-stage hip joint diseases. Currently, hip replacement has achieved good long-term survival rates, with an average cumulative revision rate of about 8% after 15 years for patients with osteoarthritis (Evans

et al., 2019). Femoral and acetabular prostheses can be implanted using cemented or uncemented techniques. The choice of femoral fixation method is currently controversial. Supporters of uncemented fixation point out that compared to cemented femoral stems in young patients, uncemented femoral stems have good long-term survival rates (Eskelinen et al., 2006) and may be easier to revise. On the other hand, supporters of cemented fixation argue that, like elderly patients, young patients would benefit from the longer lifespan of modern cemented femoral stems (Kiran et al., 2018). Due to the unique fixation method of cemented stems, stress distribution of the proximal femur is more reasonable, with less stress shielding effect compared to uncemented stems, resulting in better preservation of bone mass and reduced long-term revision rates. Additionally, revision surgery may be easier to perform (Costi et al., 2017). Follow-up data from Australian Orthopedic Association National Joint Replacement Registry (AOANJRR) over 17 years suggested that cemented polished tapered stems had lower revision rates than commonly used uncemented stems (Babazadeh et al., 2022).

In the past decade, there has been a trend towards developing shorter femoral stems, which aims at reducing stress shielding near the femur and reducing the risk of potential proximal femoral fractures. Several uncemented short stems have shown good medium to long-term clinical results (Hossain et al., 2017; Giardina et al., 2018; Zimmerer et al., 2020). However, some researchers have reported limitations of these stems, particularly in cases of poor bone mineral density (Gruner and Heller, 2015; Shin et al., 2016). Significantly decreased bone mineral density is associated with increased risk of periprosthetic fractures when using uncemented short stems (Gkagkalis et al., 2019). Cemented short stems offer potential benefits in terms of optimizing proximal femoral loading, facilitating installation and revision procedures. Research has confirmed the good long-term survival rate of cemented short stems (Santori et al., 2019).

With the population ages, there is a significant increase in the demand for hip arthroplasty. Researchers are striving to translate the potential benefits of uncemented short stems to cemented short stems. Currently, there is limited research on cemented short stems. The purpose of this study was to investigate the influence of cemented short stem on proximal femoral load distribution and evaluate its initial stability through a combination of finite element analysis (FEA) and biomechanical experiment.

2 Materials and methods

2.1 Finite element analysis

2.1.1 Finite element model

In this study, a medium-sized, left-sided, fourth-generation artificial composite femur model (3403, Sawbones, Pacific Research Laboratories, Vashon, United States) was used. To obtain the 3D model of the sawbones, it was scanned using a computed tomography (CT) machine (GE Lightspeed VCT 64, General Electric, Massachusetts, United States) with a scan interval of 1.0 mm. The CT scan data was then exported to Mimics (Version 21.0, Materialise, Leuven, Belgium) in DICOM format. After extracting the contours of each CT slice image, the contours were overlaid in three dimensions to obtain the shape and surface of the entire femur. The lines and surfaces of the 3D construction were corrected for distorted areas and then segmented to obtain the final 3D femur shape, which was exported in STL format.

FIGURE 1
ACP stem.

The imported femur model in STL format was loaded into Geomagic Wrap (Version 2021, 3D Systems, Rock Hill, United States). The model was then remeshed to achieve a smoother surface. This involved utilizing functions such as feature removal, relaxation, and pin deletion. Additionally, the offset function was employed to create a cancellous bone model by inwardly offsetting the femur bone by 2 mm. The Mesh Doctor command was used to inspect the grid status of the mesh model. Once the inspection was passed, the precise surface interface was accessed to perform a sequence of operations. These operations included detecting and editing contour lines, constructing and repairing surface patches, constructing grids, and fitting surfaces. These actions resulted in the generation of surface models for the cortical bone and cancellous bone. Finally, the shell unit model was transformed into a solid model and exported in STEP format.

We selected the ACP stem (Model: 1#, AK MEDICAL, Beijing, China) as the experimental stem. ACP stem was a high-polished, three-tapered, collarless, cemented femoral stem. The overall length of the stem was 115 mm (Figure 1). STEP format of ACP stem was collected through manufacturer datasheets.

The cortical bone, cancellous bone, and stem models were imported into Unigraphics NX software (Version 12.0, Siemens, Berlin, Germany). The resection of the femoral neck was done using a standard method. The inner side of the resection was located

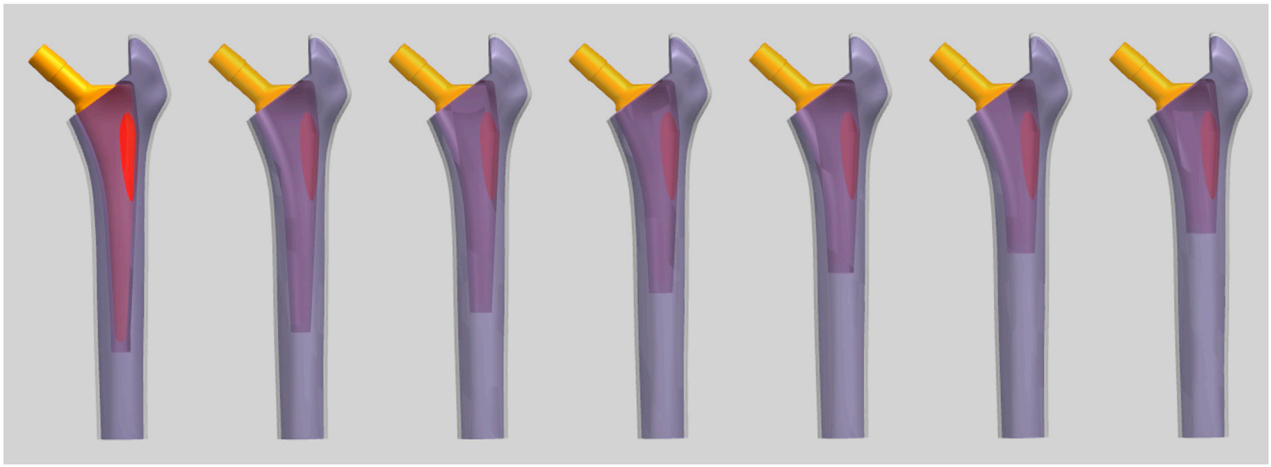

FIGURE 2
The final FEA models (From left to right, the models are labeled as ACP115 to ACP55 consecutively).

10 mm above the lesser trochanter horizontally, while the outer side was located at the level of the base of the femoral neck. The femoral neck was cut at a 45° angle along the line connecting these two points in the coronal plane, and the femoral head was subsequently removed. To minimize computational load, the distal femur was removed. Every 10 mm of the distal end of the stem was horizontally truncated once, for a total of six truncations, resulting in seven sets of stems with lengths ranging from 55 mm to 115 mm. They were named ACP55 to ACP115 based on the stem length. The length of ACP75 was equal to twice the vertical distance from the highest point of the greater trochanter of the femur to the lowest point of the lesser trochanter. So ACP55 to ACP75 were regarded as short stems by Feyen and Shimmin. (2014). The longitudinal axis of the stem was parallel to the anatomical axis of the femur in both the coronal and sagittal planes. The stem was assembled in the femur with a anteversion of 15°, and the height of the rotation center of the femoral head aligned with the highest point on the greater trochanter horizontally. By using the intersection function, the intersection surface between the stem and cancellous bone was obtained. This surface was then offset outward by 2 mm to obtain a 2 mm-thick cement mantle. The cortical bone region was removed by Boolean operations to account for the space occupied by cancellous bone and the stem. The stem-occupied space was removed from the cancellous bone. Finally, seven sets of final models were obtained and exported in PRT format as shown in Figure 2.

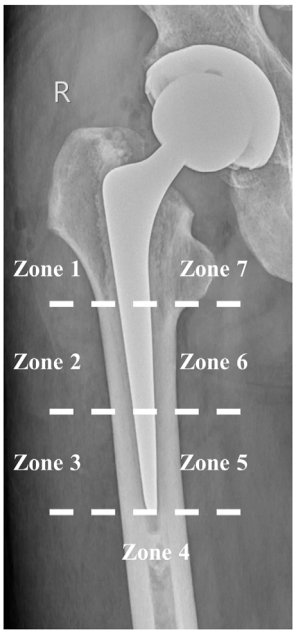

FIGURE 3
Gruen zones in cemented stems.

2.1.2 Material properties and meshing

We assumed that the bone structure had homogeneous and isotropic linear properties. The material properties were obtained from the manufacturer, respectively for cortical bone (E = 16.7 GPa, ν = 0.3), trabecular bone (E = 0.155 GPa, v = 0.3), bone cement (E = 2.2 GPa, ν = 0.3), and ACP stem (E = 210 GPa, ν = 0.3) (Naghavi et al., 2023).

We partitioned all finite element models into tetrahedral 10-node meshes. To assess mesh convergence, we constructed six groups of finite element models with different mesh densities and performed finite element analysis with the same boundary conditions. The peak value of the von-Mises stress in the femur was considered the convergence observation indicator, defined as the numerical difference between the two successive solutions under the same loading conditions being less than 5% to determine mesh convergence. Based on the results of the mesh convergence analysis, the optimal mesh sizes were determined to be: 2 mm for cortical bone, 2 mm for cancellous bone, 1 mm for bone cement, and 1.5 mm for the stem. The result of mesh quality evaluation showed that the average values of jacobian ratio and skewness were 1.037 and 0.252 (Ruggiero et al., 2019).

2.1.3 Loading and boundary conditions

Finite element analysis was performed using Ansys workbench (Version 2021 R1, ANSYS Inc, Canonsburg, United States). The ASTM F2996–13 and ISO 7206–4:2010(E) were taken into consideration when determining the loading and boundary conditions (Bergmann et al., 2016).A load of 2300N was applied to the point at the center of the maximum offset femoral head, at a 12° angle to the anatomical axis of the femur. The distal end of the femur was set as the fixed support surface. All the contact areas were considered bonded except the cement-stem interface. The coefficient of friction 0.25 was considered between cement and stem interface (Verdonschot and Huiskes, 1996).

2.1.4 Observation indicators and statistical analysis

The main purpose of this finite element analysis was to observe the following factors and statistical methods in different lengths of cemented stems after implantation in the femur: (1) Peak values and distribution characteristics of von-Mises stress in the femur; (2) Characteristics of the distribution of nodal von-Mises stress in the proximal femur. We chose Gruen zones 1 (number of nodes: 755) and 7 (number of nodes: 755) as the regions of interest (Figure 3) (Gruen et al., 1979). Because these areas are less affected by the design of the femoral stem (de Waard et al., 2021). Statical analysis was performed using IBM SPSS (Version 23, IBM, Armonk, United States). The normality test indicated that the data was nonparametric, hence the summary statistics were represented by the median and interquartile range (IQR). Spearman correlation analysis was used to find the relationship between the length of the stem and von-Mises stress in the proximal femur. When $p < 0.05$, it was considered to indicate correlation. In order to ensure comparability of the results, the Gruen partitioning of the ACP115 group was used as the partitioning criterion for the femoral models in each group.

2.2 Biomechanical experiments of cemented short stem

We used a stem with a length at the junction of the standard stem and the short stem as the experimental object, which was referred to as the ACP75 stem mentioned in the above text. The distal part of the stem was cut using a low-speed water-cooled saw to minimize damage to the remaining part of the prosthesis. After the cutting was completed, the cut surface was rounded and polished to reduce local stress concentration and adverse effects on cement during subsequent implantation.

Implant structures were prepared by experienced orthopedic surgeon (X.M). A standard femoral neck cut was made approximately 1 cm near the lesser trochanter, and then a suitable broaching rasp of the stem size was used to broach the bone for stem placement.

A distal cement plug was introduced at the distal end located at the tip of the stem. Then, Simplex bone cement (Stryker Orthopedics, Mahwah, United States) was used to bond the stem to Sawbones using a stem centralizer. A total of six models were prepared for the following experiments.

The femoral models were installed in the material testing machine (ElectroPuls E10000, Instron, Norwood, United States) and subjected to vertical loading. To ensure that the load was introduced without creating any moments, a ball bearing was placed between the device and the load cell (Figure 4). The material testing machine applied 100,000 dynamic sinusoidal load cycles at a frequency of 2 Hz between 100 and 1600 N to simulate the load during the first 6 weeks *in vivo* condition (Freitag et al., 2021). The axial displacement between the stem and the cement mantle was used as an observation parameter to evaluate the initial stability of the stem. The measurement process was performed using the PLMLAB DIC-3D system (PLMLAB Sensor Tech, Nanjing, China). This system was based on the principle of binocular stereo vision and uses three-dimensional digital image correlation methods to measure the three-dimensional shape and the three-dimensional strain field of the tested object's surface under loading. The axial displacement of the stem was determined by measuring the difference in axial distance between the highest point of the stem shoulder and the highest point of the cement mantle in the coronal plane.

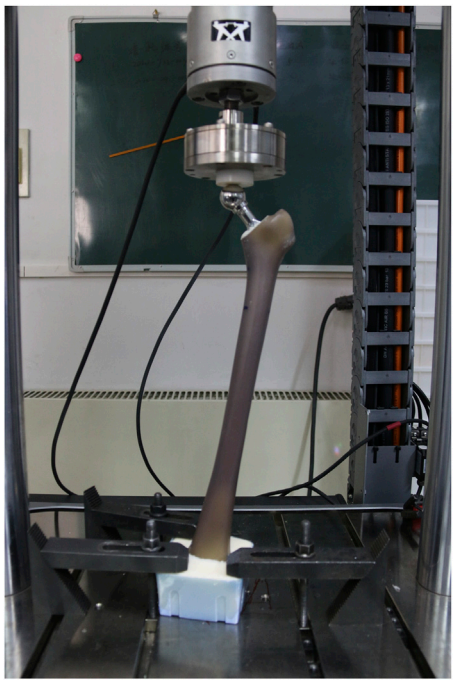

FIGURE 4
The testing machine. The femur and stem are fitted in the Instron.

3 Results

3.1 Peak values and distribution characteristics of femoral von-Mises stress

Total seven models with different stem length were analyzed, as shown in Figure 5. In general, the peak von-Mises stress tended to increase with a decrease in the stem length. Furthermore, the location of the peak Von-Mises stress was gradually shifted from the medial distal femur to the medial proximal femur. ACP115 group was 54.431 MPa, ACP105 group was 54.757 MPa,

10.3389/fbioe.2023.1289985

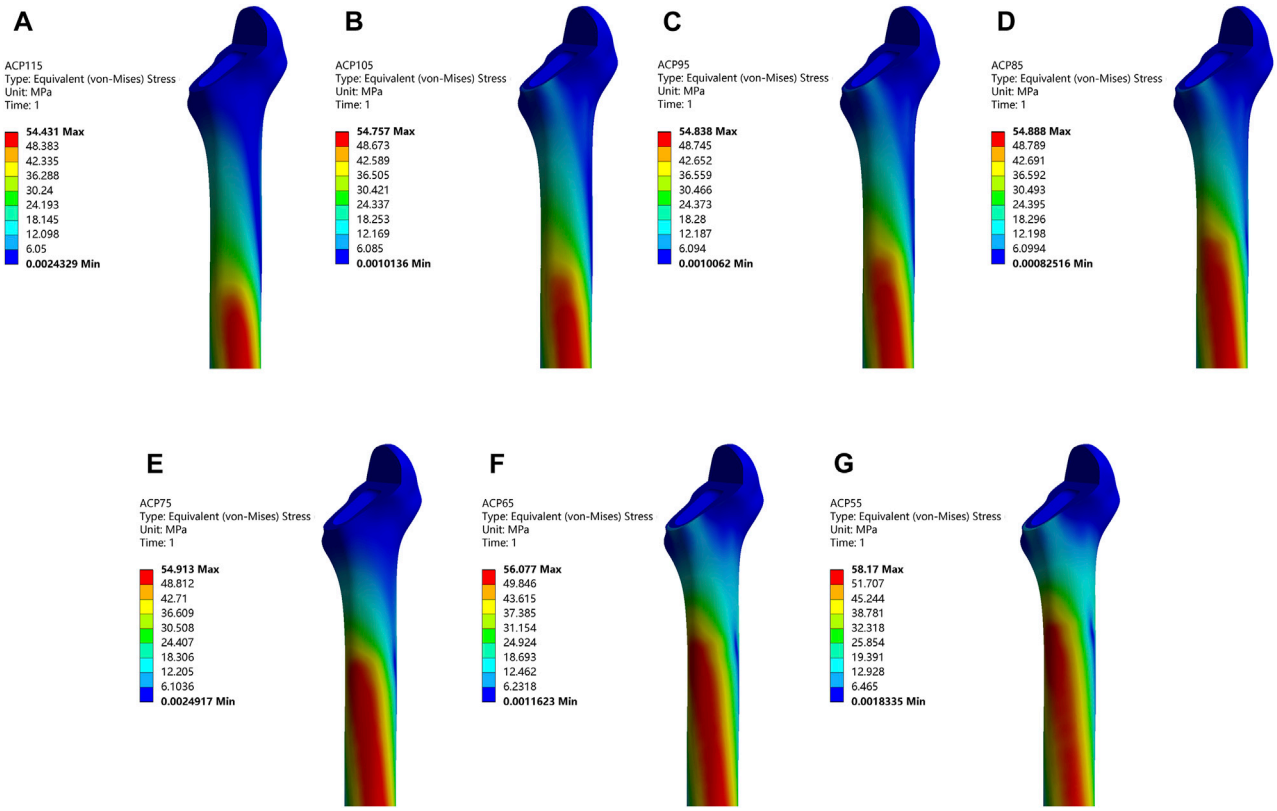

FIGURE 5
Femoral von-Mises stress distribution under different stem lengths.

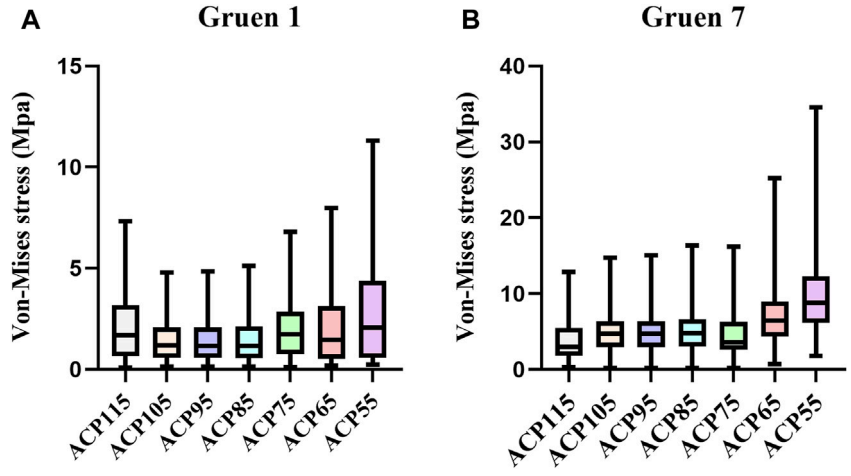

FIGURE 6
Nodal von-Mises stress in the proximal femur under different stem lengths. **(A)** Gruen zone 1 **(B)** Gruen zone 7.

ACP95 group was 54.838 MPa, ACP85 group was 54.888 MPa, ACP75 group was 54.913 MPa, ACP65 group was 56.077 MPa, ACP55 group was 58.170 MPa. The rates of increase in peak Von-Mises stress, compared to the ACP115 group, were as follows: 0.599% (ACP105), 0.748% (ACP95), 0.840% (ACP85), 0.886% (ACP75), 3.024% (ACP65), and 6.869% (ACP55).

3.2 Distribution of von-Mises stress in the proximal femur

The nodal von-Mises stress in the proximal femur of each model was calculated from the finite element results and plotted in Figure 6. In Gruen zone 1, the von-Mises stress for each group model was as

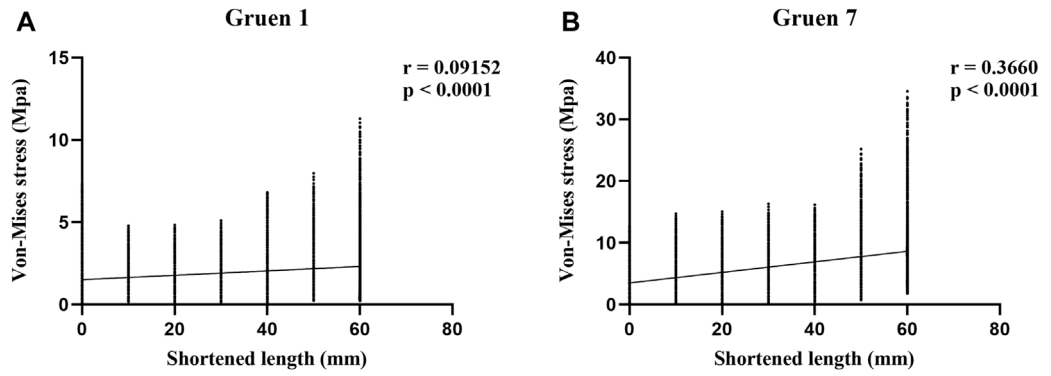

FIGURE 7
Results of Spearman correlation analysis between shortened length and von-Mises stress in the proximal femur. **(A)** Gruen zone 1 **(B)** Gruen zone 7.

follows: ACP115 (1.682 MPa, IQR 0.651–3.173), ACP105 (1.177 MPa, IQR 0.574–2.079), ACP95 (1.166 MPa, IQR 0.567–2.063), ACP85 (1.173 MPa, IQR 0.555–2.12), ACP75 (1.749 MPa, IQR 0.738–2.857), ACP65 (1.467 MPa, IQR 0.530–3.116), ACP55 (2.071 MPa, IQR 0.575–4.368). In Gruen zone 7, the von-Mises stress for each group model was as follows: ACP115 (2.987 MPa, IQR 1.810–5.522), ACP105 (4.737 MPa, IQR 2.973–6.385), ACP95 (4.711 MPa, IQR 2.961–6.395), ACP85 (4.817 MPa, IQR 3.066–6.617), ACP75 (3.597 MPa, IQR 2.639–6.276), ACP65 (6.481 MPa, IQR 4.378–8.953), ACP55 (8.823 MPa, IQR 6.172–12.332).

In order to investigate the correlation between von-Mises stress in different regions of the femur and the length of the stem, Spearman correlation analysis was performed on the von-Mises stress and shortened length of all nodes in each region, as shown in Figure 7. The results showed that the *p*-values for all regions were less than 0.0001, and the correlation coefficients (r) for each region were 0.092 (Gruen Zone 1) and 0.366 (Gruen Zone 7), which indicating a positive correlation between von-Mises stress in the proximal femur and the shortened length of the stem.

3.3 Primary stability evaluation

After 100,000 loading cycles, the irreversible axial displacement of the ACP75 stem relative to bone cement was −870 μm (SD 430 μm).

4 Discussion

Currently, limited research exists on cemented short stems. This study investigated the impact of cemented stem length on femoral load and the initial stability of cemented short stems. To eliminate the influence of metaphyseal design factors on experimental results, we progressively truncated the same stem. This approach allowed us to clearly comprehend the trend of changes in various observed indicators as the length of the cemented stem changed. Our finite element analysis demonstrated that shortening the length of cemented stems effectively enhanced the proximal load of the femur, while having minimal effects on the femur's peak stress. The peak von-Mises stresses in all groups were far below the ultimate strength of 133 Mpa, which did not increase the risk of fracture. Additionally, we conducted fatigue testing to simulate the load conditions experienced by cemented short stems during the first 6 weeks *in vivo*. Based on our findings, we observed an irreversible axial displacement of −870 μm for the cemented short stem, which fell below the predetermined criterion of 5 mm for prosthesis loosening (Santori et al., 2019). This result provided evidence for the favorable initial stability of cemented short stems.

This study demonstrated results similar to those of uncemented stems. Bieger et al. and Arno et al. have argued that reducing the stem length can decrease proximal stress shielding without compromising initial stability (Arno et al., 2012; Bieger et al., 2012). In a comparison between the Alloclassic hip system and the Mayo short stem, Boyle et al. discovered that the Mayo stem was more effective in load transmission to cancellous bone and reducing proximal bone loss (Boyle and Kim, 2011). Østbyhaug et al. conducted research on the ABG-1 stem and determined that shortening the stem by 40–50 mm could transmission stress more effectively in the metaphysis and diaphysis (Østbyhaug et al., 2009). However, shortening the uncemented stem may impact initial stability. Van Rietbergen et al. found that shorter stems had higher shear stress near the distal lateral side compared to standard stems, which could potentially lead to decreased initial stability (van Rietbergen and Huiskes, 2001). Ong et al. compared longer and shorter versions of the Omnifit hydroxyapatite stem and observed that although the shorter design had greater potential for bone formation on the medial side, the displacement of the bone-prosthesis interface at the tip of the short stem was 40%–94% greater than that of the longer stem, which may result in patient discomfort (Ong et al., 2009). Cement fixation had a significant impact on load transfer at the proximal femur (Scheerlinck and Casteleyn, 2006). The study by Freitag et al. found that cemented Optimys short stem demonstrated a smaller irreversible axial displacement after fatigue testing compared to cemented conventional straight twinSys stem (−20.4 μm ± 38.3 μm/−61.4 μm ± 92.8 μm) (Freitag et al., 2021). Although no statistical differences were observed in the result. Thomsen et al. compared the maximum fracture load and fracture pattern of cemented and uncemented stems in non-osteoporotic bone and discovered that the maximum fracture load of the cemented stem was significantly higher (Thomsen et al., 2008). Similarly, Klasan et al. conducted an experiment on cadaver bones comparing the failure loads of cemented and uncemented stems. They found that the failure load of

the cemented stem increased by 25% compared to the latter (Klasan et al., 2019). The utilization of cement technology may offer a solution to the low initial stability observed in uncemented short stems.

In recent years, several clinical studies have been published regarding cemented short stems. A study based on AOANJRR compared the 7-year follow-up results of the short and standard Exeter stem. Despite the short stem being used in a larger proportion of potential difficult cases with developmental dysplasia of the hip, there was no significant difference observed in the cumulative revision rate between the short and standard Exeter stem (Choy et al., 2013). However, another study based on the New Zealand National Joint Registry produced different result. This study found that the revision rate of the standard Exeter stem was significantly lower than that of the short Exeter stem with an offset of 35.5 mm. On the other hand, the revision rate of the shorter Exeter stem with an offset of 37 mm was similar to that of the standard stem (Wyatt et al., 2020). Another recent study also indicated that femoral stem with smaller offset carried a higher risk of revision (Wyatt et al., 2019). Therefore, for the Exeter stem, offset appears to be more important than stem length, as the proximal part provides rotational stability (Wilson et al., 2012). In addition to revision rates, a randomized controlled trial has compared the functional outcomes between short and standard Exeter stems in total hip arthroplasty. The result of this trial showed that, at an average of 2 years postoperatively, the short Exeter stem exhibited similar hip joint function, health-related quality of life, and patient satisfaction compared to the standard stem (Gaston et al., 2023). Although a greater rate of varus malalignment was found in short stem group, which may affect the stem survival rate in the future.

However, the short Exeter stem was not a truly representative short stem in the conventional sense. It was designed specifically for patients with smaller femurs. The longest follow-up results for cemented short stems were derived from the study conducted by Santori et al. The results showed that the survival rate of the Friendly cemented short stem, with aseptic loosening as the endpoint, was 100% with a maximum follow-up of 11.2 years (Santori et al., 2019). However, it was important to note that the Friendly short stem was only a modification of the Exeter stem concept, with a reduced length, limiting its comparability to the novel generation of calcar-guided short-stem concept. To date, there have been no new-generation cemented short stems used clinically. The utilization of the line-to-line technique in the development of cemented short stems may present a promising alternative for the treatment of osteoporotic bone conditions (Azari et al., 2021).

There are some limitations in this study that should be acknowledged. Firstly, the finite element analysis was performed under static load conditions, which only provided limited results. It was important to consider more realistic load conditions, such as walking, climbing stairs, and running (Kwak et al., 2021). Previous research has demonstrated that the torque generated during stair climbing poses the greatest risk for cement failure (Bergmann et al., 1995). However, in dynamic situations, it is crucial to understand the interplay between the femoral and the acetabular prosthesis. Recently, scholars have developed a novel 3D contact-lubrication model to calculate the wear performance of hip prostheses during the gait process, and they have achieved encouraging results. This may assist us in better simulating the kinematic characteristics after hip arthroplasty (Ruggiero and Sicilia, 2020). Secondly, we were hindered by the lack of a femoral canal rasp specifically designed for the shortened stem. Consequently, we utilized a femoral canal rasp that corresponded to the pre-cut stem, leading to a longer cement mantle at the distal end. However, the mechanical strength of the Sawbones primarily derived from the cortical bone, which remained unaffected by this issue. Therefore, we believed that the impact on the result was minimal. Lastly, the simulated loading employed during the first 6 weeks could only capture the initial characteristics following the implantation of the cemented short stem. The medium and long-term characteristics can only be obtained by conducting long-term clinical follow-up studies *in vivo*.

5 Conclusion

The findings of the finite element analysis indicated that, similar to an uncemented stem, reducing the length of a cement stem could effectively enhance the proximal load in the femur without posing additional fracture risk. Moreover, the biomechanical experiment validated the favorable initial stabilities of cemented short stems. However, further investigations are required to ascertain whether these findings can translate into clinical benefits.

Data availability statement

The raw data supporting the conclusion of this article will be made available by the authors, without undue reservation.

Author contributions

JL: Conceptualization, Formal Analysis, Methodology, Validation, Writing–original draft. LX: Data curation, Methodology, Writing–review and editing. CL: Data curation, Software, Writing–review and editing. XW: Software, Visualization, Writing–review and editing. XM: Conceptualization, Project administration, Resources, Supervision, Validation, Writing–review and editing.

Funding

The author(s) declare that no financial support was received for the research, authorship, and/or publication of this article.

Conflict of interest

The authors declare that the research was conducted in the absence of any commercial or financial relationships that could be construed as a potential conflict of interest.

Publisher's note

References

Arno, S., Fetto, J., Nguyen, N. Q., Kinariwala, N., Takemoto, R., Oh, C., et al. (2012). Evaluation of femoral strains with cementless proximal-fill femoral implants of varied stem length. *Clin. Biomech. (Bristol, Avon)* 27 (7), 680–685. doi:10.1016/j.clinbiomech.2012.03.006

Azari, F., Sas, A., Kutzner, K. P., Klockow, A., Scheerlinck, T., and van Lenthe, G. H. (2021). Cemented short-stem total hip arthroplasty: characteristics of line-to-line versus undersized cementing techniques using a validated CT-based finite element analysis. *J. Orthop. Res.* 39 (8), 1681–1690. doi:10.1002/jor.24887

Babazadeh, S., de Steiger, R. N., Holder, C., and van Bavel, D. (2022). Cemented polished tapered stems have lower revision rates than commonly used cementless implant up to 17 Years of follow-up: an analysis of 201,889 total hip replacements from the Australian orthopedic association national joint replacement registry. *J. Arthroplasty* 37 (1), 110–118. doi:10.1016/j.arth.2021.09.013

Bergmann, G., Bender, A., Dymke, J., Duda, G., and Damm, P. (2016). Standardized loads acting in hip implants. *PLoS One* 11 (5), e0155612. doi:10.1371/journal.pone.0155612

Bergmann, G., Graichen, F., and Rohlmann, A. (1995). Is staircase walking a risk for the fixation of hip implants? *J. Biomech.* 28 (5), 535–553. doi:10.1016/0021-9290(94)00105-d

Bieger, R., Ignatius, A., Decking, R., Claes, L., Reichel, H., and Dürselen, L. (2012). Primary stability and strain distribution of cementless hip stems as a function of implant design. *Clin. Biomech. (Bristol, Avon)* 27 (2), 158–164. doi:10.1016/j.clinbiomech.2011.08.004

Boyle, C., and Kim, I. Y. (2011). Comparison of different hip prosthesis shapes considering micro-level bone remodeling and stress-shielding criteria using three-dimensional design space topology optimization. *J. Biomech.* 44 (9), 1722–1728. doi:10.1016/j.jbiomech.2011.03.038

Choy, G. G., Roe, J. A., Whitehouse, S. L., Cashman, K. S., and Crawford, R. W. (2013). Exeter short stems compared with standard length exeter stems: experience from the Australian orthopaedic association national joint replacement registry. *J. Arthroplasty* 28 (1), 103–109. doi:10.1016/j.arth.2012.06.016

Costi, K., Solomon, L. B., McGee, M. A., Rickman, M. S., and Howie, D. W. (2017). Advantages in using cemented polished tapered stems when performing total hip arthroplasty in very young patients. *J. Arthroplasty* 32 (4), 1227–1233. doi:10.1016/j.arth.2016.11.031

de Waard, S., van der Vis, J., Venema, P., Sierevelt, I. N., Kerkhoffs, G., and Haverkamp, D. (2021). Short-term success of proximal bone stock preservation in short hip stems: a systematic review of the literature. *EFORT Open Rev.* 6 (11), 1040–1051. doi:10.1302/2058-5241.6.210030

Eskelinen, A., Remes, V., Helenius, I., Pulkkinen, P., Nevalainen, J., and Paavolainen, P. (2006). Uncemented total hip arthroplasty for primary osteoarthritis in young patients: a mid-to long-term follow-up study from the Finnish Arthroplasty Register. *Acta Orthop.* 77 (1), 57–70. doi:10.1080/1745367061004570

Evans, J. T., Evans, J. P., Walker, R. W., Blom, A. W., Whitehouse, M. R., and Sayers, A. (2019). How long does a hip replacement last? A systematic review and meta-analysis of case series and national registry reports with more than 15 years of follow-up. *Lancet* 393 (10172), 647–654. doi:10.1016/s0140-6736(18)31665-9

Feyen, H., and Shimmin, A. J. (2014). Is the length of the femoral component important in primary total hip replacement? *Bone Jt. J.* 96-b (4), 442–448. doi:10.1302/0301-620x.96b4.33036

Freitag, T., Kutzner, K. P., Bieger, R., Reichel, H., Ignatius, A., and Dürselen, L. (2021). Biomechanics of a cemented short stem: a comparative *in vitro* study regarding primary stability and maximum fracture load. *Arch. Orthop. Trauma Surg.* 141 (10), 1797–1806. doi:10.1007/s00402-021-03843-x

Gaston, P., Clement, N. D., Ohly, N. E., Macpherson, G. J., and Hamilton, D. F. (2023). Can arthroplasty stem influence outcome: a randomized controlled trial of stem length in cemented total hip arthroplasty. *J. Arthroplasty* 38 (9), 1793–1801. doi:10.1016/j.arth.2023.02.045

Giardina, F., Castagnini, F., Stea, S., Bordini, B., Montalti, M., and Toni, A. (2018). Short stems versus conventional stems in cementless total hip arthroplasty: a long-term registry study. *J. Arthroplasty* 33 (6), 1794–1799. doi:10.1016/j.arth.2018.01.005

Gkagkalis, G., Goetti, P., Mai, S., Meinecke, I., Helmy, N., Bosson, D., et al. (2019). Cementless short-stem total hip arthroplasty in the elderly patient - is it a safe option? a prospective multicentre observational study. *BMC Geriatr.* 19 (1), 112. doi:10.1186/s12877-019-1123-1

Gruen, T. A., McNeice, G. M., and Amstutz, H. C. (1979). Modes of failure" of cemented stem-type femoral components: a radiographic analysis of loosening. *Clin. Orthop. Relat. Res.* 141, 17–27. doi:10.1097/00003086-197906000-00002

Gruner, A., and Heller, K. D. (2015). Patient selection for shorter femoral stems. *Orthopedics* 38 (3 Suppl. l), S27–S32. doi:10.3928/01477447-20150215-53

Hossain, F., Konan, S., Volpin, A., and Haddad, F. S. (2017). Early performance-based and patient-reported outcomes of a contemporary taper fit bone-conserving short stem femoral component in total hip arthroplasty. *Bone Jt. J.* 99-b (4 Suppl. B), 49–55. doi:10.1302/0301-620x.99b4.Bjj-2016-1291.R1

Kiran, M., Johnston, L. R., Sripada, S., McLeod, G. G., and Jariwala, A. C. (2018). Cemented total hip replacement in patients under 55 years. *Acta Orthop.* 89 (2), 152–155. doi:10.1080/17453674.2018.1427320

Klasan, A., Bäumlein, M., Bliemel, C., Putnis, S. E., Neri, T., Schofer, M. D., et al. (2019). Cementing of the hip arthroplasty stem increases load-to-failure force: a cadaveric study. *Acta Orthop.* 90 (5), 445–449. doi:10.1080/17453674.2019.1634331

Kwak, D. K., Bang, S. H., Lee, S. J., Park, J. H., and Yoo, J. H. (2021). Effect of stem position and length on bone-stem constructs after cementless hip arthroplasty. *Bone Jt. Res.* 10 (4), 250–258. doi:10.1302/2046-3758.104.Bjr-2020-0043.R3

Naghavi, S. A., Tamaddon, M., Garcia-Souto, P., Moazen, M., Taylor, S., Hua, J., et al. (2023). A novel hybrid design and modelling of a customised graded Ti-6Al-4V porous hip implant to reduce stress-shielding: an experimental and numerical analysis. *Front. Bioeng. Biotechnol.* 11, 1092361. doi:10.3389/fbioe.2023.1092361

Ong, K. L., Day, J. S., Manley, M. T., Kurtz, S. M., and Geesink, R. (2009). Biomechanical comparison of 2 proximally coated femoral stems: effects of stem length and surface finish. *J. Arthroplasty* 24 (5), 819–824. doi:10.1016/j.arth.2008.09.012

Østbyhaug, P. O., Klaksvik, J., Romundstad, P., and Aamodt, A. (2009). An *in vitro* study of the strain distribution in human femora with anatomical and customised femoral stems. *J. Bone Jt. Surg. Br.* 91 (5), 676–682. doi:10.1302/0301-620x.91b5.21749

Ruggiero, A., D'Amato, R., and Affatato, S. (2019). Comparison of meshing strategies in THR finite element modelling. *Mater. (Basel)* 12 (14), 2332. doi:10.3390/ma12142332

Ruggiero, A., and Sicilia, A. (2020). Lubrication modeling and wear calculation in artificial hip joint during the gait. *Tribol. Int.* 142, 105993. doi:10.1016/j.triboint.2019.105993

Santori, N., Falez, F., Potestio, D., and Santori, F. S. (2019). Fourteen-year experience with short cemented stems in total hip replacement. *Int. Orthop.* 43 (1), 55–61. doi:10.1007/s00264-018-4205-3

Scheerlinck, T., and Casteleyn, P. P. (2006). The design features of cemented femoral hip implants. *J. Bone Jt. Surg. Br.* 88 (11), 1409–1418. doi:10.1302/0301-620x.88b11.17836

Shin, Y. S., Suh, D. H., Park, J. H., Kim, J. L., and Han, S. B. (2016). Comparison of specific femoral short stems and conventional-length stems in primary cementless total hip arthroplasty. *Orthopedics* 39 (2), e311–e317. doi:10.3928/01477447-20160222-04

Thomsen, M. N., Jakubowitz, E., Seeger, J. B., Lee, C., Kretzer, J. P., and Clarius, M. (2008). Fracture load for periprosthetic femoral fractures in cemented versus uncemented hip stems: an experimental *in vitro* study. *Orthopedics* 31 (7), 653. doi:10.3928/01477447-20110505-12

van Rietbergen, B., and Huiskes, R. (2001). Load transfer and stress shielding of the hydroxyapatite-ABG hip: a study of stem length and proximal fixation. *J. Arthroplasty* 16 (8 Suppl. 1), 55–63. doi:10.1054/arth.2001.28369

Verdonschot, N., and Huiskes, R. (1996). Subsidence of THA stems due to acrylic cement creep is extremely sensitive to interface friction. *J. Biomech.* 29 (12), 1569–1575. doi:10.1016/s0021-9290(96)80008-x

Wilson, L. J., Roe, J. A., Pearcy, M. J., and Crawford, R. W. (2012). Shortening cemented femoral implants: an *in vitro* investigation to quantify exeter femoral implant rotational stability vs simulated implant length. *J. Arthroplasty* 27 (6), 934–939. doi:10.1016/j.arth.2011.10.012

Wyatt, M. C., Kieser, D. C., Kemp, M. A., McHugh, G., Frampton, C. M. A., and Hooper, G. J. (2019). Does the femoral offset affect replacements? The results from a National Joint Registry. *Hip Int.* 29 (3), 289–298. doi:10.1177/1120700018780318

Wyatt, M. C., Poutawera, V., Kieser, D. C., Frampton, C. M. A., and Hooper, G. J. (2020). How do cemented short Exeter stems perform compared with standard-length Exeter stems? The experience of the New Zealand National Joint Registry. *Arthroplast Today* 6 (1), 104–111. doi:10.1016/j.artd.2020.01.003

Zimmerer, A., Slouka, S., Kinkel, S., Fritz, T., Weiss, S., Sobau, C., et al. (2020). Comparison of short-stem with conventional-stem prostheses in total hip arthroplasty: an 8-year follow-up study. *Arch. Orthop. Trauma Surg.* 140 (9), 1285–1291. doi:10.1007/s00402-020-03519-y

frontiers | Frontiers in Bioengineering and Biotechnology

TYPE Original Research
PUBLISHED 08 January 2024
DOI 10.3389/fbioe.2023.1282512

OPEN ACCESS

EDITED BY
Xijin Hua,
University of Exeter, United Kingdom

REVIEWED BY
Francesco Travascio,
University of Miami, United States
Yun Peng,
NuVasive, United States
Pengfei Yu,
Suzhou Hospital of Traditional Chinese Medicine, China

*CORRESPONDENCE
Jing-Chi Li,
Lijingchi9405@163.com
Zhi-Peng Xi,
xizhipeng1985@163.com

†These authors have contributed equally to this work and share first authorship

RECEIVED 24 August 2023
ACCEPTED 11 December 2023
PUBLISHED 08 January 2024

CITATION
Yang J-X, Luo L, Liu J-H, Wang N, Xi Z-P and Li J-C (2024), Incomplete insertion of pedicle screws triggers a higher biomechanical risk of screw loosening: mechanical tests and corresponding numerical simulations.
Front. Bioeng. Biotechnol. 11:1282512.
doi: 10.3389/fbioe.2023.1282512

Incomplete insertion of pedicle screws triggers a higher biomechanical risk of screw loosening: mechanical tests and corresponding numerical simulations

Jie-Xiang Yang[1,2†], Lin Luo[1,2†], Jin-Hui Liu[3], Nan Wang[4], Zhi-Peng Xi[4*] and Jing-Chi Li[1,2*]

[1]Department of Orthopedics, The Affiliated Traditional Chinese Medicine Hospital, Southwest Medical University, Luzhou, China, [2]Luzhou Key Laboratory of Orthopedic Disorders, Southwest Medical University, Luzhou, Sichuan, China, [3]Sichuan Provincial Laboratory of Orthopaedic Engineering, Department of Bone and Joint Surgery, Affiliated Hospital of Southwest Medical University, Luzhou, Sichuan, China, [4]Department of Orthopedics, Affiliated Hospital of Integrated Traditional Chinese and Western Medicine, Nanjing University of Chinese Medicine, Nanjing, Jiangsu, China

Screw loosening is a widely reported issue after spinal screw fixation and triggers several complications. Biomechanical deterioration initially causes screw loosening. Studies have shown that incomplete insertion of pedicle screws increases the risk of screw breakage by deteriorating the local mechanical environment. However, whether this change has a biomechanical effect on the risk of screw loosening has not been determined. This study conducted comprehensive biomechanical research using polyurethane foam mechanical tests and corresponding numerical simulations to verify this topic. Pedicle screw-fixed polyurethane foam models with screws with four different insertion depths were constructed, and the screw anchoring ability of different models was verified by toggle tests with alternating and constant loads. Moreover, the stress distribution of screw and bone-screw interfaces in different models was computed in corresponding numerical mechanical models. Mechanical tests presented better screw anchoring ability with deeper screw insertion, but parameters presented no significant difference between groups with complete thread insertion. Correspondingly, higher stress values can be recorded in the model without complete thread insertion; the difference in stress values between models with complete thread insertion was relatively slight. Therefore, incomplete thread insertion triggers local stress concentration and the corresponding risk of screw loosening; completely inserting threads could effectively alleviate local stress concentration and result in the prevention of screw loosening.

KEYWORDS

screw loosening, incomplete thread insertion, biomechanical deterioration, pedicle screw, comprehensive biomechanical research

Introduction

The pedicle screw fixation system is the most widely used spinal fixation method for treating spinal trauma and degenerative and tumoral diseases (Chen et al., 2003; Karami et al., 2015). Compared with other spinal fixation methods, this method could provide better fixation stability and could be seen as the gold standard of spinal fixation (Amaritsakul et al., 2014; Ambati et al., 2015). Screw loosening is a commonly observed complication for pedicle screw-fixed patients, which triggers the loss of fixation stability and a corresponding series of issues (Bredow et al., 2016; Marie-Hardy et al., 2020). Biomechanical deterioration initially induces screw loosening. The loss of bone-screw integration is the primary pathological phenotype of screw loosening; higher stress values at the bone-screw interface cause this phenotype and corresponding screw loosening (Li et al., 2022b; Li et al., 2022c). Therefore, any risk factors that potentially trigger stress concentration on bone-screw interfaces should be considered potential risk factors for screw loosening.

Hypertrophy of articular processes is common in patients with pedicle screw fixation (Adams et al., 2000; Adams and Roughley, 2006). This change may inhibit the complete insertion of pedicle screws. Studies have reported a lower fatigue life and a higher risk of screw breakage when threads are not completely inserted into bony structures (Chen et al., 2005; Athanasakopoulos et al., 2013). Correspondingly, higher stress values of pedicle screws can be recorded in numerical models without complete thread insertion. Since the stress concentration on screws is closely related to that on the bone screw interfaces, we hypothesize that incomplete insertion of pedicle screws may also be a significant biomechanical risk factor for screw loosening; however, this has not been verified. In this study, comprehensive research combining mechanical tests and numerical simulations was performed to verify this assumption. The corresponding results should provide a theoretical foundation for optimizing fixation stability from a biomechanical perspective.

Materials and methods

Mechanical tests on polyurethane foams

Model construction

Osteoporotic polyurethane foams (Sawbones Company, United States) were used as bone substitutes due to their homogeneous structure, consistent material properties, and availability (Brasiliense et al., 2013; Amirouche et al., 2016). Since screw loosening is commonly observed in osteoporotic patients, the density of the polyurethane foam was selected to be 0.16 g/cm3 according to the standard of the American Society of Testing Materials (ASTM) protocol (Seng et al., 2019; Weidling et al., 2020). The polyurethane foam was cut to a length of 60 mm, a width of 40 mm, and a height of 50 mm. A clinically used cylindrical titanium alloy (Ti-6Al-4V) pedicle screw (with two start threads and a parallel minor diameter) (Reach-Med Company, China) was selected for this study. The outer diameter of the pedicle screw was 6.5 mm, the inner diameter was 3.5 mm, and the screw thread length was 40 mm.

Models with four different screw insertion lengths were constructed. Models with complete thread insertion (40 mm) were considered the baseline for judging screw insertion depth. In models with incomplete screw insertion, quarter-circle threads (90°) were reserved from the test block. In contrast, in models with screw overinsertion, quarter-circle and half-circle (i.e., 90° and 180°) screws were overinserted into the test blocks, respectively (Figure 1).

Toggle tests under different loading protocols

Toggle and pull-out tests were performed on an E3000 fatigue testing machine (Instron Company, USA). Each single test was repeated ten times in different models. Each screw, connecting rod, and nut was tested only once. Before the toggle tests, the connecting rod (6.0 mm in outer diameter and 100 mm in length) was inserted into the screw tulip and secured with nails. The axis of the rod was vertical to that of the pedicle screw, and the distance from the screw axis to the tip of the rod was set at 60 mm. For toggle testing, foam blocks were fixed in the testing machine. Each group was tested five times in different parts of the toggle tests.

Toggle tests were performed under varying cyclic loading. The pedicle screw was subjected to cyclic loading in a craniocaudal direction with stepwise increasing loads. Each pedicle screw was cyclically loaded with an initial load of ±100 N; the vertical load was increased by 25 N every 30 cycles (Brasiliense et al., 2013; Kanno et al., 2019). The instantaneous values of maximum screw displacement and the corresponding vertical load were recorded 100 times per second. Cyclic loading was terminated when screw fixation failed (the maximum screw displacement reached 1 mm). Cycle times and corresponding compressive loads at fixation failure were recorded in this procedure (Figure 1).

Moreover, when performing toggle tests under a constant load of $1*10^4$ cycles, the pedicle screw was subjected to cyclic loading in the cranio-caudal direction with a load of ±200 N. This load level was selected to simulate the physiological load of a 40-kg postmenopausal woman with osteoporosis. This is a common loading environment for screw fixation in osteoporotic patients in our country. The instantaneous values of maximum screw displacement and the corresponding vertical load were recorded 100 times per second (Pelletier et al., 2017; Wang et al., 2019b). Cyclic loading was terminated after $1*10^4$ loading cycles. The differences between the first and last displacement values were also calculated and recorded in this procedure.

Pull-out tests

The foam-screw models in each group were subjected to pull-out tests after the toggle test with different loading protocols. In the pull-out tests, the foam was also rigidly fixed to the testing machine, and a custom-made fixture connected to the testing machine was then attached to the connecting rod. By this method, the axis of the screw was collinear with the pull-out force. All screws were pulled uniaxially at a rate of 5 mm/min until they were entirely pulled out of the foam (Chen et al., 2011; Cho et al., 2011). The pull-out strength was judged as the axial force value when a sudden decrease

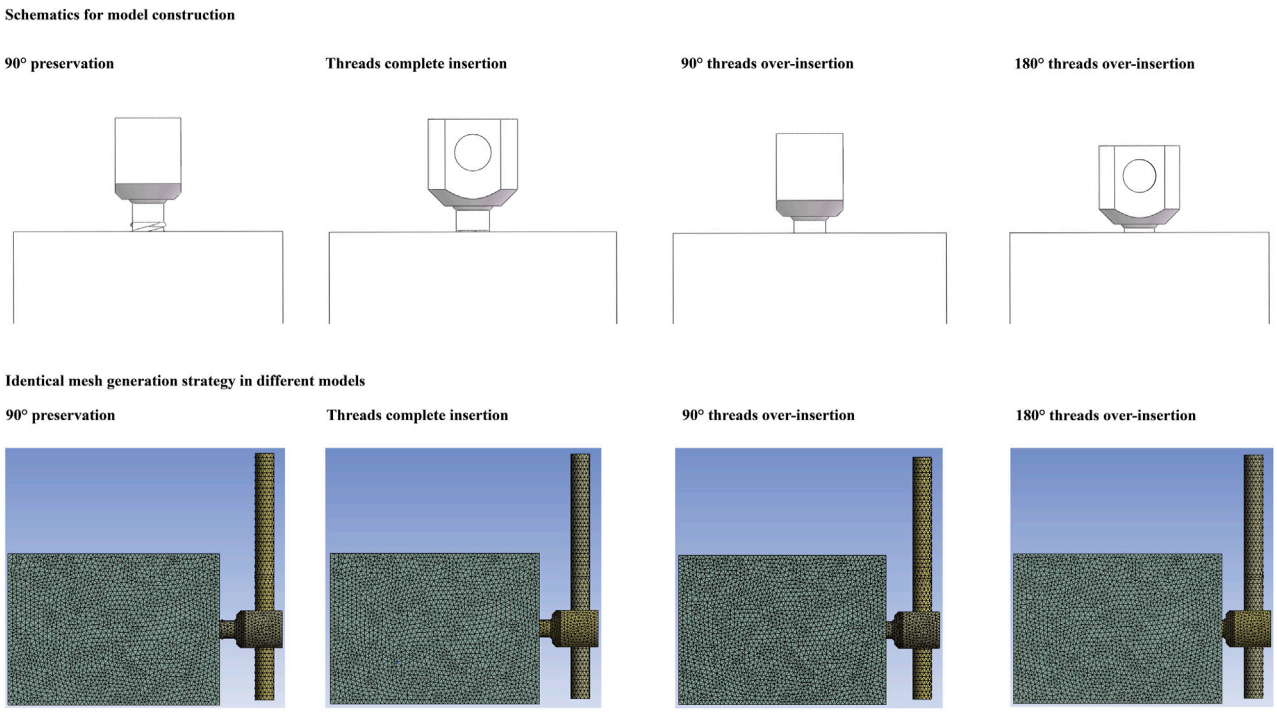

FIGURE 1
Schematic of test models with different screw insertion depths and identical mesh generation strategy in different models.

in the pull-out force was observed. The pull-out stiffness in different models was also recorded (Zhang et al., 2006; Yuan et al., 2014) (Figure 2).

Statistical analyses

Mechanically tested parameters are presented as the mean ± standard deviation (Li et al., 2023; Xi et al., 2023). Statistical analyses were conducted using SPSS software. When comparing the differences between groups with different screw insertion depths, a one-way ANOVA was used for these continuous variables. A *p*-value less than 0.05 indicated a significant difference (Burger, 2023; Chatzi and Doody, 2023).

Numerical simulations (finite element analysis)

Numerical model construction

The numerical model of the pedicle screw was constructed based on the outline of the screw used in the mechanical test. Therefore, the outline of the screw in the mechanical test and simulation were completely identical. Moreover, the model construction strategy, boundary conditions, and loading conditions in the numerical simulation of the toggle and pull-out tests are similar to those in the mechanical tests. To optimize computational efficiency, model simplifications were made in the numerical models. Specifically, the size of the test blocks in the numerical simulations was consistent with the mechanical tests (60*55*40 mm). The screw insertion depth was set at 40 mm. The connection between the screw tulip, the nut, and the spacer was simplified to a single model. The axis of the screw was vertical to the connecting rod, the distance between the axis of the screw and the tip of the rod was 60 mm, and the rod on the caudal side was deleted to reduce the number of elements (Li et al., 2022b; Li et al., 2022c). When defining the material properties of different components, the test blocks were set according to the official product parameter table of the saw-bone company.

Moreover, since the elastic deformation of the bony structures was present during the screw insertion process, the bony compaction (consolidation) effect caused by screw insertion was also simulated by upregulating the material properties of the surrounding bony structure around the screw tip (Figure 1). The elastic modulus of bone was assumed to be a power-law function of the density with an exponent of 2. The definition of the bony compaction region and the corresponding adjustment of its material properties were based on the same type of studies (Hsu et al., 2005; Chao et al., 2008; Travascio et al., 2017).

Moreover, the pedicle screw and connecting rod were defined as titanium alloy material (elastic modulus = 12 GPa and Poisson's ratio = 0.31), and the definition of the test block was also performed based on the production manual of osteoporotic polyurethane foams from the Sawbone Company (elastic modulus = 23 MPa and Poisson's ratio = 0.3). Given that the stiffness of the TC4 (120000 MPa) pedicle screw was dramatically higher than that of osteoporotic polyurethane foam (23 MPa). The deformation value of the TC4 screw was very small, so the deformation of screw can be ignored in the numerical simulaion. Therefore, the deformation of the pedicle screw was not considered in either toggle or pull-out mechanical simulations (Zhang et al., 2006; Kanno et al., 2019-2021).

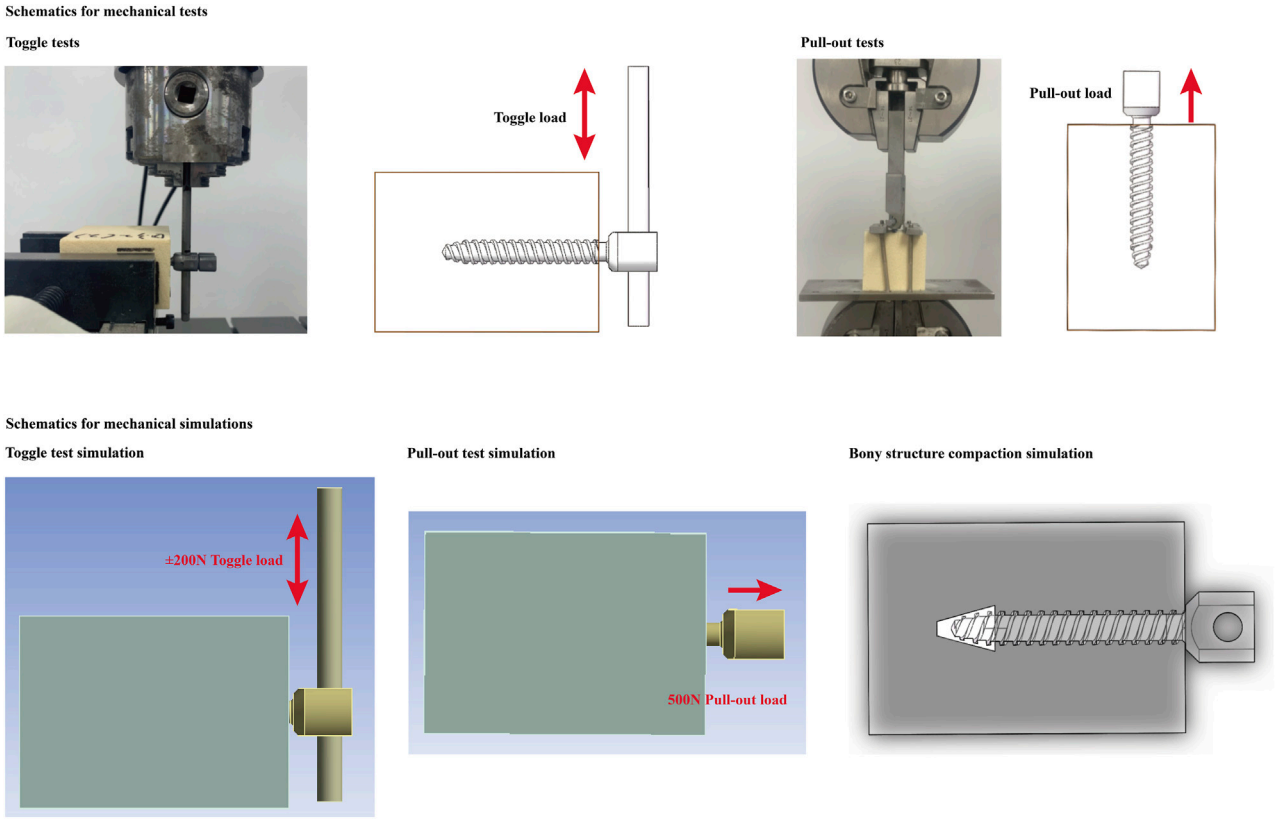

FIGURE 2
Protocols for mechanical testing and numerical simulation.

Finite element analysis under different loading protocols

Toggle test simulation

To ensure computational credibility, the boundary and loading conditions of the numerical simulation were kept identical to those of the toggle test. Contact types between different interfaces were defined according to the same type of study. The contact type between the screw and connecting rod was defined as "bonded", that between bone-screw interfaces was "frictional", and the friction coefficient was set to 0.2 (Xu et al., 2019; Takenaka et al., 2020; Li et al., 2022b). All degrees of freedom of the foam models were completely fixed, and a ±200 N load in the cranial-caudal direction was loaded on the tip of the connecting rod. To eliminate the confounding effect of mesh size, we performed a mesh convergence test on the 40 mm screw depth model. By evaluating the change in maximum equivalent stress on the pedicle screw, mesh sizes on the screw and foam were adjusted. The model was considered convergent if the change in the computed stress values was less than 3% (Ottardi et al., 2016; Li et al., 2023; Xi et al., 2023). To represent the potential risk of screw loosening, the maximum stress value of the pedicle screw and foam, the maximum shear stress and strain of the foam, and the average stress of the bone-screw interfaces were computed and recorded.

Pull-out test simulation

The material property definition, mesh size, and contact type at the bone-screw interfaces in the pull-out test were consistent with those in the toggle test. The construction of the test block and the screw models were also consistent with the toggle test, but the connecting rod in the pull-out test was removed to reduce the number of elements (Prasad et al., 2016; Nakashima et al., 2018). The degrees of freedom of the test block were completely fixed, and a 500 N load along the axis of the pedicle screw was applied to the screw tulip. The maximum screw displacement, maximum equivalent stress on the test block, and failure volume were recorded during this procedure (Krenn et al., 2008; Bianco et al., 2017) (Figure 2).

Results

Mechanical test results

Overall, screw anchoring ability increased stepwise with increasing screw insertion depth. In the alternating load toggle test, the failure load of the 90° preservation and no overinsertion groups was significantly worse than that of the 180° overinsertion groups. The failure and cycle times of the 90° preservation models

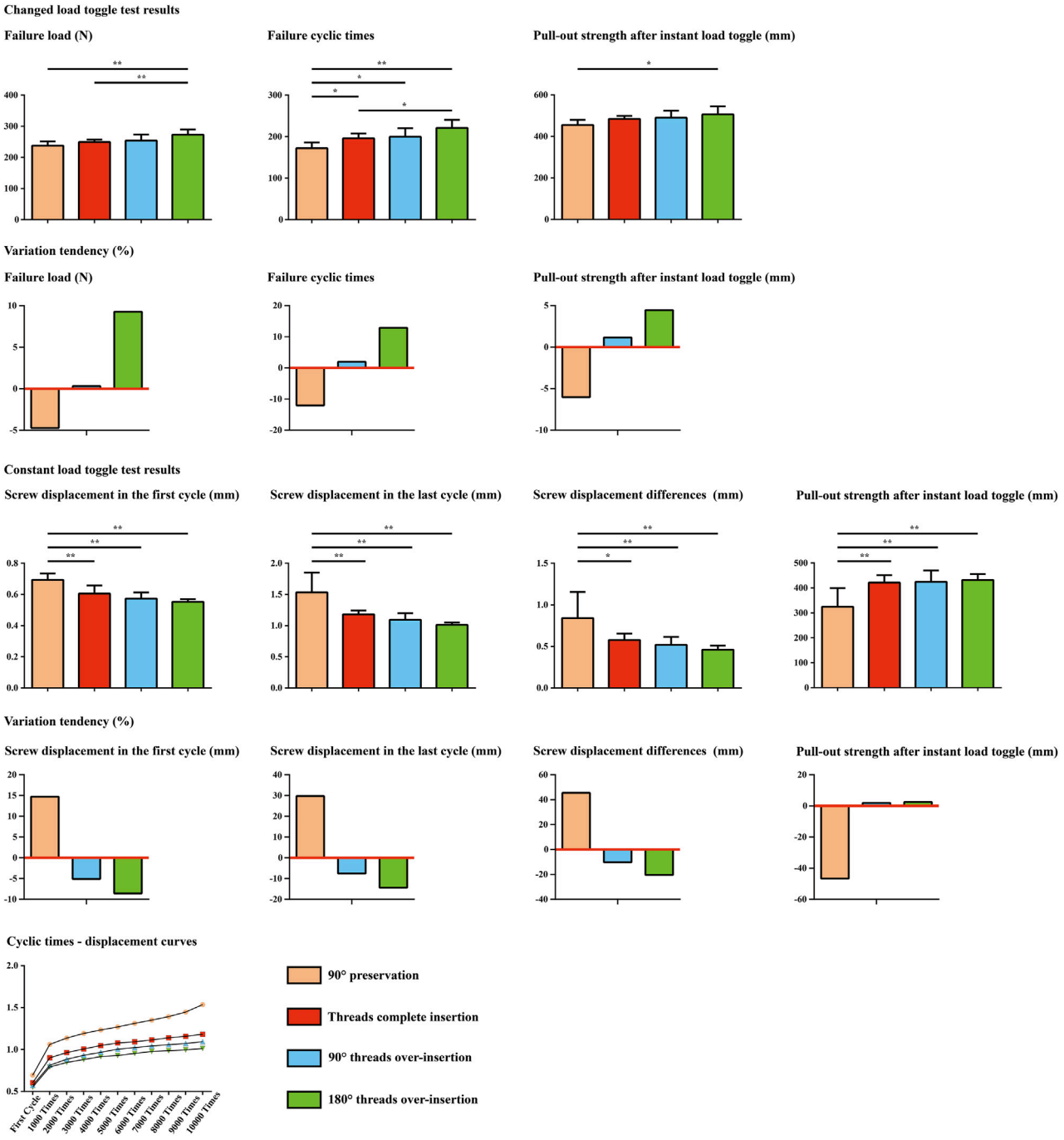

FIGURE 3
Mechanical test results in models with four different screw insertion depths.

were significantly lower than those of the other groups, and those of the models without overinsertion were also significantly lower than those of the 180° overinsertion groups. Pull-out strength in the alternating load toggle test was also significantly lower in the 90° preservation models compared to the 180° overinsertion group. Additionally, in toggle tests with a constant load, there were no significant differences in screw anchorage parameters between the complete thread insertion groups (i.e., no overinsertion and 90° and 180° overinsertion groups). The anchoring ability of the 90° preservation group was significantly worse than that of the complete thread insertion groups (Figure 2).

Numerically simulated results

An overall consistent tendency for variation could be recorded in both toggle and pull-out mechanical simulations. Specifically, a step decrease in the maximum screw displacement stress values

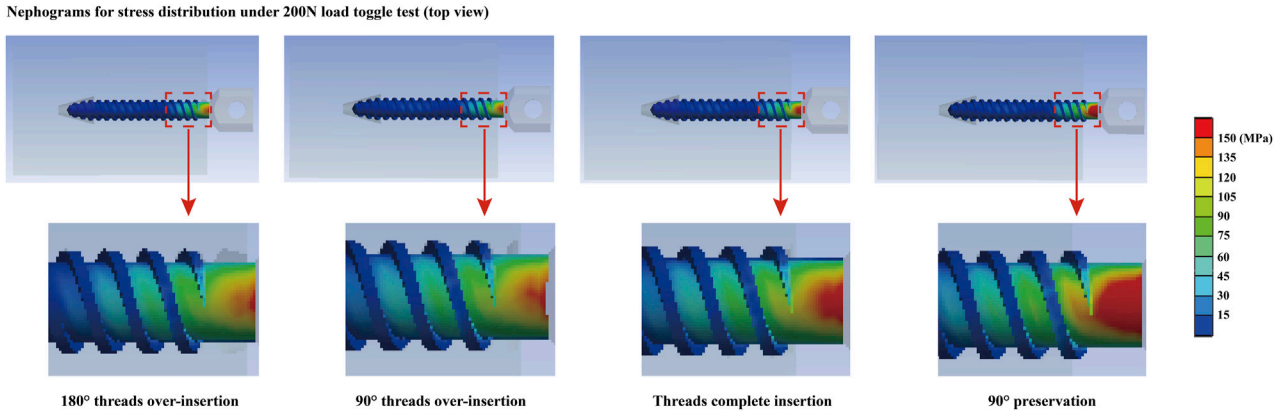

FIGURE 4
Stress distribution nephograms in models with four different screw insertion depths.

could be observed with a step increase in the screw insertion depth. Compared to the difference between models with and without complete screw thread insertion, the differences in stress and deformation values in models with complete thread insertion were relatively small. Detailed changes in stress and deformation values and corresponding variation percentage ratios are presented in Figures 3, 4.

Discussion

Biomechanical mechanisms of potential risk factors for screw loosening have been identified as a stress concentration-induced complication in published studies (Yuan et al., 2014; Wu et al., 2019; Zhang et al., 2020). Although several studies have reported incorrect screw insertion and a corresponding risk of complications (Galbusera et al., 2015; Amirouche et al., 2016), the question of whether the reservation of the thread from bony structures triggers a higher risk of screw loosening remains to be addressed. Given that the selection of the screw insertion depth is a topic arising every time a screw is inserted, identifying this could provide theoretical guidance for pedicle screw insertion to biomechanically reduce the risk of screw loosening.

By performing comprehensive research consisting of mechanical tests and numerical simulations, this study shows that incomplete thread insertion induces local stress concentration and the corresponding risk of screw loosening; complete thread insertion could effectively alleviate the local stress concentration and optimize the screw anchoring ability. In addition, although the difference between the tested and computed results was less significant in the groups with complete thread insertion, further increasing the screw insertion depth after complete thread insertion can further optimize the screw anchoring ability. Therefore, although various factors may affect the complete insertion of the screw (e.g., hypertrophy of articular processes, occlusion of soft tissues such as the facet capsule), based on the positive correlation between screw insertion depth and anchoring ability (Figures 3, 5), complete thread insertion and even overinsertion of pedicle screws are recommended to biomechanically reduce the risk of screw loosening.

From a methodological perspective, several issues should be clarified. First, polyurethane foam models with osteoporotic bone density were selected in this study rather than vertebral bodies from specimens or any laboratory animals. Polyurethane foam can well simulate the mechanical properties of cancellous bone and has the advantages of good homogeneity (effectively eliminating the confounding effect caused by existing regional differences in cancellous bone density) (Li J. et al., 2022; Li et al., 2023) and high availability (inexpensive, and more importantly, not limited by sample sources). Therefore, this test block selection strategy may improve the feasibility and standardization of experiments, thereby increasing the credibility of this study.

However, only osteoporotic models were selected in this study. The stepwise reduction in patients' BMD has been the most significant reason for poor screw anchoring ability by reducing the yield strength and degrading the biomechanical environment at the bone-screw interface (Xu et al., 2020; Zou et al., 2020). Biomechanical studies investigating the biomechanical effect of other risk factors (e.g., screw insertion angle, thread designs) on the risk of screw loosening also show that the incidence rate of screw loosening was consistently low in models with normal bone density, regardless of changes in other potential risk factors (Hsu et al., 2005; Galbusera et al., 2015). Therefore, osteoporotic models were selected for the current mechanical tests and corresponding numerical simulations. In addition, individual differences in the direction and size of the load applied to the pedicle screw existed in different patients but were not considered in this study (Mohammed et al., 2018). Alternatively, standard loading protocols widely used in published studies were selected in this study (Shi et al., 2012; Brasiliense et al., 2013; Wang et al., 2019a; Marie-Hardy et al., 2020; Kanno et al., 2021). The ±200 N toggle load carried by a single screw represents the old load of a patient with a body weight of 40 kg, and 500 N was selected in the pull-out test by referring to the average mechanically tested pull-out strength values in this study.

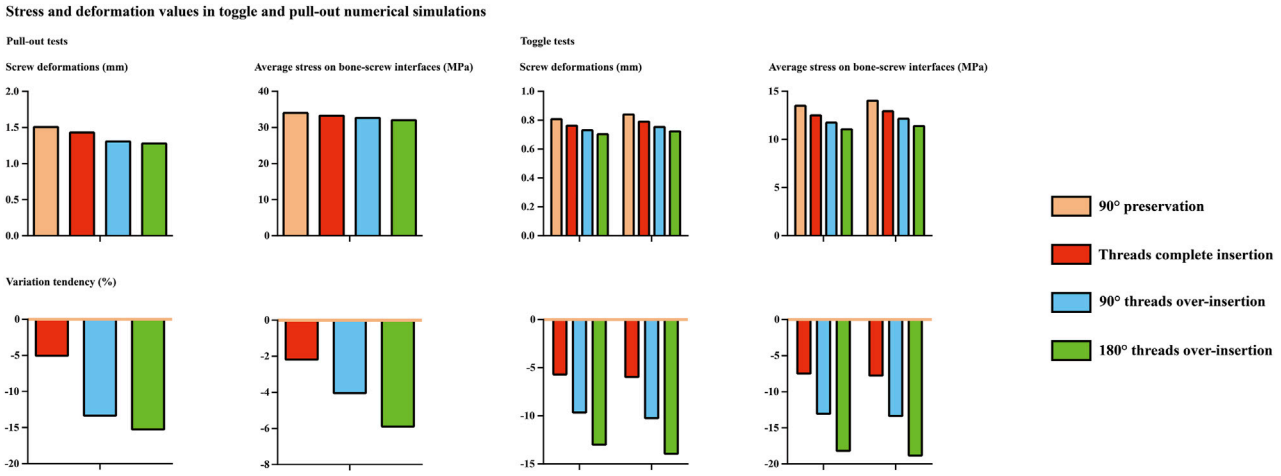

FIGURE 5
Computed stress and deformation values.

In this study, toggle tests with alternating and constant loads were performed on models with different insertion depths. Alternating load toggle tests were terminated when the maximum screw displacement value reached 1 mm because the 1 mm cavity was the standard assessment value for screw loosening. A total of $1*10^4$ times were selected in the constant load toggle tests. Screw loosening is a typical short-term complication (Galbusera et al., 2015; Amirouche et al., 2016; Ding et al., 2017). During the first $1*10^4$ cycles, the maximum screw displacement increased rapidly and remained relatively balanced (i.e., increasing the number of cycles did not significantly increase the maximum screw displacement values). Therefore, $1*10^4$ cycles are sufficient to identify the postoperative screw anchoring ability. Moreover, although the pull-out test can only directly reflect the risk of screw pull-out rather than screw loosening, this indicator has also been measured for better integration between the bone-screw interface and can optimize not only pull-out but also screw toggle strength (Wiendieck et al., 2018; Wang et al., 2019b). Consistent with this point, the current Pearson correlation analyses showed that the pull-out strength was significantly positively correlated with indicators related to the screw anchoring ability in toggle tests, and the pull-out strength was also a credible predictor when predicting the risk of screw loosening.

Mechanical tests and numerical simulations are commonly used biomechanical methods for determining screw anchoring ability (Chao et al., 2008; Solitro et al., 2022). Although mechanical tests can directly reflect screw anchoring ability by directly recording the screw displacement values in each cycle, detailed stress distribution patterns, especially at the bone-screw interfaces, cannot be directly reflected by this method. In contrast, with increasing cycle times, screw compaction on bony structures leads to higher screw displacements and results in screw loosening (Hsu et al., 2005; Boriani et al., 2018). However, this process could not be simulated in numerical models. In contrast, by comprehensively performing these two methods, the computed stress distributions can well explain the mechanism for the tested results. Also, this method can effectively optimize the reliability of the current study (Hsu et al., 2005; Chao et al., 2008).

Consisted to the same type study, direct model validation can not be performed based on the current numerical model. In finite element modeling, comparing the computed result with the mean of the test result is a common method for model validation (Li et al., 2021; Xu et al., 2022). This method is widely used in the finite element models of the intervertebral disc and facet cartilage. However, it is not suitable for screw-fixed bony structure models. Specifically, as mentioned above, bone compaction is a common phenomenon at the bone-screw interface, which can trigger an increase in bone density and elastic modulus in the compact region. Similarly, bone compaction existed not only during screw insertion but also during the toggle test process. This loading process leads to an increase in bone density around the screw, which in turn leads to an increase in screw restriction by bony structures. However, this dynamic process cannot be accurately simulated in current numerical models, which leads to the computed value of screw displacement always being larger than the tested one (this phenomenon can be observed in the current and similar studies, such as Hsu et al., 2005; Chao et al., 2008). Therefore, the above model validation method is not suitable for screw-fixed models. As an alternative, in screw anchoring ability studies where numerical simulation and mechanical tests are performed simultaneously, researchers compare the tendency of the tested and computed results, and if the trend is consistent, the numerical model is considered credible. Admittedly, this is a qualitative, rather than quantitative, approach to model validation, and screw compaction in the toggle test numerical model will be simulated in our future studies.

The neglect of cortical cells in the posterior column is an existing limitation of this study. Specifically, bony structures with irregular outlines (e.g., hypertrophied articular processes) inhibit pedicle screw insertion (Paik et al., 2012; Pelletier et al., 2017). To achieve complete screw insertion, these structures should be resected. Although cancellous bone plays a prominent role in pedicle screw anchorage, studies have also shown that this procedure damages the cortical shell of the insertion screw point and adversely affects screw anchoring ability (Paik et al., 2012; Pelletier et al., 2017; Solitro et al., 2019). The interaction between cortical damage/preservation and complete/incomplete screw insertion should be validated in future studies.

Moreover, the lack of clinical evidence was due to the difficulty in accurately quantifying incomplete thread insertion during intraoperative observation and immediate postoperative imaging examination (due to the surgical field of view and titanium artifacts). Therefore, elucidating this topic through comprehensive biomechanical research has become the only feasible method.

Additionally, several factors, including changes in connecting rod materials (Athanasakopoulos et al., 2013; Boriani et al., 2020; Massey et al., 2021), screw diameters (Chao et al., 2008; Solitro et al., 2019), screw insertion orientations (Amirouche et al., 2016; Matsukawa et al., 2017; Szczodry et al., 2018), and even different screw designs (Chao et al., 2008), have been reported to affect screw anchoring ability, and interactions between these factors and incomplete thread insertion on screw anchoring ability should also be verified in our future studies. However, because all of the above parameters (i.e., rod materials, screw diameters, and orientations) were selected in this study of the most commonly used parameters in our clinical practice (the titanium alloy connecting rod was the most commonly used material, the screw axis was parallel to the fixed vertebral body, and the outer diameter was set at 6.5mm, the most commonly used diameter of a lumbar pedicle screw), we believe that these limitations will not negatively affect the credibility of the current study.

Finally, the significance of postoperative physiological and pathological processes on screw anchoring ability (Galbusera et al., 2015; Ding et al., 2017; Volz et al., 2022), including the potential osteogenic activity of different types of screw coatings (Patel et al., 2014; Li et al., 2015; Kashii et al., 2020), cannot be determined by numerical simulations and mechanical tests on polyurethane models. However, although these limitations exist, given that the mechanical tests and numerical simulations present consistent results, complete insertion of pedicle screws, especially complete thread insertion, is recommended in patients with pedicle screw fixation to optimize screw anchoring ability.

Conclusion

Incomplete thread insertion triggers local stress concentration and higher risk of screw loosening.

Data availability statement

The original contributions presented in the study are included in the article/Supplementary Material, further inquiries can be directed to the corresponding authors.

Author contributions

J-XY: Conceptualization, Data curation, Formal Analysis, Investigation, Methodology, Project administration, Writing–original draft. LL: Conceptualization, Data curation, Formal Analysis, Investigation, Writing–original draft. J-HL: Formal Analysis, Investigation, Methodology, Supervision, Validation, Writing–original draft. NW: Formal Analysis, Investigation, Visualization, Writing–original draft. ZX: Conceptualization, Funding acquisition, Investigation, Methodology, Project administration, Validation, Writing–review and editing. J-CL: Conceptualization, Formal Analysis, Investigation, Methodology, Supervision, Writing–review and editing.

Funding

The author(s) declare financial support was received for the research, authorship, and/or publication of this article. This study was supported by Project of National Clinical Research Base of Traditional Chinese Medicine in Jiangsu Province, China (JD2022SZXMS07), Scientific Research Project of Jiangsu Provincial Health Commission (M2022095), the Seventh Batch of National Chinese Medicine.

Acknowledgments

We acknowledge Mr. Xiao-Yu Zhang for his guidance in the preparation of the figures.

Conflict of interest

The authors declare that the research was conducted in the absence of any commercial or financial relationships that could be construed as a potential conflict of interest.

Publisher's note

References

Adams, M. A., Freeman, B. J., Morrison, H. P., Nelson, I. W., and Dolan, P. (2000). Mechanical initiation of intervertebral disc degeneration. *Spine (Phila Pa 1976)* 25 (13), 1625–1636. doi:10.1097/00007632-200007010-00005

Adams, M. A., and Roughley, P. J. (2006). What is intervertebral disc degeneration, and what causes it? *Spine (Phila Pa 1976)* 31 (18), 2151–2161. doi:10.1097/01.brs.0000231761.73859.2c

Amaritsakul, Y., Chao, C. K., and Lin, J. (2014). Biomechanical evaluation of bending strength of spinal pedicle screws, including cylindrical, conical, dual core and double dual core designs using numerical simulations and mechanical tests. *Med. Eng. Phys.* 36 (9), 1218–1223. doi:10.1016/j.medengphy.2014.06.014

Ambati, D. V., Wright, E. K., Jr., Lehman, R. A., Jr., Kang, D. G., Wagner, S. C., and Dmitriev, A. E. (2015). Bilateral pedicle screw fixation provides superior biomechanical stability in transforaminal lumbar interbody fusion: a finite element study. *Spine J.* 15 (8), 1812–1822. doi:10.1016/j.spinee.2014.06.015

Amirouche, F., Solitro, G. F., and Magnan, B. P. (2016). Stability and spine pedicle screws fixation strength-A comparative study of bone density and insertion angle. *Spine Deform.* 4 (4), 261–267. doi:10.1016/j.jspd.2015.12.008

Athanasakopoulos, M., Mavrogenis, A. F., Triantafyllopoulos, G., Koufos, S., and Pneumaticos, S. G. (2013). Posterior spinal fusion using pedicle screws. *Orthopedics* 36 (7), e951–e957. doi:10.3928/01477447-20130624-28

Bianco, R. J., Arnoux, P. J., Wagnac, E., Mac-Thiong, J. M., and Aubin, C. (2017). Minimizing pedicle screw pullout risks: a detailed biomechanical analysis of screw design and placement. *Clin. Spine Surg.* 30 (3), E226–e232. doi:10.1097/bsd.0000000000000151

Boriani, S., Pipola, V., Cecchinato, R., Ghermandi, R., Tedesco, G., Fiore, M. R., et al. (2020). Composite PEEK/carbon fiber rods in the treatment for bone tumors of the cervical spine: a case series. *Eur. Spine J.* 29 (12), 3229–3236. doi:10.1007/s00586-020-06534-0

Boriani, S., Tedesco, G., Ming, L., Ghermandi, R., Amichetti, M., Fossati, P., et al. (2018). Carbon-fiber-reinforced PEEK fixation system in the treatment of spine tumors: a preliminary report. *Eur. Spine J.* 27 (4), 874–881. doi:10.1007/s00586-017-5258-5

Brasiliense, L. B., Lazaro, B. C., Reyes, P. M., Newcomb, A. G., Turner, J. L., Crandall, D. G., et al. (2013). Characteristics of immediate and fatigue strength of a dual-threaded pedicle screw in cadaveric spines. *Spine J.* 13 (8), 947–956. doi:10.1016/j.spinee.2013.03.010

Bredow, J., Boese, C. K., Werner, C. M., Siewe, J., Löhrer, L., Zarghooni, K., et al. (2016). Predictive validity of preoperative CT scans and the risk of pedicle screw loosening in spinal surgery. *Arch. Orthop. Trauma Surg.* 136 (8), 1063–1067. doi:10.1007/s00402-016-2487-8

Burger, T. (2023). Controlling for false discoveries subsequently to large scale one-way ANOVA testing in proteomics: practical considerations. *Proteomics* 23 (18), e2200406. doi:10.1002/pmic.202200406

Chao, C. K., Hsu, C. C., Wang, J. L., and Lin, J. (2008). Increasing bending strength and pullout strength in conical pedicle screws: biomechanical tests and finite element analyses. *J. Spinal Disord. Tech.* 21 (2), 130–138. doi:10.1097/bsd.0b013e318073cc4b

Chatzi, A., and Doody, O. (2023). The one-way ANOVA test explained. *Nurse Res.* 31 (3), 8–14. doi:10.7748/nr.2023.e1885

Chen, C. S., Chen, W. J., Cheng, C. K., Jao, S. H., Chueh, S. C., and Wang, C. C. (2005). Failure analysis of broken pedicle screws on spinal instrumentation. *Med. Eng. Phys.* 27 (6), 487–496. doi:10.1016/j.medengphy.2004.12.007

Chen, L. H., Tai, C. L., Lee, D. M., Lai, P. L., Lee, Y. C., Niu, C. C., et al. (2011). Pullout strength of pedicle screws with cement augmentation in severe osteoporosis: a comparative study between cannulated screws with cement injection and solid screws with cement pre-filling. *BMC Musculoskelet. Disord.* 12, 33. doi:10.1186/1471-2474-12-33

Chen, S. I., Lin, R. M., and Chang, C. H. (2003). Biomechanical investigation of pedicle screw-vertebrae complex: a finite element approach using bonded and contact interface conditions. *Med. Eng. Phys.* 25 (4), 275–282. doi:10.1016/s1350-4533(02)00219-9

Cho, W., Wu, C., Erkan, S., Kang, M. M., Mehbod, A. A., and Transfeldt, E. E. (2011). The effect on the pullout strength by the timing of pedicle screw insertion after calcium phosphate cement injection. *J. Spinal Disord. Tech.* 24 (2), 116–120. doi:10.1097/bsd.0b013e3181dd7961

Ding, Q., Chen, J., Fan, J., Li, Q., Yin, G., and Yu, L. (2017). Effect of zoledronic acid on lumbar spinal fusion in osteoporotic patients. *Eur. Spine J.* 26 (11), 2969–2977. doi:10.1007/s00586-017-5286-1

Galbusera, F., Volkheimer, D., Reitmaier, S., Berger-Roscher, N., Kienle, A., and Wilke, H. J. (2015). Pedicle screw loosening: a clinically relevant complication? *Eur. Spine J.* 24 (5), 1005–1016. doi:10.1007/s00586-015-3768-6

Hsu, C. C., Chao, C. K., Wang, J. L., Hou, S. M., Tsai, Y. T., and Lin, J. (2005). Increase of pullout strength of spinal pedicle screws with conical core: biomechanical tests and finite element analyses. *J. Orthop. Res.* 23 (4), 788–794. doi:10.1016/j.orthres.2004.11.002

Kanno, H., Aizawa, T., Hashimoto, K., and Itoi, E. (2019). Enhancing percutaneous pedicle screw fixation with hydroxyapatite granules: a biomechanical study using an osteoporotic bone model. *PLoS One* 14 (9), e0223106. doi:10.1371/journal.pone.0223106

Kanno, H., Aizawa, T., Hashimoto, K., and Itoi, E. (2021). Novel augmentation technique of percutaneous pedicle screw fixation using hydroxyapatite granules in the osteoporotic lumbar spine: a cadaveric biomechanical analysis. *Eur. Spine J.* 30 (1), 71–78. doi:10.1007/s00586-020-06451-2

Karami, K. J., Buckenmeyer, L. E., Kiapour, A. M., Kelkar, P. S., Goel, V. K., Demetropoulos, C. K., et al. (2015). Biomechanical evaluation of the pedicle screw insertion depth effect on screw stability under cyclic loading and subsequent pullout. *J. Spinal Disord. Tech.* 28 (3), E133–E139. doi:10.1097/bsd.0000000000000178

Kashii, M., Kitaguchi, K., Makino, T., and Kaito, T. (2020). Comparison in the same intervertebral space between titanium-coated and uncoated PEEK cages in lumbar interbody fusion surgery. *J. Orthop. Sci.* 25 (4), 565–570. doi:10.1016/j.jos.2019.07.004

Krenn, M. H., Piotrowski, W. P., Penzkofer, R., and Augat, P. (2008). Influence of thread design on pedicle screw fixation. Laboratory investigation. *J. Neurosurg. Spine* 9 (1), 90–95. doi:10.3171/spi/2008/9/7/090

Li, J., Xie, Y., Sun, S., Xue, C., Xu, W., Xu, C., et al. (2023). Regional differences in bone mineral density biomechanically induce a higher risk of adjacent vertebral fracture after percutaneous vertebroplasty: a case-comparative study. *Int. J. Surg.* 109, 352–363. doi:10.1097/js9.0000000000000273

Li, J., Xu, C., Zhang, X., Xi, Z., Sun, S., Zhang, K., et al. (2021). Disc measurement and nucleus calibration in a smoothened lumbar model increases the accuracy and efficiency of in-silico study. *J. Orthop. Surg. Res.* 16 (1), 498. doi:10.1186/s13018-021-02655-4

Li, J., Zhang, Z., Xie, T., Song, Z., Song, Y., and Zeng, J. (2022a). The preoperative Hounsfield unit value at the position of the future screw insertion is a better predictor of screw loosening than other methods. *Eur. Radiol.* 33, 1526–1536. doi:10.1007/s00330-022-09157-9

Li, J. C., Xie, T. H., Zhang, Z., Song, Z. T., Song, Y. M., and Zeng, J. C. (2022b). The mismatch between bony endplates and grafted bone increases screw loosening risk for OLIF patients with ALSR fixation biomechanically. *Front. Bioeng. Biotechnol.* 10, 862951. doi:10.3389/fbioe.2022.862951

Li, J. C., Yang, Z. Q., Xie, T. H., Song, Z. T., Song, Y. M., and Zeng, J. C. (2022c). Deterioration of the fixation segment's stress distribution and the strength reduction of screw holding position together cause screw loosening in ALSR fixed OLIF patients with poor BMD. *Front. Bioeng. Biotechnol.* 10, 922848. doi:10.3389/fbioe.2022.922848

Li, Y., Yang, W., Li, X., Zhang, X., Wang, C., Meng, X., et al. (2015). Improving osteointegration and osteogenesis of three-dimensional porous Ti6Al4V scaffolds by polydopamine-assisted biomimetic hydroxyapatite coating. *ACS Appl. Mater Interfaces* 7 (10), 5715–5724. doi:10.1021/acsami.5b00331

Marie-Hardy, L., Pascal-Moussellard, H., Barnaba, A., Bonaccorsi, R., and Scemama, C. (2020). Screw loosening in posterior spine fusion: prevalence and risk factors. *Glob. Spine J.* 10 (5), 598–602. doi:10.1177/2192568219864341

Massey, P. A., Hoge, S., Nelson, B. G., Ogden, A. L., Mody, M. G., Myers, M., et al. (2021). Nitinol memory rods versus titanium rods: a biomechanical comparison of posterior spinal instrumentation in a synthetic corpectomy model. *Glob. Spine J.* 11 (3), 277–282. doi:10.1177/2192568220902401

Matsukawa, K., Yato, Y., Hynes, R. A., Imabayashi, H., Hosogane, N., Asazuma, T., et al. (2017). Cortical bone trajectory for thoracic pedicle screws: a technical note. *Clin. Spine Surg.* 30 (5), E497–e504. doi:10.1097/bsd.0000000000000130

Mohammed, A., Francesco, T., Arzu, O. T., Moataz, E., and Shihab, A. J. I. J. O. I. E. (2018). *The effects of different carrying methods on locomotion stability, gait spatio-temporal parameters and spinal stresses.* 68, 81–88.

Nakashima, D., Ishii, K., Matsumoto, M., Nakamura, M., and Nagura, T. (2018). A study on the use of the Osstell apparatus to evaluate pedicle screw stability: an in-vitro study using micro-CT. *PLoS One* 13 (6), e0199362. doi:10.1371/journal.pone.0199362

Ottardi, C., Galbusera, F., Luca, A., Prosdocimo, L., Sasso, M., Brayda-Bruno, M., et al. (2016). Finite element analysis of the lumbar destabilization following pedicle subtraction osteotomy. *Med. Eng. Phys.* 38 (5), 506–509. doi:10.1016/j.medengphy.2016.02.002

Paik, H., Dmitriev, A. E., Lehman, R. A., Jr., Gaume, R. E., Ambati, D. V., Kang, D. G., et al. (2012). The biomechanical effect of pedicle screw hubbing on pullout resistance in the thoracic spine. *Spine J.* 12 (5), 417–424. doi:10.1016/j.spinee.2012.03.020

Patel, S. B., Hamlekhan, A., Royhman, D., Butt, A., Yuan, J., Shokuhfar, T., et al. (2014). Enhancing surface characteristics of Ti-6Al-4V for bio-implants using integrated anodization and thermal oxidation. *J. Mater Chem. B* 2 (23), 3597–3608. doi:10.1039/c3tb21731k

Pelletier, M. H., Bertollo, N., Al-Khawaja, D., and Walsh, W. R. (2017). The contribution of the cortical shell to pedicle screw fixation. *J. Spine Surg.* 3 (2), 184–192. doi:10.21037/jss.2017.06.07

Prasad, V., Mesfin, A., Lee, R., Reigrut, J., and Schmidt, J. (2016). Probing and tapping: are we inserting pedicle screws correctly? *Spine Deform.* 4 (6), 395–399. doi:10.1016/j.jspd.2016.06.001

Seng, W. R. D., Chou, S. M., Siddiqui, S. S., and Oh, J. Y. L. (2019). Pedicle screw designs in spinal surgery: is there a difference? A biomechanical study on primary and revision pull-out strength. *Spine (Phila Pa 1976)* 44 (3), E144–e149. doi:10.1097/brs.0000000000002789

Shi, L., Wang, L., Guo, Z., Wu, Z. X., Liu, D., Gao, M. X., et al. (2012). A study of low elastic modulus expandable pedicle screws in osteoporotic sheep. *J. Spinal Disord. Tech.* 25 (2), 123–128. doi:10.1097/bsd.0b013e31820ef9f7

Solitro, G. F., Welborn, M. C., Mehta, A. I., and Amirouche, F. (2022). How to optimize pedicle screw parameters for the thoracic spine? A biomechanical and finite element method study. *Glob. Spine J.* 14, 187–194. doi:10.1177/21925682221099470

Solitro, G. F., Whitlock, K., Amirouche, F., Mehta, A. I., and Mcdonnell, A. (2019). Currently adopted criteria for pedicle screw diameter selection. *Int. J. Spine Surg.* 13 (2), 132–145. doi:10.14444/6018

Szczodry, M., Solitro, G. F., Amirouche, F., and Patel, P. (2018). Pedicle screw with increased cortical purchase can Be inserted with same accuracy as the screw in straightforward trajectory using 3D modeling landmarks. *Spine Deform.* 6 (1), 20–27. doi:10.1016/j.jspd.2017.06.004

Takenaka, S., Kaito, T., Ishii, K., Watanabe, K., Watanabe, K., Shinohara, A., et al. (2020). Influence of novel design alteration of pedicle screw on pull-out strength: a finite element study. *J. Orthop. Sci.* 25 (1), 66–72. doi:10.1016/j.jos.2019.03.002

Travascio, F., Asfour, S., Serpieri, R., Rosati, L. J. M., and Solids, M. O. (2017). Analysis of the consolidation problem of compressible porous media by a macroscopic variational continuum approach. *Math. Mech. Solids* 22, 952–968. doi:10.1177/1081286515616049

Volz, M., Wyse-Sookoo, K. R., Travascio, F., Huang, C. Y., and Best, T. M. (2022). Mechanobiological approaches for stimulating chondrogenesis of stem cells. *Stem Cells Dev.* 31 (15-16), 460–487. doi:10.1089/scd.2022.0049

Wang, W., Pei, B., Pei, Y., Shi, Z., Kong, C., Wu, X., et al. (2019a). Biomechanical effects of posterior pedicle fixation techniques on the adjacent segment for the treatment of thoracolumbar burst fractures: a biomechanical analysis. *Comput. Methods Biomech. Biomed. Engin* 22 (13), 1083–1092. doi:10.1080/10255842.2019.1631286

Wang, W. T., Guo, C. H., Duan, K., Ma, M. J., Jiang, Y., Liu, T. J., et al. (2019b). Dual pitch titanium-coated pedicle screws improve initial and early fixation in a polyetheretherketone rod semi-rigid fixation system in sheep. *Chin. Med. J. Engl.* 132 (21), 2594–2600. doi:10.1097/cm9.0000000000000335

Weidling, M., Oefner, C., Schoenfelder, S., and Heyde, C. E. (2020). A novel parameter for the prediction of pedicle screw fixation in cancellous bone - a biomechanical study on synthetic foam. *Med. Eng. Phys.* 79, 44–51. doi:10.1016/j.medengphy.2020.03.001

Wiendieck, K., Müller, H., Buchfelder, M., and Sommer, B. (2018). Mechanical stability of a novel screw design after repeated insertion: can the double-thread screw serve as a back up? *J. Neurosurg. Sci.* 62 (3), 271–278. doi:10.23736/s0390-5616.16.03337-3

Wu, X., Shi, J., Wu, J., Cheng, Y., Peng, K., Chen, J., et al. (2019). Pedicle screw loosening: the value of radiological imagings and the identification of risk factors assessed by extraction torque during screw removal surgery. *J. Orthop. Surg. Res.* 14 (1), 6. doi:10.1186/s13018-018-1046-0

Xi, Z., Xie, Y., Chen, S., Sun, S., Zhang, X., Yang, J., et al. (2023). The cranial vertebral body suffers a higher risk of adjacent vertebral fracture due to the poor biomechanical environment in patients with percutaneous vertebralplasty. *Spine J.* 23, 1764–1777. doi:10.1016/j.spinee.2023.08.003

Xu, C., Xi, Z., Fang, Z., Zhang, X., Wang, N., Li, J., et al. (2022). Annulus calibration increases the computational accuracy of the lumbar finite element model. *Glob. Spine J.* 13, 2310–2318. 21925682221081224. doi:10.1177/21925682221081224

Xu, F., Zou, D., Li, W., Sun, Z., Jiang, S., Zhou, S., et al. (2020). Hounsfield units of the vertebral body and pedicle as predictors of pedicle screw loosening after degenerative lumbar spine surgery. *Neurosurg. Focus* 49 (2), E10. doi:10.3171/2020.5.focus20249

Xu, M., Yang, J., Lieberman, I. H., and Haddas, R. (2019). Finite element method-based study of pedicle screw-bone connection in pullout test and physiological spinal loads. *Med. Eng. Phys.* 67, 11–21. doi:10.1016/j.medengphy.2019.03.004

Yuan, Q., Han, X., Han, X., He, D., Liu, B., and Tian, W. (2014). Krag versus Caudad trajectory technique for pedicle screw insertion in osteoporotic vertebrae: biomechanical comparison and analysis. *Spine (Phila Pa 1976)* 39 (26), B27–B35. doi:10.1097/brs.0000000000000431

Zhang, Q. H., Tan, S. H., and Chou, S. M. (2006). Effects of bone materials on the screw pull-out strength in human spine. *Med. Eng. Phys.* 28 (8), 795–801. doi:10.1016/j.medengphy.2005.11.009

Zhang, W., Zhao, J., Li, L., Yu, C., Zhao, Y., and Si, H. (2020). Modelling tri-cortical pedicle screw fixation in thoracic vertebrae under osteoporotic condition: a finite element analysis based on computed tomography. *Comput. Methods Programs Biomed.* 187, 105035. doi:10.1016/j.cmpb.2019.105035

Zou, D., Sun, Z., Zhou, S., Zhong, W., and Li, W. (2020). Hounsfield units value is a better predictor of pedicle screw loosening than the T-score of DXA in patients with lumbar degenerative diseases. *Eur. Spine J.* 29 (5), 1105–1111. doi:10.1007/s00586-020-06386-8

Frontiers in
Bioengineering and Biotechnology

Accelerates the development of therapies, devices, and technologies to improve our lives

A multidisciplinary journal that accelerates the development of biological therapies, devices, processes and technologies to improve our lives by bridging the gap between discoveries and their application.

Discover the latest Research Topics

See more →

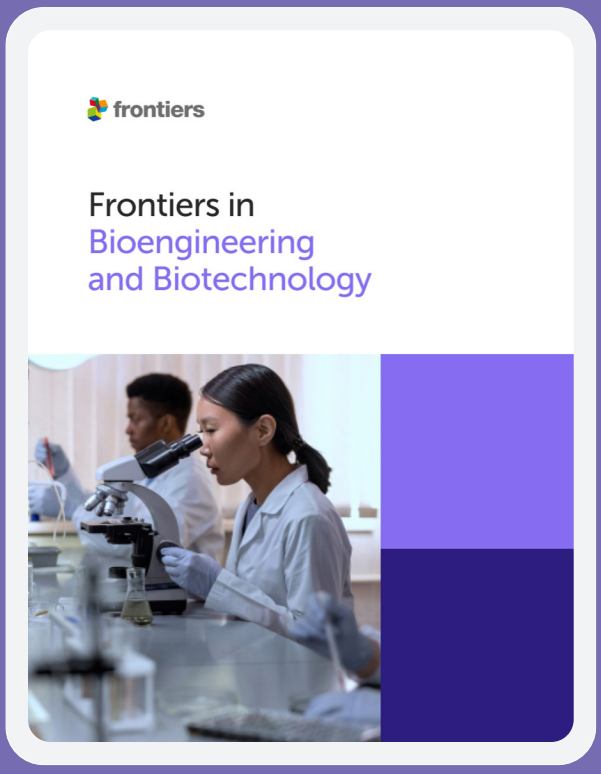

Frontiers

Avenue du Tribunal-Fédéral 34
1005 Lausanne, Switzerland
frontiersin.org

Contact us

+41 (0)21 510 17 00
frontiersin.org/about/contact